

Physicochemical Problems of Mineral Processing

Index No. 32213X



ISSN 1643-1049

Volume 48, Issue 1

2012

Physicochemical Problems of Mineral Processing 48(1), 2012

Instructions for preparation of manuscripts

It is recommended that the following guidelines be followed by the authors of the manuscripts

- Original papers dealing with the principles of mineral processing and papers on technological aspects of mineral processing will be published in the journal which appears twice a year
- The manuscript can be sent to the Editors for reviewing any time of year
- The manuscript should be written in English. For publishing in other languages an approval of the editor is necessary
- Contributors whose first language is not the language of the manuscript are urged to have their manuscript competently edited prior to submission
- The manuscript should not exceed 12 pages
- There is a 100 EUR fee for printing the paper. No fee is required for the authors participating in the Annual Symposium on Physicochemical Problems on Mineral Processing
- Manuscripts and all correspondence regarding the symposium and journal should be sent to the editor.

Submission of papers is tantamount to a transfer of copyrights by the author(s) to Oficyna Wydawnicza PWr Publisher covering publication in printed as well as electronic media (CD-ROM or Internet) of the articles and any modifications of it.

Address of the Editorial Office

Wroclaw University of Technology
Wybrzeze Wyspianskiego 27, 50-370 Wroclaw, Poland
Institute of Mining Engineering
Laboratory of Mineral Processing

Location of the Editorial Office:

pl. Teatralny 2, 50-051 Wroclaw, Poland
phone: (+48 71) 320 68 79, (+48 71) 320 68 78
fax: (+48 71) 344 81 23

jan.drzymala@pwr.wroc.pl
zygmunt.sadowski@pwr.wroc.pl
andrzej.luszczkiewicz@pwr.wroc.pl
pawel.nowak <ncnowak@cyf-kr.edu.pl>

www.minproc.pwr.wroc.pl/journal

Physicochemical Problems of Mineral Processing

**Volume 48, Issue 1
2012**

www.minproc.pwr.wroc.pl/journal



Oficyna Wydawnicza Politechniki Wrocławskiej
Wrocław 2012

Editors

Jan Drzymala editor-in-chief
Zygmunt Sadowski
Andrzej Łuszczkiewicz
Paweł Nowak

Editorial Board

Ashraf Amer, Wiesław Blaschke, Marian Brożek, Stanisław Chibowski, Tomasz Chmielewski, Beata Cwalina, Janusz Girczys, Andrzej Heim, Jan Hupka, Teofil Jesionowski, Andrzej Konieczny, Janusz Laskowski, Kazimierz Małyśa, Andrzej Pomianowski (honorary chairman), Stanisława Sanak-Rydlewska, Jerzy Sablik, Kazimierz Sztaba (chairman), Barbara Tora, Tadeusz Tumidajski

Production Editor

Przemysław B. Kowalczyk

The papers published in the Physicochemical Problems of Mineral Processing journal are abstracted in BazTech, Chemical Abstracts, Coal Abstracts, EBSCO, Google Scholar, Scopus, Thomson Reuters (Science Citation Index Expanded, Materials Science Citation Index, Journal Citation Reports) and other sources

This publication was supported in different forms by

Komitet Górnictwa PAN (Sekcja Wykorzystania Surowców Mineralnych)
Akademia Górniczo-Hutnicza w Krakowie
Politechnika Śląska w Gliwicach
Politechnika Wroclawska

©Copyright by Oficyna Wydawnicza Politechniki Wroclawskiej, Wrocław 2012

ISSN 1643-1049 (print)

previously 0137-1282

OFICyna WYDAWNICZA POLITECHNIKI WROCLAWSKIEJ
Wybrzeże Wyspiańskiego 27, 50-370 Wrocław, Poland

CONTENTS

| | |
|--|-----|
| J.M. Sokolovic, R.D. Stanojlovic, Z.S. Markovic, <i>Activation of oxidized surface of anthracite waste coal by attrition</i> | 5 |
| P. Nowak, R.P. Socha, T. Cieslik, <i>Influence of adsorption on the charge transfer reactions at the pyrite surface. Preliminary study</i> | 19 |
| R.A. Kleiv, <i>Pre-sorting of asymmetric feeds using collective particle ejection</i> | 29 |
| G. Bulut, A. Ceylan, B. Soyulu, F. Goktepe, <i>Role of starch and metabisulphite on pure pyrite and pyritic copper ore flotation</i> | 39 |
| M. Krzan, K. Malysa, <i>Influence of electrolyte presence on bubble motion in solutions of sodium n-alkylsulfates (C8, C10, C12)</i> | 49 |
| A. Laurentowska, T. Jesionowski, <i>ZnO-SiO₂ oxide composites synthesis during precipitation from emulsion system</i> | 63 |
| M. Kotyczka-Moranska, G. Tomaszewicz, G. Labojko, <i>Comparison of different methods for enhancing CO₂ capture by CaO-based sorbents. Review</i> | 77 |
| M. Ulewicz, E. Radzyminska-Lenarcik, <i>Application of supported and polymer membrane with 1 decyl-2-methylimidazole for separation of transition metal ions</i> | 91 |
| A. Przybylska, K. Siwinska-Stefanska, F. Ciesielczyk, T. Jesionowski, <i>Adsorption of C.I. Basic Blue 9 onto TiO₂-SiO₂ inorganic support</i> | 103 |
| T. Gluba, A. Obraniak, <i>Nucleation and granule formation during disc granulation process</i> | 113 |
| A. Obraniak, T. Gluba, <i>Model of energy consumption in the range of nucleation and granule growth in drum granulation of bentonite</i> | 121 |
| M. Joskowska, I. Kopczyńska, B. Debski, D. Holownia-Kedzia, R. Aranowski, J. Hupka, <i>Wetting of supports by ionic liquids used in gas separation processes</i> | 129 |
| A. Slaczka, A. Wasilczyk, <i>The effect of chemicals on the rheology of highly loaded coal water slurries (CWS)</i> . T.P. Olejnik, <i>Grinding kinetics of granite considering morphology and physical properties of grains</i> | 141 |
| A. Cybula, M. Klein, A. Zielińska-Jurek, M. Janczarek, A. Zaleska, <i>Carbon dioxide photoconversion. The effect of titanium dioxide immobilization conditions and photocatalyst type</i> | 149 |
| T. Suponik, <i>Removing contaminants from groundwater polluted by the Trzebieńka Mine settling pond located in Upper Silesia (Poland)</i> | 159 |
| K. Szwarz, K. Siwinska-Stefanska, B. Marciniak, T. Jesionowski, <i>Synthesis and characterisation of SiO₂/POSS hybrid systems obtained using the mechanical method</i> | 169 |
| M. Lezner, E. Grabowska, A. Zaleska, <i>Preparation and photocatalytic activity of iron-modified titanium dioxide photocatalyst</i> | 181 |
| J. Reszczynska, A. Iwulska, G. Sliwinski, A.Zaleska, <i>Characterization and photocatalytic activity of rare earth metal-doped titanium dioxide</i> | 193 |
| M. Nowacka, T. Jesionowski, <i>Effect of surface modification as well as type and ionic strength of electrolyte on electrokinetic properties of TiO₂ and TiO₂-SiO₂</i> | 201 |
| D. Saramak, <i>De-agglomeration in high pressure grinding roll based crushing circuits</i> | 209 |
| T. Szymura, <i>Composition reconstitution of concrete and mortars based on portland and expansive cements</i> | 219 |
| B. Pospiech, <i>Studies on platinum recovery from solutions after leaching of spent catalysts by solvent extraction</i> | 227 |
| K. Lawinska, P. Wodzinski, <i>Determination of the effective sieve blocking coefficient</i> | 239 |
| T. Depci, A.R. Kul, Y. Onal, E. Disli, S. Alkan, Z.F. Turkmenglu, <i>Adsorption of crystal violet from aqueous solution on activated carbon derived from Gölbaşı lignite</i> | 247 |
| A.A. Seifelnasr, T. Tammam, A-Z.M. Abouzeid, <i>Gravity concentration of sudanese chromite ore using laboratory shaking table</i> | 253 |
| A. Bastrzyk, I. Polowczyk, E. Szlag, Z. Sadowski, <i>Adsorption and co-adsorption of PEO-PPO-PEO block copolymers and surfactants and their influence on zeta potential of magnesite and dolomite</i> | 271 |
| A. Korkosz, A. Ptaszynska, A. Hanel, M. Niewiadomski, J. Hupka, <i>Cullet as filter medium for swimming pool water treatment</i> | 281 |
| T. Depci, T. Efe, M. Tapan, A. Ozvan, M. Aclan, T. Uner, <i>Chemical characterization of Patnos scoria (Ağrı, Turkey) and its usability for production of blended cement</i> | 295 |
| S. Chibowski, M. Paszkiewicz, J. Patkowski, <i>Adsorption of polyacrylic acid on the surface of TiO₂ in the presence of different surfactants</i> | 303 |
| | 317 |

Received May 15, 2011; reviewed; accepted May 26, 2011

ACTIVATION OF OXIDIZED SURFACE OF ANTHRACITE WASTE COAL BY ATTRITION

Jovica M. SOKOLOVIC, Rodoljub D. STANOJLOVIC, Zoran S. MARKOVIC

University of Belgrade, Technical Faculty Bor, Department of Mining, Vojske Jugoslavije 12, 19210, Bor, Serbia, Tel.: +381 30 424 555; Fax: +381 30 421 078, jsokolovic@tf.bor.ac.rs

Abstract. In this paper the activation of oxidized surface of anthracite waste coal was investigated. Coal weathering leads to physical and chemical changes on the coal surfaces and a reduction of its hydrophobicity and floatability. The changes and the presence of oxygen functional groups in the structure and surfaces coal was confirmed by the FTIR study on the raw and waste coal. The groups have remarkable impacts on surface charge and thus flotation kinetics. The floatability of oxidized coal may be improved by the creation of fresh, unoxidized surfaces on coal by attrition at high solid concentration prior to introducing coal to the froth flotation process. This paper presents the results of the effects of attrition on the floatability of the oxidized surface of waste coal, coal pyrite and alumino-silicate minerals through electrokinetics and microflotation experiments. The results show that the attrition, in the viscous pulp with the solid content of 50%, lead to the mechanical cleaning of oxidized surface and activation of the surface of coal particles, which agrees with the change of zeta potential and increasing floatability of coal by 10%. Obviously that the mechanical scrubbing may be able to restore the natural floatability of superficially oxidized coal by removing the thin oxidation layer from the coal surface. The results show that attrition time is an important parameter from the point of view of activating the oxidized coal surface, and positive changes in zeta potential and floatability. The change of zeta potential, as a measure surface charge state of coal particles, from -15 mV to about 0 mV, after attrition for 30 minutes, confirms positive application of attrition. Zeta potential approaching 0 mV resulted in increasing floatability down to the real possibilities of the attrition process prior the coal flotation.

keywords: waste coal, oxidation, FTIR, attrition, zeta potential, floatability

1. Introduction

A large amount of waste coal is created annually in the anthracite Vrska Cuka coal mine, Avramica, Serbia. It is becoming necessary to beneficiate the large quantity of discarded coal fines. Apart from adding value to a waste product, there is also an environmental issue (the fines are generally dumped into large ponds). Such waste

coal shows reduced natural floatability and it is not suitable for the application in a flotation process.

It is known that coal weathering, which occurs when coal is exposed to the atmosphere in natural conditions, is a very complex physico-chemical process (Iglesias et al., 1998). The atmospheric oxidation of coal by weathering or by storage starts with the physical adsorption of oxygen on the surface to form various oxygen functional groups such as hydroxyl (phenolic –OH), carbonyl (C=O) and carboxyl (–COOH) groups and soluble inorganic species on the coal surface (Somasundaran et al., 2000; Jia et al., 2000). The presence of these functional groups in coal structure strongly affects coal surface properties and reduces the hydrophobicity of the coal surface, as a result, its floatability (Sun, 1954; Swann et al., 1972; Wen and Sun, 1981; Fuerstenau et al., 1983, 1992; Philips et al., 1987; Laskowski, 1995), because the surface functional groups are hydrophilic (Beafore et al., 1984). According to Fuerstenau et al. (1983), coal surface properties are determined by the surface functional groups (especially the phenolic and carboxylic oxygen groups) more than by total oxygen content. Other studies have shown that coal oxidation increased oxygen functional groups such as carboxyl (COOH), carbonyl (C=O), and phenol, altering the surface hydrophobicity through the hydrophobic and hydrophilic balance (Fuerstenau et al., 1983; Miller et al., 1983).

Recently, many researchers determined these functional groups on the coal surface by various analytical techniques. FTIR methods can be a powerful tool for studying the surface components of coal and their changes during oxidation (Calemma et al., 1988; Kister et al., 1988; Xiao et al., 1990; Iglesias et al., 1998; Pietrzak and Wachowska, 2003; Saikia et al., 2007). Also, a number of indirect techniques are used to measure the degree of oxidation of coal surface by determining the wettability and floatability of the coal. The zeta potential measurement of coal can provide useful mechanism information of the surface changes. The zeta potential of oxidized coal is generally found to be lower than that of un-oxidized coal (Fuerstenau et al., 1987; Sadowski et al., 1988) and the isoelectric point usually shift toward the acid pH range (Sokolovic et al., 2006). Obviously, the zeta potential of coal is a function of active oxygen groups. An increase in the hydroxyl and carboxylic functional groups on the coal surface increases the negative zeta potential (Woodburn et al., 1983).

Yarar and Leja (1981) established a correlation between the zeta potential of weathered coal and its flotation response. It was found that naturally weathered coal flotation follows a pattern parallel to zeta potential. These studies were directed towards establishing the relationships between the degree of oxidation and surface oxidations of coal as well as its flotation response.

The floatability of minerals can be directly correlated to their zeta potentials changes. A correlation between concentration of phenolic and carboxylic groups and the flotation behavior of several different coals has been discussed by Fuerstenau et al. (1983; 1987; 1994). The ionizable phenolic and carboxylic groups have a great effect on froth flotation since these groups affect the zeta potential of coal and modify its

wettability and floatability (Sarikaya, 1995). It was shown, using film flotation and zeta potential measurements that the maximum flotation response for coal occurs close to its isoelectric point (IEP) (Fuerstenau et al., 1983; Diao and Fuerstenau, 1991; Laskowski, 2001).

It is known that floatability oxidized coals can be improved in various ways, by adding certain agents (Horsley, 1951-1952; Gayle et al., 1965; Karsilayan et al., 1992; Bolat et al., 1998; Jia et al., 2000) or application of various physical and mechanical processes (Buttermore and Slomka, 1991; Piskin and Akguen, 1997; Ozkan and Kuyumcu, 2006).

In this study we investigated the activation of oxidized surface of anthracite waste coal using attrition. The floatability of oxidized waste coal can be improved by the creation of fresh, unoxidized surface of the coal by attrition. Mechanical scrubbing may be able to restore the natural floatability of superficially oxidized coal by removing the thin oxidation layer from the coal surface (Tao et al., 2002). Various techniques, including FTIR, electrokinetic and microflotation tests have been employed in our research works. The results of investigations of the effects of attrition on the floatability of the oxidized surface of waste coal, coal pyrite and alumino-silicate minerals are presented in the paper. The results are compared with floatability and zeta potential of raw coal.

2. Material and methods

2.1. Materials

Samples were taken from anthracite coal mine Vrska Cuka in Serbia. The first pure representative samples were collected manually from raw coal (marked as coal (C)) and second, from the waste ponds (marked as waste coal (WC), alumino-silicates (AS) and coal pyrite (CP). The collected pure sample of about 250 kg was subsampled by coning and quartering to obtain a representative sample. All samples, from 50 to 100 mm size range, were crushed and screened to obtain different size fractions. The (-38+0) μm fraction was used for proximate, ultimate analyses, micro flotation tests and electrokinetic's measurements, respectively. The characterization of coal samples provides a fundamental understanding of its oxidation state. The data that is obtained usually indicates whether or not coal is easily floated. Proximate analysis includes the analytical determination of the combustion matter content, volatile matter and ash content in the coal sample. The fixed carbon content was calculated by subtracting the ash and volatile matter content from 100%. Ultimate analysis consists of measuring of carbon, hydrogen, sulphur and, nitrogen. The oxygen content of the coal is calculated by subtracting the sum of the carbon content, hydrogen content, sulphur content and nitrogen content from 100%. The results of proximate and ultimate analyses of the raw and waste samples are given in Tables 1 to 3.

The average content of ash in raw coal is about 7.5%, calorific value in comparison with other kinds of coal is higher, allways over 33.5 MJ/kg. According to data from

Table 1, a significant increased in ash content was found in the waste coal (WC) sample as a result of the coal weathering and storage. The average ash content in waste coal sample increased and was about 17.3 %.

Table 1. Proximate analysis of coal (C) and waste coal (WC) sample

| Sample | Combustion matter (%) | Volatile matter (%) | Coke (%) | Fixed carbon (%) | Calorific value (kJ/kg) | Ash (%) | Total sulphur (%) |
|-----------------|-----------------------|---------------------|----------|------------------|-------------------------|---------|-------------------|
| Coal (C) | 92.47 | 9.21 | 90.79 | 83.26 | 33586 | 7.53 | 1.40 |
| Waste coal (WC) | 82.70 | 6.43 | 93.57 | 76.27 | 29754 | 17.30 | 1.61 |

Table 2. Proximate analysis of associated mineral matters samples

| Sample | Combustion matter (%) | Calorific value (kJ/kg) | Ash (%) |
|------------------------|-----------------------|-------------------------|---------|
| Alumino-silicates (AS) | 14.05 | - | 85.95 |
| Coal pyrite (CP) | 24.85 | 5927 | 75.15 |

Table 3. Ultimate analysis of coal and waste coal and associated mineral matters samples

| Sample | Element (wt. %) | | | |
|------------------------|-----------------|------|------|-------|
| | C | N | H | S |
| Coal (C) | 73.15 | 3.15 | 2.07 | 0.72 |
| Waste coal (WC) | 56.83 | 2.84 | 1.33 | 0.50 |
| Alumino-silicates (AS) | 9.25 | 1.27 | - | - |
| Coal pyrite (CP) | 8.06 | 0.70 | - | 31.27 |

Table 4. Chemical analysis of ash of coal and waste coal and associated mineral matters samples

| Sample | Element (wt. %) | | | | | |
|------------------------|------------------|--------------------------------|-------|------|--------------------------------|-----------------|
| | SiO ₂ | Al ₂ O ₃ | CaO | MgO | Fe ₂ O ₃ | SO ₃ |
| Coal (C) | 11.56 | 10.30 | 31.00 | 3.82 | 6.29 | 28.50 |
| Waste coal (WC) | 39.68 | 18.90 | 12.72 | 1.79 | 4.59 | 11.95 |
| Alumino-silicates (AS) | 60.16 | 17.95 | 2.54 | 0.91 | 9.21 | 2.55 |
| Coal pyrite (CP) | 0.80 | 1.01 | 11.45 | 3.44 | 47.64 | 19.65 |

A comparison in the elemental composition of both coal samples is given in Table 3. The results of qualitative composition of elements in the raw and waste coal show increase of O (calculated by difference to 100 %) and reduction of C/H ratio (obtained from ultimate analysis) in the waste coal, indicating the sensitivity of the coal surface to oxidation (weathering). Chemical analysis of all analyzed samples confirms a presence of associated mineral matters such as coal pyrite and alumino-silicates.

2.2. Methods

2.2.1. FTIR spectroscopy

Infrared spectroscopy is an important and widely used analytical tool for determining the structure of coal material. FTIR spectra were recorded on a Nicolet Nexus IR 6700 with KBr pellet in the range of wave numbers 4000-400 cm^{-1} . Scans were collected at a resolution of 2 cm^{-1} . The coal/KBr disks were prepared at ratio 150 mg KBr and 1 mg sample.

2.2.2. Zeta potential measurements

Electrokinetic studies were carried on a defined size fraction of -38 μm , with 10 grams of the sample and 1 dm^3 solution of different pH values. The zeta potential was determined using a Riddick Zeta Meter and an electrophoretic cell. After conditioning, the pulp was transferred to the electrophoretic cell and the mobility of at least 10 particles was measured. The zeta potential was calculated from the electrophoretic mobility. In determining the zeta potential value adjustments were made for temperature which varied in the range of 20 to 25°C.

2.2.3. Microflotation experiments

Micro-flotation tests were carried out using a modified Hallimond flotation glass tube. Sample was conditioned in 100 cm^3 solution at the different pH values. Conditioning time was 3 minutes. Following the conditioning step, the pulp was transferred to the Hallimond tube for flotation, which was carried out for 1 minute using air at a flow rate of 0.1 dm^3/min . All experiments were conducted using distilled water. The 0.1 M HClO_4 acid and 0.1 M NaOH base solutions were used as pH modifiers.

3. Results and discussion

Current knowledge on the flotation of oxidized coals shows that the investigation of physical-chemical properties and phenomena at interfaces, as well as the identification of compounds on the surfaces of coal, can establish a correlation between the functional groups as well as zeta potential and floatability.

3.1. Identification of functional groups on the surface of coal by FTIR analysis

Concentration, type and distribution of functional groups on the surface of coal can vary widely depending on the type and degree of coal oxidation. Figures 1a and 1b present the spectra of the raw and waste coal samples.

The FTIR spectra of both studied coal samples show a certain number of common absorption bands, different shapes and intensities, with characteristic peaks, which can be divided into the following functional groups:

- bands in the range from 3600 to 3700 cm^{-1} assigned to vibrations of hydrogen strongly bonded of OH groups. These bands indicate the presence of small concentrations of alcohol and phenol

- in the wavelength range of 2850 to 2950 cm^{-1} , and 3000 to 3100 cm^{-1} , fresh raw coal shows weak bands with characteristic peaks at 2910 and 3031 cm^{-1} . Both bands assigned to asymmetric stretching vibration of CH_2 groups, or asymmetric and symmetric vibration of aromatic $=\text{C}-\text{H}$ compounds, respectively. The absence of these groups on the spectra of waste coal shows that the intensity of this bands decreases as a result of surface oxidation and the aromatic structures in coal subject to oxidation

- peak at 1587 cm^{-1} in the wavelength range 1500 to 1600 cm^{-1} in the FTIR spectra of raw coal, assigned to the symmetrical vibrations of $\text{C}-\text{C}=\text{C}$ bond of aromatic rings. These absorption bands confirms the change in surface coal

- the observed peaks of different intensities, with maximum at 1424 cm^{-1} in the spectra of raw coal (RC) and the 1434 cm^{-1} in the spectra of waste coal (WC) corresponding to the deformation of bending vibrations of methyl $-\text{CH}_3$ and methylene $-\text{CH}_2$ groups. The intensity of these vibrations are also reduced as a result of surface oxidation of coal

- the intensity of the absorption bands with maximum at 1030 cm^{-1} in the spectrum of waste coal is a consequence of the symmetrical vibration of aliphatic ether group, $\text{C}-\text{O}-\text{C}$ and possibly due to vibrations of $\text{S}=\text{O}$ groups, because the stretching vibrations of these groups occurs in the range of 1030 to 1070 cm^{-1} (Pietrzak and Wachowska, 2003). The absence of $\text{S}=\text{O}$ groups on the surfaces of raw coal, as well as the formation of sulfoxides on the surfaces of waste coal indicates the effects of surface oxidation of coal

- absorption bands with peaks at 1006, and 1004 cm^{-1} in the spectra of raw and waste coal, respectively, originate from the deformation vibration of $\text{C}-\text{H}$ group of alkenes. Lower intensity of these vibrations in the spectrum of waste coal confirms changes during coal oxidation by weathering

- formation of carboxyl group (acid) during oxidation can be explained by changes observed in the spectrum of waste coal. In the wavelength range from 880 to 960 cm^{-1} and with a characteristic peak at 910 cm^{-1} , it can be assigned to deformation vibration of $\text{OH}-\text{O}$ group

- reduction of aromatic hydrogen was observed in the spectrum of waste coal, in the wavelength range from 650 to 900 cm^{-1} , characterized by varying intensity, can be assigned to vibrations of $\text{C}-\text{H}$ groups of aromatic rings.

Comparing the FTIR spectra of raw and waste coal provide the following conclusions: on the surfaces of waste coal, as a result of oxidation, there is a formation of different oxygen functional groups (COOH , $\text{S}=\text{O}$, $\text{C}-\text{O}-\text{C}$) and absence of $\text{C}-\text{C}=\text{C}$ of the aromatic compounds and reduction of aromatic and aliphatic $\text{C}-\text{H}$ groups. All previous conclusions confirm the changes on the surfaces, which are the result of surface oxidation, occurred during weathering or storage.

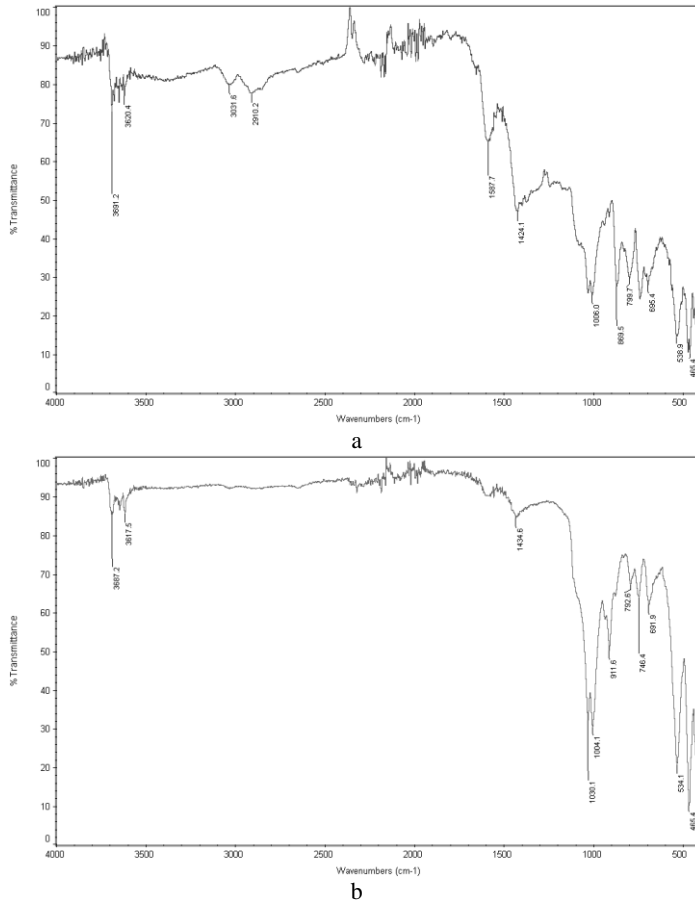


Fig. 1. FTIR spectra of a) coal (C) and b) waste coal (WC) samples

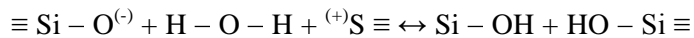
3.2. Effect of pH on the zeta potential and floatability

Correlation between zeta potentials of waste (oxidized) coal, coal-pyrite and alumino-silicates minerals from old tailings ponds and flotation responses is a useful indicator of degree of oxidation and floatability of coal. The value of the zeta potential of coal is a key tool of theoretical analyses concerning the behavior of coal in the process of coal flotation. Figure 2 shows the correlation between zeta potential and floatability of waste (oxidized) coal, coal-pyrite and alumino-silicates minerals as a function of pH.

Comparing measured zeta potential and floatability curves, different trends of curves depending on pH can be observed, both from the view point of obtaining isoelectric points of zeta potential as well as optimal flotation response that are important both at the theory and practical use of coal flotation.

The results confirm that H^+ ions are potential determining species. Therefore, different concentrations of hydronium and hydroxyl ions not only change the magnitude of the zeta potential but also its sign. The zeta potential curves show that the isoelectric point (IEP) of waste coal is about pH 6.5. Compared with IEP of raw (unoxidized) coal, which is achieved at pH 7.5 (Sokolovic et al., 2006), results show that the surface of coal particles becomes negatively charged due to oxidation. Obviously, the zeta potential of coal is a function of active oxygen groups and IEP of waste coal lies on the lower pH, as a consequence of oxidation by weathering.

The zeta potentials of aluminosilicates as a function of solution pH are given in Fig. 2b, which shows IEP of aluminosilicates and coal-pyrite at pH 5.7. The position of isoelectric point depends not only on the concentration of H^+ ions, but also the concentration of silanol groups ($HO-Si\equiv$) that are formed on the surfaces as a result of oxidation. The reaction is:



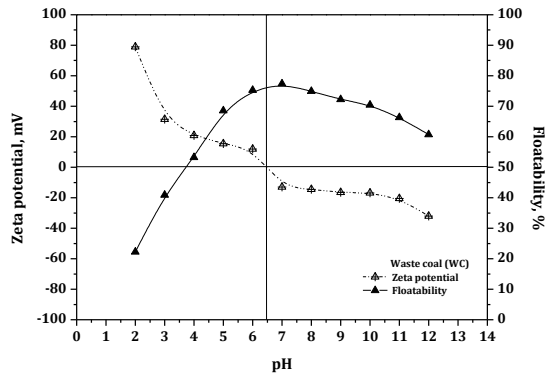
It is believed that these groups show negative charge and the potential determining ions for all SiO_2 modifications are hydroxyl ions. Figure 2b shows that coal-pyrite's isoelectric point (IEP) is at about pH of 8.4. The high IEP value obtained for coal-pyrite may be due to the presence of a high concentration of ferrous ions which results from the high solubility of coal-pyrite. Previous studies of Sokolovic et al. (2006) have shown that addition of ferrous ions shifts the IEP of ore-pyrite from pH 4.0 to 8, and the magnitude of the zeta potential of ore-pyrite is lowered. Comparing zeta potential curves, it is clear that the zeta potential behavior of coal-pyrite is analogous to that of ore-pyrite in the presence of ferrous ions with the same IEP at pH 8. Such results are consistent with the results of Jiang et al. (1998).

Floatability is a critical parameter for control of coal flotation. The flotation behaviors of all samples were found to be dependent on pH. It is shown that the maximum floatability occurs close to the isoelectric points of the coal. The relatively high floatability of waste coal, about 75%, resulted from the sampling method and lower degree of oxidation of crushed and freshly liberated particles of size range - 0.038 mm. It can be seen from Fig. 2b that aluminosilicates minerals are highly floatable (about 35 %) at a pH around 9.

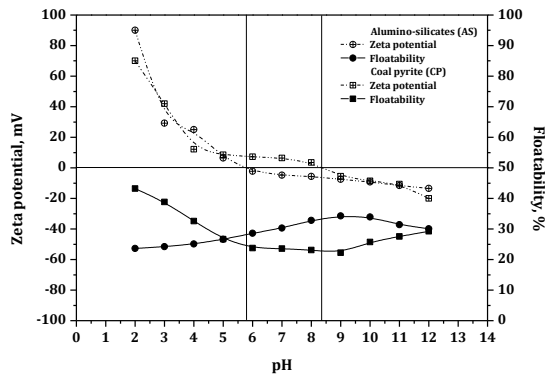
It was found that coal-pyrite is not readily floatable at neutral pH, although it becomes highly floatable at acidic pH. Also, studies have shown that floatability coal pyrite (CP) have maximum (45%) in strong acid solution. However, at around neutral pH region, the recoveries of coal-pyrite decrease drastically. Compared with floatability curves of unoxidized coal-pyrite samples, can be concluded that the waste coal-pyrite, as results of oxidation process, have better floatability properties. There may be several reasons for this behavior. It was known that in neutral and alkaline solutions, the oxidation of coal-pyrite leads to the formation of a hydrated ferric hydroxide and sulphur, which is normally intermediate product of reaction, before

formation of sulphate layers on the mineral surface (Liu et al., 1994). Obviously, the appearance of elemental sulphur, which is believed to be hydrophobic, causes better coal-pyrite floatability.

All measurement of natural floatability confirmed that maximum floatability of waste coal and minimum floatability of coal pyrite is achieved at optimal pH 7.5.



a

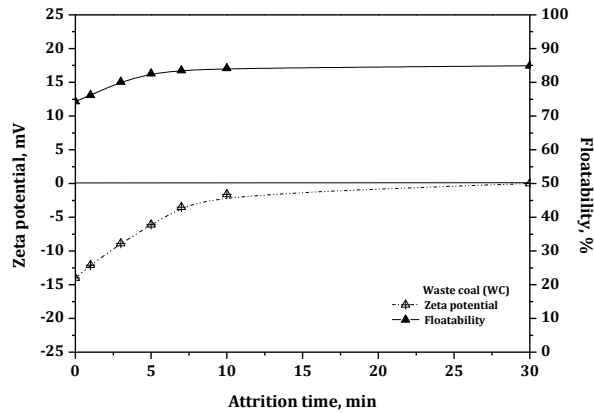


b

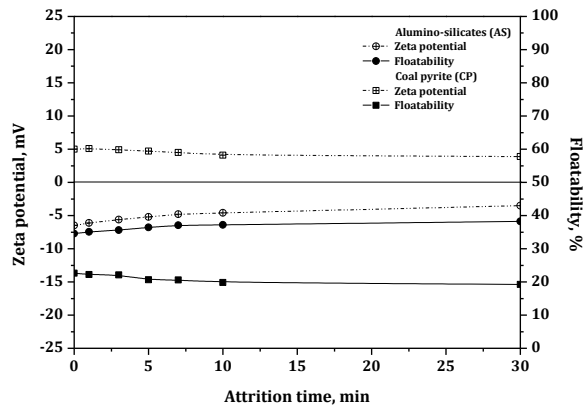
Fig. 2. Effect of pH on zeta potential and floatability of waste samples
a) coal b) associated mineral matters

3.3. The effect of attrition on the zeta potential and floatability

In order to improve floatability of waste coal, the effect of attrition time on the zeta potential and floatability of waste coal and associated minerals was investigated. All experiments were performed in attrition machine, under optimal test conditions (speed 1600 rpm, the solid content of 50% and the pH value of 7.5). The results are shown in Fig. 3.



a



b

Fig. 3. Effect of attrition time on zeta potential and floatability of waste samples
a) coal, b) associated mineral matters

It was found that the surface of coal becomes more positively charged with increasing attrition time from 1 to 30 minutes (Fig. 5a). It was found that the zeta potential changes in the range of -14 mV to 1.6 mV, where, after 20 minutes of attrition, zeta potential is asymptotically approaching 0 mV. Differences in charges suggest changes on the coal surface as a result of the attrition. Obviously the attrition process as well as mechanical scrubbing of negatively charged compounds from the surface of coal leads to the formation of fresh surfaces of coal. Therefore, increasing floatability by about 10% confirms the absence of surface functional groups as phenolic and carboxylic oxygen on the surface of coal. From the standpoint of efficiency of the flotation is a very positive phenomenon.

The change of zeta potential of coal pyrite and almino-silicates after attrition is different. Attrition time increases zeta potential of almino-silicate and decreases zeta

potential of coal-pyrite minerals. The zeta potential of coal pyrite has a positive value and under the lab-attrition conditions zeta potential decreased from approximately 5.1 mV at the beginning of the tests to 3.9 mV after 30 minutes, while the same indicator for the alumino-silicate mineral matter has a negative value and increases from -6.5 to -3.5 mV. These results clearly indicate that there have been no significant changes on the surface of associated mineral matters. It is believed that a partial removing of negative charging of silanol group from the alumino-silicates surfaces by attrition causes a minimal floatability increase to about 3%. Also, attrition of coal pyrite leads to a slight decrease of floatability from 22.64 to 19.24%. This phenomenon can be considered positive.

Based on the results, it can be concluded that attrition time is an important parameter of attrition process from the point of activating the oxidized coal surface, and positive change in zeta potential and floatability. Zeta potential approaching 0 mV can cause displacement of the coal isoelectric point (IEP) to more positive pH values and increase of floatability.

4. Conclusion

The following conclusions can be drawn from this paper.

1. The results of proximate and ultimate analyses of the raw and waste samples show increase of ash and oxygen (calculated by difference in relation to 100 %) and reduction of C/H ratio (obtained from ultimate analysis) in the waste coal, indicating the sensitivity of the coal surface to oxidation (weathering).
2. FTIR analysis of raw and waste coal have shown that on the surface of waste coal, as a result of oxidation by weathering and storing, there is a formation of different oxygen functional groups (COOH, S=O, C-O-C), the absence of C=C aromatic compounds and reduction of aromatic and aliphatic C-H groups.
3. Our research confirms that the pH value is one of the most important parameters of the process of flotation.
4. The isoelectric point (IEP) of waste coal is about pH 6.5 and similar to the IEP of raw coal. This value results from a presence of oxygen functional groups on the surfaces of waste coal as a consequence of oxidation by weathering.
5. Maximum floatability of waste coal, from about 75%, is achieved in the pH range in which lies the coal IEP. This high floatability confirms partial oxidation of coal from the dump and the consequence of the lower degree of oxidation of freshly liberated particle of size range -0.038 mm.
6. The zeta potentials of alumino-silicates and coal pyrite show IEP at pH 5.7 and 8.4, respectively. The position of isoelectric point of alumino-silicates depends on the concentration of silanol groups which are formed on the surfaces as a result of oxidation.
7. Also, floatability of coal pyrite have the maximum (45 %) in strongly acidic (pH = 2) and it is, unlike coal, don't occurs close to the isoelectric points

- (about 8.4). Such high IEP value can be explained with the presence of ferrous ions produced by dissolution of coal pyrite in the water.
8. It was stated that the maximal floatability of waste coal and minimum floatability of coal pyrite, is achieved at optimal pH 7.5.
 9. Results showed that attrition can improve floatability of waste coal.
 10. Measurements of zeta potential of waste coal, coal pyrite and alumino-silicate as a function of attrition time, from 1 to 30 minutes, showed that there is a substantial change in the magnitude of the zeta potential from -15 mV to 0 mV for coal, from -6.5 to -3.5 mV for the alumino-silicate minerals, and from 3.9 to 5.1 mV for coal pyrite.
 11. Attrition raises the floatability of waste coal and alumino-silicates minerals to 10% and 3%, respectively and reduced the floatability of coal pyrite to 3%. From the view point of flotation of waste coal samples, this phenomenon can be considered positive.
 12. Results of all electrochemical and microflotation tests confirm a positive effect of attrition on the waste coal and also the final effect on coal flotation process. The valorization of the waste coal with attrition prior flotation process may cause significant improvement in the economic value of the process of coal preparation as well as the positive contribution on the environment protection.

References

- BEAFORE, F.J., CAWIEZEL, K.E., MONTGOMERY, C.T., 1984. Oxidized coal-What it is and how it affects your preparation plant performance. *J. Coal Qual.* 3, 17-24.
- BOLAT, E., SAGLAM, S., PISKIN, S., 1998. The effect of oxidation on the flotation properties of a Turkish bituminous coal. *Fuel Process. Technol.* 55 (2), 101-105.
- BUTTERMORE, W.H., SLOMKA, B.J., 1991. Effect of sonic treatment on the floatability of oxidized coal. *Int. J. Miner. Process.* 32 (3-4), 251-257.
- CALEMMA, V., RAUSE, R., MARGARIT, R., GIRARDI, E., 1988. FTIR study of coal oxidation at low temperature, *Fuel* 67, 764-769.
- DIAO, J., FUERSTENAU, D.W., 1991. Characterization of the wettability of solid particles by film flotation: 2. Theoretical analysis. *Colloids Surf.* 60, 145-160.
- FUERSTENAU, D.W., DIAO, J., HANSON, J.S., SOTILLO, F., SOMASUNDARAN, P., 1994. Effect of weathering on the wetting behavior and flotation response of coal. In: Blaschke W.S., Ed., *New Trends in Coal Preparation Technologies and Equipment*. Gordon & Breach, pp. 747-753.
- FUERSTENAU, D.W., et al., 1992. Coal Surface Control for Advanced Fine Coal Flotation, Final Report, Project No. DE-AC22-88PC88878.
- FUERSTENAU, D.W., ROSENBAUM, J.M., LASKOWSKI, J.S., 1983. Effect of surface functional group on the flotation of coal. *Colloids Surf.* 8, 153-174.
- FUERSTENAU, D.W., YANG, G.C.C., LASKOWSKI, J.S., 1987. Oxidation phenomena in coal flotation: Part I. Correlation between oxygen functional group concentration, immersion wettability and salt flotation response. *Coal Prep.* 4, 161-182.
- GAYLE, J. B., EDDY, W.H., SHOTTS, R.Q., Laboratory investigation of the effect of oxidation on coal flotation, Report of Investigations 6620, US Bureau of Mines, 1965.
- HORSLEY, R. M., 1951-1952. Oily collectors in coal flotation. *Trans. Inst. Min. Eng.* 111 (3415), 886-894.

- IGLESIAS, M.J., DE LA PUENTE, G., FUENTE, E., PIS J.J., 1998. Compositional and structural changes during aerial oxidation of coal and their relations with technological properties. *Vib. Spectrosc.* 17, 41–52.
- JIA, R., HARRIS, G.H., FUERSTENAU, D.W., 2000. Improved class of universal collectors for the flotation of oxidized and/or low-rank coal. *Int. J. Miner. Process.* 58 (1), 99–118.
- JIANG, C. L., WANG, X. H., PAREKH, B. K., LEONARD, J. W., 1998. The surface and solution chemistry of pyrite flotation with xanthate in the presence of iron ions. *Colloids Surf., A Phys.-Chem. Eng. Aspects* 136 (1-2), 51–62.
- KARSILAYAN, H., AFSAR, H., YILMAZ, N., YANIC, C., 1992. Increase of efficiency of pine oil by heating and usage in the flotation of oxidized Amasra coal. *Fuel Sci. Technol. Int.* 10 (8), 1241–1250.
- KISTER, J., GUILIANO, M., MILLE, G., DOU, H., 1988. Changes in the chemical structure of low rank coal after low temperature oxidation or demineralization by acid treatment. *Fuel* 67, 1076–1082.
- LASKOWSKI, J.S., 1995. Coal surface chemistry and its effects on fine coal processing. In: Kawatra, S.K. Ed., *High Efficiency Coal Preparation: An International Symposium*. SME, Littleton, CO, pp. 163–176.
- LASKOWSKI, J.S., *Coal Flotation and Fine Coal Utilization*, Elsevier, Amsterdam, 2001.
- LIU, D., SOMASUNDARAN, P., VASUDEVAN, T.V., HARRIS, C.C., 1994. Role of pH and dissolved mineral species in Pittsburgh No. 8 coal flotation system: 1. Floatability of coal. *Int. J. Miner. Process.* 41, 201–214.
- MILLER, J.D., LASKOWSKI, J.S., CHANG, S.S., 1983. Dextrin adsorption by oxidized coal. *Colloids Surf.* 8 (137), 151.
- OZKAN, S.G., KUYUMCU, H.Z., 2006. Investigation of mechanism of ultrasound on coal flotation. *Int. J. Miner. Process.* 81, 201–203.
- PHILIPS, K.M., GLANVILLE, J.D., WIGHTMAN, J.P., 1987. Heat of immersion of Virginia-C coal in water as a function of surface oxidation. *Colloids Surf.* 21, 1–8.
- PIETRZAK, R., WACHOWSKA, H., 2003. Low temperature oxidation of coals of different rank and different sulphur content. *Fuel* 82, 705–713.
- PISKIN, S., AKGUEN, M., 1997. Effect of premixing on the flotation of oxidized Amasra coal. *Fuel Process. Technol.* 51 (1–2), 1–6.
- SADOWSKI, Z., VENKATADRI, R., DRUDING, J.M., MARKUSZEWSKI, R., WHEELOCK, T.D., 1988. Behaviour of oxidized coal during oil agglomeration. *Coal Prep.* 6, 17–34.
- SAIKIA, B.K., BORUAH, R.K., GOGOI, P.K. 2007. FT-IR and XRD analysis of coal from Makum coalfield of Assam. *J. Earth Syst. Sci.* 116 (6), 575–579.
- SARIKAYA, M. 1995. Flotation test as a method for studying coal weathering. *Int. J. Miner. Process.* 43, 31 – 35.
- SARIKAYA, M., OZBAYOGLU, G., 1995. Flotation characteristics of oxidised coal. *Fuel* 74 (2), 291–294.
- SOKOLOVIC, J., STANOJLOVIC, R., MARKOVIC, Z., 2006. Effect of oxidation on flotation and electrokinetic properties of coal. *J. Min. Metall. Sect. A* 42 (1), 69–81.
- SOMASUNDARAN, P., ZHANG, L., FUERSTENAU, D.W., 2000. The effect of environment, oxidation and dissolved metal species on the chemistry of coal flotation. *Int. J. Miner. Process.* 58, 85–97.
- SUN, S.C., 1954. Effects of oxidation of coals on their flotation properties. *Trans. Am. Inst. Min. Metall. Eng.*, 6, 396–401.
- SWANN, P.D., ALLARDICE, D.J., EVANS, D.G., 1972. Low-temperature oxidation of brown coal: 1. Change in internal surface due to oxidation. *Fuel* 53, 85–87.
- TAO, D., LI, B., JOHNSON, S., PAREKH, B.K., 2002. A flotation study of refuse pond coal slurry. *Fuel Process. Technol.* 76, 201– 210.
- WEN, W.W., SUN, S.C. 1981. An electrokinetic study on the oil flotation of oxidized coal. *Sep. Sci. Technol.* 16, 1491–1521.
- WOODBURN, E.T., ROBBINS, D.J., FLYNN, SA, 1983. The demineralization of a weathered coal by froth flotation. *Powder Technol.* 35, 1–15.

- XIAO, L., SOMASUNDARAN, P., VASUDEVAN, T.V., 1990. Effect of air oxidation on the floatability of bituminous coals: diffused reflectance infrared fourier transform (DRIFT) spectroscopic analysis. *Colloids Surf.* 50, 231–240.
- YARAR, B., LEJA, J., 1981. Flotation of Weathered Coal Fines from Western Canada. In: 9th International Coal Preparation Congress, New Delhi, Paper C5.

Received May 9, 2011; reviewed; accepted June 15, 2011

INFLUENCE OF ADSORPTION ON THE CHARGE TRANSFER REACTIONS AT THE PYRITE SURFACE. PRELIMINARY STUDY

Pawel NOWAK *, Robert P. SOCHA *, Tomasz CIESLIK **

* Institute of Catalysis and Surface Chemistry, Polish Academy of Sciences, Krakow, Poland,
ncnowak@cyf-kr.edu.pl

** AGH-University of Science and Technology

Abstract. Electrochemical impedance spectroscopy was used to measure the charge transfer resistance of the reaction: $\text{Fe}^{3+} + \text{e}^- = \text{Fe}^{2+}$ and electrical double layer capacitance on pyrite electrodes of different origin both freshly polished and conditioned in the solutions of several surface active substances which may be used as potential inhibitors of the oxidation of pyrite. The following substances were used for conditioning of the pyrite samples: sodium dodecylsulfate (SDS), sodium oleate (NaOL), n-octanol (n-OA), dodecyltrimethylammonium chloride (CTACl), 2-mercaptobenzthiazole (MBT) and bis(2-ethylhexyl) phosphate (D2EHP). The highest degree of adsorption, and the highest increase in the charge transfer resistance was observed for MBT, NaOL and D2EHP. Those compounds can be used as inhibitors of the pyrite oxidation.

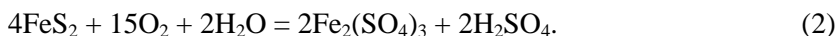
keywords: pyrite, adsorption, oxidation, corrosion prevention, mineral corrosion

1. Introduction

Since the beginning of the 20th century pyrite passed an unusual transformation from the fundamental raw material of the chemical industry to the unwanted and noxious component of the materials processed in mineral industry (Lowson, 1982). Pyrite is the most abundant sulfide mineral accompanying almost all sulfide and many non-sulfide minerals (Craig and Vaughan, 1990). Large quantities of pyrite appear in coal (Twardowska et al., 1978). At the same time pyrite has no application and in flotation process this mineral is directed to tailings. So, flotation tailings may contain as much as 60-70% of pyrite. Pyrite oxidizes relatively easily, and contrary to mono-sulfides, which oxidize to neutral sulfates, pyrite generates sulfuric acid during its oxidation



in the quantity of one mole of acid per one mole of pyrite. The amount of acid may be lower when pyrite iron oxidizes to trivalent oxidation state:



On the other hand, when pH of the surrounding aqueous phase increases above approximately 5.5 ferric sulfate hydrolyses according to the reaction:



creating additional amount of sulfuric acid. That sulfuric acid, together with dissolved trivalent iron are the main components of so-called acid mine drainage, i.e. waters flowing from worked-out mines, flotation waste deposits and sometimes from natural rocks containing pyrites (Doyle, 1990; Evangelou, 1995). Neither sulfates nor iron species belong to important environmental contaminants, however the decrease in pH of the water flowing through the wastes and soils causes the dissolution of otherwise insoluble constituents increasing the concentration of metal ions in effluents which leads to the contamination of the environment and sometimes even to catastrophes of buildings (Moore and Luoma, 1990). Pyrites appear also frequently as natural components of soils. Oxidation of those pyrites causes acidification of the soil which has detrimental influence on plants and causes contamination of the environment (Österholm and Åstrom, 2004; Åstrom and Spiro, 2005; Boman et al., 2008).

Weathering of metal sulfides may be considered as a corrosion process and, like in the case of the corrosion of metals it may be prevented by the application of inhibitors (Lipkowski, 1992; Stratmann et al., 1995). Many papers concerning the possible prevention of pyrite oxidation by application of inhibitors have appeared in the literature. Huang and Evangelou (1994) and Nyavor and Egiebor (1995) applied successfully soluble phosphates for that purpose, although Mauric and Lottermoser (2011) reported that application of phosphates in a larger scale led to only limited successes. Belzile et al. (1997) showed the applicability of several compounds (humic acids, lignosulfonates, oxalic acid, sodium silicate and acetyl acetone) in pyrite oxidation inhibition, the best inhibition was observed for the last compound. Cai et al. (2005) showed the inhibitive influence of triethylenetetramine on the oxidation of pyrrhotite. The same was showed by Güler (2005) in the case of dithiophosphate. Jiang et al. (2000) found oleic acid to be effective as an inhibitor of pyrite oxidation whereas Zhang et al. (2003) and Kargbo et al. (2004) applied successfully lipids for that purpose. Sasaki et al. (1996) applied several organic substances to suppress pyrite oxidation with some success. Pyrite leaching occurs usually with the active participation of bacteria. So, addition of antibacterial agents should depress the oxidation of pyrite. That problem was investigated by Sand et al. (2007) with a partial success.

Most of pyrites appearing in nature show good electrical conductivity (Shuey, 1975; Ennaoui, 1993) and aqueous oxidation of pyrite is an electrochemical process (Holmes and Crundwell; 2000, Rimstidt and Vaughan, 2003), so the electrochemical

methods have been intensively used in the investigations of pyrite. Furthermore, due to specific electronic structure of pyrite surface (Bronold et al., 1994; Nesbitt et al., 2000) charge transfer reactions are facilitated at the surface of pyrite and proceed with low overpotential (Salvator et al., 1991; Mishra and Osseo-Asare, 1992; Nowak and Koziol, 2002). Presence of an adsorbed layer on the surface of pyrite should impede the charge transfer (Lipkowski, 1992). So, measuring the charge transfer resistance of a correctly selected reaction occurring at the surface of a pyrite electrode should give the information on the surface coverage. Such method was previously used by one of the present authors to the investigations of adsorption at the surface of copper sulfides (Nowak and Gucwa, 2008; Nowak, 2010). The reaction of choice is:



It is an outer-sphere charge transfer reaction (Asperger, 2003) so its rate should not depend on the surface properties of the pyrite electrode but it should strongly depend on the presence of an adsorption layer. The charge transfer resistance for that reaction in the equimolar solution of trivalent iron and divalent iron sulfates was measured using electrochemical impedance spectroscopy (EIS) for several pyrite electrodes conditioned in the solutions of potential inhibitors, and compared to the values obtained for the freshly prepared electrodes. Additional information was obtained from the measured specific capacitance of the electrodes.

2. Experimental

2.1. Background of the measurements

The abstraction of a surface active substance from the solution by a sulfide minerals does not necessarily prove that the substance is adsorbed at the surface. There are other processes, like surface precipitation or surfactant decomposition that may lead to the decrease of the concentration without formation of an adsorbed layer. In the case of metallic electrodes adsorption may be conveniently estimated from the measurements of the electrical double layer (EDL) capacitance using the formula:

$$\theta = \frac{C_0 - C}{C_0 - C_{\max}}. \quad (5)$$

In that formula C means capacitance of the electrode measured at the coverage θ , C_{\max} means the electrode capacitance at full coverage and C_0 means the capacitance of the electrode not covered by the adsorbate. For such electrodes like pyrite electrode C_{\max} is difficult to be measured. However for the $C_{\max} \ll C_0$ (which is usually the case) surface coverage may be roughly estimated from the formula:

$$\theta \cong \frac{C_0 - C}{C_0} = 1 - \frac{C}{C_0}. \quad (6)$$

Application of that formula is possible only if the capacitance of EDL on the solid body side of the interface is much higher than the capacitance of EDL on the solution

side. It will be later showed that this condition is fulfilled in the case of pyrite electrodes. Surface coverage may be also estimated from the measurements of the charge transfer resistance of a conveniently selected electrode reaction. When a part of the electrode surface is covered by the layer of adsorbed molecules the charge transfer resistance may be calculated from the formula:

$$\frac{1}{R_T} = \frac{1-\theta}{R_T^0} + \frac{\theta}{R_T^{\max}}, \quad (7)$$

where R_T is the charge transfer resistance at the coverage θ , R_T^0 is the charge transfer resistance at the zero coverage and R_T^{\max} is the charge transfer resistance at the full coverage. The latter is difficult to measure but, if $R_T^{\max} \gg R_T^0$ formula (7) may be simplified to:

$$\theta \cong 1 - \frac{R_T^0}{R_T}. \quad (8)$$

Although approximate, the formulas (6) and (8) may be used for the sake of comparison between different electrodes and/or different adsorbates.

2.2. Apparatuses, procedures and materials

Five electrodes from pyrites of different origin were used in the measurements (see Table 1). The type of their conductivity was inferred from the thermoelectric force measurements. Pieces of pyrite were hand selected and embedded with epoxy resin at the end of a glass tubing. Electrical connection to the pyrite surface was made with the conducting silver-based glue. Electrodes were polished on emery papers (Struers) of the gradation: 500, 1000, 2400, and finely, 4000 before the measurements. Polishing was performed very gently to avoid heating of the electrode surface (Libowitzky, 1993). After polishing the electrode was dipped in the solution of the selected surface active compound for half an hour, thoroughly washed with distilled water and introduced to the cell. The following compounds were tested as possible pyrite oxidation inhibitors: sodium dodecylsulfate (SDS), sodium oleate (NaOL), n-octanol (n-OA), dodecyltrimethyl ammonium chloride (CTACl), 2-mercaptobenzthiazole (MBT) and bis(2-ethylhexyl) phosphate (D2EHP). All compound used were of analytical reagent purity grade. In all cases the concentration of the solution was 10^{-4} mol dm⁻³. Charge transfer resistance of the reaction (4) was measured in the solution containing: 0.5 mol dm⁻³ Na₂SO₄, 0.01 mol dm⁻³ H₂SO₄, 0.1 mol dm⁻³ FeSO₄ and 0.05 mol dm⁻³ Fe₂(SO₄)₃. For the sake of comparison the non-treated electrodes were measured too. Measurements were performed in a typical glass cell, in a three electrode configuration, with saturated calomel electrode as the reference electrode and platinum wire as a counter electrode. All measurements were performed at the temperature of 25°C. Doubly distilled water was used to prepare the solutions. Solutions were purged from oxygen by bubbling with 99.999% argon (Linde) before

the electrochemical measurements. XPS instrumentation was described in our previous paper (Nowak et al., 2000).

The impedance spectra were measured in the frequency range of 65535 - 0.125 Hz at the rest potential of the electrode. The measuring system composed of an ECI 1286 potentiostat and a FRA 1250 frequency response analyzer (both Schlumberger – Solartron, Great Britain) was used in the measurements. Charge transfer resistance and the capacitance of the electrical double layer (C_{EDL}) were then calculated from impedance spectra by fitting the proper equivalent electrical circuit (EEC) to the EIS data using the MINUIT program (James and Roos, 1975). More information on the data treatment may be found in our previous paper (Nowak et al., 2000).

Table 1. Origin and conductivity type of the pyrite electrodes used in the measurements

| Electrode description | Pyrite origin | Conductivity type |
|-----------------------|------------------------|-------------------|
| EB | Elbe, Italy | p |
| RT | Rio Tinto, Spain | n |
| UR | Ural Mountains, Russia | p |
| HU | Huenzala, Peru | n |
| HA | Halemba Mine, Poland | p |

3. Results and discussion

3.1. Impedance of the pyrite electrodes in the Fe^{2+} - Fe^{3+} equimolar solution

The rest potential of pyrite electrodes in the equimolar solution containing Fe^{2+} and Fe^{3+} ions of the concentration $0.1 \text{ mol}\cdot\text{dm}^{-3}$ was many hours stable and equal to the rest potential of a Pt electrode in the same solution, which means that the process occurring at the surface of a pyrite electrode (reaction 4) is well reversible. Figure 1 shows the impedance spectrum of one of the pyrite electrodes in that solution. The impedance plot has the shape of a depressed semicircle in accordance with the assumed EEC. Table 2 shows the results of the measurements performed on freshly polished electrodes which were not conditioned.

For the first three electrodes R_S was almost the same and rather low. It means that the value of R_S was dominated by the resistance of the solution. Both HU and HA showed much higher resistance, which may be ascribed to the low conductivity of the pyrite samples. For all investigated electrodes (except HA) R_T had the value between 13 and $21 \text{ } \Omega \text{ cm}^2$, despite different origin and type of conductivity. The differences may arise from the differences in surface roughness factor. Platinum electrode in the same solution showed similar impedance spectrum and R_T value of $14 \text{ } \Omega \text{ cm}^2$, very close to pyrite electrodes. It means that the exchange current density of reaction 4 at the pyrite electrode surface is very high. So, there is no obstruction to charge transfer at the pyrite surface, in accordance to the theoretical expectations (Bronold et al., 1994; Nesbitt et al., 2000; Salvator et al., 1991; Mishra and Osseo-Asare, 1992).

All electrodes (except HA) showed also similar EDL capacitance. Electrode made of Halemba pyrite showed not only much higher R_S but both also much higher R_T as well as much lower C_{EDL} . That electrode was not considered in adsorption

experiments. Worth mentioning is the high value of EDL capacitance of pyrite electrodes. That value is about twice as much as the electrical double layer capacitance measured in the case of non-stoichiometric copper (I) sulfide electrode and much higher than C_{EDL} measured in the case of metallic Ni electrode (Nowak et al., 2000). That high electrical double layer capacitance may be ascribed to the presence of surface iron (III) hydroxide on the surface of pyrite (Bungs and Tributsch, 1997). That problem will be discussed in our future paper.

Table 2. Parameters of the EEC from Fig. 1 fitted to the impedance data for freshly polished electrodes. R_S - solution resistance, R_T -charge transfer resistance, C_{EDL} – capacitance of the electrical double layer. Each value is a mean from at least 5 measurements

| Electrode | $R_S / \Omega\text{cm}^2$ | $R_T / \Omega\text{cm}^2$ | $C_{EDL} / \mu\text{F cm}^2$ |
|-----------|---------------------------|---------------------------|------------------------------|
| EB | 7.1±1.3 | 14.9±3.5 | 125±22 |
| RT | 8.0±0.5 | 18.6±6.5 | 97.8±13 |
| UR | 10.1±0.5 | 13.2±2 | 101.1±11 |
| HU | 86.2±6 | 21.2±5.5 | 84.4±14 |
| HA | 248.0±15.5 | 50.3±12 | 9.4±3 |

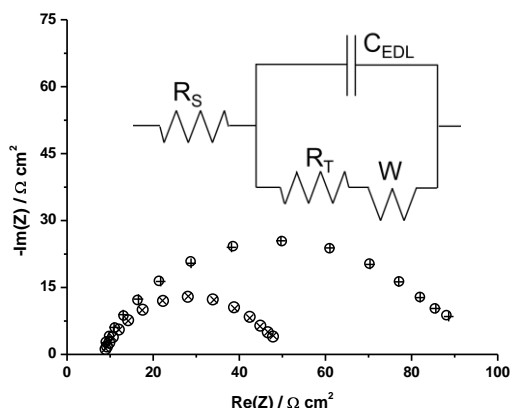


Fig. 1. Impedance spectra (Nyquist plots) of the RT electrode in the solution containing $0.5 \text{ mol dm}^{-3} \text{ Na}_2\text{SO}_4$, $0.01 \text{ mol dm}^{-3} \text{ H}_2\text{SO}_4$, $0.1 \text{ mol dm}^{-3} \text{ FeSO}_4$ and $0.05 \text{ mol dm}^{-3} \text{ Fe}_2(\text{SO}_4)_3$ at the rest potential. x – freshly polished electrode, + - the same electrode after 30 minutes of conditioning in $10^{-4} \text{ mol dm}^{-3}$ D2EHP solution, o – least-square fitted values of impedance according to the EEC from figure. R_S is the resistance of the solution, pyrite sample and the electrical connections, R_T is the charge transfer resistance, C_{EDL} is the capacitance of the electrical double layer and W is the impedance of the diffusion process (Warburg impedance)

3.2. Influence of the treatment in inhibitor solutions on the electrode impedance

Figure 1 shows the impedance spectrum of one of the pyrite electrodes after the treatment in D2EHP solution. One may see that conditioning in the D2EHP solution did not change the shape of the spectrum but only the diameter of the semicircle which means that the mechanism of the electrode reaction did not change. In the case presented in Fig.1 R_T increased more than twice. Significant decrease in the C_{EDL} was

observed too. Similar behavior was observed in the case of other investigated compounds and other electrodes. The coverage of the electrode by adsorbed layer was estimated both from formula (6) and formula (8). Those data are showed in Figs 2. It must be stated that due to the simplifications made at the derivation of the mentioned formulas those data are very approximate and may be considered only for the sake of comparison. One may see that all four considered electrodes showed similar behavior. The highest decrease in the capacitance and the highest increase in charge transfer resistance was observed in the case of MBT.

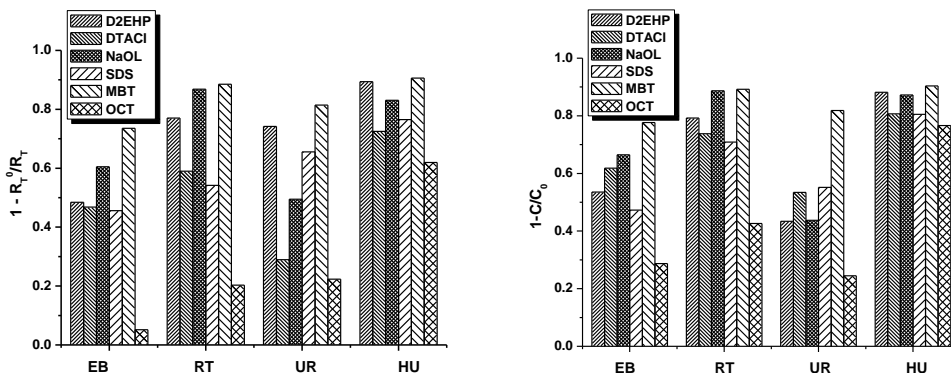


Fig. 2. Surface coverage of pyrite electrodes after 30 min of conditioning in different surfactants, estimated from impedance measurements: left from charge transfer resistance data (formula 8), right from electrical double layer capacitance data (formula 6)

Both D2EHP and NaOL showed similar (but slightly lower than MBT) value of coverage. Note that during the conditioning in a surfactant solution not only adsorption but also oxidation of the surface may occur. The lower is the adsorption the highest oxidation may be expected. Oxidation of pyrite in the mild conditions may lead to appearance of elemental sulfur at the surface and hence to passivation. That effect would obscure the dependence of coverage on adsorption. There are some differences between the electrodes. Those differences reflect probably the differences in surface properties of the pyrite sample. Note, that the biggest differences were obtained for the case of n-octanol which is expected not to adsorb strongly. Oxidation rate depends on the surface properties of the sulfide (impurities, structure faults, non-stoichiometry) and, contrary to charge transfer resistance of the reaction (4), may change from sample to sample. An example of such differences may be seen in Fig. 3, where the degree of oxidation of three different pyrites, after 4 days in air is compared from the XPS data. As can be seen, the differences in the degree of oxidation, expressed as the intensity of the XPS band which may be ascribed to oxidized iron (Fe^{3+}) and oxidized sulfur (SO_4^{2-}) are very high. Very high differences between pyrites of different origin in the corrosion rate was observed by Chmielewski and Nowak (1992).

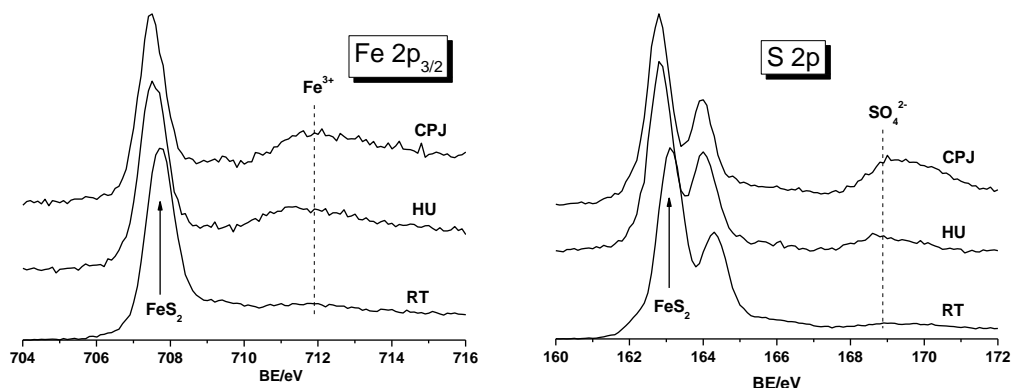


Fig. 3. XPS spectra of three different pyrites: HU, RT and coal pyrite from the Jastrzebie coal mine in Poland (CPJ) after 4 days of the oxidation in air. Surface of the samples was scraped with a steal blade before oxidation

4. Conclusions

Impedance measurements may be conveniently used for the estimation of the adsorption of surfactants at the surface of pyrite. The charge transfer resistance for the reaction $\text{Fe}^{3+} + \text{e}^- = \text{Fe}^{2+}$ as well as the electrical double layer capacitance (measured in the same measurement) do not depend on the origin of pyrite sample (providing that the resistivity of the pyrite sample is low), so this values may give the information on the degree of surface coverage. The highest adsorption was observed for 2-mercaptobenzothiazole, slightly lower, but still high for sodium oleate and bis(2-ethylhexyl) phosphate. Those compounds might be used as the inhibitors to suppress the oxidation of pyrite. Note, that during hydrothermal oxidation of metal sulfides in nature the oxidizing agent is usually Fe^{3+} ion. So one of the conjugate reactions which participate in the process of the corrosion of a metal sulfide is just the above mentioned reaction. Surface of pyrite in the solutions containing Fe^{3+} ions is covered by the surface iron(III) hydroxide, which may be inferred from the high value of electrical double layer capacitance.

Acknowledgments

This work was financed by Polish Ministry of Science and Higher Education from the financial resources for the years 2009 – 2011 (grant 4513/B/T02/2009/36).

References

- AŠPERGER, S., 2003, *Chemical Kinetics and Inorganic Reaction Mechanisms*, Kluwer Academic, New York.
- ÅSTROM, M., SPIRO, B., 2005, Sources of acidity and metals in a stream draining acid sulfate soil, till and peat, western Finland, revealed by a hydrochemical and sulphur isotope study, *Agricultural and Food Science*, 14, 34–43.

- BELZILE, N., MAKI, S., CHEN, Y.-W., GOLDSACK, D., 1997, Inhibition of pyrite oxidation by surface treatment, *Sci. Total Environ.* 196, 177-186.
- BOMAN, A., ÅSTROM, M., FRÖJDÖ, S., 2008, Sulfur dynamics in boreal acid sulfate soils rich in metastable iron sulfide – The role of artificial drainage, *Chemical Geology*, 255, 68–77.
- BRONOLD, M., TOMM, Y., JAEGERMANN, W., 1994, Surface states on cubic d-band semiconductor pyrite (FeS₂), *Surf. Sci.*, 314, L931–L936.
- BUNGS, M., TRIBUTSCH, H., 1997, Electrochemical and Photoelectrochemical Insertion and Transport of Hydrogen in Pyrite, *Ber. Bunsenges. Phys. Chem.*, 101, 1844–1850.
- CAI, M.-F., DANG, Z., CHEN, Y.-W., BELZILE, N., 2005, The passivation of pyrrhotite by surface coating, *Chemosphere* 61, 659–667.
- CHMIELEWSKI, T., NOWAK, P., 1992, Impedance Characteristics of Pyrites in Relation to their Collectorless Flotation, *Physicochemical Problems of Mineral Processing*, 25, 59–67.
- CRAIG, J.R., VAUGHAN, D.J., 1990, Compositional and textural variations of the major iron and base-metal sulfide minerals, in: *Sulfide deposits – their origin and processing* (P.M.J. Gray, G.J. Bowyer, J.F. Castle, D.J. Vaughan, N.A. Warner - editors), The Institution of Mining and Metallurgy, London, 1–16.
- DOYLE, F.M., 1990, Acid mine drainage from sulfide ore deposits, in: *Sulfide deposits – their origin and processing* (P.M.J. Gray, G.J. Bowyer, J.F. Castle, D.J. Vaughan, N.A. Warner - editors), The Institution of Mining and Metallurgy, London, 301–310.
- ENNAOUI, A., FIECHTER, S., PETTENKOFER, CH., ALONSO-VANTE, N., BÜKER, K., BRONOLD, M., HÖPFNER, CH., TRIBUTSCH, H., 1993, Iron disulfide for solar energy conversion, *Solar Energy Materials and Solar Cells*, 29, 289–370.
- EVANGELOU, V.P., 1995, *Pyrite Oxidation and its Control*, CRC Press, Boca Raton.
- GÜLER, T., 2005, Dithiophosphinate–pyrite interaction: Voltammetry and DRIFT spectroscopy investigations at oxidizing potentials, *J. Colloid Int. Sci.* 288, 319–324.
- HOLMES, P.R., CRUNDWELL, F.K., 2000, The kinetics of the oxidation of pyrite by ferric ions and dissolved oxygen: An electrochemical study, *Geochim. Cosmochim. Acta*, 64, 263–274.
- HUANG, X., EVANGELOU, V. P., 1994, Suppression of pyrite oxidation rate by phosphate addition, in : *Environmental Geochemistry of Sulfide Oxidation*, ACS Symposium Series 550, 562–573.
- JAMES, F., ROOS, M., 1975, MINUIT – a system for function minimization and analysis of the parameter errors and correlations, *Computer Phys. Commun.*, 10, 343–367.
- JIANG, C.L., WANG, X.H., PAREKH, B.K., 2000, Effect of sodium oleate on inhibiting pyrite oxidation, *Int. J. Miner. Process.*, 58, 305–318.
- KARGBO, D. M., ATALLAH, G., CHATTERJEE, S., 2004, Inhibition of Pyrite Oxidation by a Phospholipid in the Presence of Silicate, *Environ. Sci. Technol.*, 38, 3432–3441.
- LIBOWITZKY, E, 1993, Anisotropic pyrite: a polishing effect, *Phys. Chem. Miner.*, 21, 97–103.
- LIPKOWSKI, J., 1992, Ion and electron transfer across monolayers of organic surfactants, in: *Modern Aspects of Electrochemistry* (B.E. Conway, J. O'M. Bockris, R.E. White – editors), 23, 1–99.
- LOWSON, R.T., 1982, Aqueous oxidation of pyrite by molecular oxygen, *Chemical Reviews*, 82, 461–497.
- MAURIC, A., LOTTERMOSER, B. G., 2011, Phosphate amendment of metalliferous waste rocks, Century Pb-Zn mine, Australia: Laboratory and field trials, *Applied Geochemistry* 26, 45–56
- MISHRA, K.K., OSSEO-ASARE, K., 1992, Fermi level pinning at pyrite/electrolyte junctions, *J. Electrochem. Soc.*, 139, 749–752.
- MOORE, J.N., LUOMA, S.N., 1990, Hazardous wastes from large-scale metal extraction, *Environmental Science and Technology*, 24, 1278–1285.
- NESBITT, H.W., SCAINI, M., HOCHST, H., BANCROFT, G.M., SCHAUFUSS, A.G., SZARGAN, R., 2000, Synchrotron XPS evidence for Fe²⁺-S and Fe³⁺-S surface species on pyrite fracture-surfaces, and their 3D electronic states, *Am. Mineral.*, 85, 850–857.

- NOWAK, P., 2010, Influence of Surfactant Adsorption on the Leaching of Copper Sulfides, in: *Electrochemistry in Mineral and Metal Processing VIII*, ECS Transactions 28(6), (F.M. Doyle, R. Woods, G.H. Kelsall - editors), The Electrochemical Society, Pennington, USA, 143–153.
- NOWAK, P., GUCWA, A., 2008, Influence of surfactant adsorption on the leaching of copper sulfides, *Acta Metallurgica Slovaca*, 14, 196–203.
- NOWAK, P., KOZIOL, B., 2002, On the Rest Potential of Pyrite Electrode in Oxygen-Free Solutions of Iron(II) sulfate, *Physicochemical Problems of Mineral Processing*, 36, 77–88.
- NOWAK, P., SOCHA, R.P., KAISHEVA, M.K., FRANSAER, J., CELIS, J.-P., STOINOV, Z., 2000, Electrochemical Investigation of the Codeposition of SiC And SiO₂ Particles with Nickel, *J. Appl. Electrochem.*, 30, 429–437.
- NYAVOR, K., EGIEBOR, N.O., 1995, Control of pyrite oxidation by phosphate coating, *Sci. of the Total Environment*, 162, 225–237.
- ÖSTERHOLM, P., ÅSTRÖM, M., 2004, Quantification of current and future leaching of sulfur and metals from Boreal and sulfate soils, western Finland, *Australian Journal of Soil Research*, 42, 547–551.
- RIMSTIDT, J.D., VAUGHAN, D.J., 2003, Pyrite oxidation: A state-of-the-art assessment of the reaction mechanism, *Geochim. Cosmochim. Acta*, 67, 873–880.
- SALVADOR, P., TAFALLA, D., TRIBUTSCH, H., WENTZEL, H., 1991, Reaction mechanisms at the n-FeS₂/I interface, *J. Electrochem. Soc.*, 138, 3361–3369.
- SAND, W., JOZSA, P. – G., KOVACS, Z. – M., SÁSÁRAN, N., SCHIPPERS, A., 2007, Long-term evaluation of acid rock drainage mitigation measures in large lysimeters, *Journal of Geochemical Exploration*, 92, 205–211.
- SASAKI, K., TSUNEKAWA, M., TANAKA, S., KONNO, H., 1996, Suppression of microbially mediated dissolution of pyrite by originally dissolved fulvic acids and related compounds, *Colloids and Surfaces A*, 119, 241–252.
- SHUEY, R. T., 1975. *Semiconducting Ore Minerals*, Elsevier, New York.
- STRATMANN, M., FÜRBEETH, W., GRUNDMAIER, G., LÖSCH, R., REINARTZ, C.R., 1995, Corrosion inhibition by adsorbed organic monolayers, in: *Corrosion mechanisms in theory and practice*, (P. Marcus, J. Oudar - editors), Marcel Dekker, New York, 373–419.
- TWARDOWSKA, I., SZCZEPAŃSKA, J., WITCZAK, S., 1988, Influence of wastes from the coal mining industry on the aqueous environment, estimation of hazard, prediction and prevention, *Prace i Studia 35*, Ossolineum, Wrocław (in Polish).
- ZHANG, X., BORDA, M. J., SCHOONEN, M. A. A., STRONGIN, D.R., 2003, Pyrite oxidation inhibition by a cross-linked lipid coating, *Geochem. Trans.*, 4, 8–11.

Received May 12, 2011; reviewed; accepted June 9, 2011

PRE-SORTING OF ASYMMETRIC FEEDS USING COLLECTIVE PARTICLE EJECTION

Rolf Arne KLEIV

Dept. of Geology and Min. Resources Eng., Norwegian University of Science and Technology, N-7491 Trondheim, Norway, rolf.kleiv@ntnu.no

Abstract. This paper presents a theoretical analysis of the potential capacity enhancement that can be obtained by employing collective particle ejection (CPE) in automated sensor-based sorting circuits when sorting asymmetric feeds. During CPE sorting particles are examined and categorised individually, but physically separated as a set containing several particles. A CPE sorter must be placed in serial connection with a subsequent conventional individual particle ejection sorter (i.e. an IPE sorter) in order to achieve complete separation of individual particles, thus creating a CPE:IPE circuit. The relative capacity of this circuit per unit investment cost, compared with a conventional sorting circuit, depends on the relative concentration of the particle categories in the feed and decreases as the particle distribution becomes more symmetrical. As demonstrated in this paper, CPE can yield a significant capacity enhancement per unit investment cost when sorting sufficiently asymmetric feeds in situations where the capacity of conventional IPE sorting is limited by the actual physical separation of the particles and not their presentation and examination or the data analysis. The relative processing period ratio is the key parameter governing the feasibility of the CPE:IPE circuit and must be determined as a function of set size.

keywords: sensor-based sorting, ore sorting; pre-sorting, pre-concentration, sorting algorithms

1. Introduction

In spite of its long history, the revolution in computer technology and the development of fast, accurate and advanced sensors along the entire electromagnetic spectrum, automated sensor-based sorting has still to reach its full potential in the minerals industry. Reviews of sorting technology and the future prospects of modern ore sorters have been compiled and analysed by a number of investigators over the last three decades, including Wyman (1985), Salter and Wyatt (1991), Arvidson (2002), Cutmore and Eberhardt (2002), Manouchehri (2003) and Wotruba and Harbeck (2010). Salter and Wyatt (1991) give a comprehensive overview of the perceived limits to the industrial application of ore sorting and discuss their relevance and accuracy. The process related challenges aside, low capacity per unit investment cost

is perhaps, justly or unjustly, the most frequently used argument against the implementation of ore sorting.

Automated sensor-based sorting can be divided into four sub-processes comprising presentation, examination (i.e. measurement of particle properties), data analysis and physical separation. Even though all four sub-processes must be integrated to form an optimal sorting solution, and each could act as the limiting factor with respect to capacity and separation efficiency, most attention by far has been given to the examination step and the development and application of new sensors. A vast range of sophisticated measuring principles have been suggested in addition to the basic photometric or optical techniques using colour scanners or cameras. In their 1991 review of sorting technology Salter and Wyatt listed the following possible examination principles: Raman spectroscopy, FTIR, laser and glow discharge spectroscopy, scanning electron microscopy, Auger, SIMS, XPS, x-ray diffraction and fluorescence, gas and ion chromatography, mass spectroscopy, thermal analysis, inductively coupled plasma and atomic adsorption spectrometry, neutron activation analysis, radon and radioactivity measurements, particle size analysis and various electrochemical techniques. Since the early 1990s the feasibility of more and more of the techniques on this list have changed from theoretical to practical and still more techniques have been added (Wotruba and Harbeck, 2010). However, the practical application of ore sorting in the mineral industry is still dominated by photometry or the use of natural radiation sensors.

Considering the last few decades' exponential growth in data processing power and the continuing development of sensors with higher and higher acquisition speeds, the number of potential applications where the actual mechanical separation of the individual particles will represent the capacity limiting step is likely to increase. Obviously, more attention should be devoted to the development of low cost, highly efficient ejection systems. However, shifting the rate limiting step from examination to separation should also spur a closer evaluation and analysis of the fundamental algorithms on which the sorting process is based. As will be shown in this paper the concept of collective particle ejection of individually examined particles could offer a significant increase in capacity per unit investment cost when processing sufficiently asymmetric feeds (i.e. feeds dominated by one category of particles). Alternatively, the potential capacity enhancement could allow for a slower but cheaper separation solution (in terms of both investment and operating costs).

The concept proposed in this paper has limited applicability as it is by its own nature restricted by the composition of the feed and would require modified technical solutions for particle presentation and separation. However, given a case where these conditions are satisfied, the increase in capacity per unit investment cost could be economically significant and would as such contribute to extending ore sorting to new applications. With this in mind, the scope of this paper is to demonstrate the concept's potential by investigating the relative capacity enhancement per unit investment cost (i.e. relative to a conventional sorting circuit) rather than its technical implementation.

2. Concept outline

The sorting concept described in this paper is, for lack of a better phrase, referred to as collective particle ejection sorting (i.e. CPE sorting). The working principles of a CPE sorter are identical to those of a conventional sorter up until the actual separation step except for the fact that the particles are presented in discrete sets (i.e. a limited number of closely spaced particles). The particles are still being examined and categorised according to the separation criterion as individual entities. During the separation step each set is rejected or accepted as a single unit based on its composition of categorised particles. The particle sets are defined by their set size s , a parameter that simply describes the number of particles in the collection. Consequently, conventional sorting, hereby referred to as individual particle ejection sorting (i.e. IPE sorting), can be regarded as a special case of CPE sorting with a set size of 1.

Since a CPE sorter separates particle sets rather than individual particles it must be combined with a subsequent IPE sorter in order to achieve complete separation. When the sorting criterion defines two particle categories and the CPE sorter is able to produce two different products, particle sets consisting exclusively of particles belonging to the predominant category would report to one product, while sets containing both particle categories would report to another. As illustrated in Fig. 1, the latter product would then be processed by a conventional IPE sorter. It is important to note that the particles subjected to CPE sorting are still identified and categorised on an individual basis according to the same preset sorting criterion used for the IPE sorting. Hence, despite the fact that the particles are not physically separated on an individual basis, CPE sorting is fundamentally different from bulk sorting where the evaluation is based on parameters (particle averages) describing the set as a whole. Bulk sorting offers simpler ore handling and higher throughput, but has the disadvantage of less discrimination in ore selection.

As will be shown in this paper, the concept of CPE pre-sorting illustrated in Fig. 1 could offer enhanced overall capacity per unit investment cost provided that the following conditions are satisfied:

- The capacity of the IPE sorter is limited by the rate of physical separation (i.e. particle ejection) rather than particle presentation, examination and data analysis.
- The feed is sufficiently asymmetric, i.e. it is dominated by one type of particle.

In order to utilise CPE the feed particles should be presented in sets with sufficient distance on the separator belt between each set to allow effective separation. As opposed to IPE where such a distance is required between each individual particle CPE only requires sufficient spacing between the particles in the same set to correctly identify and categorise them as individual particles. Hence, if the first condition is satisfied, the CPE sorter would be able to process a higher number of particles per unit time than the IPE sorter due to a shorter average inter-particle distance of the feed.

The second condition is a result of the fact that the gain in capacity obtained from utilising a CPE pre-sorting step decreases as the feed becomes more symmetric. When

processing a near symmetric feed the majority of the particle sets will contain both particle categories and will as such have to be processed by the IPE sorter anyway (as shown in Eq. 1). Moving towards more symmetric feeds a point will be reached where the marginal capacity gain obtained by CPE pre-sorting fails to justify the investment.

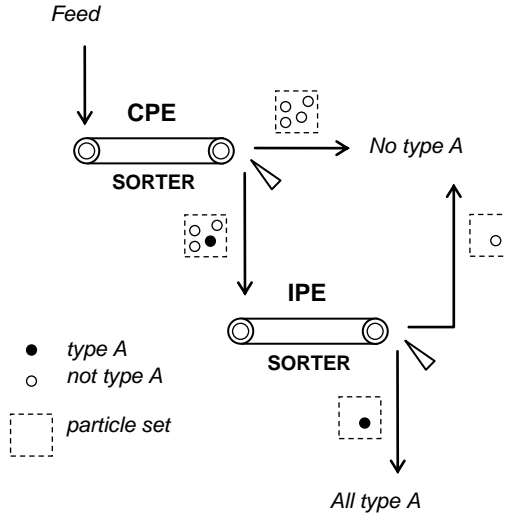


Fig. 1. The serial CPE:IPE circuit processing a feed dominated by 'not type A' particles

When assessing the capacity per unit investment cost of the proposed CPE:IPE circuit it could, as a starting point, be compared to a circuit consisting of two parallel IPE sorters. It is reasonable to assume that these two alternatives would represent roughly similar investment costs as they rely on the same number of sensors, data processing units and physical presentation and separation systems. However, the CPE:IPE circuit holds a potential for further capacity enhancement per unit investment cost if the information obtained during the pre-sorting step can be utilised by the subsequent IPE sorter. If the order of the particles that have been categorised by the CPE sorter can be preserved until they are fed to the IPE sorter, the latter sorting step simply becomes a matter of identifying the position of the already categorised particles prior to the physical separation. This would require some engineering with respect to the ejection system of the CPE sorter, but it would allow for the use of a very simple (i.e. inexpensive) optical sensor during the subsequent IPE step. Alternatively, the CPE sorter could 'tag' the particles (e.g. by using an ink jet) thus eliminating the need to keep the particle order undisturbed. When the sorting criterion relies on the use of expensive advanced sensors, either option would reduce the investment cost by limiting the need for these sensors to the pre-sorting step alone. Hence, in the extreme (and unlikely) case where the cost of the advanced sensors

completely dominates the investment costs the capacity of the proposed CPE:IPE circuit should be compared to that of a single IPE sorter.

3. Mathematical modelling and analysis

3.1. Derivation of relative capacity

Consider the CPE:IPE circuit shown in Fig. 1, where a CPE sorter with a fixed set size s operates in serial connection with a subsequent IPE sorter. Assume that the individual particles of the original feed can be classified according to a preset definition as either 'type A' or 'not type A'. Let x represent the number fraction (i.e. the concentration) of 'type A' particles in the feed to the CPE sorter and assume further that 'type A' defines the minority category. According to this definition x is always smaller than or equal to 0.5. The fraction of the total feed that still needs to be processed by the IPE sorter is then given by:

$$\alpha = 1 - (1 - x)^s . \quad (1)$$

This is easily derived from the fundamental laws of probability, as the fraction α is equal to the relative number of selections that only contain 'not type A' particles.

Assume that the CPE sorter is fed at a constant feed rate. Let t_s represent the processing period for a single set of size s processed by the CPE sorter. The processing period can be defined as the average time interval between the separations of two consecutive sets. Hence, the inverse of this value represents the total number of sets processed per time unit. Correspondingly, let t_1 represent the IPE sorter processing period for a single particle (i.e. the processing period for a set of size $s = 1$). Since the sorter is fed at a constant rate both t_s and t_1 can be assumed to be constants.

The two sorters operate in a serial connection and either could in theory act as the capacity limiting step. As the IPE sorter only has to process the fraction α of the original feed (i.e. the feed entering the CPE sorter) it follows that the overall capacity of the circuit is limited by the capacity of the IPE sorter only when:

$$\alpha t_1 > \frac{t_s}{s} . \quad (2)$$

As shown by Eq. (1), this condition is also a function of x . Consequently, by combining Eqs. (1) and (2), the IPE sorter represents the capacity limiting step when:

$$x > 1 - \left(\frac{s - \beta}{s} \right)^{\frac{1}{s}} , \quad (3)$$

where β , the relative processing period ratio, is defined as:

$$\beta = \frac{t_s}{t_1} . \quad (4)$$

Hence, the concentration of 'type A' particles in the original feed that will produce capacity equilibrium between the two sorting steps is given by:

$$x_E = 1 - \left(\frac{s - \beta}{s} \right)^{\frac{1}{s}}. \quad (5)$$

The overall capacity of the CPE:IPE circuit, in terms of the number of original feed particles processed per unit time, can then be expressed as:

$$C_{CPE:IPE} = \frac{s}{t_s}, \quad \text{when } x \leq x_E, \quad (6.a)$$

$$C_{CPE:IPE} = \frac{1}{\alpha t_1}, \quad \text{when } x > x_E. \quad (6.b)$$

In comparison, the overall capacity of a single IPE is simply given by:

$$C_{IPE} = \frac{1}{t_1}. \quad (7)$$

To facilitate easy comparison, the relative capacity per unit investment cost of the proposed CPE:IPE circuit can be defined as:

$$\varepsilon = \frac{C_{CPE:IPE}}{\gamma \cdot C_{IPE}}. \quad (8)$$

Here, the factor γ determines the basis of comparison in terms of the number of IPE sorters that could be purchased for the same investment cost. As explained in chapter 2, the value of γ could vary between 1 and 2 (2 being a far more likely value and 1 being the 'theoretical limit'). Combining Eqs. (1), (6), (7) and (8) will then yield:

$$\varepsilon = \frac{s}{\gamma \beta}, \quad \text{when } x \leq x_E, \quad (9.a)$$

$$\varepsilon = \frac{1}{\gamma - \gamma(1-x)^s}, \quad \text{when } x > x_E. \quad (9.b)$$

The proposed CPE:IPE circuit will represent an improvement in overall capacity when $\varepsilon > 1$. When $x > x_E$ the function $\varepsilon(x)$ is continuously decreasing (see Eq. (9b)). When $x \leq x_E$ the relative capacity is not a function of concentration (see Eq. (9a)) and ε is at its maximum. It is also clear from Eq. (9.a) that $\varepsilon \geq 1$ implies that $s \geq \gamma\beta$. Hence, as long as the latter condition is satisfied, x_c given by Eq. (10) represents the critical concentration of 'type A' particles in the original feed (i.e. the upper concentration limit) with respect to the useful applicability of the CPE:IPE circuit.

$$x_C = 1 - \left(\frac{\gamma - 1}{\gamma} \right)^{\frac{1}{s}}, \quad \text{when } s \geq \gamma\beta. \quad (10)$$

When $x \geq x_C$, the feed is too symmetric to benefit from CPE pre-sorting.

3.2. Exploring relative capacity

As shown in section 3.1, the relative capacity of the CPE:IPE circuit is easily determined once the set size s and the relative processing period ratio β is given. As a starting point, the value of β could be assumed to be close to 1 since the processing periods are largely governed by the response and return time of the ejection system and not the number of particles that are ejected during each separation. However, depending on the engineering solution, larger sets could require higher values for β . Fig. 2 presents the relative capacity of the CPE:IPE circuit per unit investment cost as a function of x for different values of s at $\beta = 1$ and $\gamma = 2$, whereas Fig 3 exemplifies how the relative capacity depends on the value of β for a fixed set size $s = 4$. In practice, the exact relationship between s and β should be determined for the actual sorter in question.

Figures 2 and 3 demonstrate the relative capacity's strong dependency on concentration when the latter grows larger than x_E . The maximum capacity for a given set size is achieved in the concentration range where the CPE sorter is the capacity limiting step (i.e. $x \leq x_E$). In this region the relative capacity is independent of concentration. From a practical point of view, it is necessary to determine the optimal set size for a given concentration. As can be seen from Fig. 2, the concentration variable can be divided into discrete intervals; each with their own optimal value of s . Equating Eq. (9.a) using a set size of $s - 1$ with Eq. (9.b) with a set size of s will yield the following upper concentration limit for s as the optimal set size:

$$x_U = 1 - \left(\frac{(s-1) - \beta}{(s-1)} \right)^{\frac{1}{s}}. \quad (11)$$

The corresponding lower limit x_L is easily found since $x_L(s) = x_U(s+1)$:

$$x_L = 1 - \left(\frac{s - \beta}{s} \right)^{\frac{1}{s+1}}. \quad (12)$$

Table 1 summarises the information found in Fig. 2 by presenting the characteristic concentrations x_E , x_C , x_U and x_L and the maximum relative capacity $\varepsilon(x_E)$ as a function of set size for $\beta = 1$ and $\gamma = 2$.

Note that x_E , x_U and x_L are independent of γ but depends on β , whereas x_C is independent of β (provided that $s \geq \gamma\beta$ so that x_C is defined), but depend on γ . The maximum relative capacity (i.e. $\varepsilon(x_E)$) at a given set size is simply proportional to

$1/\gamma\beta$. Hence, as shown in Fig. 3, halving the value of γ from the default value of 2 would double the relative capacity of the circuit.

Table 1. Characteristic concentration and maximum relative capacity for $\beta=1$ and $\gamma=2$.

| s | 2 | 3 | 4 | 5 | 6 |
|--------------------|-------|-------|-------|-------|-------|
| x_E | 0.293 | 0.126 | 0.069 | 0.044 | 0.030 |
| x_C | 0.293 | 0.206 | 0.159 | 0.129 | 0.109 |
| x_U | - | 0.206 | 0.096 | 0.056 | 0.037 |
| x_L | 0.206 | 0.096 | 0.056 | 0.037 | 0.026 |
| $\varepsilon(x_E)$ | 1 | 1.5 | 2 | 2.5 | 3 |

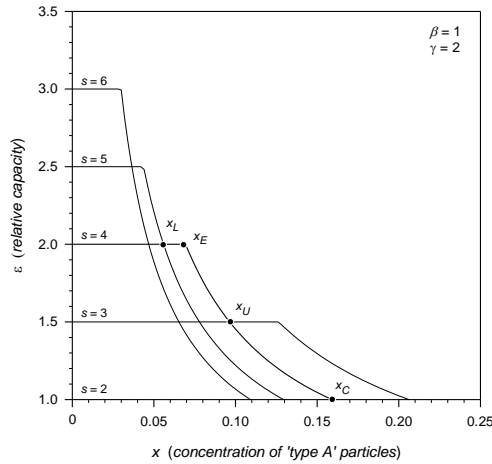


Fig. 2. Relative capacity as a function of x and s at $\beta=1$ and $\gamma=2$. The characteristic concentrations x_E , x_C , x_U and x_L (see Eqs. 5, 10, 11 and 12, respectively) are shown for $s=4$.

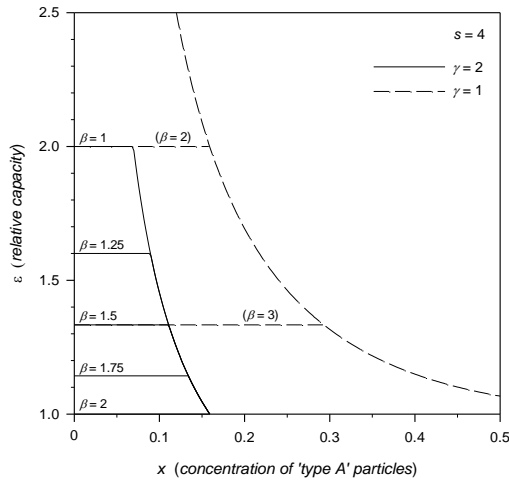


Fig. 3. Relative capacity as a function of x and β at $s=4$

3.3. Theoretical limitations and practical applications

The useful applicability of the CPE:IPE concept is limited by its underlying premise; i.e. that the capacity is not limited by presentation, examination or data analysis, but by the actual physical separation of the particles. In other words, the average amount of time required to correctly categorise a single particle and relay the information to the ejector system must be lower than the processing period t_s divided by the set size s . In practice, the function $t_s(s)$ (and consequently $\beta(s)$) will very effectively limit the value of s and the potential gain in relative capacity. However, even $s = 3$ would yield a significant gain provided that the feed is sufficiently asymmetric and β is not too large. Using this set size the maximum capacity increase of 50% at $\beta = 1$ is attainable up to $x = 0.126$, whereas $\beta = 1.25$ offers a maximum increase of 20% up to 0.164.

The practical feasibility of the CPE sorting concept hinges on the relative processing period β which is a function of the technical solutions on which the sorter's ejection system is based. As argued earlier in this paper, small set sizes could offer t_s values close to that of t_1 , thus yielding a β close to unity. This is likely to be the case for the sorting of coarse particles where mechanical ejector systems (e.g. mechanical flaps) are used rather than air nozzles to achieve physical separation. Mechanical ejector systems require less energy during operation, but are slower than air nozzles and are replaced by the latter when the feed particle size becomes too small for the mechanical systems to handle efficiently. This offers an alternative scope for the proposed CPE sorting concept as it could equally well be used to extend the useful size range of mechanical flaps by trading the potential capacity enhancement for lower energy costs during operation as well as reduced investment costs.

As stated in the introduction and emphasised further in chapter 2 the proposed CPE:IPE circuit would require modified technical solutions for particle presentation and separation. A variety of different implementations would be possible and cost-efficient elements could probably be adapted from packing and sorting machines utilised in the food Industry. However, discussing the design and construction of such systems are beyond the scope of this paper.

4. Conclusions

The following conclusions can be drawn from the theoretical analysis comparing the concept of collective particle ejection sorting (i.e. CPE sorting) of particle sets containing several particles with conventional individual particle ejection sorting (i.e. IPE sorting):

- CPE can yield a significant capacity enhancement per unit investment cost when sorting sufficiently asymmetric feeds in situations where the capacity of conventional IPE sorting is limited by the actual physical separation of the particles and not their presentation and examination or the data analysis.

- A CPE sorter must be placed in serial connection with a subsequent IPE sorter in order to achieve complete separation of individual particles. For a given set size, as long as the relative concentration of particles belonging to the minority category is sufficiently low the capacity of this circuit (i.e. the CPE:IPE circuit) is limited by the CPE step. When this is the case the capacity is at its maximum level and does not depend upon the concentration.
- The relative processing period ratio is the key parameter governing the feasibility of the CPE:IPE circuit and must be determined as a function of set size.
- The relative capacity per unit investment cost of the CPE:IPE circuit can be further enhanced if the information obtained during the CPE step can be utilised by the subsequent IPE step, thus omitting the need for a dual set of advanced sensors.
- CPE can be used to extend the useful size range of mechanical flaps by trading the potential capacity enhancement for lower energy costs during operation.

References

- ARVIDSON, B., 2002, Photometric ore sorting. In: *Minerals Processing Plant Design, Practice and Control Proceedings*, vol. 1, Mular, A.L., Halbe, D.N., Barratt, D.J. (Eds), SME, Littleton, USA, 1033–1048.
- CUTMORE, N.G., EBERHARDT, J.E., 2002, The Future of Ore Sorting in Mineral Processing. In: *Proc. International Conference on the Sustainable Processing of Minerals*, Cairns, 287–289.
- MANOUCHEHRI, H.R., 2003, Sorting: possibilities, limitations and future. In: *Proc. of Conference of Mineral Processing*, Luleå, 1–17.
- SALTER, J.D., WYATT, N.P.G., 1991, Sorting in the Minerals Industry: Past, Present, and Future. *Minerals Engineering*, 4 (7–11), 779–796.
- WOTRUBA, H., HARBECK, H., 2010, Sensor-Based Sorting. In: *Ullmann's Encyclopedia of Industrial Chemistry*, Wiley-VCH Verlag.
- WYMAN, R.A., 1985, Sorting by electronic selection. *SME-Handbook on Mineral Processing*, Weiss, N.L. (Ed.), SME, New York, 7.5–7.35.

Received May 5, 2011; reviewed; accepted July 7, 2011

ROLE OF STARCH AND METABISUPHITE ON PURE PYRITE AND PYRITIC COPPER ORE FLOTATION

Gulay BULUT *, Adnan CEYLAN**, Burhan SOYLU ***, Ferihan GOKTEPE ****

* Istanbul Technical University, Faculty of Mines, Mineral Processing Department, 34469, Maslak, Istanbul, TURKEY, e-mail: gbulut@itu.edu.tr

** Head Engineer, Park Electric Production Mining and Industry A.Ş., Madenköy, Şirvan-SİİRT/TURKEY, e-mail: adnanceylan1@hotmail.com

*** bsoylu85@hotmail.com

**** Balıkesir University, Balıkesir Technical College, Mining Department, 10145, Balıkesir/TURKEY, e-mail: fgoktepe@balikesir.edu.tr

Abstract. Depression of pyrite is very important in sulphide ore flotation. This paper investigates the role of non-toxic depressants on the flotation of pyrite. Starch and meta bisulphite were used as a depressant for pure pyrite sample and a pyritic copper ore at two different pHs values. pH was 6.5 and 10 in pure pyrite study while it was 6.9 and 12 in pyritic ore study. This study showed that metabisulphite is more effective at pH 6.5 or 6.9 than pH 10 or 12, while starch is more effective at pH 12. Also, higher dosages of meta bisulphite are required for depression of pyrite. Pure pyrite and pyritic copper ore study gave similar results.

keywords: flotation, pyrite, depressant, starch, metabisulphite

1. Introduction

Chalcopyrite is often associated with pyrite and economical extraction of copper demands selective depression of pyrite from chalcopyrite. Conventionally sodium cyanide is used as a depressant in alkaline conditions for the selective depression of pyrite from chalcopyrite during the froth flotation process, leading to potentially disastrous environmental consequences (Ball and Rickards, 1976). Therefore, development of alternate reagents, concerning environment, have been interested in for researchers. Polysaccharide based reagents have been utilized in the mineral industry, principally as a depressant for a variety of minerals. These organic polymers are not only nontoxic but are also biodegradable and relatively inexpensive (Rath et al., 1991).

Pioneering contributions have been made by Laskowski et al. (1991, 2007), Laskowski and Liu (1999a, 1999b), Liu et al. (2000) and by Lopez et al. (2004) with respect to interaction of dextrin with several sulfides and oxides. These studies

revealed that unmodified natural polysaccharides, such as dextrin, starch or guar gum, adsorbed on mineral surfaces through interactions with metal-hydroxylated species on the mineral surface. The direct consequence of the interaction of natural polysaccharides with metal-hydroxylated species and thus the adsorption is strongly dependent on pH.

Sulphur-oxy depressants are added to the flotation pulp in the form of sulphite (SO_3^{2-}), bisulphite (HSO_3^-), meta bisulphite ($\text{S}_2\text{O}_5^{2-}$) or sulphur dioxide (SO_2) for depression of pyrite, sphalerite and galena (Grano et al., 1997a, 1997b; Khemeleva et al., 2003, 2005, 2006; Shen et al., 2001; Chander and Khan, 2000). In general, mechanisms governing sulphide mineral flotation behavior by sulphur-oxy species can be grouped according to those that involve interaction of sulphite with collector (xanthate), either in solution or its adsorbed state (Grano et al., 1997).

Shen et al. (2001) studied the effect of sodium sulphite on the flotation of sphalerite and pyrite in the presence of copper ions and they reported that sulphite promoted the formation of copper hydroxide on the surface of pyrite leading depression. Yamamoto (1980) proposed that sulphite ions depressed pyrite by desorbing xanthate species from the surface.

Although the use of metabisulphite for the depression of sulphide minerals is rather limited, Gül (2007) and Gül et al. (2008) used non-toxic reagents such as sodium metabisulphate, coustic starch, zinc sulphate and activated carbon instead of highly toxic reagents potassium bichromate and sodium cyanide that successfully depressed pyrite and separation of chalcopyrite, galena and sphalerite have been achieved.

In this comparative study, starch and metabisulphite are used as an alternative and non-toxic depressant for the depression of pure pyrite. Then pyritic copper ore was used to compare the results with pure pyrite sample.

2. Experimental

2.1. Material

In this study pure a pyrite sample for fundamental studies and pyritic copper ore to prove fundamental studies in real situation were used. Pure pyrite sample was obtained from Murgul-Artvin in the northeast of Turkey. The sample was upgraded by hand picking and purified using some mineral processing methods such as jigging. Chemical analyses of pure pyrite and ore samples are given in Table 1. Analyses proved that the pyrite sample contained 97% pyrite, 1-2% chalcopyrite and 1-2% quartz. Chemical analyses and XRD results indicated that the pyrite sample is highly pure. Pyritic copper ore sample was taken from Siirt-Madenköy Copper Mine in South-East of Turkey. According to the mineralogical analyses, the ore sample contains chalcopyrite (CuFeS_2), sphalerite (ZnS), pyrite (FeS_2), galena (PbS), hematite (Fe_2O_3), limonite ($\text{FeO}(\text{OH})\cdot n\text{H}_2\text{O}$), calcite (CaCO_3) and quartz (SiO_2) (Ceylan, 2009 and Ceylan and Bulut, 2010). Figure 1 shows the above minerals growth in the ore.

Mineralogical study also showed that about 50% of ore is formed by pyrite, as a major mineral in the ore.

Table 1. Chemical analyses of the samples

| Compound | Pure Pyrite Sample % | Pyritic Copper Ore Sample % |
|------------------|----------------------|-----------------------------|
| Fe | 42.43 | 27.65 |
| S | 49.40 | 27.22 |
| Pb | 0.025 | 0.13 |
| Zn | 0.005 | 0.43 |
| Cu | 0.056 | 1.60 |
| SiO ₂ | 0.595 | 20.35 |

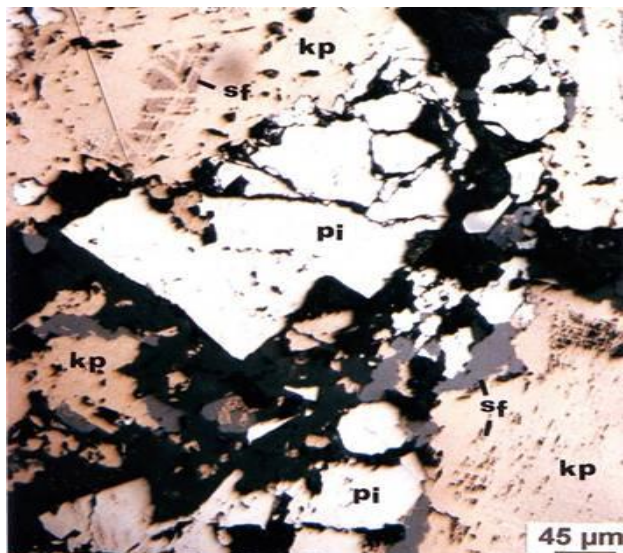


Fig. 1. Growth of minerals in the pyritic copper ore: chalcopyrite (kp) and sphalerite (sf) phases locked with cataclastic pyrite (pi) structure

2.2. Method

Experimental studies have been carried out with Denver flotation machines using 40 g of -100 μm pure pyrite in one dm^3 cell for pure pyrite study and 1 kg of approximately 53 μm ore sample in 2.5 liter cell for pyritic copper ore study. An agate mortar and pestle was used for grinding the pure pyrite sample while ore sample was ground with a ball mill prior to each test. In these experiments the effects of depressant type and dosages at two different pHs for flotation behavior of pyrite were investigated. The flotation flow-sheet with copper ore is given in Figure 2. Three stages cleaning were applied after obtaining a rougher-copper concentrate. Pyrite was removed with gangue minerals as tailings (Ceylan, 2009). In the rougher stage, reagents were added in three stages and 5 minutes flotation time was given for all the

stages. Therefore flotation time was totally 15 minutes in the rougher stage. In the cleaning stages, 8 minutes, 6 minutes and 4 minutes flotation times were given for the first, the second and the third stages respectively.

Aerophine 3418 A, which is a P-based sulphide collector and belongs to dialkyl dithiophosphinate group, was used as a collector in the flotation of pyrite. Sodium meta bisulphite ($\text{Na}_2\text{S}_2\text{O}_5$) and caustified starch were used as depressants. Methyl isobutyl carbinol (MIBC) was used as a frother, and lime and H_2SO_4 were used as pH regulators.

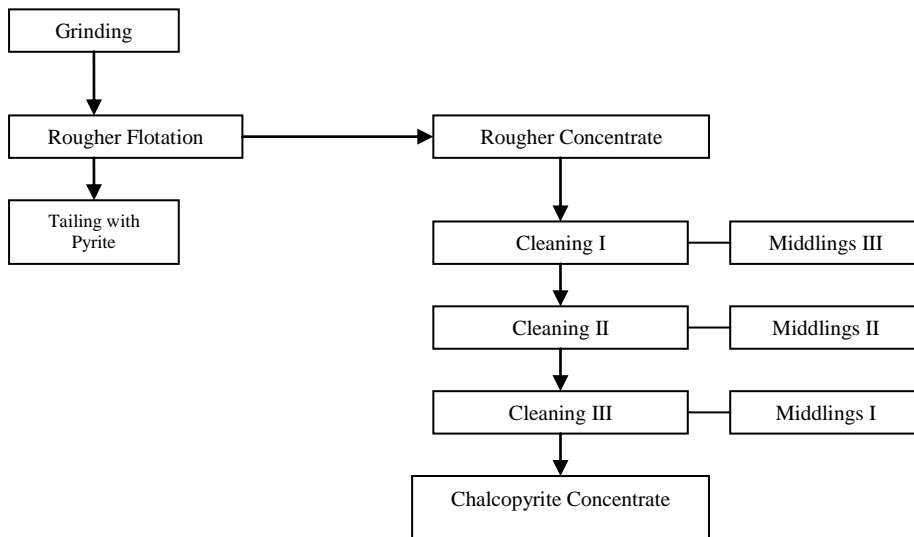


Fig. 2. The flow-sheet of ore flotation tests

3. Results and discussion

3.1. Pure pyrite study

3.1.1. Effect of starch

Starch was employed as a depressant on pyrite flotation at dosages between 1.7 and 17 mg/dm^3 at two different pHs; 6.5 (natural pH of sample) and 10. Aerophine 3418 A was used at 40 mg/dm^3 dosages and MIBC was used at 10 mg/dm^3 dosages. Collector dosages, frother dosages and conditioning time (3 min.) and flotation time (5 min.) were kept constant. The experimental results are given in Figure 3. This figure shows that flotation recovery decreased from 43.5 to 10.4% at pH 10 and it decreased from 74.9 to 59.2 % at pH 6.5. This shows that starch was more effective at pH 10 than pH 6.5. Although maximum depression was obtained with 1.7 mg/dm^3 starch at pH 6.5, increasing the starch dosages did not effect the pyrite flotation. In case of pH 10, again maximum depression occurred at 1.7 mg/dm^3 starch then increasing starch amount slightly depressed the pyrite. This shows that at low pH about 10% depression

occurred with 1.7 mg/dm^3 , while 21% depression occurred with the same dosages of starch at pH 6.5 where pyrite flotation is expected to be weak at pH 10. This can be explained as because starch adsorbed on mineral surface through the interaction with metal-hydroxylated species on the pyrite. So that increasing the pH caused the metal hydroxylated species on the pyrite and the adsorption of the starch occurred and more depression is occurred (Laskowski et al., 1991). Also organic reagents such as starch do not ionize in solution but form colloidal particles in the pulp which can be deposited on the mineral surfaces, preventing flotation in a similar manner to a slime coating (Wills, 1988). Similar results were obtained by Rath et al. (2000) who investigated the interaction of dextrin and guar gum with pyrite for adsorption, flotation and electrokinetic tests. They reported that higher adsorption densities of polysaccharides onto pyrite reveal in the pH range 7.5-11, that is maximum around pH 10 for dextrin and guar gum.

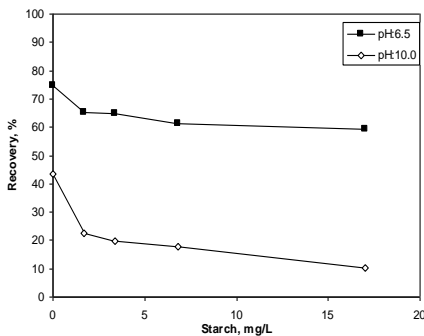


Fig. 3. The effect of starch on pure pyrite flotation

3.1.2. Effect of $\text{Na}_2\text{S}_2\text{O}_5$

The effect of $\text{Na}_2\text{S}_2\text{O}_5$ was investigated at pH 6.5 and 10. The amount of $\text{Na}_2\text{S}_2\text{O}_5$ was between 34 mg/dm^3 and 134 mg/dm^3 , and the amounts of Aerophine 3418 A and MIBC were the same as in starch experiments. The results are given in Fig. 4. Flotation recovery decreased from 43% to 4% at pH 10, and from 75% to 23.3% at pH 6.5 with 134 mg/dm^3 metabisulphide addition. Decrease in recovery with metabisulphate was about 40% at pH 10 where pyrite flotation is already low due to high pH and about 50% decrease in recovery was obtained at pH 6.5. Test results reveal that metabisulphite is more effective at pH 6.5 than at pH 10 but trend was similar. Actually almost complete depression has already occurred at 100 mg/dm^3 dosage at pH 10. But at pH 6.5, maximum depression, about 25%, was obtained by increasing dosages from 100 mg/dm^3 to 134 mg/dm^3 . That means that higher dosages are required to depress pyrite at lower pHs. In the literature it has been reported that when sulphur-oxy depressants are used these involve interaction of sulphite with collector either in solution or its adsorbed state and sulphite ions depressed pyrite by desorbing xanthate species from the surface (Grano et al., 1997 and Yamamoto, 1980).

The surface of pyrite can adsorb sulphite ions which prevent collector adsorption (Wills, 1988). Therefore the change in mineral floatability indicates that sulphide or

sulphite should have a greater affinity for surface sites than the adsorbed collector species. On the other hand, according to Woods (1972) activation and depression during flotation is worth considering in terms of mixed potential mechanism. In the literature, it is proposed that sulphide and sulphite prevent the flotation of pyrite because their oxidation potentials in alkaline solutions are more positive than that of xanthate (Hoyack and Raghavan, 1987). Janetski et al. (1977) investigated pyrite flotation and depression and reported that the solution containing sulphide, xanthate and oxygen, a mixed potential will be cathodic to the xanthate / dixanthogen potential and hence dixanthogen will not be formed and mineral will not be rendered floatable. Therefore presence of sulphide in solution introduces an anodic process which will occur in preference to xanthate oxidation. The mechanism for depression of sulphides floated with xanthate with addition of sodium sulphide producing a drop in the redox potential causing desorption of xanthate from the mineral (chemical displacement process) and a subsequent loss of flotation (Gebhardth and Kotlayar, 1991). Figure 5 shows the relation of pulp potential and depressant amount and pyrite recovery (Goktepe, 1992). This shows that increasing the addition of NaSH depresses pyrite and 1500 g/Mg dosage addition, complete depression occurred. Pulp potential was also recorded and the change in potential shows that pulp potential decreased as NaSH amount increased. When pulp potential-recovery and NaSH amount are considered together, it can be seen that recovery decreased as pulp potential decreased. In the literature there are some studies showing that solution redox potential may be reduced by the introduction of sulphite.

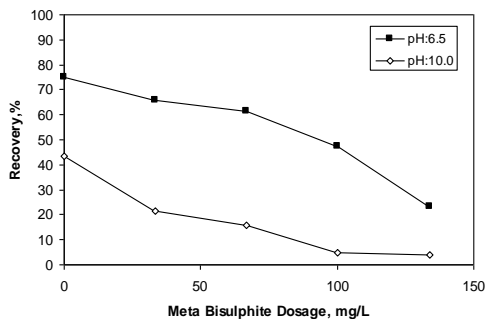


Fig. 4. The effect of sodium meta bisulphite on pyrite flotation

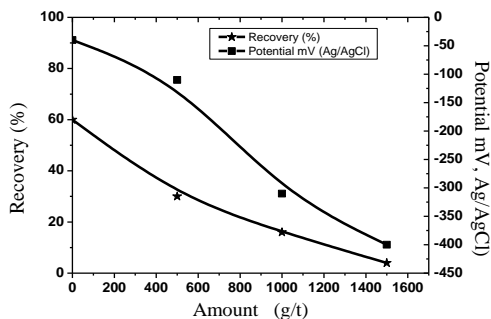


Fig. 5. Effect of NaSH amount for pyrite flotation and for pulp potential. (conditions: 2 mg/dm³ xanthate, pH 6, NaSH as a reducing reagent and potential was measured by platinum electrode) (Goktepe, 1992)

Miller (1970) considered that sulphite should act as a depressant for pyrite, due both to its reducing properties as well as its specific adsorption onto pyrite. As xanthate adsorption onto pyrite and a variety of other sulphide minerals is believed to take place via xanthate dimerisation to dixanthogen, the introduction of a more reducing couple may minimise adsorption via this mechanism but this mechanism is not specific with respect to the mineral Miller (1970). Zeta potential of pyrite in the

presence and absence of sodium sulphite was also measured by Miller (1970), which gave evidence of specific adsorption of sulphite ion onto pyrite.

When Figures 3 and 4 are compared to show the effect of depressant types, it can be said that to obtain the similar amount of depression, higher dosages of meta bisulphite is required than starch but metabisulphite is more effective as a depressant.

3.2. Pyritic copper ore

3.2.1. Effect of starch

First, flotation was carried out with ore sample without any depressant at natural pH of sample (pH: 6.9) where 50 g/ton Aerophine 3418 A and 50 g/ton MIBC (Methyl iso-butyl carbinol) were used as reagents in rougher stage. Three cleaning stages were applied and only 25 g/ton MIBC was used in these stages. Then the effect of starch was investigated at pHs 6.9 and 12.1 where 50 g/ton starch, 50 g/ton Aerophine 3418 A and 50 g/ton MIBC were kept constant in all rougher tests. In the three cleaning stages only 25 g/ton starch and 20 g/ton MIBC were used. The results are shown in Table 2.

Table 2. The effect of starch on the pyritic copper ore flotation

| pH | Products | Weight (%) | Cu (%) | |
|------------------------------|-------------|------------|--------|----------|
| | | | Grade | Recovery |
| 6.9 without depressant | Concentrate | 9.30 | 10.22 | 63.00 |
| | Middling 1 | 1.90 | 4.01 | 5.10 |
| | Middling 2 | 1.70 | 3.59 | 4.00 |
| | Middling 3 | 6.20 | 1.28 | 5.30 |
| | Tailing | 80.90 | 0.42 | 22.60 |
| | Total | 100.00 | 1.504 | 100.00 |
| 6.9 | Concentrate | 3.20 | 11.91 | 23.80 |
| | Middling 1 | 4.20 | 6.82 | 18.30 |
| | Middling 2 | 5.10 | 3.92 | 12.60 |
| | Middling 3 | 13.30 | 2.81 | 23.70 |
| | Tailing | 74.20 | 0.46 | 21.60 |
| | Total | 100.00 | 1.58 | 100.00 |
| 12.1 | Concentrate | 4.20 | 19.92 | 52.20 |
| | Middling 1 | 1.60 | 11.23 | 11.70 |
| | Middling 2 | 1.60 | 6.57 | 6.70 |
| | Middling 3 | 5.80 | 3.02 | 10.90 |
| | Tailing | 86.80 | 0.34 | 18.50 |
| | Total | 100.00 | 1.59 | 100.00 |

As Table 2 shows, using starch as a depressant at pH 6.9 did not improve the results, besides lower recovery obtained at concentrate. This means that starch also depresses the copper as well. It can be seen that starch depresses pyrite at higher pH level more selectively but still lower recovery obtained comparing to the flotation without starch. It is generally believed that the depressive behavior of polysaccharides in differential flotation is not specific, or not as specific as inorganic depressants.

Because starch does not ionize in solution but form colloidal particles in the pulp which can be deposited on the mineral surface, preventing flotation in a similar manner to slime coating. Large quantities of these reagents will depress all minerals and they are not as selective as the electrolytic depressants (Wills, 1988). Although the adsorption mechanism of the polysaccharides has not yet been fully understood (Yamamoto, 1980; Bogusz et al., 1997) pointed out that, in interaction polysaccharides with mineral surface metal-hydroxylated species, selective adsorption of polysaccharides would not likely be achieved. This is because the flotation pulp contains various metal ions derived from dissolution of minerals, which inevitably mask the surfaces of minerals and make them all similar. In this study, especially at natural pH, starch also depressed copper when it is used in cleaning stages.

3.2.2. Effect of $\text{Na}_2\text{S}_2\text{O}_5$

The effect of $\text{Na}_2\text{S}_2\text{O}_5$ was investigated at pHs 6.9 and 12.1 and 5000 g/ton $\text{Na}_2\text{S}_2\text{O}_5$, 50 g/Mg Aerophine 3418 A and 50 g/Mg MIBC were used in all rougher stage. In the three cleaning stages only 20 g/Mg MIBC was used and results are given in Table 3. It can be seen from Table 3 that at pH 6.9 copper grade and recovery are better than at pH 12.1.

Table 3. The effect of $\text{Na}_2\text{S}_2\text{O}_5$ on the pyritic copper ore flotation

| pH | Products | Weight (%) | Cu (%) | |
|------|-------------|------------|--------|----------|
| | | | Grade | Recovery |
| 6.9 | Concentrate | 3.10 | 22.62 | 44.90 |
| | Middling 1 | 0.40 | 11.35 | 2.70 |
| | Middling 2 | 0.60 | 7.40 | 2.70 |
| | Middling 3 | 4.90 | 3.46 | 10.50 |
| | Tailing | 91.00 | 0.69 | 39.20 |
| | Total | 100.00 | 1.60 | 100.00 |
| 12.1 | Concentrate | 2.40 | 21.20 | 31.30 |
| | Middling 1 | 2.60 | 15.43 | 25.10 |
| | Middling 2 | 3.20 | 7.93 | 15.90 |
| | Middling 3 | 5.90 | 2.64 | 9.80 |
| | Tailing | 85.90 | 0.33 | 17.90 |
| | Total | 100.00 | 1.59 | 100.00 |

A copper concentrate with 22.62% Cu grade and 44.9% metal recovery was obtained at pH 6.9. Although grade of copper concentrate was 21.2% with 31.3% recovery at pH 12.1. These results prove that pyrite is depressed more effectively at lower pH level with $\text{Na}_2\text{S}_2\text{O}_5$. But incase of middlings higher grades and recoveries were obtained at pH 12.1. If two tailings were compared, lower grade and lower recovery obtained at pH 12.1, which shows that copper loss in tailing is lower at pH 12.1.

When two depressants were compared by considering only concentrate, $\text{Na}_2\text{S}_2\text{O}_5$ looks more effective depressant than starch. If middlings were added to the concentrate or if tailings were considered for the loss of copper at pH 12.1, it can be seen that similar results were obtained. These results confirm to the results obtained from pure mineral study. When two depressants are compared, $\text{Na}_2\text{S}_2\text{O}_5$ ensures more selectivity than starch.

4. Conclusions

It was found that starch is an effective depressant for pyrite even with a very small amount of addition. Furthermore, the effect of starch is more pronounced at alkaline pH than natural pH. The sodium metabisulphite ensures more selectivity compared to starch at natural pH for pure pyrite and pyritic copper ore flotation. Fundamental findings of this study (pure mineral) can be applied to an ore sample. The findings confirms each other. Overall both metabisulphite and starch can be an alternative depressant for pyrite instead of toxic depressants such as cyanide in the industrial applications.

References

- BALL B., RICKHARD R.S., 1976, A. M. Gaudin Memorial Volume, edited by M.C. Fuerstenau, American Institute of Mining Metallurgical and Petroleum Engineers, New York, 458.
- BOGUSZ E., BRIENNE S.R., BUTLER I., RAO S.R., FINCH J.A., 1997, Metal Ions and Dextrin Adsorption on Pyrite, *Minerals Engineering*, 10, 441–445.
- CEYLAN A., 2009, Concentration of the Siirt-Madenköy ores with flotation method, [Master thesis], (in Turkish), Istanbul Technical University.
- CEYLAN A., BULUT G., 2010, Treatment of the Siirt-Madenköy ores by flotation, in *Proceedings of XXV International Mineral Processing Congress (IMPC)*, Brisbane, Australia, 1737–1762.
- CHANDER S., KHAN A., 2000, Effect of Sulfur Dioxide on Flotation of Chalcopyrite, *International Journal of Mineral Processing*, 58, 45–55.
- GEBHARDT J.E., KOTLYAR D.G., 1991, Hydrosulphide depression of copper-sulphide minerals floated by xanthate and thionocarbamate collectors, [in] *Proceedings of the Copper 91, International Symposium, Vol.II, Mineral Processing and Process Control*, Ottawa, Canada, Pergamon Press, 201–215.
- GÖKTEPE F., 1992, Electrochemical potentials in flotation of complex sulphide ores, [PhD Thesis] (in English), University of Wales College of Cardiff, UK.
- GRANO S.R., JOHNSON N.W., RALSTON J., 1997a, Control of the solution interaction of metabisulphite and ethyl xanthate in the flotation of the Hilton ore of Mount Isa Mines Limited, Australia, *Minerals Engineering*, 10, No.1, 17–45.
- GRANO S.R., PRESTIDGE C.A., RALSTON J., 1997b, Solution interaction of ethyl xanthate and sulphite and its effect on galena flotation and xanthate adsorption, *International Journal of Mineral Processing*, 52, 161–186.
- GRANO S.R., CNOSSEN H., SKINNER W., PRESTIDGE C.A., RALSTON J., 1997, Surface modifications in the chalcopyrite-sulphite ion system. II. dithiophosphate collector adsorption study, *International Journal of Mineral Processing*, 50, 27–45.
- GÜL A., 2007, The role of $\text{Na}_2\text{S}_2\text{O}_5$ and activated carbon on the selective flotation of chalcopyrite from a copper ore using a dithiophosphine -type collector, *Mineral Processing. Extractive Metal.Rev.*, 28, 235–245.

- GÜL A., YÜCE A.E., SİRKECİ A.A., ÖZER M., 2008, Use of non-toxic depressants in the selective flotation of copper lead-zinc ores, *Canadian Metallurgical Quarterly*, 47, No.2, 111–118.
- HOYACK M.E. AND RAGHAVAN S., 1987, Interactions of aqueous sodium sulphite with pyrite and sphalerite, *Trans.Instn.Mining and Metallurgy (Section C:Mineral Process and Ext. Metallurgy)*, 96, C173–C178.
- JANETSKI N.D., WOODBURN S.I. AND WOOD R., 1977, An electrochemical investigation of pyrite flotation and depression, *International Journal of Mineral Processing*, 4, 227–239.
- KHMELEVA T.N., SKINNER W.M., BEATTIE D.A., 2005, Depression mechanisms of sodium bisulphite in the xanthate-collectorless flotation of copper activated sphalerite, *International Journal of Mineral Processing*, 76, 43–53.
- KHMELEVA T.N., CHAPELET J.K., SKINNER W.M., BEATTIE D.A., 2006, Depression mechanisms of sodium bisulphite in the xanthate-induced flotation of copper activated sphalerite, *International Journal of Mineral Processing*, 79, 61–75.
- KHMELEVA T.N., BEATTIE D.A., GEORGIEV T.V., SKINNER W.M., 2003, Surface study of the effect of sulphite ions on copper-activated pyrite pre-treated with xanthate, *Minerals Engineering*, 16, 601–608.
- LASKOWSKI J.S., LIU Q., BOLIN N.J., 1991, Polysaccharides in flotation of sulphides. Part 1. adsorption of polysaccharides onto mineral surfaces, *International Journal of Mineral Processing*, 33, 1–4, 223–234.
- LASKOWSKI J.S., LIU Q., 1999a, Polymers Mineral Processing- On the adsorption mechanism of carboxymethyl cellulose, edited by J.S. Laskowski, *MetSoc of CIM*, 357–373.
- LASKOWSKI J.S., LIU Q., 1999b, Polymers Mineral Processing- Adsorption of polysaccharides onto sulfides and their use in sulphide flotation, edited by J.S. Laskowski, *MetSoc of CIM*, 71–89.
- LASKOWSKI J.S., LIU Q., O'CONNOR C.T., 2007, Current understanding of the mechanism of polysaccharide adsorption at the mineral /aqueous solution interface, *International Journal of Mineral Processing*, 84, 59–68.
- LIU Q., ZHANG Y., LASKOWSKI J.S., 2000, The adsorption of polysaccharides onto mineral surfaces : an acid/base interaction, *International Journal of Mineral Processing*, 60, 229–245.
- LÓPEZ VALDIVIESO A., CELEDÓN CERVANTES T., SONG S., ROBLEDO CABRERA A., LASKOWSKI J. S., 2004, Dextrin as a non-toxic depressant for pyrite in flotation with xanthates as collector, *Minerals Engineering*, 17, Issues 9–10, 1001–1006.
- MILLER J.D., 1970, Pyrite depression by reduction of solution oxidation potential. Report to EPA Water Quality Office, Grant No. 12010 DIM.
- RATH R.K., SUBRAMANIAN S. AND PRADEEP T., 2000, Surface chemical studies on pyrite in the presence of polysaccharide-based flotation depressant, *Journal of Colloid and Interface Science*, 229, 82–91.
- SHEN W.Z., FORNASIERO D., RALSTON J., 2001, Flotation of sphalerite and pyrite in the presence of sodium sulfite, *International Journal of Mineral Processing*, 63, 17–28.
- WILLS B.A., 1988, *Mineral Processing Technology*, Fourth Edition, Published by the Pergamon Press,
- WOOD R., 1972, Electrochemistry of sulphide flotation, *Proc.Aust.Min.Met.*, 241, 53–61.
- YAMAMOTO T., 1980, Mechanism of depression of pyrite and sphalerite by sulphite, complex sulphide ores, edited by M.J. Jones, London, Institute of Mining and Metallurgy, 71–78.

Received April 23, 2011; reviewed; accepted June 20, 2011

INFLUENCE OF ELECTROLYTE PRESENCE ON BUBBLE MOTION IN SOLUTIONS OF SODIUM N-ALKYLSULFATES (C8, C10, C12)

Marcel KRZAN, Kazimierz MALYSA

J. Haber Institute of Catalysis and Surface Chemistry Polish Academy of Sciences, ul. Niezapominajek 8, 30-239 Krakow, Poland, nckrzan@cyf-kr.edu.pl

Abstract. Influence of sodium chloride (NaCl) addition on bubble velocity in solutions of sodium n-octylsulfate (SOS), n-decylsulfate (SDS) and n-dodecylsulfate (SDDS) was studied. The NaCl concentration was varied from 0.0001 to 0.05 M. Profiles of the bubble local velocity, that is, variations of the bubble local velocity with distance from the point of the bubble formation (capillary), were determined. At low sodium n-alkylsulfates concentrations the bubbles, after the acceleration stage, reached a maximum velocity followed by a deceleration stage tending to attain their terminal velocity. The maximum disappeared at high SOS, SDS and SDDS concentrations. Electrolyte alone did not affect the bubble velocity. However, addition of even small amounts of NaCl into solutions of sodium n-alkylsulfates affected the bubble motion. The effect was especially significant at low concentrations of the surfactants studied, where the bubble terminal velocity was lowered from ca. 30-34 cm/s (no electrolyte) down to ca. 15 cm/s in 0.01M NaCl presence. The electrolyte affected the bubble motion via its influence on state of the Dynamic Adsorption Layer formed over surface of the bubbles rising in sodium n-alkylsulfates solutions.

keywords: sodium n-octyl-, n-decyl-, n-dodecylsulfates, bubble velocity, adsorption coverage, electrolyte, surface tension, surface fluidity, dynamic adsorption layer

1. Introduction

Sodium n-alkylsulfates are typical anionic surfactants and some of them (n-dodecylsulfate) are used in froth flotation of various metals, salts, as frothers or/and collectors (Laskowski, 1998, 2010; Ceylan and Kucuk, 2004; Hu et al., 2005 and 2008; Watasharing et al., 2009; Rujirawanich, 2010). As sodium n-alkylsulfates adsorb strongly at solution/gas interfaces so their adsorption at surface of the rising bubbles affects (lowers) the bubble velocity. Adsorption of surface active substances (frothers) at bubble surface prevents also their coalescence, assures a froth layer formation and facilitates the grain attachment to bubbles (Laskowski, 1998; Nguyen and Schulze, 2004; Leja, 1982). Lower rise velocity means that the contact time between the colliding bubble and particle is longer and therefore, the probabilities of

the three phase contact (TPC) and stable bubble-grain aggregate formation are increased. Moreover, the bubble residence time and corresponding gas holdup are higher in the flotation column when the bubble rise velocity is smaller (Azgoni et al., 2007).

Presence and state of adsorption layer at the rising bubble surface can slow down in a great extent the bubble velocity as a result of retardation of fluidity of the gas/liquid interface (Clift et al., 1978; Sam et al., 1996; Krzan and Malysa, 2002ab; Krzan et al., 2007; Krzan and Malysa, 2009). When the bubble is formed in surfactant solution then adsorption coverage is uniform over its surface. Motion leads to inducement of uneven distribution of adsorbed molecules over the bubble surface as a result of viscous drag exerted by fluid on surface of the rising bubble. When the bubble starts to rise with a constant velocity (terminal velocity) it indicates that the dynamic architecture of adsorption layer (DAL) is established over the bubble interface. Establishment of the DAL means that the adsorption coverage is at minimum on the bubble top pole, while on the bottom the coverage is higher than the equilibrium one. It means that the surface tension gradient is induced over interface of the rising bubble, which retards mobility of the bubble interface. As a result of the bubble interface immobilization the hydrodynamic drag for the bubble motion is increased and the bubble rising velocity can be reduced, even by over 50%. For complete immobilization of interface of the rising bubbles a definite degree of adsorption coverage is needed, which magnitude is different for various surface active substances (Krzan and Malysa, 2002ab; Krzan et al., 2007). In the case of ionic surfactant their degree of adsorption coverage at solution/gas interface is strongly affected by the electrolyte presence, due to the electrolyte influence on electrostatic interaction in the adsorption layer formed.

Adsorption of ionic surfactant is affected by the properties of electric double layer (EDL) at the solution/gas interface. Electrostatic interactions (repulsive) in the EDL hinder the adsorption of further surfactant ions and facilitate the counterions adsorption. Davies and Rideal applied the Frumkin adsorption isotherm by considering the ionic interactions in the diffuse part of EDL under the assumption that the surfactant ions are adsorbed in the Stern layer (Davies and Rideal, 1963). However, their model overestimated the diffuse layer potential. Kalinin and Radke (1996) assumed that part of the counterions can form a pair with surfactant ions in the Stern layer, while another (not bonded part) is located in the diffusive region of EDL. Their model was applied successfully to describe experimental data of several authors concerning the dependence of the surface tension of air/aqueous and oil/aqueous solutions. Most recently an alternative model was proposed by Warszynski et al. (1998a), which assumes a penetration of counterions into the Stern layer and formation of the “surface quasi-two-dimensional electrolyte” (STDE). According to the STDE model the electroneutrality condition is not fulfilled at the interface, which bears a surface charge originating from the difference in surfactant ion and counterion surface concentrations. A good agreement between experimental data and theoretical calculations was obtained under an assumption that the ion specific effect is caused by

the difference of size of hydrated counterions. Warszynski et al. (1998a) showed that due to neutralization of the surface charge of adsorbed ionic surfactant molecules by counterions adsorbed in the Stern layer the surface tension of SDDS solutions can be shifted towards lower concentrations by more than order of magnitude. It was also shown recently (Krzan and Malysa, 2009) that addition of 0.05M of some inorganic electrolytes (NaCl/KCl/HCl/NaOH) and/or the pH variation caused significant diminishing the local velocity in low concentrations of SDDS solutions.

The paper presents results of studies on influence of sodium chloride (NaCl) addition on bubble motion in solutions of sodium n-octylsulfate, n-decylsulfate and n-dodecylsulfate of different concentrations. Variations of the bubble local velocity with distance from the point of the bubble formation (capillary) and the terminal velocity values were determined. The electrolyte (NaCl) concentration was varied from 0.0001 to 0.05M and it was found that NaCl presence even at so small amount as 0.001M can significantly affect motion of the rising bubbles. It is showed that the electrolyte affected the bubble motion via its influence on state of the Dynamic Adsorption Layer formed over surface of the bubbles rising in sodium n-alkylsulfates solutions.

2. Experimental

The experimental setup and procedures of the measurements were described in details elsewhere (Krzan and Malysa, 2002a; 2009). Single bubbles were formed in a controlled way at the capillary of inner diameter 0.075 mm and their motion after detachment was monitored over approximately 500 mm distance from the capillary using the Moticam 2000 camera and stroboscopic illumination (100 Hz). Values of the local velocity U of the bubble, at the given distance L from the capillary, were calculated as:

$$U = \frac{\sqrt{(x_2 - x_1)^2 + (y_2 - y_1)^2}}{\Delta t}$$

where (x_2, y_2) and (x_1, y_1) are coordinates of the subsequent positions of the bubble bottom pole, and Δt is the time interval (10 ms) between the stroboscopic lamp flashes. The distance L was measured as a distance between the capillary orifice and the bottom pole of the rising bubble. Bubble shape deformations were determined by measurements the horizontal and vertical diameters of the rising bubble.

Sodium n-octylsulfate (SOS), n-decylsulfate (SDS) and n-dodecylsulfate (SDDS) were the commercial reagents (Sigma-Aldrich and Fluka) and were used as received. Sodium chloride was heated up to 550°C in order to get rid of any surfactant contaminations. The solutions were prepared immediately before experiment to avoid any long term hydrolysis. Distilled water (Millipore – surface tension 72.4 mN/m, conductivity 0.05 μ S) was used for solution preparation.

The measurements were carried out at room temperature $22 \pm 1^\circ\text{C}$.

3. Results and discussion

Figure 1 presents the dependencies of the bubble local velocity on distance from the capillary for sodium n-octylsulfate (Fig. 1A), n-decylsulfate (Fig. 1B) and n-dodecylsulfate solutions of different concentrations. The dependence for the bubble local velocities in distilled water is presented as a reference to show effect of the surfactants studied on the velocity profiles. As seen in pure water the bubble terminal velocity, V_{term} , that is, the bubble constant velocity, was 34.8 ± 0.3 cm/s for the bubbles of diameter 1.48 ± 0.03 mm, formed at the capillary used in the study (inner diameter 0.075 mm). It is worthy to add here that the bubble terminal velocity depends on the bubble size as documented by Cliff et al. (1978). In our previous studies (Zawala et al., 2007ab, Malysa et al., 2011) we showed that when the bubble diameter varied from 1.22 to 1.66 mm (capillaries of inner diameters 0.05–0.1mm) then magnitude of the bubble terminal velocity varied from 31.5 ± 0.2 to 36.7 ± 0.2 cm/s, but character of variations of the local velocity profiles was similar. As seen in Fig. 1 the velocity profiles are varying with n-alkylsulfates concentration, in a similar way as in the case non-ionic and ionic surfactants studied earlier (Krzan and Malysa, 2002ab and 2009; Krzan et al., 2004 and 2007; Malysa et al., 2005 and 2011). Immediately after detachment the bubble accelerates rapidly over a distance of ca. 20mm, depending on the solution concentration. In distilled water the bubble acceleration was ca. 925cm/s^2 (Krzan et al., 2007) and after the acceleration stage the bubble achieved its terminal velocity of 34.8 ± 0.3 cm/s at the distance ca. 2-3 cm from the capillary. In low concentrations of sodium n-alkylsulfates the bubbles reached, after the acceleration stage, a maximum velocity followed by a deceleration stage tending to attain their terminal velocity (see Fig. 1). A general tendency can be easily noted in Fig. 1 that position, height and width of the maximum depend on concentration of the sodium n-alkylsulfates solutions. Higher solution concentration caused lowering the maximum height and width. Finally, the maximum disappeared and the bubbles attained their terminal velocity immediately after the acceleration stage at concentrations high enough.

Presence of the maximum on the velocity profiles is an indication that the dynamic architecture of the adsorption layer (DAL) hasn't yet been fully established (Krzan and Malysa, 2002ab and 2009; Krzan et al., 2004 and 2007; Malysa et al., 2005 and 2011). The maximum disappearance means that the DAL has been established at the acceleration stage of the bubble motion. Variations of the maximum velocity with concentrations of sodium n-octylsulfate, n-decylsulfate and n-dodecylsulfate are compared in Fig. 2A. As seen there and in Fig. 1 the concentration of the maximum disappearance was the lowest in the case of sodium n-dodecylsulfate solutions, due to its highest surface activity. Figure 2B presents the dependencies of the bubble terminal velocity on concentrations of these solutions and again here the reagent of highest surface activity (sodium n-dodecylsulfate) lowered the bubble terminal velocity at lowest solution concentrations. It needs to be added here that values of the terminal velocity for low concentrations of sodium n-octylsulfate should be treated with a

caution (as approximates only) because at these concentrations, as can be observed in Fig. 1A, the bubble local velocities were still not constant even at distances 25-30 cm from the capillary orifice. Note please (Figs. 1 and 2) that at high concentration of sodium n-octylsulfate, n-decylsulfate and n-dodecylsulfate the bubbles terminal velocity was similar, ca. 15 cm/s, that is over 50% smaller than in distilled water. Moreover, the bubble terminal velocity practically stopped to depend on the solution concentration above a “threshold” concentration, which value depends on the reagent type.

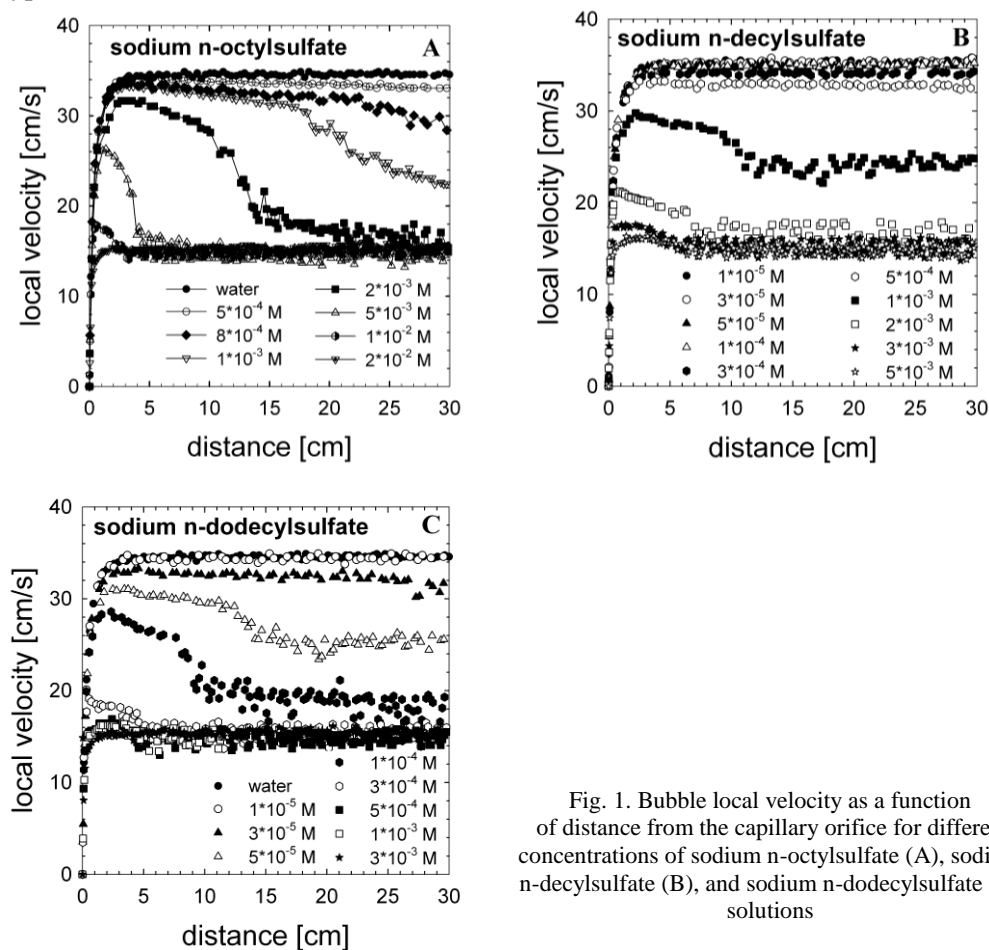


Fig. 1. Bubble local velocity as a function of distance from the capillary orifice for different concentrations of sodium n-octylsulfate (A), sodium n-decylsulfate (B), and sodium n-dodecylsulfate (C) solutions

Lowering of the bubble terminal velocity in surfactant solutions is caused by retardation fluidity of the bubble surface due to formation a dynamic architecture of the adsorption layer (DAL) over surface of the rising bubble. As surface tension of solutions of ionic surfactants (Warszynski et al., 1998a and 2002; Adamczyk et al., 1999ab; Para et al., 2005; Jarek et al. 2010), that is adsorption coverage under equilibrium condition, is strongly affected by electrolyte presence so the velocity

profiles of the rising bubbles should also depend on the electrolyte contents in their solutions. It has already been shown that the addition of 0.05M of electrolyte (NaCl or KCl) strongly affected the parameters of the bubble motion in sodium n-dodecylsulfate solutions (Krzan and Malysa, 2009). In presence of 0.05M NaCl or KCl the bubble local velocities were significantly diminished even in low concentrations of the SDDS solutions. As there is a lack of systematic studies on influence of electrolyte concentration so we studied effect of sodium chloride on the bubble velocity in SOS, SDS and SDDS solutions of different concentrations to find a minimum electrolyte concentration, which can affect the bubble motion. Photos of Figs. 3 and 4 illustrate clearly that increasing concentration of inert electrolyte can significantly affect velocity of the bubbles rising in solutions of $1 \cdot 10^{-3}$ M sodium n-decylsulfate (Fig. 3) and $3 \cdot 10^{-5}$ M sodium n-dodecylsulfate (Fig. 4). As all these experiments were carried out under identical frequency of the stroboscopic illumination (100 flashes/sec) so changes in distances between positions of the subsequent images show immediately influence of electrolyte concentration on the bubble velocity. The effect is really huge and it is clearly seen that at constant concentrations of the anionic surfactants the bubble velocity decreases quickly when the electrolyte concentration is increasing. It needs to be noted and underlined here that in $1 \cdot 10^{-3}$ M SDS and $3 \cdot 10^{-5}$ M SDDS solutions there were a distinct maximum (see Figs. 1B and 1C) indicating that fluidity of the bubble interface was not fully retarded in these solutions. Lower velocity in the SDS and SDDS solutions containing sodium chloride is an indication that the electrolyte presence caused higher retardation of the bubble surface fluidity.

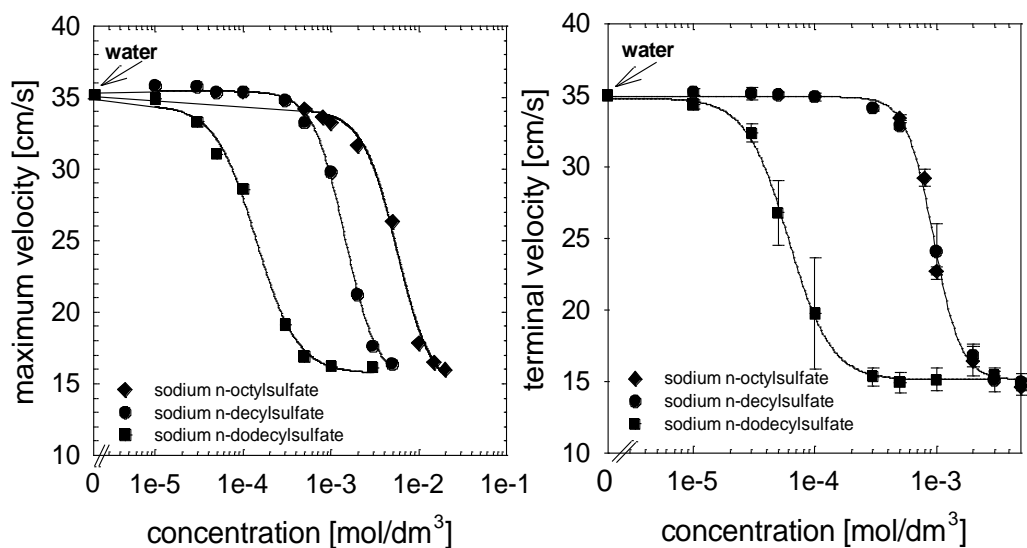


Fig. 2. Variations of the bubble maximum and terminal velocity with concentration of sodium n-alkylsulfates

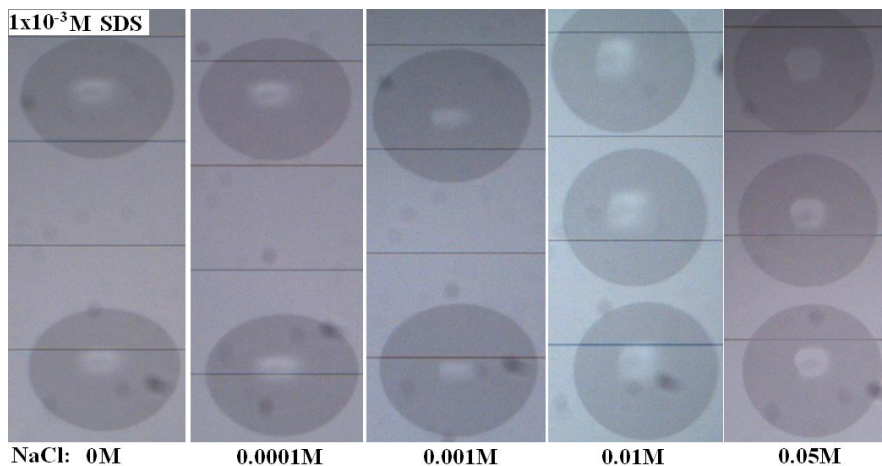


Fig. 3. Images of the bubbles rising in $1 \cdot 10^{-3}$ M SDS solutions containing different amounts of sodium chloride (distance 1cm from the capillary orifice). Strobe frequency-100 flashes per second

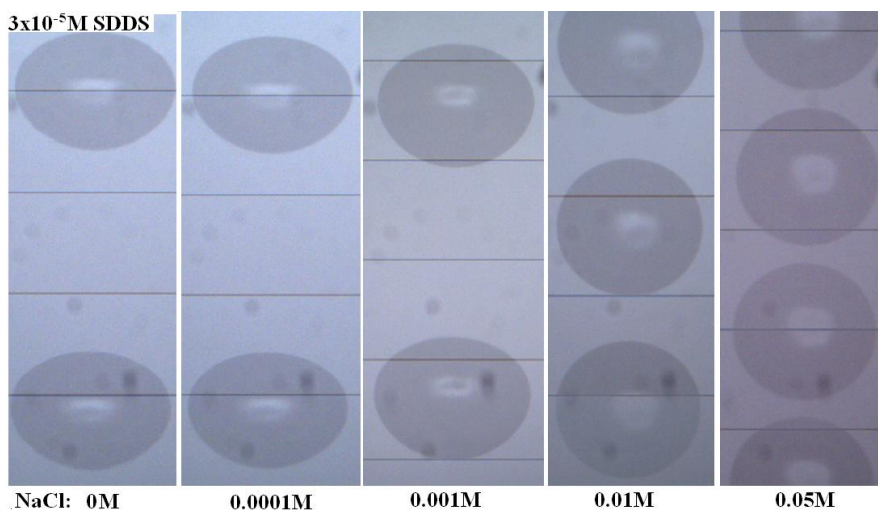


Fig. 4. Images of the bubbles rising in $3 \cdot 10^{-5}$ M SDDS solutions containing different amounts of sodium chloride (distance 1cm from the capillary orifice). Strobe frequency-100 flashes per second

Figures 5A-5D present the quantitative data on influence of sodium chloride addition on profiles of the bubble local velocity in solutions of $5 \cdot 10^{-4}$ M sodium n-octylsulfate (Fig. 5A), $1 \cdot 10^{-3}$ M sodium n-decylsulfate (Fig. 5B), $3 \cdot 10^{-5}$ M sodium n-dodecylsulfate (Fig. 5C) and $1 \cdot 10^{-4}$ M sodium n-dodecylsulfate (Fig. 5D). The sodium chloride concentration was varied from 0.0001 to 0.05 M. The dashed lines in Figs. 5A-5D refer to the bubbles motion in solution of 0.05M NaCl without any surfactant

added. As seen the profiles of the bubble local velocity in 0.05 M NaCl and in distilled water (compare Figs. 5 and 1) are identical – after the acceleration stage the bubbles attained their terminal velocity of 34.8 ± 0.3 cm/s at the distance ca. 2-3 cm from the capillary. Identical values of the terminal velocity for distilled water and 0.05 M NaCl solution shows two important things: i) presence of inert electrolyte alone does not affect the bubble motion, and ii) there was no even traces of surface active contaminations in the sodium chloride used. When SOS, SDS or SDDS was present then the situation was completely different (see Figs. 5A-D). With increasing NaCl concentration the local velocity profiles in solutions of $5 \cdot 10^{-4}$ M SOS, 1×10^{-3} M SDS, $3 \cdot 10^{-5}$ M SDDS and 1×10^{-4} M SDDS were changed very significantly. Values of the maximum velocity in solutions containing $5 \cdot 10^{-4}$ M SOS, $1 \cdot 10^{-3}$ M SDS, $3 \cdot 10^{-5}$ M SDDS and $1 \cdot 10^{-4}$ M SDDS were clearly decreasing with increasing NaCl concentration. The bubbles terminal velocity was also changed. For example in $1 \cdot 10^{-3}$ M SDS and $3 \cdot 10^{-5}$ M SDDS the bubble terminal velocities were lowered from 24.1 ± 0.7 cm/s and 31.4 ± 0.6 cm/s to 15.2 ± 0.5 cm/s and 14.6 ± 0.5 cm/s, respectively (see Figs. 5B and 5C), when the electrolyte concentration was changed from 0 to 0.05 M. Thus, the increasing electrolyte concentration affected the bubble motion parameters in a similar way as increasing surfactant concentration in solutions without inert electrolyte. Explanation of these findings is rather obvious and consistent with literature data on influence of inert electrolytes on surface tension isotherms of ionic surfactants (Kalinin and Radke, 1996; Warszynski et al., 1998a and 2002; Adamczyk et al., 1999ab; Para et al., 2005; Jarek et al., 2010) – surface activity of the sodium n-alkylsulfates studied was increased due to the electrolyte presence as a result of damping electrostatic interactions in their adsorption layers.

When molecules of the ionic surfactant are adsorbed at solution/gas interface, the electrical double layer (EDL) is built and, as a result, an energetic barrier of electrostatic origin appears. Due to repulsive interactions between the adsorbed ionic surfactant molecules within the adsorption layer the adsorption coverage is significantly lower than in the case of similar but nonionic surfactants. Addition of electrolyte can increase the ionic surfactant adsorption. For example in the case of the SDDS solutions the surface tension isotherm can be shifted towards lower concentrations by more than order of magnitude (Warszynski et al., 1998a). This effect of lowering of surface tension of ionic surfactant solutions in electrolyte presence is due to neutralization of the surface charge of adsorbed ionic surfactant molecules by counterions adsorbed in the Stern layer (Kalinin and Radke, 1996; Warszynski et al., 1998a and 2002; Adamczyk et al., 1999ab; Para et al., 2005; Jarek et al., 2010). The counterions adsorption in the EDL region causes that interface is almost “neutral” for the adsorbing surfactant, and thus, the surface activity of the ionic surfactant almost approaches the surface activity of nonionic surfactant with the same carbon chain length. In other words the electrolyte presence means that at identical bulk concentration the surface tension of sodium n-alkylsulfates solutions is lowered.

Presence of the maximum on the local velocity profiles is an indication, as showed elsewhere (Krzan and Malysa, 2002ab; Krzan et al., 2007), that dynamic structure of the adsorption layer, i.e., uneven, steady state distribution of the surfactant molecules over the bubble surface, has not been established at the acceleration stage of the bubble motion.

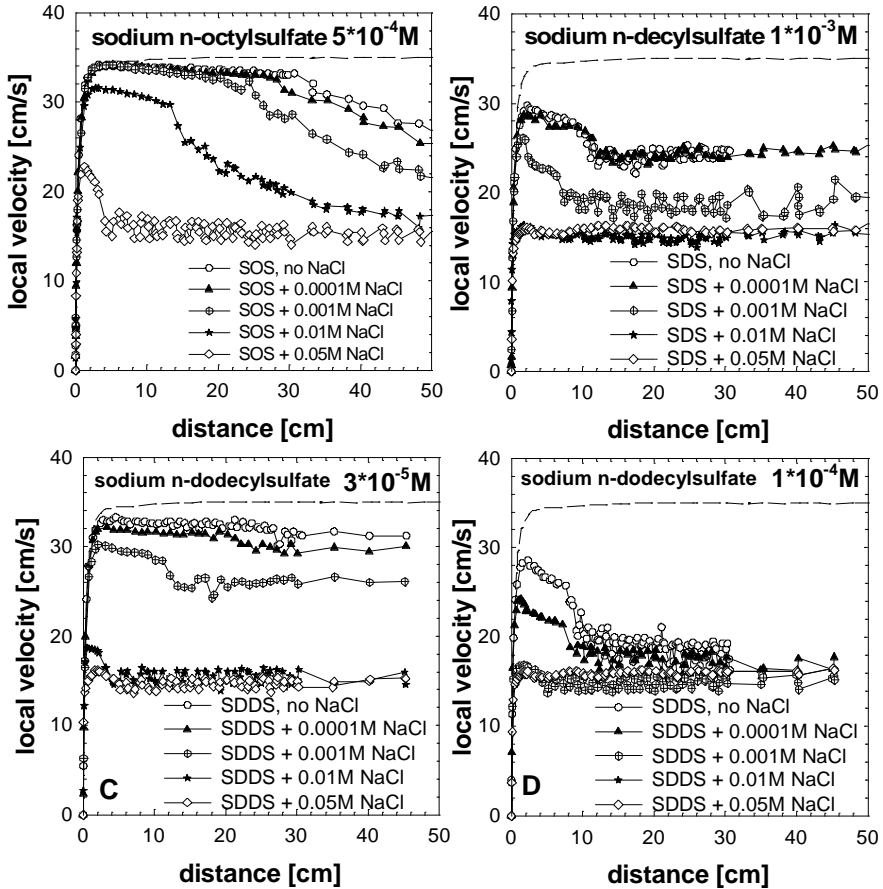


Fig. 5. Influence of sodium chloride concentration on local velocity profiles of the bubbles rising in $5 \cdot 10^{-4} \text{M}$ sodium n-octylsulfate (A), $1 \cdot 10^{-3} \text{M}$ sodium n-decylsulfate (B), $3 \cdot 10^{-5} \text{M}$ (C) and $1 \cdot 10^{-4} \text{M}$ sodium n-dodecylsulfate (D) solutions. The dashed line shows the bubble local velocities in 0.05 M NaCl solution, without any surfactant

The maximum is observed at low concentrations of various surfactants and diminishes with increasing surfactant concentration (see Figs. 1 and 2A). It has also been showed (Krzan and Malysa, 2002a; Krzan et al., 2007) that when a maximum is observed on the bubble velocity profiles then there are observed shape pulsations of the rising bubbles. These shape pulsations mean variations of the interfacial area and adsorption-desorption processes, counteracting expansion of the interfacial area, and

are strong confirmation that there was not yet established a steady state distribution of the adsorbed surfactant molecules. The bubble shape pulsations are decreasing, similarly as the height and width of the maximum on the velocity profiles, when the surfactant concentration is increasing. As discussed above the electrolyte presence in solution causes an increase of n-alkylsulfates surface activity as a result of damping electrostatic interactions in the adsorption layers. Increased surface activity means that there is higher adsorption coverage at a given solution bulk concentration. Thus, there should also exist a correlation between variations of the bubble shape and the local velocity values when the electrolyte concentration is increasing at the constant n-alkylsulfate concentrations.

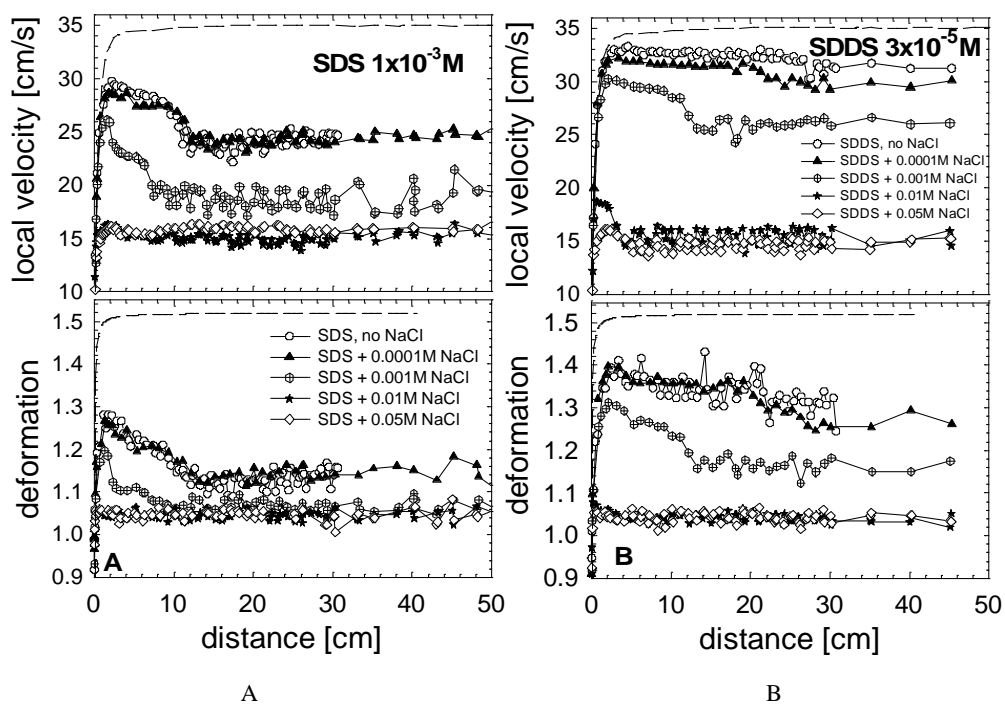


Fig. 6. Influence of sodium chloride concentration on local velocity and degree of the shape variations with distance from the bubble detachment in $1 \cdot 10^{-3}$ M SDS (Fig. 6A) and $3 \cdot 10^{-5}$ M SDDS (Fig. 6B) solutions. The dashed line shows the bubble local velocities and deformations in 0.05 M NaCl solution, without any surfactant

Figures 6A and 6B present a comparison of variations of the bubble local velocity and the bubble shape deformations with distance from the capillary in $1 \cdot 10^{-3}$ M SDS and $3 \cdot 10^{-5}$ M SDDS solutions. The bubble shape variations are expressed as a ratio (d_h/d_v) of the horizontal (d_h) and vertical (d_v) diameters. A good correlation between variations of the bubble shape and the local velocity values can be observed there.

Both parameters show maxima at similar distances from the capillary and in a similar way the maxima are changing and shifting with changes of the solution concentration. Shape pulsations mean variations of the interfacial area and variations in surface tension gradients induced, which affect fluidity of the bubble interface. Consequently, these variations in the bubble surface fluidity lead to changes of the bubble velocity. Existence of correlations between local velocity changes and shape variations shows that electrolyte presence caused, indeed, variations of adsorption coverage over surface of the rising bubbles. Influence of electrolyte concentration on degree of adsorption coverage over surface of the bubble growing at the capillary orifice can be determined using the convective-diffusion model elaborated by Warszynski et al. (1998b). In calculations the available literature data (Warszynski et al., 1998a) on influence of electrolyte on adsorption isotherms of sodium n-dodecylsulfate were used. Table 1 presents data on degree of adsorption coverage at the moment of the bubble detachment from the capillary in $3 \cdot 10^{-5}$ M and $1 \cdot 10^{-4}$ M sodium n-dodecylsulfate solutions without and containing 0.01 M NaCl. As seen the adsorption coverage at the detaching bubble (θ_{det}) was ca. 5–6 fold higher in SDDS solutions containing 0.01 M NaCl. In $3 \cdot 10^{-5}$ M SDDS solution the adsorption coverage was increased from 1% to 6% in presence of 0.01 M NaCl. Simultaneously, as showed above, the bubble maximum and terminal velocities were lowered from 33.3 and 31.4 cm/s to 18.7 and 15.4 cm/s, respectively. Thus, the data presented in Fig. 4 and Table 1 show straightforward that electrolyte presence affects the bubble velocity as a result of variation of the adsorption coverage of the anionic surfactants over surface of the rising bubbles.

Table 1. Adsorption coverage on bubble growing in sodium n-dodecylsulfate solutions without and containing 0.01 M NaCl. Time of the bubble growth 1.6 s

| Conc. | No electrolyte | | | 0.01M NaCl | | |
|---------------------|----------------|------------|-----------|----------------|------------|-----------|
| | θ_{det} | V_{term} | V_{max} | θ_{det} | V_{term} | V_{max} |
| $3 \cdot 10^{-5}$ M | 0.01 | 31.4±0.6 | 33.3 | 0.06 | 15.4±0.7 | 18.7 |
| $1 \cdot 10^{-4}$ M | 0.036 | 17.7±1.3 | 28.6 | 0.2 | 15.9±0.3 | 16.5 |

Figure 7 presents influence of NaCl concentration on the bubble maximum (7A) and terminal (7B) velocities in SOS, SDS and SDDS solutions. As seen the electrolyte presence, even at so low concentrations as 0.0001 and 0.001M, affect the bubble motion in solutions of sodium n-alkylsulfates. In the case of lowest concentrations of sodium n-alkylsulfates solutions the terminal velocities are lowered from ca. 30-35 cm/s (no electrolyte) down to ca. 23-28 cm/s (0.001M NaCl). When the electrolyte concentration was increased to 0.01 M NaCl then the bubble terminal velocity was reduced to the level of ca. 15cm/s in all SOS, SDS and SDDS solutions studied, what means that fluidity of the bubble surface was practically fully retarded. At higher SOS,

SDS and SDDS concentrations the electrolyte caused also lowering the bubble velocity but the effect was less spectacular because the “starting point” was lower, that is, the bubble velocity in solutions without any electrolyte was lower. Nevertheless, the data obtained show clearly how strongly the electrolyte presence can lower the bubble velocity in solutions of anionic surfactants. As lowering of the bubble velocity is advantageous for probability of the grain attachment to the bubble in every flotation system (lower velocity means a longer contact time during their collisions) so a practical implication from these studies is the following – lower dosage of ionic frother can be applied when electrolyte is present in flotation system.

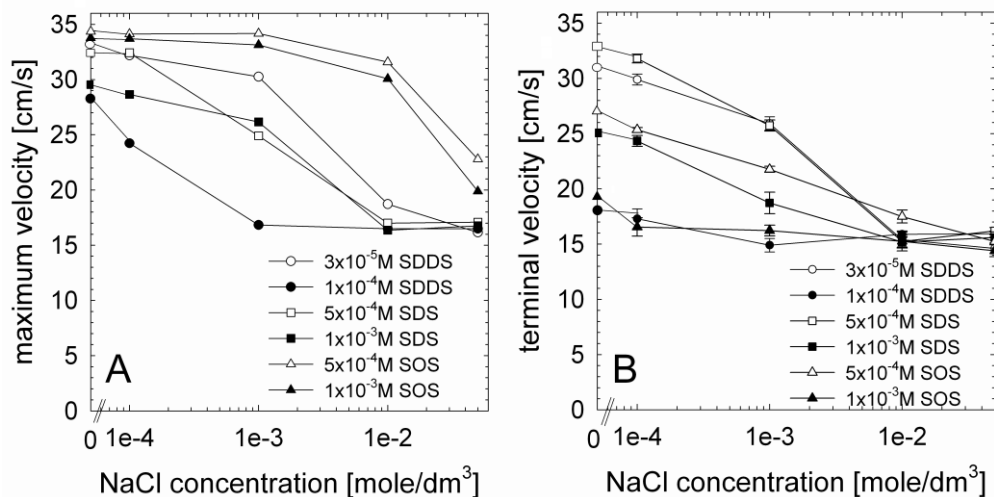


Fig. 7. Influence of electrolyte concentration on maximum (Fig. 7A) and terminal (7B) velocities of bubbles in SDDS, SDS and SOS solutions.

4. Conclusions

Presence of electrolyte (sodium chloride) in sodium n-alkylsulfate solutions affects strongly motion of the rising bubbles. Electrolyte alone, i.e. without any sodium n-alkylsulfate presence, has no effect on the bubble motion and the bubble terminal velocity in 0.05M NaCl was identical as in distilled water (34.8 ± 0.3 cm/s). At low sodium n-alkylsulfates concentrations the effect of electrolyte addition is huge and even at very low NaCl dosage (0.0001 and 0.001M) the bubbles terminal velocity was lowered from ca. 30-34 cm/s (no electrolyte) down to ca. 23-28 cm/s (0.001M NaCl). When the electrolyte concentration was increased to 0.01M NaCl then the bubble terminal velocity was reduced to the level ca. 15 cm/s in all SOS, SDS and SDDS solutions studied. It was found that increasing electrolyte concentration affected the bubble motion parameters in a similar way as increasing concentration of sodium n-alkylsulfates, what shows that due to the electrolyte presence the degree of adsorption

coverage over the bubble surface was increased. Higher adsorption coverage means an increased retardation of the bubble surface fluidity and lower bubble velocity. Minimum adsorption coverage needed for complete retardation of the bubble surface mobility was determined for sodium n-dodecylsulfate solutions without electrolyte and with 0.01M NaCl. It was found that the SDDS adsorption coverage over surface of the rising bubble was ca. 5–6-fold higher when 0.01 M of NaCl was added.

In flotation systems the bubble velocity lowering is advantageous because lower velocity means a longer contact time during collisions of the bubbles and grains and increased probability of formation a stable bubble-grain aggregates. Thus, a practical implication can be drawn from these studies that lower dosage of anionic frother can be applied when electrolyte is present in flotation system.

Acknowledgments

Financial support from Ministry of Science and Higher Education (grant PBS 45/N-COST/2007/0) is gratefully acknowledged.

References

- ADAMCZYK, Z., PARA, G., WARSZYNSKI, P., 1999, Influence of ionic strength on surface tension of cetyltrimethylammonium bromid, *Langmuir* 15, 8383–8387.
- ADAMCZYK, Z., PARA, G., WARSZYNSKI, P., 1999, Surface tension of sodium dodecyl sulphate in the presence of a simple electrolyte, *Bull. Pol. Ac. Sci.* 47, 175–186.
- AYGOMI, F., GOMEZ, C.O., FINCH, J.A., 2007, Correspondence of gas holdup and bubble size in presence of different frothers, *Int. J. Miner. Process.* 83, 1–11.
- CEYLAN, K., ZEKI KUCUK, M., 2004, Effectiveness of the dense medium and the froth flotation methods in cleaning some Turkish lignites, *Energ. Convers. Manag.* 45, 1407–1418.
- CLIFT, R., GRACE, J.R., WEBER, M.E, 1978, *Bubbles, Drops and Particles*, Academic Press.
- DAVIES, J.T., RIDEAL, E.K., 1963, *Interfacial Phenomena*, Academic Press, New York.
- HU, C.Y., LO, S.L., KUAN, W.H., LEE, Y.D., 2005, Removal of fluoride from semiconductor wastewater by electrocoagulation-flotation, *Water Res.* 39, 895–901.
- HU, C.Y., LO, S.L., KUAN, W.H., LEE, Y.D., 2008, Treatment of high fluorite-content wastewater by continuous electrocoagulation-flotation system with bipolar aluminum electrodes, *Sep. Purif. Technol.*, 60, 1–5.
- JACHIMSKA, B., WARSZYNSKI, P., MALYSA, K., 2001, Influence of adsorption kinetics and bubble motion on stability of the foam films formed at n-octanol, n-hexanol and n-butanol solution surface, *Colloids Surf. A* 192, 177–193.
- JAREK, E., JASINSKI, T., BARZYK, W., WARSZYNSKI, P., 2010, The pH regulated surface activity of alkanolic acids, *Colloids Surf. A* 354, 188–196.
- KALININ, V.V., RADKE, C.J., 1996, An ion-binding model for ionic surfactant adsorption at aqueous-fluid interfaces, *Colloids Surf. A* 114, 337–350.
- KRZAN, M., MALYSA, K., 2002a, Profiles of local velocities of bubbles in n-butanol, n-hexanol and n-nonanol solutions, *Colloids Surf. A*, 207, 279–291.
- KRZAN, M., MALYSA, K., 2002b, Influence of frother concentration on bubble dimension and rising velocities, *Physicochem. Problems Mineral Process.* 36, 65–76.
- KRZAN, M., LUNKENHEIMER, K., MALYSA, K., 2004, On the influence of the surfactant's polar group on the local and terminal velocities of bubbles, *Colloids Surf. A* 250, 431–441.
- KRZAN, M., ZAWALA, J., MALYSA, K., 2007, Development of steady state adsorption distribution over interface of a bubble rising in solutions of n-alkanols (C5, C8) and n-alkyltrimethylammonium bromides (C8, C12, C16), *Colloids Surf. A* 298, 42–51.

- KRZAN, M., MALYSKA, K., 2009, Influence of solution pH and electrolyte presence on bubble velocity in anionic surfactant solutions, *Physicochem. Problems Mineral Process.* 43, 43–58.
- LASKOWSKI, J., 1998, Frothers and Frothing in Frothing in Flotation - II. (J.Laskowski and E.T.Woodburn - Eds.), Gordon and Breach Publishers, chap.1.
- LASKOWSKI, J., 2010, A new approach to classification of flotation collectors, *Can. Metall. Q.*, 49(4), 397–404.
- LEJA, J., 1982, *Chemistry of Froth Flotation*, Plenum Press, New York and London.
- MALYSKA, K., KRASOWSKA, M., KRZAN, M., 2005, Influence of surface active substances on bubble motion and collision with various interfaces, *Adv. Colloid Interface Sci.* 114–115C: 205–225.
- MALYSKA, K., ZAWALA, J., KRZAN, M., KRASOWSKA, M., 2011, Bubbles Rising in Solutions; Local and Terminal Velocities, Shape Variations and Collisions with Free Surface, Chapter 11 in: *Bubble and Drops Interfaces*, ISBN 9789004174955, 243–292.
- NGUYEN, A.V., SCHULZE, H.J., 2004, *Colloidal Science in Flotation*, Marcel Dekker.
- PARA, G., JAREK, E., WARSZYNSKI, P., 2005, The surface tension of aqueous solution of cetyltrimethylammonium cationic surfactants in presence of bromide and chloride counterions, *Colloids Surf. A* 261, 65–73.
- RALSTON, J., DUKHIN, S.S., 1999, The interaction between particles and bubbles, *Colloids Surf. A* 151, 3–14.
- RUJIRAWANICH, V., CHAVADEJ, S., RUJIRAVANIT, R., 2010, Removal of trace Cd²⁺ using continuous multistage ion foam fractionation: Part 1 -The effect of feed SDS/Cd molar ratio, *J. Hazard. Mater.* 182, 812–819.
- SAM, A., GOMEZ, C.O., FINCH, J.A., 1996, Axial velocity profiles of single bubbles in water/frother solutions, *Int. J. Miner. Process.* 47, 177–196.
- SCHIMMOLER, B.K., LUTRELL, G.H., YOON, R-H., 1993, A combined hydrodynamic-surface force model for bubble- particle collection, XVIII Int. Miner. Process. Congress. 3, 751–756.
- WARSZYNSKI, P., BARZYK, W., LUNKENHEIMER, K., FRUHNER, H., 1998a, Surface tension and surface potential of Na n-dodecylsulfate at the air solution interface: Model and experiment, *J. Phys. Chem. B* 102, 10948–10957.
- WARSZYNSKI, P., WANTKE, K.-D., FRUHNER, H., 1998b, Surface elasticity of oscillating spherical interfaces, *Colloids Surf. A* 139, 137–153.
- WARSZYNSKI, P., LUNKENHEIMER, K., CICHOCKI, G., 2002, Effect of counterions on the adsorption of ionic surfactants at fluid–fluid interfaces, *Langmuir* 18, 2506–2514.
- WATCHARASING, S., KONGKOWIT, W., CHAVADEJ, S., 2009, Motor oil removal from water by continuous froth flotation using extended surfactants: Effects of air bubble parameters and surfactant concentration, *Sep. Purif. Technol.* 70, 179–189.
- ZAWALA, J., KRASOWSKA, M., DABROS, T. and MALYSKA, K., 2007a, Influence of Bubble Kinetic Energy on its Bouncing During Collisions with Various Interfaces, *Can. J. Chem. Eng.* 85, 669–678
- ZAWALA, J., SWIECH, K., MALYSKA, K., 2007b, A simple physicochemical method for detection of organic contaminations in water, *Colloids Surf. A* 302, 293–300.

Received April 29, 2011; reviewed; accepted June 25, 2011

ZnO-SiO₂ OXIDE COMPOSITES SYNTHESIS DURING PRECIPITATION FROM EMULSION SYSTEM

Agnieszka LAURENTOWSKA, Teofil JESIONOWSKI

Poznan University of Technology, Institute of Chemical Technology and Engineering M. Skłodowskiej-Curie 2, PL-60965 Poznan, e-mail: teofil.jesionowski@put.poznan.pl, phone: +48(61)6653720, fax: +48(61)6653649

Abstract. A new method of obtaining a ZnO-SiO₂ synthetic composite from emulsion systems is described. The reagents were solutions of sodium silicate and zinc sulphate, cyclohexane was used as an organic solvent and non-ionic surfactants as modifiers. The influence of the mode of reagents dosing and type of emulsifiers on the physicochemical properties, structure and particle size of ZnO-SiO₂ was evaluated. The choice of the optimum emulsifier or mixture of emulsifiers and their amounts needed for the process of precipitation and ensuring getting products of uniform particles and the smallest possible size was proposed. The ZnO-SiO₂ composite obtained was characterised by micrometric particle size. The oxide composites obtained were subjected to thorough analyses to determine their physicochemical properties, dispersion and morphology. Particle size distributions were evaluated by the NIBS technique and laser diffraction method. The products were also characterised by sedimentation profiles, wettability with water and colorimetric analyses, determination of bulk density or ZnO and SiO₂ contents.

keywords: ZnO-SiO₂, precipitation, particle size distribution, surface morphology, wettability, sedimentation, emulsion

1. Introduction

Silica and silica-based materials have found widespread application for industrial, technological and domestic purposes. The demand for improved silica types with specific properties such as mechanical strength, pore volume and size distribution, surface area or reactivity is fueling the search for innovative production of such materials (Sun 2004). For many years, silicates have attracted great attention due to their special physicochemical properties, low cost and abundant supply, and have been widely applied in many fields, e.g. as molecular sieves (Ying 1999), catalyst supports (Fotopoulos 2007), for gas absorption and separation (Kalinkin 2009), and as raw materials for the glass industry (Yang 2010).

In recent years, ZnO nanoparticle embedded SiO₂ composites have attracted extensive research interests. It has been found that these materials have improved luminescence efficiency compared to bulk ZnO materials. Excellent nonlinear optical properties, saturable absorption and optical bistability have also been reported for these composites (Mo 1998, Fu 2003, Chakrabarti 2004, Zhao 2007). ZnO-based nanocomposites are promising materials in ceramic technology for application as varistors, sensor elements, photoconductors in electrophotography (Cannas 1999), and for electroluminescent applications such as in flat-panel displays, photoelectronics integrated devices, and semiconductor lasers. However, the luminescence efficiency of ZnO-based nanocomposites needs to be improved for the above applications (Fu 2003). Yao et al. (2000) have reported band gap luminescence from ZnO in mesoporous silica, and they have found that Zn–O–Si cross-linking bonds that formed at the interface between ZnO and the pore walls of silica had a great influence on the optical properties of ZnO/SiO₂. Much attention has been paid to the UV barrier properties of fabrics modified with ZnO-SiO₂. It has been shown that coating of fabrics with a paste of ZnO-SiO₂ is an effective method of surface modification (Sójka-Ledakowicz 2010).

Recently, intense research has been dedicated to preparation of materials of desired properties (e. g. spherical shape of particles, high adsorption activity) (Jesionowski 2009). In the production of highly dispersed synthetic silicates a particularly important are the technological conditions of the process. They affect the physicochemical properties of the products obtained and surface modification permits improvement of the product properties (Krysztafkiewicz 2004). In conventional methods, uncontrolled nucleation and subsequent growth of the precipitated particles in a bulk aqueous medium finally generates large particles with a wide size distribution (Lee 2006). To overcome these problems, many recent studies have used emulsions to control the size, distribution and morphology of the fine particles (Ganguli 1997). Emulsions consist of droplets of one liquid dispersed throughout another one referred to as the continuous phase (Robins 2002). They are used in a wide spectrum of industrial applications including production of pharmaceuticals, food, cosmetics and textiles. Due to a small droplet size of the dispersed phase, the total interfacial area in the emulsion is very large. Since the creation of interfacial area incurs a positive free energy, the emulsions are usually thermodynamically unstable. Nevertheless, it is possible to make highly stable emulsions by the use of emulsifiers. Emulsifiers accumulate at the oil/water interface and make an energy barrier against flocculation and coalescence of the droplets. The emulsifiers can be ionic, non-ionic or zwitterionic surfactants, proteins or amphiphilic polymers (Somasundaran 2006). Midmore (2001) observed that the addition of non-ionic surfactants, used to flocculate silica dispersions, caused synergistic effects on the stability of oil-in-water (o/w) emulsions containing silica.

In this study ZnO-SiO₂ synthetic oxide composites were obtained by precipitation from emulsion. The reagents were water solutions of sodium silicate and zinc

sulphate, cyclohexane (organic solvent) and non-ionic emulsifiers. The effects of different modes of the reagent dosing were analysed. The main aim of the study was to identify an emulsifier or a mixture of emulsifiers needed for the process of precipitation and its or their amounts whose use would ensure getting a product of optimum properties made of uniform particles of the smallest possible diameters.

2. Experimental

2.1. Materials

The reagents used to obtain ZnO-SiO₂ oxide composite were 5% water solutions of zinc sulphate of analytical grade (Chempur) and sodium silicate of technological grade (Vitrosilicon SA). The non-ionic surfactants were nonylphenylpolyoxyethyleneglycol ethers of a medium oxyethylenation degree 3, 5 and 6 (NP3, NP5 and NP6) – Sigma Aldrich. Cyclohexane of analytical grade was used as an organic solvent (POCH SA).

2.2. Methods of studies

The process of ZnO-SiO₂ precipitation was performed in a reactor of 0.5 dm³ in capacity, equipped in a high speed stirrer 1700 rpm (Eurostar Digital, IKA Werke), to which a 5% solution of zinc sulphate or earlier prepared emulsion E1 were introduced. Emulsion E1 was made by mixing 110 cm³ of cyclohexane and 100 cm³ of sodium silicate to which NP3, NP5 or NP6 emulsifier or a mixture of two emulsifiers was added. Using a peristaltic pump Ismatec ISM833A the reagents were introduced at a constant rate of 4.2 cm³/min. Precipitation was performed at room temperature. A scheme illustrating the synthesis of ZnO-SiO₂ composite is presented in Fig. 1.

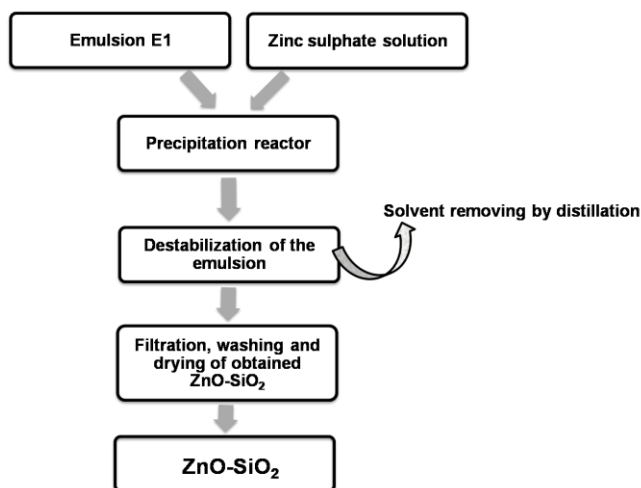


Fig. 1. Synthesis of ZnO-SiO₂ oxide composite from the emulsion systems

The oxide composite ZnO-SiO₂ was characterised by determination of the particle size distribution, surface morphology and wettability with water. The particle size distribution was evaluated by measurements with the apparatuses Malvern Instruments Ltd: Zetasizer Nano ZS (non-invasive backscattering method – NIBS) and Mastersizer 2000 (laser diffraction technique). Surface morphology of the surfaces of the products studied was evaluated by scanning electron microscopy SEM (Zeiss VO40). The colour of the products was classified with the use of a colorimeter Specbos 4000 (JETI Technische Instrumente GmbH). Intensity of the colour was expressed in the CIE L*a*b* system where L* describes lightness, C* colour saturation, h* colour hue and +a informs about the contribution of red, -a – a contribution of green, +b – a contribution of yellow. dE describes total color change which is a resultant of differences in particular components (dL*, da*, db*). The profiles of ZnO-SiO₂ sedimentation and wettability with water were measured with the help of a tensiometer K100 (Krüss) with special equipments. Chemical analysis of the products was made by titration analysis with EDTA solution.

3. Results and discussion

In the first stage the synthesis of ZnO-SiO₂ composites was performed by introducing E1 emulsion in the volume of 210 cm³ into 200 cm³ of a 5% solution of ZnSO₄. E1 emulsion was made with 110 cm³ of cyclohexane and 100 cm³ of a 5% sodium silicate solution with addition of surfactants NP3, NP5 or NP6. Table 1 presents the conditions of precipitation depending on the type of emulsifier and particle size and polydispersity indices obtained at this stage of the study.

The particle size distribution of sample M1 according to intensity (Fig. 2a) reveals three bands. The first covers the diameter range 255 – 295 nm, with the maximum intensity of 4.2% for particles 255 nm in diameter. The second one covers the diameter range 396 – 531 nm, with the maximum intensity of 7.7% for particles of 459 nm in diameter. The third band covers the range of diameters 1280 – 5560 nm and has the maximum intensity of 8.4% for agglomerates of 1990 nm in diameter. For sample M2 only one band is obtained covering the diameter range from 459 nm to 1280 nm, Fig. 2b, with the maximum intensity of 25.8% corresponding to particles of 825 nm. Sample M2 is characterised by a relatively low polydispersity index of 0.476, which means that despite the presence of clusters of secondary agglomerates this composite is rather homogeneous. The particle size distribution of M3 (Fig. 2c) has only one band covering the diameters from 1720 to 3580 nm. Its maximum intensity of 32.4% corresponds to agglomerates of 2300 nm in diameter. Fig. 2d shows the particle size distribution for sample M4 with two bands. The first covers the range 68 nm – 92 nm, with the maximum intensity of 40.6% for particles of 79 nm in diameter, while the second covers the range 4150 – 5560 nm, with the maximum intensity of 20.8% for secondary agglomerates of 5560 nm in diameter. For sample M5 the particle size distribution shows two bands (Fig. 2e), the first covers the diameters from 220 to 396 nm, with the maximum intensity of 26.0% corresponding to particles of

295 nm in diameter, while the second covers the range 531 – 712 nm, with the maximum of 9.3% for particles of 615 nm in diameter.

Table 1. Analysis of particle size distribution and PdI versus the type of emulsifier

| Sample | Type/amount of emulsifier (g) | | | Particle diameter (nm) | PdI |
|--------|-------------------------------|-----|-----|---------------------------------|-------|
| | NP3 | NP5 | NP6 | | |
| M1 | 1.5 | - | 1.0 | 255-295 396-531 1280-5560 | 0.837 |
| M2 | - | - | 2.0 | 459-1280 | 0.476 |
| M3 | 3.4 | - | - | 1720-3580 | 0.807 |
| M4 | - | 2.4 | - | 68-92 4150-5560 | 0.625 |
| M5 | 1.4 | 1.2 | - | 220-396 531-712 | 0.879 |

Analysis of morphological and dispersive properties of ZnO-SiO₂ samples synthesised with the use of one ether or a mixture of ethers has pointed to the beneficial effect of using a mixture of non-ionic surfactants NP3 and NP5 on nucleation of the crystal phase and formation of relatively uniform particles of small diameters. In the same sample (M5) a drawback observed was the undesirable tendency towards formation of secondary agglomerations, confirmed by a relatively high polydispersity index PdI= 0.879 (Fig. 2f). In the ZnO-SiO₂ sample precipitated in a water system in similar process conditions, the particle size changes from 225 to 351 nm and from 1350 to 2115 nm (Michalska 2003).

The beneficial effect of a mixture of emulsifiers NP3 and NP5 (sample M5) used in the process of precipitation on the dispersion of ZnO-SiO₂ is best illustrated by the particle size distribution curves recorded by Mastersizer 2000. As follows from Fig. 3, sample M5 shows the presence of ZnO-SiO₂ particles of the smallest diameter of 8.7 μm which in this sample bring the greatest volume contribution (5.7%).

Sedimentation is a phenomenon of free fall of solid particles in liquid and is used to increase a density of suspension under the effect of gravitational field. The rate of fall depends on the diameter and shape of particles and on the material density. Figure 4a presents sedimentation profiles of the ZnO-SiO₂ samples studied as mass increase vs. time. From the profiles the rate of particles fall can be determined. Analysis of the curves shows that the greatest increase in mass over the same period is noted for sample M1. The angle of the curve inclination to the X-axis is the smallest for M1, which corresponds to the fastest sedimentation. For this sample the fast sedimentation is related mainly to large size of particles and their shapes often differ from spherical and can be close to other geometrical figures. Moreover, solid particles of undefined shape can show a tendency to flocculation. The process of sedimentation

was the slowest for sample M4, built of very fine particles and few secondary agglomerates whose influence on the process of M4 sedimentation was negligible.

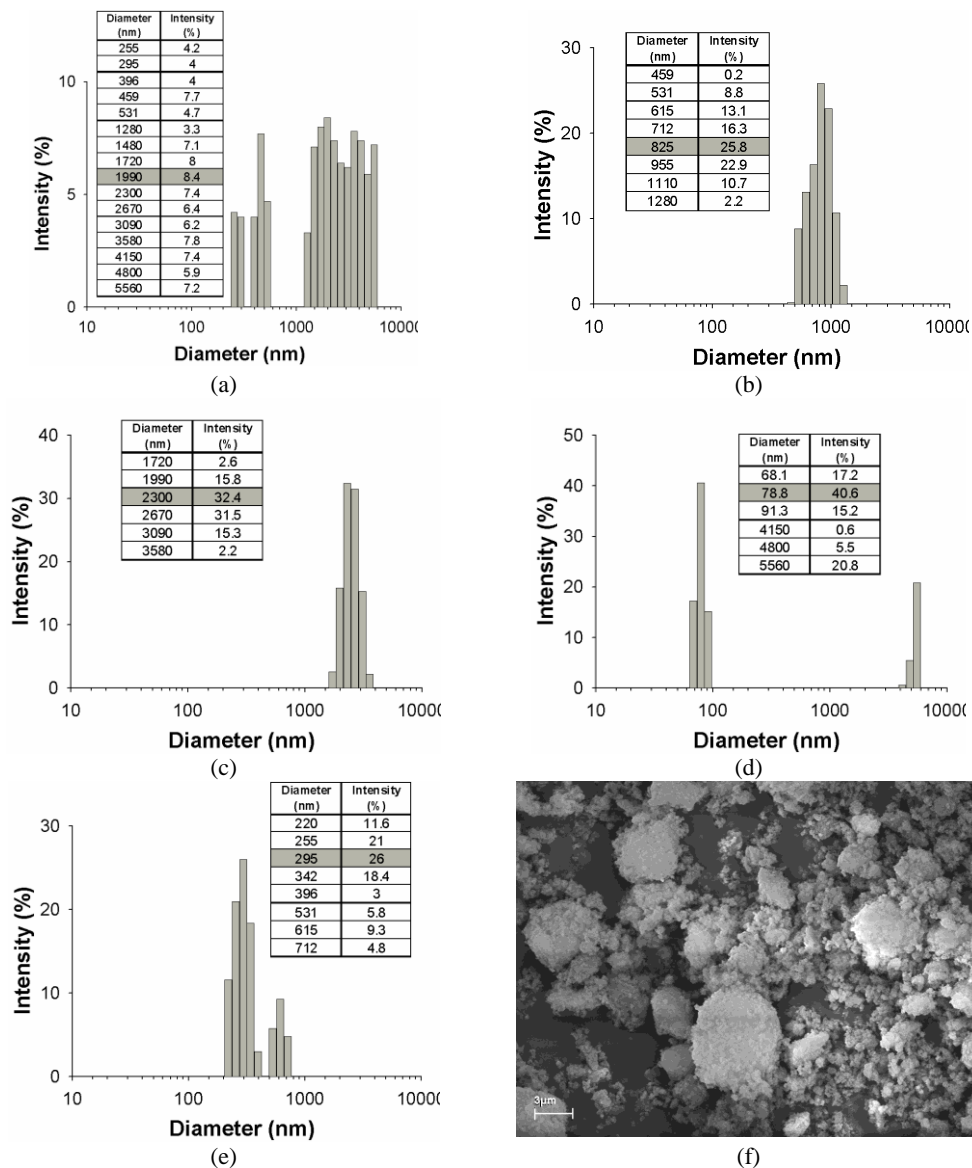


Fig. 2. Particle size distributions according to intensity evaluated for ZnO-SiO₂ oxide composites obtained on introducing E1 emulsion into zinc sulphate (a) M1, (b) M2, (c) M3, (d) M4, (e) M5, (f) SEM image of M5 sample

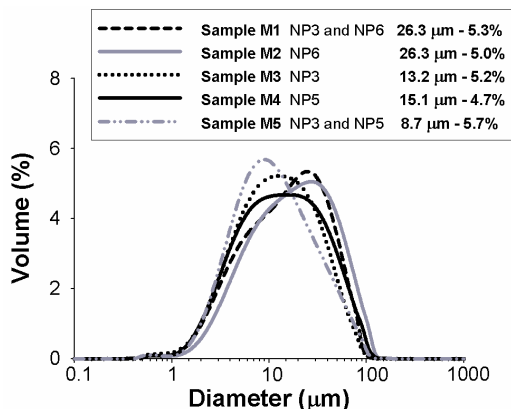


Fig. 3. Comparison of particle size distributions in micrometric range for ZnO-SiO₂ composites precipitated on introducing E1 emulsion into zinc sulphate using different types of emulsifiers

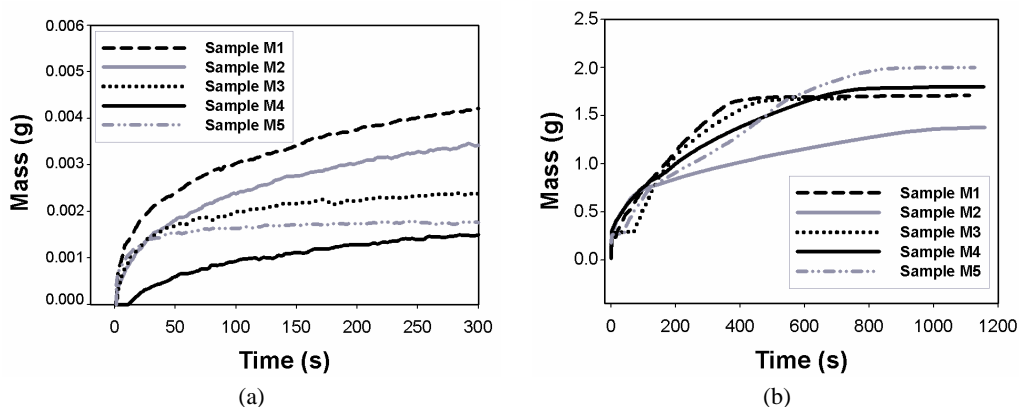


Fig. 4. Profiles of sedimentation (a) and wettability with water (b) for ZnO-SiO₂ oxide composites precipitated by introducing E1 emulsion into zinc sulphate

Another important parameter determining the use of materials for certain applications is the ability to absorb water. Much attention at many research centres has been paid to obtain maximally hydrophobic powders by relatively simple and cheap methods. Figure 4b presents the profiles of wettability with water recorded for the ZnO-SiO₂ samples studied. The curves illustrate the ability to absorb water by individual samples. The greatest mass increase in time was observed for sample M5, which means that this sample has the greatest wettability. Most probably the presence of relatively small particles showing a tendency to aggregation and their non-uniform morphology are responsible for the high ability to absorb water. The most hydrophobic was sample M2. Its hydrophobicity was related mostly to microstructural differences or partial adsorption of non-ionic surfactants on the surface of ZnO-SiO₂ particles.

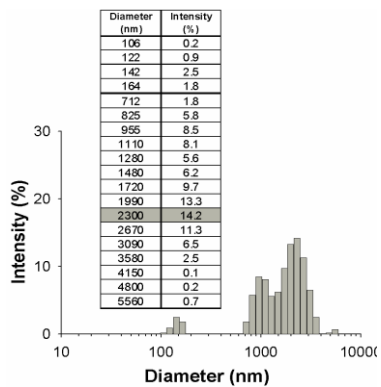
In the second stage of the study, the synthesis of ZnO-SiO₂ composites was performed in a different mode; 200 cm³ of zinc sulphate was introduced into 210 cm³ of E1 emulsion. E1 emulsion was made of 110 cm³ cyclohexane and 100 cm³ of a 5% solution of sodium silicate with surfactants NP3, NP5 or NP6.

Table 2 presents the dispersion parameters for ZnO-SiO₂ samples precipitated with different amount of emulsifier or a mixture of two emulsifiers.

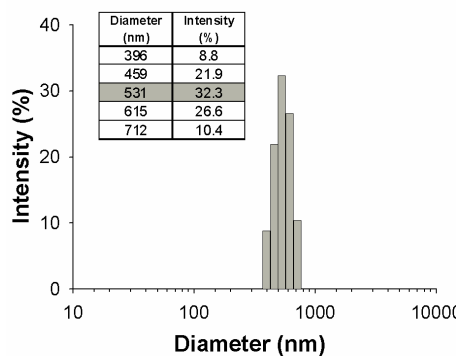
Table 2. Analysis of particle size distributions and PDI for different surfactants used in the process of ZnO-SiO₂ samples synthesis

| Sample | Type/amount of emulsifier (g) | | | Particle diameter (nm) | PDI |
|--------|-------------------------------|-----|-----|------------------------|-------|
| | NP3 | NP5 | NP6 | | |
| M6 | 1.5 | - | 1.0 | 106-164 712-5560 | 0.598 |
| M7 | - | - | 2.0 | 396-712 | 0.861 |
| M8 | 3.4 | - | - | 50-68 1280-5560 | 0.682 |
| M9 | - | 2.4 | - | 220-342 | 0.910 |
| M10 | 1.4 | 1.2 | - | 164-459 | 0.317 |

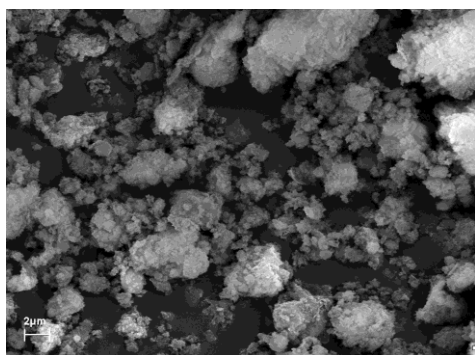
Figure 5a presents the particle size distribution according to intensity, obtained for sample M6. It shows two bands covering diameters from the ranges 106 – 164 nm and 712 – 5560 nm. In the first band the maximum intensity of 2.5% corresponded to the particle diameter 142 nm. The maximum intensity of 14.2% in the second band corresponds to the particle diameter 2300 nm. Sample M6 is characterised by the low polydispersity index (PDI=0.598), which points to high homogeneity of the particles despite the presence of secondary aggregates. The particle size distribution according to intensity, recorded for M7 is presented in Fig. 5b. It shows one band covering the diameter range 396 – 712 nm, with the maximum intensity of 32.3% corresponding to 531 nm. Figure 5c presents the SEM image of M7 confirming the presence of particles of non-uniform structure. The particle size distribution of sample M8 (Fig. 5d) shows two bands. One of them is relatively narrow and covers the diameters from the range 50 – 68 nm with the maximum of 9.6% corresponding to particles of 68 nm in diameter. The other band covering the range 1280 – 5560 nm testifies to the presence of secondary agglomerates. Its maximum of 14.0% corresponds to agglomerates of 5560 nm in diameter. The particle size distribution obtained for sample M9, Fig. 5e, shows one band covering the diameters 220 – 342 nm, with the maximum intensity of 37.8% corresponding to particles of 255 nm in diameter. Besides having single almost spherical particles of small diameter (Fig. 5f), sample M9 shows a tendency to flocculation hence its high polydispersity index of 0.910.



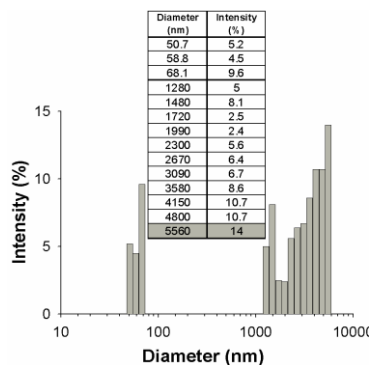
(a)



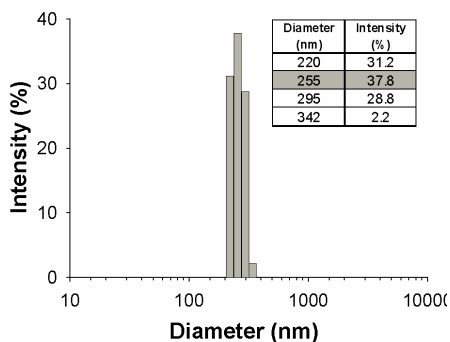
(b)



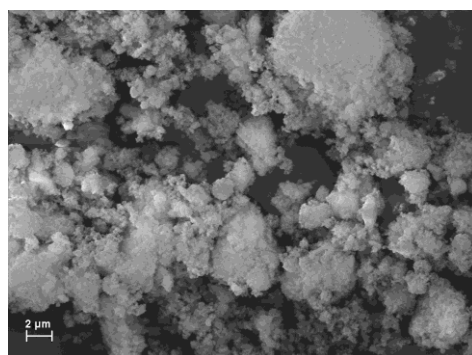
(c)



(d)



(e)

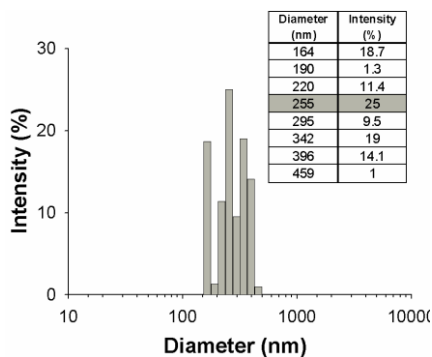


(f)

Fig. 5. Particle size distributions according to intensity of ZnO-SiO₂ composites obtained by introducing zinc sulphate to E1 emulsion: (a) M6, (b) M7, (c) SEM of M7, (d) M8, (e) M9, (f) SEM of M9, (g) M10

(continued)

Fig. 5. Continued



(g)

The next plot is the particle size distribution of sample M10 (Fig. 5g). It has only one band covering the particle diameters from 164 to 459 nm, reaching a maximum intensity of 25.0% for particles of 255 nm in diameter. The lowest polydispersity index ($PdI=0.317$) and small sizes of particles illustrate the beneficial effect of a mixture of surfactants NP3 and NP5 on the process of ZnO-SiO₂ nucleation.

ZnO-SiO₂ has also been reported to be obtained from water systems with the use of zinc chloride. The particle size distribution obtained for this sample showed the highest intensities of 15.7% and 15.2% corresponding to particles of 531 nm and 220 nm, respectively. The non-uniform character of its particles and a tendency to formation of aggregates and agglomerates had direct influence on the surface activity of the precipitated ZnO-SiO₂ (Sójka-Ledakowicz 2010).

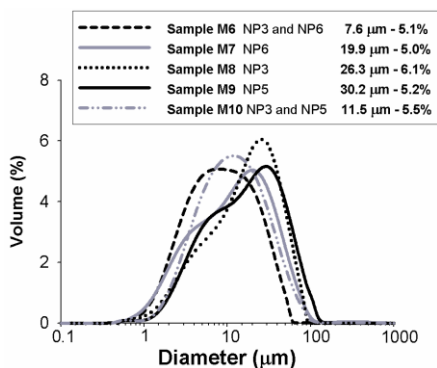


Fig. 6. Comparison of particle size distributions in the micrometric range for the samples obtained by introducing zinc sulphate into E1 emulsion for different emulsifiers or their mixtures

The influence of surfactants on the size of ZnO-SiO₂ particles is best illustrated by the particle size distribution curves plotted on the basis of laser diffraction measurement data. Figure 6 shows the particle size distribution curves for the samples

obtained with the use of different emulsifiers. The particle size distribution in the micrometric range according to volume contribution of sample M8 showed that the greatest volume contribution of 6.1% was brought by particles of 26.3 μm in diameter. In the sample M6 the smallest particles of diameters close to 7.6 μm , bring a volume contribution of 5.1%. These results illustrate the beneficial effect of emulsifiers NP3 and NP6 in the process of precipitation

The rate of a particle free fall depends on the physical properties of the liquid and particle, in particular on the difference in their densities, on viscosity of the liquid and size and shape of the particle. As follows from Fig. 7a, the sedimentation profile of sample M6 is inclined at the smallest angle to the Y-axis, which means that in this sample the rate of particles fall is the highest. The addition of a mixture of NP3 and NP6 surfactants in the process of ZnO-SiO₂ precipitation irrespective of its mode, favours the appearance of particles showing a tendency to fast falling. This observation was interpreted as related most probably to a change in the interaction between the solid particles or between the solid particles and the liquid. The lowest sedimentation manifested by the smallest mass increase in time was noted for sample M9. This sample is built of particles of the smallest diameters so their falling can be more uniform. Moreover the use of NP5 emulsifier during precipitation (irrespective of the direction of reagents introduction) influences the hydrodynamic interactions in the systems studied.

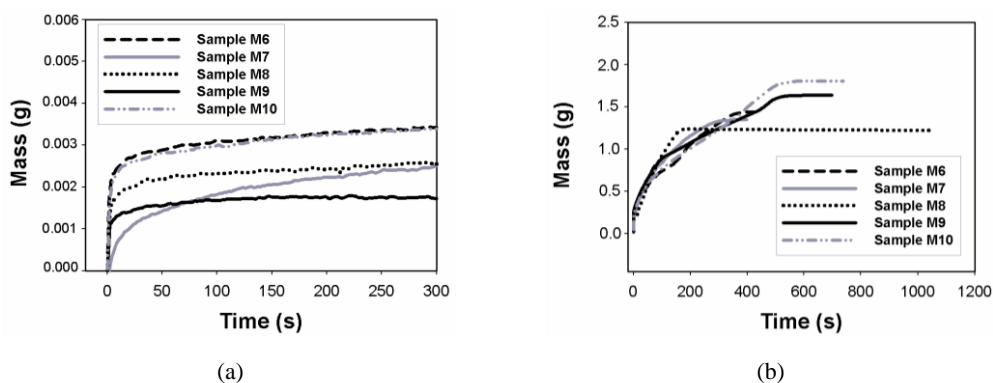


Fig. 7. Sedimentation profiles (a) and wettability with water (b) of ZnO-SiO₂ samples precipitated on introducing zinc sulphate into E1 emulsion

On the basis of the wettability profiles shown in Fig. 7b the samples tendency to absorb water (in other words their hydrophobic-hydrophilic properties) was characterised. The greatest water absorption ability or greatest affinity to water was observed for sample M10, which testifies to a high free energy of this composite. The smallest mass increase in time was detected for M8, whose surface shows the weakest interaction with water and hence poor water absorption. This behaviour of sample M8 can most probably be attributed by adsorption of NP3 surfactant on the particles of ZnO-SiO₂ leading to changes in the free energy of this composite.

Table 3 presents the properties of ZnO-SiO₂ composites obtained, including bulk density and percent contributions of the two oxide components in the appropriate sample.

Table 3. Chemical compositions and bulk densities of ZnO-SiO₂ oxide composites

| Sample | Chemical composition of ZnO-SiO ₂ composites (%) | | | Bulk density (g/dm ³) |
|--------|---|------------------|------------------|-----------------------------------|
| | ZnO | SiO ₂ | H ₂ O | |
| M1 | 25.2 | 52.8 | 22.0 | 25 |
| M2 | 27.0 | 54.5 | 18.5 | 111 |
| M3 | 24.8 | 53.8 | 21.4 | 134 |
| M4 | 26.2 | 49.5 | 24.3 | 112 |
| M5 | 28.5 | 51.0 | 20.5 | 91 |
| M6 | 23.5 | 51.5 | 25.0 | 140 |
| M7 | 24.0 | 51.4 | 24.6 | 149 |
| M8 | 21.3 | 57.5 | 21.2 | 190 |
| M9 | 27.8 | 55.9 | 16.3 | 122 |
| M10 | 26.9 | 52.2 | 20.9 | 109 |

The greatest content of ZnO in the composites obtained is 28.5% in sample M5 which also shows the lowest bulk density of 91 g/dm³. The greatest content of SiO₂ reaching 57.5% is determined for sample M8 showing the highest bulk density of 190 g/dm³.

In ZnO-SiO₂ oxide composites obtained from 5% water solutions of zinc chloride and sodium silicate, the greatest content of zinc oxide was 35.0 – 37.3%, while the lowest 28.2 – 28.9%. The greatest percent contribution of silica in the samples precipitated from water solutions was 56.7 – 58.8%, while the lowest was 49.0 – 49.5% (Laurentowska 2010). These data indicate that the percent contribution of particular oxides depends first of all on the concentration of substrates and not on the environment of the reaction.

Table 4 presents the colorimetric data on the ZnO-SiO₂ precipitated from the emulsion systems.

Table 4 presents colorimetric properties of ZnO-SiO₂ samples ordered according to the type of emulsifier used in the process of precipitation. The reference standard was the ZnO-SiO₂ composite obtained upon introduction of a 5% solution of sodium silicate to a 5% solution of zinc sulphate at 20°C. The lightness of all samples, L* takes similar values for all samples. The highest L* (94.32) was observed for M6, which also showed a greatest contribution of yellow, of 4.09. The lowest lightness L* of 92.22 was found for sample M1. The contribution of red varied from 0.04 (sample M8) to 0.42 (sample M9).

Table 4. Colorimetric characterisation of ZnO-SiO₂ oxide composites precipitated from the emulsion systems

| Sample | Colorimetric properties | | | | | |
|--------|-------------------------|------|------|------|-------|------|
| | L* | a* | b* | C* | h* | dE* |
| M0 | 93.83 | 0.26 | 2.75 | 2.76 | 84.53 | - |
| M1 | 92.22 | 0.31 | 2.71 | 2.73 | 83.53 | 1.61 |
| M2 | 92.76 | 0.26 | 2.96 | 2.97 | 84.99 | 1.09 |
| M3 | 93.08 | 0.25 | 2.96 | 3.03 | 85.20 | 0.78 |
| M4 | 93.96 | 0.34 | 3.35 | 3.36 | 84.13 | 0.53 |
| M5 | 92.58 | 0.25 | 2.83 | 2.84 | 84.86 | 1.25 |
| M6 | 94.32 | 0.21 | 4.09 | 4.10 | 87.12 | 1.32 |
| M7 | 94.28 | 0.36 | 3.34 | 3.36 | 83.82 | 0.66 |
| M8 | 93.43 | 0.04 | 3.03 | 3.03 | 89.23 | 0.50 |
| M9 | 93.42 | 0.42 | 3.36 | 3.39 | 82.93 | 0.73 |
| M10 | 92.39 | 0.17 | 2.63 | 2.63 | 86.21 | 1.44 |

4. Conclusions

The performed reactions of synthesis of ZnO-SiO₂ composites from emulsion system gave products of particles whose diameters were mainly in the micrometric range. The particle size analysis by NIBS method showed that the sample of the smallest particles (220 – 342 nm) was obtained by introducing zinc sulphate into E1 emulsion with addition of emulsifier NP5, which proves a beneficial effect of NP5 on dispersion and morphology of the composite. According to the results of the particle size analysis by laser diffraction method, the direction of substrates introduction significantly affects the process of precipitation. The SEM images confirmed the presence of particles of micrometric sizes showing a tendency to formation of agglomerates and aggregates. The hydrophobic or hydrophilic properties of the products obtained were evaluated on the basis of profiles of wettability with water. Differences in the hydrophobic-hydrophilic properties of the products were attributed mainly by microstructural properties and partial adsorption of surfactants on the particle surface. The rates of sedimentation obtained from the sedimentation profiles permitted indirect characterisation of hydrodynamic interactions in the systems studied. Colorimetric analysis provided the information on the colours of the oxide composites studied and in particular confirmed the suitability of using ZnO-SiO₂ as a white pigment of high lightness.

Acknowledgements

This publication was prepared within the key project – PO IG no. 01.03.01-00-006/08 cofinanced from the funds of European Regional Development Fund within the framework of the Operational Programme Innovative Economy.

References

- CANNAS C., CASU M., LAI A., MUSINO A., PICCALUGA G., 1999, *XRD, TEM and ^{29}Si MAS NMR study of sol-gel ZnO-SiO₂ nanocomposites*, J. Mater. Chem., 9, 1765–1769.
- CHAKRABARTI S., GANGULI D., CHAUDHURI S., 2004, *Excitonic and defect related transitions in ZnO-SiO₂ nanocomposites synthesized by sol-gel technique*, Phys. Status Solidi, 201, 2134–2142.
- FOTOPOULOS A. P., TRIANTAFYLIDIS K. S., 2007, *Ethylene epoxidation on Ag catalyst supported on non-porous, microporous and mesoporous silicates*, Catal. Today, 127, 148–156.
- FU Z., YANG B., LI L., DONG W., JIA C., WU W., 2003, *An intense ultraviolet photoluminescence in sol-gel ZnO-SiO₂ nanocomposites*, J. Phys. Condens. Mat., 15, 2867–2873.
- GANGULI D., CHATTERJEE M., 1997, *Ceramic Powder Preparation: A Handbook*, Kluwer, Boston.
- JESIONOWSKI T., 2009, *Preparation of spherical silica in emulsion systems using the co-precipitation technique*, Mater. Chem. Phys., 113, 839–849.
- KALINKIN A. M., KALINKINA E. V., ZALKIND O. A., 2009, *Mechanosorption of carbon dioxide by Ca- and Mg-containing silicates and aluminosilicates sorption of CO₂ and structure-related chemical changes*, Colloid J., 71, 185–192.
- KRYSZTAFKIEWICZ A., LIPSKA L. K., CIESIELCZYK F., JESIONOWSKI T., 2004, *Amorphous magnesium silicate – synthesis, physicochemical properties and surface morphology*, Adv. Powder Technol., 15, 549–565.
- LAURENTOWSKA A., CIESIELCZYK F., JÓZWIAK K., JESIONOWSKI T., 2010, *Syntetyczne kompozyty tlenkowe typu ZnO-SiO₂ o dużym stopniu zdyspersgowania*, Przem. Chem., 89, 1351–1356.
- LEE S. G., JANG Y. S., PARK S. S., KANG B. S., MOON B. Y., PARK H. C., 2006, *Synthesis of fine sodium-free silica powder from sodium silicate using w/o emulsion*, Mater. Chem. Phys., 100, 503–506.
- MICHALSKA I., KRYSZTAFKIEWICZ A., BOGACKI M. B., JESIONOWSKI T., 2003, *Preparation and characterisation of precipitated zinc silicates*, J. Chem. Technol. Biot., 78, 452–460.
- MIDMORE B. R., 2001, *Interaction between colloidal silica and a nonionic surfactant hexagonal liquid crystalline phase*, Colloids Surf. A, 182, 83–92.
- MO C. M., LI Y. H., LIU Y. S., ZHANG Y., ZHANG L. D., 1998, *Enhancement effect of photoluminescence in assemblies of nano-ZnO particles/silica aerogels*, J. Appl. Phys., 83, 4389–4391.
- ROBINS M. M., WATSON A. D., WILDE P. J., 2002, *Emulsions – creaming and rheology*, Curr. Opin. Coll. Interface Sci., 7, 419–425.
- SOMASUNDARAN P., MEHTA S. C., PUROHIT P., 2006, *Silicone emulsion*, Adv. Colloid Interface Sci., 128–130, 103–109.
- SÓJKA-LEDAKOWICZ J., OLCZYK J., WALAWSKA A., LAURENTOWSKA A., KOŁODZIEJCZAK-RADZIMSKA A., JESIONOWSKI T., 2010, *Modyfikacja wyrobów włókienniczych przy wykorzystaniu tlenku cynku o cząstkach nanometrycznych oraz kompozytu tlenkowego ZnO-SiO₂*, Przem. Chem., 89, 1648–1652.
- SUN Q., VRIELING E. G., VAN SANTEN R. A., SOMMERDIJK N. A. J. M., 2004, *Bioinspired synthesis of mesoporous silicas*, Curr. Opin. Solid St. M., 8, 111–120.
- YANG Y., ZHUANG Y., HE Y., BAI B., WANG X., 2010, *Fine tuning of the dimensionality of zinc silicate nanostructures and their application as highly efficient absorbents for toxic metal ions*, Nano Res., 3, 581–593.
- YAO B. D., SHI H. Z., BI H. J., ZHANG L. D., 2000, *Optical properties of ZnO loaded in mesoporous silica*, J. Phys.: Condens. Matter, 12, 6265–6270.
- YING J. Y., MEHNERT C. P., WONG M. S., 1999, *Synthesis and applications of supramolecular-templated mesoporous materials*, Angew. Chem. Int. Edit., 38, 56–77.
- ZHAO S., JI Z., YANG Y., HUO D., LV Y., 2007, *Nano-ZnO embedded SiO₂ glass with intense ultraviolet emission*, Mater. Lett., 61, 2547–2550.

Received April 29, 2011; reviewed; accepted July 7, 2011

COMPARISON OF DIFFERENT METHODS FOR ENHANCING CO₂ CAPTURE BY CaO-BASED SORBENTS. REVIEW

Michalina KOTYCZKA-MORANSKA , Grzegorz TOMASZEWICZ
Grzegorz LABOJKO

Institute for Chemical Processing of Coal, Zamkowa 1 41-801 Zabrze, mmoranska@ichpw.zabrze.pl

Abstract. CaO-based sorbent looping cycle, i.e. cyclic calcination/carbonation, is one of the most perspective technologies for CO₂ capture during coal combustion and gasification processes. This study deals with different methods of enhancing CaO based sorbents activity. We also present the results of our research on the use of dolomite from Siewierz and limestone from Czatkowice. The limestone carbonation conversion in the initial cycles is worse than pure CaO, but its carbon dioxide capture parameters are better than the parameters of dolomite. Sintering appears to play a significant role in the decay of CaO-based sorbents. The annealing effect for different sorbents was investigated. Tests were performed for calcium acetate, calcium hydroxide, dolomite from Siewierz and pure CaO.

keywords: calcium looping, CO₂ capture, CaO-based sorbents

1. Introduction

Nowadays, global warming is considered to be an important problem of the world. Extensive efforts are being made worldwide to reduce CO₂ emissions to the atmosphere. About 75% of the anthropogenic CO₂ emissions to the atmosphere during the past 20 years are due to fossil fuel burning (Solieman et al., 2009). It is widely accepted that the CO₂ concentration was about 280 ppm before the Industrial Revolution, and that it increased from 315 ppmv in 1950 to 355 ppmv in 1990. The increasing use of fossil fuels to meet energy needs has led to increased atmospheric CO₂ levels (Wang et al., 2010). CO₂ capture and sequestration is emerging as a viable option to achieve very deep cuts in emissions that might be needed in the medium term. This has led to proposals to capture the CO₂ from combustion gases, and then release it separately in a concentrated stream, which can be fixed more efficiently than diluted combustion gases (Shimizu et al., 1999). According to some research, CO₂ capture and storage technologies (CCS) could reduce CO₂ emissions in industry sectors by over 50% by 2050 (Florin and Harris, 2009). Therefore, reducing the CO₂ emissions will be the greatest industrial challenge of the 21st century (Fang et al.,

2009). Currently, the most common commercial technology to capture CO₂ is amine-based absorption, but its application is limited to a small scale (102 Mg/day) and low temperature (40-150°C). Alternatively, these drawbacks can be overcome by using metal-oxide-based inorganic sorbents to capture CO₂ selectively from flue gas streams. Suitable sorbents should exhibit fast carbonation and regeneration within the temperature range of 200-800°C. To date, CaO-based sorbents have been the most promising candidates for CO₂ capture and are cost-effective (Manovic and Anthony, 2008a). Because power plants are the biggest CO₂ emitters, the extensive efforts to reduce CO₂ emission resulted in rapid development of carbon capture and storage technologies. It is widely recognized that there is scope for large reductions in capture costs by applying new concepts for separating carbon dioxide from combustion flue gases in the capture system. The most popular separating systems are presented in Fig. 1.

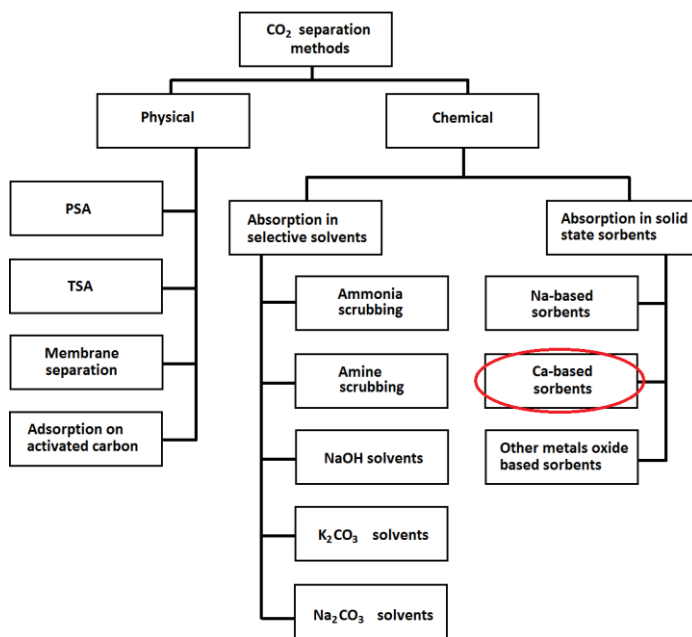


Fig. 1. The most popular CO₂ separating methods

There are three groups of technologies for carbon dioxide reduction from flue gases:

- post-combustion - carbonate looping processes are based on the capture of carbon dioxide from the flue gases of an existing power plant.
- pre-combustion - CO₂ can be captured prior to power generation, where fossil fuels are decarbonised.
- oxy-combustion of fuel in boilers or gas turbines with pure O₂ mixed with recirculated exhausts (95–99%) separated from the air.

2. CaO-based sorbents

Silaban et al. (1996) and Shimizu et al. (1999) proposed the use of calcium-based sorbents to capture CO₂ from gases at high temperatures based on the reversibility of the reaction:



The basic carbonation/calcination loop was successfully tested in the Acceptor Gasification Process in the USA during the late 1960s, in a 40 Mg/day pilot plant, where the calcinations were conducted under air. In the case of the CO₂ post-combustion capture system, the carbonation reaction makes use of CO₂ contained in the exhaust gases of the boiler. The calcination of the formed CaCO₃, which is carried out in a reactor where the part of the fuel is burned with oxygen, generates a concentrated stream of CO₂ ready for storage (Li et al., 2009).

The adsorbent used in the capture system must have (Yong et al., 2002):

- (1) high selectivity and adsorption capacity for carbon dioxide at high temperature;
- (2) adequate adsorption/desorption kinetics for carbon dioxide at operating conditions;
- (3) stable adsorption capacity of carbon dioxide after repeated adsorption/desorption cycles;
- (4) adequate mechanical strength of adsorbent particles after cyclic exposure to high pressure streams;
- (5) adequate pore size distribution and large pore volume;
- (6) large active surface of sorbent.

The main advantages of the calcium sorbents obtained from limestone are:

- low price of sorbent (from limestone),
- non-toxicity and environmental impact,
- easy use in fluidized bed reactors,
- CO₂ capture in temperature higher than 500°C (possibility of heat recovery),
- possibility to reuse the sorbent for cement production,
- possibility for CO₂ removal from flue gases and hydrogen production.

Because the equilibrium pressure of CO₂ at 1 atm (1013.25 hPa) occurs above 850°C, the process of calcination should be carried out just above this temperature. On the other hand, using temperature higher than 950°C and long calcination times result in a decrease in sorption capacity. However, absorption of CO₂ using CaO (carbonation) can occur at temperatures above 600°C, which is undoubtedly a great advantage of calcium sorbents (Salvador et al., 2004). The efficiency of the CO₂ capture depends on many parameters i.e. diffusion resistance, which depends on the size of sorbent particles, volume and the pore structure, as well as surface size and reaction kinetics (Hughes et al., 2004). These parameters influence carbonation, but many of them also influence calcination. Typical calcination/carbonation parameters and research methods for different CaO precursors are shown in Table 1. As shown in

the literature reports, the most important parameters characterizing the sorbents are (Grasa and Abanades, 2006; Abanades et al., 2008; Alvarez and Abanades, 2005a):

- the chemical composition (pollution, doping),
- calcination temperature,
- calcination and carbonation time,
- reactor type (determines thermal stress of the sorbent particles),
- effective concentration of CO₂ during calcination.

Table 1. Summary of research methods and calcination/carbonation parameters

| Sorbent | Calcination temperature | Carbonation temperature | Conditions | Calcination time | Carbonation time | Ref. |
|---|--|---|---|------------------|------------------|-----------------------------------|
| Kelly Rock CaCO ₃ La Blanca CaCO ₃ | 900°C (100%N ₂) | 800°C (50%CO ₂) | TGA, thermal pretreating, 30mg | 10 min | 30 min | (Manovic et al., 2008a) |
| Kelly Rock CaCO ₃ La Blanca CaCO ₃ Katowice CaCO ₃ | - | - | TGA, thermal pretreating, Flow rate CO ₂ 200cm ³ /min, 3g | 30 min | 10 min | (Manovic et al., 2009) |
| Ca(OH) ₂ | 950°C (100% CO ₂) | | | | | |
| Ca(CH ₃ COO) ₂ | 700°C 850°C (30%CO ₂) | 650°C | TGA, 20mg | - | 100 min 5 min | (Grasa et al., 2007) |
| CaO-KMnO ₄ | 780-980°C (21%O ₂ 79%N ₂) | 550-750°C (15%O ₂ 85%N ₂) | TGA | 15 min | 20 min | (Li et al., 2010) |
| Ca(CH ₃ COO) ₂ ⇒ CaO-Ca ₁₂ Al ₁₄ O ₃₃ | 900°C | 690°C | TGA, thermal pretreating - 890°C, 20 min, N ₂ | 10 min | 30 min | (Martavaltzi and Lemonidou, 2008) |
| Ca(OH) ₂ ⇒ CaO-Ca ₁₂ Al ₁₄ O ₃₃ | 850°C | 690°C | | | | |
| CaCO ₃ ⇒Ca(CH ₃ COO) ₂ | 850°C | - | TGA, 0,1cm ³ | 2h | | (Wu et al., 2005) |
| Ca(OH) ₂ | 700°C 800°C 900°C | 700°C | TGA | - | - | (Jia et al., 2005) |
| CaCO ₃ | 700°C (100%N ₂) | 600°C (15%CO ₂ 85%N ₂) | TGA, 10mg | - | - | (Fang et al., 2009) |
| Ca(CH ₃ COO) ₂ ⇒ CaO-Ca ₁₂ Al ₁₄ O ₃₃ | 850°C (N ₂) | 690°C (N ₂) | TGA, thermal pretreating 900°C, 1.5h | 10 min | 30 min | (Martavaltzi et al., 2010) |
| CaO | | 300°C; 325°C; 350°C; 400°C; 450°C; (CO ₂) | | | | |
| Ca(OH) ₂ | | 200°C; 250°C; 300°C; 350°C; 375°C; 400°C; 425°C; (CO ₂); (50%H ₂ O) | - | - | - | (Nikulshina et al., 2007) |
| CaO⇒ CaO-Ca ₁₂ Al ₁₄ O ₃₃ | 650°C 850°C | 600°C; 650°C; 700°C (15%CO ₂ 85%N ₂) | TGA, 10-15 mg | 5 min | 30 min | (Li and Cai, 2007) |
| CaO CaO⇒ Ca(CH ₃ COO) ₂ | 920°C 1100°C | 600°C-700°C | TGA | - | - | (Li et al., 2009) |

(continued)

Table 1. Continued

| | | | | | | |
|--|---|---|--------------------------|--------------|--------|---|
| CaO/NaOH | 700°C (CO ₂) | 315°C (CO ₂) | TGA | - | - | (Siriwardane et al., 2007) |
| Kelly Rock CaCO ₃ | 750°C (50% CO ₂ 50% N ₂) | 750°C (100% N ₂) | TGA | 90 min | 30 min | (Manovic and Anthony, 2008b) |
| La Blanca CaCO ₃ | 960°C (100% CO ₂) | 650°C (100% CO ₂) | TGA | 10 min | 30 min | (Alvarez and Abanades, 2005a) |
| nano CaCO ₃ | 850°C (N ₂) | 650°C (15% CO ₂ 85% N ₂) | TGA, 5mg | 10 min | 24h | (Florin and Harris, 2009) |
| CaCO ₃ ⇒CaO Ca(OH) ₂ ⇒CaO nano CaO | 700°C (N ₂) | 600°C (15% CO ₂ 85% N ₂) | TGA, 2,5mg | 20 min 5h | 20 min | (Florin and Harris, 2008a) |
| Tamuin CaCO ₃ | 850°C (N ₂) | 650°C (N ₂) | TGA 5g | 40 min | 30 min | (Bouquet et al., 2009) |
| Kozani CaCO ₃ _MgCO ₃ Fermion Mount.CaCO ₃ _MgCO ₃ | 1005°C 1200°C | - | TGA 40mg | - | - | (Chrissafis and Paraskevopoulos, 2005a) |
| Kozani CaCO ₃ _MgCO ₃ Fermion Moun.CaCO ₃ _MgCO ₃ | 1100°C (CO ₂) | - | TGA | - | - | (Chrissafis et al., 2005b) |
| CaCO ₃ (>98%) | 650°C | - | 20kg FCB (INCAR-CSIC) | - | - | (Abanades et al., 2009) |
| Havelock CaCO ₃ Cadomin CaCO ₃ Kelly Rock CaCO ₃ Havelock CaCO ₃ +NaCl+Na ₂ CO ₃ | 850°C (N ₂) | 700°C (15% CO ₂ 85% N ₂) | TGA 22-23g CFBC 5kg | - | - | (Fang et al., 2009) |
| CaCO ₃ _MgCO ₃ | 950°C | 650°C | 80-100g Bubbling FBR | - | - | (Fang et al., 2009) |
| Purbeck CaCO ₃ Katowice CaCO ₃ Havelock CaCO ₃ Kelly Rock CaCO ₃ | 900°C | 650°C | TGA | 5 min | 5 min | (Wu et al., 2004) |
| CaCO ₃ SoyuzChimProm (Russia) | 800°C | 800°C | TGA | 15 min | 15 min | (Lysikov et al., 2008) |
| CaCO ₃ | >900°C (CO ₂) | 600-700°C | 20 kg CFBC | - | - | (Alonso et al., 2010) |
| CaCO ₃ Zi-Bo (China) | 920°C | 649°C (15% CO ₂ 85% air) | CFB | - | - | (Cao et al., 2010) |
| CaCO ₃ Swabian Alp | 630-700°C | 850°C | DBF | - | - | (Charitos et al., 2010) |

However, many studies showed that the capture capacity of CaO-based sorbents decreases during operation cycles (Manovic et al., 2009; Florin and Harris, 2008b). This is a major challenge for the future application of CaO-based technology for capturing CO₂. Therefore, it is required to improve sorbent reversibility for extended operation purpose.

The carbonation process proceeds in micropores, on mesopores and on grain boundaries (Bouquet et al., 2009; Manovic and Anthony, 2008c). Carbonation in micropores proceeds up to pore filling. The limited capacity of the micropores has been used by Bhatia and Perlmutter (1983) to calculate the conversion level of

carbonation after the calcination. Carbonation in the second region is limited by carbon dioxide diffusion through a layer of CaCO_3 . Critical layer thickness of the product covering the walls of pores was determined by Alvarez, using a model assuming cylindrical pores (Alvarez and Abanades, 2005b). In the process presented in the paper (Florin and Harris 2008b), reagent CaCO_3 was used (Sigma-Aldrich) with a grain size $<45 \mu\text{m}$. Carbonation was conducted at 600°C , in 15% CO_2 in N_2 , and calcination at 700°C in N_2 atmosphere. Decrease in absorption capacity is associated with sintering of the sorbent surface because of the influence of temperature, and the reduction in porosity and active surface (Wang et al., 2010; Manovic et al., 2008a,b; Alvarez and Abanades, 2005a; Manovic et al., 2009; Bouquet et al., 2009; Lysikov et al., 2008; Stanmore and Gilot, 2005). Other factors that reduce the activity of sorbents are the attrition of sorbent grains during the process and chemical inactivation. The reaction with sulfur oxide (SO_2) is competitive to the carbonation reaction (Li et al., 2009; Manovic and Anthony, 2007, 2010a). Sulfurization and carbonation reactions are similar because of being heterogeneous and occurring in the porous structure of the sorbent. However, sulfurization is irreversible in the range $500\text{--}900^\circ\text{C}$, occurs in small pores and covers the surface of the sorbent (Manovic and Anthony, 2010b; Adanez et al., 1999; Patsias et al., 2005; Nimmo et al., 2004). Bouquet et al. (2009) developed a simple micrograins model, describing the decline in capacity during subsequent cycles of carbonation. His model predicts the active area of the sorbent surface after a certain number of carbonations. However, Silaban et al. (1996) concluded that dolomite has better properties than limestone as a sorbent, and this is due to differences in structure. Further research in this field was conducted by Chrissafis et al. (2005a,b). He noted that at the temperature of 1005°C sintering of the surface significantly reduces the degree of carbonation of limestone, opposite to dolomite. Decrease in absorption capacity after 45 cycles was 60% for limestone, 40% for dolomite and less than 20% for huntite (Bandi et al., 2002).

Intensive research has been carried out to improve the performance of CaO-based sorbents by enhancing the CaO conversion and reducing performance decay. The main goal is to increase its porosity and surface area to enhance conversion. Designing synthetic sorbents (carrying chemical promotions or applying specific processing steps) to enhance performance stability is also a very important issue. The decrease in CO_2 absorption by CaO can be limited in several ways. The factors which have the greatest impact are:

- the kind of raw material used to obtain a calcium-based sorbent,
- thermal pretreatment of the sorbent,
- doping sorbent with Na_2CO_3 , NaCl , KCl , KMnO_4 , MgCl_2 , CaCl_2 , $\text{Mg}(\text{NO}_3)_2$,
- steam reactivation,
- other metals contained in limestone,
- grain size of sorbent.

The impact of the raw compound on the properties of the calcium oxide obtained was presented by Alvarez (Alvarez and Abanades, 2005a; Lu et al., 2006). In that

research calcium oxide was prepared from precursors such as Ca(NO₃)₂, Ca(CH₃COO)₂, CaCO₃ and Ca(OH)₂. As can be seen in the case of calcium oxide obtained from calcium acetate, the degree of CaO conversion was close to 100% and it corresponds to 76% CO₂ saturation. The properties of CaO obtained from calcium acetate are better than the properties of CaO obtained from natural limestone - it has a much better conversion (Manovic et al., 2008a) and greater durability (Li et al., 2009). In addition, calcium acetate has a high uptake capacity, but its reversibility occurs when the regeneration takes place under mild conditions (700°C in He) and the carbonation reaction carries on long enough (about 300 min. per cycle). Martavaltzi found that calcium acetate has a greater ability to capture CO₂ than Ca(OH)₂ due to differences in surface morphology (Martavaltzi and Lemonidou, 2008). Calcium hydroxide has a large tortuosity of the surface, which inhibits the attachment of CO₂ molecules to the active surface. Simultaneously, a key role in the pore structure of calcium hydroxide is played by the heating rate and calcination temperature (Jia et al., 2005). However, the decrease in maximum carbonation conversion for CaO obtained from both sorbents limits their application (Wu et al., 2005). In the case of industrial application of these absorbents it is necessary to use them in the form of pellets. The comparison of calcium oxide in powder and pellet form has shown a higher sorption capacity of sorbent in the powdered form (Wu et al., 2007). The sorption capacity of the pellets can be significantly raised using steam reactivation of sorbent during cycles (Manovic and Anthony, 2010b,c). As noted in paper of Manovic and Anthony, (2010c) the effect of steam reactivation raised the conversion of carbonation from 25% to 75%. The advantage of the application of the CaO steam reactivation is that it does not need to drain the excess water from the system. The sorbent does not require drying and it is not degraded during this process (Manovic and Anthony, 2007). Another way to increase the activity of absorption is the thermal pretreating of the sorbent (Manovic et al., 2009, 2008a). As concluded in paper by Manovic et al. (2009), sorbent annealing at temperatures 1000–1200°C reduces transformation activity in the initial cycles. In subsequent cycles it results in abnormal conversion, compared to not annealed sorbents. This is due to the increase in the hardness of sorbent grains, and their viability in reactors (Manovic and Anthony, 2008b). This phenomenon is more pronounced in the case of sorbents obtained by synthesis than those obtained by grinding. Sorbent activity may be increased up to ~ 50% in 30 cycles. The phenomenon of increased conversion of sorbent with an increasing number of cycles is called self-reactivation. The effect of heating of sorbent on its viability and activity was also investigated by Manovic et al. (2009). Annealing was performed in a tube furnace for the following temperatures: 900, 950, 1000 and 1100°C in the atmosphere of CO₂ and N₂. It was found that better performance is obtained for the sorbent heated in CO₂. Alvarez and Abanades (2005c) determined that the final conversion of CaO carbonation depends not only on the surface area but also on its geometry. It should be noted that long periods between the normal cycles of calcination decrease the activity of the sorbent (Florin and Harris, 2009; Manovic and

Anthony, 2008b). As already mentioned, one of the ways to prevent the reduction of sorbent capacity is impregnation using solutions of Na_2CO_3 , NaCl , KCl , KMnO_4 , MgCl_2 , CaCl_2 , $\text{Mg}(\text{NO}_3)_2$.

The experiments described in the literature do not allow to state clearly which of the impregnation procedures makes it possible to obtain a low-cost sorbent, characterized by very high efficiency in CO_2 capture and long life. As concluded by Li et al. (2010), CaCO_3 impregnated with KMnO_4 shows a greater capacity for CO_2 uptake only in the temperature range from 660°C to 710°C . In this range of temperature a sorbent has a longer viability than the undoped one. However, above this temperature the sorbent does not show a satisfactory performance. Also, impregnation of the sorbents with Na_2CO_3 and NaCl solution can improve their performance, but only when the sorbent is doped with a very small amount of impregnating salt (Salvador et al., 2003; Seo et al., 2007; Fennell et al., 2007). After the steam rehydration, sorbents doped with NaCl and Na_2CO_3 can be operated at temperatures of $130\text{--}300^\circ\text{C}$ for calcination and 50°C for carbonation (Seo et al., 2007). The experiments carried out with commercially available Aldrich calcium oxide as a sorbent showed its good absorption properties. The systems containing metal oxides of the first group of the periodic table (Li, Na, K, Rb, Cs) were also prepared. Their application results in an increase in the sorption capacity of CaO with an increase in the atomic radius of the doping metal. Thus, calcium oxide doped with cesium oxide showed the largest sorption capacity of all these compounds. The kind of cesium oxide precursor also influences the absorption capacity of CaO . The absorption capacity is the best for CsOH . Also important was the percentage of doping. It was found that for a sorbent with the highest absorption capacity the content was 20% (Reddy and Smirniotis, 2004). Using mixed alumina and calcium ($\text{Ca}_{12}\text{Al}_{14}\text{O}_{33}$) as a carrier of calcium oxide led to a significant improvement in regenerative properties of calcium-based sorbent. Also in this case the kind of precursor of calcium oxide (CaO , $\text{Ca}(\text{CH}_3\text{COO})_2$, CaCO_3 and $\text{Ca}(\text{OH})_2$) influences the absorption capacity. Calcination temperature influences the volume and surface area of sorbent. Together with the increase in temperature, active surface decreases, and consequently the sorption capacity is reduced. In order to maintain relatively high absorption capacity of the sorbent, a weight ratio 75:25 of $\text{CaO}:\text{Ca}_{12}\text{Al}_{14}\text{O}_{33}$ should be used (Li et al., 2006). Thermal stability of pure calcium oxide - although it showed a high absorption capacity - was not satisfactory, either. In the following cleaning cycles (apart from the initial one), a gradual decrease in the absorption capacity of CaO was observed. In the case of calcium oxide deposited on a mixed oxide of calcium and aluminum, the absorption capacity lower than the capacity of pure CaO was observed. The number of cycles does not affect its sorption capacity, either. In an experiment executed with $\text{CaO}-\text{Ca}_{12}\text{Al}_{14}\text{O}_{33}$, during 45 cycles CO_2 carbonation and regeneration activity of sorbent was almost constant. As already mentioned, the particle size of sorbent used also influences the degree of carbonation. The effect of a different grain size of limestone on the degree of carbonation was shown in paper (Grasa et al., 2008). With

the increase in the grain size the resistance of CO₂ diffusion inside CaO particles also increases and consequently the degree of conversion is reduced. Table 2 presents the literature review of CaO-based sorbents granulation used in experiments.

Table 2. Summary of sorbent granulation based in literature data

| Sorbent | Grain size μm | Ref. |
|---|--|---|
| Kelly Rock CaCO ₃ La Blanca CaCO ₃ | 300-425 400-600 | (Manovic et al., 2008a) |
| Kelly Rock CaCO ₃ La Blanca CaCO ₃ Katowice CaCO ₃ | 300-425 400-600 400-800 | (Manovic et al., 2009) |
| CaO Ca(OH) ₂ | 17,3 15,6 | (Grasa et al., 2007) |
| Kelly Rock CaCO ₃ La Blanca CaCO ₃ | 75-150 400-600 | (Manovic and Anthony, 2008b) (Alvarez and Abanades, 2005c) |
| nano CaCO ₃ Tamuin CaCO ₃ | 0,04 125-160 | (Florin and Harris, 2009) (Bouquet et al., 2009) |
| Kozani CaCO ₃ _MgCO ₃ Fermion Mount.CaCO ₃ _MgCO ₃ | <125 | (Chrissafis and Paraskevopoulos, 2005a) |
| CaCO ₃ CaCO ₃ _MgCO ₃ | <350 200-450 | (Abanades et al., 2009) (Fang et al., 2009) |
| Havelock CaCO ₃ Havelock CaCO ₃ | 250-425 400-800 | (Symonds et al., 2009) (Manovic et al., 2008c) |
| La Blanca CaCO ₃ | 100-250 400-600 600-800 | (Abanades and Alvarez, 2003) |
| ReaChim CaCO ₃ Havelock CaCO ₃ Kelly Rock CaCO ₃ Cadomin CaCO ₃ | 800-900 250-300 650-1675 | (Okunev et al., 2008) (Salvador et al., 2003) |
| Purbeck CaCO ₃ Katowice CaCO ₃ Havelock CaCO ₃ Kelly Rock CaCO ₃ | 710-1000 400-800 710-1000 600-800 | (Alonso et al., 2010) |
| SoyuzChimProm CaCO ₃ (Russia) CaCO ₃ | 3-10 <350 | (Li et al., 2010) (Nimmo et al., 2004) |
| Zi-Bo CaCO ₃ (China) CaCO ₃ Swabian Alp (Germany) | 250-1000 340 | (Grasa et al., 2008) (Charitos et al., 2010) |

3. Results and conclusions

In our study we examined the degree of carbonation of the dolomite from Siewierz, limestone from Czatkowice and pure calcium oxide (POCH S.A.). The experiments were performed using thermogravimetric analyzer Netzsch STA 409 PG. Sorbents were tested alternately during carbonation and calcination with heating and cooling rate of 20 K/min. Carbonation was conducted at 600°C, in 50% CO₂ in N₂, and calcination at 900°C in N₂ atmosphere. The results are shown in Figure 2.

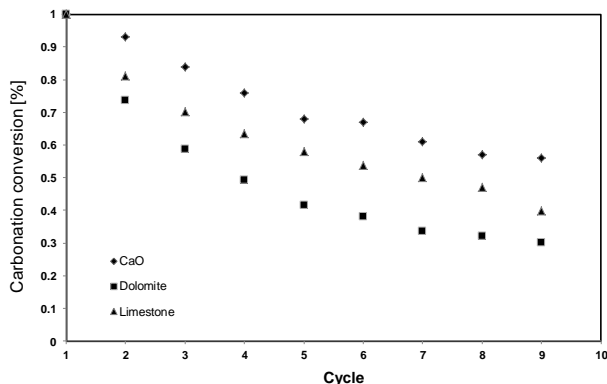


Fig. 2. Comparison of the degree of carbonation conversion of limestone, dolomite and CaO

As can be seen, although the limestone carbonation conversion in the initial cycles is worse than pure CaO, its CO₂ capture parameters are better than the parameters of dolomite. Decrease in the carbonation conversion is associated with sintering of the sorbent active surface. Moreover, annealing effect for different sorbents was investigated. Tests were performed for calcium acetate, calcium hydroxide, dolomite from Siewierz and pure CaO. Sorbents were thermally pretreated in 1000°C for 1h. The results are shown in Figure 3. In our experiments pre-sintering at 1000°C resulted in a significant drop in conversion in the first CO₂-capture reaction followed by an enhancement through ~10 cycles. The results are similar to these published by Manovic and Anthony (2008d).

The technology using lime in cyclic post-combustion capture is only about 15 years old. It seems that the technology will be developed widely in the nearest future and will be able to offer an economical CO₂ removal method using lime-based solids. Calcines of natural limestone can be used as high-temperature sorbents to capture CO₂ at the wide range of parameters. However, the decay of their maximum carbonation conversion during many carbonation/calcination cycles can limit their applicability. There is a close similarity between the conversion decay trends obtained in our research and that of other authors using different starting limestones. The decay of CaO-based sorbents ability to absorb CO₂ during the cycles is comparable to pure CaO. It was found that neither limestone from Czatkowice nor dolomite from Siewierz are effective for capturing CO₂.

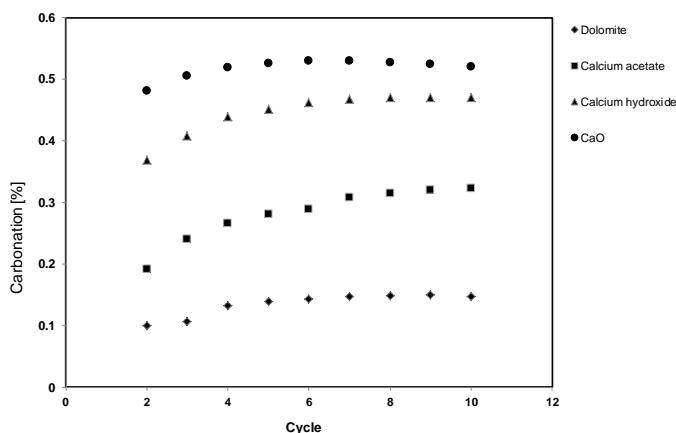


Fig. 3. Comparison of the degree of carbonation conversion thermal pretreated sorbents

References

- ABANADES, J., ALVAREZ, D., 2003, Conversion Limits in the Reaction of CO₂ with Lime, *Energy & Fuels*, 17, 308–315.
- ABANADES, J., ALONSO, M., RODRIGUES, N., GONZÁLEZ, B., GRASA, G., MURILLO, R., 2009, Capturing CO₂ from combustion flue gases with a carbonation calcination loop, *En. Procedia.*, 1, 1147–1154.
- ABANADES, J., MANOVIC, V., ANTHONY, E., GRASA, G., 2008, CO₂ Looping Cycle Performance of a High-Purity Limestone after Thermal Activation/Doping, *Energy & Fuels*, 22, 3258–3264.
- ADANEZ, J., de DIEGO, L., GARCIA-LABIANO, F., 1999, Calcination of calcium acetate and calcium magnesium acetate: effect of the reacting atmosphere, *Fuel* 78, 583–592.
- ALONSO, M., RODRÍGUEZ, N., GONZÁLEZ, B., GRASA, G., MURILLO, R., ABANADES, J., 2010, Carbon dioxide capture from combustion flue gases with a calcium oxide chemical loop. Experimental results and process development, *Int. J. Greenhouse Gas Cont.*, 4, 167–173.
- ALVAREZ, D., ABANADES, J., 2005a, Pore-Size and Shape Effects on the Recarbonation Performance of Calcium Oxide Submitted to Repeated Calcination/Recarbonation Cycles, *Energy & Fuels*, 19, 270–278.
- ALVAREZ, D., ABANADES, J., 2005b, Determination of the critical product layer thickness in the reaction of CaO with CO₂, *Ind. Eng. Chem. Res.* 44, 5608–5615.
- ALVAREZ, D., ABANADES, J., 2005c, Pore-Size and Shape Effects on the Recarbonation Performance of Calcium Oxide Submitted to Repeated Calcination/Recarbonation Cycles, *Energy & Fuels*, 19, 270–278.
- BANDI, A., SPECHT, M., SICHLER, P., NICOLOSO, N., 2002. In Situ Gas. Conditioning in Fuel Reforming for Hydrogen Generation., 5th Int.Symposium on Gas Cleaning at High Temperature, Morgantown
- BHATIA, S., PERLMUTTER, D., 1983, Effect of the product layer on the kinetics of the CO₂–lime reaction., *A. I. Ch. E. Journal* 29, 79–86.
- BOUQUET, E., LEYSSENS, G., SCHÖNNENBECK, C., GILOT, P., 2009, The decrease of carbonation efficiency of CaO along calcination–carbonation cycles: Experiments and modeling, *Chem. Eng. Sci.*, 64, 2136–2146.

- CAO, Ch., ZHANG, K., HE, Ch., ZHAO, Y., GUO, Q., 2010, Investigation into a Gas–Solid–Solid Three–Phase Fluidized Bed Carbonator to Capture CO₂ from Combustion Flue Gas; *Chem. Eng. Sci.*; 66, 375–383.
- CHARITOS, A., HAWTHORNE, C., BIDWE, A., SIVALINGAM, S., SCHUSTER, A., SPLIETHOFF, H., SCHEFFKNECHT, G., 2011, Parametric investigation of the calcium looping process for CO₂ capture in a 10kWh dual fluidized bed; *Int. J. Greenhouse Gas Cont.*, 4, 852–859.
- CHRISAFIS, K., PARASKEVOPOULOS, K., 2005a, The effect of sintering on the maximum capture efficiency of CO₂ using a carbonation/calcination cycle of carbonate rocks; *J. Therm. Anal. Cal.*, 81, 463–468.
- CHRISAFIS, K., DAGOUNAKI, C., PARASKEVOPOULOS, K., 2005b, The effects of procedural variables on the maximum capture efficiency of CO₂ using a carbonation/calcination cycle of carbonate rocks; *Thermochimica Acta*, 428, 193–198.
- FANG, F., LI, Z., CAI, N., 2009, Experiment and Modeling of CO₂ Capture from Flue Gases at High Temperature in a Fluidized Bed Reactor with Ca-Based Sorbents, *Energy & Fuels*, 23, 207–216.
- FENNELL, P., PACCIANI, R., DENNIS, J., DAVIDSON, J., HAYHURST, A., 2007, The Effects of Repeated Cycles of Calcination and Carbonation on a Variety of Different Limestones, as Measured in a Hot Fluidized Bed of Sand, *Energy & Fuels* 21, 2072–2081.
- FLORIN, N., HARRIS, A., 2008a, Screening CaO-Based Sorbents for CO₂ Capture in Biomass Gasifiers, *Energy & Fuels* 22, 2734–2742.
- FLORIN, N., HARRIS, A., 2008b, Enhanced hydrogen production from biomass with in situ carbon dioxide capture using calcium oxide sorbents, *Chem. Eng. Sci.*, 63, 287–316.
- FLORIN, N., HARRIS, A., 2009, Reactivity of CaO derived from nano-sized CaCO₃ particles through multiple CO₂ capture-and-release cycles, *Chemical Engineering Science*, 64, 187–191.
- GRASA, G., ABANADES, J., ALONSO, M., GONZÁLEZ, B., 2008, Reactivity of highly cycled particles of CaO in a carbonation/calcination loop, *Chem. Eng. J.*, 137, 561–567.
- GRASA, G., GONZÁLEZ, B., ALONSO, M., ABANADES, J., 2007, Comparison of CaO-Based Synthetic CO₂ Sorbents under Realistic Calcination Conditions, *Energy & Fuels*, 21, 3560–3562.
- GRASA, G., ABANADES, J., 2006, CO₂ Capture Capacity of CaO in Long Series of Carbonation/Calcination Cycles, *Industrial & Engineering Chemistry Research*, 45, 8846–8851.
- HUGHES, R., LU, D., ANTHONY, E., WU, Y., 2004, Improved long-term conversion of limestone-derived sorbents for in situ capture of CO₂ in a fluidized bed combustor, *Ind. Eng. Chem. Res.*, 43, 5529–5539.
- JIA, L., ZENG, Y., ZHANG, T., 2005, Experimental Study on Pore Distribution Characters and Convert Rate of CaO, *Journal of Thermal Science*, 14, 87–91.
- KOGEL, J., TRIVEDI, N., BARKER, J., KRUKOWSKI S., 2006, *Industrial minerals & rocks: commodities, markets, and uses*, Society for Mining Metallurgy & Exploration 570.
- LI, Y., ZHAO, Ch., CHEN, H., LIANG, C., DUAN, L., ZHOU, W., 2009, Modified CaO-based sorbent looping cycle for CO₂ mitigation, *Fuel* 88, 697–704.
- LI, Y., ZHAO, Ch., CHEN, H., DUAN, L., CHEN, X., 2010, Cyclic CO₂ capture behavior of KMnO₄-doped CaO-based sorbent, *Fuel* 89, 642–649.
- LI, Z., CAI, N., 2007, Modeling of Multiple Cycles for Sorption-Enhanced Steam Methane Reforming and Sorbent Regeneration in Fixed Bed Reactor, *Energy & Fuels*, 21, 2909–2918.
- LI, Z., CAI, N., HUANG, Y., 2006, Effect of preparation temperature on cyclic CO₂ capture and multiple carbonation-calcination cycles for a new Ca-based CO₂ sorbent, *Industrial & Engineering Chemistry Research* 45, 1911–1917.
- LU, H., REDDY, E., SMIRNIOTIS, P., 2006, Calcium Oxide Based Sorbents for Capture of Carbon Dioxide at High Temperatures, *Industrial & Engineering Chemistry Research* 45, 3944–3949.
- LYSIKOV, A., TRUKHAN, S., OKUNEV, A., 2008, Sorption enhanced hydrocarbons reforming for fuel cell powered generators, *Int. J. Hydrogen Energy* 33, 3061–3066.
- MANOVIC, V., ANTHONY, E., GRASA, G., ABANADES, J., 2008a, CO₂ Looping Cycle Performance of a High-Purity Limestone after Thermal Activation/Doping, *Energy & Fuels* 22, 3258–3264.

- MANOVIC, V., ANTHONY, E., 2008b, Parametric Study on the CO₂ Capture Capacity of CaO-Based Sorbents in Looping Cycles, *Energy & Fuels*, 22, 1851–1857.
- MANOVIC, V., ANTHONY, E., GRASA G., ABANADES J., 2008c, CO₂ Looping Cycle Performance of a High-Purity Limestone after Thermal Activation/Doping, *Fuel*, 87, 3344–3352.
- MANOVIC, V., ANTHONY, E., 2008d, Thermal activation of CaO-based sorbent and self-reactivation during CO₂ capture looping cycles, *Env. Sci. Tech.* 42, 4170–4174.
- MANOVIC, V., ANTHONY, E., LONCAREVIC D., 2009, CO₂ looping cycles with CaO-based sorbent pretreated in CO₂ at high temperature, *Chem. Eng. Sci.* 64, 3236–3245.
- MANOVIC, V., ANTHONY, E., 2007, SO₂ retention by reactivated CaO-based sorbent from multiple CO₂ Capture Cycles, *Environ. Sci. Technol.* 41, 4435–4440.
- MANOVIC, V., ANTHONY, E., 2010a, Sulfation Performance of CaO-Based Pellets Supported by Calcium Aluminate Cements Designed for High-Temperature CO₂ Capture, *Energy Fuels* 24, 1414–1420.
- MANOVIC, V., ANTHONY, E., 2010b, CO₂ Carrying behavior of calcium aluminate pellets under high-temperature/high-CO₂ concentration calcination conditions, *Ind. Eng. Chem. Res.* 49, 6916–6922.
- MANOVIC, V., ANTHONY, E., 2010c, Lime-Based Sorbents for High-Temperature CO₂ Capture—A Review of Sorbent Modification Methods *Int. J. Environ. Res. Public Health* 7, 3129–3140.
- MARTAVALTZI, Ch., LEMONIDOU, A., 2008, Development of new CaO based sorbent materials for CO₂ removal at high temperature, *Microporous and Mesoporous Materials* 110, 119–127.
- MARTAVALTZI, Ch., PAMPAKA, E., KORKAKAKI, E., LEMONIDOU, A., 2010, Hydrogen Production via Steam Reforming of Methane with Simultaneous CO₂ Capture over CaO-Ca₁₂Al₁₄O₃₃, *Energy Fuels* 24, 2589–2595.
- NIKULSHINA, V., GÁLVEZ, M., STEINFELD, A., 2007, Kinetic analysis of the carbonation reactions for the capture of CO₂ from air via the Ca(OH)₂–CaCO₃–CaO solar thermochemical cycle, *Chemical Engineering Journal* 129, 75–83.
- NIMMO, W., PATSIAS, A., HAMPARTSOUMIAN, E., GIBBS, B., FAIRWEATHER, M., WILLIAMS, P., 2004, Calcium magnesium acetate and urea advanced reburning for NO control with simultaneous SO₂ reduction, *Fuel*, 83, 1143–1150.
- OKUNEV, A., NESTERENKO, S., LYSIKOV, A., 2008, Decarbonation Rates of Cycled CaO Absorbents, *Energy & Fuels*, 22, 1911–1916.
- PATSIAS, A., NIMMO, W., GIBBS, B., WILLIAMS P., 2005, Calcium-based sorbents for simultaneous NO_x/SO_x reduction in a down-fired furnace, *Fuel*, 84, 1864–1873.
- REDDY, E., SMIRNIOTIS, P., 2004, Sorption of CO₂ by alkali metals doped CaO sorbents, *Journal of Physical Chemistry B*, 108, 7794–7800.
- SALVADOR, C., et al., 2005, Proceedings of the 7th International Conference on Greenhouse Gas Control Technologies, 5 September 2004, Vancouver, Canada 1107–1113.
- SALVADOR, C., LU, D., ANTHONY, E., ABANADES, J., 2003, Enhancement of CaO for CO₂ capture in an FBC environment, *Chemical Engineering Journal*, 96, 187–195.
- SEO, Y., JO, S., RYU, Ch., YI, Ch., 2007, Effects of water vapor pretreatment time and reaction temperature on CO₂ capture characteristics of a sodium-based solid sorbent in a bubbling fluidized-bed reactor, *Chemosphere*, 69, 712–718.
- SHIMIZU, T., HIRAMA, T., HOSODA, H., KITANO, K., INAGAKI, M., TEJIMA, K., 1999A, Twin Fluid-Bed Reactor for Removal of CO₂ from Combustion Processes, *Chemical Engineering Research and Design*, 77A, 62–68.
- SILABAN, A., NARCIDA, M., HARRISON, D., 1996, Characteristics of the reversible reaction between CO_{2(g)} and calcined dolomite, *Chem. Eng. Com.* 146, 149–162.
- SIRIWARDANE, R., ROBINSON, C., SHEN, M., SIMONYI, T., 2007, Novel Regenerable Sodium-Based Sorbents for CO₂ Capture at Warm Gas Temperatures, *Energy & Fuels*, 21, 2088–2097.
- SOLIEMAN, A., DIJKSTRA, W., HAIJE, P., COBDEN, R., 2009, Brink Calcium oxide for CO₂ capture: Operational window and efficiency penalty in sorption-enhanced steam methane reforming, *Int. J. Greenhouse Gas Cont.* 3, 393–400.

- STANMORE, B., GILOT, P., 2005, Review—calcination and carbonation of limestone during thermal cycling for CO₂ sequestration; *Fuel Proc. Tech.*, 86, 1707–1743.
- SYMONDS, R., LU, D., MACCHI, A., HUGHES, R., ANTHONY, E., 2009, CO₂ capture from syngas via cyclic carbonation/calcination for a naturally occurring limestone: Modelling and bench-scale testing, *Chemical Engineering Science*, 64, 3536–3543.
- WANG, J., MANOVIC, V., WU, Y., ANTHONY, E., 2010, A study on the activity of CaO-based sorbents for capturing CO₂ in clean energy processes, *Applied Energy*, 87, 1453–1458.
- WU, S. , BEUM, T., YANG, J., KIM, J., 2007, Properties of Ca-base CO₂ sorbent using Ca(OH)₂ as precursor, *Industrial & Engineering Chemistry Research*, 46, 7896–7899.
- WU, S., UDDIN, Md., SASAOKA, E., 2005, Effect of Pore Size Distribution of Calcium Oxide High-Temperature Desulfurization Sorbent on Its Sulfurization and Consecutive Oxidative Decomposition, *Energy & Fuels*, 19, 864–868.
- WU, S., UDDIN, Md., NAGAMINE, S., SASAOKA, E., 2004, Role of water vapor in oxidative decomposition of calcium sulfide, *Fuel*, 83, 671–677.
- YONG, A., MATA, V., RODRIGUES, A., 2002, Adsorption of carbon dioxide at high temperature—a review, *Sep. Pur. Technol.*, 26, 195–205.

Received April 21, 2011; reviewed; accepted July 16, 2011

APPLICATION OF SUPPORTED AND POLYMER MEMBRANE WITH 1 DECYL-2-METHYLIMIDAZOLE FOR SEPARATION OF TRANSITION METAL IONS

Malgorzata ULEWICZ *, Elzbieta RADZYMINSKA-LENARCIK **

* Department of Metal Extraction and Recirculation, Czestochowa University of Technology, 42-200 Czestochowa, Armii Krajowej 19, ulewicz@min.pcz.czyst.pl

** Department of Inorganic Chemistry, University of Technology and Life Sciences, Seminaryjna 3, 85-326 Bydgoszcz, elaradz@utp.edu.pl

Abstract. The facilitated transport of Cu(II), Zn(II), Co(II), and Ni(II) ions from different aqueous nitrate source phases ($c_{Me} = 0.001M$, pH 6.0) across polymer inclusion membranes (PIMs) consisting of cellulose triacetate (support) and 2-nitrophenylpentyl ether (plasticizer) doped with 1-decyl-2-methylimidazol as ion carrier was reported. The membrane is characterised by atomic force microscopy (AFM) and thermal analysis (DTA and TG) techniques. The results show that Cu^{2+} can be separated very effectively from other transition metal cations as Zn^{2+} , Co^{2+} , and Ni^{2+} from different equimolar mixtures of these ions. The recovery factor of Cu^{2+} ions during transport across PIM from different mixture is equal to 92-95.1%. The comparative transport of Cu(II), Zn(II), Co(II), and Ni(II) ions from aqueous nitrate source phase across supported (SLMs) containing 1-decyl-2-methylimidazol as ion carrier was reported.

keywords: polymer inclusion membrane (PIM), supported liquid membrane (SLM), separation ions, copper(II), zinc(II), nickel(II), cobalt(II), imidazole derivatives

1. Introduction

Liquid membrane techniques are slowly though continuously becoming a very important and promising alternative to solvent extraction for metal ions recovery and separation from aqueous solutions. In recent years a remarkable increase in the application of emulsion membranes for zinc(II) recovery from spent solutions after the production of cellulose fibres has been observed. Moreover, pilot plants for Zn(II) recovery from the zinc production process and for the recovery of metals (including zinc, copper, cobalt cadmium and lead) from spent water generated in municipal waste incineration plants was activated. The wider use of liquid membranes in practice is considerably limited by their low durability and instability of operation, resulting mainly from their structures and compositions. It is important now to enhance the

stability of liquid membranes and extend the time of their operation, so that they could be used in practice, because, as has been demonstrated by numerous studies (Kislik, 2010; Nghiem et al., 2006), separation of many metals is possible in the process of transport through liquid membranes.

As metal ion carriers in the membrane processes, the same organic substances as those used in extraction processes are employed (Walkowiak et al., 2002). For the separation of nonferrous ions in the liquid membrane transport process both classical and new types of carriers are used (Nghiem et al., 2006). Commercial carriers of metal cations commonly used in the membrane technique enable the effective separation of ions but their selectivity is rather poor. Therefore, new complexing reagents are searched which selectively separate metal ions from aqueous solutions.

Gherrou et al. (2002) reported on the selective proton-driven transport of silver(I) ions in presence of nonferrous cations (Cu^{2+} , Zn^{2+}) across supported membranes with DB18C6. The transport selectivity of SLM was as follows: $\text{Ag}^+ > \text{Cu}^{2+} > \text{Zn}^{2+}$. Gherrou et al. (2005) also obtained optimal compositions of the polymer membrane for copper(II) transported using DB18C6. Selective facilitated transport of Cu^{2+} across PLM with 1, 10-didecyl-1,10-diaza-18-crown-6 or 1,7-diaza-15-crown-5 as ion carrier was studied by Parthasarathy and Buffle (1991) as well as Dadfarnia and Shamsipur (1992). The competitive transport of Cu^{2+} from solutions containing Mn^{2+} , Co^{2+} , Cd^{2+} , Ni^{2+} , and Pb^{2+} ions across bulk liquid membrane doped with DA18C6 was observed by Cho et al. (1988). Ulewicz et al. (2004) examined the competitive transport of Cd^{2+} from solutions containing Zn^{2+} and Cu^{2+} ions from aqueous chloride source phase through polymer inclusion membranes containing side-armed lariat ether-type derivatives of diphosphaza-16-crown-6 as ion carrier. The initial fluxes of all investigated cations increase with the acidity of the feed phase and the selectivity order was as follows: $\text{Cd(II)} > \text{Zn(II)} > \text{Cu(II)}$.

The cations Zn^{2+} , Pb^{2+} , Cu^{2+} , Ni^{2+} , Co^{2+} and Cd^{2+} which are transported across PIMs containing azocrown and thioazocrown imidazole derivatives were investigated by Ulewicz et al. (2007, 2009). The linear decrease in the values of the initial metal ions transport fluxes was observed with the increase in the hydrophilic-hydrophobic balance (HLB) index of the imidazole crown ether derivatives. The transport selectivity of PIM with azocrown imidazole was as follows $\text{Pb(II)} > \text{Zn(II)} > \text{Cu(II)} > \text{Co(II)} > \text{Ni(II)} > \text{Cd(II)}$. Recently, pyrrole azocrown ethers in ordinary bulk membrane systems were also found to preferentially transport lead(II) from equimolar mixture of Co^{2+} , Ni^{2+} , Cu^{2+} , Zn^{2+} , Cd^{2+} , Ag^+ and Pb^{2+} ions (Luboch et al., 2006).

The results of the authors' investigation of the separation of nonferrous metal ions using 1-alkylimidazoles as ion carriers are presented in their previous work (Ulewicz and Radzymińska-Lenarcik, 2011). In this work, the authors present the results of their investigation of the competitive transport of copper(II), zinc(II), cobalt(II), and nickel(II) ions across inclusion membranes containing 1-dodecyl-2-methylimidazoles from dilute nitrate solutions.

2. Experimental

2.1. Reagents

The inorganic chemicals, i.e. copper(II), zinc(II), nickel(II), and cobalt(II) nitrate were of analytical grade and were purchased from POCh (Gliwice, Poland). The organic reagents, i.e. cellulose triacetate (CTA), *o*-nitrophenylphenyl ether (*o*-NPPE) and dichloromethane were also of analytical grade and were purchased from Fluka and used without further purification. The 1-decyl-2-methylimidazol was synthesized according to a method reported in the literature (Pernak et al. 1987).

2.2. Supported and polymer membrane preparation and characterization

The polymer membranes were prepared according to the procedure reported in the previous paper (Ulewicz et al., 2007). A solution of cellulose triacetate as the support, plasticizer and 1-decyl-2-methylimidazol as ion carrier in dichloromethane was prepared. A specified portion of this solution was poured into a membrane mould comprised of a 9.0 cm in diameter glass ring placed on a glass plate with cellulose triacetate-dichloromethane glue. After slow solvent evaporation overnight the resulting membrane was peeled off from the glass plate by immersion in cold water. Then the membrane was soaked for 12 hours in distilled water to achieve their homogeneity. Microporous polypropylene membrane Celgard 2500 (Celgard, LLC) was used as the solid support. The membrane was soaked for 24 h in 1.0 M 1-decyl-2-methylimidazol in dichloromethane. Two samples of PIM and SLM membrane were cut from the same membrane film for duplicate transport experiments.

A surface characterization study of the membranes was performed by atomic force microscopy (AFM) according to the procedure described in our earlier paper (Ulewicz et al., 2010). The analysis of surface pore characteristics of polymer membrane was made using the AFM image processing program NanoScope v.5.12, which enabled the calculation of two parameters, roughness (R_q) and porosity (ϵ). The PIM's thermal analysis in nitrogen atmosphere (150 cm³/min) were done using Netzsch TG 209 F3 Tarsus. Scanning speed was 15°C/min.

2.3. Transport studies

Transport experiments were carried out in a permeation module cell described in our earlier paper (Ulewicz et al., 2007). The membrane film (at surface area of 4.9 cm²) was tightly clamped between two cell compartments. Both, i.e. the source and receiving aqueous phases (45 cm³ each) were mechanically stirred at 600 rpm. The receiving phase was deionized water. The SLM and PIM transport experiments were carried out at the temperature of 20 ± 0.2°C. Metal concentration was determined by withdrawing small samples (0.1 cm³ each) of the aqueous receiving phase at different time intervals and analysing by atomic absorption spectroscopy method (AAS Spectrometer, Solaar 939, Unicam). The source phase pH was kept

constant (pH = 5.0) and controlled by pH meter (pH meter, CX-731 Elmetron, with combine pH electrode, ERH-126, Hydromet, Poland). The permeability coefficient (P , m/s) of metal ions across membranes was described by the following equation (Danesi, 1984-85):

$$\ln\left(\frac{c}{c_i}\right) = -\frac{A}{V} \cdot P \cdot t, \quad (1)$$

where c is the metal ions concentration (M) in the source aqueous phase at some given time, c_i is the initial metal ions concentration in the source phase, t is the time of transport (s), V is volume of the aqueous source phase (m³), and A is an effective area of membrane (m²).

A linear dependence of $\ln(c/c_i)$ in the source phase versus time was obtained and the permeability coefficient was calculated from the slope of the straight line that fits the experimental data. The initial flux (J_i) was determined as equal to:

$$J_i = P \cdot c_i. \quad (2)$$

The selectivity coefficient (S) was defined as the ratio of initial fluxes for $M1$ and $M2$ metal ions, respectively:

$$S = J_{i,M1} / J_{i,M2}. \quad (3)$$

To describe the efficiency of metal removal from the source phase, the recovery factor (RF) was calculated:

$$RF = \frac{c_i - c}{c_i} \cdot 100\% \quad (4)$$

The reported values correspond to the average values of three replicates, with the standard deviation within 5%.

3. Results and discussion

The imidazole ring is a stable molecule that, according to Pearson's HSAB principle, is ranged among the intermediate class of bases. Although its basicity is by an order of magnitude lower than that of ammonia, imidazole forms more stable complexes with metal ions belonging to the intermediate class of Pearson's acids (Schaekers et al., 2004). Decyl substituents at position 1 of the imidazole ring distinctly affect the hydrophobic properties of the molecule and weakly strengthen its basicity ($pK_a = 7.43$) (Lenarcik and Ojczenasz, 2002). An additional methyl substituent at position 2 of the imidazole ring has been found to increase basicity by one order of magnitude, compared with that of 1-decylimidazoles ($pK_a = 8.47$), though at the same time the stability of the 1-decyl-2-methylimidazole complexes declined

due to the effect of $\pi_{M \rightarrow L}$ back-bonding and the steric effect of the substituent at position 2.

The initial flux transport of Cu^{2+} , Zn^{2+} , Co^{2+} and Ni^{2+} ions across the polymer inclusion membrane doped with 1-decyl-2-methylimidazole vs. 2-nitrophenyl pentyl ether concentration is shown in Fig. 1. As can be seen, 53.4% of the plasticizer in the membrane containing the imidazole derivative is an optimal concentration. Neither too low nor too high concentrations of the plasticizer in the membrane are desirable. Below this concentration an anti-softening effect occurs and the membrane becomes very brittle. Also, an excess of the plasticizer proved to be negative, because the plasticizer migrating into the aqueous phase formed at the interface of a barrier to the transfer of the metal ions. Furthermore, an increase in the plasticizer concentration resulted in an excessive increase in the thickness of the membrane, which also adversely affects the stream of ionic transfer. A similar phenomenon has also been reported by Gyves et al. (2006) during the transfer of Cu^{2+} across a membrane containing LIX 84 using tri-n-butoxyethyl phosphate (TBEP) as a plasticizer and by Gherrou et al. (2005) across a polymeric membrane containing DB18C6 using 2-nitrooctyl ether (oNPOE) as a plasticizer.

The AFM image of PIM's consists of 53.4% plasticizer, 20% CTA and 26.6% 1-decyl-2-methylimidazole in a two-dimensional form with the format $5.0 \times 5.0 \mu\text{m}$ shown in Fig.2. The porosity (ε) and roughness (R_q) of the polymer membrane were calculated using atomic force microscopy (AFM) and were equal to 17.2% and 6.8 nm, respectively. The effective pore size was $0.064 \mu\text{m}$. The distribution of the carrier in the investigated membrane after evaporation of dichloromethane is homogeneous on the entire surface. The membrane tortuosity was determined from the relationship developed by Wolf and Strieder (1990): $\tau = 1 - \ln \varepsilon$ and equal to 2.76 (for $\varepsilon = 0.172$). The values of initial fluxes, selectivity order and selectivity ratio for the competitive transport of divalent metal ions from different equimolar mixtures across PIM doped with 1-decyl-2-methylimidazole are summarised in Table 1. The values of initial fluxes of Cu(II) ions transport across PIM are higher than any of the components of the investigated equimolar mixtures. The selectivity order of metal ions transported from a mixture containing three metal ions decreases in the sequence: $\text{Cu(II)} > \text{Co(II)} > \text{Ni(II)}$, whereas from the mixture containing four metal ions – in the sequence: $\text{Cu(II)} > \text{Zn(II)} > \text{Co(II)}, \text{Ni(II)}$. The stability constants ($\log \beta_1$) of Co(II), Ni(II), and the Zn(II) complexes with 1-decylimidazole and 1-decyl-2-methylimidazole are presented in Table 2 (Lenarcik and Ojczenasz, 2004; Lenarcik and Kierzkowska, 2004, 2006; Radzimska-Lenarcik, 2007, 2008, 2011). The stability constants of the 1-decyl-2-methylimidazole complexes are lower, compared with those of 1-decylimidazole, except Zn(II) ion. The steric effect of the substituent at position 2 decreases the stability constants of octahedral complexes of all the metals studied though it does not hinder the formation of tetrahedral species. Therefore, the Co (II), Zn (II) and Cu (II) ions, which are able to form such compounds, have larger overall stability constants. The formation of tetrahedral complexes with 1-alkylimidazoles has been proven for

the Co (II), Zn (II) and Cu (II) ions (Lenarcik and Ojczenasz, 2004; Lenarcik and Kierzkowska, 2004; Lenarcik and Rauckyte, 2004; Radzaminska-Lenarcik, 2007). It seems that the initial flux values correspond to those of the stability constants of the complexes.

The highest percentage removals Cu^{2+} was obtained from the source phase containing an equimolar mixture of three metal ions and was equal to 95.1%. Recovery factors for Ni(II) and Co(II) were not very high, they did not exceed 24%. The percentage removals of Cu^{2+} from the source phase containing an equimolar mixture Cu^{2+} - Zn^{2+} , and Cu^{2+} - Zn^{2+} - Co^{2+} - Ni^{2+} ions were above 92%.

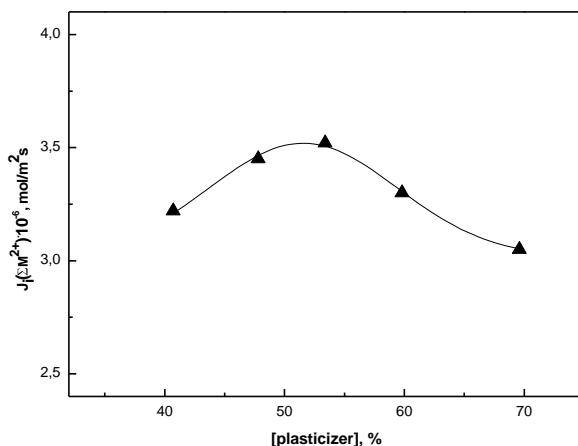


Fig. 1. Summary initial flux for competitive transport of Zn^{2+} , Co^{2+} , Cu^{2+} , and Ni^{2+} ions transport across PIM doped with 1-decyl-2-methylimidazol vs. of plasticizer concentration, membrane: 7.65 mg/cm^2 CTA and 2.26 mg/cm^2 1-decyl-2-methylimidazole

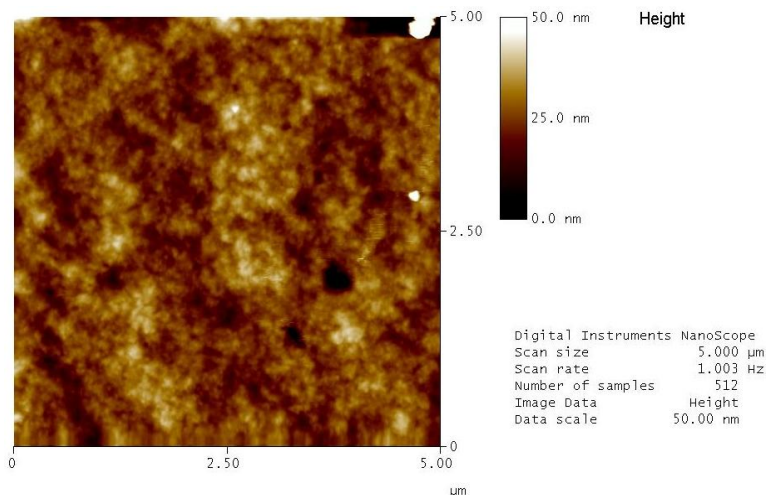


Fig. 2. 2D atomic force microscopy for PIM with 1-decyl-2-methylimidazole

Table 1. Initial fluxes, selectivity order and selectivity coefficients for competitive transport of Cu(II), Zn(II), Co(II), and Ni(II) ions across PIM doped with 1-decyl-2-methylimidazole; membrane: 53.4% plasticizer, 20% CTA and 26.6% 1-decyl-2-methylimidazole

| Mixture | Metal ions | J, $\mu\text{mol}/\text{m}^2\cdot\text{s}$ | $S_{\text{Cu(II)/Me(II)}}$ |
|---------|------------|--|--|
| 1 | Cu(II) | 2.89 | Cu(II) > Co(II) > Ni(II) 10.3 13.8 |
| | Co(II) | 0.28 | |
| | Ni(II) | 0.21 | |
| 2 | Cu(II) | 2.36 | Cu(II) > Zn(II) 2.6 |
| | Zn(II) | 0.92 | |
| 3 | Cu(II) | 2.35 | Cu(II) > Zn(II) > Co(II), Ni(II) 2.9 13.1 |
| | Zn(II) | 0.81 | |
| | Co(II) | 0.18 | |
| | Ni(II) | 0.18 | |

Table 2. Comparison of the stability constants ($\log \beta_1$) of Co(II), Ni(II), Cu(II), and Zn(II) complexes with 1-decylimidazole and 1-decyl-2-methylimidazole

| | Co(II) | Ni(II) | Cu(II) | Zn(II) |
|---------------------------|--------|--------|--------|--------|
| 1-decylimidazole | 4.67 | 4.24 | 4.15 | 4.28 |
| 1-decyl-2-methylimidazole | 3.32 | 2.68 | 3.54 | 5.1 |

The thermal stability of the polymeric membrane has also been examined (Fig. 3). In general, the thermal stability of polymeric membranes depends on the networking as well as on the presence of aromatic rings and degradable functional groups. Degradation of the CTA membrane proceeds in two steps. The first step extends over the temperature range of 292–320°C (the main step) and the other does over the range of 450–476°C (charring of dust) (Gharrou et al., 2004 and 2005, Arous et al., 2004). Other authors have reported a single degradation step only of a cellulose triacetate membrane at 300°C (Benosmane et al., 2009), although only *ca* 80% of CTA had been degraded at that temperature. Also a degradation temperature of 350°C can be found for CTA in the literature (Resina et al., 2007). CTA-oNPE membranes containing 1-decyl-2-methylimidazole underwent degradation to an extent of 80.09% at 251.3°C and to 5.12% at 359.1°C. The onset of degradation of that membrane has also been recorded at 192.1°C (in 71.69%) and charring of the products at 361.2°C (with a 19.89% loss in weight).

Then a comparative study was made of the separation of the d-electron metal ions during their transfer across Celgard-2500-based membranes. The AFM image of SLM in a two-dimensional form with the format 5.0x5.0 μm is shown in Fig.4. The membrane Celgard 2500 was characterized by porosity 0.55, thickness 25 μm , and effective pore size 0.209x0.054 μm . The SLM membrane tortuosity was determined also from the relationship developed by Wolf and Strieder (1990) and was found to be equal to 1.60 (for $\varepsilon=0.550$). The values of initial fluxes, selectivity order and selectivity ratio for the competitive transport of divalent metal ions from different equimolar mixtures across SLM containing 1-decyl-2-methylimidazole are summarised in Table 3. As it is seen from these Tables, the values of initial fluxes of Cu(II) ions

are higher than that for any of the other components of the mixture. For a mixture of the fourth metal ion, the initial fluxes of metal ions transport across SLMs with 1-decyl-2-methylimidazole decreases in the sequence: $\text{Cu(II)} > \text{Zn(II)} > \text{Co(II)} > \text{Ni(II)}$. The selectivity coefficient Cu^{2+} of other divalent metal ions during transport across SLM are lower than that across PIM. The percentage of removals of Cu^{2+} from the source phase after 24h obtained for this (1, 2 and 3) mixture are 82.7; 77.2 and 82.0%, respectively.

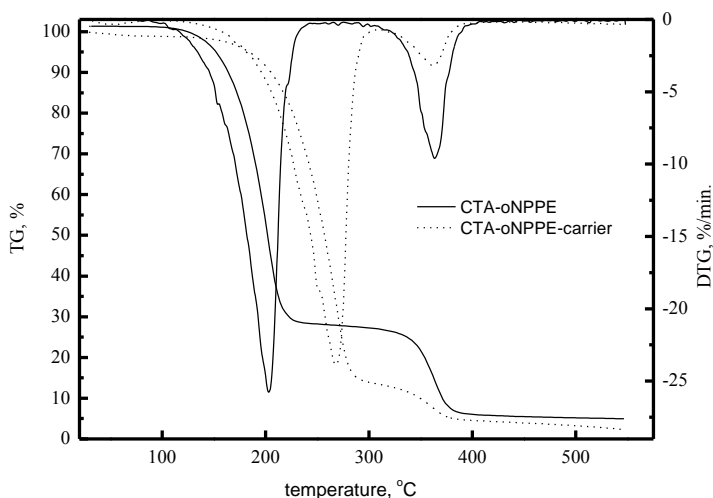


Fig. 3. Thermograms of CTA-oNPPE and CTA-oNPPE-1-decyl-2-methylimidazole

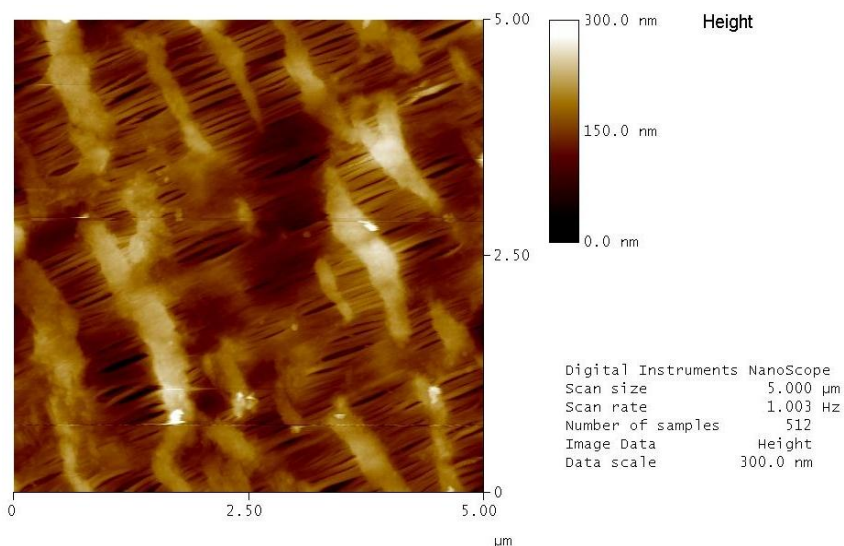


Fig. 4. 2D atomic force microscopy for SLM with 1-decyl-2-methylimidazole

To compare the magnitude of the stream of ionic transfer across Celgard-2500-based membranes and polymeric ones, structural differences between them should be accounted for (Tayeb et al., 2005). Because the carrier concentrations in both membranes are equal, a standardized stream of the transfer across the membranes can be described by the following equation (Tayeb et al., 2005)

$$J_{N(PIM)} = J_{\text{exp}(PIM)} \cdot \frac{d_{PIM} \tau_{PIM}}{\varepsilon_{PIM}} \cdot \frac{\varepsilon_{SLM}}{d_{SML} \tau_{SLM}}, \quad (5)$$

where d is the thickness of the membrane, ε denotes porosity and τ is tortuosity.

The normalized PIM flux calculated by Eq.(5) for Cu^{2+} from the mixture 1, 2 and 3 were 0.437; 0.357 and 0.355 $\mu\text{mol}/\text{m}^2\cdot\text{s}$, respectively. Accordingly, the stream of the transfer of Cu^{2+} ions across Accurel-based membranes is larger than that across polymeric ones. The finding is compatible with that of Tayeb et al. (2005) reported for the transfer of Cd^{2+} ions across membranes with low concentrations of a *Lasalocid A* carrier. On the other hand, larger streams of the transfer of alkali metal ions across membranes with the DC18C6 ether than those across Celgard-2500-based membranes have been reported by Schow et al. (1996) and by Kim et al. (2000) who studied the transfer of Cs^+ ions across membranes doped with a calix[4]-crown-6 derivative. However, the authors did not account for the structural features of the membranes. The advantage of the polymeric membranes over the carrier-based ones is their stable performance. From the latter, the carrier is washed off already during the first cycle of operation and its re-use is possible only after a repeated immobilization of the carrier in the pores of the polypropylene film. On the other hand, the polymeric membranes (PIM) can be re-used and the stream of the Cu^{2+} transfer does not diminish during another cycle of operation.

Table 3. Initial fluxes, selectivity order and selectivity coefficients for competitive transport of Cu(II), Zn(II), Co(II), and Ni(II) ions across SLM containing 0.5 M 1-decyl-2-methylimidazole

| Mixture | Metal ions | J, $\mu\text{mol}/\text{m}^2\cdot\text{s}$ | $S_{\text{Cu(II)/Me(II)}}$ |
|---------|------------|--|--|
| 1 | Cu(II) | 1.75 | Cu(II) >> Co(II) > Ni(II) 3.4 4.5 |
| | Co(II) | 0.51 | |
| | Ni(II) | 0.39 | |
| 2 | Cu(II) | 1.54 | Cu(II) > Zn(II) 1.7 |
| | Zn(II) | 0.91 | |
| 3 | Cu(II) | 1.23 | Cu(II) > Zn(II) > Co(II) > Ni(II) 1.6 8.2 8.8 |
| | Zn(II) | 0.74 | |
| | Co(II) | 0.15 | |
| | Ni(II) | 0.14 | |

4. Conclusion

Copper(II) cations can be effectively removed from aqueous nitrate solutions in the hydrometallurgical process of supported and polymer inclusion membrane transport with 1-decyl-2-methylimidazole as ion carriers. The optimum composition of

membranes is 53.4% plasticizer, 20% CTA and 26.6% 1-decyl-2-methylimidazole. The selectivity coefficients of $\text{Cu}^{2+}/\text{Zn}^{2+}$, $\text{Cu}^{2+}/\text{Co}^{2+}$ and $\text{Cu}^{2+}/\text{Ni}^{2+}$ obtained during transport across polymer membranes are higher than supported membranes containing a carrier at the same concentration. The percentage removals of Cu^{2+} from the source phase containing an equimolar mixture $\text{Cu}^{2+}\text{-Zn}^{2+}$, and $\text{Cu}^{2+}\text{-Zn}^{2+}\text{-Co}^{2+}\text{-Ni}^{2+}$ ions were above 92%. Owing to the steric effect, 1-decyl-2-methylimidazole fairly well differentiates the properties of its complexes with Co(II), Ni(II), Cu(II) and Zn(II).

Acknowledgments

The authors wish to thank Celgard LLC for their kind contribution of the membrane Celgard 2500.

References

- AROUS O., AMARA M., KERDJOUJ H., 2004, Synthesis and characterization of cellulose triacetate and poly(ethylene imine) membranes containing a polyether macrobicyclic: Their application to the separation of copper(II) and silver(I) ions, *J. Applied Polymer Sci.*, 93, 1401–1410.
- BENOSMANE N., HAMDY S.M., HAMDY M., BOUTEMEUR B., 2009, Selective transport of metal ions across polymer inclusion membranes containing calix[4]resorcinarenes, *Sep. Purif. Technol.*, 65, 211–219.
- CHO M. H., SEON-WOO K. H., HEO M. Y., LEE I. C., YOON C. J., KIM S. J., (1988) Studies on the macrocycles mediated transport in bulk liquid membrane system of transport metal ions, *Bull. Korean Chem. Soc.* 9, 292–295.
- DANESI P.R., 1984–1985, Separation of metal species by supported liquid membranes, *Sep. Sci. Technol.*, 19, 857–894.
- DADFARNIA, M. SHAMSIPUR, 1992, Specific membrane transport of copper(II) ion by a cooperative carrier composed of 1,7-diaza-15-crown5 and palmitic acid, *J. Membr. Sci.*, 75, 61–68.
- GHERROU A., KERDJOUJ H., MOLINARI R., SETA P., 2005, Preparation and characterization of polymeric plasticized membranes (PPM) embedding a crown ether carrier application to copper ions transport, *Mat. Sci. Eng.*, 25, 436–443.
- GHERROU A., KERDJOUJ H., MOLINARI R., DRIOLI E., 2002, Facilitated co-transport of Ag(I), Cu(II) and Zn(II) ions by using a crown ether as carrier: influence of the SLM preparation methods on ions flux, *Sep. Sci. Technol.*, 37, 2317–2336.
- GHERROU A., KERDJOUJ H., MOLINARI R., SETA P., DRIOLI E., 2004, Fixed sites plasticized cellulose triacetate membranes containing crown ethers for silver(I), copper(II) and gold(III) ions transport, *J. Membr. Sci.* 228, 149–157.
- GYVES J. de, HERNANDEZ-ANDALUZ A. M., MIGUEL E.R.D.S., 2006, LIX(R)-loaded polymer inclusion membrane for copper(II) transport. 2. Optimization of the efficiency factors (permeability, selectivity, and stability) for LIX(R) 84-I, *J. Membr. Sci.* 268, 142–149.
- KIM J. S., KIM S.K, KO J.W., KIM E.T, YU S.H, CHO M.H., KWON S.G, LEE E.H., 2000, Selective transport of cesium ion in polymeric CTA membrane containing calixcrown ethers, *Talanta*, 52, 1143–1148.
- KISLIK V.S. (eds) 2010, *Liquid membranes. Principles and application in chemical. separation and wastewater treatment*, Elsevier, UK.
- LENARCIK, B.; OJCZENASZ, P., 2002, The influence of the size and position of the alkyl groups in alkylimidazole molecules on their acid – base properties. *J. Heterocyclic Chem.* 39, 287–290.
- LENARCIK B., OJCZENASZ P., 2004, Investigation of the stability constants of Co(II) complexes with a homologous series of 1-alkylimidazoles in aqueous solution by using a partition method with several solvents, *Sep. Sci. Technol.*, 39, 199–226.

- LENARCIK B., KIERZKOWSKA A., 2004, The influence of alkyl length on stability constants of Zn(II) complexes with 1-alkylimidazoles in aqueous solutions and their partition between aqueous phase and organic solvent, *Solv. Extr. Ion Exch.*, 22, 449–471.
- LENARCIK B.; KIERZKOWSKA A., 2006, The influence of alkyl chain length and steric effect on extraction of zinc(II) complexes with 1-alkyl-2-methylimidazoles, *Solv. Extr. Ion Exch.*, 24, 433.
- LENARCIK B., RAUCKYTE T., 2004, the influence of alkyl length on extraction equilibria of Ni(II) complexes with 1-alkylimidazoles in aqueous solution/organic solvent systems, *Sep. Sci. Technol.*, 39, 3353–3372.
- LUBOCH, E., WAGNER-WYSIECKA, E., FAINERMAN-MELNIKOVA M., LINDOY L. F., BIERNAT J.F., 2006, Pyrrole azocrown ethers. Synthesis, complexation, selective lead transport and ion-selective membrane electrode studies, *Supramol. Chem.*, 18, 593.
- NGHIEM L.D., MORRIS P., POTTER, I.D., PERERA, J.M., CATRALL, R.W., KOLEV, S.D., 2006, Extraction and transport of metal ions and small organic compounds using polymer inclusion membranes (PIMs), *J. Membrane Sci.*, 281, 7–41.
- PARTHASARATHY N., BUFFLE J., 1991, Supported liquid membrane for analytical separation of transition metal ions. Part II. Appraisal of lipophilic 1, 10-didecyl, 1, 10-diaza-18-crown-6 as metal ion carrier in membrane, *Anal. Chimica Acta*, 254, 9–19.
- PERNAK J., KRYSINSKI J., SKRZYPCZAK A., 1987, Bakterizide wirkung von iminiumverbindungen, *A. Tenside Surfact. Det.*, 24, 276–286.
- RADZYMIŃSKA-LENARCIK E., 2007, The influence of the alkyl chain length on extraction equilibrium of Cu(II) complexes with 1-alkylimidazoles in aqueous solution/ organic solvent systems. *Solv. Extr. Ion Exch.* 25, 53–64.
- RADZYMIŃSKA-LENARCIK, E., 2007, Effect of alkyl chain length on the extraction of copper(II) complexes with 1-alkyl-2-methylimidazoles. *Sep. Sci. Technol.*, 42, 2661–2675.
- RADZYMIŃSKA-LENARCIK, E., 2008, Search for the possibility of utilizing the differences in complex-forming capacities of alkylimidazoles for selective extraction of some metal ions from aqueous solutions. *Pol. J. Chem. Technol.*, 10, 73–78.
- RADZYMIŃSKA-LENARCIK E., 2011, Influence of the solvent donor number on the O/W partition ratio of Cu(II) complexes with 1,2-dialkylimidazoles. *Chem. Pap.* 65, 226–232.
- RESINA M., MACANAS J., GYVESB J. de, MUNOZ M., 2007, Development and characterization of hybrid membranes based on an organic matrix modified with silanes for metal separation, *J. Membr. Sci.*, 289, 150–158.
- SCHOW A. J., PETERSON R. T., LAMB J.D., 1996, Polymer inclusion membranes containing macrocyclic carriers for use in cation separations, *J. Membr. Sci.* 111, 291–295.
- TAYEB R., FONTAS C., DHAHBI M., TINGRY S., SETA P., 2005, Cd(II) transport across supported liquid membranes (SLM) and polymeric plasticized membranes (PPM) mediated by Lasalocid A, *Sep. Purif. Technol.* 42, 189–193.
- ULEWICZ M., KOZŁOWSKI C.A., WALKOWIAK W., 2004, Removal of Zn(II), Cd(II) and Cu(II) ions by polymer inclusion membrane with side-armed diphosphaza-16-crown-6-ethers, *Physicochem. Probl. Miner. Process.*, 38, 2004, 131–138
- ULEWICZ M., LESINSKA U., BOCHENSKA M., 2010, Transport of lead across polymer inclusion membrane with p-tert-butylcalix[4]arene derivative, *Physicochem. Probl. Miner. Process.*, 44, 245–256.
- ULEWICZ M., RADZYMIŃSKA –LENARCIK E., 2011, Transport of metal ions across polymer inclusion membrane with 1-alkylimidazole, *Physicochem. Probl. Miner. Process.*, 46, 119–130.
- ULEWICZ M., SADOWSKA K., BIERNAT J.F., 2007, Transport of Zn(II), Cd(II) and Pb(II) across polymer inclusion membrane doped with imidazole azocrown ethers, *Desalination*, 214, 352–364.
- ULEWICZ M., SADOWSKA K., BIERNAT J.F., 2007, Selective transport of Pb(II) across polymer inclusion membrane using imidazole azocrown ethers as carriers, *Physicochem. Probl. Miner. Process.*, 41, 133–143.
- ULEWICZ M., SZCZYGELSKA –TAO J., BIERNAT J.F., 2009, Selectivity of Pb(II) transport across polymer inclusion membranes doped with imidazole azothiacrown ethers, *J. Membr. Sci.*, 344, 32–38.

- WALKOWIAK W., ULEWICZ M., KOZŁOWSKI C.A., 2002, Application of macrocyclic compounds for metal ions separation and removal – a review, *Ars Separatoria Acta*, 1, 87–98.
- WOLF J.R., STRIEDER W., 1990, Toruosities for a random fiber bed: overlapping, parallel cylinders of several radii, *J. Membr. Sci.*, 49, 103–115.

Received May 6, 2011; reviewed; accepted July 7, 2011

ADSORPTION OF C.I. BASIC BLUE 9 ONTO TiO₂–SiO₂ INORGANIC SUPPORT

Agnieszka PRZYBYLSKA, Katarzyna SIWINSKA-STEFANSKA
Filip CIESIELCZYK, Teofil JESIONOWSKI

Poznan University of Technology, Institute of Chemical Technology and Engineering, M. Skłodowskiej-Curie 2, 60-965 Poznan, Poland, e-mail: teofil.jesionowski@put.poznan.pl, phone: +48(61)6653720, fax: +48(61)6653649

Abstract. Adsorption of C.I. Basic Blue 9 (Methylene Blue Hydrate) on the surface of TiO₂–SiO₂ oxide composite unmodified or functionalized with N-2-(aminoethyl)-3-amino propyltrimethoxysilane was investigated. The organic dye was supported on inorganic TiO₂–SiO₂ oxide composite precipitated in the emulsion system. The process of adsorption was performed for the dye concentrations from 100 to 3000 mg/dm³. Specific surface area of support was determined prior to and after modification with aminosilane. The pigments obtained were subjected to characterization of their physicochemical properties, including particle size distributions and surface morphology as well as colorimetric analysis. Elemental analysis allowed evaluation of the degree of support coverage with the dye. The data obtained permitted assessment of the pigments quality and the effectiveness of support surface modification.

keywords: TiO₂–SiO₂ oxide composite, emulsion precipitation, adsorption, C.I. Basic Blue 9, pigments, morphological properties

1. Introduction

At many research groups intense investigation is carried out aimed at obtaining of inorganic fillers characterized with relatively high surface activity, based on activated carbon, SiO₂, TiO₂, Al₂O₃, MgO, MgSiO₃ etc. (Malik 2002; Wu 2006; Jesionowski 2009a, 2009b; Siwinska-Stefanska 2010; Ciesielczyk 2011; Pilarska 2011).

Titanium dioxide is well known not only as a filler or support but also as a photocatalyst used in the processes of air or wastewater purification (Cho 2008). TiO₂ exists in three crystallographic forms of anatase, rutile and brookite. To improve its properties suitable for particular application as a component of paints or cosmetic products, its surface is covered with a layer of inert oxide (e.g. SiO₂) to make a composite containing a ≡Ti–O–Si≡ bond.

Most often produced inorganic oxides are titanium-silica ($\text{TiO}_2\text{-SiO}_2$), titanium-zirconium ($\text{TiO}_2\text{-ZrO}_2$) and titanium-aluminium ($\text{TiO}_2\text{-Al}_2\text{O}_3$) oxide composites. Coverage of titanium core with a silica layer can reduce the photocatalytic properties of TiO_2 , while addition of silicon dioxide increases TiO_2 resistance to atmospheric elements and facilitates dispersion in liquids.

Many methods for the synthesis of titania-silica composite have been proposed, including the sol-gel method (Dutoit 1995) and chemical precipitation method (Liu 2008). Recently an interesting proposed method is the synthesis of $\text{TiO}_2\text{-SiO}_2$ from emulsion system using solutions of sodium silicate and titanium sulphate as Si and Ti precursors, and an organic solvent has been performed (Siwinska-Stefanska 2010).

Among others, titania-silica support has been used for adsorption of dyes to get hybrid pigments of widespread use in food and cosmetic industry, in production of lacquers, etc. The pigments have been also employed for colouration of plastics, while in food industry for colouration of food products and drinks, and in pharmaceutical industry for colouration of drugs and tablets. The pigments are also used for colouration of paper. The above examples illustrate the wide range of pigments application. They are met in almost all spheres of everyday life and thanks to the use of new technologies they have become more environmentally friendly.

Adsorption of organic dyes on the surface of $\text{TiO}_2\text{-SiO}_2$ composite can be performed by many methods (Messina 2006). For example it can be carried out in a special reactor at a controlled temperature or on titanium dioxide modified with aminosilane. In another method the dyes (C.I. Reactive Blue 19 and C.I. Acid Orange 7) have been adsorbed by introducing a water solution of the dye onto unmodified or modified titanium dioxide (Andrzejewska 2004). Different dyes (cationic and anionic) have been adsorbed on unmodified $\text{TiO}_2\text{-SiO}_2$ composite at different pH of the reaction environment (Park 2007). The yield of adsorption and its character have been found to depend on the surface charge of the $\text{TiO}_2\text{-SiO}_2$ composite. At $\text{pH}>3$ the surface of the support is negatively charged, while at $\text{pH}<3$ positively. For a negatively charged surface the adsorption of anionic dyes is less effective than cationic ones, while a positively charged surface the adsorption of anionic dyes is more effective.

The study presented was aimed at synthesis of hybrid pigments by adsorption of C.I. Basic Blue 9 organic dye on the surface of inorganic support $\text{TiO}_2\text{-SiO}_2$ unmodified or functionalized with aminosilane U-15D. Moreover, the effect of the support's surface modification on the physicochemical properties of the pigments obtained was established.

2. Experimental

$\text{TiO}_2\text{-SiO}_2$ oxide composite was synthesised by emulsion precipitation method using solutions of sodium silicate and titanium sulphate as precursors of silica and titanium dioxides, moreover the organic solvent (cyclohexane) was used. The precipitated composite was calcined at 950°C for 2 hours to get the rutile form of

titanium dioxide. The TiO₂-SiO₂ hybrid system obtained was modified with 3 wt./wt. of *N*-2-(aminoethyl)-3-aminopropyltrimethoxysilane (U-15D), made by Unisil. The modification was performed in a reactor of 0.5 dm³ in capacity, charged with 20 g of the hybrid system and a solution of U-15D in an appropriate volume of the solvent composed of water and methanol at the 1:4 volume ratio. The choice of modifier was made on the basis of earlier studies (Jesionowski 2002, 2003; Andrzejewska 2004). The amine groups from silane are needed to form stable chemical bond with the dye adsorbed. Functionalization of titanium dioxide support with U-15D has been reported to significantly increase the yield of adsorption (Andrzejewska 2004; Jesionowski 2008). The modification process was detailed described by Jesionowski et al. (2000).

The C.I. Basic Blue 9 dye used to obtain the studied pigments was purchased from Sigma-Aldrich. The process of adsorption was carried out in a reactor containing 7.5 g of unmodified or functionalized hybrid oxide to which 250 cm³ of a water solution of the dye in appropriate concentration was added. The suspension was stirred for 2 hours with a R05 magnetic stirrer made by IKA Werke GmbH. Then, the whole system was filtered off under reduced pressure, the filtrate was dried by the convection method at 105°C. The TiO₂-SiO₂ hybrid system precipitated and the pigments obtained were characterized by a thorough physicochemical analysis.

Particle size distributions of the hybrid system and pigments obtained were determined with the use of a Zetasizer Nano ZS working on the basis of non-invasive backscattering method (NIBS) made by Malvern Instruments Ltd. The degree of dispersion and morphology of the products were evaluated by a scanning electron microscope (Zeiss VO40). Crystalline structure of TiO₂-SiO₂ was determined by the X-Ray diffraction method (WAXS) using a TUR-M62 diffractometer. Hydrophilic/hydrophobic properties of the samples studied were evaluated by a K100 tensiometer made by Krüss, on the basis of capillary penetration of water in the samples. Adsorption properties of selected samples were characterized by determination of their specific surface area using an ASAP 2020 instrument made by Micromeritics Instrument Co. Chemical analysis of the products was performed on an Elemental apparatus, model Vario EL Cube. Colorimetric characterization of the samples was made using the CIE L*a*b* system on a SPECBOS 4000 colorimeter (made by YETI Technische Instrumente GmbH). The results are given in the CIE L*a*b* system, where: L* – lightness, +a* – contribution of red colour, -a* – contribution of green colour, +b* – contribution of yellow colour, -b* – contribution of blue colour, also colour saturation – C* and total change in colour – ΔE*.

3. Results and discussion

In the first stage of the study, the TiO₂-SiO₂ oxide hybrid unmodified and modified with 3 wt./wt. of *N*-2-(aminoethyl)-3-aminopropyltrimethoxysilane was subjected to dispersive and morphological analysis. The particle size distribution of unmodified TiO₂-SiO₂ shows a single band covering the range of diameters from 459 to 1110 nm (Fig. 1). An analogous distribution of TiO₂-SiO₂ subjected to surface modification

with aminosilane has two bands covering the ranges from 342 to 1720 nm and from 3580 to 6440 nm. A comparison of the particle size distributions obtained for these two samples reveals that the modification brings about the appearance of a band corresponding to secondary agglomerates. The polydispersity index of $\text{TiO}_2\text{-SiO}_2$ unmodified and grafted with U-15D is 0.375 and 0.314, respectively. The particles in both samples show a tendency towards formation of agglomerates of approximately spherical shape. The modified sample is a bit less uniform, which follows from a greater tendency of its particles to agglomerate. The SEM images (Fig. 2a and 2b) confirm the presence of secondary agglomerates.

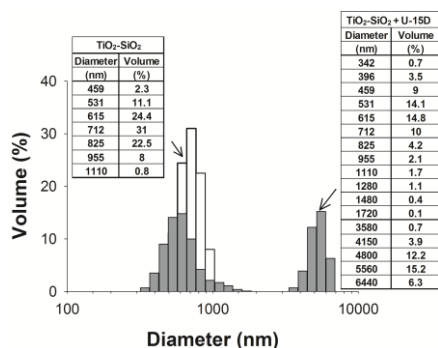


Fig. 1. Comparison of particle size distributions according to volume contributions of unmodified and modified $\text{TiO}_2\text{-SiO}_2$

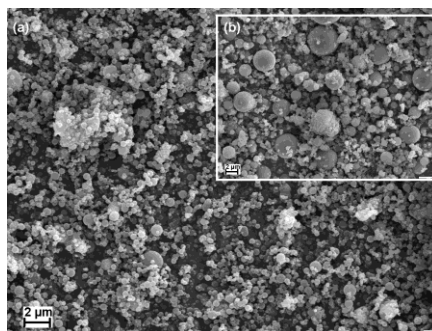


Fig. 2. SEM images of $\text{TiO}_2\text{-SiO}_2$ (a) unmodified and (b) modified

The studies were planned to be performed on $\text{TiO}_2\text{-SiO}_2$ with titanium dioxide of rutile structure because this crystalline form is highly stable and does not induce photocatalytic destruction of the dye. As follows from XRD measurements, titanium dioxide of rutile form gives intensity peaks at 2θ of 27.45, 36.08, 39.18, 41.22, 44.05, 54.32 and 56.64, while that of anatase variety gives peaks at 2θ of 25.28, 32, 33, 33.50, 48.05 and 55.06 (Siwinska-Stefanska 2010; Valverde-Aguilar 2011). According to the diffractogram shown in Fig. 3, the $\text{TiO}_2\text{-SiO}_2$ composite synthesized is mainly composed of the rutile form of TiO_2 (the presence of a low contribution of the anatase variety is indicated by the diffraction maximum at 2θ of 25.28).

The next stage of our study was concerned with assessment of the effect of composite surface modification with U-15D on the hydrophilic/hydrophobic as well as adsorptive properties. The profiles of wettability with water recorded for the unmodified and modified samples indicated that the functionalization of the composite surface reduced its affinity to water, see Fig. 4. The increase in mass of the modified sample was smaller than that of the unmodified one, which proves that the surface functionalization leads the sample more hydrophobic.

Adsorption capacity of the samples was determined by recording nitrogen adsorption/desorption isotherms (Fig. 5) showing that the amount of nitrogen adsorbed by the modified sample was smaller. The specific surface area increased from $3.4 \text{ m}^2/\text{g}$

for the unmodified sample to $5.4 \text{ m}^2/\text{g}$ for the modified one, but the pore volume (V_p) and the mean pore diameter (S_p) decreased for the modified sample (see Table 1).

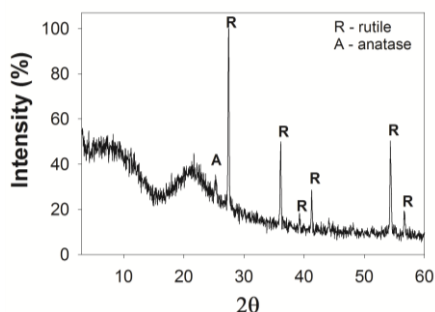


Fig. 3. X-Ray diffractogram of the $\text{TiO}_2\text{-SiO}_2$ support

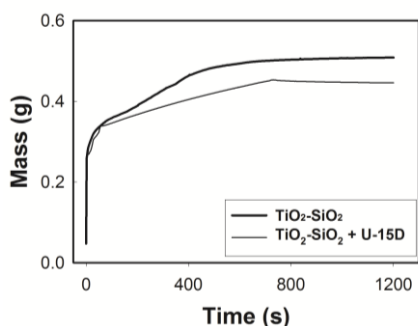


Fig. 4. Profiles of wettability with water recorded for unmodified and modified (3 wt./wt. of U-15D) $\text{TiO}_2\text{-SiO}_2$ composite

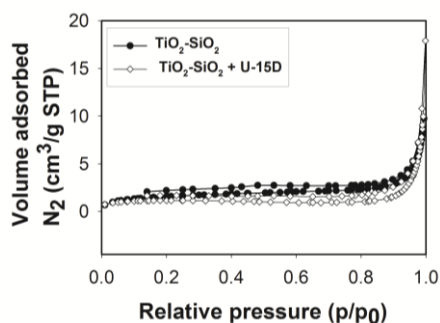


Fig. 5. Nitrogen adsorption/desorption isotherms for unmodified and modified $\text{TiO}_2\text{-SiO}_2$ composites

Table 1. Adsorptive properties of the modified and unmodified $\text{TiO}_2\text{-SiO}_2$ supports used in adsorption of C.I. Basic Blue 9

| adsorptive properties | $\text{TiO}_2\text{-SiO}_2$ | $\text{TiO}_2\text{-SiO}_2 + \text{U-15D}$ |
|--|-----------------------------|--|
| surface area, A_{BET} (m^2/g) | 3.4 | 5.4 |
| total volume of pores, V_p (cm^3/g) | 0.015 | 0.011 |
| mean size of pores, S_p (nm) | 13.3 | 8.1 |

The pigments obtained in this study can be applied, e.g. in production of paints. For this application very important is the shape and size of pigment particles determining the rheological properties of the paint, hue, resistance to atmospheric elements and easy dispersion. Usually the pigment particles diameters are in the range from 1 to $10 \mu\text{m}$. If pigment particles represent a variety of sizes, the coat of paint will be more resistant to atmospheric elements. Therefore, from the point of view of this application, the dispersive and morphological characterization of pigments is very important. The relevant physicochemical analyses have been rather broadly presented in literature (Binkowski, 2000; Andrzejewska, 2007). The use of $\text{TiO}_2\text{-SiO}_2$ composite precipitated in emulsion system as a support of organic dyes, gave pigments of

particles of spherical shape and much smaller diameters than those met in other commonly used pigments based on other types of supports. The use of the functionalized $\text{TiO}_2\text{-SiO}_2$ as a support of the organic dye studied led to pigments of diameters smaller than those in the pigments based on unmodified support. The particle size distributions according to volume contribution obtained for the pigments prepared by adsorption of C.I. Basic Blue 9 in concentrations of 500 or 3000 mg/dm^3 on unmodified $\text{TiO}_2\text{-SiO}_2$ (Fig. 6) visible two bands covering the diameter ranges 342–955 nm and 255–955 nm. An analogous particle size distribution for the pigment obtained by adsorption of C.I. Basic Blue 9 in concentration of 500 mg/dm^3 on the modified support shows a band covering the range 220–712 nm instead of the band covering the range 342–955 nm visible for the unmodified support. A similar shift was observed for the pigment obtained by adsorption of C.I. Basic Blue 9 in concentration of 3000 mg/dm^3 .

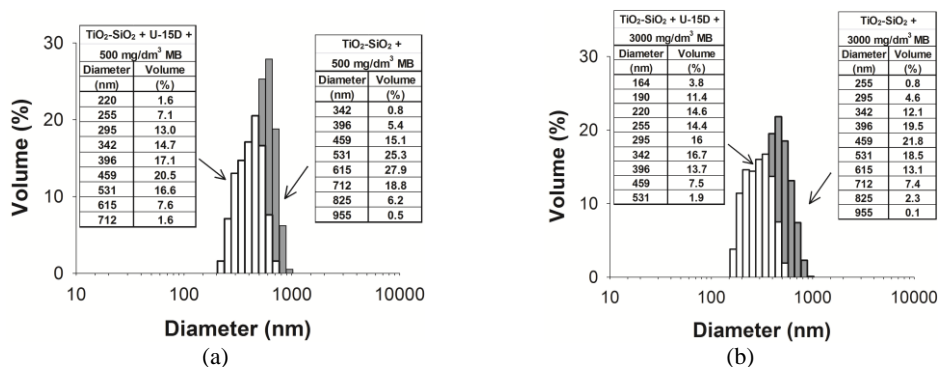


Fig. 6. Comparison of the particle size distributions according to volume contributions evaluated for the pigments obtained by adsorption of C.I. Basic Blue 9 in concentration (a) 500 mg/dm^3 and (b) 3000 mg/dm^3 on unmodified and functionalized $\text{TiO}_2\text{-SiO}_2$ support

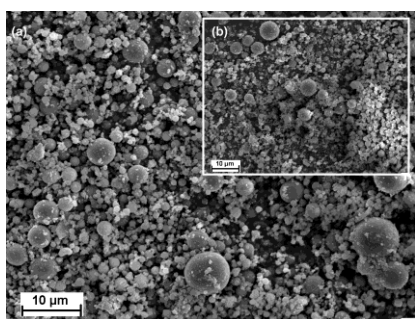


Fig. 7. SEM images of the pigments obtained by adsorption of C.I. Basic Blue 9 in concentration of 3000 mg/dm^3 on (a) unmodified and (b) modified $\text{TiO}_2\text{-SiO}_2$ support

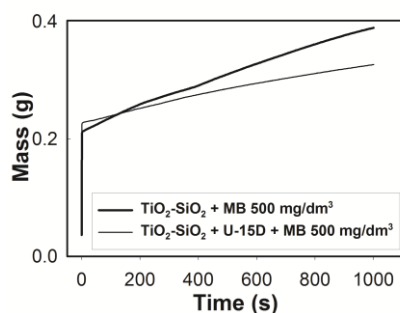


Fig. 8. Profiles of wettability with water estimated for the pigments obtained by adsorption of C.I. Basic Blue 9 in concentration of 500 mg/dm^3 on $\text{TiO}_2\text{-SiO}_2$ and $\text{TiO}_2\text{-SiO}_2 + \text{U-15D}$

Table 2. Elemental content and degree of coverage for the pigments obtained by adsorption of C.I. Basic Blue 9 on unmodified and modified TiO₂-SiO₂ support

| Initial dye concentration (mg/dm ³) | TiO ₂ -SiO ₂ | | | | TiO ₂ -SiO ₂ + U-15D | | | |
|---|------------------------------------|-------|-------|---|--|-------|-------|---|
| | Content (%) | | | Degree of coverage (μmol/m ²) | Content (%) | | | Degree of coverage (μmol/m ²) |
| | N | C | S | | N | C | S | |
| 0 | 0.003 | 0.030 | 0.015 | – | 0.301 | 0.346 | 0.005 | – |
| 100 | 0.015 | 0.142 | 0.034 | 2.16 | 0.322 | 0.513 | 0.026 | 4.99 |
| 500 | 0.033 | 0.188 | 0.036 | 2.87 | 0.493 | 0.521 | 0.028 | 5.06 |
| 1000 | 0.036 | 0.192 | 0.043 | 2.93 | 0.495 | 0.532 | 0.031 | 5.18 |
| 1500 | 0.040 | 0.208 | 0.049 | 3.17 | 0.498 | 0.552 | 0.032 | 5.37 |
| 2000 | 0.045 | 0.223 | 0.056 | 3.40 | 0.499 | 0.559 | 0.034 | 5.44 |
| 2500 | 0.049 | 0.246 | 0.058 | 3.76 | 0.501 | 0.567 | 0.038 | 5.52 |
| 3000 | 0.051 | 0.258 | 0.063 | 3.94 | 0.505 | 0.582 | 0.040 | 5.67 |

Table 3. Colorimetric data for the pigments obtained by adsorption of C.I. Basic Blue 9 onto unmodified and functionalized TiO₂-SiO₂ support

| Initial dye concentration (mg/dm ³) | TiO ₂ -SiO ₂ | | | | | TiO ₂ -SiO ₂ + U-15D | | | | |
|---|------------------------------------|-------|--------|-------|-------|--|------|--------|-------|-------|
| | Colorimetric data | | | | | | | | | |
| | L* | a* | b* | C* | ΔE* | L* | a* | b* | C* | ΔE* |
| 0 | 93.70 | 0.29 | 2.76 | 2.70 | – | 93.73 | 0.30 | 2.68 | 2.78 | – |
| 100 | 85.41 | 8.13 | -6.34 | 24.39 | 41.71 | 62.14 | 0.86 | -23.00 | 8.97 | 15.34 |
| 500 | 78.07 | 9.53 | -12.46 | 25.39 | 43.03 | 61.22 | 1.43 | -23.53 | 12.54 | 22.11 |
| 1000 | 77.20 | 9.13 | -13.27 | 27.84 | 46.15 | 59.27 | 1.95 | -26.31 | 13.04 | 24.45 |
| 1500 | 75.62 | 11.04 | -14.15 | 28.77 | 47.72 | 57.95 | 2.73 | -26.57 | 14.95 | 26.56 |
| 2000 | 72.33 | 11.61 | -15.03 | 30.55 | 51.08 | 55.04 | 3.01 | -28.26 | 15.66 | 28.98 |
| 2500 | 70.36 | 12.10 | -15.80 | 30.97 | 51.81 | 54.28 | 3.58 | -28.51 | 16.20 | 30.28 |
| 3000 | 67.99 | 12.05 | -18.02 | 30.36 | 54.67 | 53.90 | 5.32 | -28.91 | 18.79 | 33.73 |

The pigment based on unmodified support has particles of diameters from the range 255–955 nm, while that based on functionalized support has particles of diameters shifted towards smaller values – from 164 to 531 nm.

As follows from the SEM images presented in Fig. 7, the pigments based on unmodified TiO₂-SiO₂ support are built of spherical shape particles and show rather low uniformity. Analysis of the wettability profiles with water (Fig. 8) indicates that the mass increase in time for the pigment based on the functionalized support is lower than that for the pigment based on the unmodified support.

The products obtained were also subjected to determination of chemical composition by elemental analysis. As follows from the results presented in Table 2, the content of C, N and S elements increases with increasing initial concentration of the dye, which is related to the degree of coverage. Many authors have used the notion a support degree of coverage with an organic dye for evaluation of the yield of adsorption (Harris, 2001; Jesionowski, 2011). The degree of coverage can be calculated from the expression proposed by Berendsen and de Golan (1978). In our study the degree of coverage increased with increasing initial concentration of the dye. For the pigment obtained by adsorption of C.I. Basic Blue 9 in the initial concentration

of 100 mg/dm^3 the degree of coverage was $2.16 \text{ } \mu\text{mol/m}^2$, while for the initial concentration of the dye of 3000 mg/dm^3 the degree of coverage was $3.94 \text{ } \mu\text{mol/m}^2$. Modification of inorganic support surface with aminosilane (U-15D) causes an increase in this parameter. For the pigment obtained by adsorption of C.I. Basic Blue 9 of the initial concentration of 100 mg/dm^3 on the unmodified support the degree of coverage is $2.16 \text{ } \mu\text{mol/m}^2$, while for that obtained by adsorption of the same dye in the same concentration on the modified support the degree of coverage is $4.99 \text{ } \mu\text{mol/m}^2$. An analogous tendency has been observed for C.I. Basic Red 5 adsorption on the silica support (Jesionowski, 2008).

The effect of $\text{TiO}_2\text{-SiO}_2$ support modification and concentration of the dye on the colour of the pigments obtained was evaluated with the use of the CIE $L^*a^*b^*$ colour space system. According to the data presented in Table 3, the lightness of the products obtained decreases with increasing initial concentration of the dye adsorbed. The greatest total change in colour ΔE^* 54.67 was observed for the pigment obtained by adsorption of C.I. Basic Blue 9 of the initial concentration 3000 mg/dm^3 on the unmodified $\text{TiO}_2\text{-SiO}_2$ support. The total change in colour ΔE^* for the pigment obtained by adsorption of C.I. Basic Blue 9 on the modified $\text{TiO}_2\text{-SiO}_2$ support was much smaller 33.73.

4. Conclusions

The proposed method for the synthesis of $\text{TiO}_2\text{-SiO}_2$ oxide composite by precipitation from emulsion gives products characterized by a monomodal particle size distribution and specific surface area of $3.42 \text{ m}^2/\text{g}$. Functionalization of the composite surface with aminosilane resulted in deterioration of the dispersive and morphological properties but also in specific surface area increase to $5.42 \text{ m}^2/\text{g}$. The pigments obtained on the basis of the functionalized support showed better dispersive properties and more intense colour than those based on the unmodified $\text{TiO}_2\text{-SiO}_2$ support. Surface functionalization of $\text{TiO}_2\text{-SiO}_2$ composite with aminosilane (U-15D) also brought about an increase in the degree of coverage with the dye and gave pigments characterized with a lower affinity to water. Colorimetric analysis of $\text{TiO}_2\text{-SiO}_2$ functionalized with U-15D and the use of this support for adsorption of C.I. Basic Blue 9 proved the greater colour intensity of the pigment obtained then that obtained on unmodified $\text{TiO}_2\text{-SiO}_2$.

Acknowledgements

This publication was prepared within the key project – PO IG no. 01.03.01-00-006/08 cofinanced by the European Regional Development Fund within the framework of the Operational Programme Innovative Economy.

References

ANDRZEJEWSKA A., KRYSZTAFKIEWICZ A., JESIONOWSKI T., 2007, Treatment of textile dye wastewater using modified silica, *Dyes Pigments*, 75, 116–124.

- ANDRZEJEWSKA A., KRYSZTAFKIEWICZ A., JESIONOWSKI T., 2004, Adsorption of organic dyes on the aminosilane modified TiO₂ surface, *Dyes Pigments*, 62, 121–130.
- BERENDSEN G.E., de GOLAN L., 1978, Preparation and chromatographic properties of some chemically bonded phases for reversed-phase liquid chromatography, *J. Liq. Chromatogr.*, 1, 561–586.
- BINKOWSKI S., JESIONOWSKI T., KRYSZTAFKIEWICZ A., 2000, Preparation of pigments on modified precipitated silica, *Dyes Pigments*, 47, 247–257.
- CHO K., CHANG H., PARK J.H., KIM B.G., JANG H.D., 2008, Effect of molar ratio of TiO₂/SiO₂ on the properties of particles synthesized by flame spray pyrolysis, *J. Ind. Eng. Chem.*, 14, 860–863.
- CIESIELCZYK F., JESIONOWSKI T., 2011, Characterization of highly dispersed magnesium silicates prepared from silica sols and selected magnesium salts, *Physicochem. Probl. Miner. Process.* 46, 279–288.
- DUTOIT D.C.M., SCHNEIDER M., BAIKER A., 1995, Titania-silica mixed oxides: I. Influence of sol-gel and drying conditions on structural properties, *J. Catal.*, 153, 165–176.
- HARRIS R.G., WELLS J.D., JOHNSON B.B., 2001, Selective adsorption of dyes and other organic molecules to kaolinite and oxide surfaces, *Colloids Surf. A*, 180, 131–140.
- JESIONOWSKI T., KRYSZTAFKIEWICZ A., 2000, Comparison of the techniques used to modify amorphous hydrated silicas, *J Non-Cryst. Solids*, 277, 45–57.
- JESIONOWSKI T., 2002, Synthesis of organic-inorganic hybrids via adsorption of dye on the aminosilane-functionalised silica surface, *Dyes Pigments*, 55, 133–141.
- JESIONOWSKI T., POKORA M., TYLUS W., DEC A., KRYSZTAFKIEWICZ A., 2003, Effect of N-2-(aminoethyl)-3-aminopropyltrimethoxysilane surface modification and C.I. Acid Red 18 dye adsorption on physicochemical properties of silicas precipitated in an emulsion route, used as a pigment and filler in acrylic paints, *Dyes Pigments*, 57, 29–41
- JESIONOWSKI T., ANDRZEJEWSKA A., KRYSZTAFKIEWICZ A., 2008, Adsorption of basic dyes from model aqueous solutions onto novel spherical silica support, *Color. Technol.*, 124, 165–172.
- JESIONOWSKI T., KRYSZTAFKIEWICZ A., ŻURAWSKA J., BULA K., 2009, Novel precipitated silicas – an active filler of synthetic rubber, *J. Mater Sci.*, 44, 759–769.
- JESIONOWSKI T., 2009, Preparation of spherical silica in emulsion systems using the co-precipitation technique, *Mater. Chem. Phys.*, 113, 839–849.
- JESIONOWSKI T., PRZYBYLSKA A., KURC B., CIESIELCZYK F., 2011, The preparation of pigment composites by adsorption of C.I. Mordant Red 11 and 9-aminoacridine on both unmodified and aminosilane-grafted silica supports, *Dyes Pigments*, 88, 116–124.
- LIU Y., GE Ch., REN M., YIN H., WANG A., ZHANG D., LIU Ch., CHEN J., FENG H., YAO H., JIANG T., 2008, Effects of coating parameters on the morphology of SiO₂-coated TiO₂ and the pigmentary properties, *Appl. Surf. Sci.*, 254, 2809–2819.
- MALIK D.J., STRELKO Jr. V., STREAT M., PUZYI A.M., 2002, Characterisation of novel modified active carbons and marine algal biomass for the selective adsorption of lead, *Water Res.*, 36, 1527–1538.
- MESSINA V.P., SCHULTZ C.P., 2006, Adsorption of reactive dyes on titania-silica mesoporous materials, *J. Colloid Interface Sci.*, 299, 305–320.
- PARK J.-K., KIM J.-K., KIM H.-K., 2007, TiO₂-SiO₂ composite filler for thin paper, *J. Mater. Process. Tech.*, 186, 367–369.
- PILARSKA A., JESIONOWSKI T., 2011, Synthesis of MgO in magnesium hydroxide carbonatization process, *Physicochem. Probl. Miner. Process.* 46, 83–94.
- SIWINSKA-STEFANSKA K., KRYSZTAFKIEWICZ A., CIESIELCZYK F., PAUKSZTA D., SOJKA-LEDAKOWICZ J., JESIONOWSKI T., 2010, Physicochemical and structural properties of TiO₂ precipitated in an emulsion system, *Physicochem. Probl. Miner. Process.* 44, 231–244.
- SIWINSKA-STEFANSKA K., PRZYBYLSKA A., JESIONOWSKI T., SOJKA-LEDAKOWICZ J., OLCZYK J., WALAWSKA A., 2010, Wpływ kompozytu tlenkowego TiO₂-SiO₂ na właściwości barierowe wyrobów włókienniczych, *Przem. Chem.*, 89, 1661–1666.

- VALVARDE-AGUILAR G., GARCIA-MACEDO J.A., RENTERIA-TAPIA V., 2011, Photoconductivity studies of gold nanoparticles supported on amorphous and crystalline TiO₂ matrix prepared by sol-gel method, *Rev. Mex. Fis.* 57, 13–18.
- WU F.-C., TSENG R.-L., 2006, Preparation of highly porous carbon from fir wood by KOH etching and CO₂ gasification for adsorption of dyes and phenols from water, *J. Colloid Interface Sci.*, 294, 21–30.

Received April 29, 2011; reviewed; accepted June 17, 2011

NUCLEATION AND GRANULE FORMATION DURING DISC GRANULATION PROCESS

Tadeusz GLUBA, Andrzej OBRANIAK

Faculty of Process and Environmental Engineering, Technical University of Lodz, Poland Wolczanska 213, 90-924 Lodz, gluba@wipos.p.lodz.pl

Abstract. The study of nucleation and granule formation in a bed of fine-grained material during the phase of batch damping in the process of periodical disc granulation was conducted. The study was carried out on laboratory disc (diameter - 0.5 m), with the use of constant disc filling with powder material, constant slope angle 50° between the disk axis and level and constant rotational speed of device. Foundry bentonite was used as the examined material and distilled water as a binding liquid. The binding liquid was added in the form of droplets having constant size. The size of droplets was changed in the range 2.4÷4.9 mm. The influence of number and size of binding liquid droplets delivered to bed, as well as of their delivery height on the size distribution of nuclei generated in the dumping phase was determined.

keywords: nucleation, disc granulation, size distribution, drop impact energy

1. Introduction

The flow of liquid through porous substances poses a serious problem, solution of which is necessary to carry out some operations taking place in three-phase systems such as granulation. Wet granulation is characterized by the participation of two disperse phases: grained powder and liquid phase introduced in the form of droplets and compact phase – the air. Their interaction, which depends on the degree of both phases dispersion, determines the progression of a given operation.

Wet granulation processes may be divided into three main stages: wetting and nucleation, consolidation and growth, and granule attrition and breakage (Ennis and Litster, 1997; Tardos et al., 1997; Iveson et al., 2001; Litster and Ennis, 2004). During the wetting and nucleation stage, the liquid binder is sprayed onto the tumbling fine-grained material (in rotary drums, disks) where it wets the powder and forms granule nuclei. The conditions of liquid distribution have a great effect on nucleation and final properties of the granule produced (Gluba, 2002; Hapgood et al., 2003; Gluba, 2003).

The phenomena of liquid drop impacts on powder beds plays an important role during nucleation in wet granulation processes.

When the drop size is larger than the particle size, wetting the powder with the liquid gives a distribution of seed granules or nuclei. When the drop size is small compared to the unit particle size, the liquid will coat the particles. The coating is produced by collision between the drop and the particle followed by spreading of the liquid over the particle surface.

If the liquid drop breaks on impact, then this will effectively increase the number of granule nuclei formed and decrease their size. If the liquid drop spreads out a large amount before it soaks into the powder, then this will increase the surface coverage term and may prematurely cause nuclei coalescence and caking at the powder surface.

Only a few studies concern the phenomena occurring during the collision of liquid droplets with the surface of the porous material powder (Agland and Iveson, 1999; Hapgood et al., 2002; Nguyen et al., 2009; Tan et al., 2009). However, most of them relate to other research systems and there is no simple transfer to the conditions of nucleation in wet granulation process.

2. Aim of the study

The aim of this study was to determine the effect of conditions for the supply of binding liquid droplets to bed in a disc granulator on the formation and growth of granule nuclei.

3. Experimental

Investigations of binding liquid droplet penetration in a moving bed of powder material located in a disc granulator were carried out on an experimental stand the scheme of which is shown in Fig. 1.

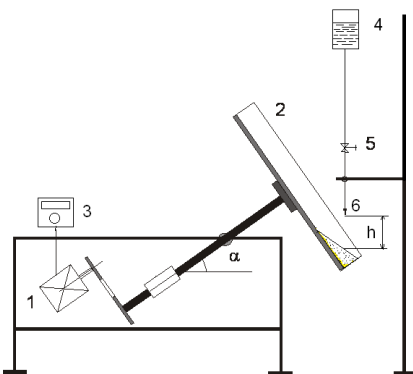


Fig. 1. Schematic diagram of the equipment.
1. engine with reducer, 2. disc, 3. inverter,
4. tank, 5. valve, 6. Needle. h - height of the needle
tip above the bed, α - angle of disk axis
inclination

Disc granulator (2) of diameter 0.5 m and height of the rim 0.1 m was mounted on a rotating shaft, inclined at an angle $\alpha = 50^\circ$. A shaft was driven by an electric motor with reducer (1) and inverter (3). During the tests a constant rotational speed of plate

was equal to 10 rpm and constant mass of fine-grained material equal to 0.3 kg. A wetting liquid was provided drop-wise from a dropping funnel (6) supplied from the tank (4) on a bed in the disc. The assumed value of the liquid flow intensity was determined by means of a valve (5). Binding liquid was supplied drop wise of various fixed size resulting from the size of applied funnel tips. The size of droplets generated for each tip was determined based on the weight and the number of drops supplied at a given time. The calculations assumed spherical shape of drops.

Three different heights of the binding liquid droplets supply resulting from the location of the funnel outlet tips at different heights h above the bed.

The parameters of the wetting liquid supply to the bed are summarized in Table 1.

Table 1. The wetting parameters used in the investigations

| Hight of the needle tip above the bed, h [m] | Drop diameter d_d [mm] | Drops number n_d [-] | Liquid flow rate Q_w [cm ³ /s] |
|---|-----------------------------|---------------------------|--|
| 0.02 0.52 1.02 | 3.0, 3.3, 4.9 | 100, 200, 300 | 0.043 |
| 0.02 0.52 1.02 | 2.4, 3.3 | 100, 200, 300 | 0.025 |

A model experimental material was foundry bentonite. The basic properties of the raw material were: density $\rho = 2150 \text{ kg/m}^3$, mean bulk density $\rho_b = 865 \text{ kg/m}^3$, mean volumetric size $d_m = 0.013 \text{ mm}$. Distilled water was used as the wetting liquid.

Fine-grained material bed in the disc was given a specified number of liquid drops n_d and then the unit was stopped and obtained feed was separated into size fractions using a set of sieves. For each size fraction mass m_n and the number of granule nuclei n_n which formed in the course of dispensing drops of liquid to the bed were determined. At the same conditions of liquid supply a second attempt was performed each time during which after the supply of liquid to bed the process was continued over a fixed time $t_g = 10 \text{ min}$. The feed obtained after this time period was separated into size fractions and weight of each fraction m_{n10} and the number of granules in a given size class n_{n10} were determined.

4. Results

The results of this study indicate that the conditions for the supply of binding liquid to the powder bed significantly influence the penetration of the liquid in the bed and the associated process of creating granules nuclei. Depending on the size of dispensed droplets, their number, and the height of their supply the conditions of their nucleation quite clearly change. For example, Fig. 2 shows the change in the number of nuclei created at the stage of dispensing drops of a size $d_d = 4.9 \text{ mm}$, depending on the height h , for a different number of supplied drops n_d .

From Fig. 2 it follows that in the case of dispensing liquid just above the bed ($h = 0.02\text{m}$), the number of resulting nuclei is similar to the number of supplied liquid drops, which means that every drop approximately seeks to create a single germ. With the increase of height h there follows a significant increase in the number of resulting nuclei, which means that the supplied drops are prone to break-up, which results in a greater number of nuclei. The dependence of number of created nuclei to the specified number of drops ratio defined with a coefficient $\zeta = n_n/n_d$, on the height h for different sizes of droplets is compared in Fig. 3.

Figure 3 shows that the coefficient ζ considerably increases with the increase of droplet size, and for $d_d = 3.0$ take values close to 1. This means that in case of this droplet size no break-up occurs and the number of nuclei is virtually equal to the number of given drops.

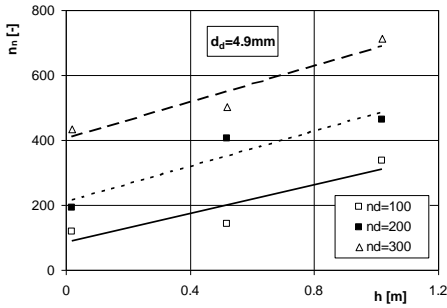


Fig. 2. Effect of liquid droplets supply height on the number of resulting nuclei

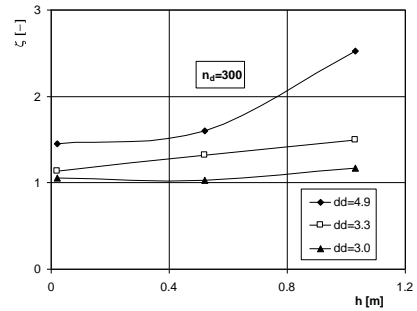


Fig. 3. Dependence of coefficient ζ on the height h , for different sizes of droplets d_d

Obtained dependencies indicate that the behavior of drops in a powder bed determines both its size (mass) and the speed with which it hits the bed. The speed of a drop hitting the material u was calculated based on correlation proposed by Range and Feuillebois (1998):

$$u = \sqrt{\frac{g}{A}(1 - e^{-2Ah})}, \quad (1)$$

$$\text{with } A = \frac{3c_f \cdot \rho_a}{4\rho_d \cdot d_d},$$

where $c_f = 0.796$ is the friction coefficient for a drop falling in air

g - gravitational acceleration, m/s^2

h - height of the needle tip above the bed, m

ρ_a - air density, kg/m^3

ρ_d - drop density (distilled water), kg/m^3

d_d - drop diameter, m .

Taking into account the weight of a falling drop m_d and its speed at impact u the kinetic energy of the drop was determined from the formula:

$$E_d = 0.5m_d \cdot u^2 . \tag{2}$$

Calculated speeds and kinetic energy of drops at the moment of impact with the powder are summarized in Table. 2.

The effect of drop kinetic energy on the value of coefficient ζ , with a fixed number of added drops n_d is shown in Fig. 4.

From Fig. 4 it follows that the effect of liquid supply height and drop size on their degree of decomposition, expressed with coefficient ζ , may be well defined with the kinetic energy of droplets colliding with the powder. A certain influence of the total number of droplets of liquid supplied to the bed may be observed here. The higher the value n_d coefficient ζ decreases. This can be elucidated by the fact that with a greater number of drops supplied to the bed a greater probability of their coalescence exists which influences a smaller number of obtained nuclei. An analogous relationship, shown in Fig. 5, was also obtained for a smaller intensity of binding liquid drop dispensing $Q_w = 0.025 \text{ cm}^3/\text{s}$.

Table 2. Drop impact velocity and energy

| Drop diameter d_d [m] | High of the needle tip above the bed h [m] | Drop impact velocity u [m/s] | Drop mass m_d [kg] | Drop impact energy E_d [J] |
|-------------------------|--|--------------------------------|----------------------|------------------------------|
| $2.4 \cdot 10^{-3}$ | 0.02 | 0.625 | $7.24 \cdot 10^{-6}$ | $1.412 \cdot 10^{-6}$ |
| | 0.52 | 2.962 | | $3.174 \cdot 10^{-5}$ |
| | 1.02 | 3.872 | | $5.425 \cdot 10^{-5}$ |
| $3.0 \cdot 10^{-3}$ | 0.02 | 0.625 | $1.41 \cdot 10^{-5}$ | $2.761 \cdot 10^{-6}$ |
| | 0.52 | 3.006 | | $6.386 \cdot 10^{-5}$ |
| | 1.02 | 3.980 | | $11.198 \cdot 10^{-5}$ |
| $3.3 \cdot 10^{-3}$ | 0.02 | 0.625 | $1.88 \cdot 10^{-5}$ | $3.676 \cdot 10^{-6}$ |
| | 0.52 | 3.022 | | $8.592 \cdot 10^{-5}$ |
| | 1.02 | 4.021 | | $15.212 \cdot 10^{-5}$ |
| $4.9 \cdot 10^{-3}$ | 0.02 | 0.626 | $6.16 \cdot 10^{-5}$ | $1.205 \cdot 10^{-5}$ |
| | 0.52 | 3.076 | | $29.151 \cdot 10^{-5}$ |
| | 1.02 | 4.160 | | $53.297 \cdot 10^{-5}$ |

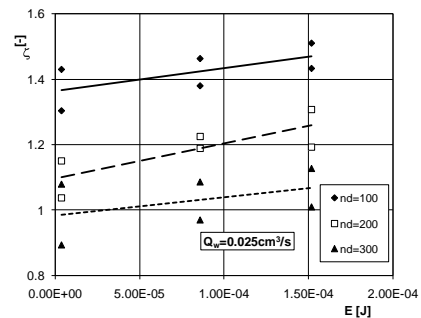
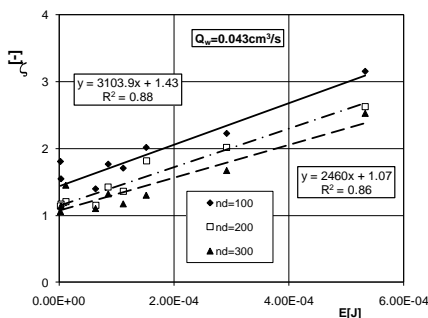


Fig. 4. Dependence of coefficient ζ on the kinetic energy of drops falling on the bed

Fig. 5. Dependence of the coefficient ζ on the kinetic energy of drops falling on the bed

One may conclude about the mechanisms of formation and growth of nuclei at the stage of supply of binding liquid droplets to bed based on the size of nuclei created. When every drop strives to create a single germ, their dimensions are a reflection of the size of dispensed droplets. When it comes to breaking up of droplets, there can be created a greater number of droplets of smaller size. During the movement of wet powder bed, other mechanisms influencing the number and size of nuclei created, i.e. coalescence, wear, layering may occur. The importance of individual mechanisms may depend on the conditions for the supply of liquid to the bed and change during the process.

For example, Fig. 6 shows the comparison of curves of quantitative size composition for different heights of liquid supply at a specified size and number of drops, and Fig. 7 compares mass-distribution curves at the same conditions of drops supply.

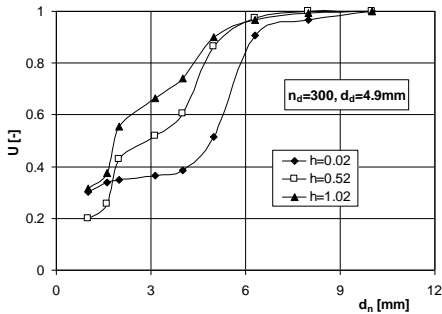


Fig. 6. Comparison of quantity-size distributions of nuclei

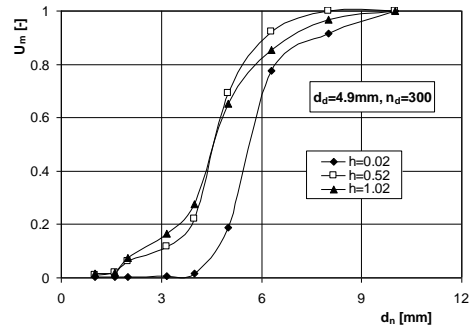


Fig. 7. Comparison of mass-size distributions of nuclei

In both graphs presented similar relationships can be observed. The increase in the amount of droplet supply results in increased quantitative and mass fraction of nuclei of a smaller size, which confirms previously observed trends regarding the conditions for liquid droplets break-up.

Figure 8 shows the comparison of the impact of liquid droplets supply on the average size of nuclei for the two droplet sizes, with a fixed number of them. For the droplet size $d_d = 4.9$ mm the increase of height h causes a reduction in the average quantitative size of nuclei, while for droplets of size $d_d = 3.0$ mm this impact was very slight. Figure 8 shows the comparison of changes in the average size of nuclei after 10 minutes of further granulation from the end of dispensing liquid.

It was found that during 10 min of granulation after the supply of liquids, the drop of germ size occurs. This may be caused by the destruction of even very weak agglomerates and minor thickening of their internal structure. The nuclei mass fraction in the total feed mass is very slight yet and nuclei are virtually suspended in the powder material which hinders their contact and mutual interaction. During this period, the liquid is no longer fed, and so there is no driving force for further formation and growth of nuclei and destructive mechanisms may play a greater role.

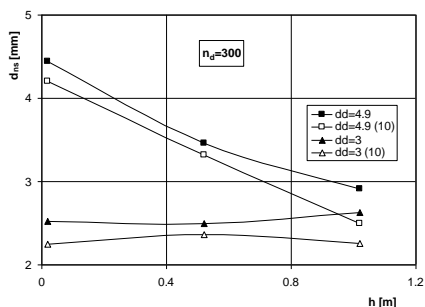


Fig. 8. Effect of liquid supply height on the average size of nuclei

5. Conclusions

On the basis of the obtained results the following conclusions were drawn.

1. Parameters of binding liquid droplets supplied to the powder material bed significantly affect the conditions of formation and growth of granule nuclei.
2. Effect of droplet size and their supply height above the bed on the number of resulting nuclei may be described with the kinetic energy of drops falling on the bed.
3. The increase of droplet supply height results in increased quantitative and mass fraction of nuclei of smaller size.
4. For larger droplets ($d_d = 4.9$ mm) the increase in the liquid supply height brings about reduction in the average quantitative size of nuclei while for smaller droplets ($d_d = 3.0$ mm) the effect is negligible.

Acknowledgments

The work was carried out under research project no. N N209 096135 financed by the Ministry of Science and Higher Education for the years 2008-2011.

References

- AGLAND S., IVESON S.M., 1999, The impact of liquid drops on powder bed surfaces, CHEMECA 99, New Castle, Australia.
- ENNIS, B.J. LITSTER J.D., 1997, Particle size enlargement in Perry's Chemical Engineers' Handbook, Eds. Perry, R. and Green, D., 7th Ed., 20–56 to 20–89.
- GLUBA T., 2002, The effect of wetting conditions on the strength of granules, Physicochemical Problems of Mineral Processing, 36, 233–242.
- GLUBA T., 2003, The effect of wetting liquid droplet size on the growth of agglomerates during wet drum granulation, Powder Technology, 130, 219–224.
- HAPGOOD K.P., LITSTER J.D., BIGGS S.R., HOWES T., 2002, Drop penetration into porous powder beds. Journal of Colloid and Interface Science 253 (2), 353–366.
- HAPGOOD K.P., LITSTER J.D., SMITH R., 2003, Nucleation Regime Map for Liquid Bound Granules, AIChE Journal, 49 No.2.
- IVESON S.M., LITSTER J.D., HAPGOOD K., ENNIS B.J., 2001, Nucleation, growth and breakage phenomena in agitated wet granulation processes: a review, Powder Technology 117, 3–39.
- LITSTER J.D., ENNIS B.J., 2004, The Science and Engineering of Granulation Processes. Particle Technology Series. B. Scarlett, Kluwer Academic Publishers, Dordrecht, The Netherlands.
- NGUYEN T., SHEN W., HAPGOOD K., 2009, Drop penetration time in heterogeneous powder beds, 64, 5210–5221.

- RANGE K., FEUILLEBOIS F., 1998, Influence of Surface Roughness on Liquid Drop Impact, *J. Colloid & Interface Sci.*, 203, 16–30.
- TAN M.X.L., WONG L.S., LUM K.H., HAPGOOD K.P., 2009, Foam and drop penetration kinetics into loosely packed powder beds, *Chem. Eng. Science*, 64, 2826–2836.
- TARDOS G.I., IRFAN-KHAN M., MORT P.R., 1997, Critical Parameters and limiting conditions in binder granulation of fine powders, *Powder Technol.* 94, 245–258.

Received April 29, 2011; reviewed; accepted July 20, 2011

MODEL OF ENERGY CONSUMPTION IN THE RANGE OF NUCLEATION AND GRANULE GROWTH IN DRUM GRANULATION OF BENTONITE

Andrzej OBRANIAK, Tadeusz GLUBA

Faculty of Process and Environmental Engineering, Technical University of Lodz, Poland Wolczanska 213, 90-924 Lodz, obraniak@wipos.p.lodz.pl

Abstract. The energy consumption during granulation process in horizontal drum granulators at variable process and equipment parameters: drum diameter, angular velocity and the degree of drum filling with raw material was investigated. The feed was wetted drop-wise during tumbling at a constant liquid flow rate. During the whole process the instantaneous values of the driving torque on the shaft were measured. The effect of the drum diameter, its angular velocity, drum filling degree and moisture content of the feed on energy consumption was evaluated. A model of the dependence of energy needed for nucleation and granules growth during wet granulation for different process and equipment parameters was proposed in the paper.

keywords: agglomeration, granulation energy, drum granulation, bentonite

1. Introduction

The dynamics of a granular bed in drum granulators, i.e. the motion of the bed and individual particles, as well as forces of their interactions, determine the value of torque measured on the granulator shaft, and as a result, the power of a driving motor and energy used to carry out the process.

The analysis of static and dynamic equilibrium of the granulated bed, and also results obtained by Heim et al. (2001, 2004) prove that inertia and friction forces in the tumbling feed depend significantly on such equipment and process parameters as bed moisture content, drum diameter, its filling degree and rotational velocity of the granulator.

The changes of reduced torque as a function of feed moisture content were investigated by Heim et al. (1999). The obtained results are shown in Fig. 1.

In the graphs representing the relations of the reduced torque, three ranges can be distinguished, for which different characters of the relation were obtained. In the first range the dependence of torque on moisture content has approximately the form of square function. In the second range a decrease of the value is observed, and in the

third range the value is constant. At the end of the third range there is an abrupt drop of the torque. Particularly interesting is the initial torque increase and its further fixing. Such a character of the torque can be explained by changes in the parameters characterising the granulated bed during the process such as granulation degree, granule diameter, bulk density of the feed and due to liquid supply the total mass of the bed. The influence of some of these parameters on the bed dynamics was investigated both in model mixing of the granular bed in a horizontal tumbling mill (Forsberg and Zeng, 1991; Rajamani et al., 2000) and in drum and disk granulators: (Heim, 2004; Mellmann, 2001), and during grinding in ball mills (Hogg and Fuerstenau, 1972; Kapur et al., 1992). However, there are a few studies devoted to energy consumption required to circulate the processed bed, and hence discussing the costs of drum granulation process.

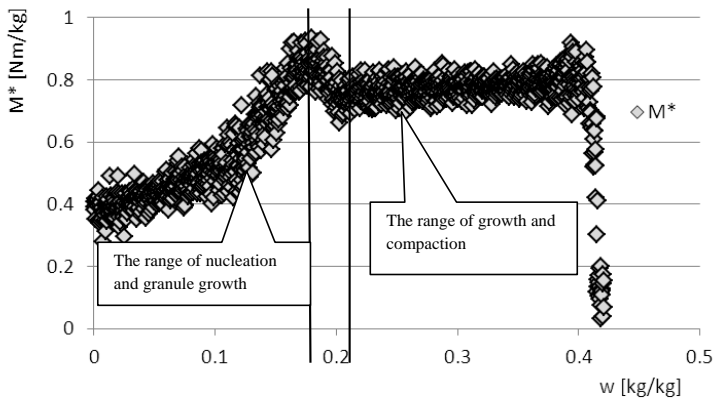


Fig. 1. The effect of feed moisture content on the reduced torque ($D=0.4$ m; $\varphi=20\%$; $\omega=1.4$ rad/s) (Heim et al., 1999)

2. Aim of the study and range of investigations

Aim of the study was to determine the effect of drum diameter, rotational velocity of the granulator and degree of its filling with raw material on the energy required for the transformation of powder material into granulated product.

The following ranges of changes in the parameters were used in the studies: diameter of granulator drum $D = 0.25; 0.3; 0.35$ and 0.40 m, drums length $L=0.4$ m, filling of the drum with granular material $\varphi = 5\%$ to 20% , angular velocity of the drum $\omega = 1.05$ to 3.35 rad/s. The investigations were performed in four drums that had the same length L and different diameters. The range's change of drum angular velocity was select in such way to provide cascading - the typical feed movement for drum tumbling granulators.

The degree of drum filling with raw material φ was changed gradually by 2.5% or 5% in the range $5\div 20\%$ of the inner drum volume, depending on drum diameter. Such a filling range ensures correctness of granulation process. The proposed ranges of

changes of process and equipment parameters (D , ω , φ) overlap the ranges used in drum granulation processes.

The tested material was foundry bentonite and the wetting liquid was distilled water.

3. Equipment and measuring methods

A schematic diagram of the experimental set up is shown in Fig. 2. Drum (1) was driven by motoreducer (6) by means of a belt transmission and a clutch. A fluent change of rotational velocity of the drum was obtained by means of inverter (7), and controlled by a revolution counter. Instantaneous torque values were measured by torque meter (3) and reading device (4). Next, they were processed and recorded by computer (5). The granular bed placed in the drum was wetted drop-wise by means of sprinkler (2), which was introduced axially to the device that ensured a uniform liquid supply. The sprinkler was mounted on tripod (8), which was independent of the granulator. The wetting liquid (distilled water) was supplied from tank (10), placed at the height of 2.5 m from the drum axis and its constant flow rate ($Q = 10^{-6} \text{ m}^3/\text{s}$) was fixed by means of rotameter (9). During the trial, a constant liquid level was kept in the tank, which guaranteed a constant pressure of supplied liquid. The granular bed was wetted until the material got overwetted which caused that the bed stuck to the inner wall of the granulator.

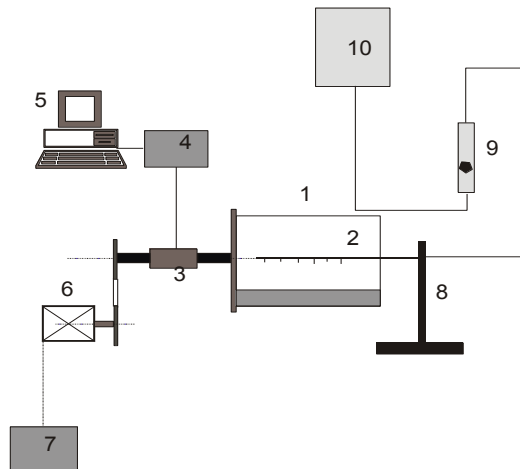


Fig. 2. Schematic diagram of the equipment. 1- drum granulator; 2- sprinkler; 3- torque meter; 4- reading device; 5- computer, 6- motoreducer; 7- inverter; 8- tripod; 9- rotameter; 10- tank

Every 120 s a sample was taken, subjected to sieve analysis and returned to the drum. The process of granulation was carried out batch-wise, each time at determined process and equipment parameters: drum filling with material, rotational velocity of the granulator and drum diameter.

4. Results

Results of the measurement of instantaneous torque values $M(t)$ read in 1s time intervals on the granulator shaft during granulation (wetting stage) of the granular bed tumbling in the drum were converted to the values of reduced torque $M^*(t)$.

The instantaneous values of reduced torque $M^*(t)$ were calculated on the basis of instantaneous torque $M(t)$, as well as on the basis of the torque of idle run (at empty granulator) M_j and the total feed mass in the drum (raw material m_s and wetting liquid $m_w(t)$) from Eq. (1):

$$M^*(t) = \frac{M(t) - M_j}{m_s + m_w(t)}. \quad (1)$$

Due to the fact that the wetting liquid was supplied all the time during granulation process with constant volume flow rate, the changes of reduced torque vs. wetting time were the same as the torque changes vs. bed moisture content w . Moisture content of the feed at the time t was calculated from Eq. (2).

$$w = \frac{m_w(t)}{m_s} = \frac{Q \cdot t \cdot \rho_w}{m_s}. \quad (2)$$

In the case when the wetting liquid is supplied continuously at a constant flow rate to the system, the reduced moment in time is analogous to the torque in the function of feed moisture content.

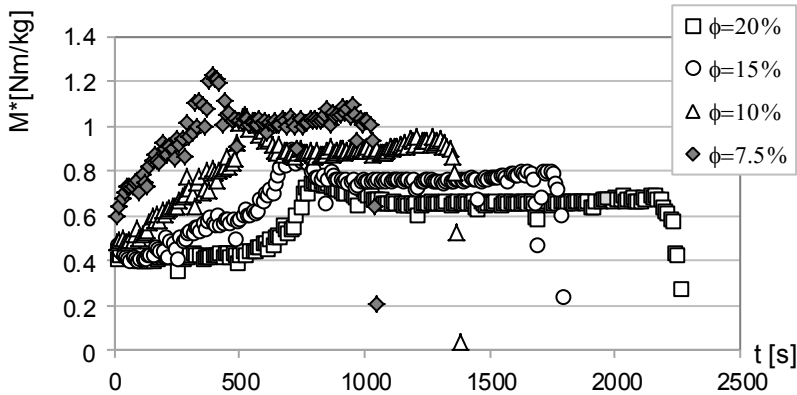


Fig. 3. Comparison of changes in reduced torque vs. time for different values of drum filling ϕ ($D = 0.4$ m; $\omega = 1.4$ rad/s)

From analysis of the obtained results it follows that the value of torque during granulation in a tumbling drum with wetted bed depends also on such equipment and process parameters as drum diameter, filling of the drum ϕ and its rotational velocity. This is confirmed by a comparison of changes in the reduced torque during bed

wetting for various degrees of drum filling φ shown in Fig. 3. Diagrams in this figure were prepared for mean values of the torque from 10 subsequent measuring points, (every 10 s). It was found that the reduced torque was decreasing with an increase of drum filling, which is related most probably to the bed – drum wall contact surface, which with volume increase grows slower than the feed mass.

Similar relations were obtained for different diameters and angular velocities of the drum. It follows from them that the reduced moment increases with an increasing drum diameter and its angular velocity. This is probably caused by an increasing distance between the bed mass centre and drum axis and an increase of the friction forces due to the increase of centrifugal force.

To specify how much changes of the torque, and consequently power, can provide information on the granulation process, a comparison was made between changes in the reduced torque and changes in the mass fraction of the smallest particles which was considered as not granulated material. This relation is illustrated in Fig. 4. The comparison of changes in the torque and total fraction of not granulated mass U_s made it also possible to determine the time interval in which the whole raw material was processed into granulated product. It can be observed that the mass of not granulated material reduced rapidly for moisture content (and also time), at which the reduced torque reached a maximum. The fraction of not granulated material corresponding to this maximum value is about 10% and decreases to ca. 5% after setting up the torque M^* .

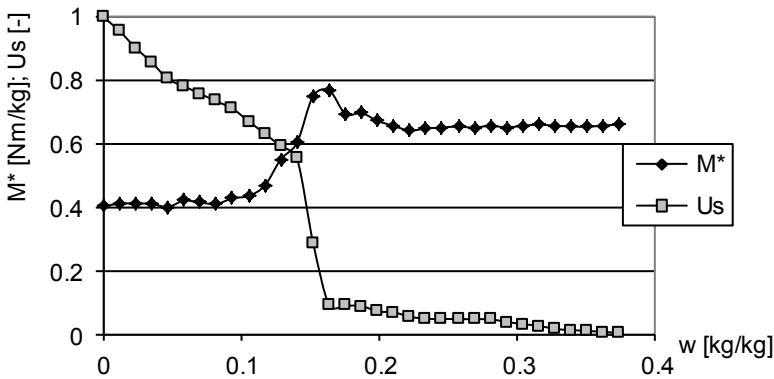


Fig. 4. Comparison of changes in reduced torque and mass fraction of not granulated material vs. moisture content ($D = 0.4$ m; $\varphi = 15\%$; $\omega = 1.05$ rad/s)

Values of the torque shown in Fig. 5 were calculated as an average from 10 subsequent measuring points after every minute of the measurement.

On the basis of the values of reduced torque the values of unit power demand were calculated from equation (3):

$$N^*(t) = M^*(t) \cdot \omega . \tag{3}$$

Due to the fact that practically all fine-grained material is processed into granulated product at the first stage of the process (later only growth and concentration of the previously formed agglomerates is observed) the energy required to form granulated product, was determined on the basis of power changes at the first stage of the process. Experimental points of power change at the first stage were approximated by quadratic polynomial.

At the second stage of the process a stabilized value of the unit power can be observed. It is a result of stable movement of previously formed granules and subsequent lack of changes in dynamics of tumbling feed. An example of power changes in both stages is shown in Fig. 5.

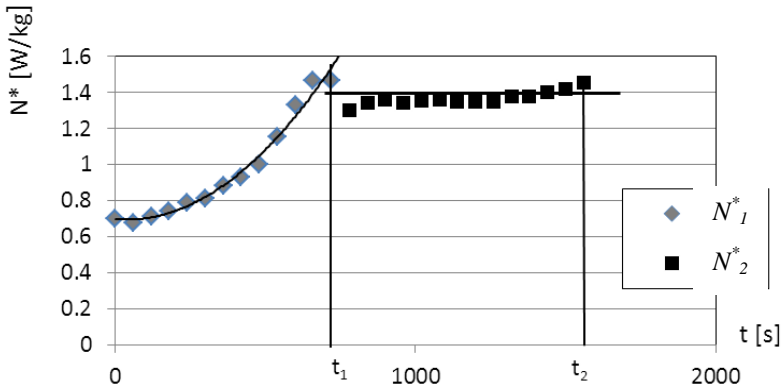


Fig. 5. Approximation of the results by mathematical functions

The energy required for the transformation of powder feed into granules was determined from the equation (4):

$$E_1^* = \int_0^{t_1} N_1^*(t) dt . \quad (4)$$

and the energy consumption for the subsequent growth and concentration of previously formed granules from equation (5):

$$E_2^* = \int_{t_1}^{t_2} N_2^*(t) dt . \quad (5)$$

The values of energy obtained as a result of integration of the functions approximating all experimental power changes (75) was related to equipment and process parameters used in the experiments.

For the stage of nucleation and granule formation a power function at correlation coefficient $R^2 = 0.945$ was derived:

$$E_1^* = 10^{2.64} \cdot D^{2.92} \cdot \varphi^{0.72} \cdot \omega^{0.87} . \quad (6)$$

The second stage of process in which granules grow as a result of layering and coalescence is described by power equation (7):

$$E_2^* = 31600 \cdot D^{3.12} \cdot \varphi^{0.82} \cdot \omega^{1.15} \quad (7)$$

The correlation coefficient for this equation was $R^2 = 0.965$. Figure 6 presents the example of comparison between the energy values obtained as the result of integration of quadratic equations and those calculated from Eq. 6.

Based on analysis of the results it was found that energy required for raw material granulation in a drum granulator depended on equipment and process parameters, at which the process was carried out.

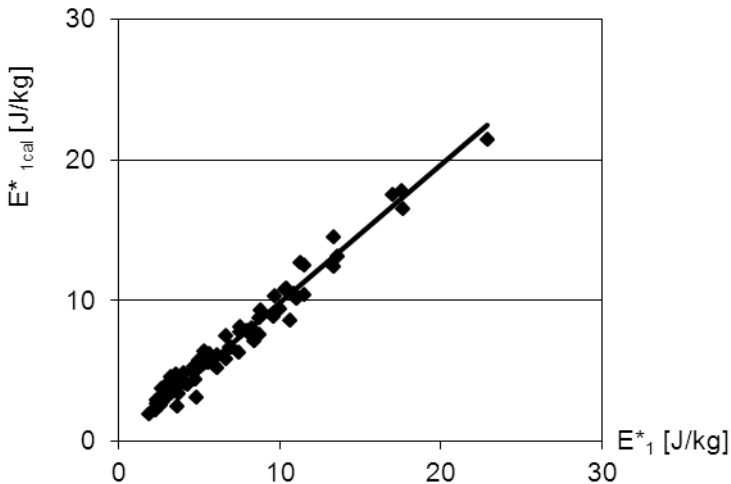


Fig. 6. Comparison of energy obtained from integration of square functions and calculated from Eq. 6

5. CONCLUSIONS

The analysis of results demonstrated that the energy required during nucleation (the initiation of agglomerates formation) as well as their growth and concentration for the granulation of powder material in drum granulator depends on process and equipment parameters. The analysis of the obtained power equations indicates that the energy requirement in both stages of granulation is proportional to the volume of transformed raw material (exponent by drum diameter is close to 3). More significant influence of the rest of analyzed parameters on energy requirement during the stage of growth and concentration of formed granules were also observed.

The result of energetic parameters measurements during granulation may be the indicator of process realisation. It can be observed that the mass of not granulated material reduced rapidly for moisture content (and also time), at which the reduced torque reached a maximum value.

Nomenclature

- E^* - unit energy, J/kg
 M - torque on drum shaft, Nm
 M_j - torque of idle run, Nm
 M^* - reduced torque, Nm/kg
 N - power supplied, W
 N^* - reduced power, W/kg
 Q - volume flow rate of liquid, m³/s
 m_s - mass of raw material, kg
 m_w - mass of wetting liquid, kg
 t - wetting (granulation) time, s
 w - bed moisture content, kg/kg
 ρ_w - water density, kg/m³
 ω - angular velocity, rad/s.

Acknowledgements

The study was carried out under the research project N N209 096135 in the Department of Process Equipment in the years 2008–2011.

References

- FORSSBERG E., ZENG Y., 1991, Effect of powder filling fraction on particle size and energy consumption in coarse grinding, *Scandinavian Journal of Metallurgy*, 20, 300–304.
- HEIM A., GLUBA T., OBRANIAK A.; 2001, Bed dynamics during granulation in rotating drums, *Proceedings of the 7th International Symposium on Agglomeration (Albi, France 29-31.05)*, 887–896.
- HEIM A., GLUBA T., OBRANIAK A., 2004, The effect of the wetting droplets size on power consumption during drum granulation, *Granular Matter* 6, 137–143.
- HEIM A., GLUBA T., OBRANIAK A.; 1999, Badania momentu obrotowego podczas granulacji bębnowej, *Physicochemical Problems of Mineral Processing, XXXVI Symposium*, 49–62.
- HEIM A., KAŻMIERCZAK R., OBRANIAK A., 2004, Model dynamiki złoża ziarnistego w granulatorze talerzowym, *Inżynieria Chemiczna i Procesowa* 25 (3/2), 993–998.
- HOGG R., FUERSTENAU D.W., 1972, Power relationships for tumbling mills, *Trans. SME-AIME*, 252, 418–423.
- KAPUR P.C., RANJAN S., FUERSTENAU D.W., 1992, A cascade-cataract charge flow model for power draft of tumbling mills, *International Journal of Mineral Processing* 36, 9–29.
- MELLMANN J., 2001, The transverse motion of solids in rotating cylinders – forms of motion and transition behaviour, *Powder Technology*, 118, 251–270.
- RAJAMANI R. K., MISCHRA B.K., VENUGOPAL R., DATTA A., 2000, Discrete element analysis of tumbling mills, *Powder Technology*, 109, 105–112.

Received June 17, 201; reviewed; accepted July 20, 2011

WETTING OF SUPPORTS BY IONIC LIQUIDS USED IN GAS SEPARATION PROCESSES

Monika JOSKOWSKA, Iwona KOPCZYNSKA, Bartosz DEBSKI,
Daria HOLOWNIA-KEDZIA, Robert ARANOWSKI, Jan HUPKA

Department of Chemical Technology, Chemical Faculty, Gdansk University of Technology, 80-952 Gdansk, Poland, aran@chem.pg.gda.pl

Abstract. Ionic liquids were found to be selective solvents for separation of gases. They are widely used in supported ionic liquid membranes (SILMs) technology, especially in gas separation and purification processes. This work has characterized commercially available porous membranes employed in such purposes. Characterization of supports and membrane phases was carried out in order to determine factors influencing membrane stability. Scanning electron microscopy (SEM) was used to determine morphology of membrane surface. In this work wetting of the polymeric support with [Emim][TfO], [Emim][Tf₂N], [Bmim][TfO] and [Bmim][Tf₂N] and swelling of the membrane impregnated with ionic liquids have been investigated.

keywords: imidazolium ionic liquids, liquid membrane, wettability

1. Introduction

Supported liquid membranes (SLMs) have been an object of growing interest in recent years. They present several advantages in separation processes, such as requirement of very small quantities applications. The reason of this state is mainly low stability (Kemperman et al., 1996). Mechanisms of instability are reported in the literature (Kocherginsky et al., 2007). Stability is mostly affected by loss of liquid membrane phase from the support (Naplenbroek et al., 1992). Due to the fact that membrane phase is kept in the membrane pores by capillary forces, it is obvious that this process can be either evaporation, dissolution in surrounding phases or high pressure difference. These effects have influence on flux and selectivity of the system (Takeuchet et al., 1987; Zha et al., 1995). Stability of SLMs depends on the properties of polymeric or ceramic support, membrane phase, possible carriers and operating conditions. Physicochemical properties of membrane phase play important role in membrane stability. Proper choice of these materials can improve significantly system lifetime. Problems mentioned above can be avoided by using ionic liquids as a membrane phase filling pores of the support. Some researchers report that water

concentration in organic phase is also important in SLMs stability, whereas when it is less than 15 g/l it shows proper stability (Zha et al., 1995).

In recent years ionic liquids have been widely used as an alternative to traditional organic solvents in catalysis, as a reaction media and in separation and purification processes. Ionic liquids have many unique properties, for example, they have non-measurable vapor pressure, they are non-flammable and liquid in a wide range of temperatures, they solvate wide range of organic and inorganic species (Earle et al., 2000; Marsh et al. 2004; Pernak, 2000). Ionic liquids give a possibility of adjusting their physicochemical properties by choosing proper ions. Proper choice of organic phase allows to avoid the problem of solvating IL in receiving phase and only the excess amount of ILs from the membrane surface is removed (De Los Rios, 2007; 2009). These properties give SILMs advantage over traditional SLMs (Fortunato et al. 2004; Gan et al, 2006; Hernandez-Fernandez et al., 2009). Non-measurable vapor pressure allows to overcome the problem with loss of membrane phase by evaporation. Since ILs consist of large asymmetric organic cation and small anion and this structure prevents crystallization, they are liquid in a wide range of temperatures. As mentioned above, stability depends on capillary forces that is why size and morphology of membrane pores affect the stability (Kemperman et al., 1996). Minimum transmembrane pressure required to push out the impregnating phase from membrane pores is given by the Young–Laplace equation:

$$P = \frac{2 \cdot \gamma \cdot \cos\theta}{r}, \quad (1)$$

where: γ is the interfacial tension, θ is the contact angle, r is the pore radius.

This equation is true for cylindrical pores. Commercially available membranes have highly irregular pores geometry. Calculated pressure is then higher than real critical level. It can be concluded that generally membranes with smaller pore size are more stable than those with bigger pores.

This work focused on the use of polymeric porous membranes which can be applied as support for liquid membranes. Experimental procedures based on capillary rise method are widely used for porous media characterization (i.e. pore radius, contact angle). Measurements of penetration distance and liquid mass increase are two main experimental methods, in which Washburn equation is a basic instrument to analyze the obtained results (Trong et al., 2005; 2006). Capillary rise method was used for contact angle determination for polymeric material wetted by ionic liquids. Influence of imidazolium-based ionic liquids composition on wettability of porous supports was investigated. The family of 1-alkyl-3-methylimidazolium compounds ($C_n\text{mim}$) with variable alkyl chain lengths in cation and changeable anions were taken into account.

2. Experimental

2.1. Material, experimental apparatus and method

Seven ionic liquids were used in this study: 1-ethyl-3-methylimidazolium bis(trifluoromethylsulfonyl)imide [EMIM][Tf₂N], 1-ethyl-3-methylimidazolium trifluoromethanesulfone [EMIM][TfO], 1-butyl-3-methylimidazolium bis(trifluoromethylsulfonyl)imide [BMIM][Tf₂N], 1-butyl-3-methylimidazolium trifluoromethanesulfone [BMIM][TfO]. All chemicals were supplied by Merck Chemicals Company, Darmstadt, Germany with purity higher than 99%. The molecular structures of ILs cations and anions used in this study are shown in Fig.1 and Fig.2.

In order to determine the effect of chemical structure of the ionic liquids on wetting, different alkyl chain lengths of the cations and different anions were selected.

Polymeric supports: the four hydrophilic membranes were used: GH Polypro (polypropylene) - PP, FP VericelTM (polyvinylidene fluoride) - PVDF, NylafloTM (polyamide) - Nylon, Supor[®] (polyethersulfone) - PES, (Pall, Gelman Laboratory, USA). Table 1 shows the physicochemical properties of polymeric supports used in the experiments declared by Pall, Gelman Laboratory.



Fig. 1. Structure of ionic liquids cations used in the experiments

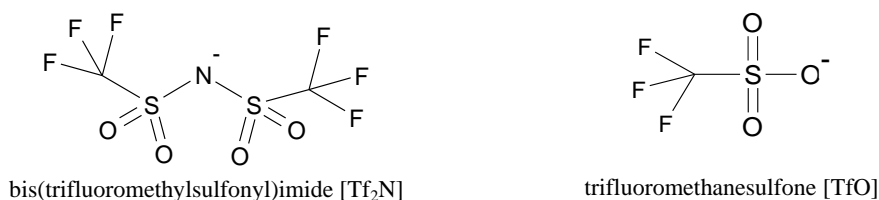


Fig. 2. Structure of ionic liquids anions used in the experiments

Table 1. Physicochemical parameters of polymeric supports reported by producer

| Support | Density [kg/m ³] | Pore size [μm] | Porosity [%] | Thickness [μm] |
|---------|---------------------------------|-------------------|-----------------|-------------------|
| PP | 900 | 0.2 | 80 | 92 |
| PVDF | 1790 | 0.2 | 80 | 123 |
| Nylon | 1130 | 0.2 | 80 | 110 |
| PES | 1370-1510 | 0.2 | 80 | 148 |

SEM characterization

The scanning electron microscope (SEM) Philips-FEI XL 30 ESEM (Environmental Scanning Electron Microscope) was used to determine the morphological properties and the pore size distribution. Before the SEM observation, the samples of supports were dusted with ultrathin layer of gold which significantly improved the quality of obtained images. Fig.4 (a), (b), (c) and (d) are SEM micrographs of the supports – polypropylene PP, polyvinylidene fluoride PVDF, polyamide Nylon, polyethersulfone PES (5000x) (scale bar = 5µm).

IR spectra of PP membrane

PP support has a hydrophilic, modified surface. The manufacturer (Pall) does not provide information about the type of modification. Membrane surface modification was calculated by ATR (Attenuated Total Reflection) technique on camera - FT-IR Spectrometer Tensor using zinc selenide optics and diamond crystal (Golden Gate's snap Specac). Analyses were performed using the following parameters: the spectral range 4000 - 600 cm⁻¹, resolution 2 cm⁻¹, the number of scans: 64. Figure 5 shows the IR spectra.

Thickness of the membrane and swelling in ionic liquids

Thickness of the membrane after immobilization step was determined by optical method using Epi-fluorescent Microscope L3001 with a compatible digital camera, Power Shot A650 IS. This method allows to measure the change of the thickness of the polymer after immersing it in ionic liquid for 24h. Glass holder was used to place the membrane in z direction to measure thickness.

Wetting of the membrane

The capillary rise method is based on the Washburn approach that has been derived from the Poiseuille equation:

$$dV = \frac{r^4 \cdot \Delta P \cdot \pi}{8\eta \cdot h} dt \quad , \quad (2)$$

and the Washburn equation:

$$h^2 = \frac{r \cdot \gamma \cdot \cos \theta}{2\eta} t \quad . \quad (3)$$

Additionally, the following simplifications are employed in the capillary rise method:

- a) the flow is laminar and stationary,
- b) there is no slip, i.e. no flow on the solid body - liquid interface,
- c) no internal pressure.

One way of determining contact angle value is an investigation of two liquids – reference and examined (Studebaker, 1955). For reference liquid:

$$h^2 = \frac{r\gamma_0}{2\eta_0} t_0. \quad (4)$$

When two beds are identical, r is constant, and for another liquid we have:

$$h^2 = \frac{r\gamma_1 \cos \theta}{2\eta_1} t_1. \quad (5)$$

Dividing equation (4) by (5) we obtain:

$$\cos \theta = K \frac{t_0}{t_1}, \quad (6)$$

where

$$K = \frac{\gamma_0 \cdot \eta_1}{\gamma_1 \cdot \eta_0}, \quad (7)$$

where

t_0 , γ_0 , η_0 are time of penetration, surface tension and viscosity of reference liquid, and t_1 , γ_1 , η_1 are time of penetration, surface tension and viscosity of liquid investigated, respectively.

The apparatus for the capillary rise experiments is shown in Fig. 3.

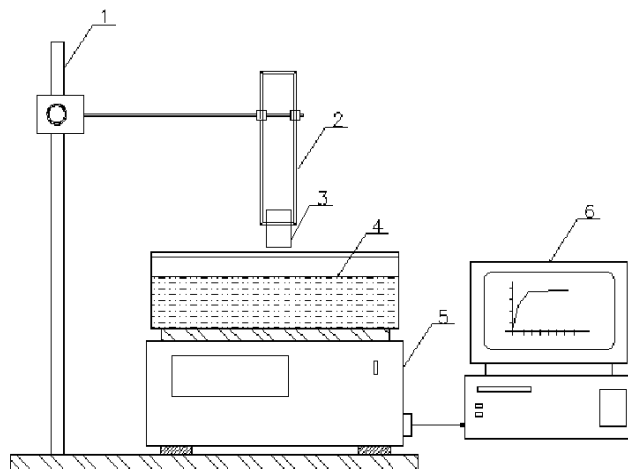


Fig. 3. Capillary rise measuring apparatus: 1 - support, 2 – glass matrix holder, 3 – polymeric membrane, 4 – vessel with ionic liquid, 5 - balance, 6 -computer

In the experiment, polymeric membrane samples sized 10x10 mm were cut out. The line at 5 mm height was made. The sample was placed in a glass holder. The increase in height of liquid penetrating into polymeric membrane and decrease in mass of the liquid in a container was recorded every second using timer and electronic balance, attached to a computer. The time $t = 0$ approximately corresponded to the moment of membrane submersion in the wetting liquid. The time of penetration up to 5 mm of membrane was measured. The experiments were repeated eight times (two times for each side) and the mean value was calculated. Based on measurement of ionic liquid penetration time in polymeric support, angle values were calculated using Equations 5 and 6. The results are shown in Table 2.

The second method for contact angle determination was the dynamic sessile drop method. The surface tensions of the ionic liquids were determined by the pendant drop method using Tensiometer Kruss DSA 10. Dynamic sessile drop study determines the largest contact angle possible without increasing solid/liquid interfacial area by adding volume of liquid dynamically. This maximum angle is the advancing angle θ_a . Volume is removed to produce the smallest possible angle, the receding angle θ_r . The difference between the advancing and receding angle $\theta_a - \theta_r$ is the contact angle hysteresis. The results are shown in Table 3.

3. Results and discussion

In the experiments imidazolium ionic liquids with different anions and cations were applied. Selected ionic liquids are widely used in gas separation technology. Imidazolium salts containing alkyl fluoride anions: bis(trifluoromethanesulfonyl) amide ([Tf₂N]) and trifluoromethanesulfonate ([TfO]) selectively separate carbon (IV) oxide from other gases, for example methane (Anderson et al., 2007; Anthony et al., 2005; Baltus et al., 2004; Bara et al., 2009; Bates et al., 2002; Chin et al., 2006; Joskowska et al., 2010; Joskowska et al. 2011).

The morphology of commercial membranes was studied by SEM. SEM (Fig.4) micrographs present highly porous material. The pores are heterogenic and not cylindrical.

Figure 4 indicates, that the 0.2 μm pore size declared by the manufacturer is not the size of the smallest pores, but the average size of all the pores in the membranes.

IR spectra illustrate intense stretching vibrations of C-H bond - methyl group at 2951 cm^{-1} (asymmetric) and 2868 cm^{-1} (symmetric) and methylene group at 2919 cm^{-1} (asymmetric) and 2839 cm^{-1} (symmetric) are visible in the IR spectra of PP membrane (Fig. 5). Stretching vibrations of the double bond occurred at 1728 cm^{-1} . IR spectra shows also intense bending vibrations of symmetric methylene group at 1453 cm^{-1} and bending vibrations of asymmetric methyl groups at 1376 and 1358 cm^{-1} .

Therefore, it can be concluded that the surface of PP membrane is modified with compounds containing C-O-C bonds, as evidenced by the emergence of asymmetric stretching vibration of C-O-C bond at 1256 cm^{-1} and asymmetric at 1105 cm^{-1} band

swing vibration of methyl groups below 1000 cm^{-1} . IR spectra of PVDF, PES and Nylon membranes perfectly fit to the IR spectra of model sample.

Contact angle θ is a quantitative way of showing wettability of solid with liquid. It is geometrically defined as an angle formed at tri-phase border liquids – gas – solid. The low value of contact angle indicates spreading of liquid on a surface – good wettability; high value indicates weak wettability. If the contact angle is below 90° it can be concluded, that liquid wets solid. If the angle is over 90° , liquids does not wet solid.

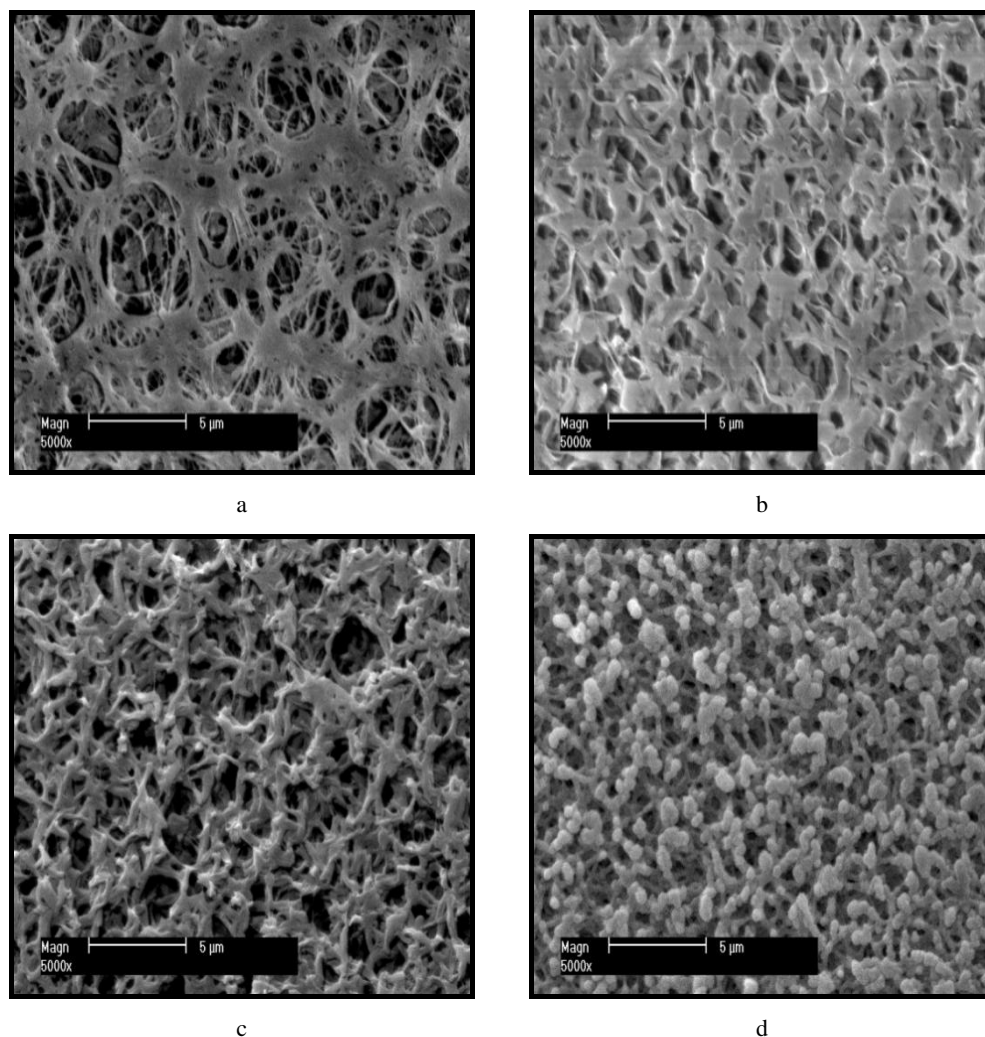


Fig. 4. Scanning electron micrographs of (a) PP, (b) PVDF, (c) Nylon, (d) PES (500x) (scale bar = $5\text{ }\mu\text{m}$)

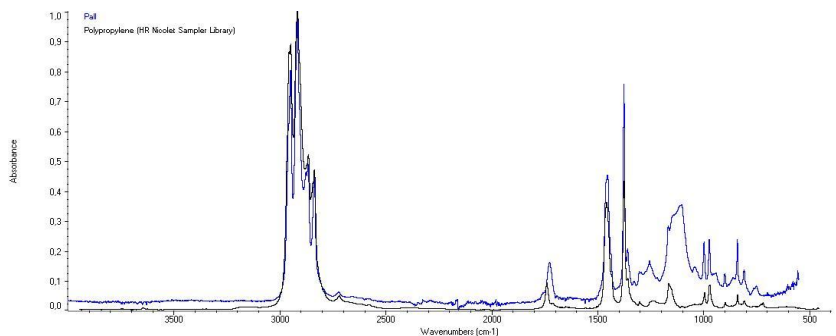


Fig. 5. IR spectra of PP membrane

Table 2. The physicochemical properties and time of penetration of reference liquids

| Support | Reference liquid | Surface tension, N/m | Viscosity, Pa·s | Time of penetration, s |
|---------|------------------|----------------------|-----------------|------------------------|
| PES | Hexane | 0.0179 | 0.00029 | 2 |
| PVDF | Hexane | 0.0179 | 0.00029 | 5 |
| Nylon | Toluene | 0.0278 | 0.00055 | 4 |
| PP | Methanol | 0.0221 | 0.00054 | 4 |

Table 3. The physicochemical properties of ionic liquids and contact angle determination by Washburn equation

| Ionic Liquid | Surface tension [N/m] | Viscosity [Pa·s] | Support | Time of penetration t_1 [s] | k | $\cos\theta$ | θ [deg] |
|---------------------------|-----------------------|------------------|---------|-------------------------------|-------|--------------|----------------|
| [EMIM][Tf ₂ N] | 0.041 | 0.026 | PES | 367 | 38.2 | 0.208 | 78 |
| | | | PVDF | 471 | 38.2 | 0.406 | 66 |
| | | | Nylon | 209 | 31.5 | 0.602 | 53 |
| | | | PP | 212 | 25.3 | 0.478 | 61 |
| [EMIM][TfO] | 0.044 | 0.040 | PES | 297 | 55.7 | 0.239 | 66 |
| | | | PVDF | 707 | 55.7 | 0.332 | 67 |
| | | | Nylon | 247 | 45.8 | 0.492 | 42 |
| | | | PP | 213 | 36.9 | 0.374 | 46 |
| [BMIM][Tf ₂ N] | 0.037 | 0.032 | PES | 444 | 53.0 | 0.489 | 76 |
| | | | PVDF | 799 | 53.0 | 0.802 | 71 |
| | | | Nylon | 354 | 43.6 | 0.977 | 60 |
| | | | PP | 376 | 35.1 | 0.681 | 68 |
| [BMIM][TfO] | 0.034 | 0.070 | PES | 530 | 129.7 | 0.489 | 61 |
| | | | PVDF | 809 | 129.7 | 0.802 | 37 |
| | | | Nylon | 437 | 106.7 | 0.977 | 12 |
| | | | PP | 505 | 86.0 | 0.681 | 47 |

Capillary rise experiments were carried out in order to investigate wettability of the polymeric support by selected ionic liquids. The first experiment including water, toluene, ethanol, methanol, isopropanol, acetone, hexane and cyclohexane was done in order to determine a reference wetting liquid for each support. Methanol was the best penetrating liquid for PP, hexane for PES and PVDF. For Nylon membrane toluene (see table 2) occurred to be the best. Based on the time of penetration in polymeric matrix measurements of reference liquids and examined ionic liquids, contact angles values were calculated (see table 3). For all the examined ionic liquids wettability decreases in following order Nylon > PP (except for BMIM TfO) > PVDF > PES. The lowest value of contact angles for all supports has been determined for BMIM TfO. Contact angle, θ , increases as the surface tension of the ionic liquid, γ increases. Similar findings have been reported earlier by Sedev (2011).

The Washburn equation presents linear dependence of squared height of liquid penetration in capillary and time of the experiment. However, in the case of porous system, Washburn established the model of system as a bunch of cylindrical capillaries. Capillary radius r is then the average or effective pores radius. Another simplification in Washburn method is connected with flow which should be laminar and stationary and without flow in the phase boarder.

Examined polymer supports do not meet Washburn assumptions. Therefore, sessile drop method was used.

Values of contact angles calculated from sessile drop contact angle measurements are below 20° , therefore all the ionic liquids examined are suitable for perfect wetting of supports (table 4). The best wettability was observed for Nylon membrane, successively for PP, PVDF and PES.

Assumption of best wetting for liquids with the lowest surface tension was confirmed ([Bmim][TfO]). Increase in ionic liquid hydrocarbon chain in cation structure does not affect wettability.

Taking into account values of contact angles (table 4) it can be concluded that each of chosen supports is perfectly wetted by ionic liquids.

Izak et al. (2007) observed that degree of swelling of the membrane can be related with the water activity of the ionic liquid. The measured water content of ionic liquids used was [Emim][TfO] – 1.370%, [Bmim][TfO] – 0.134%, [Emim][Tf₂N] – 0.001%, [Bmim][Tf₂N] – 0.109%. However, ionic liquids are highly hygroscopic and we have to keep in mind that water content can change during the experiment (Izak et al., 2007).

All the investigated supports show higher thickness after immobilization with ionic liquid. According to presented data it can be concluded that the longer is hydrocarbon chain in the cation structure, the higher swelling effect is observed. However, Nylon membrane shows similar thickness for all ionic liquids used in this study. Thickness of PVDF membrane was difficult to measure due to transparency of the membrane when immobilized with ionic liquid as indicated by standard deviations values. Such

behavior of polymeric membranes can affect mechanical stability of the membranes and affects value of maximum possible gas pressure without breaking of support.

Table 4. Contact angle determination by sessile drop method

| Ionic Liquid | Support | Advancing angle θ_a [deg] | Receding angle θ_r [deg] | Hysteresis $\theta_a - \theta_r$ [deg] |
|---------------------------|---------|-------------------------------------|------------------------------------|---|
| [EMIM][Tf ₂ N] | PES | 16.6±0.2 | 9.6±0.2 | 7.0 |
| | PVDF | 12.5±0.7 | 7.4±0.1 | 5.1 |
| | Nylon | 10.3±0.5 | 6.8±0.6 | 3.5 |
| | PP | 12.3±0.5 | 7.8±0.6 | 4.5 |
| [EMIM][TfO] | PES | 14.5±0.6 | 8.3±0.2 | 6.2 |
| | PVDF | 15.5±0.6 | 8.4±0.19 | 7.1 |
| | Nylon | 14.2±0.3 | 8.1±0.2 | 6.1 |
| | PP | 11.8±0.9 | 5.6±0.7 | 6.2 |
| [BMIM][Tf ₂ N] | PES | 16.9±0.2 | 8.2±0.2 | 8.7 |
| | PVDF | 19.2±0.5 | 10.9±0.5 | 8.3 |
| | Nylon | 10.7±0.4 | 8.4±0.3 | 2.3 |
| | PP | 13.9±0.4 | 8.0±0.3 | 5.9 |
| [BMIM][TfO] | PES | 15.5±0.2 | 8.1±0.2 | 7.4 |
| | PVDF | 18.3±0.6 | 10.4±0.7 | 7.9 |
| | Nylon | 8.1±0.3 | 6.6±0.1 | 1.5 |
| | PP | 10.5±0.3 | 8.8±0.5 | 1.7 |

Table 5. Thickness of pure and immobilized with ionic liquid membranes

| Support | Ionic Liquid | Thickness [μm] |
|---------|---------------------------|--------------------------------|
| PES | none | 117.73 ± 2.52 |
| | [EMIM][Tf ₂ N] | 133.52 ± 8.56 |
| | [EMIM][TfO] | 138.40 ± 2.07 |
| | [BMIM][Tf ₂ N] | 148.85 ± 4.50 |
| | [BMIM][TfO] | 144.17 ± 1.93 |
| PVDF | none | 159.92 ± 1.83 |
| | [EMIM][Tf ₂ N] | 179.95 ± 5.34 |
| | [EMIM][TfO] | 170.01 ± 2.80 |
| | [BMIM][Tf ₂ N] | 186.78 ± 3.89 |
| | [BMIM][TfO] | 204.57 ± 7.37 |
| Nylon | none | 114.51 ± 3.24 |
| | [EMIM][Tf ₂ N] | 121.10 ± 3.62 |
| | [EMIM][TfO] | 122.61 ± 3.27 |
| | [BMIM][Tf ₂ N] | 117.15 ± 2.34 |
| | [BMIM][TfO] | 119.15 ± 3.29 |
| PP | none | 74.57 ± 2.29 |
| | [EMIM][Tf ₂ N] | 86.93 ± 2.31 |
| | [EMIM][TfO] | 82.39 ± 2.63 |
| | [BMIM][Tf ₂ N] | 105.80 ± 6.44 |
| | [BMIM][TfO] | 104.80 ± 5.63 |

4. Summary

Properties of commercial membranes characterized in this study affect the effectiveness of gas separation processes based on supported ionic liquid membranes. One of the major factors affecting such processes is membrane stability. Stability of systems is then characterized for example by pressure resistance, wettability and swelling of the support. Wettability of polymeric support with ionic liquids was examined. The results show that it is possible to use ionic liquids as the membrane phase in the supported ionic liquid membranes and to apply such systems for selective separation of carbon dioxide from other gases (Joskowska et al., 2010).

Acknowledgements

Financial support was provided by the Polish Ministry of Science and Higher Education No.: N209 181536 and co-financed by European Social Fund "InnoDoktorant" - Scholarships for PhD students, I" and State budget and Pomorskie.

References

- ANDERSON, J.A., DIXON, J.K., BRENNECKE, J.F., 2007, Solubility of CO₂, CH₄, C₂H₆, O₂, N₂ in 1-hexyl-3-methylpyridinium Bis(trifluoromethylsulfonyl)imide: Comparison to Other Ionic Liquids. *Acc. Chem. Res.*, 40, 1208–1216.
- ANTHONY, J.L., ANDERSON, J.A., MAGINN, E.J., BRENNECKE, J.F., 2005, Anion effects on gas solubility in ionic liquids. *J. Phys. Chem. B*, 109, 6366–6374.
- BALTUS, R.E., CULBERTSON, B.H., DAI, S., LUO, H., W DEPAOLI D., 2004, Low-Pressure solubility of carbon dioxide in room-temperature ionic liquids measured with a quartz crystal microbalance. *J. Phys. Chem. B*, 108, 721–727.
- BARA, J.E., GABRIEL, CH. J., CARLISLE, T.K., CAMPER, D.E., FINOTELLO, A., GIN, D.L., NOBLE, R.D., 2009, Gas separations in fluoroalkyl-functionalized room-temperature ionic liquids using supported liquid membranes. *Chem. Eng. J.*, 147, 43–50.
- BATES, E.D., MAYTON, R.D., NTAI, I., DAVIS, J.H., JR., 2002, CO₂ capture by a task-specific ionic liquid. *J. Am. Chem. Soc.*, 124, 926–927.
- CHINN, D., VU, DE Q., DRIVER, M.S., BOUDREAU, L.C., 2006, CO₂ removal from gas using ionic liquids absorbents. United States Patent, US 2006/0251558 A1.
- DE LOS RIOS, A.P., HERNÁNDEZ-FERNÁNDEZ, F.J., TOMAS-ALONSO, F., PALACIOS, J.M., GOMEZ, D., RUBIO, M., VILLORA, G., 2007, A SEM-EDX study of highly stable supported liquid membranes based on ionic liquids. *J. Membr. Sci.*, 300, 88–94.
- DE LOS RIOS, A.P., HERNÁNDEZ-FERNÁNDEZ, F.J., TOMAS-ALONSO, F., PALACIOS, J.M., VILLORA, G., 2009, Stability studies of supported liquid membranes based on ionic liquids: Effect of surrounding phase nature. *Desalin.*, 245, 776–782.
- EARLE, M.J., SEDDON, K.R., 2000, Green solvents for the future. *Pure Appl. Chem.*, 72, 1391–1398.
- FORTUNATO, R., AFONSO, C., REIS, A., CRESPO, J., 2004, Supported ionic liquid membranes using ionic liquids: study of stability and transport mechanism. *J. Membr. Sci.*, 242, 197.
- GAN, Q., ROONEY, D., XUE, D., THOMPSON, G., ZOU, Y., 2006, An experimental study of gas transport and separation properties of ionic liquids supported on nanofiltration membranes. *J. Membr. Sci.*, 280, 948.
- GAN, Q., ROONEY, D., ZOU, Y., 2006, Supported ionic liquid membranes in nanopore structure for gas separation and transport studies. *Desalin.*, 199, 535–537.
- HERNANDEZ-FERNANDEZ, F., DE LOS RIOS, A., TOMAS-ALONSO, F., PALACIOS, J., VILLORA, G., 2009, Preparation of supported ionic liquid membrane: Influence of the ionic liquid immobilization method on their operational stability. *J. Membr. Sci.*, 341, 172.

- IZAK, P., HOVORKA, S., BARTOVSKY, T., BARTOVSKA, L., CRESPO, J.G., 2007, Swelling of polymeric membranes in room temperature ionic liquids. *J. Membr. Sci.*, 296, 131–138.
- JOSKOWSKA, M., DEBSKI, B., LUCZAK, J., MARKIEWICZ, M., ARANOWKI, R., HUPKA, J., 2010, Determination of carbon dioxide diffusion coefficients in supported ionic liquids membranes. *Przem. Chem.*, 89, 1189–1193.
- JOSKOWSKA, M., LUCZAK, J., ARANOWSKI, R., HUPKA, J., 2011, Use of imidazolium ionic liquids for carbon dioxide separation from gas mixtures. *Przem. Chem.*, 90, 174–180.
- KEMPERMAN, A.J.B., BOOMGAARD, D.B.T., STRATHMANN, H., 1996, Stability of Supported Liquids Membranes: State of the Art. *Sep. Purif. Techno.*, 31, 2733–2762.
- KOCHERGINSKY, N.M., LALITHA SEELAM, Q.Y., 2007, Recent advances in supported liquid membrane technology. *Sep. Purif. Techno.*, 53, 71–177.
- MARSH., K.N., BOXALL, J.A., LICHTENHALL, R., 2004, Room temperature ionic liquids and their mixtures – a review. *Fluid Phase Equilib.*, 219, 93–98.
- NAPLENBROEK, A.M., SMOLDERS, C.A., 1992, Supported liquid membranes: instability effects. *J. Membr. Sci.*, 67, 121–132.
- PERNAK, J., 2000, Ciecze jonowe – rozpuszczalniki XXI wieku. *Przem. Chem.*, 79, 150–153.
- SEDEV, R., 2011, Surface tension, interfacial tension and contact angles of ionic liquids. *Curr. Opin. Colloid Interface Sci.*, article in press, doi:10.1016/j.cocis.2011.01.011.
- TAKEUCHI, H., TAKAHASHI, K., GOTO, W., 1897, Some observations on the stability of supported liquid membranes. *J. Membr. Sci.*, 34, 19–31.
- TRONG, D., HUPKA, J., 2005, Characterization of porous materials by capillary rise method. *Physicochem. Probl. Miner. Process.*, 39, 47–65.
- TRONG, D., HUPKA, J., DRZYMALA, J., 2006, Impact of roughness on hydrophobicity of particles measured by the Washburn method. *Physicochem. Probl. Miner. Process.* 40, 45–52.
- ZHA, F.F., FANE, A.G., FELL, C.J.D., 1995, Instability mechanisms of supported liquid membranes in phenol transport process. *J. Membr. Sci.*, 107, 59–107.

Received April 20, 2011; reviewed; accepted July 18, 2011

THE EFFECT OF CHEMICALS ON THE RHEOLOGY OF HIGHLY LOADED COAL WATER SLURRIES (CWS)

Andrzej SLACZKA, Adam WASILCZYK

Silesian University of Technology, Faculty of Mining and Geology, Department of Mineral Processing and Waste Utilization, ul. Akademicka 2, 44-100 Gliwice, Poland, andrzej.slaczka@polsl.pl, adam.wasilczyk@polsl.pl

Abstract. In this study the influence of chosen detergents on the rheology of highly loaded coal-water slurries (60%_{wf}) made up from coals of different degree of carbonization from steam coal rank of 31.2 through 33 to coking coal rank of 35.1 according to Polish Standards were tested. In the experiments the nonionic types of chemicals - Rokwinol 60 (polyoxyethylated sorbitol oleate, C₆₄H₁₂₄O₂₆), Rokanol LO18 (RO (CH₂CH₂O)_n H, where R – alkyl radical consisting of 16 to 18 carbon atoms in the carbon chain and "n" is around 18), manufactured by Chemical Factory "ROKITA " in Brzeg Dolny, Poland as well as anionic sodium lignosulphonate LSP, a by-product from cellulose production, were used. The detergents used were of a commercial purity. They were chosen taking into account the structure of molecules. Molecules of the surfactants used differ in space structure. Rokanol LO18 has a linear structure, Rokwinol 60 as a derivative of sorbitol has a branched structure whereas sodium lignosulphonate has complicated space structure. The price and accessibility of the detergents used were also considered.

The test results clearly showed that the rheological properties of the CWS depend significantly on both the type of coal and the type of surfactant. The slurries prepared in this study exhibit pseudoplastic and dilatant properties. The same surfactant, depending on the type of coal, may give the CWS of different rheological behaviour.

It was supposed that besides of electrostatic and dispersing forces the steric effect plays a significant role in the CWSs fluidity.

The coal-water slurries, made up from all tested coals without addition of detergents, had consistency of dense mud and their viscosities were not measured..

keywords: coal-water slurries, CWS, coal-water slurry fuels, CWSF, rheology, surfactants

1. Introduction

In recent years, considerable research has been devoted to producing concentrated coal-water slurries, which can be used as a suitable replacement for oil in several industrial applications. Such slurries, which can be shipped and pipelined, are now

commercially providing a convenient way of transporting coal over long distances. Coal slurries can also be stored in tanks, which is beneficial in industrial areas.

Several physical properties have been identified as responsible for controlling the properties of the suspensions. They are: the physicochemical properties of the coal, solids volume fraction and particle size distribution, inter-particle interactions in the suspension which are affected by the nature of the surface groups, pH and the presence of electrolytes and chemical additives as well as the temperature of the suspension (Laskowski, 2001; Dincer et al., 2003; Boylu et al., 2004).

In general, it has been shown, that coal particles that have been rendered mutually repulsive (e.g. through the adsorption of ionic or non-ionic surfactants) form a well-dispersed suspension. These suspensions are characterized by low viscosity but form hard sediments that are difficult to redisperse when left to stand (Tudor et al., 1996).

A state of weak flocculation exists in these suspensions when the attractive forces exceed the repulsive forces, and this results in the particles being held together in loose aggregates or flocs. This flocculated state avoids the formation of hard sediments (Tudor et al., 1996).

The mutual interactions between coal grains in the slurry depend on its surface energy which one is the result of slurry composition and may be the measure of the slurry response (Slaczka et al., 2005; Slaczka and Wasilczyk, 2010).

Due to the calorific value, coal concentration in the slurry should be not less than 55% wt. One of the major requirements to be met in preparing Coal–Water Slurry Fuels is that it must have as high as possible coal concentration and a minimum viscosity, to allow ease of handling during preparation, storage, transfer and atomization. However, it is generally known, that the viscosity of CWS increases with the coal concentration in the slurry, and that the stability of the suspension becomes poor if the viscosity is reduced (Papachristodoulou and Tras, 1987; Henderson et al., 1983). Consequently, the problem is how to maintain the highest possible solid concentration and stability simultaneously, at a given or optimum viscosity. To obtain such properties it is necessary to manipulate essentially two major factors: the concentration of the slurry and the addition of suitable fluidizers and stabilizers.

Accordingly, chemical additives are very important in enhancing the fluidity of the coal-water slurries, and the selection of excellent dispersing additives should be recognized as one of the most essential factors in the preparation of highly loaded CWS fuels with reasonably low viscosities.

The rheological properties of CWSs in relation to different additives were subject of interest of many researchers. They investigated the influence of different factors on the apparent viscosity of CWSs (Turian et al., 2002; Logos, 1996; Slaczka, 2004). Therefore in practical terms, the slurry must have a low viscosity at the moderate shear rates that are characteristic of pumping ($10\text{--}200\text{ s}^{-1}$). Also, the slurry should possess low viscosity at shear rates corresponding to the atomization process ($5000\text{--}30000\text{ s}^{-1}$), because it has been found that low slurry viscosity leads to small droplet sizes during atomization of CWS and hence an increase in the carbon conversion efficiency in a

boiler or furnace. Therefore, it is believed that desirable rheological characteristics of CWS would include the phenomenon of pseudoplastic response to increasing shear rate (Nam-Sun et al., 1995).

In this study, the effects of different chemicals used as dispersing agents on the viscosity of CWS were investigated. The coal samples used were Polish coals of different ranks. Two types of surfactant, nonionic and anionic, were used as dispersing agents.

2. Experimental

2.1. Materials

2.1.1. Coals

CWS were made up from coal samples of different degrees of carbonification from steam coal rank of 31.2 through 33 to coking coal rank of 35.1 according to Polish Standards.

The proximate analysis of the coal samples and their ranks are given in Table 1.

Table 1. Proximate analysis of investigated coals

| Coal | Ash [%] | Sulphur [%] | Higher calorific value [MJ/kg] | Volatile matter [%] | Rank | |
|------|---------|-------------|--------------------------------|---------------------|-----------------|------------------------|
| | | | | | Polish Standard | ECC Geneva |
| A | 6.9 | 0.6 | 27.8 | 32.3 | 31.2 | 06 0 1 3 0 38 07 06 33 |
| B | 3.4 | 0.4 | 33.1 | 30.1 | 33 | 09 0 3 2 6 30 03 04 35 |
| C | 4.7 | 0.4 | 34.2 | 23.8 | 35.1 | 11 0 2 1 8 24 04 04 36 |

2.1.2 Detergents

Additives, which are mainly surfactants and potentially may be used as fluidizers and stabilizes in CWSF technology are numerous.

This work is focused on three of them belonging to three different groups of chemicals: Rokanol LO18 (nonionic surfactant, $RO (CH_2 CH_2 O)_n H$, where R means unsaturated alkyl radical consists of 16 to 18 carbon atoms in the chain and n equal to around 18), Rokwinol 60 (nonionic surfactant being polyoxyethylated sorbitol stearate, $C_{64}H_{124}O_{26}$, molecular weight of around 1300), and sodium lignosulphonate LSP (anionic compound which is a by-product of cellulose production. It was of commercial purity grade). The detergents were chosen taking the structure of molecules into account. The price and accessibility of the detergent used were also considered. Rokanol LO18 has a linear structure, while Rokwinol 60, as a derivative of sorbitol, has a branched structure, whereas sodium lignosulphonate has a complicated space structure.

2.2. Slurry preparation

The grain size of the coal sample was reduced below 1 mm using laboratory scale jaw crusher, cone mill and disintegrator. Then, the coal samples were rubbed in an agate mortar for 30 minutes together with water and proper additive to get a slurry of coal concentration equal to 60 wt% and 1.0 wt% of dispersant (based on dry coal). The slurries obtained in this way contained 95% grains below 0.1 mm.

The frequency distribution of the grain size in the slurries were very similar. For example Fig. 1 provides the frequency distribution of the slurry prepared from coal B.

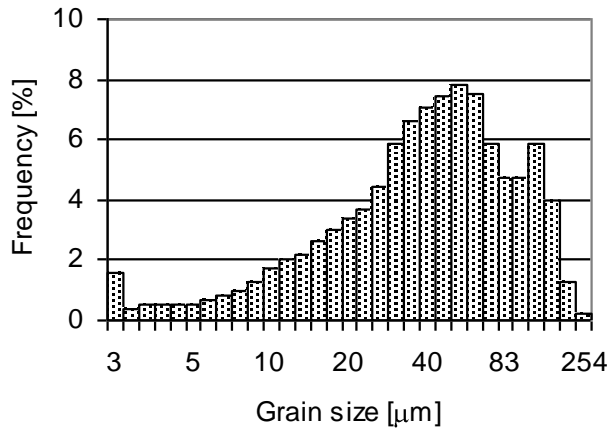


Fig. 1. Grain size distribution of coal B in the slurry

2.3. Rheology measurements

The rheological curves were obtained using a Rheotest 2 viscometer with the vane spindle at 25 to 500 rev/min. The pH value of the slurry varied between 5.8 and 6.0 in all the experiments. The temperature was kept constant within 20 and 21°C. The shear stress-shear rate curves obtained from the experiments were fitted to the Ostwald-de Waele or power law model

$$\tau = K\dot{\gamma}^n$$

where K and n are rheological constants referred to a fluid consistency coefficient and flow behavior index, respectively. For $n = 1$ this equation reduces to Newton's law of viscosity with $K = \tau/\dot{\gamma}$, hence the departure of n from unity indicates the degree of deviation from the Newtonian behaviour. Rheograms of shear stress versus shear rate as well as apparent viscosity versus shear rate are presented in Fig. 2.

Coal-water slurries made up from the all tested coals without addition detergents had consistency of a dense mud. Therefore, their rheological curves were not determined.

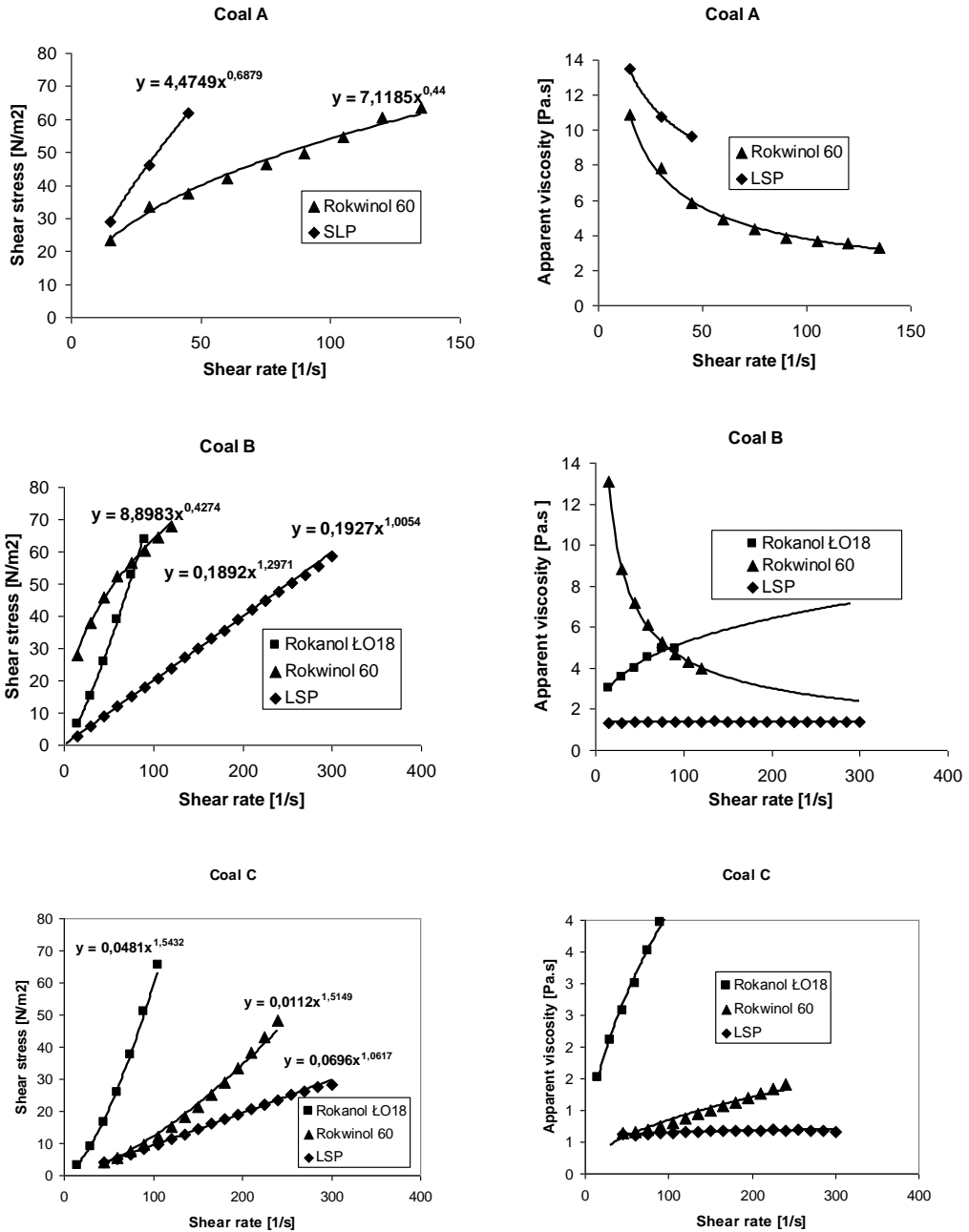


Fig. 2. Effect of surfactant on the rheological behavior of the slurries tested

In the Figures there are also given the best fit power law equations describing the rheological properties of the slurries tested.

The flow behavior indices n taken from the best fit power law model formulas are given in the Table 1.

Table 1. Effect of surfactant addition on flow behavior index of the slurries tested

| Coal | Flow behavior index (n) | | |
|------|-----------------------------|-------------|--------------|
| | LSP | Rokwinol 60 | Rokanol LO18 |
| A | 0.688 | 0.440 | -- |
| B | 1.005 | 0.427 | 1.297 |
| C | 1.062 | 1.514 | 1.542 |

3. Results and discussion

From Figure 2 it is visible, that the rheological behavior of all the tested slurries fits the Ostwald-de Waele model. Nevertheless, Fig. 2 and Table 1 also show large differences in slurry rheological responses between different kinds of coal and surfactant used.

The results showed that the slurry based on coal A (rank of 31.2) exhibits shear thinning, i.e. pseudoplastic behaviour ($n < 1$). That means it has lower apparent viscosity at higher shear rates both for Rokwinol 60 and LSP used as additives. In that case, one can observe rapidly decreasing of apparent viscosity when the shear rate grows. However, in the case of the Rokanol LO18 used as the additive, the slurry was devoid of the fluidity at all (there is no proper curves in Figure 2).

The slurries made up from coal B (rank of 33) and coal C (rank of 35.1) exhibit different rheological response, depending on the additive used. Namely, it was found that the slurry based on coal B with Rokwinol 60 reveals pseudoplastic behaviour ($n < 1$), whereas with Rokanol LO18 it is shear-thickening or dilatant fluid ($n > 1$). This means that it increases its apparent viscosity at higher shear rates. The same slurry with the LSP reveals almost Newtonian behavior ($n = 1.005$) and rather low apparent viscosity.

The slurries made up from coal C (rank of 35.1) with Rokanol LO18 and Rokwinol 60 exhibits dilatant behaviour ($n > 1$), whereas with the LSP the slurry becomes practically Newtonian fluid of low apparent viscosity.

Typically, SLP as the anionic surfactant in a CWS adsorbs on hydrophobic sites of the coal and consequently impart a negative charge to the coal particles. Since the counter-cations are strongly attracted to the interfaces, and electrical double layer is formed. These counter-cations are usually distributed in the diffuse layer when there is no specific adsorption. Alternatively, some of the counter-cations are associated with the surface in the Stern layer. This electrical double layer creates repulsive interaction forces caused by the overlap of the double layers, preventing the aggregation of the

coal particles. It leads to increase in fluidity of the slurry in the presence of the SLP (coals B and C).

One should notice that the detergents used differ in the space structure. Molecules of Rokanol LO18 has a linear structure, Rokwinol 60 has branched molecules whereas LSP molecules has complex and space structure. Experiments showed that introducing SLP to the CWSs based on coals B and C leads to almost Newtonian fluids of low viscosities. It indicates that besides of electrostatic and dispersing forces, the space structure of detergents molecules used as fluidizers in CWSs preparation, plays the significant role.

Adsorption on coal grains molecules of the SLP, branched in space, creates large distances between coal grains in the slurry. Water fills these spaces and acts as a lubricant which leads to a decrease in apparent viscosity.

In the case of coals A and B with nonionic Rokwinol 60 (molecular weight about 1300) one can suppose that the large molecular chains adsorbed on the coal surface tumble at random and affect large volumes of fluid under low shear, but that they gradually align themselves in the direction of increasing shear and produce less resistance. The decrease in apparent viscosity of CWSs influenced by Rokwinol 60 may be explained also by another mechanism. Hydrophilic spots on the coal surface attach hydrophilic poles of the surfactant. The hydrophobic poles of the surfactant will thus orient itself towards the aqueous phase. In this case, water acts as a lubricating material between the coal particles. In contrast, if the hydrophilic part orients itself towards the aqueous phase, the amount of water at the surface of the coal particle will be increased by hydrogen bonding with the polyethoxy chain. This will produce a hydration layer or solvation shell of water around the coal particles and prevent agglomeration by eliminating preference between other coal particles and water. This might decrease the viscosity if the hydrophilic chains act to separate the coal particles by cushioning them and allowing them to slip against one another.

It is obvious, that slurries of dilatant properties are not useful as slurry fuels. Such properties make impossible pumping them and atomization in burners as well.

Summarizing, one can say that among tested systems for preparation of Coal-Water Slurry fuels the best are these composed of coal C and LSP and of coal B with LSP or Rokwinol 60 as the additives.

4. Conclusions

The test results clearly show that the rheological properties of CWSs depend significantly on both the type of coal and surfactant. The slurries prepared in this study exhibit pseudoplastic as well as dilatant properties. The same surfactant, depending on the type of coal, may give the CWS of different rheological behavior.

The experiments showed that LSP has a considerable influence on the rheological properties of the coal-water slurries. The slurries of coals B and C in which LSP used as the additive reveal almost newtonian behavior and its apparent viscosity was diminished significantly.

It was supposed that besides of electrostatic and dispersing forces, the steric effects play a significant role in the CWSs fluidity.

The coal-water slurries made up from all the tested coals without addition of detergents had consistency of dense mud and their viscosities were not measured.

Acknowledgements

The authors wish to thank the Polish Committee for Scientific Research for financial support (grant No: N N524 167435).

References

- Boylu, F., Dincer, H., Atesok, G., 2004, Effect of coal particle size distribution, volume fraction and rank on the rheology of coal-water slurries, *Fuel Processing Technology* 85, 241–250.
- Dincer, H., Boylu F., Sirkeci A.A, Atesok G., 2003, The effect of chemicals on the viscosity and stability of coal water slurries, *International Journal of Mineral Processing* 70, 41–45.
- Henderson, C.B., Scheffee, R.S., McHale, E.T, 1983, Coal-water slurries - a low-cost liquid fuel for boilers, *Energy Progress*, (United States), 3(2), 69–75.
- Laskowski, J.S., 2001, Rheological Measurements in Mineral Processing Related Research, IX Balkan Mineral Processing Congress, Beri Ofset, Istanbul, Turkey 41–57.
- Logos C., Nguen Q.D., 1996, Effect of particle size on the flow properties of s Soyth Australian coal-water slurry, *Powder Technology* 88, 55–58
- Nam-Sun R, Dae-Hyun S., Dong-Chan K., Jong-Duk K. 1995, Rheological behaviour of coal-water mixtures 1. Effects of coal type. loading and particle size, *Fuel* 74 (8), 1220–1225.
- Papachristodoulou, G., Trass, O., 1987, Coal slurry fuel technology, *The Canadian Journal of Chemical Engineering* 65(2), 177–201.
- Slaczka A., Piszczynski Z., Polo F.G. 2005., Coal-Water Slurry Fuels (CWSF); Influence of Detergents on The Surface Energy of Coal Grains, *Inżynieria Mineralna (Journal of The Polish Mineral Engineering Society)* No 2(15), 13–20 .
- Slaczka A., Wasilczyk A., 2010, Surface Energy of Coal Grains in the System Coal-Water-Additive in Relation to the Stability of Highly Loaded Coal-Water Slurries, XVI International Coal Preparation Congress - Lexington, USA. Conference proceedings 931–936.
- Slaczka A, 2004, Rheology of Highly Loaded Coal-Water Slurries , *Inżynieria Mineralna (Journal of The Polish Mineral Engineering Society)* No 1(12), 9–18.
- Turian R.M., Attal J.F., Sung D.J., Wedgewood L.F. 2002, Properties and rheology of coal-water mixtures using different coals, *Fuel* 81, 2019–2033.
- Tudor P.R, Atkinson D., Crawford R. J., Mainwaring D.E., 1996, The effect of adsorbed and non-adsorbed additives on the stability of coal-water suspensions, *Fuel* 75(4), 443–452.

Received April 29, 2011; reviewed; accepted July 26, 2011

GRINDING KINETICS OF GRANITE CONSIDERING MORPHOLOGY AND PHYSICAL PROPERTIES OF GRAINS

Tomasz P. OLEJNIK

Faculty of Process and Environmental Engineering, Technical University of Lodz, Wolczanska 213, 90-924 Lodz, tomasz.olejnik@p.lodz.pl

Abstract. The article presents the results of studies on the kinetics of grinding of granite taking into consideration the morphology and mechanical properties of particular size fractions of the feed. The study was conducted in a mill on a semi-technical scale. Milling was carried out periodically using several sets of grinding media. The output fraction of the ground material was of size 3-5 mm. The granulometric analysis of the raw material was carried out in a multiple manner. The granulometric composition of milling product was analyzed every 30 minutes. Simultaneously, ground material was subjected to an analysis of the shape of grains and microscopic analysis of morphology and chemical composition. Strength tests of grains were performed applying selected fractions of particle size ranges. The change of particle breakage rate function S_i , for selected particles size ranges, was described with the Austin-Gardner expression. The influence of destructive force on kinetics of grinding was defined.

keywords: ball mill, specific grinding rate, grain morphology, contact points

1. Introduction

The grinding mechanism comes down to the division of solid particles into the grains of smaller size and that this process is evoked by the action of external loads, exceeding the limit of endurance and can damage the atomic or molecular bonds (Blumenauer and Pusch 1981). Since each rupture of the material in each zone of load precedes deformation, the implementation of the process of grinding requires provision of the necessary amount of energy. This amount being conditioned with the size of deformation, elastic properties of deformed material and the type of load.

Simultaneously, uneven internal structure of the material to be ground, numerous micro and macro cracks weaken the cohesion forces between particles forming a crystallographic network of grain. Destruction of the internal cohesion of the grain, cracking the grains into smaller sized items, requires exceeding the required levels of cohesion force distribution (under the action of external forces). The described phenomenon may be caused by normal stretching or shearing stresses (Mostafa 2003).

The grinding in ball mills is determined by a complex nature of the impact of grinding media on the ground raw material. Main geometrical dimensions of drum grinding mill and the size and type of motion affect the speed of the grinding process as well as the final composition of grinding. The grinding is performed primarily through a complex interaction of grinding media on the ground material being located between them or between the inner surface of grinding media. Grains of material to be ground that will be in these areas are mainly abraded and thinned, with the possibility of participation of the crushing mechanism (Lynch 1974; Shipway and Hutchings 1993). Energy transfer is conditioned by the energy level of the working parts of the mill. The basic energy level assumed in the potential energy of the Earth's gravity conditions. A measure of the energy level grinding is therefore the ratio of the dynamic forces to the forces of gravity or kinetic energy into potential energy of grinding media (Cole and Peters 2007).

Practically low efficiency of the grinding process forces engineers to look for process parameters being optimal from the point of view of energy inputs to obtain the shortest possible milling time. Considering this point of view, examined the effects of grinding in a ball mill, taking into account the analysis of the results, the morphological structure and chemical composition of grains, and their resistance to normal stresses.

The objective of the investigation was to determine the effect of a variable number of grinding media for grinding process, taking into account the individual properties of particles such as yield strength for normal forces and the shape of the grain (Hornaga et al., 2009). Mechanical properties of the grain may determine the change in value of breakage rate function S_i in the corresponding size frictions of the grains. The study was conducted for granite. Due to the morphology of particles of granite, which is characterized by a very heterogeneous structure, it is expected that the fragmentation process takes place in such a way that it provides very different grain size particles, and substantially different shape. The observed diversity of the feed may determine the value of parameters in the Austin-Gardner equation (Eq. 1), and the specific numerical values may depend on process parameters such as number and size of grinding media.

2. Process parameters

The grinding process was conducted under dry conditions. Kinetic studies of milling were carried out for a semi-technical mill. Basic technical information concerning the mill is shown in Table 1

Granite was subjected to crushing in a ball mill. This is a solid, acidic magma-deep rock, medium or thickly-crystalline of overtly-crystalline structure distinguished by a clear symmetry planes, usually in three orthogonal directions (Cappell and White 2001). The bulk density of granite, was determined after a freely drop and after 10 minutes of shaking of the measurement sample. Bulk density was, respectively, equal to 1394 kg/m^3 and 1410 kg/m^3 , and its average value was equal to 1402 kg/m^3 .

Material used for milling was from 5 to 8 mm in size. Filling the mill with grinding media with a feed accounted for 30% of the total capacity of the mill.

Milling process was carried out in a batch mode using several sets of balls. The total mass of the balls used for milling was about 41 kg. Sampling of the feed was measured every 30 minutes, taking a mass of about 0.6 kg for analysis. Milling was performed using four sets of balls, labeled sequentially I, II, III and IV. Size and weight of balls for each measurement series are provided in Table 2. Furthermore, the statistical estimated number of contact points for each set of balls was determined (Mort 2003).

Table 1. Basic parameters of a semi-industrial mill

| | |
|---|-------|
| internal diameter, m | 0.5 |
| total capacity, m ³ | 0.112 |
| rotation frequency n, min ⁻¹ | 31 |

Table 2. Number composition and ball mass for particular series

| Series | I | II | III | IV |
|-------------------|--|--------------|--------------|------------|
| Ball diameter, mm | Ball mass, kg / Number of contact points | | | |
| 10 | - | 6 / 27588 | 1 / 6424 | - |
| 20 | - | 12.3 / 11176 | 12.5 / 11363 | 11 / 9999 |
| 30 | - | 12.3 / 2035 | 12.5 / 2068 | 15 / 2475 |
| 40 | - | 10 / 671 | 15 / 1001 | 15 / 1001 |
| 60 | 40 / 512 | - | - | - |
| Sum | 40 / 512 | 40.6 / 50611 | 41 / 14432 | 41 / 13475 |

3. Analysis of results

Samples were subjected to granulometric, morphological, chemical and strength analyses. The chemical composition, determined by the number of atoms of different elements included in the composition of chemical compounds and grain morphology, were examined using a scanning electron microscope. The analysis of the shape of grains and grain composition was performed using Analyzer 3D AWK made by Kamika Instruments. Furthermore, a fractional sieve analysis was carried out to rule out a measurement error associated with the testing method applied. The results of the analysis allowed to determine the granulometric composition of milled material at particular moments of grinding time. To determine the shape of particles fraction analysis according to Zingg (1935) was used.

Table 3 shows the chemical composition and atomic fractions of particular chemical elements of particular chemical elements for chosen size fraction of grains.

In combination with a chemical composition analysis, an optical grain analysis was carried out. With this aim in mind, a scanning microscope was utilized. Figures 1 and

2 show a selected granite surface for a size fraction of 1.6 – 2.0 and 0.2 – 0.3 mm.

Selected grains from each size fraction were subjected to strength examinations. Single grains were exposed to shearing stresses. Crushing tests were performed with INSTRON 3300. To make the results uniform, for each grain size fraction multiple tests were conducted to exclude the measurement error. The results of strength analyses, that is the values of compression forces and destructive stresses evoked by them, are summarized in Table 5.

Table 3. Atomic fractions of elements present in the chemical compound composition associated with the structure of granite

| A chemical compound / element | Grain size fraction | | | | |
|-------------------------------------|---------------------|------------|-----------|-----------|-----------|
| | 1.6 – 2.0 | 1.25 – 1.4 | 0.8 – 1.0 | 0.4 – 0.5 | 0.2 – 0.3 |
| Atomic fractions, % | | | | | |
| CaCO ₃ / C | 4.58 | 4.82 | 11.52 | 9.91 | 8.39 |
| SiO ₂ / O | 64.72 | 65.77 | 56.36 | 63.05 | 66.85 |
| Allbite / Na | 1.71 | 1.87 | 1.78 | 0.63 | 1.43 |
| MgO / Mg | 0.52 | 0.64 | 0.38 | 0.24 | 0.31 |
| Al ₂ O ₃ / Al | 4.66 | 4.60 | 5.29 | 1.39 | 2.91 |
| SiO ₂ / Si | 19.78 | 17.51 | 18.63 | 23.56 | 18.2 |
| Feldspar / K | 1.81 | 1.91 | 1.83 | 0.56 | 0.81 |
| Wollastonite / Ca | 0.53 | 0.50 | 0.96 | 0.12 | 0.3 |
| / Ti | 0.18 | 0.23 | 0.26 | - | 0.09 |
| / Fe | 1.54 | 2.14 | 2.92 | 0.54 | 0.70 |

Basing on the granulometric composition changes, disintegration rates of particular size fractions using authors' computer program were calculated (Olejnik 2009, 2010). For calculations, Eq. 1 of Gardner and Austin was applied for discrete values of fractions, assuming ideal mixing of the milled material:

$$\frac{\Delta w_i(t)}{\Delta t} = -S_i w_i(t) + \sum_{j=1, j>i}^{i-1} S_j b_{i,j,t} \cdot w_j(t), \quad (1)$$

where

$b_{i,j,t}$ – particle size distribution function in time

S_i, S_j – specific grinding rate (distribution parameter) of particles in fraction i or j

T – grinding time, min

Δt – time increment

w_i – the mass of grains from size grade i

w_j – the mass of grains from size grade j

$\Delta w_i(t)$ – increment of the mass of grains from size grade i .

For better presentation of results, we defined also the mean geometrical grain size by using Eq. 2:

$$d_s = \sum_{i=1}^n d_{si} \cdot x_i \tag{2}$$

where, x_i – mass fraction of particles in size fraction i ; d_{si} – mean (arithmetic) particle size in size fraction i , mm.

The rate coefficients S_i for particular size fractions are shown in Table 4. For particles of granite, characterized by distinct cracks and fissures, devastating impact of grinding media causes a rapid change in the particle size. Granite used in the study is characterized with a high susceptibility to grinding being reflected in a high value of distribution parameter (Table 4) for all tested grain size ranges.

Strength tests were performed for selected grains, with the appropriate fraction size ranges. To eliminate measurement error, the sample test was repeated several times, averaging the results while calculating the average measurement error and standard deviation.

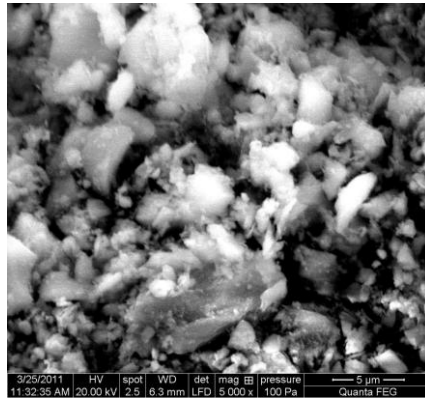


Fig. 1. Granite grain, size fraction of 1.6 – 2.0 mm. Magnification about 5000x

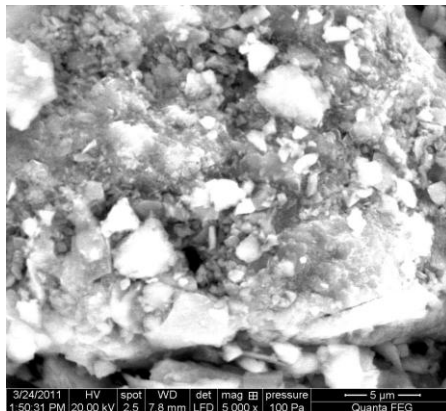


Fig. 2. Granite grain, size fraction of 0.2 – 0.3 mm. Magnification about 5000x

Table 4. Disintegration rates S_i (distribution parameter) of grain fractions d_s for investigated series

| d_s | $S_{i(I)}, \text{min}^{-1}$ | $S_{i(II)}, \text{min}^{-1}$ | $S_{i(III)}, \text{min}^{-1}$ | $S_{i(IV)}, \text{min}^{-1}$ |
|-------|-----------------------------|------------------------------|-------------------------------|------------------------------|
| 2.5 | 0.00244 | 0.0115 | 0.00517 | 0.00781 |
| 1.8 | 0.00221 | 0.015 | 0.00806 | 0.01208 |
| 1.5 | 0.00115 | 0.017 | 0.00911 | 0.01018 |
| 1.32 | 0.00372 | 0.0165 | 0.0147 | 0.0147 |
| 1.13 | 0.00306 | 0.0169 | 0.0163 | 0.0203 |
| 0.9 | 0.00291 | 0.0197 | 0.0224 | 0.0128 |
| 0.4 | 0.0198 | 0.0356 | 0.0071 | 0.0211 |

Table 5. The values of normal forces and destructive stresses

| Grain size fraction, mm | Mean destructive force, N | Mean destructive stresses, MPa |
|-------------------------|---------------------------|--------------------------------|
| 3 ÷ 2 | 279.4 | 14.01 |
| 1.6 ÷ 2.0 | 135 | 13.27 |
| 1.25 ÷ 1.4 | 126.4 | 22.93 |
| 0.8 ÷ 1.0 | 57.66 | 22.67 |
| 0.4 ÷ 0.5 | 64.98 | 48.72 |

For a size fraction of granite grains between 2 and 3 mm, there are the highest average grain destructive forces. Their value is more than 270 N. In the course of destruction tests, there was a tendency to reduce the medium destructive forces with decreasing average grain size. For the smallest particles in the range of 0.5 to 0.8 mm, destructive forces were approximately 60 N.

Simultaneously, with the decreasing grain size, the opposite trend was observed concerning the normal stress. For the largest particles, the destructive stress was around 14 MPa, and increased to a value of about 50 MPa, for the smallest ones. The observed trend may be elucidated by the morphology of the grains. From the physico-chemical analysis – the zone investigated with the application of a scanning electron microscope it may be inferred that the change in grain size does not entail a change in the atomic composition and indirectly, chemical composition (Table 3). Simultaneously, Zingg's analysis points to the fact that the grains in the whole range of variation of its size, have a shape resembling a sphere. The example results of analysis of samples taken at 30th and 210th minute after the start of grinding, for series I are given respectively in Fig. 3 and 4.

The observed tendency concerning the growth of destructive stresses at a simultaneous reduction of the size of the load can be explained by the increase in deformation of the grain structure without losing the cohesiveness of the material. While for the larger particles it is possible to obtain the presence of a soft matrix, weakening the structure of the material, then for smaller particles subjected to fragmentation one obtains a homogeneous material. However, the analysis of image of the surface of grains does not confirm this assumption.

For large and small grains, we have similar elemental compositions, which is tantamount to saying that for the investigated range of variation of grain size of granite, there occur the same chemicals. And if so, the grains should have similar mechanical properties. Even more interesting conclusions can be drawn by analyzing the rate of grinding balls for different compositions of balls. The observed differences in susceptibility of the tested materials to grinding can lead to a differentiated composition and size, and hence, masses of balls.

For relatively large particles, a crucial mechanism causing fragmentation of the granite will be crushing. Grinding effect for the smallest particles can be determined by abrasion. For large particles the grinding media should have a sufficiently large kinetic energy that is apt to overcome the internal forces of cohesion within the grain. If the milling is conducted for a composition of balls of large diameter, increased energy of balls will occur for the largest grains. In this case, wearing of large grains causes the formation of the smallest fraction but not necessarily a transition of destroyed grain to a fraction of finer grains. Only long-time wear can reduce the grain size large enough to make it over into a smaller size ranges.

An analysis of grinding speed leads to the conclusion on the mechanism of crushing that the impact grinding occurs at the initial stage of grinding. The effect of grinding is greater for larger particles and smaller broken grains are mainly ground by the mechanism of wear. This is due to the fact of a greater probability of finding the grain in the area between grinding media. While the impact effect on large grains increases with increasing weight of the grinding media, so for small particles a decisive meaning is played by abrasive action grinding occurring between the grinding media and feed.

The shortest times of grinding needed to obtain a suitable granulation product were attained for two measurement series I and II. This corresponds to two different configurations of the balls. For series I there occurs a small number of theoretical contact points (512). On the other hand, for series II, one has the greatest number of all contact points (Table 2). Considering the economic criterion, the two compositions of balls are justified, however, the analysis of disintegration rate of individual size fractions indicates more favorable conditions for the milling of series II (Table 4, refer to column $S_i(\text{II})$).

Grains with relatively small size in comparison to the size of balls, have a smaller chance of being in the area of impact grinding (Georgalli and Reuter, 2008). Therefore, from the grinding efficiency point of view, the most important is point contact of the particles with the balls. This is when replace of large grinding media with smaller media. Changing the size of balls, is changed the number of contact points. Due to the fact that the rate of milling of small size fractions increases with the number of contact points can describe mathematically the size of grinding media most appropriate for the economy grinding process. The expression for mathematical models will be possible after examination of the grinding process of other minerals with a different morphology.

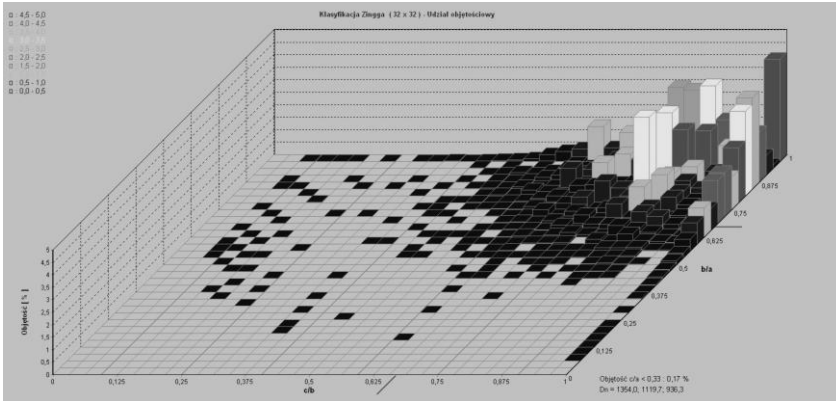


Fig. 3. Distribution of granite grain shape obtained after 30 minutes of milling. Measurement series I

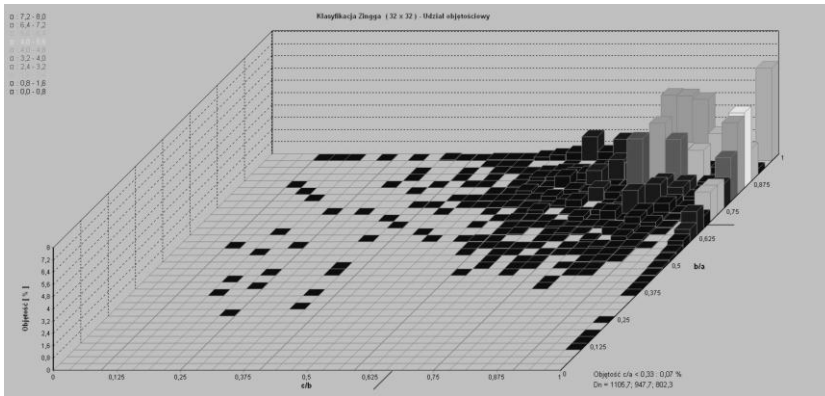


Fig. 4. Distribution of granite grain shape obtained after 210 minutes of milling. Measurement series I

Economic aspects of milling is shown in Fig. 5 containing curves of the average grain size changes in time using different sets of grinding media. Therefore, the change of the characteristic (diameter) grain size is accompanied by a change in grain cross-section. The mathematical expression describing the relationship between these values is changed to the second power of linear dimension. Considering the state of stress in the two grains of granite differing significantly in terms of characteristic size, it is possible with the application of weaker destructive power, in favor of smaller grains. Trends of decreasing normal forces and the corresponding increase of destructive stress for smaller grains are shown in Table 5.

For measurement series II, there are greater milling rates of small size fractions (of the order from 0.0197 to 0.0356 min^{-1}). Thus, the theoretical total decay time of size fraction of 0.9 mm is circa 50 minutes for measurement series II and until 341 minutes for Series I. The difference in the time of the disappearance of size fractions illustrates

the positive impact of increased number of contact points on the process kinetics for the small size fractions.

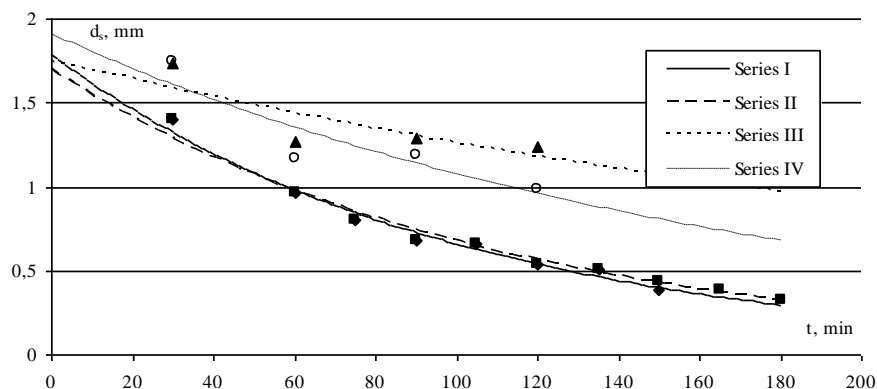


Fig. 5. The curves of change in time of the mean grain size of granite for four compositions of balls

4. Conclusions

Basing on the results, the following conclusions can be drawn. The kinetics of milling is determined by the strength of the stress-destructive particles depending on the morphology of the shredded material. Variation in size of balls may significantly affect the dominant mechanism of grinding of the grain. It is feasible to attain the required granulometric composition through the selection of the size of grinding media.

Acknowledgments

The project was financed within the framework W-10/1/2011 Dz. St. of the Faculty of Process and Environmental Protection, Technical University of Lodz.

References

- BLUMENAUER H., PUSCH G., 1981, Technische Bruchmechanik. VEB Deutscher Verlag für Grundstoffindustrie, Leipzig.
- CHAPPELL, B.W. and WHITE, A.J.R., 2001, Two contrasting granite types: 25 years later. Australian Journal of Earth Sciences 48, 489–499.
- COLE D. M., PETERS J. F., 2007, A physically based approach to granular media mechanics: grain-scale experiments, initial results and implications to numerical modeling, Granular Matter 9, 309–321.
- GEORGALLI G. A., REUTER M. A., 2008, A particle packing algorithm for packed beds with size distribution, Granular Matter 10: 257–262.
- HORNGA J.-H., WEI C.-C., TSAI H.-J., SHINA B.C., 2009, A study of surface friction and particle friction between rough surfaces, Wear 267, 1257–1263.
- LYNCH A.J., 1974, Mineral crushing and grinding circuits, Oxford, New York.
- MORT P.R., 2003, Proceedings of the 4th International Conference for conveying and handling of particulate solids 2, 12.98–12.104, Budapest, 27-30.05.2003.

- MOSTAFA M.E., 2003, General rock failure criterion, Mining Technology, (Trans. Inst. Min. Metall A.), A68, 112, April 2003.
- OLEJNIK T.P., 2009, Kinetics of Grinding of the Raw Materials Considering of the Compression Strength of Grains, Proceedings of CHoPS+ICBMH, 166–169, Brisbane.
- OLEJNIK T.P., 2010, Milling rate of chosen mineral materials in a ball mill under changing apparatus-process conditions”, Proceedings of Comminution’10, CD, 1–11, Cape Town.
- SHIPWAY P.H., HUTCHINGS I.M., 1993, Fracture of brittle spheres under compression and impact loading, II Results for lead-glass and sapphire spheres, Phil. Magaz. A, 67, 1389–1404.
- ZINGG T., 1935, Beitrag zur Schotteranalyse. Mineralogische und Petrologische Mitteilungen 15, 39–140.

Received July 20, 2011; reviewed; accepted August 18, 2011

CARBON DIOXIDE PHOTOCONVERSION. THE EFFECT OF TITANIUM DIOXIDE IMMOBILIZATION CONDITIONS AND PHOTOCATALYST TYPE

Anna CYBULA, Marek KLEIN, Anna ZIELIŃSKA-JUREK, Marcin JANCZAREK,
Adriana ZALESKA

Department of Chemical Technology, Gdansk University of Technology, 80-233 Gdansk, Poland, e-mail:
adriana.zaleska@pg.gda.pl

Abstract. Carbon dioxide and water vapor were effectively photoconverted to methane using either pure or modified-TiO₂ and UV-Vis irradiation. The process of photoconversion in the gas phase was carried out in a tubular reactor equipped with a perforated TiO₂-coated support. The effect of selected parameters of TiO₂ immobilization procedure, such as the time and temperature of drying step and the photocatalyst amount, on photocatalytic efficiency was investigated. The effect of TiO₂ loading with Ag/Au nanoparticles on CO₂ photoconversion efficiency was also studied. CH₄ was found to be the major photoreduction product. The highest methane production was observed after irradiation of CO₂+H₂O mixture over Au-TiO₂ photocatalyst. After one hour of UV-Vis irradiation 503 ppm of methane was formed.

keywords: TiO₂, photoreduction, CO₂ photoconversion, titanium dioxide

1. Introduction

The reduction of carbon dioxide has recently been regarded as an important research area in chemical technology, not only for solving the problems resulting from environmental pollution, but also for finding ways to maintain carbon resources, which are being depleted by burning fossil fuels. Photocatalytic CO₂ conversion offers a promising way for clean, low cost and environmentally friendly production of fuels by solar energy. Photocatalytic reduction of CO₂ could be carried out in CO₂-saturated aqueous solution containing suspended TiO₂ (Li et al., 2010; Dey et al., 2004) liquid CO₂ (Kaneco et al., 1997), high pressure CO₂ system with TiO₂ powders suspended in isopropyl alcohol (Kaneco et al., 1998) and in the gas phase - CO₂ with H₂O vapor irradiated over TiO₂ (Tan et al., 2008; Xia et al., 2007; Nguyen et al., 2008; Tan et al., 2006). The UV-irradiated TiO₂ surface can generate electrons to reduce the CO₂ molecules present in aqueous and gaseous streams at ambient temperature and pressure conditions. Photogenerated electron-hole pairs migrate to the surface and in the presence of H₂O molecules lead to the reduction of CO₂ in CH₄ and compounds

such as C_2H_2 , CH_3OH , C_2H_5OH at the solid-gas interface (Usubharatana et al., 2006; Varghese et al., 2009).

Photocatalytic reactions could be carried out in the presence of pure and modified TiO_2 (Fujishima et al., 2006; Chatterjee et al. 2005; Zaleska, 2008). Zhang et al. (2011) studied the effect of calcination temperature (375, 450, 550°C) and dopant concentration of iodine (I_2) (5, 10, 15 wt.%) on the efficiency of photoconversion. A fixed amount of powder catalyst (200 mg) was dispersed on a glass-fiber filter and placed at the bottom of the cylindrical photoreactor. The photocatalytic activities of the I- TiO_2 powders were investigated by photocatalytic reduction of CO_2 with H_2O under visible light (>400 nm) and also under UV-visible illumination. CO was found to be the major photoreduction product. A high efficiency of CO_2 reduction was observed for 10 wt.% I- TiO_2 photocatalysts (the highest CO yield equivalent to $2.4 \mu mol \cdot g^{-1} \cdot h^{-1}$) under visible light. The highest activity in the presence of UV-Vis light showed 5 wt.% I- TiO_2 , calcined at 375°C (600 ppm after 90 minutes), and the increase in calcination temperature decreased the efficiency of the process of photoreduction. Too high iodine doping level may result in recombination centers and thus lower the photocatalytic activity (Zhang et al., 2011). Photocatalytic reduction of CO_2 with H_2O in the gaseous phase was studied by Chen et al. (2009) using thin films P-25 (prepared by reactive magnetron sputtering) under UV irradiation (100 W). The main product of the reaction of methane was also detected in the form of trace amounts of other hydrocarbons such as methanol. The highest concentration of the products was observed for pure anatase, and the lowest for pure rutile. Chen et al. (2009) have shown that there is synergy between CO_2 concentration and the temperature of the process. The highest methane yields were produced under the optimal combination of high CO_2 concentration (approximate 45% volume) and elevated temperature (approximately 80°C). Under these conditions, after 4 h of irradiation 200 nmol of methane were received. It was also noted that conditions of TiO_2 film synthesis at the surface of boro-silicate glass (e.g. deposition angle during current magnetron sputtering) affected the effectiveness of the process (Chen et al., 2009). The results obtained by Tan et al. (2006) confirmed that CO_2 could be reformed in the presence of water vapor and TiO_2 -P 25 pellets into CH_4 under continuous UV irradiation at ambient conditions. Total CH_4 yield was 200 ppm and lower than 100 ppm after 48 h of irradiation with UVC (253.7 nm) and UVA (365 nm), respectively (Tan et al., 2006). Li et al. (2010) studied a photoconversion process using Cu/ TiO_2 - SiO_2 . Glass wool was placed in the reactor as the support for the glass fiber filter loaded with a thick film of powder catalysts. The glass wool support was also moisturized with 3.0 g deionized water to maintain saturated water vapor in the reactor. Irradiation source was a Xenon lamp (irradiation intensity 2.4 mW/cm^2). The measured production rate of the products increased with the irradiation time and reached a peak value at around 4 h. The methane production rate was $13.2 \mu mol/(g \cdot h)$. It was found that a photocatalyst after regeneration can be used again for photoconversion process but its activity is already significantly lower (Li et al., 2010).

Photocatalytic reduction of CO₂ with H₂O in the gaseous phase was studied by Nguyen et al. (2008) using Cu-Fe/TiO₂ catalyst coated on optical fibers under UVA and UVC irradiation. Methane and ethylene were observed as the main products to evolve from this photoreactor. The presence of Fe as a co-dopant in Cu/TiO₂ photocatalyst was found to synergistically reduce CO₂ with H₂O to ethylene at the quantum yield and total energy efficiency of 0.024% and 0.016%, respectively. This phenomenon could be explained by an efficient charge transfer mechanism between TiO₂ as a support and Cu as well as Fe as co-dopants. Methane was formed more favorably than ethylene on Cu/TiO₂. Meanwhile, Fe as a co-dopant on Cu/TiO₂ photocatalyst was found to depress methane formation. The highest ethylene production rate was observed for TiO₂ doped with 0.25 wt.% of Cu and 0.25 wt.% of Fe and it was 0.53 μmol(g·h)⁻¹ (Nguyen et al., 2008). Thus, the efficiency of currently available TiO₂-based photocatalysts is still not sufficient for practical use. Therefore, the development of new ones and optimization of existing photocatalysts exhibiting activity upon visible light with surface characteristics of improved performance and of high chemical and physical stability are crucial for broader scale utilization of photocatalytic systems in commercial applications. To avoid the above listed problems and to improve solar photocatalytic CO₂-to-light hydrocarbons conversion two main approaches are proposed: (1) TiO₂ modification to increase the spectral sensitivity of TiO₂-based photocatalysts to visible light and to compete with electron-hole recombination (by metal and non-metal co-doping), and (2) enhancement of interface surface area by photoreactor design.

Apart from photocatalyst properties, the activity is also affected by the method and parameters of a photocatalyst immobilization procedure. In our investigation, TiO₂-based photocatalyst was deposited on the surface of a flat perforated steel tray, easily removable from the reactor. The photoreactor was equipped with a parabolic, aluminum mirror to concentrate light. Thus, the aim of this study was to investigate the effect of selected parameters of immobilization step, such as the time and temperature of drying and the photocatalyst amount, on photocatalytic efficiency.

2. Experimental

2.1. Materials

TiO₂ P-25 having mixed anatase and rutile structure 4:1 (particle size 40 nm, S_{BET} = 50m²/g), was obtained from Evonik, Germany. Titanium isopropoxide (pure p.a.; TIP) was purchased from Aldrich and used as titanium source for the preparation of TiO₂ nanoparticles. Hydrogen tetrachloroaurate(III) tetrahydrate (99.9%) and silver nitrate were provided by POCh and used as starting materials for the preparation of gold/silver nanoparticles. Sodium borohydride and ascorbic acid (99%) were purchased from Aldrich and used as reducing agents. Cyclohexane was used as continuous oil phase, sodium bis-(2-ethylhexyl) sulfosuccinate (AOT) purchased from

Aldrich as surfactants, 2-propanol as a cosurfactant and aqueous solution as the dispersed phase.

2.2. Photocatalytic conversion of carbon dioxide

Compressed CO₂ from a cylinder was led to the photoreactor via a gas flow meter, a safety tank equipped with a manometer and an absorber with demineralized water. The reactor chamber was purged with CO₂ gas for 30 min with 80 dm³·h⁻¹ gas flow rate. The reaction system was maintained at 4903 Pa positive pressure. After 30 min purging, the reaction chamber was closed and irradiated using 1000 W Xenon lamp (Oriel), which emits both UV and visible light. The optical path included a 10 cm thick water filter to cut off IR. A schematic illustration of the batch reactor system for the CO₂ photoreduction test is shown in Fig. 1.

The photocatalytic reduction CO₂ was tested in a bench-scale photocatalytic reactor (V=314 cm³) with a perforated TiO₂-cover tray. The reactor chamber was made of a cylindrical quartz tube (i.d. 50 mm, length 160 mm) and equipped with inlet and outlet valves, as shown in Fig. 2.

Perforated removable trays were placed in the quartz tube, which served as a reaction chamber and was positioned over aluminum parabolic mirror with 188.4 cm² collecting area. Thus, the in-going gas phase passed through the perforated barrier and was irradiated from the top by incident radiation, and from the bottom by reflected light.

The TiO₂ suspension was prepared by addition of an appropriate amount of water to 0.5 g of the photocatalyst. Both sides of the internal element of the photoreactor were coated with TiO₂-based suspension by painting procedure. The obtained TiO₂-coated support was dried from 5 to 35 hours at different temperatures (80, 120 or 160°C). A steel or plastic support was used to check the impact of such a support on the effectiveness of the process.

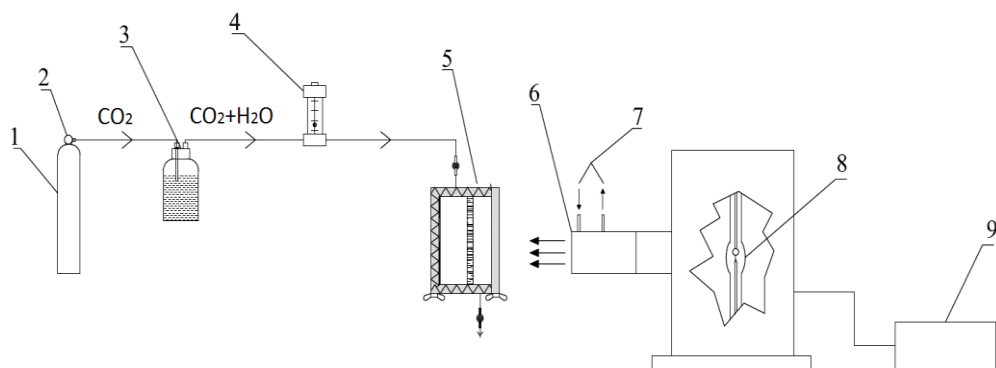


Fig. 1. Schematic illustration of the batch reactor system for the CO₂ photoreduction test:
1) cylinder of CO₂; 2) gas cylinder valve; 3) water bubbler; 4) gas flow meter; 5) photoreactor equipped with a quartz window; 6) water filter; 7) inlet and outlet cooling water; 8) xenon lamp; 9) feeder

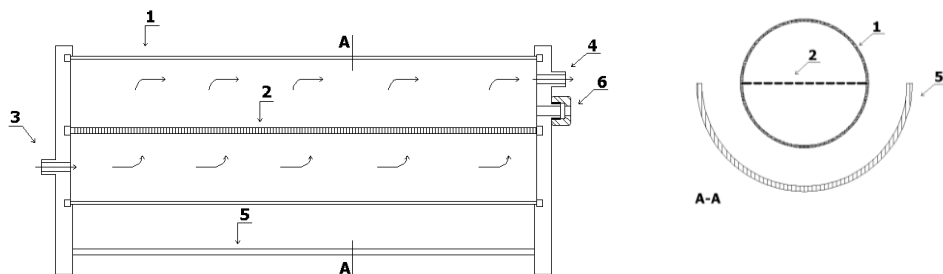


Fig. 2. Schematic diagram of the photoreactor: 1) quartz tube; 2) perforated TiO_2 -covered tray; 3) gas inlet; 4) gas outlet; 5) parabolic mirror; 6) sampling port

2.3. Gas chromatographic analysis

A Perkin-Elmer model Clarus 500 gas chromatograph was used together with a porapak-Q 100-120 mesh column (2 m x 2.1 mm i.d.) equipped with a flame ionization detector. In each case a 0.200 cm^3 of gaseous sample were injected in a splitless mode. The operating conditions were as follows: the initial GC column temperature 105°C . The injector temperature was 150°C and the detector temperature was 220°C . The carrier gas used was nitrogen. The flow was kept at a constant $17 \text{ cm}^3/\text{min}$. The gas phase from the reaction chamber was sampled by the gas-tight membrane. The gas samples were analyzed in a duplicate at given periods of time. The retention time for methane, ethene and ethane was respectively 0.74, 1.31 and 1.58 minutes.

3. Results and discussion

For studying the photocatalytic conversion of CO_2 into light hydrocarbon with the TiO_2 , it was necessary to investigate the influence of the selected parameters affecting the step of photocatalyst immobilization (e.g. the drying temperature and time, the type of support and TiO_2 amount). The efficiency of CO_2 photoconversion was estimated as methane concentration after 1 h irradiation of $\text{CO}_2 + \text{H}_2\text{O}$ mixture over TiO_2 supported on the surface of a flat perforated steel tray. The TiO_2 P-25/UV-Vis system was chosen as a reference generating methane as the main product of CO_2 photoconversion. Commercially available TiO_2 P25 was chosen for this investigation as a standard used in heterogeneous photocatalysis. The effect of these parameters was achieved in separate experiments and is presented in Tables 1-3. Table 1 shows the efficiency of methane generation in the presence of P-25 dried in different temperatures after a coating process. It was found that the increase of drying temperature from 80 to 120°C resulted in the increase of methane concentration from 36 to 66 ppm, respectively. However, as the drying temperature increased up to 160°C , CH_4 concentration decreased, reaching the lowest value equal to 4.7 ppm (see Table 1).

The effect of the drying time of TiO₂ suspension deposited on the surface of a flat perforated steel tray on CO₂ photoconversion efficiency is presented in Table 2. The obtained data suggested, that the increase in drying time from 5 to 20 h resulted in the increase of methane concentration from 24 to 90 ppm. However, time elongation to 35 h caused only slight increase in methane concentration. After 60 min. irradiation of CO₂+H₂O mixture over TiO₂ dried in 35 h, methane concentration was 99 ppm. Thus, a 20-hour drying time was chosen for further investigations to save energy during the preparation procedure.

Table 1. The effect of drying temperature TiO₂ on CO₂ photoconversion efficiency (drying time: 20 h, photocatalyst: P-25, average photocatalyst amount: 0.37 g)

| Drying temperature [°C] | Methane concentration after 1h exposure for UV-Vis irradiation [ppm] |
|-------------------------|--|
| 80 | 36 |
| 120 | 66 |
| 160 | 4.7 |

Table 2. The effect of drying time TiO₂ on CO₂ photoconversion efficiency (drying temperature: 120°C, photocatalyst: P-25, average photocatalyst amount: 0.37 g)

| Drying time [h] | Methane concentration after 1h exposure for UV-Vis irradiation [ppm] |
|-----------------|--|
| 5 | 24 |
| 20 | 90 |
| 35 | 99 |

The influence of TiO₂ amount applied to the surface during coating procedure on CO₂ photoconversion was also investigated and is presented in Table 3. The enhancement in the photocatalytic efficiency for higher amount of P-25 deposited on the porous steel tray was observed. It is expected that introducing a higher amount of TiO₂ can extend the surface area of the available photocatalyst and raise efficiency of CO₂ photoconversion. Methane concentration will amount to 39, 90 and 135 ppm for TiO₂ mass equal to 0.2541, 0.3642 and 0.4825 g, respectively. Further increase in TiO₂ amount resulted in mechanical instability of the obtained TiO₂ thin film. It was noticed that for a higher amount of the photocatalyst, TiO₂ layer suffered cracking and TiO₂ partly fell away during the photoconversion process.

Steel and plastic trays were tested as TiO₂ support materials. Both trays had the same size and perforation pattern. The same coating procedure resulted in a much lower amount deposited on the surface of the plastic tray due to weaker adhesive properties. The amount of the photocatalyst deposited on the surface of the steel and plastic plates was equal to 0.37 and 0.08 g of TiO₂, respectively. Thus, the application

of a plastic support caused the decrease in methane concentration to 34 ppm after 1 h of irradiation (see Table 4).

Table 3. The effect of TiO₂ amount on CO₂ photoconversion efficiency (drying temperature 120°C, drying time 20 h, photocatalyst P-25)

| Mass of the photocatalyst deposited on the surface of a perforated steel tray [g] | Methane concentration after 1h exposure for UV-Vis irradiation [ppm] |
|---|--|
| 0.2541 | 39 |
| 0.3642 | 90 |
| 0.4825 | 135 |

Table 4. The effect of the type of support on CO₂ photoconversion efficiency (drying temperature 120 °C, drying time 20 h, photocatalyst P-25)

| Type of support | Methane concentration after 1h exposure for UV-Vis irradiation [ppm] |
|-----------------|--|
| steel | 90 |
| plastic | 34 |

After selecting conditions of the photocatalyst immobilization step, TiO₂ modified with noble metals was used for CO₂ photoconversion. TiO₂ modified with monometallic nanoparticles (Ag or Au) and TiO₂ modified with bimetallic nanoparticles (Ag/Au) were prepared using a microemulsion system (water/AOT/cyclohexane) according to the procedure described by Zielinska-Jurek et al. (2011). The efficiency of methane generation, after a 1 h exposure of CO₂+H₂O mixture to UV-Vis irradiation over noble metal modified TiO₂, are presented in Table 5.

Table 5. The efficiency of CO₂ photoconversion in the presence of TiO₂ modified with noble metal nanoparticles (immobilization conditions: drying temperature 120°C, drying time 20 h, a steel perforated tray)

| Type of dopant | Metal precursor used during preparation | Amount of metal precursors used during preparation [mol. %] | | TiO ₂ source ¹ | Methane concentration after 1h exposure to UV-Vis irradiation [ppm] | Mass of the photocatalyst [g] |
|----------------|--|---|-----|--------------------------------------|---|-------------------------------|
| | | Au | Ag | | | |
| Ag | AgNO ₃ | - | 6.5 | TIP | 493 | 0.4002 |
| Au | HAuCl ₄ | 1.5 | - | TIP | 503 | 0.4165 |
| Ag/Au | AgNO ₃ and HAuCl ₄ | 0.5 | 2.5 | TIP | 164 | 0.4636 |

¹TIP – TiO₂ obtained by hydrolysis of titanium(IV) isopropoxide in the microemulsion system

Higher efficiency of CO₂ photoconversion was observed for TiO₂ modified with gold nanoparticles. 503 ppm of methane were obtained in the presence of the sample 1.5% Au/TiO₂ after one hour of exposure to UV-Vis irradiation. Photoconversion efficiency for the modified photocatalyst bimetal nanoparticles Ag-Au/TiO₂ after a 1 h exposure to UV-Vis irradiation was 164 ppm. The obtained results suggested that the deposition of gold or silver nanoparticles on the surface of TiO₂ resulted in the enhancement of CO₂ photoconversion efficiency. Noble metals deposited or doped with TiO₂ have high Schottky barriers among the metals and thus act as electron traps, facilitating electron-hole separation and promoting the interfacial electron transfer process (Li et al., 2010; Dey et al., 2004). Additionally, noble-metal nanoparticles have often been used to extend the absorption properties from the ultraviolet to visible region and to enhance the photocatalytic activity of titanium(IV) oxide (Kaneco et al., 1997; Tan et al., 2008; Xia et al., 2007; Nguyen et al., 2008). Silver and gold nanoparticles possess the ability to absorb visible light, due to localized surface plasmon resonance (LSPR).

4. Conclusions

Selected parameters of TiO₂ immobilization on the surface of inert support in the CO₂ photoconversion were investigated. It was found that drying temperature and time, the type of support, as well as the amount of used TiO₂ significantly affected the efficiency of the CO₂ photoreduction process. The highest methane concentration was observed since TiO₂ was deposited on the surface of a perforated steel tray and dried at 120°C for 20 h. It has been found that with the increase of the mass of TiO₂ the efficiency of the process increases. Up to five-fold higher methane concentration was observed after 1 h irradiation in the presence of TiO₂ modified with noble metal nanoparticles than that of pure TiO₂.

Acknowledgments

This research was financially supported by Polish Ministry of Science and Higher Education (grant No. N N305 320736), National Centre for Research and Development (grant No. SP/L465786/10/28maja2010) and by Voivodeship Fund for Environmental Protection and Water Management in Gdansk, Scholarships for MSc Students WFOŚ/D/703/166/2010.

References

- CHATTERJEE, D., DASGUPTA, S., 2005, Visible light induced photocatalytic degradation of organic pollutants, *J. Photochem. Photobiol. C* 6, 186–205.
- CHEN, L., GRAHAM, M., LI G., GENTER, D., DIMITRIJEVIC, N., GRAY, K., 2009, Photoreduction of CO₂ by TiO₂ nanocomposites synthesized through reactive direct current magnetron sputter deposition, *Thin Sol. Films* 517, 5641–5645.
- DEY, G.R., BELAPURKAR, A.D., KISHORE, K., 2004, Photo-catalytic reduction of carbon dioxide to methane using TiO₂ as suspension in water, *J. Photochem. Photobiol. A*, 163, 503–508.
- FUJISHIMA, A., ZHANG, X., 2006, Titanium dioxide photocatalysis: present situation and future approaches, *C.R. Chimie*, 9, 750–760.

- KANECO, S., KURIMOTO, H., OHTA, K., MIZUNO, T., SAJI, 1997, A., Photocatalytic reduction of CO₂ using TiO₂ powders in liquid CO₂ medium, *J. Photochem. Photobiolog. A* 109, 59–62.
- KANECO, S., SHIMIZU, Y., OHTA, K., MIZUNO, T., 1998, Photocatalytic reduction of high pressure carbon dioxide using TiO₂ powders with a positive hole scavenger, *J. Photochem. Photobiol. A*, 115, 223–226.
- LI, Y., WANG, W., ZHAN, Z., WOO, M., PRATIM, B., 2010, Photocatalytic reduction of CO₂ with H₂O on mesoporous silica supported Cu/TiO₂ catalysts, *Appl. Catal. B*, 100, 386–392.
- NGUYEN, T.V., WU, J.C.S., CHIOU, C.H., 2008, Photoreduction of CO₂ over Ruthenium dye-sensitized TiO₂-based catalysts under concentrated natural sunlight, *Catal. Commun.* 9, 2073–2076.
- NGUYEN, T.V., WU, J.C.S., 2008, Photoreduction of CO₂ in an optical-fiber photoreactor: Effects of metals addition and catalyst carrier, *Appl. Catal. A: Gen.* 335, 112–120.
- TAN, S.S., ZOU, L., HU, E., 2008, Kinetic modelling for photosynthesis of hydrogen and methane through catalytic reduction of carbon dioxide with water vapour, *Cat. Today* 138, 125–129.
- TAN, S.S., ZOU, L., HU, E., 2006, Photocatalytic reduction of carbon dioxide into gaseous hydrocarbon using TiO₂ pellets, *Cat. Today*, 115, 269–273.
- USUBHARATANA, P., MCMARTIN, D., VEAWAB, A., TONTIWACHWUTHIKUL, P., 2006, Photocatalytic Process for CO₂ Emission Reduction from Industrial Flue Gas Streams, *Ind. Eng. Chem. Res.* 45, 2558–2568.
- VARGHESE, O.K., PAULOSE, M. LATEMPA, T.J. GRIMES C.A., 2009, High-Rate Solar Photocatalytic Conversion of CO₂ and Water Vapor to Hydrocarbon Fuels, *Nano Letters* 9, 731–737.
- XIA, X.H., JIA, Z.J., YU, Y., LIANG, Y., WANG, Z., MA, L.L., 2007, Preparation of multi-walled carbon nanotube supported TiO₂ and its photocatalytic activity in the reduction of CO₂ with H₂O, *Carbon* 45, 717–721.
- ZALESKA, A., 2008, Doped-TiO₂: A Review, *Recent Pat. Eng.* 2, 157–164.
- ZHANG, Q., LI Y., ACKERMAN E., GAJDARDZISKA-JOSIFOVSKA M., LI H., 2011, Visible light responsive iodine-doped TiO₂ for photocatalytic reduction of CO₂ fuels, *Appl. Catal. A: Gen.* 400, 195–202.
- ZIELIŃSKA-JUREK A., KOWALSKA E., SOBCZAK J., LISOWSKI W., OHTANI B., ZALESKA, A., 2011, Preparation and characterization of monometallic (Au) and bimetallic (Ag/Au) modified-titania photocatalysts activated by visible light, *Appl. Catal. B* 101, 504–514.

Received April 22, 2011; reviewed; accepted July 23, 2011

REMOVING CONTAMINANTS FROM GROUNDWATER POLLUTED BY THE TRZEBIONKA MINE SETTLING POND LOCATED IN UPPER SILESIA (POLAND)

Tomasz SUPONIK

Politechnika Śląska, Wydział Górnictwa i Geologii, Akademicka 2, 44-100 Gliwice, tomasz.suponik@polsl.pl

Abstract. The Trzebionka Mine settling pond is located in south Poland and has a significant impact on quality of surrounding soil and groundwater. This is mainly due to toxic elements present in wastes disposed in the pond. The wastes are mainly flotation tailings after processing of zinc and lead ores. In the paper, chemical composition of the wastes is presented. Problems with surface water contamination by the Trzebionka Mine settling pond are also presented in the article. It was shown that most problems result from contaminants flowing down in the unsaturated zone, reaching ground waters and then flowing horizontally leading to pollution of the surface water. As a result, the canal surrounding the post-flotation pond as well as Luszowka and Wodna streams and finally the Chechlo river are contaminated. In order to protect these waters a permeable reactive barrier (PRB) technology is proposed to be used in the vicinity of the considered dumping site. The PRB technology is a technique of groundwater remediation in which the contaminants are removed from an aquifer by flowing through a PRB filled with a special material called reactive material. The processes which can be used to treat groundwater contaminated by the Trzebionka Mine settling pond are redox reactions, adsorption and biochemical reactions. At the end of the article a proper selection of reactive materials, and thus treating processes, for efficient PRB application in the considered dumping site area is suggested.

keywords: flotation waste of Pb-Zn production, metals and non-metals in groundwater and in surface water, remediation, PRB Technology

1. Introduction

The Silesia and Cracow province has been developing for hundreds of years. There are mining, power and metallurgical industries in this region. As a result of heavy industry expansion, many dumping sites exist in the area. Some of them are old and forgotten, some are still used, and new are being created. The dumping sites affect the quality of ground and surface water in this region (Cabala, 2005, 2009; Girczys and Sobik-Szołtysek, 2002; Labus, 1999).

The flotation wastes from Trzebionka Mining Company plant processing Zn and Pb ores had been located in the Trzebionka Mine settling pond for over half a century. Rainfall water either flows through the dumping site or forms a surface run-off, and consequently contains different contaminants. Water flows down in the unsaturated zone, reaches the groundwater and then flows horizontally polluting surface water. The leachate from the dumping site may contain different kinds of chemicals like inorganic anions, oxyanions and cations. To remove them from the groundwater, and thus to protect surface water, PRB (Permeable Reactive Barrier) technology may be used. This technology is a technique of groundwater remediation where contaminants are removed from an aquifer by the groundwater flow through a PRB filled with a special material called reactive material. The PRB technique of groundwater remediation is a passive one. Contaminants treatment can be accomplished may occur with the reactive material through physicochemical, chemical and/or biochemical processes. The PRB technology has the potential to effectively remediate subsurface contamination at many types of sites with significant cost savings compared to other approaches. The economic benefits of the PRB technique results from the fact that relatively little energy or labour input is necessary.

The primary goals of this study were to present the impact of the Trzebionka Mine settling pond on groundwater and then on surface water, as well as to present the processes and reactive materials that can be used in the PRB technology for treating groundwater contaminated with metals and non-metals by the Trzebionka Mine settling pond.

2. The impact of settling pond the Trzebionka Mine on water environment

The Trzebionka Mine settling pond (Fig. 1) is located between Chrzanow and Trzebinia towns in the southern part of the Silesia-Cracow Upland. It belongs to Trzebionka Mining Company (presently under liquidation) and occupies ca. 0,65 km² (Nowak, 2008). In the dumping site the flotation waste of zinc and lead ores had been stored in the form of suspension containing dolomite, quartz mixed with zinc sulphides (sphalerite ZnS) and lead carbonates (cerussite PbCO₃) (Jarosiński et al., 2006; Nowak, 2008). The chemical composition of the Zn-Pb waste is presented in Table 1.

The contaminants present in the Zn-Pb waste pollute nearby Luszowka and Wodna streams. Both streams discharge their waters into the Chechlo river (Fig. 1). To confirm that the ground and surface water are polluted by the dumping site leaching tests for wastes taken from the considered dumping site were made. The experiments were performed according to EU Standard (2006). The liquid/solid ratio (L/S) in the leaching tests was 10.

Eight samples of wastes (ca. 1 kg each) were taken from the dumping site. Each sample was made homogeneous before the test. The locations of samples collection are shown in Fig. 1. The depth of sampling points amounted to ca. 0.5 m below ground surface. The wastes were sampled with the use of a paddle.

The concentrations of following elements As, Cd, Ni, Pb, Zn in wastes (for each sample) were measured with the help of Mass Spectrometry (ICP-AES). The results are presented in Table 2.

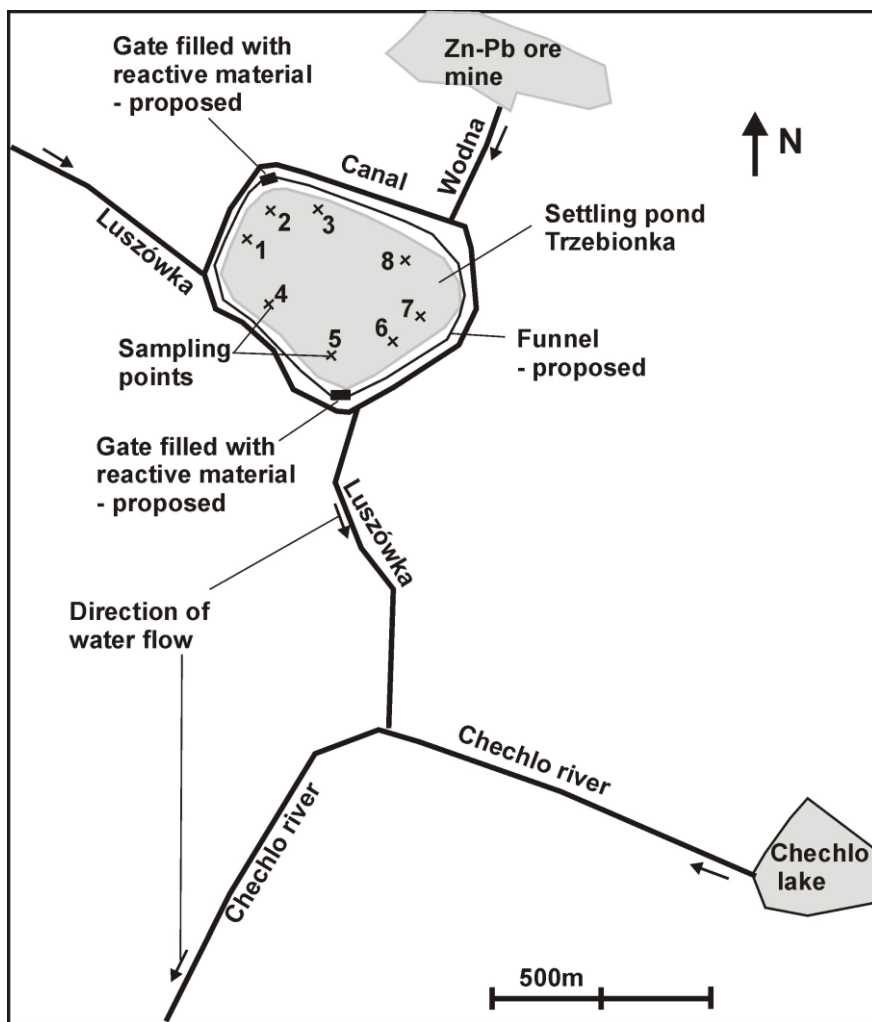


Fig. 1. Surface water in the region of the Trzebieńka Mine settling pond plotted using own data and Mapa Turystyczna (2011)

The arithmetic average and maximum concentration of chosen elements leached from wastes amounted to: $As_{av} = 94$ mg/kg; $As_{max} = 155$ mg/kg; $Cd_{av} = 48$ mg/kg; $Cd_{max} = 81$ mg/kg; $Ni_{av} = 42$ mg/kg; $Ni_{max} = 68$ mg/kg; $Pb_{av} = 129$ mg/kg; $Pb_{max} = 192$ mg/kg; $Zn_{av} = 936$ mg/kg; $Zn_{max} = 1232$ mg/kg, whereas $pH = 7.31$ and $EC = 4.820$ mS/cm. The results show that there is high probability that investigated elements can be leached from the Trzebieńka Mine settling pond under prevalent pH conditions.

Table 1. Chemical composition of flotation waste from Trzebionka Mining Company (Jarosiński et al., 2006)

| Component | mean value [%] | Component | mean value [%] |
|--------------------------------|----------------|-----------|----------------|
| CaO | 30.08 | S | 0.76 |
| MgO | 17.50 | Sn | 0.042 |
| CO ₂ | 39.2 | As | 0.039 |
| Al ₂ O ₃ | 2.10 | Cu | 0.021 |
| SiO ₂ | 2.07 | Mn | 0.02 |
| Fe | 2.03 | Cl | 0.015 |
| Zn | 0.89 | Cd | 0.009 |
| Pb | 0.40 | Sb | 0.0014 |
| ZnO | 0.49 | Ag | 0.0003 |
| PbO | 0.33 | | |

Table 2. Concentration of As, Cd, Ni, Pb, Zn leached from wastes taken from the investigated dumping site (Fig. 1)

| Element | Concentration of elements leached from wastes taken from the indicated sampling point | | | | | | | |
|---------|---|-----|------|-----|------|-----|------|------|
| | [in mg/kg] | | | | | | | |
| | 1 | 2 | 3 | 4 | 5 | 6 | 7 | 8 |
| As | 95 | 118 | 155 | 45 | 88 | 71 | 81 | 99 |
| Cd | 37 | 81 | 70 | 41 | 15 | 24 | 73 | 44 |
| Ni | 17 | 61 | 59 | 44 | 55 | 68 | 22 | 10 |
| Pb | 88 | 118 | 104 | 75 | 192 | 126 | 155 | 174 |
| Zn | 472 | 988 | 1174 | 658 | 1064 | 893 | 1007 | 1232 |

High concentration of metals and non-metals in surface water (Table 3) located nearby the settling pond confirms also the surface water pollution by the dumping site. Water in Luszowka stream and in the draining canal area of the post-flotation settling pond is slightly alkaline (pH 8) (Pasiczna et al., 2008). Electric conductivity (EC) in these waters amounted to 0.79 mS/cm and 3.96 mS/cm (median values), respectively (Pasiczna et al., 2008). Since an electric conductivity value above 2 mS/cm indicates substandard water, such a high value of EC proves strong contamination of water in the canal.

The measurements, which results are presented in Table 3, were made in the years of 2003-2005, that is before liquidation of Trzebionka Mining Company. During this time the settling pond was not the only source of surface water contamination. Some wastewater (slightly contaminated with Zn, Pb, Cd) from the ore mine and from ore concentration plant was poured in the Wodna stream (Fig. 1) and in the Trzebionka Mine settling pond (with flotation waste) (Jarosiński et al., 2006; Pasiczna et al.,

2008). Nevertheless, it can be said that the presented in Fig. 1 dumping site was one of the main sources of groundwater and because of that surface water contamination.

Due to toxicity of chemical components of the waste (Table 1) and their high concentration in the surface water (Table 3) and in eluates (Table 2), arsenic, cadmium, nickel, lead, thallium, uranium, and zinc create hazards for the aqueous environment.

Table 3. Concentration of contaminants (metals and non-metals and other selected compounds) in surface water contaminated by the Trzebieonka Mine settling pond (flotation waste of Zn-Pb ores) considered by Pasieczna et al. (2008) as a presumable source of contamination (on the bases of the Chrzanów map sheet by Pasieczna et al. (2008))

| Contaminant | Concentration of contaminants in: | |
|-------------------------------|--|---|
| | Luszwonka stream | canal surrounding post-flotation pond |
| As | max 10 µg/dm ³ ; median 2 µg/dm ³ | max 6 µg/dm ³ ; median 3 µg/dm ³ |
| Ba | max 83.41 µg/dm ³ ; median 58,17 µg/dm ³ | max 10 µg/dm ³ ; median 2 µg/dm ³ |
| B | max 627µg/dm ³ ; median 200 µg/dm ³ | max 131 µg/dm ³ ; median 107 µg/dm ³ |
| Cd | max 10.5 µg/dm ³ ; median <0.2 µg/dm ³ | max 3.8 µg/dm ³ ; median 1.0 µg/dm ³ |
| Pb | max 21.0 µg/dm ³ ; median 1.1 µg/dm ³ | max 31.9 µg/dm ³ ; median 9.4 µg/dm ³ |
| Li | max 10 µg/dm ³ ; median 7 µg/dm ³ | max 26 µg/dm ³ ; median 9 µg/dm ³ |
| Mo | max 3.86 µg/dm ³ ; median 2.21 µg/dm ³ | max 8.41 µg/dm ³ ; median 4.68 µg/dm ³ |
| Ni | max 7 µg/dm ³ ; median 1 µg/dm ³ | max 48 µg/dm ³ ; median 6 µg/dm ³ |
| Rb | max 12.4 µg/dm ³ ; median 5.0 µg/dm ³ | max 16 µg/dm ³ ; median 7.6 µg/dm ³ |
| Sr | max 970.5 µg/dm ³ ; median 424.5 µg/dm ³ | max 1018.4 µg/dm ³ ; median 854.1 µg/dm ³ |
| Tl | max 0.75 µg/dm ³ ; median 0.09 µg/dm ³ | max 10.79 µg/dm ³ ; median 0.74 µg/dm ³ |
| U | max 1.03 µg/dm ³ ; median 0.60 µg/dm ³ | max 1.25 µg/dm ³ ; median 0.82 µg/dm ³ |
| SO ₄ ²⁻ | max 1347 mg/dm ³ ; median 181 mg/dm ³ | max 4593 mg/dm ³ ; median 3181 mg/dm ³ |
| Zn | max 1491 µg/dm ³ ; median 140 µg/dm ³ | max 6602 µg/dm ³ ; median 1681 µg/dm ³ |

3. Selection of processes and reactive materials for treating groundwater contaminated by the Trzebieonka Mine settling pond

According to future plans (Gazeta Krakowska, 2011) 70-m-high the Trzebieonka Mine settling pond will be a place for viewing and admiring the landscape. Although the wastewater from the ore concentration plant and the mine will not be directed (after liquidation) to the settling pond and to surface water any longer, the problem connected with leaching elements from the waste to groundwater and to surface water will remain. Therefore, in order to protect these waters, the PRB technology can be used in the vicinity of the dumping sites.

The PRB technology is a technique of groundwater remediation. With the use of it, many toxic contaminants can be removed from groundwater. This technique is a passive one, in which contaminants are removed from an aquifer by flowing through a reactive barrier filled with a reactive material (Gavaskar et al., 2000; ITRC, 2005;

Meggyes et al., 1998; Puls et al., 1998; Suponik, 2010). The processes applied to treat groundwater contaminated with metals and non-metals are (Suponik, 2008) include: redox reactions which lead to precipitation of metals, pH control (precipitation), adsorption, and biochemical reactions which lead to precipitation of metals by sulphate-reducing bacteria.

Table 4. Reactive materials used in laboratory or field test for different kind of inorganic contaminants (Gavaskar et al., 2000; ITRC, 2005; Koziol-Komosinska and Kukulka, 2008; Koziol, 2002; Puls et al., 1998; Suponik and Lutynski, 2009; U.S. Department of Energy, 1998; Wilkin and Puls, 2003)

| inorganic contaminants | | | reactive material | type of process |
|--|-----------|--|--|--|
| metal | non-metal | other compounds | | |
| Al, Sb, Ba, Cd, Cr ⁶⁺ , Co, Cu, Pb, Mn, Mo, Ni, Ag, ⁹⁰ Sr, Tl, Tc, U | As, Se | NO ₃ ⁻ , SO ₄ ²⁻ | zero-valent metals (iron) | precipitation barriers - redox reactions |
| Cr, Mo, Tc, U | As | | ferrous hydroxide, ferrous carbonate, ferrous sulphide | |
| Cd, Mo, U | As, Se | SO ₄ ²⁻ | limestone | precipitation barriers - pH control |
| | As, Se | | activated alumina | |
| Sb, Bi, Cs, Cr, Co, Hg, Mo, Ag, Tc, tin Sn, U, Zr | As | | activated carbon | adsorption barriers |
| Tc, U | | | exchange resins | |
| Cr, Pb, Mo, U, Cu, Cd, Zn, Ni | As | SO ₄ ²⁻ | peat, lignite, brown coal | |
| Al, Ba, Cd, Co, Cs, Cr, Cu, Pb, Mn, Hg, Ni, ⁹⁰ Sr, U, Zn | As, Se | | zeolite | |
| Cd, Co, Cu, Pb, Mn, Hg, Ni, Sn, Zn | | SO ₄ ²⁻ | coastal hay, wood chips, saw dust, livestock manure, sludge, compost | precipitation barriers – biochemical reactions |

The crucial question in the case of contaminated groundwater is whether it is possible to use the PRB technology in an effective way. In the paper by Suponik and Lutynski (2009) factors that limit PRB application were discussed. One of the most important factor during reactive material (and thus process) selection is the type of contaminants. A compilation of laboratory and field research into chemicals treated

with reactive material is provided in Table 4 (Gavaskar et al., 2000; ITRC, 2005; Kyzioł-Komosinska and Kukułka, 2008; Kyzioł, 2002; Puls et al., 1998; Suponik and Lutynski, 2009; U.S. Department of Energy, 1998; Wilkin and Puls, 2003). It is classified into the type of inorganic contaminant, reactive material type, and finally in the type of the principal process which allows to remove contaminants from groundwater.

On the basis of Table 4 it can be claimed, that the possible processes and reactive materials for use with PRB to remove As, Cd, Ni, Pb, Tl, U, Zn from groundwater are:

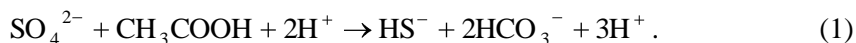
1. redox reactions with the use of zero-valent iron – there is no evidence that this barrier removes Zn,
2. biochemical reactions with the use of biomaterial presented in Table 4 – there is no evidence that this barrier removes As, Tl, U,
3. adsorption with the use of zeolite – there is no evidence that this barrier removes Tl.

These processes are shortly discussed below.

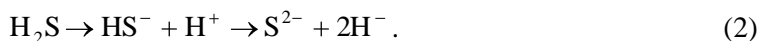
Zero-valent iron Fe(0) is an efficient, easy to use and cheap reactive material for removing metals and non-metals by redox reactions. It is applied when groundwater contains positively charged inorganic cations such as Cd²⁺, Co²⁺, Cu²⁺, Ni²⁺, Pb²⁺, and negatively charged anions and oxyanions containing As(III), As(V), Cr(VI), Se(VI), Tc(VII).

Reactive barriers filled with Fe(0) have several advantages over others ones. Zero-valent iron can work effectively and long (without replacement the material). So, the maintenance costs are rather low. Moreover, scrap iron is relatively cheap and can be obtained in a granular form in large quantities.

Heavy metals can be treated through biochemical reactions in the PRB (ITRC, 2005). In accordance with many studies (e.g. Canova, 2006) the primary removal mechanisms for the metals are sulphate-reducing bacteria (SRB). Bacteria obtain their energy by oxidizing simple organic compounds or molecular hydrogen H₂ while reducing sulphates SO₄²⁻ to sulphides, especially to hydrogen sulphide H₂S (Schulze and Mooney, 1994). An example of a biomaterial that encourages growth of sulphate-reducing bacteria in PRB are coastal hay, wood chips, saw dust, livestock manure (Canova, 2006), sludge and compost. The SRB obligates anaerobes, which prefer the following conditions: pH between 5 and 8; Eh ca. -200mV. A typical overall conversion equation (neglecting the small amount of organic material required to produce biomass) is:



The reduction product of reaction (1), hydrogen sulphide, is a volatile gas. The form in which sulphide occurs depends on the pH. HS⁻ and S²⁻, which occur at neutral and high pH respectively, are both water soluble. H₂S is the predominant form at low pH <6 (Cohen, 2006) because:



The sulphides react with metal ions to precipitate them as metal sulphides, many of which are stable under anaerobic conditions of the treatment system (Cohen, 2006). The heavy metal ions react with dissolved sulphide according to the following reaction:



Bio-barriers are considered a unique type of PRB. Due to delivering amendments into the subsurface (e.g. compost, correction of pH) this PRB works less passively than filled with Fe(0) and may incur greater operation and maintenance costs.

Adsorption is a process that occurs when a liquid solute accumulates on the surface of a solid adsorbent, forming a molecular or atomic film (the adsorbate). The manner and strength of fixation is of great importance in relation to the possibility of remobilisation, and is strongly influenced by parameters such as concentration, solubility, and speciation of the contaminants and co-solvents, and the prevalent pH, oxidation-reduction potential and temperature conditions (Roehl et al., 2000). Sorption material must meet the following conditions: high sorption capacity, high selectivity for the target contaminants, fast reaction kinetics, high hydraulic permeability, long-term effectiveness. It should be non-harmful to the environment, available at reasonable costs (Kowal and Swiderska-Broz, 1996; Roehl et al., 2000), insoluble, not biodegradable, and easy to apply. Unfortunately, sorption material should be replaced and regenerated frequently due to the effects of potential desorption or reversed ion-exchange. This aspect makes adsorption barrier rather expensive and not attractive comparing to other types.

Since the bio-barrier works less passively than reactive barrier filled with Fe(0) and adsorption material (zeolite) needs to be replaced and regenerated frequently, the zero-valent iron seems to be the best reactive material for treating groundwater contaminated with As, Cd, Ni, Pb, Tl, U. It is effective, relatively cheap and works long.

Unfortunately, zinc is the only toxic element (among contaminants presented in Table 3) that is not treatable by Fe(0). With regard to this element, it can be removed from groundwater by adsorption on zeolite, peat or lignite (Table 4), or by biochemical reactions with the use of the SRB (Table 4). Both processes are able to remove also organic and inorganic chemicals from groundwater.

In general, granulated zero-valent iron might be used in the first segment of the reactive barrier, whereas adsorbent or bio-material might be used as a second segment. Since most chemicals can be removed with Fe(0), the material applied in the second segment would not be used completely and it could treat residual contaminants.

To take a decision whether the PRB can be accepted or not in the initial stage of the assessment of possibilities of using the PRB technology, various additional data are needed to be either obtained or measured (Suponik and Lutyński, 2009). They are:

hydrogeological, geological and site, and contaminated groundwater characteristics. Furthermore, in order to assess the effectiveness of suggested processes, laboratory tests with the use of contaminated groundwater and chosen reactive materials need to be performed.

The PRB is currently built in two basic configurations: Continuous Reactive Barrier and Funnel-and-Gate System (Puls et al., 1998; Roehl et al., 2005) divided into: Funnel-and-Gate Open System and Funnel-and-Gate Closed System. The Funnel-and-Gate Closed System was proposed for the area of The Trzebionka Mine settling pond, because it uses impermeable walls (funnel) to closed contaminated region (Fig. 1). The funnel directs the contaminant plume to a “gate(s)” containing the reactive material. Thanks to this configuration it uses less reactive material. In this case the gate(s) should be located in a place which is characterized by the highest discharge of the water flux and the highest concentrations of contaminants. Therefore, to properly locate gate(s) in the vicinity of dumping sites the flow direction of contaminated groundwater should be assessed (location of gates presented in Fig. 1 is only a proposal). The configuration of the PRB proposed in Fig. 1 consists of two gates, each ca. 25 m long and approximately 1.8 km of impermeable walls.

Estimating the cost of the PRB is a difficult task in this stage of consideration, since a number of factors need to be evaluated, including:

- site characterization costs: complete vertical and horizontal delineation of the groundwater plume and characterization of hydrogeologic, geochemical, geotechnical, and microbiological conditions,
- design costs: treatability studies and modelling,
- construction costs: purchase and installation of reactive material and impermeable wall,
- operation and maintenance costs: monitoring and reporting costs and replacement of reactive material.

The total costs of the PRBs vary widely depending on the site type and PRB characteristics. In general, the depth and length of the PRB continue to drive the costs of PRB application (Gavaskar et al., 2000). For example (in the USA the costs is different from that in Poland) the cost was:

- from \$100 000 in Mountain View, California. Fe(0) was used in Continuous Reactive Barrier. Treatment zone depth ca. 5 m; reactive zone length ca. 14 m, total mass reactant 90 Mg (Puls et al., 1998),
- to \$1 000 000 in Lakewood, Colorado. Fe(0) was used in the Funnel-and-Gate Open System. Funnel material: Sealable Joint Sheet Piles, funnel length 320 m, No. of gates 4, treatment zone depth ca. 7 m, reactive zone length 4x12 m=48 m, total mass reactant - no information available, total system length 368 m (Puls et al., 1998).

Since the second segment of the reactive barrier consisted of adsorbent or bio-material and length of the proposed (in the area of The Trzebionka Mine settling pond) PRB is high, the total costs may be high. Originally, the cost of a PRB was compared to a pump-and-treat system (alternative method). According to Gavaskar et al. (2000),

ITRC (2005), Puls et al. (1998) this system is generally more expensive than PRB. Therefore, today, pump-and-treat systems are not being used at the same number of sites as in past years. This reduction is partially due to issues involving overall effectiveness and the high cost of operation and maintenance for the pump-and-treat systems. Therefore, it may turned out that the PRB with Fe(0) in the first segment of the reactive barrier and adsorbent or bio-material in the second segment is the cheapest and the most effective method for protecting Luszowka and Wodna streams, and, as a result of it, the Chechlo river.

4. Conclusions

The Trzebionka Mine settling pond has a significant impact on the quality of groundwater, and thereby on the surface water, Luszowka and Wodna streams and Chechlo river. The chemical composition of flotation waste located in it shows high concentration of various metals and non-metals. Leaching tests confirm that they migrate to water. The metals and non-metals flow down (in the form of dissolved in water) in the unsaturated zone, reach the groundwater and then flow horizontally and pollute surface water (with arsenic, cadmium, nickel, lead, thallium, uranium, and zinc). There are three processes in the PRB technology that are able to remove metals and non-metals from groundwater contaminated by the Trzebionka Mine settling pond. They are: redox and biochemical reactions and adsorption. In order to keep the operation and maintenance cost of the PRB relatively low and to achieve high effectiveness of the treatment process the redox reaction with zero-valent iron was chosen and proposed to be used as a first segment of the reactive barrier, and biochemical reactions with SRB or adsorption process with zeolite, peat or lignite were proposed to be used as a second segment - to remove zinc from groundwater and to treat residual contaminants (remained after first segment).

References

- CABALA J., 2005, Kwaśny drenaż odpadów poflotacyjnych rud Zn-Pb; zmiany składu mineralnego w strefach ryzosferowych rozwiniętych na składowiskach, Zesz. Nauk. Politechniki Śląskiej; Górnictwo z. 267, Gliwice, 63–70.
- CABALA J., 2009, Metale ciężkie w środowisku glebowym olkuskiego rejonu eksploatacji rud Zn-Pb, Wydawnictwo Uniwersytetu Śląskiego, Katowice.
- CANOVA J., 2006, Pilot-Scale Bioreactive PRB Removes Metals from Ground-Water Plume Within One Year, Technology News and Trends, Issue 22, US EPA .
- COHEN R.H., 2006, Use of microbes for cost reduction of metal removal from metals and mining industry waste streams, Journal of Cleaner Production Vol. 14. Issues 12-13, 1146–1157.
- EU STANDARDS, 2006, PN – EN 12457-4:2006, Charakteryzowanie odpadów - Wymywanie - Badanie zgodności w odniesieniu do wymywania ziarnistych materiałów odpadowych i osadów - Część 4: Jednostopniowe badanie porcjowe przy stosunku cieczy do fazy stałej 10 l/kg w przypadku materiałów o wielkości cząstek poniżej 10 mm (bez redukcji lub z redukcją wielkości), ISBN: 83-243-8906–7.

- GAVASKAR A., GUPTA N., SASS B., JANOSY R., HICKS J., 2000, Design guidance for application of permeable reactive barriers for groundwater remediation, Florida: Battelle Columbus Operations Ohio.
- GAZETA KRAKOWSKA, 2009, Chrzanów: Na hałdzie będzie punkt widokowy, nr 174, Grupa Wydawnicza Polskapresse sp. z o.o., Oddział Prasa Krakowska, Warszawa, www.gazetakrakowska.pl.
- GIRCZYS J., SOBIK-SZOLTYSEK J., 2002, Odpady przemysłu cynkowo-olowiowego. Wydawnictwo Politechniki Częstochowskiej, Częstochowa.
- ITRC (Interstate Technology & Regulatory Council), 2005, Permeable Reactive Barriers: Lessons learned/new directions, Washington: <http://www.itrcweb.org>.
- JAROSINSKI A., NOWAK A. K., WŁODARCZYK B., 2006, Charakterystyka odpadów i ścieków z ZG „The Trzebieńka Mine” SA, Ekotechnika nr 1/37, 43–45.
- KOWAL A. L., ŚWIDERSKA-BRÓŻ M., 1996, Oczyszczanie wody, Wydawnictwo Naukowe PWN, Warszawa-Wrocław.
- KYZIOŁ J., 2002, Sorpcja i siła wiązania wybranych jonów metali ciężkich z substancją organiczną (na przykładzie torfów), IPIŚ PAN, Zabrze.
- KYZIOŁ-KOMOSIŃSKA J., KUKUŁKA L., 2008, Wykorzystanie kopalin towarzyszących pokładom złóż węgla brunatnych do usuwania metali ciężkich z wód i ścieków, IPIŚ PAN; Works & Studies - Prace i Studia no 75, Zabrze.
- LABUS K., 1999, Stopień zanieczyszczenia i identyfikacja ognisk zanieczyszczeń kadmem, ołowiem i cynkiem wód powierzchniowych i podziemnych zlewni Białej Przemszy, Wydawnictwo Instytutu Gospodarki Surowcami Mineralnymi i Energią PAN, Kraków.
- MAPA TURYSTYCZNA, 2010, Śląskie, część południowa, skala 1:100 000, Śląska Organizacja Turystyczna, Katowice, ISBN: 978-83-62001-36-1.
- MEGGYES T., HOLZLOHNER U., AUGUST H., 1998, A multidisciplinary approach to improving the safety and durability of landfill barriers, In Contaminated and derelict land (Sarsby R.W. (ed)), Kraków. Thomas Telford, London, 413–420.
- NOWAK A. K., 2008, Ekologiczno-techniczne aspekty pozyskiwania koncentratów cynku i ołowiu, Praca doktorska. Wdział Inżynierii i Technologii Chemicznej Politechnika Krakowska. Kraków.
- PASIECZNA A., LIS J., SZUWARZYŃSKI M., DUSZA-DOBEK A., WITKOWSKA A., 2008, Szczegółowa mapa geochemiczna Górnego Śląska 1:25 000, Arkusz Chrzanów, Państwowy Instytut Geologiczny, Warszawa.
- PULS R. W., POWELL M. R., BLOWES D. W., GILLHAM R. W., SCHULTZ D., SIVAVEC T., VOGAN J. L., POWELL P. D., 1998, Permeable reactive barrier technologies for contaminant remediation, Washington: United States Environmental Protection Agency.
- ROEHL K. E. et al., 2005, Permeable reactive barriers; Long-term Performance of Permeable Reactive Barriers, editors: K.E. ROEHL, T. MEGGYES, F. G. SIMON, D. I. STEWART, ELSEVIER Vol.7, ISBN: 0-444-51536-4.
- ROEHL K. E., HETTENLOCH P., CZURDA K., 2000, Permeable sorption barriers for in-situ remediation of polluted groundwater reactive materials and reaction mechanisms, Proceedings of the 3rd International Symposium on Geotechnics Related to the European Environment, Berlin. Thomas Telford, London, 465–473.
- SCHULZE E. D., MOONEY H. A.(Eds.), 1994, Biodiversity and Ecosystem Function, Springer-Verlag. Berlin Heidelberg.
- SUPONIK T., 2008, The use of waste from iron finishing in groundwater treatment, Górnictwo i Geologia vol. 3, no. 3, The Publishing House of the Silesian University of Technology, 61–70.
- SUPONIK T., 2010, Ensuring Permeable Reactive Barrier Efficacy and Longevity, Archives Of Environmental Protection, vol.36, no.3, 59–73.

- SUPONIK T., LUTYŃSKI M., 2009, Possibility of Using Permeable Reactive Barrier in Two Selected Dumping Sites, Archives Of Environmental Protection, vol.35, no.3, 109–122.
- U.S. DEPARTMENT OF ENERGY, 1998, Research and Application of Permeable Reactive Barriers, Grand Junction Office.
- WILKIN R. T., PULS R.W., 2003, Capstone report on the application, monitoring, and performance of permeable reactive barriers for ground-water remediation, Vol-1, Office of Research and Development, US EPA, Cincinnati.

Received July 5, 2011; reviewed; accepted August 5, 2011

SYNTHESIS AND CHARACTERISATION OF SiO₂/POSS HYBRID SYSTEMS OBTAINED USING THE MECHANICAL METHOD

Karolina SZWARC *, Katarzyna SIWINSKA-STEFAŃSKA *,
Bogdan MARCINIEC **, Teofil JESIONOWSKI *

* Poznan University of Technology, Institute of Chemical Technology and Engineering, M. Skłodowskiej–Curie 2, PL-60965, Poznan, Poland, Teofil.Jesionowski@put.poznan.pl, phone: +48(61)6653720, fax: +48(61)6653649

** Adam Mickiewicz University, Department of Organometallic Chemistry, Faculty of Chemistry, Grunwaldzka 6, PL-60780, Poznan, Poland

Abstract. Hybrid systems of silica and polyhedral oligomeric silsesquioxanes (SiO₂/POSS) were obtained by the mechanical method with the use of spherical or hydrated silicas, precipitated in the emulsion or aqueous environment. The SiO₂ surface was modified with the following cage silsesquioxanes: hepta(isobutyl)2-triethoxysilylethyloctasilsesquioxane, octakis ({3-glycidoxy-propyl}dimethylsiloxy)octasilsesquioxane and octakis ({3-methacryloxypropyl}dimethylsiloxy)-octasilsesquioxane. The nanofillers obtained were subjected to thorough dispersive analysis (NIBS method) and morphological analysis (transmission electron microscopy). Their wettability in water systems was evaluated and their adsorption activity was characterised by determination of the specific surface area BET, pore diameters and volume. Thermal stability of the nanofillers was checked. The effect of surface modification on the degree of coverage was assessed on the basis of elemental analysis.

keywords: SiO₂, hybrid nanofillers, polyhedral oligomeric silsesquioxanes, mechanical treatment, surface morphology

1. Introduction

Nanotechnology is a new highly attractive field of science that combines the achievements in chemistry, physics, biotechnology, informatics and material science (Makles, 2005; Swiderski, 2008). It includes fundamental studies and application at either molecular or atomic levels. The size of nanoparticles varies from 1 to 100 nm (Huang, 2010). Mineral nanomaterials are commonly used as fillers of polymer composites and their addition improves certain important parameters of the composites like thermal stability (Swiderski, 2008). Extended range of application of polymer materials has stimulated the need for new and versatile materials of improved properties. The search for new nanofillers has led to development of new organic-

inorganic hybrid materials such as polyhedral oligomeric silsesquioxanes (POSS).

POSS are described by the chemical formula of $(\text{RSiO}_{1.5})_n$ (Carmo do Ribeiro, 2007) and are intermediates between silica SiO_2 and silicones RSiO (Iyer, 2007). The R group localised at the corners of the cage can be an arbitrary organic substituent.

Hybrid-ceramic structure of oligosilsesquioxanes ensures high thermal stability and makes it possible to maintain the original mechanical properties of these compounds while in polymer composites (DeArmitt, 2008).

Moreover, the compounds have a wide range of melting points and decomposition temperatures and very low volatility (Chiu, 2010).

Silica which is the main skeleton or matrix of silsesquioxanes is the most common component of the Earth crust. It occurs in the amorphous or crystalline (quartz, tridymite) forms (Oldenburg, 1998; Westcott, 1998). Silica has been widely applied in nanotechnology, glass production, electronic industry, construction industry and many other areas. It is highly stable, chemically inert, shows high mechanical strength and high susceptibility to modifications (Georgakilas, 2008). Functionalisation of silica particles has been proved very successful and has been most often performed with silane proadhesive compounds, polymers and single metal atoms (Oldenburg, 1998; Westcott, 1998).

The hitherto achievements in functionalisation of the surface of silica fillers have prompted the attempts at modification of silica surface with oligosilsesquioxanes by the mechanical method and production of SiO_2 /POSS type hybrid systems as a new class of nanofillers. The study is aimed at an attempt of binding POSS compounds to the silica surface to get the best possible adhesion and/ or chemical interactions between the support and the modifier. So far no such attempts have been made.

2. Experimental

POSS compounds were obtained by a two-stage synthesis including the “corner capping” and hydrosilylation reactions performed in the same conditions over a Karstedt catalyst in the amount of $1 \cdot 10^{-5}$ mol Pt/mol Si–H and toluene or tetrahydrofuran (THF) as a solvent. The syntheses of monosubstituted and octasubstituted oligosilsesquioxanes are presented in Figs. 1 and 2 (Dutkiewicz, 2009; Marciniak, 2010).

The process of hybrid production was begun with obtaining silica under laboratory conditions in the quarter-technical scale.

The silica precipitation process was preceded by preparation of two emulsions, of which the alkaline one (E1) contained appropriate volume of sodium silicate solution and cyclohexane. The other was an acidic emulsion (E2) and contained hydrochloric acid and an organic solvent. The third component of both emulsion involved the same emulsifier, added to the emulsions in various amounts. Emulsion E2 was placed in a reactor and emulsion E1 was introduced in doses to the reactor while its entire content was mixed using a homogeniser. The precipitated silica was destabilised and then, the organic solvent was distilled off.

Another sample of silica was precipitated from water solution. A 5% solution of sodium silicate and a 5% solution of sulphuric acid were added in doses to aqueous solution of the hydrophobising agent (unsaturated fatty alcohol of a medium degree of oxyethylenation 7). The coagulating agent added to this reaction mixture was sodium sulphate. The product of the reaction was white silica precipitate, which was separated from the post-reaction mixture by vacuum filtration. The precipitate was washed a few times with hot water to remove the residues of the post-reaction salt and the surfactant, then the precipitate was subjected to convection drying at 105°C for 24h.

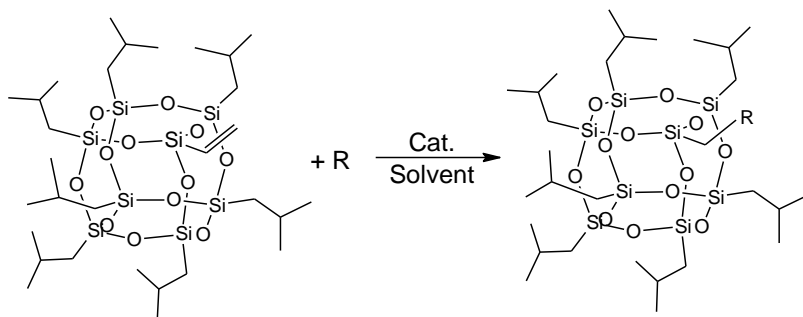


Fig. 1. Synthesis of monosubstituted polyhedral oligomeric silsesquioxanes

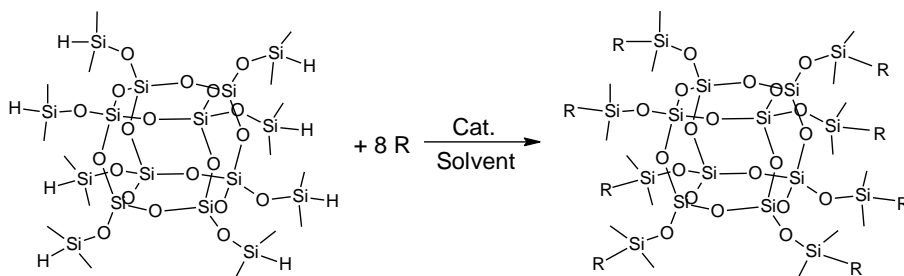


Fig. 2. Synthesis of octasubstituted polyhedral oligomeric silsesquioxanes

The hybrid nanofillers of SiO₂/POSS type were obtained by the mechanical method in an electric mortar RM 100 made by Retsch. A portion of silica precipitated in the emulsion or water system was placed in the mortar and then a mixture of POSS and 10 cm³ of toluene was introduced by a peristaltic pump PP1B-05A made by Zalimp, at a constant rate of 0.3 cm³/min. The modifying mixture was introduced in the amounts of 3, 5 or 10 weight parts by mass of SiO₂. After introduction of the whole portion of the mixture the contents were ground for 30 minutes. Then, the whole content was moved to a flask of 500 cm³ in capacity and placed in a vacuum evaporator Rotavapor RII made by Büchi Labortechnik AG to remove the solvent. The final step was drying by convection at 120°C for 48 h (chamber drier SEL-I3, made by Memmert). The method of obtaining the hybrid nanofillers is schematically illustrated in Fig. 3.

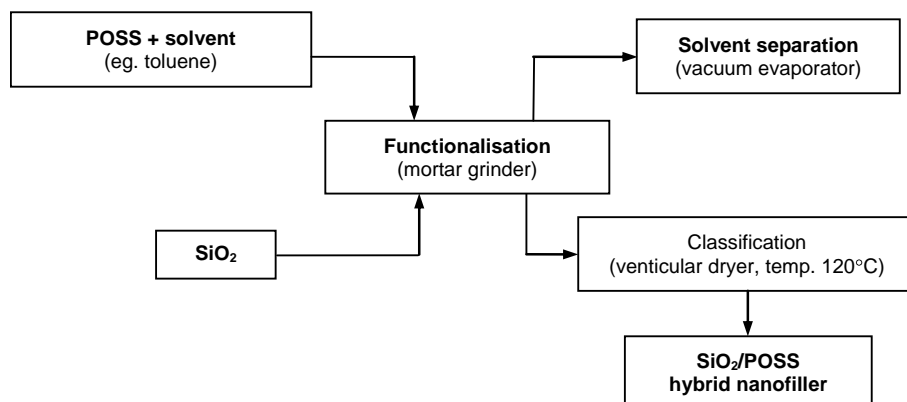


Fig. 3. Scheme of functional nanofillers mechanical preparation

The final product was accurately characterised by a number of methods. The particle size distributions of the samples were measured by a Zetasizer Nano ZS, made by Malvern Instruments Ltd., enabling measurements in the range 0.6–6000 nm (NIBS method). Microstructures of the samples were analysed in the images obtained by the transmission (TEM Joel, 1200 EX II) and scanning electron microscopy (SEM Zeiss, VO40). The wettability with water was measured by a tensiometer K100 made by Krüss equipped with necessary attachments. For selected hybrid systems the nitrogen adsorption/desorption isotherms were recorded using an ASAP 2020 analyser, made by Micromeritics Instrument Co., to measure the specific surface area BET (S_{BET}) and then obtain the pore diameter (S_p) and volume (V_p). Thermal stability of the nanomaterials obtained was assessed by thermogravimetric analysis TG/DTA (Jupiter STA 449 F3, Netzsch). The degree of coverage was evaluated on the basis of the Berendsen and de Golan formula (Berendsen, 1978), on the basis of the data from the elemental analysis (Vario EL Cube, Elementar) and specific surface area of the initial silica.

3. Results and discussion

Hybrid nanofillers were prepared on the basis of silica obtained either in the emulsion or aqueous system. The modifying substances were some monosubstituted cage silsesquioxanes hepta(isobutyl)2-triethoxysilylethyl octasilsesquioxane (K-POSS), and octasubstituted ones octakis ({3-glycidoxypropyl}dimethyl-siloxy) octasilsesquioxane (G-POSS) and octakis ({3-methacryloxypropyl }-dimethylsiloxy) octasilsesquioxane (M-POSS). The initial silicas precipitated in the emulsion or water systems were functionalised with the cage silsesquioxanes by the mechanical method. Table 1 presents results of measurements of the dispersive and physico-chemical parameters.

Table 1. Dispersive and physico-chemical properties of hybrid nanofillers made of silica precipitated in the emulsion or water systems and cage silsesquioxanes

| Sample No. | Hybrid nanofillers | | Dispersive properties | |
|------------|--------------------|--|-----------------------------------|---|
| | Acronym | Amount of POSS modifiers (weigh parts) | Bulk density (g/dm ³) | Particle diameter from Zetasizer Nano ZS (nm) |
| 1 | KU | – | 212 | 91–220; 3090–6440 |
| 2 | M-KU-G3 | 3 | 274 | 59–142; 1990–6440 |
| 3 | M-KU-G5 | 5 | 260 | 68–164; 825–1720; 2300–6440 |
| 4 | M-KU-G10 | 10 | 257 | 79–190; 1990–6440 |
| 5 | M-KU-M3 | 3 | 275 | 106–190; 3580–6440 |
| 6 | M-KU-M5 | 5 | 270 | 91–164; 2670–6440 |
| 7 | M-KU-M10 | 10 | 268 | 79–220; 2300–6440 |
| 8 | M-KU-K3 | 3 | 252 | 79–220; 1110–6440 |
| 9 | M-KU-K5 | 5 | 248 | 91–142; 2670–6440 |
| 10 | M-KU-K10 | 10 | 233 | 122–220; 4150–6440 |
| 11 | KE | – | 273 | 295–825 |
| 12 | M-KE-G3 | 3 | 331 | 142–295 |
| 13 | M-KE-G5 | 5 | 332 | 122–295 |
| 14 | M-KE-G10 | 10 | 339 | 106–1480 |
| 15 | M-KE-M3 | 3 | 342 | 142–459 |
| 16 | M-KE-M5 | 5 | 345 | 122–396 |
| 17 | M-KE-M10 | 10 | 347 | 164–396; 2300–4800 |
| 18 | M-KE-K3 | 3 | 337 | 164–459 |
| 19 | M-KE-K5 | 5 | 351 | 164–531 |
| 20 | M-KE-K10 | 10 | 380 | 142–1110 |

The hybrids obtained by the mechanical method have non-uniform structure. Nevertheless, the final effect is satisfactory as the hybrids show a high degree of refinement and contain particles of very small diameters (~200 nm) thanks to the use of a mortar. The unmodified silica obtained in the water system (amorphous) (Sample 1) as well as that obtained in the emulsion system (Sample 11) are characterised by the lowest bulk densities. After the surface functionalisation, the samples based on silica precipitated in the water system have bulk densities from 233 to 274 g/dm³. For the hybrids based on silica precipitated from the emulsion system the bulk densities are even higher and vary from 331 g/dm³ (Sample 12) to 380 g/dm³ (Sample 20). The best dispersive features were obtained for the hybrids made of silica of either type and octakis({3-glycidoxypropyl}dimethylsiloxy)octasil- sesquioxanes. The amorphous hydrated silica shows great refinement because of its hydrophilic character. Figures 4 and 5 present the particle size distribution and TEM images of the unmodified hydrated silica and the hybrid made of this silica functionalised with 5 wt./wt. of octakis({3-glycidoxypropyl}dimethylsiloxy)- octasilsesquioxane (Samples 1 and 3). Figures 4a and 5a present bimodal particle size distribution for sample 1, with two bands covering the diameter ranges 91–220 and 3090–6440 nm. The TEM image shows particles of irregular surface having a high tendency to formation of secondary agglomerates.

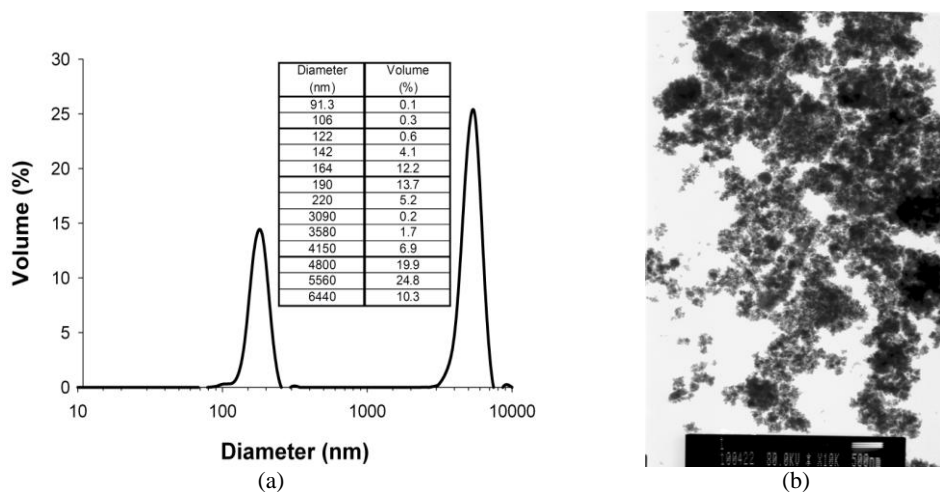


Fig. 4. (a) Particle size distribution (Zetasizer Nano ZS) and (b) TEM microphotograph of unmodified hydrated silica

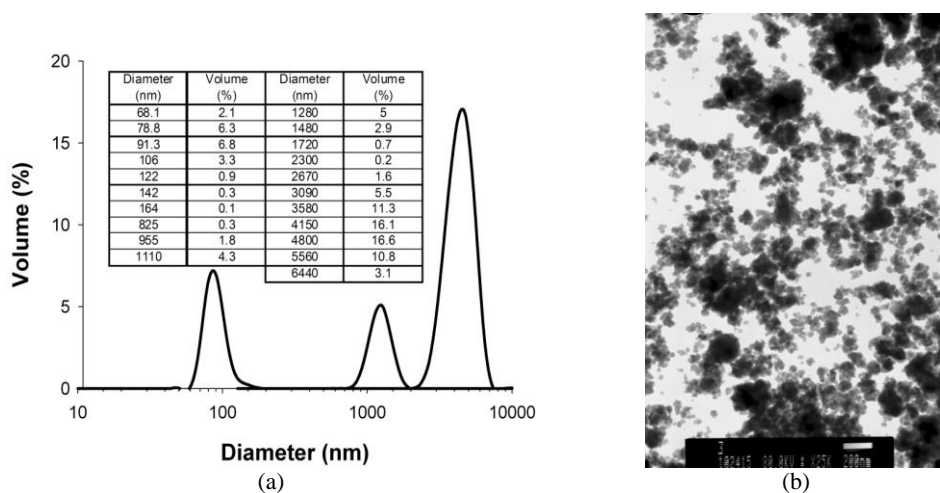
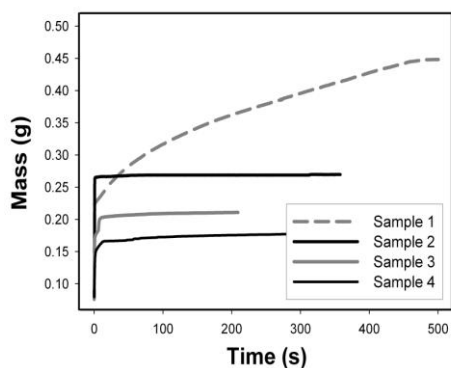


Fig. 5. (a) Particle size distribution (Zetasizer Nano ZS) and (b) TEM microphotograph of hydrated silica modified with 5 wt./wt. of octakis({3-glycidoxypropyl}dimethylsiloxy)octasilsesquioxane

Sample 3 has much different dispersive and morphological features. The particle size distribution in Fig. 5a displays three bands covering the diameter ranges 68–164, 825–1720 and 2300–6440 nm. The TEM (Fig. 5b) image reveals highly refined particles with a low tendency to agglomeration.

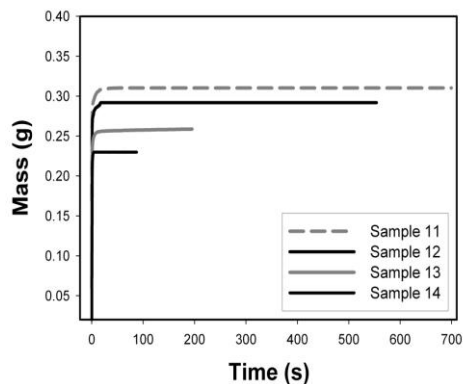
The hybrid systems functionalised with octakis({3-glycidoxypropyl}-dimethylsiloxy)octasilsesquioxane was also subjected to determination of wettability. Figure 6 presents the wettability profiles of the initial hydrated silica and the hybrids

obtained with 3, 5 or 10 wt./wt. of POSS (Samples 1–4). Figure 7 shows the wettability profiles of the silica obtained by precipitation in the emulsion system and the hybrids obtained on its basis (Samples 11–14). The highest tendency to water absorption was noted for Sample 1 (0.45 g), while the lowest for Sample 4 functionalised with 10 wt./wt. G-POSS (0.17 g). As follows from the character of the wettability curves, increase in the amount of the modifying substances enhances the hydrophobicity of the product which should have beneficial effect for its application as polymer filler.



(a)

Fig. 6. Profiles of wettability with water recorded for the initial hydrated silica and selected SiO₂/POSS hybrid systems



(b)

Fig. 7. Profiles of wettability with water recorded for the initial silica precipitated in the emulsion system and selected SiO₂/POSS hybrid systems

The tendency to water absorption was also observed for the hybrid systems based on the silica precipitated from the emulsion system. From among these samples the greatest sorption of 0.32 g was noted for Sample 11, while the lowest for Sample 14 obtained after modification with 10 wt./wt. of octakis({3-glycidoxypropyl}dimethylsiloxy)octasilsesquioxanes. To verify the right course of modification the adsorption activity was evaluated on the basis of nitrogen adsorption/desorption. Analysis of the isotherms recorded for SiO₂/POSS fillers permitted determination of specific surface area, pore diameter and pore volume (see Table 2). The specific surface area of the initial amorphous silica is 110 m²/g. Functionalisation of the silica surface with POSS led to a significant decrease in the surface activity as the specific surface area decreased to 24–41 m²/g. This effect is a consequence of blocking the active centres on the SiO₂ surface by the molecules of oligosilsesquioxanes. According to pore size, the materials were classified as mesoporous.

Figure 8 presents the adsorption/desorption isotherms obtained for the unmodified silicas of both types and the hybrids functionalised with 10 wt./wt. G-POSS. A systematic increase in the relative pressure and in the volume of adsorbed nitrogen

was noted with a maximum value of $240 \text{ cm}^3/\text{g}$ for Sample 1 at $p/p_0=1$. For the hybrids, the increase in the volume of adsorbed nitrogen after the threshold value was much smoother and the maximum values reached at $p/p_0=1$ were much lower.

Table 2. Adsorptive properties of unmodified hydrated and emulsion silicas and hybrid nanofillers modified with octakis({3-glycidoxypropyl}dimethylsiloxy)octasilsesquioxane in different amounts

| Sample No. | BET surface area, S_{BET} (m^2/g) | Total volume of pores, V_p (cm^3/g) | Mean size of pores, S_p (nm) |
|------------|--|---|--------------------------------|
| 1 | 110 | 0.37 | 13 |
| 2 | 41 | 0.02 | 3 |
| 3 | 34 | 0.02 | 3 |
| 4 | 24 | 0.02 | 3 |
| 11 | 40 | 0.17 | 16 |
| 12 | 24 | 0.01 | 2 |
| 13 | 17 | 0.01 | 2 |
| 14 | 8 | 0.01 | 2 |

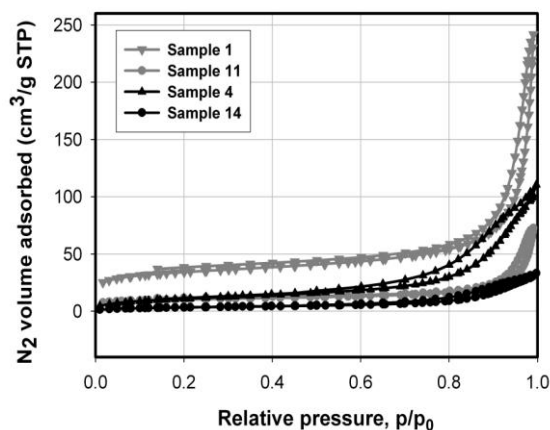


Fig. 8. Nitrogen adsorption/desorption isotherms for the unmodified silica of two types (Samples 1 and 11), and for the samples functionalised with 10 wt./wt. of octakis({3-glycidoxypropyl}dimethylsiloxy)octasilsesquioxanes (Samples 4 and 14)

Thermal stability of the unmodified silica and selected hybrids functionalised with octakis({3-glycidoxypropyl}dimethylsiloxy)octasilsesquioxanes was evaluated on the basis of thermogravimetric analysis. Measurements were made in the nitrogen atmosphere at temperature changed from 25 to 1000°C at a step of $10^\circ\text{C}/\text{min}$. The thermogravimetric (TGA) curves obtained are presented in Figs. 9 and 10.

Decomposition of hydrated silica (Sample 1) begins already at 25°C and occurs in a single step (Fig. 9). The mass loss observed in the range $25\text{--}150^\circ\text{C}$ is rather abrupt. Above 700°C the sample gets stabilised and its mass almost does not change. In the temperature range $25\text{--}1000^\circ\text{C}$, pure hydrated silica loses only 10% of the total mass. The process of degradation of the hybrids takes place in two steps, the first is related to the loss of water and the second to the decomposition of the functional groups in the corners of the silsesquioxane cage. Figure 10 shows the TGA curve for the unmodified silica precipitated in the emulsion system and based on it hybrids modified with 3 wt./wt. and 10 wt./wt. of G-POSS, recorded on heating. Decomposition of Sample 11 run at two steps, in contrast to that of Sample 1. The first mass loss noted in the range from about 25 to about 300°C is most probably related to the loss of water. In this range the mass loss reaches a little more than 8%. For the hybrids obtained as a result of modification with 3 or 10 wt./wt. G-POSS the TGA curves display two inflection points: the first at about 300°C and the second at about 325°C .

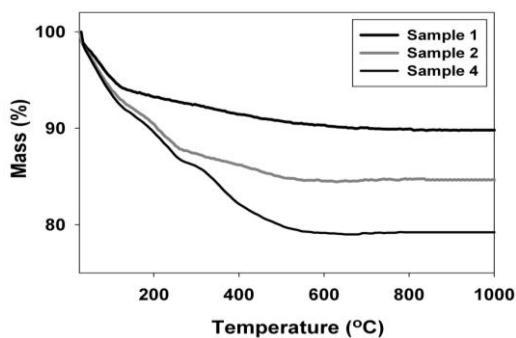


Fig. 9. TGA curves for the unmodified hydrated silica (Sample 1) and hybrids functionalised with octakis ({3-glycidoxypropyl} dimethylsiloxy)octasilsesquioxanes (Samples 2 and 4)

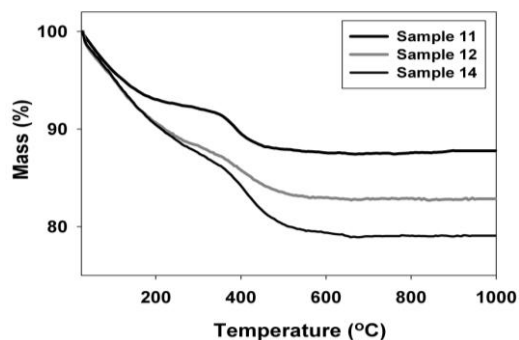


Fig. 10. TGA curves recorded for the unmodified silica precipitated in the emulsion system (Sample 11) and for the samples functionalised with octakis ({3-glycidoxypropyl} dimethylsiloxy) octasilsesquioxanes (Samples 12 and 14)

It is presumed that the first temperature corresponds to the beginning of degradation of the organic substituents at the silica atoms in POSS skeleton. Until reaching 600°C a considerable mass loss is observed, above this temperature the mass loss is slight. In the range from 25 to 1000°C Sample 14 loses a bit over 20% of the total mass.

Elemental analysis of the samples studied (Figs. 11 and 12) has proved that the content of carbon increased with increasing mass of the POSS modifier, which was also related to increasing degree of surface coverage. The latter parameter was calculated from the Berendsen and de Golan formula.

The hybrid systems (Fig. 11) obtained as a result of functionalisation with octakis({3-glycidoxypropyl}dimethylsiloxy)octasilsesquioxane have the highest percent content of carbon. For Sample 4 the carbon content is 5%, while the degree of

coverage for the same sample is $0.738 \mu\text{mol}/\text{m}^2$. The smallest degree of coverage was found for the hydrated silica functionalised with octakis({3-glycidoxypropyl}dimethylsiloxy)octasilsesquioxanes (Samples 5-7). The hybrids obtained on the basis of the silica precipitated from the emulsion system showed a similar tendencies (see Fig. 12).

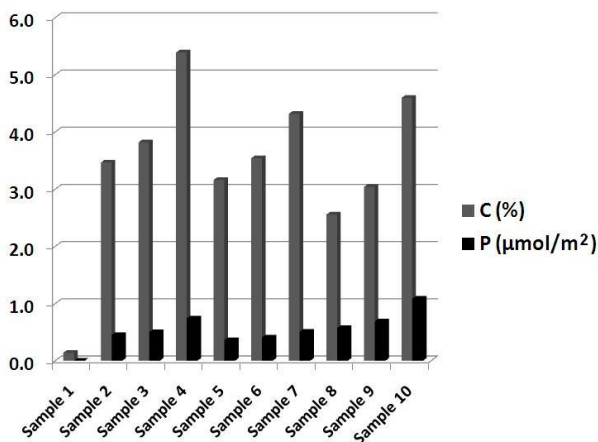


Fig. 11. Carbon content and coverage degree for the unmodified hydrated silica and based on it functionalised hybrids

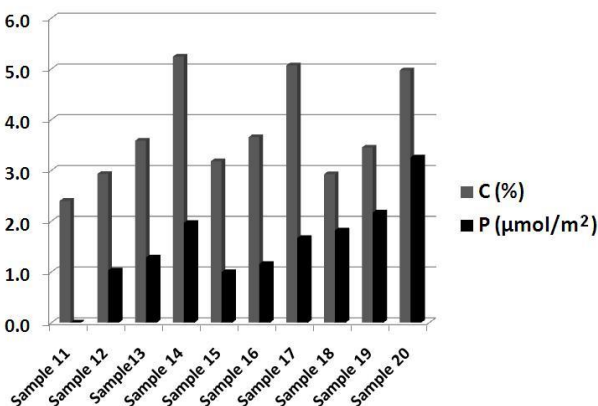


Fig. 12. Carbon content and coverage degree measured for the unmodified silica precipitated in the emulsion system and based on it hybrids

4. Conclusions

The products obtained by the proposed method of mechanical modification in general had more beneficial dispersion properties than the pure silicas. Functionalisation of the silica surface with G-POSS gave hybrid materials made of

smaller size particles than those of the silica, irrespective of the amount of the modifier used. With increasing amount of the POSS modifier, the products revealed increasing hydrophobicity, which is beneficial from the point of view of their application as polymer fillers.

The specific surface area BET was observed to decrease from 110 m²/g for the unmodified silica to 24 m²/g for some hybrids. Thermal stability of the hybrids was found to depend on the thermal degradability of the functional groups of the silsesquioxanes used. Modification of silica surface with POSS leads to an increase in the degree of coverage, which is reflected in the percent content of carbon in the hybrids. This increase is particularly pronounced for the samples functionalised with octakis({3-glycidoxypropyl}dimethylsiloxy)octasilsesquioxanes.

Acknowledgements

The study was realised within the Development Project POIG 01.03.01-30-173/09 Nanosil from the European Fund of Regional Development within the operation programme Innovative Economy.

References

- BERENDSEN G.E., de GOLAN L., 1978, Preparation and chromatographic properties of some chemically bonded phases for reversed-phase liquid chromatography, *Journal of Liquid Chromatography*, 1, 561–586.
- CARMO DO RIBEIRO D., FILHO DIAS L.N., PAIM L.L., STRADIOTTO R.N., 2007, Preparation, characterization and application of a nanostructured composite: octakis(cyanopropyl dimethylsiloxy)octasilsesquioxanes, *Applied Surface Science*, 253, 3683–3689.
- CHIU Y-C., RIANG L., CHOU I-C., MA C-C.M., CHIANG C-L., YANG C-C., 2010, The POSS side chain epoxy nanocomposite: Synthesis and thermal properties, *Journal of Polymer Science, Part B*, 48, 643–652.
- DeARMITT CH., WHEELER P., 2008, POSS - keeps high temperature plastics flowing, *Plastics Additives and Compounding*, 10, 36–39.
- DUTKIEWICZ M., MACIEJEWSKI H., MARCINIEC B., 2009, Functionalization of polyhedral oligomeric silsesquioxane (POSS) via nucleophilic substitution, *Synthesis*, 12, 2019–2024.
- GEORGAKILAS V., BOURLINOS A.B., ZBORIL R., TRAPALIS C., 2008, Synthesis, characterization and aspects of superhydrophobic functionalized carbon nanotubes, *Chemistry of Materials*, 20, 2884–2886.
- HUANG F.W., HUANG F.R., ZHOU Y., DU L., 2010, Thermal properties of new bismaleimide resins containing hydrogen silsesquioxane and diallyl Bisphenol A, *Journal of Applied Polymer Science*, 117, 2932–2936.
- IYER S., ABU-ALI A., DETWILER A., SEHIRALDI A., 2007, Transparent polymer – polyhedral oligomeric silsesquioxane composites, *ACS Symposium Series (Science and Technology of Silicones and Silicone-Modified Materials)*, Cleveland, 964, 313–325.
- MAKLES Z., 2005, Nanomateriały – nowe możliwości, nowe zagrożenia, *Bezpieczeństwo Pracy - Nauka i Praktyka*, 2, 2–4.
- MARCINIEC B., 2010, Funkcjonalizowane oktasilseskwioxany klatkowe (T8) jako podstawa hybrydowych nanokompozytów polimerowych, *Przemysł Chemiczny*, 89, 1184–1187.
- OLDENBURG S.J., AVERITT R.D., WESTCOTT S.L., HALAS N.J., 1998, Nanoengineering of optical resonances, *Chemical Physics Letters*, 288, 243–247.

- ŚWIDERSKI F., ROBAK-WASZKIEWICZ B., Nanotechnologia – korzyści i zagrożenia zdrowotne, Bromatologia i Chemia Toksykologiczna, 3, 202–208.
- WESTCOTT S., OLDENBURG S., LEE T.R., HALAS N.J., 1998, Formation and adsorption of gold nanoparticle-cluster on functionalized silica nanoparticle surfaces, Langmuir, 14, 5396–5401.

Received July 20, 2011, reviewed, accepted August 25, 2011

PREPARATION AND PHOTOCATALYTIC ACTIVITY OF IRON-MODIFIED TITANIUM DIOXIDE PHOTOCATALYST

Marta LEZNER, Ewelina GRABOWSKA, Adriana ZALESKA

Department of Chemical Technology, Faculty of Chemistry, Gdansk University of Technology, Gdansk, Poland, e-mail: adriana.zaleska@pg.gda.pl

Abstract. Iron modified TiO₂ was prepared by the sol-gel method and surface modification method followed by calcination at 400°C. Two types of titanium dioxide: TiO₂ ST-01 (Ishihara Sangyo Ltd., Japan; 300 m²/g), and TiO₂ P25 (Evonik, Germany, 50 m²/g) were used in the grinding procedure. The photocatalysts were characterized by UV-VIS absorption and BET surface area measurements. The photocatalytic activity of the obtained powders in UV-Vis and visible light was estimated by measuring the decomposition rate of phenol (0.21 mmol/dm³) in an aqueous solution. The best photoactivity under visible light was observed for iron doped TiO₂ with 0.5% by grinding the TiO₂ ST-01.

keywords: photocatalysis, modified TiO₂, iron nanoparticles, photocatalysis

1. Introduction

The process of photocatalysis using semiconductor suspension is a method widely used in environmental protection. One of the most commonly used photocatalysts, due to its characteristics (inexpensive, insoluble under most conditions, photochemically stable and non toxic), is titanium dioxide used, *inter alia*, for the elimination of organic substances from gas and liquid phases and recently also for reduction of CO₂ into the light hydrocarbons. Since pure TiO₂ absorbs UV almost exclusively, most of the work carried out in the world is focused on obtaining TiO₂ active under visible light. Modification of metals may increase the activity of titanium oxide(IV) in the range of visible light ($\lambda > 400$ nm), and thus allows the use of renewable energy - solar radiation in the environment (Valenzuela et al., 2009). Among various dopants, the Fe³⁺-dopant is the most frequently employed one, owing to its unique half-filled electronic configuration, which narrows the energy gap while inducing new intermediate energy levels and may also diminish the recombination of electrons and holes by capturing photogenerated carriers (Liu et al., 2011; Zhou et al., 2006). Liu et al. (2011) proposed the possible mechanism of Fe³⁺-dopant effect on photocatalytic activities. According to the energy level chart of Fe³⁺-dopants in TiO₂ proposed by

previous researches, the $\text{Fe}^{3+}/\text{Fe}^{2+}$ energy level is just below the conduction band of TiO_2 while the $\text{Fe}^{3+}/\text{Fe}^{4+}$ energy level is slightly above the valence band of TiO_2 . The Fe^{3+} -dopant can act not only as a temporary trapping site of photo-induced electrons but also as a shallow capturing site of photo-induced holes, which will efficiently separate the photo-excited electrons and holes and prolong their lifetime. Furthermore, according to the viewpoint of crystal field theory, the Fe^{3+} -dopant is more stable in TiO_2 because of its $3d^5$ (half-filled high spin) electronic configuration, so the captured electrons or holes can be easily released from Fe^{2+} or Fe^{4+} to regenerate Fe^{3+} and then migrate to the photocatalysts' surface to initiate the photocatalytic reactions. On the other hand, Fe^{3+} -dopant effectively extends the UV-Vis spectra of TiO_2 into visible light region (Liu et al., 2011).

Synthetic iron oxide magnetite (Fe_3O_4) nanoparticles have been widely studied in the last decades, and an increasing number of scientific and technological applications have been developed, such as catalysts, pigments, gas sensors, biotechnology, and data storage solid support for enzymes, such as cellulase, glucose oxidase, bovine serum albumin homing peptides and lipase. Magnetite bounded to chitosan acts as a nano-absorbant for the removal of heavy metals, and when using a highly active heterogeneous Fenton system based on iron metal and magnetite, $\text{Fe}^0/\text{Fe}_3\text{O}_4$ has been used to oxidize synthetic dyes (Valenzuela et al., 2009; Jiao et al., 2010). Hematite nanoparticles are an interesting material for fundamental research because of their magnetic characteristic (Zboril et al., 2002). They can display three critical temperatures: Neel temperature, Morin temperature and blocking temperature (Zysler et al., 2001).

Recently, several methods have been developed to prepare Fe_2O_3 - TiO_2 composites, which usually exhibit improved properties. Liu et al. (2011) prepared the Fe-doped TiO_2 nanorod clusters and monodispersed nanoparticles by a modified hydrothermal and solvothermal method. The well-controlled microstructures and morphologies enhance specific surface areas of the Fe-doped TiO_2 photocatalysts compared with P25 and N-doped TiO_2 nanoparticles. High photocatalytic activities of the Fe-doped photocatalysts could be related to enhanced specific surface areas, visible light responses and diminish recombination rates of the photo-excited carriers (Liu et al., 2011).

Shi et al. (2011) obtained co-doped titanium dioxide (Fe-La- TiO_2) photocatalysts by a sol-gel method. Co-doping causes absorption spectra of Fe-La- TiO_2 to shift to the visible region and photocatalytic activity of Fe,La- TiO_2 is markedly improved due to the cooperative action of the two dopants, Fe and La (Shi et al., 2011). Iron(III)-doped titanium dioxide photocatalysts from aqueous titanium(III) chloride solution in the presence of dissolved FeCl_3 (0–10.0 at.% relative to TiCl_3) by the co-precipitation method were prepared by Ambrus et al. (2008). The photocatalytic efficiency of iron-doped titanias was found to be superior to the bare TiO_2 under UV-Vis irradiation. The photocatalyst with 3.0 at.% iron was the most efficient for the photocatalytic decomposition of phenol in UV-vis experiments. The optimal iron content was found

to be 1.2 at.% for VIS light irradiation. At higher iron contents (6.0– 10.0 at.%) the photocatalytic performance under Vis irradiation was worse relative to the undoped TiO_2 (Ambrus et al., 2008).

When titania suspensions are used, the photocatalyst must be recovered at the end of the treatment, either by filtration or sedimentation, which is expensive in terms of time and reagents. The aim of this study was to develop a method for obtaining TiO_2 modified with magnetic iron oxide (Fe_2O_3) nanoparticles and to characterize the obtained photocatalysts. BET surface area measurements, UV-Vis spectroscopy and photooxidation of phenol (under UV-Vis and visible light) were used to characterize and evaluate the photocatalytic activity of the obtained samples.

2. Materials and methods

ST-01 TiO_2 powder having anatase crystal structure was obtained from Ishihara Sangyo, Japan (anatase, surface area $300 \text{ m}^2/\text{g}$, particle size 7 nm) and P-25 from Evonik GmbH, Germany (anatase:rutile = 80:20, surface area $50 \text{ m}^2/\text{g}$, particle size 8 nm). Titanium(IV) isopropoxide, TIP, (97%) was obtained from Aldrich Chem. Fe_2O_3 nanoparticles (20 wt. % in ethanol, particle size < 110 nm) from Sigma-Aldrich Co. was used as iron source in the preparation procedure without further purification.

Gemini V (model 2365) was used for measurements of BET surface area of the catalysts. All the samples were degassed at 200°C prior to nitrogen adsorption measurements. BET surface area was determined by a multipoint BET method using the adsorption data in the relative pressure (P/P_0) range of 0.05–0.3.

The diffuse reflectance spectra DRS were characterized using the UV–Vis spectrometer (UVD 3500 Labomed, USA) equipped with an integrating sphere accessory for diffuse reflectance.

In the sol–gel method, Fe-doped TiO_2 catalysts were prepared from titanium(IV) isopropoxide, known to be the titanium source origin for the anatase-type TiO_2 . Titanium(IV) isopropoxide ($V = 20 \text{ cm}^3$) were mixed with an appropriate amount of the dopant precursor (solution of iron oxide in ethanol) and distilled water ($V = 35 \text{ cm}^3$). The solution was being stirred at room temperature for 30 min, followed by a 24-hour thermal treatment (80°C) and calcinations at 400°C for 2 h. The procedure is presented by a simplified block diagram in Fig. 1A.

In the second procedure iron-modified TiO_2 powders were prepared by grinding 3 g of either ST-01 TiO_2 or P25 TiO_2 in an agate mortar with iron oxide in ethanol. The obtained powders were dried for 24 h at the temperature of 80°C and calcinated at 400°C for 2 h.. The procedure is presented by a simplified block diagram in Fig 1B.

The photocatalytic activity was determined by measuring the decomposition rate of phenol (0.21 mM) aqueous solution which was selected as a model contaminant under UV-Vis and visible irradiation. Photocatalytic degradation runs were preceded by blind tests in the absence of a catalyst or illumination.

Twenty five milliliters of a photocatalyst suspension (125 mg) were stirred using magnetic stirrer and aerated ($5 \text{ dm}^3/\text{h}$) prior and during the photocatalytic process.

Aliquots of 1.0 cm^3 of the aqueous suspension were collected at regular time periods during irradiation and filtered through syringe filters ($\text{Ø} = 0.2 \text{ mm}$) to remove photocatalyst particles. Phenol concentration was estimated by a colorimetric method using a UV–Vis spectrophotometer. The suspension was irradiated using 1000 W Xenon lamp (Oriol), which emits both UV and Vis light. To limit the irradiation wavelength, the light beam was passed through GG 420 to cut-off wavelengths shorter than 420 nm.

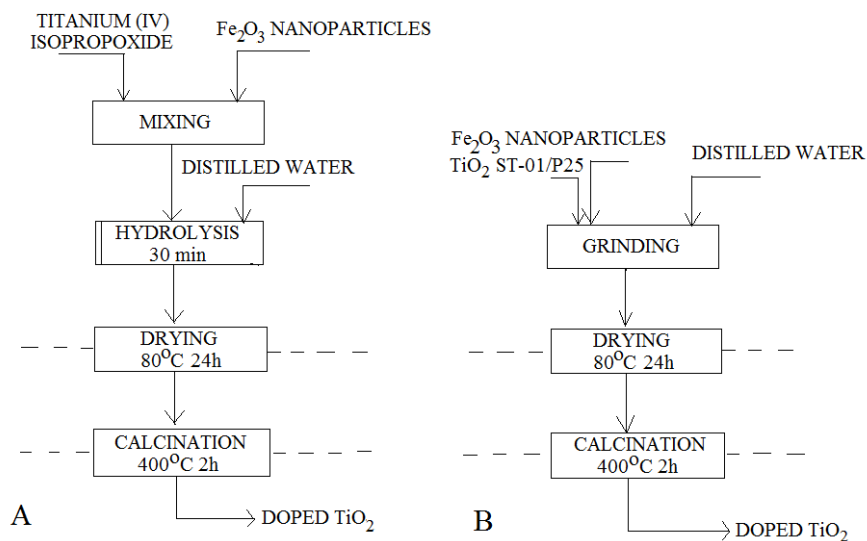


Fig. 1. Block diagram of Fe-doped TiO₂ prepared by (a) sol-gel method, (b) impregnation method

3. Result and discussion

The amount of the dopant taken for photocatalyst preparation was calculated on the assumption that the content of iron in the photocatalyst after synthesis should be equal to from 0.5 to 10 wt.% of the catalyst dry mass. Sample numbers, the amount of the dopant used during preparation, TiO₂ matrix and BET surface area are presented in Table 1. All the photocatalysts obtained in this work were in the form of orange powders.

Photocatalytic activity of the obtained TiO₂ powders was estimated by measuring the decomposition rate of phenol in aqueous solution in the presence of UV-Vis or visible light irradiation ($\lambda > 420 \text{ nm}$). No degradation of phenol was observed in the absence of either photocatalyst or illumination. Pure TiO₂ synthesized by the sol-gel method without any dopant, P25 TiO₂ and ST-01 TiO₂ were used as the reference system. Photocatalytic activity under UV-Vis or visible light is presented as phenol degradation rate (Table 1) and as efficiency of phenol removal after 60 min of irradiation (Fig. 2).

Table 1 . Surface properties and photocatalytic activity of iron-doped TiO₂ photocatalysts – the influence of dopant and preparation method

| Sample label | Metal precursor | TiO ₂ matrix ^a | Content of metal precursor [wt. %] | BET [m ² /g] | Phenol degradation rate [μmol·dm ⁻³ ·min ⁻¹] | |
|------------------|--------------------------------------|--------------------------------------|------------------------------------|-------------------------|---|----------------|
| | | | | | UV/Vis | Vis (λ>420 nm) |
| Fe(0,5)_H | Fe ₂ O ₃ /EtOH | TIP | 0.5 | 180 | 3.04 | 0.33 |
| Fe(1)_H | | | 1 | 166 | 2.54 | 0.26 |
| Fe(2)_H | | | 2 | 154 | 1.16 | 0.29 |
| Fe(3)_H | | | 3 | 152 | 1.26 | 0.19 |
| Fe(5)_H | | | 5 | 152 | 0.72 | 0.57 |
| Fe(10)_H | | | 10 | 143 | 0.87 | 0.09 |
| Fe(0,5)_ST | Fe ₂ O ₃ /EtOH | ST-01 | 0.5 | 215 | 3.04 | 2.00 |
| Fe(1)_ST | | | 1 | 149 | 2.01 | 0.76 |
| Fe(2)_ST | | | 2 | 151 | 1.96 | 0.54 |
| Fe(3)_ST | | | 3 | 140 | 1.15 | 0.85 |
| Fe(5)_ST | | | 5 | 129 | 1.49 | 0.78 |
| Fe(10)_ST | | | 10 | 129 | 1.48 | 0.22 |
| Fe(0,5)_P25 | Fe ₂ O ₃ /EtOH | P25 | 0.5 | 58 | 3.08 | 0.34 |
| Fe(1)_P25 | | | 1 | 53 | 3.80 | 0.23 |
| Fe(2)_P25 | | | 2 | 55 | 3.63 | 0.07 |
| Fe(3)_P25 | | | 3 | 56 | 2.92 | 0.39 |
| Fe(5)_P25 | | | 5 | 56 | 3.24 | 0.06 |
| Fe(10)_P25 | | | 10 | 62 | 2.36 | 0.09 |
| P25 | - | - | - | 50 (58 ^b) | 2.90 | 0.18 |
| ST-01 | - | - | - | 300 (278 ^b) | 2.82 | 0.50 |
| TiO ₂ | - | - | - | 161 | 3.07 | 0.16 |

^aTIP – TiO₂ obtained by titanium(IV) isopropoxide hydrolysis; P-25 – mixture of anatase and rutile with majority of anatase (particle size: 40 nm, S_{BET} = 50 m²/g, supplier: Evonik, Germany); ST-01 – anatase (particle size: 8 nm, S_{BET} = 300 m²/g, supplier: Ishihara Sangyo Ltd., Japan); ^b As-measured data

Doping with iron increases the photocatalytic activity under UV-Vis and visible light. Under UV-Vis light irradiation, the rate of phenol degradation in the presence of pure TiO₂ obtained by the sol-gel method, TiO₂ST01 and TiO₂ P25 was estimated to be 3.07, 2.92 and 2.82 μmol·dm⁻³·min⁻¹, respectively. The most active were the photocatalysts prepared by grinding TiO₂ P25 with a dopant. The observed rate was increased to 3.80 μmol·dm⁻³·min⁻¹ in the presence of Fe(1)_P25 doped with 1% wt. of iron. Iron modified TiO₂ST-01 and sol-gel TiO₂ showed slightly enhanced photocatalytic activities under UV-Vis irradiation as compared to pure TiO₂ST01 and sol-gel TiO₂. The highest phenol degradation rate was 3.04 μmol dm⁻³ min⁻¹ for the sample with 0.5% wt. of iron - Fe(0,5)_ST and Fe(0,5)_H prepared by grinding TiO₂ST01 and by the sol-gel method.

Photocatalysts prepared by surface impregnation of TiO₂ ST-01 showed the highest activity in the phenol degradation reaction under visible light than those used with other arrays of TiO₂.

Under visible light irradiation, the rate of phenol degradation in the presence of pure TiO₂ obtained by the sol-gel method, TiO₂ ST01 and TiO₂ P25 was estimated to be 0.52, 0.50 and 0.12 $\mu\text{mol}\cdot\text{dm}^{-3}\cdot\text{min}^{-1}$, respectively. The best photoactivity under visible light was observed for the sample prepared by grinding TiO₂ ST-01 with 0.5% wt. of iron. In the presence of the Fe(0.5)_ST sample, phenol was degraded in 61% after 60 min. of irradiation. Using the TiO₂P25 matrix, we could notice the lack of photocatalytic activity under visible light.

Figure 2 shows a comparison of characteristics of the most photoactive samples prepared using three types of TiO₂ matrix under UV-Vis (Fig. 2A) and visible (Fig. 2B) light. All the photocatalysts revealed the highest photoactivity under UV-Vis and visible light comparable to that of pure TiO₂.

The amount of the dopant also influenced the specific surface area BET of the obtained photocatalysts (Table 1). The specific surface area of pure TiO₂, obtained by TIP hydrolysis, TiO₂ ST-01 and TiO₂ P25 was 161, 278 and 58 m²/g, respectively. The value of BET surface area generally decreases with increasing of iron concentration (Table 1). For all the samples prepared by the surface impregnation method the BET surface area was lower than that for pure TiO₂ST-01 and ranged from 129 to 215 m²/g. Not too much difference in the surface area was observed for the samples obtained by surface impregnation of TiO₂ P25 (the surface area varied from 53 to 62 m²/g). For the samples obtained by the sol-gel method, the surface area decreased from 180 to 143 m²/g since the amount of iron precursor added during the preparation increased from 0.5 to 10 wt.%.

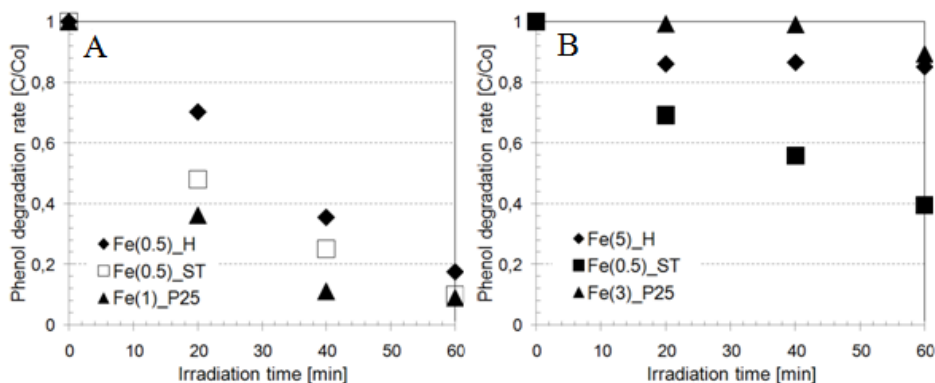


Fig. 2. Photoactivity under (A) UV-Vis and (B) Vis light of Fe-TiO₂ photocatalysts. Experimental conditions: $C_o=0.21$ mM; m (TiO₂) = 125 mg, $T=10^\circ\text{C}$, $Q_{\text{air}}=5$ dm³/h

The visible light absorbance is an important ability for photocatalysts, since solar light usage is a widely concerned issue in the practical application of photocatalysts. Absorption properties of iron-doped TiO₂ were estimated by UV-Vis spectroscopy to characterize the light absorption ability of the prepared photocatalysts. For

comparison, the spectrum of pure TiO_2 is also shown. The spectrum of bare TiO_2 clearly shows an absorption onset at about 395 nm which is in good agreement with the band gap value of bulk anatase ($\lambda = 387$ nm corresponding to 3.2 eV).

Figure 3 shows the absorption spectra of Fe- TiO_2 . The measurement of the samples was made at the wavelength of light in the range from 300 to 600 nm. When the value was of 350 to 400 nm, we observed a sharp increase in absorbance. Experimental data clearly indicate a correlation between absorption and the amount of a dopant. The higher the concentration of iron the stronger absorption in the visible range. Photocatalysts prepared by surface impregnation of TiO_2 P25 were inactive in the reaction of phenol degradation under visible light, but they revealed stronger absorption in the visible region than pure TiO_2 P25.

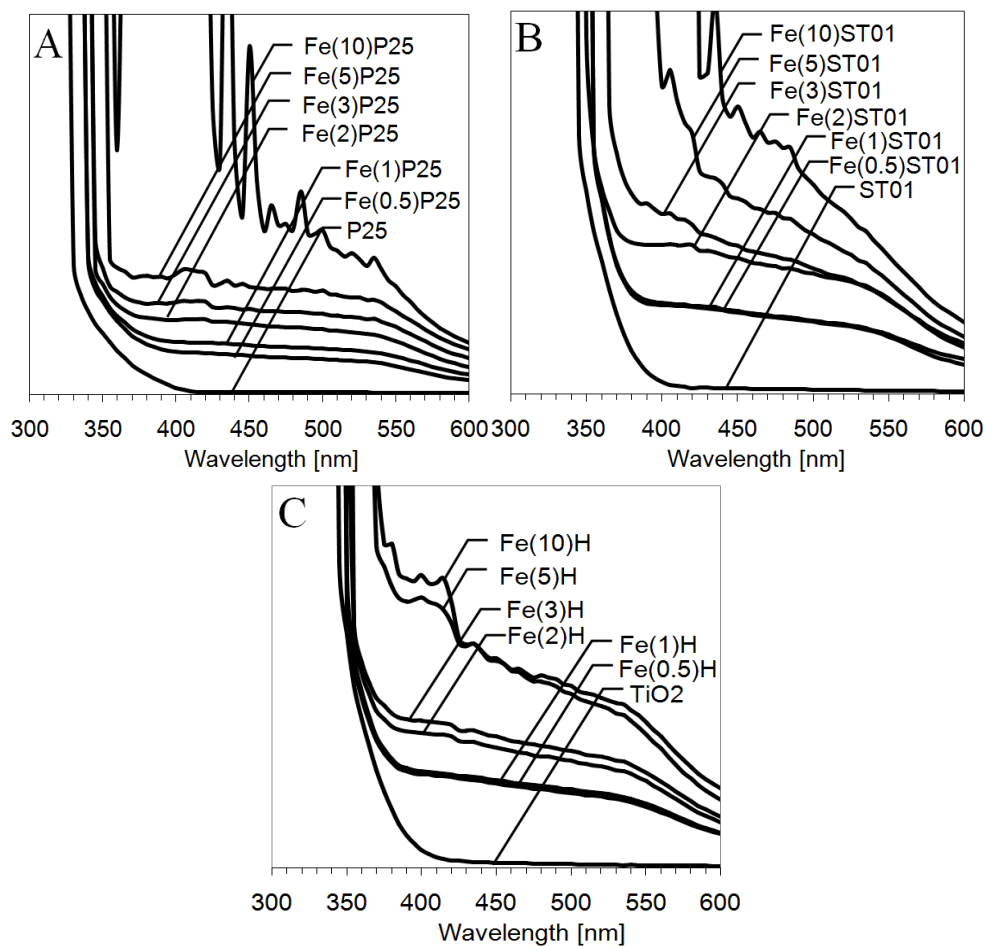


Fig. 3. Diffuse reflectance spectra of pure and Fe-modified TiO_2 prepared by (A) grinding TiO_2 P25 with a dopant (B) grinding TiO_2 ST-01 with a dopant (C) sol-gel method

4. Conclusion

Fe-modified TiO₂ nanopowders were prepared by the sol-gel and impregnation method. The amount of Fe(III) ions incorporated into TiO₂ significantly affected the characteristics and activity of the photocatalysts. The co-doped TiO₂ powders possessed a specific surface area in the range of 53-215 m²/g. The photocatalytic activity of TiO₂ was enhanced under UV-Vis light and the absorption range was extended towards the visible region. A photocatalytic degradation process was developed using phenol as a model compound.

Photocatalysts prepared by grinding TiO₂ ST-01 with a dopant were active in the reaction of phenol degradation ($\lambda > 420$ nm). The sample Fe(0.5)_ST containing 0.5 wt%. iron, calcined at 400°C (1h), showed the highest activity. After 60 min of irradiation under visible light 61% of phenol was degraded. Photocatalysts prepared by sol-gel and impregnation of TiO₂ P25 are nonactive in the reaction of phenol degradation under visible light.

All Fe-TiO₂ nanopowders were active under UV-Vis light. Sample Fe(1)_P25 showed the highest activity. After 60 min of irradiation under UV-Vis light 91% of phenol was degraded.

Acknowledgments

This work was supported by Polish Ministry of Science and Higher Education (N N523 568438 and N N523 420137).

References

- AMBRUS Z., BALAZS N., ALAPI T., WITTMANN G., SIPOS P., DOMBI A., MOGYOROSI K., 2008, Synthesis, structure and photocatalytic properties of Fe(III)-doped TiO₂ prepared from TiCl₃, *Appl. Catal. B: Environ.* 81, 27–37.
- JIAO S., CHEN Y., XU M., ZHANG Y., WANG D., PANG G., FENG S., 2010, Fabrication and magnetic property of α -Fe₂O₃ nanoparticles/TiO₂ nanowires hybrid structure, *Matter Letter* 64, 1704–1706.
- LIU Y., WEI J.H., XIONG R., PAN C.X., SHI J., 2011, Enhanced visible light photocatalytic properties of Fe-doped TiO₂ nanorod clusters and monodispersed nanoparticles, *Appl Surf Sci* 257, 8121–8126.
- SHI Z., ZHANG X., YAO S., 2011, Preparation and photocatalytic activity of TiO₂ nanoparticles co-doped with Fe and La. *Particuology*, 9, 260–264.
- VALENZUELA R., FUENTES M. C., PARRA C., BAEZA J., DURAN N., SHARMA S.K., KNOBEL M., FREER J., 2009, Influence of stirring velocity on the synthesis of magnetite nanoparticles (Fe₃O₄) by the co-precipitation method, *J. Alloy Compd.* 488, 227–231.
- ZBORIL R., MASHIAN M., PETRIDIS D., 2002, Iron(III) Oxides from Thermal Processes Synthesis, Structural and Magnetic Properties, Mössbauer Spectroscopy Characterization, and Applications, *Chem Mater* 14, 969–82.
- ZHOU M., YU J., CHENG B., 2006, Effects of Fe-doping on the photocatalytic activity of mesoporous TiO₂ powders prepared by an ultrasonic method, *J Hazard Mater* B137, 1838–1847.
- ZYSLER R. D., VASQUEZ M., ARCIPRETE C., DIMITRIJEWITS M., RODRIGUEZ-SIERRA D. D., SARAGOVI C., 2001, Structure and magnetic properties of thermally treated nanohematite *J Magn Mater* 224, 39–48.

Received July 18, 2011, reviewed, accepted September 1, 2011

CHARACTERIZATION AND PHOTOCATALYTIC ACTIVITY OF RARE EARTH METAL-DOPED TITANIUM DIOXIDE

Joanna RESZCZYNSKA *, Anna IWULSKA **, Gerard SLIWINSKI **,
Adriana ZALESKA *

* Department of Chemical Technology, Faculty of Chemistry, Gdansk University of Technology, Gdansk, Poland, e-mail: adriana.zaleska@pg.gda.pl

** Photophysics Department, Institute of Fluid-flow Machinery, Polish Academy of Sciences, Gdansk, Poland

Abstract. The aim of this research was to prepare rare metal (Er, Yb)-modified TiO₂ nanoparticles by a sol-gel method. The obtained nanoparticles were characterized by BET measurements, UV-Vis spectra and the Laser-induced fluorescence (LIF) method. Visible light photocatalytic activity of the sample was studied by photodegradation of phenol while considering the influence of the dopant concentration. The obtained results showed that a smaller amount of the dopant gave better photocatalytic activity of a semiconductor. The absorption spectra of Yb³⁺-doped and Er³⁺-TiO₂ samples show stronger absorption in the UV-Vis region than pure TiO₂. The presence of erbium was found more beneficial for visible light activation of TiO₂ doped photocatalysts than ytterbium.

keywords: photocatalysis, rare earth metal, modified TiO₂, luminescence

1. Introduction

Heterogeneous photocatalytic oxidation, developed in the 1970s, has attracted considerable attention particularly when used under solar light (Teh and Mohamed, 2011). Over the past 10 years, the semiconductor TiO₂, as a photocatalyst, has become the focus of numerous studies owing to its attractive characteristics and applications in the treatment of environmental contaminants (Lin and Yu, 1998). There are a lot of applications of TiO₂ for photodegradation of organic compounds (Hoffmann et al., 1995), inorganic reagents (Bakarat et al., 2004), removing odors from closed spaces, and self-cleaning surfaces (Fujishima et al., 2000). There are some examples of photocatalytic decomposition of water (Khan et al., 2002) and photoconversion of CO₂ (Tan et al., 2006) for methane in the presence of TiO₂.

In this respect the most important challenge is to increase the efficiency of the processes of photoconversion and extension of the spectral sensitivity of TiO₂. In this context, most of the work carried out in the world in recent years has aimed at

modification of TiO_2 , in order to obtain the activated photocatalyst with visible light. The TiO_2 -based photocatalysts, exhibiting higher activity under UV or visible light, can be obtained by: addition of transition metal ions, preparation of reduced forms of TiO_{2-x} (Takeuchi et al., 2000), sensitization of TiO_2 using dyes (Chatterjee and Mahata, 2001), TiO_2 sensitization using a smaller width of the semiconductor band gap E_g (Hirai et al., 2001), and doping non-metals (Asahi et al., 2001; Ohno et al., 2003; Janus and Morawski, 2007; Korosi and Dekany, 2006; Zaleska et al., 2007).

Rare earth elements are especially suitable for optical applications, since they have unfilled 4f and 5d shells. The effect of upconversion or Anti-Stokes emission is generally known from laser physics. The light of lower energy is up-converted in the light with a shorter wavelength. Several mechanisms are possible, which act either alone or in combination. The three main excitation processes are: excited-state absorption, energy-transfer upconversion and photon avalanche (Feng et al., 2008). Cacciotti et al. (2011) fabricated Tb-dopant and Yb-dopant TiO_2 by electrospinning technique. All the samples showed luminescent properties. Yang et al. (2011) prepared inverse opal photonic crystals of Yb^{3+} , Er^{3+} co-doped TiO_2 ($\text{TiO}_2\text{:Yb, Er}$) by a self-assembly technique in combination with a sol-gel method. They observed luminescence properties of the inverse opals. Gao et al. (2011) synthesized $\text{Er}^{3+}\text{:YAlO}_3/\text{Fe}$ -doped $\text{TiO}_2\text{-ZnO}$ composite by ultrasonic dispersion and a liquid boiling method. They showed that $\text{Er}^{3+}\text{:YAlO}_3$ can transform the visible light in solar energy into ultraviolet light, satisfying the requirement of $\text{TiO}_2\text{-ZnO}$ composite for photocatalytic degradation (Acid Red B dye). Wang et al. (2006, 2007a; 2007b) and Feng et al. (2008) mixed upconversion materials with TiO_2 and reported that the photocatalytic activity of the upconversion-doped TiO_2 is higher than that of the undoped one. Upconversion materials, which were synthesized without Y-Al-O compounds, were only reported by Shang et al. (2008). They prepared $\text{Er}^{3+}\text{-Yb}^{3+}$ co-doped TiO_2 nanocrystals by a sol-gel method. However, the activity of the obtained photocatalysts were examined only in the process of the degradation of dyes (which may act as sensitizer and thereby cause a misstatement of the effectiveness assessment of the degradation). In accessible literature there is no available information on the stability of photocatalysts (the possibility of recycling and stability of photocatalysts during storage).

Here we report a preparation method and characteristics of erbium- and ytterbium-modified TiO_2 photocatalysts. Rare earth metal-doped TiO_2 was prepared by a sol-gel method.

2. Experimental

2.1. Materials and instruments

Titanium isopropoxide (pure p.a.) was purchased from Aldrich and used as titanium source for the preparation of TiO_2 nanoparticles. $\text{Er}(\text{NO}_3)_3\cdot 6\text{H}_2\text{O}$ and $\text{Yb}(\text{NO}_3)_3\cdot 6\text{H}_2\text{O}$ salts were freshly prepared by the reaction of Er_2O_3 and Yb_2O_3 with

nitric acid. Er_2O_3 (99.9%) and Yb_2O_3 (99.9%) were obtained from Sigma Aldrich while TiO_2 P25 from Evonik, Germany (surface area $50 \text{ m}^2/\text{g}$). All the chemicals were used as received without further purification. Deionized water was used for all the reactions and treatment processes.

Nitrogen adsorption-desorption isotherms were recorded at liquid nitrogen temperature (77 K) on a Micromeritics Gemini V (model 2365) and specific surface areas were determined by the Brunauer–Emmett–Teller (BET) method.

The diffuse reflectance spectra DRS were characterized using UV–Vis spectrometer (Labomed, Inc.) equipped with an integrating sphere accessory for diffuse reflectance.

To measure the fluorescence spectra (LIF, Laser-induced fluorescence) a UV-Vis spectrometer equipped with a SR-303i monochromator and ICCD camera iStar DH 740 using a diffraction grating 600 lines/mm were used. The quantity counts were: 100 Laser: Nd: YAG laser with a wavelength of 532 nm.

2.2. Preparation of doped TiO_2 photocatalysts

TiO_2 -based photocatalysts were obtained according to the procedures presented by a simplified block diagram in Fig. 1. A sample of 12.2 cm^3 titanium isopropoxide was added to the mixture of 6.0 cm^3 acetic acid and 48 cm^3 ethanol. The sol was stirred for 10 min, then 3.0 cm^3 water was added dropwise. Then, a certain amount of $\text{Er}(\text{NO}_3)_3$ and $\text{Yb}(\text{NO}_3)_3$ was added and the sol was stirred for one more hour. The obtained gel was dried at 60°C for 20 h in a vacuum oven and ground to obtain powder. The heat-treatment of 400°C for 2.5 h in the air was applied to the sample. The concentration of metal precursors, which varied from 0.25 to 1.0 mol.% was related to the concentration of TIP in the sol-gel system.

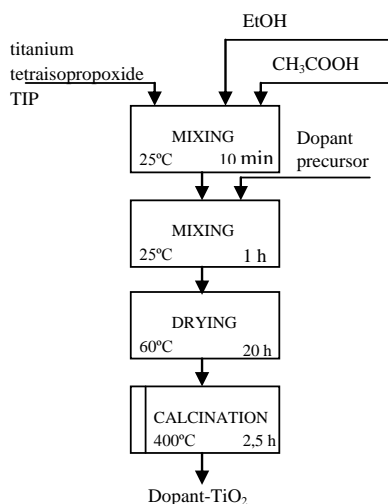


Fig. 1. Block diagram of RE-doped TiO_2 prepared by a sol-gel method

2.3. Measurements of photocatalytic activity

The photocatalytic activity of RE-TiO₂ powders in visible light was estimated by measuring the decomposition rate of phenol (0.21 mmol/dm³) in an aqueous solution. Photocatalytic degradation runs were preceded by blind tests in the absence of a catalyst or illumination. Twenty five milliliters of catalyst suspension (125 mg) were stirred using a magnetic stirrer and aerated (5 dm³/h) prior and during the photocatalytic process. Aliquots of 1.0 cm³ of the aqueous suspension were collected at regular time periods during irradiation and filtered through syringe filters (Ø = 0.2 mm) to remove catalyst particles. Phenol concentration was estimated by a colorimetric method using UV-Vis spectrophotometer (DU-520, Beckman). The suspension was irradiated using 1000 W Xenon lamp (Oriel), which emits both UV and Vis light. To limit the irradiation wavelength, the light beam was passed through GG400 filter to cut-off wavelengths shorter than 400 nm.

3. Results and discussion

Table 1 presents the BET surface area, pore volume and photocatalytic activity results for the erbium- and ytterbium-doped TiO₂ nanoparticles. The Er³⁺-TiO₂ photocatalyst modified with 0.5 mol.% of Er has the lowest BET surface area and pore volume of about 113 m²/g and 0.056 cm³/g, respectively. The Yb³⁺-TiO₂, modified with 0.5 mol.% Yb, has the highest surface area and pore volume equal to about 132 m²/g and 0.065 cm³/g, respectively. For other Er³⁺-TiO₂ and Yb³⁺-TiO₂ samples containing from 0.25 to 1.0 mol.% of metal the surface areas varied from 119 to 126m²/g. It was observed that metal dopant affects the surface area of TiO₂ powder samples. The obtained results indicated that other parameters, such as erbium or ytterbium presence cause their enhancement in photoactivity, rather than the surface area.

Table 1. BET surface area, pore volume and photocatalytic activity of RE-TiO₂ photocatalysts

| Photocatalysts type | Amount of metal precursor [mol %] | S _{BET} [m ² /g] | Pore volume [cm ³ /g] | Phenol degradation after 1h exposure to Vis irradiation (λ>400 nm) [%] |
|------------------------------------|-----------------------------------|--------------------------------------|----------------------------------|--|
| TiO ₂ | - | 118 | 0.058 | 24 |
| Er ³⁺ -TiO ₂ | 0.25 | 126 | 0.062 | 38 |
| Er ³⁺ -TiO ₂ | 0.5 | 113 | 0.056 | 31 |
| Er ³⁺ -TiO ₂ | 1.0 | 123 | 0.061 | 21 |
| Yb ³⁺ -TiO ₂ | 0.25 | 119 | 0.059 | 25 |
| Yb ³⁺ -TiO ₂ | 0.5 | 132 | 0.065 | 31 |
| Yb ³⁺ -TiO ₂ | 1.0 | 125 | 0.061 | 26 |

To study the optical absorption properties of as-prepared samples, UV-Vis absorption spectra in the range 350 – 700 nm were investigated, and the results are shown in Fig. 2. It can be seen that the modification of titania with erbium significantly affected the light absorption property of the photocatalysts. Furthermore,

it can be seen that there are three typical absorption peaks located at 490, 535 and 655 nm. The spectrum in Fig. 2 is characteristic for Er^{3+} -doped colloid with absorption bands identified with the transitions from the $^4\text{I}_{15/2}$ ground state to the excited states of the Er^{3+} ions (Pang et al., 2010).

The absorption spectra of Yb^{3+} -doped and Er^{3+} - TiO_2 samples show stronger absorption in the UV-Vis region than commercially available P25.

The photoluminescence spectra were measured on Er^{3+} - TiO_2 and Yb^{3+} - TiO_2 samples under excitation at 532 nm. Emission bands were observed at 670 nm for erbium and at 580 and 640 nm for ytterbium. Figure 3 shows the photoluminescence spectra of the prepared powders. These spectra show the concentration quenching of erbium and ytterbium luminescence, as expected. When the concentration of rare earth metal decreased, then erbium and ytterbium emission was enhanced.

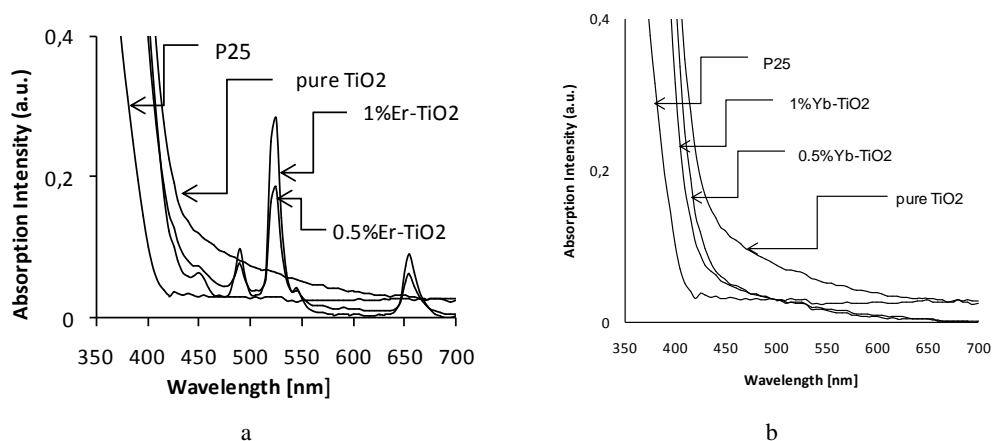


Fig. 2. Absorption properties of RE- TiO_2 prepared by a sol-gel method, a) Er^{3+} - TiO_2 , b) Yb^{3+} - TiO_2

The photocatalytic activity of the rare earth metal-doped TiO_2 nanoparticles was evaluated by measuring the decomposition of phenol. The efficiency of phenol degradation after 60 min of exposure to Vis irradiation in the presence of Er^{3+} - TiO_2 and Yb^{3+} - TiO_2 nanoparticles is presented in Table 1 and Fig. 4.

The photodegradation efficiency under visible light decreased with the increase in the ytterbium loading up to 0.5 mol.% and then decreased. When erbium was the dopant, the photodegradation efficiency under visible light decreased with the increase in the erbium loading up to 0.25 mol.%. The efficiency of phenol decomposition measured in the presence of the sample 0.25% Er^{3+} - TiO_2 after 60 min of irradiation was 38%. It indicates that the presence of erbium was more beneficial for visible light activation of TiO_2 doped photocatalysts than ytterbium, where maximum efficiency of phenol decomposition was 31% for the sample 0.5% Yb^{3+} - TiO_2 . All rare earth metal-doped photocatalysts have better photocatalytic activity than the undoped ones.

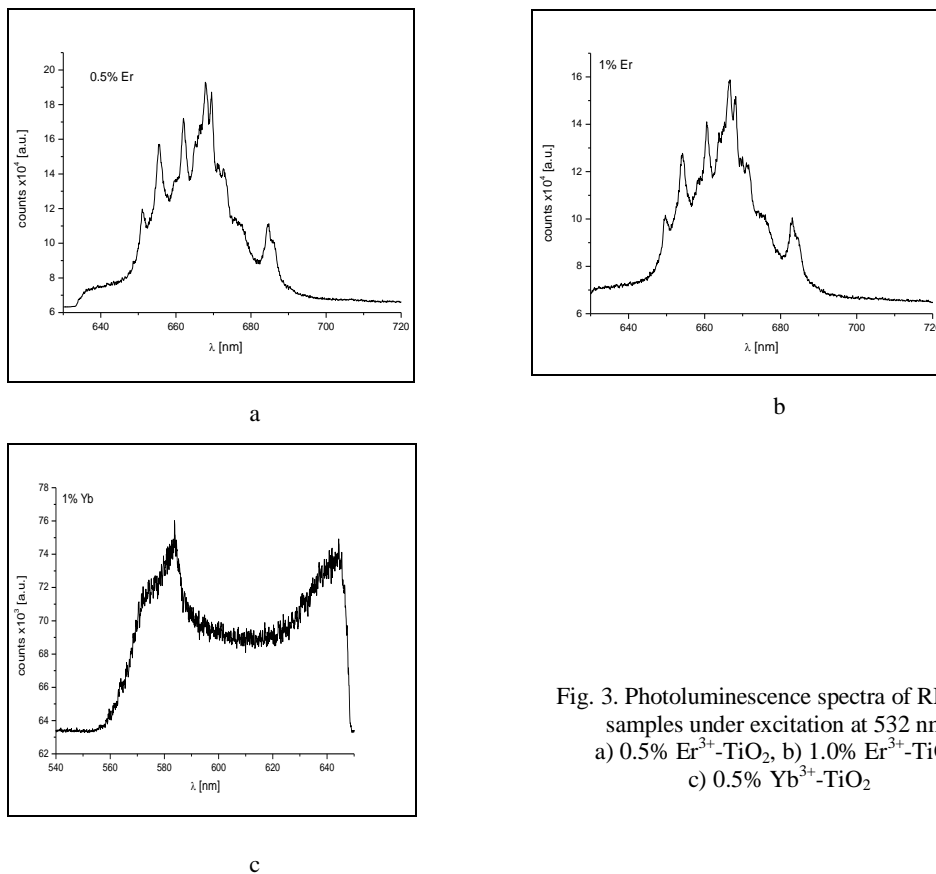


Fig. 3. Photoluminescence spectra of RE-TiO₂ samples under excitation at 532 nm, a) 0.5% Er³⁺-TiO₂, b) 1.0% Er³⁺-TiO₂, c) 0.5% Yb³⁺-TiO₂

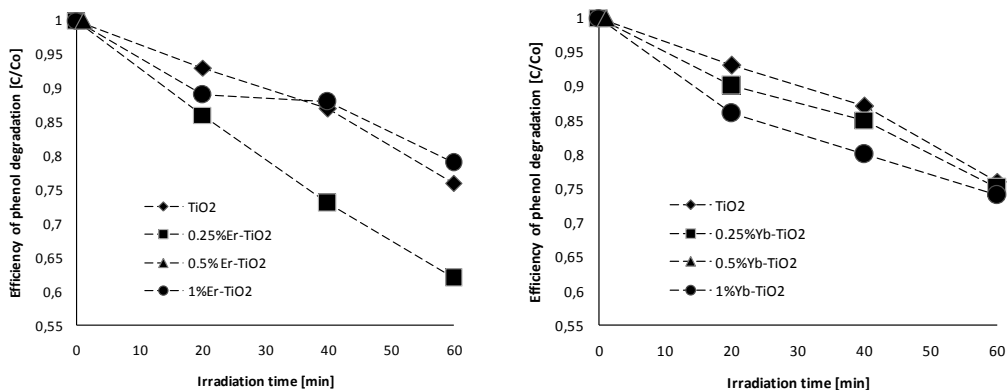


Fig. 4. Efficiency of phenol photodegradation in the presence of RE-doped TiO₂ under visible light ($\lambda > 400$ nm). Experimental conditions: $C_0 = 0.21$ mM, $m(\text{TiO}_2) = 125$ mg, $T = 10^\circ\text{C}$, $Q_{\text{air}} = 5$ dm³/h, a) Er³⁺-TiO₂, b) Yb³⁺-TiO₂

3. Conclusion

The photocatalysts based on TiO₂ and doped with rare earth metal have luminescence properties. The effect of metal modification on photocatalytic activity depends on the type of metal and metal precursor concentration used during the preparation. It was found that titania surface modification with erbium and ytterbium caused an increase of the photocatalytic activity under visible irradiation and it was observed that a metal dopant affects the surface area of TiO₂ powder samples. The absorption spectra of Yb³⁺-doped and Er³⁺-TiO₂ samples show stronger absorption in the UV–Vis region than commercially available TiO₂ P25. It can be seen that for Er³⁺-TiO₂ there are three typical absorption peaks located at 490, 535 and 655 nm.

Acknowledgments

This work was supported by Polish Ministry of Science and Higher Education (No. N N523 420137).

References

- ASAHI R., MORIKAWA T., OHWAKI T., AOKI K., TAGA Y., 2001, Visible-light photocatalysis in nitrogen-doped titanium oxides, *Science* 293, 269–271.
- BAKARAT M.A., CHEN Y.T., HUANG C.P., 2004, Removal of Toxic Cyanide and Cu(II) Ions from Water by Illuminated TiO₂ Catalyst, *Appl. Catal. B* 53, 13–20.
- CACCIOTTI I., BIANCO A., PEZZOTTI G., GUSMANO G., 2011, Terbium and ytterbium-doped titania luminescent nanofibers by means of electrospinning technique, *Mat. Chem. Phys.* 126, 532–541.
- CHATTERJEE D., MAHATA A., 2001, Demineralization of organic pollutants on the dye modified TiO₂ semiconductor particulate system using visible light, *Appl. Catal. B Environ.* 33, 119–125.
- FENG G., LIU S., XIU Z., ZHANG Y., YU J., CHEN Y., WANG P., YU X., 2008, Visible light photocatalytic activities of TiO₂ nanocrystals doped with up-conversion luminescence agent, *J. Phys. Chem. C* 112, 13692–13699.
- FUJISHIMA A., RAO T.N., TRYK D.A., 2000, Titanium dioxide photocatalysis, *J. Photochem. Photobiol. C: Photochem. Rev.* 1, 1–21.
- GAO J., LUAN X., WANG J., WANG B., LI K., LI Y., KANG P., HAN G., 2011, Preparation of Er³⁺:YAlO₃/Fe-doped TiO₂-ZnO and its application in photocatalytic degradation of dyes under solar light irradiation, *Chem. Eng. J.* 268, 68–75.
- HIRAI T., SUZUKI K., KOMASAWA I., 2001, Preparation and photocatalytic properties of composite CdS nanoparticles-titanium dioxide particles, *J. Colloid Interface Sci.* 244, 262–265.
- HOFFMANN M.R., MARTIN S.T., CHOI W., BAHNEMANN D.W., 1995, Environmental applications of semiconductor photocatalysis, *Chem. Rev.* 95, 69–96.
- JANUS M., MORAWSKI A.W., 2007, New method of improving photocatalytic activity of commercial Degussa P25 for azo dyes decomposition, *Appl. Catal. B* 75, 118–123.
- KHAN S.U., AL-SHAHRY M., INGLER W.B. JR., 2002, Efficient photochemical water splitting by a chemically modified n-TiO₂, *Science* 297, 2243–2245.
- KOROSI L., DEKANY I., 2006, Preparation and investigation of structural and photocatalytic properties of phosphate modified titanium dioxide, *Colloids Surf., A* 280, 146–154.
- LIN J., YU J.C., 1998, An investigation on photocatalytic activities of mixed TiO₂-rare earth oxides for the oxidation of acetone in air, *J. Photochem. Photobiol. A: Chem.* 116, 63–67.
- NAKAMURA I., NEGISHI N., KUTSUNA S., IHARA T., SUGIHARA S., TAKEUCHI K., 2000, Role of oxygen vacancy in the plasma-treated TiO₂ photocatalyst with visible light activity for NO removal, *J. Mol. Catal. A: Chem.* 161, 205–212.

- OHNO T, MITSUI T., MATSUMURA M., 2003, Photocatalytic activity of S-doped TiO₂ photocatalyst under visible light, *Chem. Lett.* 32, 364–365.
- PANG S., LI X., SHI Z., YANG G., CUI Z., 2010, Preparation and characterization of sol-gel derived Er³⁺-Yb³⁺ codoped SiO₂/TiO₂ core-shell nanoparticles, *Mat. Lett.* 64, 846–848.
- SHANG Q., YU H., KONG X., WANG H., WANG X., SUN Y., ZHANG Y., ZENG Q., 2008, Green and red up-conversion emissions of Er³⁺-Yb³⁺ Co-doped TiO₂ nanocrystals prepared by sol-gel method. *J. Lumin.* 128, 1211–1216.
- TAN S.S., ZOU L., HU E., 2006, Photocatalytic reduction of carbon dioxide into gaseous hydrocarbon using TiO₂ pellets, *Cataly. Tod.* 115, 269–273.
- TEH C.M., MOHAMED A.R., 2011, Roles of titanium dioxide and ion-doped titanium dioxide on photocatalytic degradation of organic pollutants (phenolic compounds and dyes) in aqueous solutions: A review, *J. All. Comp.* 509, 1648-1660.
- WANG J., LI R., ZHANG Z., SUN W., XU R., XIE Y., XING Z., ZHANG X., 2007a, Efficient photocatalytic degradation of organic dyes over titanium dioxide coating upconversion luminescence agent under visible and sunlight irradiation, *Appl. Cat. A, Gen.* 334, 227–233.
- WANG J., MA T., ZHANG G., ZHANG Z., ZHANG X., JIANG Y., ZHAO G., ZHANG P., 2007b, Preparation of novel nanometer TiO₂ catalyst doped with upconversion luminescence agent and investigation on degradation of acid red B dye using visible light, *Cat. Comm.* 8, 607–611.
- WANG J., WEN F.Y., ZHANG Z.H., ZHANG X.D., PAN Z.J., ZHANG P., KANG P.L., TONG J., WANG L., XU L., 2006, Investigation on degradation of dyestuff wastewater using visible light in the presence of a novel nano TiO₂ catalyst doped with upconversion luminescence agent, *J. Photochem. Photobiol., A: Chem.* 180, 189–195.
- YANG Z., ZHU K., SONG Z., ZHOU D., YIN Z., QIU J., 2011, Preparation and upconversion emission properties of TiO₂:Yb, Er inverse opals, *Sol. Stat. Comm.* 151, 364–367.
- ZALESKA A., SOBCZAK J.W., GRABOWSKA E., HUPKA J., 2007, Preparation and photocatalytic activity of boron-modified TiO₂ under UV and visible light, *Appl. Catal. B* 78, 92–100.

Received July 18, 2011; reviewed; accepted September 1, 2011

EFFECT OF SURFACE MODIFICATION AS WELL AS TYPE AND IONIC STRENGTH OF ELECTROLYTE ON ELECTROKINETIC PROPERTIES OF TiO₂ AND TiO₂-SiO₂

Magdalena NOWACKA, Teofil JESIONOWSKI

Poznan University of Technology, Institute of Chemical Technology and Engineering, M. Skłodowskiej-Curie 2, 60-965 Poznan, Poland, Teofil.Jesionowski@put.poznan.pl, phone: +48(61)6653720, fax: +48(61)6653649

Abstract. Electrokinetic properties of the commercial titanium white (Tytanpol[®] RS) and precipitated TiO₂-SiO₂ composite were studied. As they depend mainly on the character of the surface of materials studied, the effect of the amount and type of surface modifying agents on the electrokinetic potential was analysed. The study was performed on the commercial titania and TiO₂-SiO₂ composite precipitated from an emulsion system, both either unmodified or modified with three organofunctional silanes applied in three different concentrations. The effect of ionic strength of the electrolyte used (KCl, NaNO₃ or AlCl₃) on the electrokinetic potential of the two systems studied was established. Stability of the dispersive systems studied was evaluated.

keywords: zeta potential, electrophoretic mobility, TiO₂ and TiO₂-SiO₂ oxide composite, electrokinetic stability, surface modification

1. Introduction

Electrokinetic phenomena belongs to the oldest and the most important area of surface and colloid science. Discovery of such electrokinetic phenomena as electrophoresis, electroosmosis and streaming potential, permitted a description of the electric double layer, which has been of great importance for understanding of the stability of colloids. Results collected from investigation of electrokinetic phenomena have permitted prediction of specific aspects of colloidal systems behaviour (Wall 2010).

The notion of colloidal or dispersive systems, has been for the first time used by Graham and since that time its meaning has evolved. At present the colloidal systems are defined as those having two phases: a dispersed phase (internal phase) and a continuous phase (dispersion medium).

Colloidal systems belong to unstable systems. Their stability depends e.g. on electric charge and surface charge density. Colloidal particles dispersed in the solution

are surrounded by ions bearing the opposite charge, which leads to formation of an adsorbed layer. In the neighbourhood of this layer there is formed another one known as diffuse layer. The electrical double layer (e.d.l.) is formed at the interface between the solid and liquid phases (Otterstedt 1998). Between the adsorbed and diffuse layers the electrokinetic (zeta) potential appears.

This potential denoted as ζ , is one of the most important parameters characterising particles of solid suspended in polar and non-polar solutions (Alkan 2005). It permits the calculation of strength and energy of interaction between the two colloidal particles which brings information on stability of the system (resistance to coagulation), dispersion viscosity, floating properties and can help choosing appropriate reagents for their modification (Hunter 1981). Low value of ζ close to zero is characteristic of instable systems, while a high value (either positive or negative) informs about a stable colloidal state (Kosmulski 2001). Strongly charged particles repel one another, which delays or prevents the ageing processes and implies that the fastest coagulation takes place at the isoelectric point (i.e.p.).

In 1941, Derjaguin and Landau explained the phenomena taking place in stable aggregations on the basis of the interplay between the attractive van der Waals forces and electrostatic repulsion force. In 1948, Verwey and Overbeek formulated a theory of liophobic colloids, which was practically identical to that proposed by Derjaguin and Landau and that is why it has been referred to as the DLVO theory (Yoon 1996; Wu 1999; Bergua 2006). Unfortunately, the theory does not work for the interactions between closely neighbouring particles. The extended XDLVO theory also takes into account the acid-base interactions according to the Lewis theory. The XDLVO theory claims the total energy of interactions between particles is a sum of the energies of van der Waals interactions, electrical double layer and Lewis acid-base interactions.

The knowledge of ζ potential brings information on several properties of dispersed systems. The potential depends to a significant degree on the type of particles, type of the medium in which they are dispersed and the type of ions present in the medium. The zeta potential responds to changes in pH, temperature and concentration of particular components (Jayaweera 1993; Leong 2005; Erdemoglu 2006) as well as in the ionic strength of the electrolyte used. Increase in the ionic strength leads to a compression of the diffuse layer and reduction in the zeta potential. High ionic strength leads to a decrease in the zeta potential values at a constant pH at all types of surfaces. It has been proved that at low concentrations of electrolyte (0.001M) the zeta potential takes values close to that of the surface potential. There are exceptions to the rule, when the electrophoretic mobility and zeta potential are independent of the ionic strength in a certain pH range, e.g. the electrokinetic curve is insensitive to ionic strength in an acidic medium. With increasing ionic strength the zeta potential of silica in an acidic environment decreases (Kosmulski 2010).

Zeta potential measurements have been widely used in advanced industrial technologies, like in water treatment, purification of building walls, biomedicine or in paper production. Determination of the potential has been used for evaluation of the

effect of each substrate in colloidal phase which is of particular importance in pharmaceutical, cosmetic and food industries to get stable colloidal systems. Values of zeta potential are also used for prediction of long-term stability of paints or lacquers (Vane 1997; Hunter 2001).

Many papers on TiO₂ zeta potential evaluations have been published (Kosmulski 2009a, 2009b, 2010), but this data are commonly investigated for ungrafted titania, e.g. TiO₂ P25.

The aim of study is to establish the effect of surface modification, type and ionic strength of the electrolyte used on the electrokinetic properties of commercial titanium white and TiO₂-SiO₂ hybrid systems.

2. Experimental

2.1. Materials

The study was performed on the commercial titanium white produced by the sulphate method by the Chemical Works "POLICE" SA, Poland, Tytanpol[®] RS and TiO₂-SiO₂ hybrid systems precipitated from emulsion according to the method described previously (Siwinska-Stefanska 2010, 2011; Walkowiak 2010).

Changes in the surface morphology of Tytanpol[®] RS and TiO₂-SiO₂ systems and their hydrophilic properties (into hydrophobic ones) were achieved by addition of silane proadhesive compounds (purchased from Unisil) in the amounts of 0.5, 1 or 3 weight parts in relation to powder (Table 1). The effect of varied amount of the silane introduced on the zeta potential was also of interest in this study.

Table 1. Proadhesive silane compounds used for surface modification of the systems studied

| Name | Formula |
|---|--|
| <i>N</i> -2-(aminoethyl)-3-aminopropyltrimethoxysilane (U-15D) | H ₂ N(CH ₂) ₂ NH(CH ₂) ₃ Si(OCH ₃) ₃ |
| 3-methacryloxypropyltrimethoxysilane (U-511) | CH ₂ =C(CH ₃)COO(CH ₂) ₃ Si(OCH ₃) ₃ |
| vinyltrimethoxysilane (U-611) | CH ₂ =CHSi(OCH ₃) ₃ |

2.2. Methods

The colloidal systems studied were characterised by determination of their electrokinetic properties (zeta potential and electrophoretic mobility) influence of modification of TiO₂ and TiO₂-SiO₂ oxide composite with proadhesive silanes in different amounts and that of ionic strength (0.001–0.1M) and type of electrolyte (KCl, NaNO₃, AlCl₃) on the electrokinetic properties.

Measurements were made by Zetasizer Nano ZS equipped with an autotitrator (Malvern Instruments Ltd.). At first a certain amount of a sample to be studied was dispersed in a given electrolyte solution. Then, pH was measured by the autotitrator using a glass electrode and a desired pH value was adjusted by introducing a solution of 0.2 M HCl or 0.2 M NaOH. A fraction of the sample was then pumped by a peristaltic pump to a measuring cell in which electrophoretic mobility was measured. Finally, on the basis of the results the zeta potential was calculated from the Henry equation.

3. Results and discussion

The first stage of the study was devoted to determination of the influence of modification of the commercial titanium white and TiO₂-SiO₂ system with selected alkoxy silanes (U-15D, U-511, U-611) on the zeta potential. Figure 1a presents the zeta potential as a function of pH for unmodified TiO₂ RS and TiO₂ RS modified with 0.5, 1 or 3 wt./wt. of *N*-2-(aminoethyl)-3-aminopropyl-trimethoxysilane (U-15D). Measurements were performed in a 0.001M KCl solution for pH in the range from 1.7 to 11.

The zeta potential of unmodified TiO₂ RS, took almost exclusively negative values varied from 7 to (-43) mV for the above pH range. The isoelectric point was reached at pH close to 2.4. After modification with U-15D in the amount of 0.5 wt./wt. and for pH in the range 1.7–8.5, the zeta potential assumed positive values. The sample was stable at pH from 1.7 to 5.3. An increase in *N*-2-(aminoethyl)-3-aminopropyltrimethoxysilane content to 1 wt./wt. caused a small shift of the electrokinetic curve towards more basic pH relative to those modified with 0.5 wt./wt. of this silane. The isoelectric point was reached at pH close to 8.9. The zeta potential of this system varied from 49 to -24 mV for pH varying from 1.7 to 11 and was stable for pH from 1.7 to 6.5. When the TiO₂ RS system was modified with 3 wt./wt. of U-15D, the shift of the electrokinetic curve towards higher pH was the most pronounced and the zeta potential took almost only positive values, varying from 54 to -11 mV and reaching i.e.p. at pH close to 10.

Modification of TiO₂ RS system surface with *N*-2-(aminoethyl)-3aminopropyl-trimethoxysilane resulted in a significant shift of the electrokinetic curve towards higher pH, relative to the curve for the unmodified sample. An important process for this sample is the ionisation of -NH₂ groups. High density of H⁺ ions induces formation of NH₃⁺ groups, so that the modified surface has positive sign. With increasing H⁺ ions concentration the ionisation becomes limited and the surface charge is reduced (Jesionowski 2010). The following reactions take place: -NH₂ + H⁺ = -NH₃⁺ and -NH₃⁺ + OH⁻ = -NH₂ + H₂O.

Surface modification with amine compounds leads to high values of the isoelectric point, which is related to basic character of the surface. The TiO₂ or TiO₂-SiO₂ oxide composite surface treatment with aminosilane is illustrated in Fig. 1.

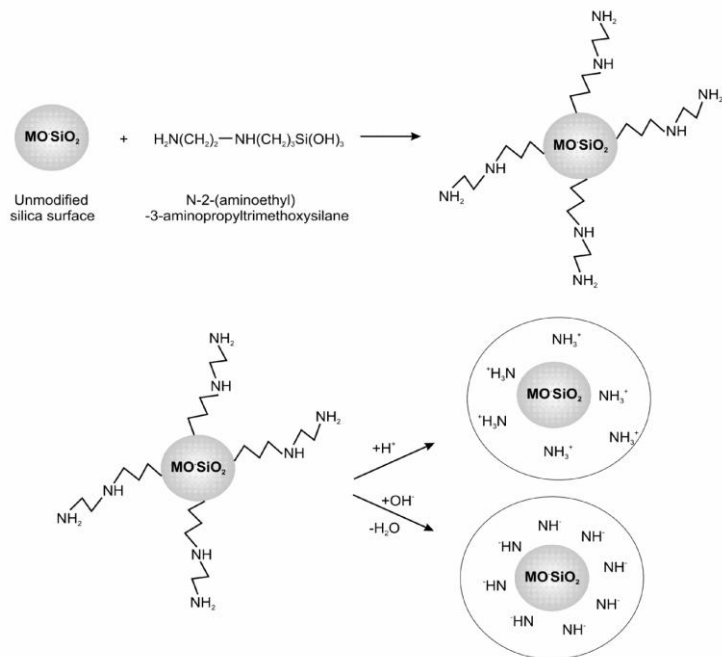


Fig. 1. Scheme of inorganic support modification with N-2-(aminoethyl)-3-aminopropyltrimethoxysilane

Plots of zeta potential measured in a 0.001M KCl solution versus pH for the TiO_2 RS unmodified and modified with 0.5, 1 and 3 wt./wt. of 3-methacryloxypropyltrimethoxysilane (U-511) are presented in Fig. 2b. The electrokinetic curve obtained for the TiO_2 RS sample modified with 0.5 wt./wt. of U-511 reaches the isoelectric point at pH close to 5.8. The zeta potential varied from 33 to -29 mV over pH from 1.7 to 11. Modification of titanium white with 1 and 3 wt./wt. of U-511 leads to a small shift of the electrokinetic curves towards lower pH values with respect to the curve for the sample modified with 0.5 wt./wt. of 3-methacryloxypropyltrimethoxysilane. Both former curves reach i.e.p. at pH close to 4.3 and the potential values vary between 28 and -38 mV. The sample modified with 1 wt./wt. of U-511 shows high stability for pH 8.5 to 11, while that modified with 3 wt./wt. for pH range of 7.7–11.

Changes in the zeta potential as a function of pH for TiO_2 RS unmodified and modified with 0.5, 1 and 3 wt./wt. of vinyltrimethoxysilane (U-611), measured in a 0.001M solution of KCl, are presented in Fig. 2c. The sample modified with 0.5 wt./wt. of U-611 is characterised by the electrokinetic curve shifted towards basic pH values with respect to that recorded for the unmodified sample, reaching i.e.p. at pH close to 4.6. This sample is stable at pH from the 9 to 11 and its zeta potential values vary from 25 to -33 mV over the pH range analysed. For the sample of

TiO₂ RS modified with 1 wt./wt. of U-611 the isoelectric point is reached at pH close to 4.8. The zeta potential of this sample varies from 21 to -46 mV and the sample is stable for pH from 7.9 to 11. For the sample modified with 3 wt./wt. of vinyltrimethoxysilane the zeta potential varies from 18 to -50 mV and i.e.p. is reached at pH near 3.6.

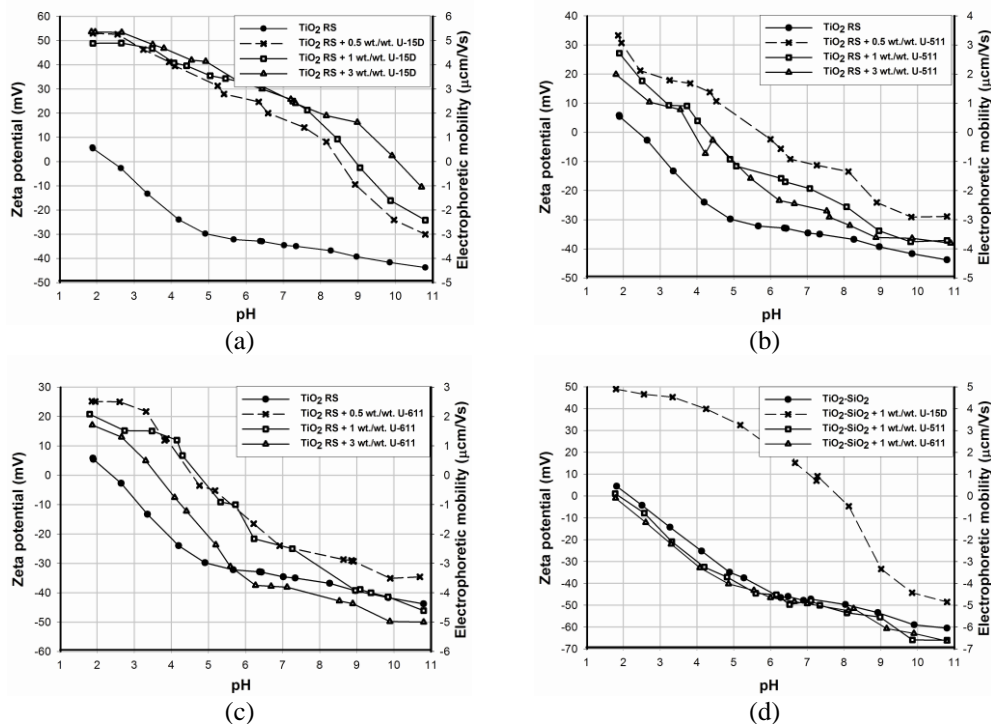


Fig. 2. Zeta potential and electrophoretic mobility versus pH for TiO₂ RS unmodified and modified with 0.5, 1 or 3 wt./wt. of (a) U-15D, (b) U-511, (c) U-611 and (d) for TiO₂-SiO₂ oxide composite

The electrokinetic curves estimated for TiO₂-SiO₂ composite modified with 1 wt./wt. of the silanes U-15D, U-511 and U-611 are shown in Fig. 2d. Relations between the curves are similar to those observed for the analogously modified surface of TiO₂ RS. The most pronounced changes in the electrokinetic properties were noted as a result of modification of 1 wt./wt. of U-15D, while the changes caused by modification with 1 wt./wt. of U-511 and U-611 with respect to the curve obtained for the unmodified TiO₂-SiO₂ sample were insignificant.

In the next stage of the study the subject of concern was the influence of ionic strength and type of the electrolyte on the zeta potential of TiO₂ and TiO₂-SiO₂ hybrid systems. The plots of zeta potential as a function of pH for solutions of different ionic strength obtained for TiO₂ RS and TiO₂-SiO₂ are presented in Fig. 3 a, b. The increase in concentration of the electrolyte used in the study (from 0.001 to 0.1M KCl),

resulted in a shift of the electrokinetic curve towards lower values of zeta potential. When 0.001M solution was used, then over the whole pH range, the zeta potential changed from 7 to -37 mV for TiO_2 RS and from 11 to -40 mV for $\text{TiO}_2\text{-SiO}_2$. The zeta potential values obtained in the KCl solution of 0.1 M varied from 12 to -17 mV for TiO_2 RS and from 11 to -21 mV for $\text{TiO}_2\text{-SiO}_2$.

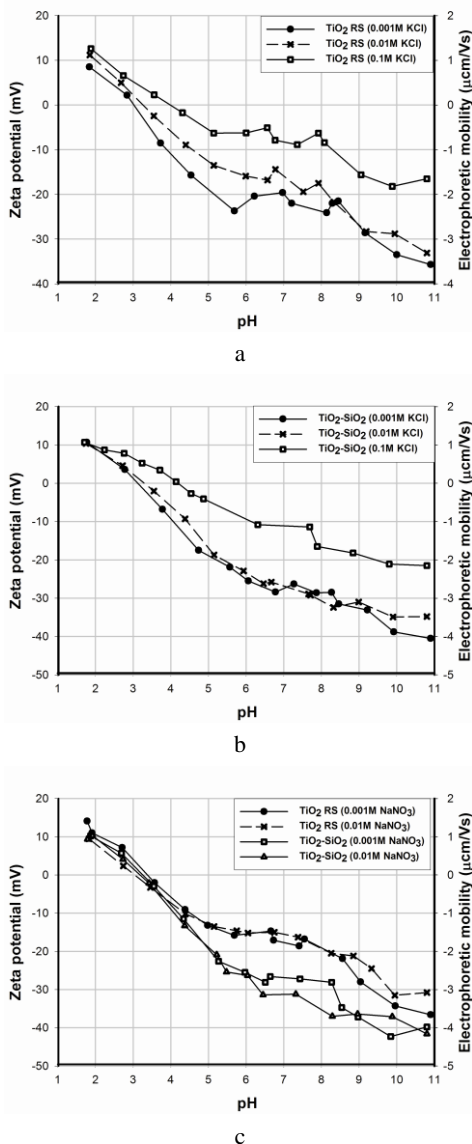


Fig. 3. Zeta potential versus pH for TiO_2 RS and $\text{TiO}_2\text{-SiO}_2$ for different ionic strengths of the electrolyte (KCl, NaNO_3)

Figure 3c presents the zeta potential measured versus pH for TiO₂ RS and TiO₂-SiO₂ for different ionic strengths of the NaNO₃ solution used as an electrolyte. Changes in the ionic strength of the electrolyte were found to have a significant effect on the zeta potential values, especially in the alkaline pH range. Results confirmed the literature reports describing the influence of the ionic strength on the zeta potential (Kosmulski 2010).

Aqueous solutions of electrolytes are divided into neutral (e.g. KNO₃) and those containing specifically adsorbing ions (e.g. Ca(NO₃)₂ or Pb(NO₃)₂). The monovalent counterions (Na⁺) cause a compression of the electrical double layer and that is why they reduce the zeta potential, but they do not change the charge on the particle of a given material. The multivalent cations or their hydrated forms reverse the sign of the charge by adsorption in the Stern layer. Adsorption of Al(OH)₃ in the Stern layer is favoured because of hydrogen bonds formation between the OH groups and oxygen ions and hydroxyl groups on the particles of a given material (Lyklema 1984; Hiemenz 1997).

The plots of zeta potential versus pH for TiO₂-SiO₂ measured in a solution of AlCl₃ are presented in Fig. 4. The use of AlCl₃ as an electrolyte resulted in increased zeta potential values which reached a maximum value at pH close to 4.5, irrespectively of the ionic strength. For higher pH (from 4.5 to 11) the zeta potential values decrease.

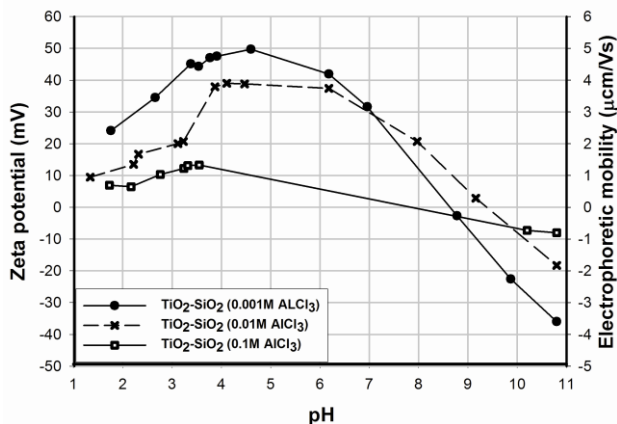


Fig. 4. Zeta potential versus pH of TiO₂-SiO₂ for different ionic strength of AlCl₃

4. Conclusions

The above presented and discussed results have shown that the electrokinetic behaviour of the commercial titanium white differed from that of the synthesised TiO₂-SiO₂ hybrid system. The most pronounced affect on the zeta potential values had the modification with U-15D silane. With increasing amount of this modifier used, the electrokinetic curves were shifted towards higher pH and the zeta potential took mostly positive values in the pH range studied. The modification with U-511 and

U-611 silanes did not cause significant changes in the character of electrokinetic curves. The type of electrolyte used (KCl, NaNO₃ or AlCl₃) and changes in its ionic strength also had important effect on the values of zeta potential.

Acknowledgement

This work was supported by the Poznan University of Technology research grant no. 32-204/2011 DS-MK.

References

- ALKAN M., DEMIRBAŞ Ö., 2005, Electrokinetic properties of kaolinite in mono- and multivalent electrolyte solutions, *Micropor. Mesopor. Mat.* 83, 51–59.
- BERGUA U., ROBERTS W., 2006, *Colloidal silica: fundamentals and applications*, CRC Press, New York.
- ERDEMOGLU M., SARIKAYA M., 2006, Effects of heavy metals and oxalate on the zeta potential of magnetite, *J. Colloid Interface Sci.* 300, 795–804.
- HIEMENZ P.C., RAJAGOPALAN R., 1997, *Principles of colloid and surface chemistry*, Marcel Dekker, New York.
- HUNTER R., 1981, *Zeta potential in colloid science*, Academic Press, Sydney.
- HUNTER R., 2001, Measuring zeta potential in concentrated industrial slurries, *Colloids Surf. A* 195, 205–214.
- JAYAWEERA P., HETTIARACHCHI S., 1993, Determination of zeta-potential and pH of zero charge of oxides at high-temperatures, *Rev. Sci. Instrum.* 64, 524–528.
- JESIONOWSKI T., CIESIELCZYK F., KRYSZTAFKIEWICZ A., Influence of selected alkoxy silanes on dispersive properties and surface chemistry of spherical silica precipitated in emulsion media, *Mat. Chem. Phys.* 119, 65–74.
- KOSMULSKI M., 2001, *Chemical properties of material surfaces*, Marcel Dekker, New York.
- KOSMULSKI M., PROCHNIAK P., ROSENHOLM J.B., 2009a, Electroacoustic study of titania at high concentrations of 1-2, 2-1 and 2-2 electrolytes, *Colloids Surf. B* 1-3, 106–111.
- KOSMULSKI M., PROCHNIAK P., ROSENHOLM J.B., 2009b, Electrokinetic study of adsorption of ionic surfactants on titania from organic solvents, *Colloids Surf. A* 1-3, 298–300.
- KOSMULSKI M., 2010, *Surface charging and points of zero charge*, CRC Press, New York.
- LEONG Y. K., 2005, Yield stress and zeta potential of nanoparticulate silica dispersions under the influence of adsorbed hydrolysis products of metal ions - Cu(II), Al(III) and Th(IV), *J. Colloid Interface Sci.* 292, 557–566.
- LYKLEMA J., 1984, Points of zero charge in the presence of the specific adsorption, *J. Colloid Interface Sci.* 99, 109–117.
- OTTERSTEDT J.E., BRANDRETH D.A., 1998, *Small particles technology*, Plenum Press, New York.
- SIWINSKA-STEFANSKA K., PRZYBYLSKA A., JESIONOWSKI T., SOJKA-LEDAKOWICZ J., OLCZYK J., WALAWSKA A., 2010, Wpływ kompozytu tlenkowego TiO₂-SiO₂ na właściwości barierowe wyrobów włókienniczych, *Przem. Chem.* 89, 1661–1666.
- SIWINSKA-STEFANSKA K., PAUKSZTA D., JESIONOWSKI T., 2011, Właściwości fizykochemiczne kompozytów TiO₂/SiO₂ otrzymanych w wyniku nukleacji układu reakcyjnego, *Przem. Chem.* 90, 1–11.
- VANE L.M., ZANG G.M., Effect of aqueous phase properties on clay particle zeta potential and electroosmotic permeability for electrokinetic soil remediation processes, *J. Hazard. Mater.* 55, 1–22.
- WALKOWIAK M., OSINSKA M., JESIONOWSKI T., SIWINSKA-STEFANSKA K., 2010, Synthesis and characterization of a new hybrid TiO₂-SiO₂ filler for lithium conducting gel electrolytes, *Cent. Eur. J. Chem.* 8 (6), 1311–1317.
- WALL S., 2010, The history of electrokinetic phenomena, *J. Colloid Interface Sci.* 15, 119–124.

- WU W., GIESE R.F., van OSS C.J., 1999, Stability versus flocculation of particle suspensions in water – correlation with the extended DLVO approach for aqueous system, compared with classical DLVO theory, *Colloids Surf. B* 14, 47–55.
- YOON R., MAO L., 1996, Application of extended DLVO theory, *J. Colloid Interface Sci.* 181, 613–26.

Received May 14, 2011; reviewed; accepted August 5, 2011

DE-AGGLOMERATION IN HIGH PRESSURE GRINDING ROLL BASED CRUSHING CIRCUITS

Daniel SARAMAK

Department of Environmental Engineering and Mineral Processing, Faculty of Mining and Geoengineering, AGH UST, dsaramak@agh.edu.pl

Abstract. The problems of possible application of de-agglomeration operations into industrial HPGR-based crushing circuits, were presented in the paper. The HPGR technology has the potential to provide a significant circuit efficiency increases from technological (better comminution efficiency) and economic (lower energy- consumption of crushing process) scopes. However, the HPGR product is usually compressed into a flake product, what may constitute a technical challenge in effective classification of crushing product and the overall efficiency of the circuit.

Three methods of flakes disintegration were investigated in the paper: an impact de-agglomeration, drum de-agglomeration and the wet one. Results showed that the wet and drum de-agglomeration operations are the most favourable methods of flakes disintegration. Additionally the wet process is especially beneficial for material with lower moisture content.

keywords: comminution, agglomeration, disintegration, flakes, efficiency

1. Introduction

High-pressure comminution is regarded as an important technology in mineral processing circuits primarily because it offers considerable energy savings. There are also many evidences in literature (Morley, 2003) that High Pressure Grinding Roll (HPGR) technology is more energy-efficient than typical tumbling comminution machines including autogenous, semi-autogenous and ball mills, as well as vertimills (Kalinowski, 2006). The HPGR technology has been widely used in the cement industry and, to a lesser extent, in the diamond industry, but still relatively rarely in the hard ores processing industry (Celik and Oner, 2006; Morrell, 2008; Persio et al. 2011).

Application of the HPGR technology has the potential to provide a significant circuit capacity increases in existing plants because the HPGR product has a significantly lower Bond Work Index. As a result of that the grinding time in downstream milling process can be reduced, because required size of product on that comminution stage is obtained more quickly than after conventional crushers on

second stage (Ergun et al., 2004; Norgate and Weller, 1994). Other benefits of the high-pressure comminution concern the following issues:

- the energy efficiency of the circuit increases with the proportion of comminution degree obtained in HPGR
- the micro-crack generation is observable, what significantly lowers the energy-consumption in downstream grinding processes
- the specific capital costs per unit capacity for the HPGR-ball mill circuit are more than 20% lower than for the SABC circuits (Pahl, 1993)
- the energy-consumption of circuit is also more beneficial for the HPGR-ball mill option, SABC circuit utilizes 20 to 30% more of energy (Saramak, 2011)
- the term of delivery in new machines implementation is also shorter for HPGR units than for SAG mills
- considerable smaller footprint of HPGR comparing to the SAG unit
- comparable costs of linings, but no costs of grinding media costs for HPGR machines.

The HPGR machines usually work in a closed circuit combined with the screen (Fig. 1), from where the oversize product is recycled to the press (van der Meer and Gruendken, 2010; Naziemiec and Saramak, 2009; Saramak, 2011).

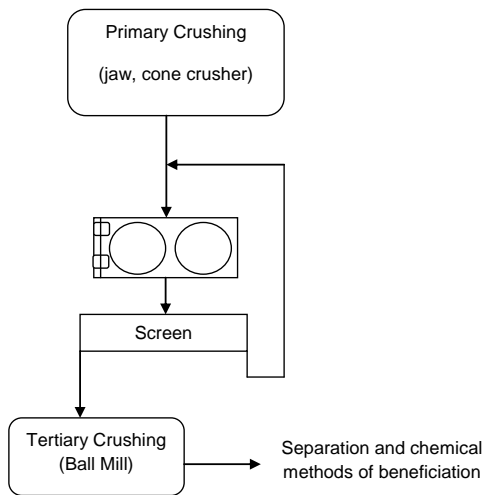


Fig. 1. Comminution circuit with HPGR device on second crushing stage (Saramak et al., 2010)

1.1. Problem definition

The technical challenge in achieving effective classification of crushing product occurs because the HPGR product is usually compressed into a flake product. The strength of flakes is a proportional functional relationship of the operating pressure. Even though the comminution degree increases together with the higher volumes of operating pressure, also the greater weight recovery of more competent flakes is observable in the HPGR product. Investigations in that matter carried out by the

author show that an extensive generation of flakes takes place especially for higher volumes of operating pressure in middle and coarser size fractions of the product (Fig. 2).

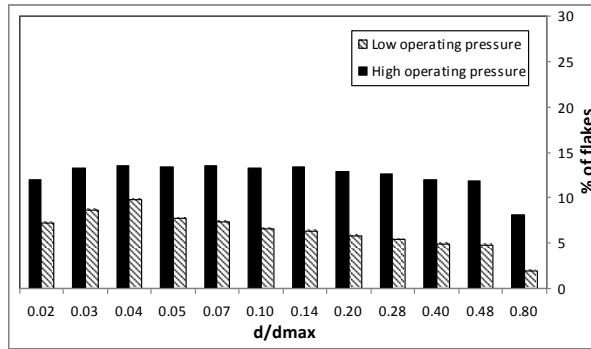


Fig. 2. Flakes mass recoveries in HPGR products crushed under high and low operating pressure

On-site experiments in iron and gold ore processing plants enable author to state that together with increasing the operating pressure in the HPGR press, the mass flow of the oversize screening product, which is recycled to the press, is higher too. The greater volume of operating pressure, the more considerable share of flakes in recycle mass flow what significantly decreases the overall efficiency of comminution circuit. Apart from the operating pressure, the flakes competency is a function of the ore type and the moisture content. Generally, competent flakes are being generated to a larger extent in softer ores or those with increased clay content (like kimberlites), while harder ores tend to produce rather fragile flakes.

1.2. De-agglomeration process

A method of overcoming of competent flakes generation is the implementation to the circuit the operation of the HPGR product de-agglomeration. This operation can be also utilized depending on the technological process requirements or the flakes competency. This is a significant issue in the flow-sheet development; it enhances the circuit efficiency, reducing the recirculation of already crushed material, which could be otherwise recycled to the press within the flakes.

Various de-agglomeration methods can be applied into the flow-sheet. Flakes product may be de-agglomerated by using rotary drum scrubbers, drums with lifter bars, by handling in chutes and bins, utilizing the impact forces (hammer mill or vertical impactor followed by the screening operation) or even on vibrating screens (especially in wet screening operations). Wet screening of the HPGR product is regarded as a mild de-agglomeration. When intense de-agglomeration is required, the HPGR product is delivered directly to the mill, the mill discharge is screened and the screen oversize is returned to the HPGR. Some methods of de-agglomeration are possible to implement without the need of adding any extra machines to the

technological circuit. An impact de-agglomeration can be done even on the vibrating screen, where either the dry or wet process can be carried out.

The technological flow-sheet configuration for a given material is driven by the requirements of the process and consideration of the crushing devices characteristics (mainly HPGR). In particular, the mass of possible fines recirculation and existence of a separate de-agglomeration operation will have a significant effect on the formulation of the flow-sheet technological and economic efficiency. The need and type of possible de-agglomeration operation can be assessed by suitable tests. The main aim of such tests is to identify suitable de-agglomeration and classification variant for the HPGR product disintegration.

2. Experimental programme

The main aim of the paper was to examine different methods of de-agglomeration. Two tests were carried out in following manner: test one was proceeded for material under natural moisture condition (about 2%), while in test 2 the feed moisture was increased to about 4%. This enabled to investigate an influence of both the method of de-agglomeration and the selected feed condition (the moisture) on the de-agglomeration process efficiency. In laboratory tests the iron ore with the bulk density approximately 2.0 g/cm³ and the hematite content about 60% was used, which was entirely crushed in laboratory HPGR unit. Table 1 summarizes technological parameters of the HPGR crushing process.

Table 1. HPGR tests summary

| | Test 1 | Test 2 |
|-------------------------------|----------|----------|
| Operating pressing force [kN] | 8 000 | 8 000 |
| Speed of rolls [m/s] | 0.4 | 0.4 |
| Roller diameter [m] | 0.2 | 0.2 |
| Roller width [m] | 0.15 | 0.15 |
| Type of linings | plain | plain |
| Type of material | Iron ore | Iron ore |
| Feed d_{\max} [mm] | 10 | 10 |
| Feed moisture content [%] | 2 | 4 |

The HPGR centre product from each test was then split into three representative samples designed for further de-agglomeration tests. Sample 1 was de-agglomerated in hands to obtain ideal disintegration of flakes and this sample was treated as a reference one. The flakes content in every single sample was analyzed within the size fraction of 1.168–4 mm, additionally the mass recoveries of -3.15 mm material were determined.

3. Experimental results

Screen analyses of both reference samples together with particle size distribution curve of feed are presented in Fig. 3.

The results has shown that both de-agglomerated samples have a content of almost 80% of particles smaller than 3.15 mm and the influence of different moisture of samples is of a rather low importance if about the HPGR product particle size.

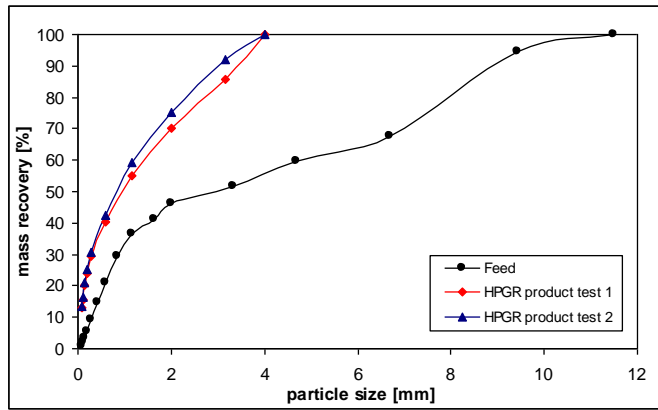


Fig. 3. Particle size distribution curves of feed and crushing products

3.1. Impact de-agglomeration

The first de-agglomeration method under investigation was the drop test. In that test the influence of impact forces on the de-agglomeration process were examined. The material flakes were dropped from the height of 1 meter, and then screened.

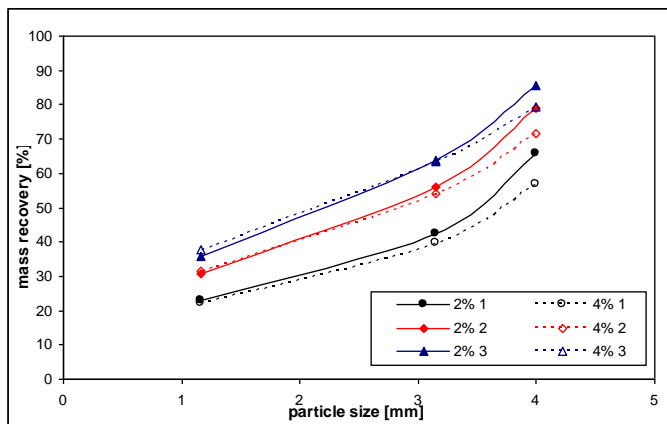


Fig. 4. Impact de-agglomeration

The procedure has been repeated three times for each sample. Results are presented in Fig. 4. The results show that with every drop the mass recovery of particles smaller than 3,15 mm steadily increasing, but even after third drop it cannot even approach the value of 80% obtained for HPGR products. The impact de-agglomeration is also more

efficient for the material with lower moisture content for several percent. After each consecutive drop the weight recovery of -3.15mm product increases, but the growth is smaller than after previous drop.

The impact de-agglomeration is relatively simple to implement, even without adding no machine to the circuit. It can be obtained for example during the screening process by implementing a suitable screen evoking a higher vertical trajectory of the particle movement.

3.2. Drum de-agglomeration

On the contrary to the impact de-agglomeration, the drum de-agglomeration process must take place in a separate machine, usually the rotary drum with lifters or rotors. A laboratory test was carried out in a 0.5 m diameter drum with two lifter bars. The samples were treated in the drum for 10, 20 and 30 seconds, while the drum rotated with speed slightly lower than 1 rev/s. After each test, the sieve analysis was performed and results are presented in Fig. 5.

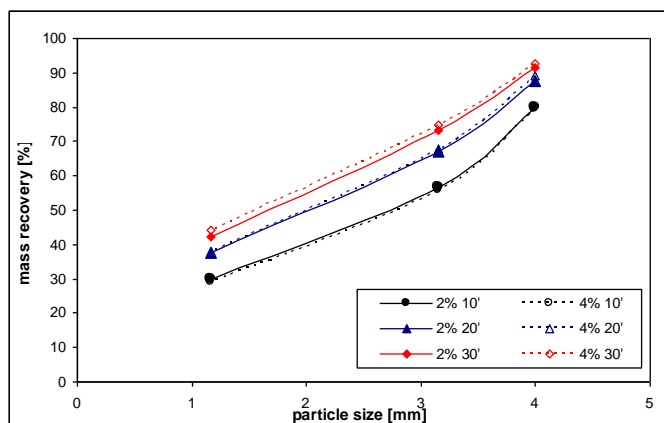


Fig. 5. Drum de-agglomeration results

The test has shown that obtained results are better comparing to the drop tests. Just after 10 seconds of material tumbling, the de-agglomeration results were more favorable than after two drops in impact tests. After 30 seconds of tumbling time the products contained only 10 – 15% of flakes exceeding 3.15 mm ($+3.15\text{mm}$ particles content was 75% for drum de-agglomeration and 85-90% for the de-agglomerated HPGR product – see Fig. 3). Furthermore, the moisture influence on the obtained results is of a minor importance.

3.4. Wet de-agglomeration

Apart from the above investigations, an additional test was carried out. The sample was laid for several minutes in a water bath. After the water treatment the material was

screened on a sieve with 3.15 mm mesh. This method of de-agglomeration can be obtained by the wet screening of the HPGR product. Under operating conditions, the screening process should be modified respectively, because the material should be intensively sprinkled with water, and the screening time needs to be optimized as well.

The sample with 4% of moisture was investigated by that method and the weight recovery of -3.15 mm particles was as high as 83%. The result for 2%-sample was practically identical. This result shows that the soaking of material is the most efficient method of de-agglomeration, because the flakes content in screen oversize product (-3.15 mm) is 3 to 8%. Table 2 also presents comminution degrees obtained in impact and drum de-agglomeration processes.

Table 3 summarizes the test results presented in the paper.

Table 2. Technological effects for both de-agglomeration methods

| | HPGR product | | Impact de-agglomeration | | Drum de-agglomeration | |
|-----|--------------|------|-------------------------|------|-----------------------|------|
| | 2% | 4% | 2% | 4% | 2% | 4% |
| S50 | 3.2 | 3.44 | 1.34 | 1.39 | 1.76 | 1.89 |
| S80 | 2.92 | 3.42 | 2.10 | 1.86 | 2.29 | 2.33 |

Table 3. Percentage weight recoveries of -3.15 mm particle fraction in all samples

| Type of test | 2% moisture content | 4% moisture content |
|-------------------------|---------------------|---------------------|
| De-agglomerated product | 85.9 | 92.2 |
| Impact de-agglomeration | 63.8 | 63.5 |
| Drum de-agglomeration | 73.2 | 74.8 |
| Wet de-agglomeration | 83 | |

4. Summary and conclusions

Results show that the wet de-agglomeration and next the drum process are two the most favorable methods of flakes disintegration. The wet process is especially beneficial for material with lower moisture content, because only about 3% of material stays as flakes. The satisfactory flakes disintegration can be also obtained when the drum de-agglomeration method is implemented. For material moisture content of 2% the flakes content is about 10% or less. The impact de-agglomeration for this type of material appeared as a less efficient method.

The material with higher moisture content produced a more favorable value of overall comminution degree, no matter of the method of de-agglomeration. However, the higher comminution level was weakened by the lower ratio of disintegrated flakes (Table 3) for products with higher moisture content. As a result of that, a part of undersize fines stays in the oversize screening product as flakes and they are recycled to the press again, decreasing the process efficiency.

The proper selection of de-agglomeration method should be made in general on the basis of three aspects: the first issue ought to take into account the type of material crushed, the second one should consider the desired degree of flakes disintegration,

while the third one the technological parameters of the HPGR operation. Application of the de-agglomeration operation into the technological circuit can be carry out in several ways. Connecting points between two conveyors can be a suitable place for installation the impact plates (mild de-agglomeration), if the height is as high as 2 meters or more. Another solution of mild de-agglomeration is the flushing of material onto the screen with excessive addition of water. When the process involves more intense process of particle disintegration, the drums should be applied together with mechanical treatment of moist flakes during the screening process.

Acknowledgments

The article is an effect of Polish Ministry of Science research grant N N524 466139.

References

- Celik I.B., Oner M., 2006, The influence of grinding mechanism on the liberation characteristics of clinker minerals, *Cement and Concrete Research*, 36 (3), 422–427.
- Ergün L., Ekmekçi Z., Gülsoy O., Benzer H., 2004, Modelling and simulation of grinding circuit in Madneuli copper concentrator, *Physicochemical Problems of Mineral Processing* 38, 231–240.
- Kalinowski W., 2006, Modernizacja procesów przemiałowych w przemyśle cementowym w świetle wymagań najlepszych dostępnych technik, *Surowce i Maszyny Budowlane* no. 1/2006.
- Morley C., 2003, HPGR in hard rock applications, *Mining Magazine*, IX/2003.
- Morrell S., 2008, A method for predicting the specific energy requirement of comminution circuits and assessing their energy utilization efficiency, *Minerals Engineering* 21, 224–233.
- Naziemiec Z., Saramak D., 2009, Analiza zmian obciążenia materiału w strefie zgniotu pras walcowych, *Górnictwo i Geoinżynieria* 4.
- Norgate, T.E., Weller K.R., 1994, Selection and operation of high pressure grinding rolls circuits for minimum energy consumption, *Minerals Engineering*, 7 (10), 1253–1267.
- Pahl M. H., 1993, *Praxiswissen Verfahrenstechnik – Zerkleinerungstechnik*. Fachbuchverlag Leipzig/Verlag TÜV Rheinland, Köln.
- Persio Rosario P, Hall R., Grundy M., Klein B., 2011, A preliminary investigation into the feasibility of a novel HPGR-based circuit for hard, weathered ores containing clayish material, *Minerals Engineering*, 24 (3–4), 290–302.
- Saramak D., 2010, Analiza powiązań pomiędzy parametrami technologicznymi pras walcowych z wykorzystaniem analizy czynnikowej, *ZN AGH Górnictwo i Geoinżynieria*, rok 34, zeszyt 4/1.
- Saramak D., 2011, Technological issues of High-Pressure Grinding Rolls operation in ore comminution processes, *Archives of Mining Sciences*, 56 (in press).
- Saramak D., Tumidajski T., Brożek M., Gawenda T., Naziemiec Z., 2010, Aspects of comminution flowsheets design in processing of mineral raw materials, *Gospodarka Surowcami Mineralnymi* 26, 4, 59–69.
- van der Meer F.P., Gruendken A., 2010, Flowsheet considerations for optimal use of high pressure grinding rolls, *Minerals Engineering*, 23 (9), 663–669.

Received May 9, 2011; reviewed; accepted August 25, 2011

COMPOSITION RECONSTITUTION OF CONCRETE AND MORTARS BASED ON PORTLAND AND EXPANSIVE CEMENTS

Teresa SZYMURA

Faculty of Architecture and Construction Engineering, Lublin University of Technology, 20-618 Lublin
Nadbystrzycka 40, t.szymura@pollub.pl

Abstract. Preliminary research aiming at the reconstitution of concrete and mortar substrate composition with the application of classical analytical methods and XRF is described. Approximate calculations of the substrate composition have been performed on the basis of an algorithm that consists in determining content proportions of calcium oxide, silica, alumina, iron oxide, sulfur trioxide and chlorides in substrates and products, elaborating linear equations with material balance for individual oxides in substrates and products, setting equation systems of two unknowns (cement, sand) for mortars and three unknowns (cement sand, coarse aggregate) for concretes, and finally solving all possible arrangements of equations with the use of a computer software. Mean values of all possible solutions have been accepted as final results. The determined initial composition is close to the real one with maximum differences of about 3%. The elaborated algorithm cannot be applied to calculate substrate composition when sulfur oxides and aluminum occur simultaneously in the balance equation.

keywords: cement binders, concrete mix composition, chemical analysis of cementitious materials

1. Introduction

Artificial stone, that is materials produced on the basis of cement, is the most often used material in construction engineering. Mortars and concretes belong to that group. They form, as a result of setting and hardening, a mixture which basic components are cement, aggregate and mixing water combined in adequate proportions. Hazard condition assessment and analysis of concrete construction damages that would lead to the determination of causes of those damages make an essential problem (Jamrozy, 2008). Cementitious materials compose or enter the composition of structural (load-bearing) elements and that is why they should exhibit adequate strength properties that considerably depend on their chemical composition (Czarnecki, 2004; Kurdowski, 2000). For that reason determination of chemical and mineral composition of concretes or mortars makes possible to find out many of their properties and thereby to establish some technical characteristics (physical-chemical and mechanical

properties). Chemical composition of cement as well as many other construction materials can be determined by means of chemical analysis methods (classical or instrumental) with the application of modern computational techniques that can be referred to as chemometry (Mazerski, 2000; Massart et al., 1998).

Although cementitious materials are very popular and the knowledge of their production technologies is very extensive, it happens that the end products do not meet designed strength standards or undergo unexpected corrosion (Czarnecki and Emmons, 2002). In such cases it is necessary to reconstitute the composition of the mixture out of which the faulty material has been produced (Jakubowska et al., 2009). Such analysis is not an easy task as the tested materials, that is concretes and mortars, are not uniform. Successful reconstitution of composition depends on numerous data concerning origin and kinds of the applied substrates as well as of the products whose initial composition is to be determined.

Within the presented research project, cement-based materials have been designed and produced under laboratory conditions. Their raw-material composition has been reconstituted with the application of chemical analysis methods and mathematical calculations that consist in the elaboration of many material-balance equation systems for individual determined components (CaO , MgO , SiO_2 , Fe_2O_3 , Al_2O_3 , SO_3 , Cl) where substrate components (e.g. cement, sand, aggregate) are the unknowns. The calculations have been performed with the use of computer software and the obtained results have been compared to the real data.

The experiments on raw-material composition reconstitution have been performed for mortars and concrete produced on the basis of portland cement and expansive cement (Krol and Tur, 1999; Peukert, 2000).

2. Characteristics of the tested materials: substrates and products

Mineral materials with a hydraulic binder (cement) as their main component have been tested.

2.1 Cements

Presently, among cements the portland cement is the most often used in the building industry. A variety of strength values and curing rates characterize that kind of cement (Kurdowski, 1991). It is produced in special kilns out of natural rock materials like limestone, clay, marlstone, chalk, diatomaceous earth, or high-silica sand. After having been processed the mentioned raw materials assume a form of porous baked nodules whose dimensions do not exceed 20 mm and are called portland cement clinker. In order to control the setting behavior gypsum is added during the clinker grinding process. The ground mixture of clinker and gypsum is referred to as portland cement. Portland cement clinker makes also a basis for the production of other cement varieties. Its properties influence physical-chemical characteristics of the

final product. That is the reason why it is essential to adequately proportion individual raw materials, make them uniform and process properly.

Properly prepared rawmix should include components shown in Table 1. The components can be found in limestone and clay or in marlstone, in a bonded form.

Table 1. Main chemical components of cement (Jamroz, 2008)

| No. | Component | Proportion in the portland cement composition (%) |
|-----|--------------------------------------|---|
| 1 | CaO | 60-70 |
| 2 | SiO ₂ | 18-25 |
| 3 | Al ₂ O ₃ | 4-9 |
| 4 | Fe ₂ O ₃ | 1-5 |
| 5 | MgO | 1-5 |
| 6 | SO ₃ | 1-3 |
| 7 | Na ₂ O + K ₂ O | 0.5 – 1.8 |

The following four mineralogical phases can be distinguished in the final product:

- alite – C₃S or tricalcium silicate 3CaO·SiO₂, participates in the formation of initial mechanical strength, longtime strength also depends on the mineral, content from 30 to 65%
- belite – C₂S or dicalcium silicate 2CaO·SiO₂, it sets slower than C₃S, content from 15 to 45%
- tricalcium aluminate (celite) – C₃A or 3CaO·Al₂O₃, the quickest reaction with water, content from 5 to 15%
- brownmillerite – C₄AF or tetracalcium aluminoferrite 4CaO·Al₂O₃·Fe₂O₃, one of the ferrites (there are also C₆A₂F, C₆AF₂), content from 5 to 15%.

Individual minerals differ in the way they undergo the hydration process (different reactivity with water) as well as in their share in the formation of chemical resistance and mechanical strength of the hardened cement paste.

Three characteristic processes that change structures of individual minerals can be distinguished as the process of setting and hardening runs (Kurdowski, 2008): dissolution of some minerals in water, hydrolysis, that is a chemical reaction of the mineral with water that makes the mineral decompose into constituent elements, and hydration, that is chemical binding of water by the mineral.

The addition of gypsum makes sulfate ions SO₄²⁻ react with already hydrating C₃A, which forms a layer of ettringite (3CaO·Al₂O₃·3CaSO₄·32H₂O) on its surface that inhibits the disadvantageous process of C₃A hydration and makes hydration of calcium silicates (mainly of alite) run in an undisturbed way. The reaction produces a phase denoted by the formula CSH. It makes the main component of most cement pastes and the most essential factor that determines strength of the hardening mix. At the same time calcium hydroxide (portlandite) forms.

3. Experimental

3.1. Results and discussion

The presented research project has aimed at elaborating an algorithm for the determination of an initial raw-material composition of concretes and mortars and evaluating its accuracy by the comparison of the obtained substrate content values to the quantities real-time used for the product production.

The testing range has included tests on the content proportions of basic elements in substrates (cements, mixing water, sand, aggregate) and in products (mortars and concretes). The following components have been determined: CaO, SiO₂, Al₂O₃, Fe₂O₃, SO₃ and chlorides.

Quantitative analysis testing has been performed by classical methods concordant with operative standards and partly by means of XRF techniques with the application of an x-ray fluorescence spectrometer, manufactured by Philips, model PW 1606. .

Chemical-analysis techniques that meet the PN-EN 206-1:2006 standard requirements and concern cement testing are of the status of standard model methods or alternative ones. Some of instrumental methods can be alternatively applied but only in the case when they use certified calibration patterns, Within the presented research work testing of all raw-material components as well as of mortar and concrete (after 28 days of the setting period) has been performed by classical methods described in the PN-EN standard while cement analyses have been done by both kinds of methods as only for that case calibration patterns have been available.

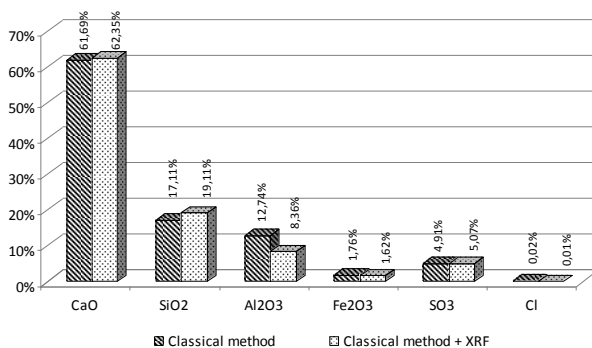


Fig. 1. Analysis results for expansive cement (Krol and Tur, 1999) sampled from the store of the Lublin University of Technology and tested by classical and instrumental (XRF) methods

The use of XRF techniques for chemical testing of building materials yields fast and accurate results but requires the application of calibration patterns that presently are not available for aggregates, mortars and concretes and that is why chemical composition of those materials cannot be determined that way. Chemical testing of building materials performed by classical methods recommended in the PN-EN 206-1:2006 Standard is characterized by lower accuracy and is more time-consuming but makes possible to determine chemical composition not only of cements bur also of

aggregates, mortars and concretes with their samples adequately prepared prior to the testing.

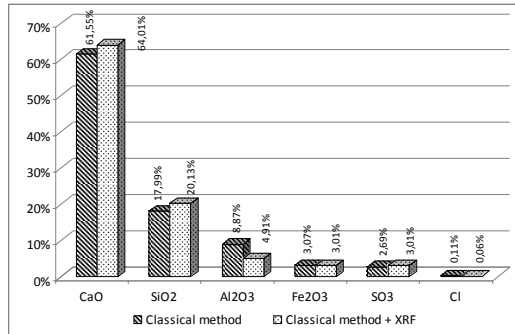


Fig. 2. Analysis results obtained by classical and XRF methods for portland cement CEM I 32,5 R of Chelm Cement Plant

Accuracy of the results depends mainly on a kind of the performed analysis, the determined component, applied reagents, and careful preparation of the sample. Some of the needed reagents are expensive and hard to obtain. Additionally, some of them can be a source of contamination. The performed testing has shown that the most inaccurate result has been obtained for a sample of aluminum oxide. For that reason additional calculations have been performed using interpolation of the obtained concentrations of individual materials determined both by classical and XRF methods.

Reconstitution of initial composition shown by the example of concretes and expansive mortars

Determination of the initial chemical composition for concretes and mortars with the application of research methods starts at the assumption that oxide constitutions of individual substrates and products are already known.

Table 2 presents oxide constitution of substrates and expansive products. An analysis of the presented materials indicates that there are also other compounds that enter their constitution. Notably, a coarse aggregate (gravel) sample has included carbonate rock chips. In the course of pyroprocessing its mass decrement of ca 20% has occurred and has complemented component balance of the aggregate as well as of the concrete with bonded water taken into account.

For the determination of raw-material composition of cementitious materials an algorithm in the form of an equation system has been proposed. It uses mathematical apparatus including matrix determinants. Calculations have been performed with the use of the Microsoft Office Excel software.

Based on the obtained results concerning oxide constitution of cement, sand, and gravel as well as of concrete and mortar material balance has been elaborated for each of the components. For concrete, many alternative equation arrangements in systems, of three equations with three unknowns representing components required for its manufacture (cement, sand, gravel) have been elaborated. In the case of mortar the

elaborated systems included two equations with two unknowns representing percent proportions of cement and sand. The following symbols have been used in the equations to denote the unknowns:

- c – percentage of portland or expansive cement in a product (concrete or mortar)
- p – percentage of sand in a product (concrete and mortar)
- z – percentage of gravel in a product (only concrete).

Table 2. Chemical composition of the tested materials obtained by means of classical analyses

| Chemical composition | Expansive concrete | Expansive mortar | Sand | | Gravel |
|--------------------------------|--------------------|------------------|-------------|--|--------|
| | | | Content (%) | | |
| CaO | 24.27 | 27.82 | 3.2 | | 20.37 |
| SiO ₂ | 47.74 | 45.59 | 87.74 | | 53.27 |
| Al ₂ O ₃ | 3.88 | 5.71 | 0.58 | | 1.19 |
| Fe ₂ O ₃ | 0.96 | 0.94 | 0.44 | | 1.17 |
| SO ₃ | 1.17 | 2.1 | 0.02 | | 0.08 |
| Cl | 0.1 | 0.07 | 0.15 | | 0.15 |
| Sum | 78.12 | 82.23 | 92.13 | | 76.23 |

For the sake of clarity in presenting all the arrangements composed of equations for individual chemical components, the following notation has been used to represent the components in each of the tables:

C – calcium oxide (CaO); S – silica (SiO₂); A – alumina (Al₂O₃); F – iron oxide (Fe₂O₃);

S – sulfur trioxide (SO₃); Cl – chloride ions (Cl⁻).

In the equations, water components have been neglected considering their low concentrations. In final calculations, water quantity has been established as the remaining part when from the sample whole a total of the calculated components has been subtracted.

A number of all possible arrangements has been calculated (Nahorska, 2002):

$$C_k^n = \frac{n!}{k!(n-k)!},$$

where: n – number of all possible equations, k – number of equations in a system.

Respectively:

– for concretes: $C_3^6 = \frac{6!}{3!(6-3)!} = 20$

– for mortars: $C_2^6 = \frac{6!}{2!(6-2)!} = 15$

Equation systems have been elaborated with the use of computer software (MathCad and Microsoft Office Excel).

Below given are example balance equations for expansive concrete and expansive mortar analyzed by classical methods:

for concrete:

$$0.6169c + 0.0320p + 0.2037k = 24.2700 \text{ calcium oxide}$$

$$0.1274c + 0.0058p + 0.0119k = 3.8800 \text{ alumina}$$

$$0.1711c + 0.8774p + 0.5327k = 47.7400 \text{ silica,}$$

boundary conditions:

$$c + p + k < 100, c > 0, p > 0, k > 0,$$

solution of the equation system:

$$c = 25.787, p = 27.037, k = 36.804,$$

where: c, p, k – percent proportions of expansive cement, sand, coarse aggregate in expansive concrete.

For mortar:

$$0.1274c + 0.0058p = 5.7100 \text{ alumina}$$

$$0.1711c + 0.8774p = 45.5900 \text{ silica}$$

$$c + p < 100, c > 0, p > 0$$

solution of the equation system: $c = 42.834, p = 43.607$, where: c, p – percent proportions of expansive cement and sand in expansive mortar.

Tables 3 and 4 present example balance arrangements and solutions of equation systems. Percent proportions of individual concrete or mortar components have been calculated as arithmetic means of results obtained for all the arrangements. In all the elaborated equations water fraction has been neglected as it contains only minute quantities of the balanced chemical components. Two repeating arrangements of equations for concrete: $\text{CaO} + \text{SO}_3 + \text{Al}_2\text{O}_3$ and $\text{CaO} + \text{SO}_3 + \text{Fe}_2\text{O}_3$, have been rejected because of a disproportionate difference in the results.

All the equations systems have been solved with the use of matrix determinants. In the case of concrete (three variables), at calculating main determinants W for individual equation systems Sarrus rule has been applied and values of all the unknowns (c, p, z) have been calculated based on Cramer formulas (Krysicki and Wlodarski, 2005). Determinants for all the equation systems, both for mortar and concrete, have been calculated using software of the Microsoft Office Excel 2003.

Both for mortar and concrete, correct solutions have been obtained only by equation systems with a non-zero main determinant that is by determined systems that have only one solution in the form of the searched values of unknowns with all those calculated values (c, p, z for concrete and c, p for mortar) meeting earlier determined boundary conditions. It has been noted that results obtained for expansive and portland cements by the C+S+A i C+S+F arrangements (Table 3) do not meet boundary conditions which means that mathematical equations.

It has been noted that results obtained for expansive and portland cements by the C+S+A i C+S+F arrangements (Table 3) do not meet boundary conditions which means that mathematical equations with the calcium sulfate participation are more implicit.

Figures 3 and 4 present raw-material composition of expansive materials – concrete and mortar. It has been calculated on the basis of chemical analyses and the elaborated algorithm. Percent proportions of individual mix components obtained with

the use of classical analytic methods and with classical + instrumental methods have been marked. The calculated results have been compared to real-time raw-material composition. Figures 5 and 6 present results obtained for mortar and concrete based on portland cement CEM I 32,5 R.

Table 3. The obtained results set by arrangements based on analyses performed for expansive concrete with the use of classical methods only and with classical methods + XRF method

| Arrangements | Classical methods | | | Classical and instrumental analytical methods | | |
|--------------|-------------------|----------|------------|---|----------|------------|
| | Cement (%) | Sand (%) | Gravel (%) | Cement (%) | Sand (%) | Gravel (%) |
| A+S+C | 25.787 | 27.037 | 36.804 | 25.892 | 27.140 | 35.629 |
| A+S+S | - | - | - | - | - | - |
| A+S+Cl | 25.889 | 27.856 | 35.424 | 25.918 | 27.364 | 35.251 |
| A+S+F | 25.913 | 27.973 | 35.227 | 25.857 | 26.842 | 36.161 |
| C+S+S | 23.051 | 22.08 | 45.852 | 22.994 | 21.883 | 45.321 |
| S+C+Cl | 26.184 | 27.773 | 35.469 | 26.000 | 27.335 | 35.269 |
| S+C+F | 26.695 | 28.701 | 33.776 | 25.607 | 26.622 | 36.583 |
| C+S+Cl | 23.059 | 17.039 | 46.62 | 23.002 | 16.918 | 46.082 |
| C+S+F | - | - | - | 23.019 | 6.808 | 47.619 |
| C+S+A | - | - | - | 22.095 | 1.152 | 33.410 |
| S+Cl+F | 23.119 | 21.961 | 41.69 | 23.047 | 20.601 | 42.392 |
| S+Cl+A | - | - | - | - | - | - |
| S+Cl+S | 23.201 | 28.639 | 35.001 | 23.141 | 28.336 | 34.645 |
| Cl+F+A | 25.911 | 28.095 | 35.184 | 25.846 | 26.256 | 36.366 |
| Cl+F+S | 25.814 | 27.881 | 35.411 | 26.342 | 27.215 | 35.343 |
| Cl+F+C | 26.929 | 30.332 | 32.81 | 25.450 | 25.427 | 37.249 |
| F+A+C | 25.965 | 23.621 | 36.785 | 25.839 | 28.393 | 35.597 |
| F+A+S | - | - | - | - | - | - |
| A+Cl+C | 25.838 | 26.538 | 36.705 | 25.899 | 26.984 | 35.633 |
| F+S+S | 23.126 | 25.38 | 40.394 | 23.055 | 24.563 | 40.891 |
| mean | 25.10 | 26.07 | 37.54 | 24.93 | 25.46 | 37.91 |

It needs to be noted that the value defined as “water” that has been obtained by subtracting the total of determined components from the whole is not exactly the amount of water that has been used to produce expansive concrete and expansive mortar. Practically, it is a total of the amount of water participating in the setting process, of water remaining in the pores, of evaporated water and also of carbon dioxide CO₂ bonded in the process of the binder carbonization.

Table 4. The obtained results set by arrangements based on analyses performed for expansive mortar with the use of classical methods only and with classical methods + XRF methods

| Balance equations | Classical methods | | Classical methods + instrumental methods | |
|-------------------|-------------------|----------|--|---------|
| | Cement (%) | Sand (%) | Cement (%) | Sand(%) |
| A+S | 42.834 | 43.607 | 42.920 | 42.612 |
| A+C | 42.821 | 43.934 | 43.157 | 37.395 |
| A+S | 42.611 | 48.549 | 42.605 | 49.522 |
| A+Cl | 42.838 | 43.555 | 42.607 | 49.499 |
| A+F | 42.884 | 42.556 | 42.210 | 58.228 |
| S+C | 42.838 | 43.612 | 42.427 | 42.720 |
| S+S | 42.631 | 43.652 | 42.632 | 42.675 |
| S+Cl | 43.764 | 43.431 | 46.683 | 41.793 |
| S+F | 42.609 | 43.657 | 46.673 | 41.795 |
| C+S | 42.613 | 47.936 | 42.649 | 38.378 |
| C+Cl | 42.841 | 43.555 | 42.445 | 42.363 |
| C+F | 42.895 | 42.512 | 41.496 | 60.857 |
| S+Cl | 42.631 | 43.583 | 42.634 | 42.338 |
| S+F | 42.631 | 43.567 | 42.619 | 43.797 |
| Cl+F | 42.627 | 43.583 | 43.001 | 42.288 |
| mean | 42.81 | 44.09 | 43.05 | 45.04 |

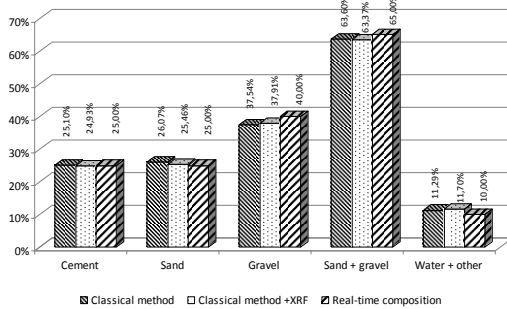


Fig. 3. Raw-material composition of expansive concrete

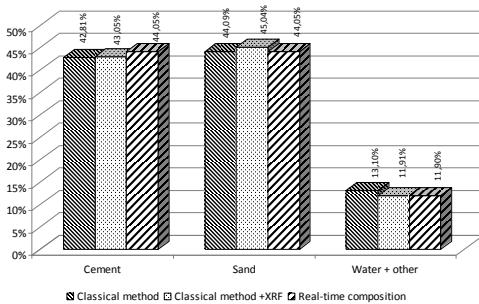


Fig. 4. Raw-material composition of expansive mortar

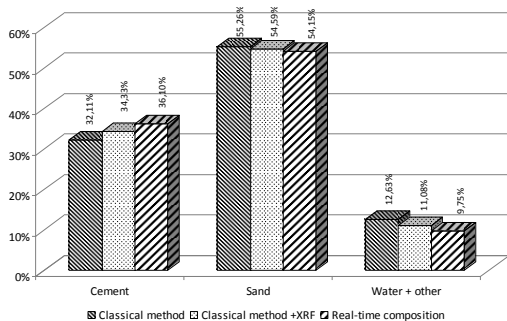


Fig. 5. Raw-material composition of ordinary mortar

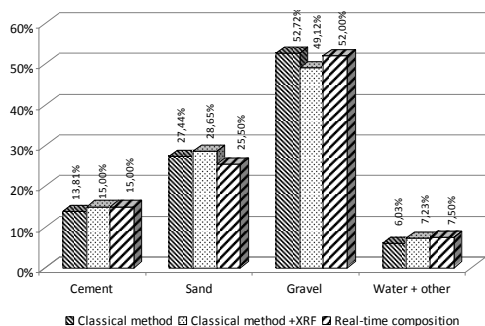


Fig. 6. Raw-material composition of ordinary concrete

4. Determination of concrete composition by the Gawlicki method

Determination of concrete and aggregate content proportions has been also performed by a method described by Gawlicki (Malolepszy, 2000). The method has been elaborated for an ordinary concrete, where Portland cement has been used as a binder without any additives. The presented research work attempts a reconstitution of the portland and expansive concrete composition taking into account that aggregate contains carbonate rock chips.

Table 5. Composition of ordinary concrete

| | Cement | Sand + gravel |
|---------------------------|--------|---------------|
| Real-time value (%) | 15.00 | 77.50 |
| Calculated value (%) | 11.81 | 75.72 |
| Difference in results (%) | 21.27 | 2.30 |

Table 6. Composition of expansive concrete

| | Cement | Sand + gravel |
|---------------------------|--------|---------------|
| Real-time value (%) | 25.00 | 65.00 |
| Calculated value (%) | 17.27 | 68.13 |
| Difference in results (%) | 30.92 | 4.59 |

5. Conclusions

Quantitative analyses of cement performed by classical methods according to the operative standards seem to be less accurate than analyses performed by X-ray fluorescence techniques. Alumina concentration sets a particular example of that. In the case of portland cement it is of 12.74% (Fig. 2) and the value is too high as compared to the standard values of 4-9% (Table 1). Percent proportions of the remaining chemical components calculated by the both kinds of methods do not exceed content value ranges given by the standards. Analytic results obtained by classical methods and by the instrumental one approach each other and their distribution do not exceed a few per cent. The greatest differences occur in the case of chlorides and in that case exorbitant values obtained by classical methods can result from the chloride contamination of reagents applied to the analyses. In each case it is important that samples to be analyzed are adequately prepared with their homogenization to be particularly careful. The applicability of instrumental methods to quantitative analyses of building materials is limited as they can be used for that purpose only when adequate calibration patterns exist. The application range of classical chemical-analysis methods is wider and includes assessment of the corrosion hazard for those materials and other expertise projects with the reconstitution of quantitative composition of concrete mixtures in that number. With interpolation applied to determine concentrations of chemical components required for the reconstitution of the real-time composition of cementitious materials it is possible to obtain more accurate results in the case of mortars and concretes based on Portland and expansive cements.

Estimated amounts of individual substrates calculated with the elaborated algorithm based on the results obtained by classical methods as well as by the XRF techniques approach real-time composition of concretes and mortars, ordinary and expansive ones, tested within the presented research project. In order to generalize the above observation over a wider range of cases, it is necessary to perform more extensive testing with the use of extended range of substrates proportioned various ways.

At the reconstitution of concrete and mortar substrate composition the greatest discrepancies have been observed for the case of the “water” component (water + the other). However, it should be emphasized that substrate water cannot be balanced for the end product. Practically, it is a total of the amount of water participating in the setting process, of water remaining in the pores, of evaporated water and also of a new component, that is carbon dioxide CO_2 bonded in the process of the binder carbonization.

The elaborated algorithm to be used for the reconstitution of real-time composition of concretes and mortars is characterized by relatively high accuracy. In order to enhance its reliability it is enough to minimize sources of faulty solutions of the balance equation systems. The most important are efficient methods of chemical

analysis that make possible to accurately determine chemical composition of individual materials.

In the case of calculating mixture composition of both kinds of concretes, strikingly disproportionate results have been obtained with equation systems that included A+S, both for classical methods and instrumental techniques. It can be related to the occurrence of ettringite, $3\text{CaO}\cdot\text{Al}_2\text{O}_3\cdot 3\text{CaSO}_4\cdot 32\text{H}_2\text{O}$, in the composition of concretes. Further investigations of a similar kind are necessary in order to describe that relation in the form of a mathematical equation.

Results obtained by the method of Gawlicki (Malolepszy, 2000) show differences between real-time and calculated values of the order of a few percent for sand and gravel and of over 20 and 30% for cements (Table 5 and 6).

References

- CZARNECKI L. I EMMONS P. H., 2002. Naprawa i ochrona konstrukcji betonowych, Polski Cement Sp. z o.o., Kraków.
- CZARNECKI L. I INNI., 1994. Chemia w budownictwie, Arkady, Warszawa.
- JAKUBOWSKA M., KALARUS D., KOT A., KUBIAK W., 2009. Metody chemometryczne w identyfikacji źródeł pochodzenia klinkieru oraz cementu, Materiały Ceramiczne /Ceramic Materials/, 61, 1, 12-15.
- JAMROZY Z., 2008. Beton i jego technologie, PWN, Warszawa.
- KOBYLINSKI A., SZYMANSKI E., 1978. Materiały budowlane, PWN, Warszawa.
- KROL M., TUR W., 1999. Beton ekspansywny, Arkady, Warszawa.
- KRYSICKI W., WŁODARSKI L., 2005. Analiza matematyczna w zadaniach, wyd. 29, t. 1, Warszawa, PWN
- KURDOWSKI W., 2000. Chemia materiałów budowlanych, UWN-D, Kraków.
- KURDOWSKI W., 2008. Faza C-S-H - stan zagadnienia cz.1, Cement, Wapno, Beton, 4, 216–222.
- KURDOWSKI W., 2008. Faza C-S-H - stan zagadnienia cz.2, Cement, Wapno, Beton, 5, 258–268.
- KURDOWSKI W., 2002. Korozja chlorkowa betonu, Cement Wapno Beton, 2, 56-60.
- KURDOWSKI W., 1991. Chemia cementu, PWN, Warszawa.
- MALOLEPSZY J. et al., 2000. Technologia betonu - metody badan, UWND, Kraków.
- MASSART D.L., VANDEGINSTE M.B.G., BUYDENS L.M.C., DE JONG S., LEWI P.J., SMEYERS-VERBEKE J., 1998. Handbook of chemometrics and qualimetrics: part B, Elsevier Amsterdam.
- MAZERSKI J., 2000. Podstawy chemometrii, Wyd. Politechniki Gdanskiej Gdansk.
- NAHORSKA H. et al., 2002. Tablice matematyczne, Podkowa, Gdansk.
- NONAT A., 2004. Cement and Concrete Research 34, 1521.
- PEUKERT S., 2000. Cementy powszechnego uzytku i specjalne – podstawy produkcji, właściwosci i zastosowanie, Polski Cement Sp. z o.o., Krakow.
- PN-B-06712, 1986. Kruszywa mineralne do betonu.
- PN-EN 206-1, 2000. Beton – Część 1: Wymagania, właściwości, produkcja i zgodność.
- SORRENTINO F., 2008. Nowe spojrzenie na moduł nasycenia wapnem, Cement Wapno Beton, 2, 82–88.

Received April 30, 2011; reviewed; accepted July 25, 2011

STUDIES ON PLATINUM RECOVERY FROM SOLUTIONS AFTER LEACHING OF SPENT CATALYSTS BY SOLVENT EXTRACTION

Beata POSPIECH

Department of Chemistry, Czestochowa University of Technology, 42-200 Czestochowa, Armii Krajowej 19, Poland, bak@wip.pcz.pl

Abstract. The results of studies on the separation of platinum(IV) ions by solvent extraction from aqueous solutions after leaching of spent catalysts have been reviewed. The following processes have been discussed: acid leaching of spent catalysts and solvent extraction of platinum(IV) ions by using organophosphorous acids, amines and oximes as the extractants. In hydrometallurgical leaching of spent automobile catalysts many reagents such as *aqua regia* solutions, aluminum chloride solutions with low concentrations of nitric acid as an oxidant, and sodium cyanide solutions were tested. After leaching, the metal ions in leach solutions have to be separated and purified by solvent extraction. Typical leach liquor contains economically valuable metal ions such as platinum(IV), palladium(II), rhodium(III) nickel(II) and manganese(II). The influence of several factors on the efficiency and selectivity of platinum(IV) ions extraction from leach solutions was shown. The optimum conditions of these processes were also reported on the ground of literature survey.

keywords: platinum, spent catalyst, leaching, solvent extraction

1. Introduction

Spent catalysts from automobile industry contain a number of important nonferrous metals such as platinum (Pt), palladium (Pd), nickel (Ni), iron (Fe) and manganese (Mn). Platinum exhibits excellent catalytic activity, therefore platinum is also used in petrochemical industry for the catalytic reforming process. Actually, an increasing demand for platinum is observed. Natural resources of platinum group metals (PGMs) are limited. On the other hand, the demand for these metals increases throughout due to their use as conductors in the electronic industries, automobile and industrial catalysts, jewellery, biomedical devices, dental and medical prosthesis, etc. (Swain et al. 2010; Lee et al. 2010; Angelidis et al. 1996). Spent catalysts are the potential source of important metals and it is also a source of hazardous, toxic chemical element such as Pb, Hg, Cd, V and their association. Therefore, the spent catalysts are hazardous industrial waste. Environmental laws concerning spent catalyst disposal

have become increasingly more severe in recent years (Singh 2009; Marafi and Stanislaus 2003).

This paper reports leaching of spent catalysts and the solvent extraction separation of platinum ions from leach liquors. The aim of this paper is to show the possibility of selective platinum recovery by hydrometallurgical processes. In this paper, the platinum supply, demand, and recycling were shown.

2. Platinum production and demand

Initially, catalysts containing mainly nickel, cobalt, copper and iron had been assessed as autocatalysts. They were susceptible to poisons derived from the fuel. The eventually chosen catalysts were based on the highly active platinum group metals (Tweeg 1999). The PGM recovery from spent catalysts has been increased during the last 10 years. The increase of PGMs in industry is connected mainly with the still growing number of cars. Catalysts allow to reduce considerably three major impurities in the atmosphere, that is carbon monoxide (CO), hydrocarbons (HC) and nitrogen oxide (NO) (Saternus and Fornalczyk 2009).

Table 1. Platinum supply, demand and recycling (2005 to 2010) (Matthey 2011)

| Mega grams | 2005 | 2006 | 2007 | 2008 | 2009 | 2010 |
|------------------------------|--------------|--------------|--------------|--------------|--------------|--------------|
| Supply | | | | | | |
| South Africa | 159.1 | 164.7 | 157.7 | 140.4 | 144.2 | 144.2 |
| Russia | 27.7 | 28.6 | 28.5 | 25.1 | 24.4 | 25.7 |
| North America | 11.3 | 10.7 | 10.1 | 10.1 | 8.1 | 6.5 |
| Zimbabwe | 4.8 | 5.1 | 5.3 | 5.6 | 7.2 | 8.7 |
| Others | 3.6 | 3.3 | 3.7 | 3.6 | 3.6 | 3.4 |
| Total Supply | 206.5 | 212.4 | 205.3 | 184.8 | 187.4 | 188.5 |
| Demand by Application | | | | | | |
| Autocatalyst | 118.1 | 121.5 | 128.9 | 113.7 | 68.0 | 97.2 |
| Chemical | 10.1 | 12.3 | 13.1 | 12.4 | 9.0 | 13.8 |
| Electrical | 11.2 | 11.2 | 7.9 | 7.1 | 5.9 | 6.8 |
| Glass | 11.2 | 12.6 | 14.6 | 9.8 | 0.3 | 10.7 |
| Investment | 0.5 | -1.2 | 5.3 | 17.3 | 20.5 | 20.2 |
| Jewellery | 76.6 | 68.02 | 65.6 | 64.1 | 87.4 | 75.1 |
| Medical & Biomedical | 7.7 | 7.8 | 7.2 | 7.6 | 7.8 | 7.9 |
| Petroleum | 5.4 | 5.6 | 6.5 | 7.5 | 6.5 | 5.3 |
| Other | 7.0 | 7.4 | 8.2 | 9.0 | 5.9 | 7.9 |
| Total Demand | 247.8 | 245.4 | 257.3 | 248.5 | 211.3 | 245.1 |
| Recycling | | | | | | |
| Autocatalyst | -24.0 | -26.8 | -29.1 | -35.1 | -25.8 | -33.7 |
| Electrical | 0.0 | 0.0 | 0.0 | -0.2 | -0.3 | -0.3 |
| Jewellery | -15.5 | -17.2 | -20.4 | -21.6 | -17.6 | -23.2 |
| Total Recycling | -39.5 | -44.0 | -49.5 | -56.9 | -43.7 | -57.2 |

South Africa is the largest producer of platinum. About 80% of the world's PGM come from the Bushveld complex in South Africa. Russia is the second largest

supplier of platinum, accounting for roughly 10%. Platinum production capacity is estimated to grow to approximately 0.281 gigagram (Gg) in 2010 from about 0.192 Gg in 2002. Before 1999, supply and demand were largely balanced and prices were stable. The platinum demand has outgrown supply almost every year since 1999. As a consequence, the balance between supply and demand has become increasingly unsettled. Table 1 gives platinum supply, demand by application, and recycling since 2005 to 2010 (Matthey 2011).

Growing demand in spite of rapid price rise indicates very low demand elasticity. Actually, platinum remains heavily used for jewelry. Demand from that sector dropped from 40% to 32% in 2010, due to higher platinum prices (Yang 2009). Figure 1 shows the price of platinum since 2007 to 2011 (Matthey 2011).

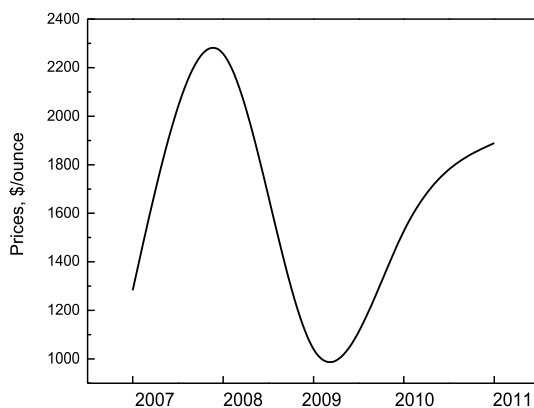


Fig.1. Platinum price in years 2007–2011 (Matthey 2011)

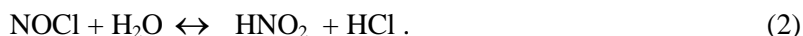
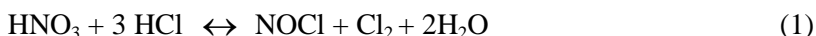
3. Main available processes of PGMs from spent catalysts

Nowadays the spent auto catalysts are reworked with the use of hydrometallurgical methods and high temperature treatment of the material. The aim of these technologies is the extraction of pure metal (Brumby et al. 2005; Fornalczyk and Saternus 2007, 2010). Recovery of valuable metals from spent catalyst requires application of the modern, technically advanced, economically valuable and environmentally friendly hydrometallurgical technology. The solvent extraction process enables recovery of valuable metals such as platinum from secondary or spent materials and protects the environment from hazardous and toxic compounds (Charewicz et al. 2001, Chmielewski et al. 2005). Hydrometallurgical processes may be classified in two major groups (Angelidis et al. 1996): a) feed digestion (leaching), b) solution purification with metals separation using solvent extraction (the noble metals are extracted from the substrate by oxidant acidic solution, leaving the bulk of the substrate unaffected). The conventional methods such as precipitation, cementation, ion-exchange and reductive exchange have been used to separation of platinum from

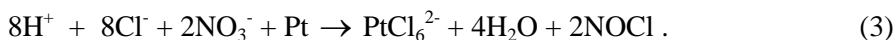
liquid wastes. Solvent extraction (SX) is one of the most important processes in hydrometallurgy and is applied for the recovery of many valuable metals.

4. Acid leaching of spent catalysts

Many authors have investigated the recovery of valuable metals such as Pt from a spent catalyst by HNO₃/HCl mixture leaching. They studied also the kinetics of platinum extraction from spent reforming catalysts in *aqua regia* solutions under atmospheric pressure and at temperature up to 100°C (Baghalha et al. 2009). HNO₃ and HCl in *aqua regia* undergo reactions (1) and (2):

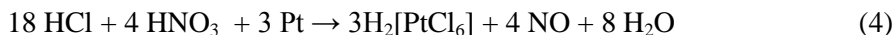


The role of HNO₃ (NO₃⁻) is to be the oxidant. The role of HCl is to provide the complexing agent (Cl⁻). Dissolution of Pt from the catalyst is a redox and complexing reaction:



By kinetic modeling using a power-law rate equation for Pt extraction, the reaction order was calculated to be 1.5 for Pt concentration in solid and 1.3 for the hydrogen ion molarity in the solution. The effect of temperature on Pt extraction kinetics was modeled using the Arrhenius equation. The activation energy for the Pt extraction equal to 72.1 kJ/mol. This value indicates that Pt extraction in *aqua regia* is controlled by the surface chemical reaction of Pt dissolution.

Jafarifar et al. (2005) studied also the leaching of the catalyst in freshly prepared *aqua regia*. The sample of the catalyst contained 0.20% Pt, 0.43% Re and other impurities such as iron oxide and large amount of aluminosilicate supporting carrier. This work has investigated two alternative methods for leaching. In the first method spent catalyst was refluxed with *aqua regia* at the liquid/solid ratio of 5 for 2.5 h. In the solution after leaching the concentration of Pt was approximately 30 g/dm³. In the second method, microwave radiation was used at a power of 150 W with *aqua regia* at liquid/solid ratio of 2 for 5 min. The reactions were:



After leaching the platinum was separated from rhenium and recovered as diammonium hexachloroplatinate with efficiency of 96.5% and 98.3%, respectively by these methods. The platinum precipitate was converted to platinum powder at 400°C according to reaction:



Studies on platinum dissolution from a spent Pt-NiO/Al₂O₃ industrial catalyst were carried on by Angelidis and Skouraki (1996). Aluminium chloride solution with low concentrations of nitric acid as an oxidant instead of *aqua regia* was used to leach the spent catalyst. The Pt recovery increases as nitric acid concentration increases. It was confirmed that it does not affect platinum dissolution yield, but minimizes excess reagents consumption.

Pt recovery from a spent dehydrogenation catalyst using cyanide leaching was studied by Shams et al. (2004). The best Pt recovery results were obtained for pH values in range of 8-9 at 140-180°C. Decoking of the coked catalysts is not necessary during high temperature cyanide leaching from catalysts. The level of platinum recovery obtained by cyanide leaching compared with others hydrometallurgical methods using, for example, *aqua regia* or hydrochloric acid, which has a recovery of more than 95%, looks too low for a cost effective platinum recovery procedure.

Aqua regia leaching was used to recovery of platinum from the dust of spent catalyst arising from nitric acid production plant (Barakad and Mahmoud 2004). *Aqua regia* was prepared by mixing concentrated hydrochloric acid (36%) and concentrated nitric acid (65%) by the volume ratio of 3 HCl to 1 HNO₃. The maximum recovery of 98% was attained with a liquid/solid ratio of 10 at 109°C after 1.5 h. Solvent extraction with 10% trioctylamine (TOA) in kerosene was proposed for separation of iron(III) from Pt(IV) ions from solution containing 0.1 g/dm³ Pt(IV) and Fe(III). Pt(IV) ions were extracted with TOA by an ion exchange mechanism. The effect of HCl concentration in aqueous solution was investigated. Solutions containing Pt(IV) and Fe(III) ions were prepared in the presence of different hydrochloric acid concentration (0.01 M – 7 M). Excellent separation of Pt(IV) from Fe(III) was obtained utilizing 0.01 M HCl. The separation factor (*D*) for platinum over iron reached a value of > 4000 in 0.01 M HCl. Platinum was separated from the leach liquor as diammonium hexachloroplatinate (NH₄)₂PtCl₆ by precipitation using ammonium chloride.

5. Solvent extraction of platinum

Many researcher have studied the extraction of metals from spent catalysts. The physical and chemical properties of PGMs are very similar, and thus, is difficult to separate these metals from aqueous solutions. Literature reports that Pt(II) forms mainly chloride complexes PtCl₄²⁻ in aqueous chloride solutions. Pt(IV) forms in chloride solutions stable anionic complexes PtCl₆²⁻. Table 2 shows the values of stability constants of chloride complexes for Pt(IV) at different ionic strengths (Stability, 1982). The platinum(IV) chloride complexes PtCl₆²⁻ are stable at pH values below 1 to prevent hydrolysis and in the presence of excess chloride ions to prevent adsorption on the undissolved substrate (Angelidis et al., 1996). The values of stability constants of PtCl₆²⁻ complexes at constant ionic strength (*I* = 3.0 M) is equal to 2.76.

The separation of Pt and Pd from aqueous solutions is very difficult. The commercial organophosphorus compounds, amines, oximes, thio-phosphoric

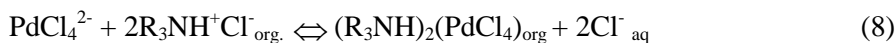
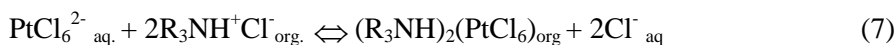
acids, phosphonic acids, thiophosphinic acid, thiourea have been proposed for the extraction in order to separate of Pt(IV) from other metal ions. Several publications have dealt with the application of organophosphorus acids and the derivatives of organophosphorus compounds in extraction of platinum from aqueous chloride solutions. The studies on application of tributyl phosphate (TBP) and Aliquat 336 in selective extraction of Pt(IV) from solution after leaching automobile catalyst containing Pd(II), Fe(III), Ni(II), Mn(II) and Cr(VI) by solvent extraction were reported by Lee et al. (2010). The extraction behaviour of Pt and other metal ions from aqueous phase (pH 3.2) as a function of Aliquat 336 concentration in kerosene was investigated. The efficiency of platinum(IV) ions extraction increased with the increase of extractant concentration. The best separation factor was obtained with 0.011 M Aliquat 336. This extractant can be used to separations of Pt(IV) and Pd(II) ions with efficiency 99.9 % and 99.8 %, respectively.

The separation of Pt(IV) and Pd(II) from associated metals like Fe(III), Cu(II), Ni(II), Zn(II), Al(III) from synthetic solutions containing 1 g/dm³ of Pt(IV) and 1 g/dm³ Pd(II) were investigated by solvent extraction with 0.5 vol.% LIX 841 (2-hydroxy-5-nonylacetophenone oxime in mixture with a high flash point hydrocarbon dilent) in kerosene. A 5 vol.% solution of Alamine 336 (tertiary amine of mixed tri-octyl/decyl amine) in kerosene was used for co-extraction of Pt(IV) and Fe(III). The 0.5 M thiourea and dilute 0.1 M HCl solution were used for stripping of these metals. Purity of the Pd(II) and Pt(IV) strip solutions were 99.7% (Reddy et al. 2010).

Table 2. Values of stability constants of chloride complexes for Pt(IV) (Stability, 1982)

| Medium and ions strength, M | β_1 | β_2 | β_3 | β_4 | β_5 | β_6 |
|------------------------------------|-----------|-----------|-----------|-----------|-----------|-----------|
| 0.1 NaNO ₃ | - | - | 3.08 | 2.46 | - | - |
| 1.0 NaNO ₃ | - | - | 3.15 | 2.55 | - | - |
| 3.0 NaClO ₄ | - 0.25 | - | - | - | - | - |
| 3.0 H ₂ SO ₄ | - | - | - | - | - | 2.76 |

Separation of Pt(IV) and Pd(II) from chloride solution using Alamine 300 at concentrations from 0.001 to 0.01 M in the presence of 0.5 M HCl in aqueous phase was also studied (Swain et al. 2010). The extraction reaction can be explained with equations:



The loaded organic phase was stripped by NaSCN as H₂Pt(Cl)₄(SCN)₂. NaSCN was the best stripping agent for platinum and (NH₂)₂Cs with HCl was the best stripping agent for palladium. Platinum of about 99.99% purity and 98% pure

palladium can be separated from a mixed solution of Pt and Pd chloride by this process.

Liquid-liquid extraction of platinum, palladium, and rhodium with Cyanex 921 (tri-octyl phosphine oxide) from aqueous hydrochloric acid media has been studied by Mhaske and Dhadke (2001). A synthetic solution was similar in composition to that expected from the leaching of spent catalysts in 6.0 M HCl. The separation of these metal ions from their mixtures was carried out by taking advantage of their different extraction and stripping conditions with Cyanex 921. The effect of HCl concentration was investigated. It was observed that extraction of Pt(IV), Pd(II) and Rh(III) decreases at higher concentration of HCl due to the mass action effect of the chloride ions. Platinum metals were extracted also with different concentrations of Cyanex 921 from 1 to 100 mmol/dm³ in toluene. The Cyanex 921 concentration for Pt(IV) was optimised at 6.0 M HCl and in the presence of 250 mmol/dm³ tin(II) chloride. The stripping of Pt(IV) was observed at 4.0 to 6.0 M HNO₃. The proposed method is rapid for the separation of Pt, Pd and Rh with recovery efficiency about 99.8 %.

6. Conclusion

The recycling of catalysts is required for economic and environmental reasons. Platinum, along with some other platinum group metals (PGMs), is the main active component of industrial and automobile catalysts. Leaching and separation conditions for the recovery of platinum from spent catalyst have been evaluated. Leaching with *aqua regia* at temperatures above 70°C is difficult in industrial practice because of the highly aggressive nature of this solution and decomposition of gaseous products. The study showed that the substitution of hydrochloric acid by aluminum chloride and the use of low nitric acid concentrations instead of *aqua regia* do not affect considerably platinum recovery from powdered industrial platinum based catalysts. Literature survey indicated that solvent extraction of platinum(IV) ions is simple, rapid and suitable for metal ions separation from solution after leaching of spent catalysts. The results of investigations indicate that the hydrometallurgical techniques for recovery of platinum are cost effective and environmentally friendly.

References

- ANGELIDIS T.N., SKOURAKI E., 1996, Preliminary studies of platinum dissolution from a spent industrial catalyst, Applied Catalysis A: General, 142, 387–395.
- BAGHALHA M., KHOSRAVIAN H.G.H., MOTAHEB H.R., 2009, Kinetics of platinum extraction from spent reforming catalysts in aqua-regia solutions, Hydrometallurgy 95, 247–253.
- BARAKAT M.A., MAHMOUD M.H.H., 2004, Recovery of platinum from spent catalyst, Hydrometallurgy 72, 179–184.
- BRUMBY A., VERHELST M., CHERET D., 2005, Recycling GTL catalysts. A new challenge, Catalysis Today 106, 166–169.
- CHAREWICZ W., CHMIELEWSKI T., WALKOWIAK W., 2001, Srebro i platynowce – występowanie, właściwości, zastosowanie, Mat. VI Seminarium Hydrometalurgia srebra i platynowców, 5–22.

- CHMIELEWSKI T., WALKOWIAK W., CHAREWICZ W., 2005, Wybrane uwarunkowania rozwoju hydrometalurgicznych technologii otrzymywania ołowiu, niklu, kobaltu srebra, złota i platynowców, *Mat. X Seminarium Hydrometalurgia metali towarzyszących*, 7–43.
- FORNALCZYK A., SATERNUS M., 2007, Recykling zużytych katalizatorów samochodowych, *Rudy i Metale Nieżelazne* 6, 326–331.
- FORNALCZYK A., 2010, Zużyte katalizatory samochodowe, *Recykling* 12, 21–23.
- JAFARIFAR D., DARYANAVARD M.R., SHEIBANI S., 2005, Ultra fast microwave-assisted leaching for recovery of platinum from spent catalyst, *Hydrometallurgy* 78, 166–171.
- LEE J.Y., RAJU B., KUMAR B.N., KUMAR J.R., PARK H.K., REDDY B.R., 2010, Solvent extraction separation and recovery of palladium and platinum from chloride leach liquors of spent automobile catalyst, *Separation and Purification Technology*, 73, 213–218.
- MARAFI M., STANISLAUS A., 2003, Options and processes for spent catalyst handling and utilization, *Journal of Hazardous Materials B101*, 123–132.
- MHASKE A.A., DHADKE P.M., 2001, Extraction separation studies of Rh, Pt and Pd using Cyanex 921 in toluene – a possible application to recovery from spent catalyst, *Hydrometallurgy* 61, 143–150.
- MATTHEY, 2011, Platinum 2011, *Platinum Metals Review*, 55, 201–202.
- REDDY B.R., RAJU B., LEE J.Y., PARK H.K., 2010, Process for the separation and recovery of palladium and platinum from spent automobile catalyst leach liquor using LIX 841 and Alamine 336, *Journal of Hazardous Materials*, 180, 253–258.
- SATERNUS M., FORNALCZYK A., 2009, Zużyte katalizatory samochodowe jako źródło platynowców, *Rudy i Metale Nieżelazne* 2, 59–67.
- SHAMS K., BEIGGY M.R., SHIRAZI A.G., 2004, Platinum from a spent industrial dehydrogenation catalyst using cyanide leaching followed by ion exchange, *Applied Catalysis A: General*, 258, 3227–234.
- SINGH B., 2009, Treatment of spent catalysts from the nitrogenous fertilizer industry – A review of the available methods of regeneration, recovery and disposal, *Journal of Hazardous Materials* 167, 24–37.
- SWAIN B., JEONG J., KIM S., LEE J., 2010, Separation of platinum and palladium from chloride solutions by solvent extraction using Alamine 300, *Hydrometallurgy* 104, 1–7.
- STABILITY CONSTANTS OF METAL-IONS COMPLEXES, 1982, Part A: Inorganic Ligands, Compiled by E. Högfeltdt, Pergamon Press
- TWIGG M. V., 1999, Twenty-Five Years of Autocatalysts, *Platinum Metals Review* 43, (4), 168–171
- YANG C.J., 2009, An impending platinum crisis and its implications for the future of the automobile, *Energy Policy* 37, 1805–1808

Received May 15, 2011; reviewed; accepted August 16, 2011

DETERMINATION OF THE EFFECTIVE SIEVE BLOCKING COEFFICIENT

Katarzyna LAWINSKA, Piotr WODZINSKI

Department of Process Equipment, Technical University of Lodz, wodzinsk@wipos.p.lodz.pl

Abstract. This paper presents the results of considerations concerning the ratio of blocking of screen holes and the importance of particular independent variables affecting the process of blocking of sieve holes. The phenomenon of blocking the holes is unfavorable since it reduces the flow area of the lower size fraction through a sieve under scrutiny. The study was conducted, using laboratory sieves. Fine-grained materials: sand (loose sedimentary rock of irregular form) and agalite (spherical mineral) were applied as investigated mineral media.

keywords: screening, sieve, granular material

1. Introduction

The phenomenon of blocking the holes of the sieve is a process resulting from two processes occurring simultaneously at the time of clogging and declogging of sieves (Beeckmans et al., 1985). The fundamental relationship that appears in this case is $f = f(t)$, where f is the coefficient of screen blocking and t denotes time. It is defined as the ratio of the number of free holes to the total number of sieve holes. Furthermore, one can define it as the ratio of surface area occupied by grains clogged in the holes (or slots) of grain and the total area of the screen. It is a dimensionless value (Apling 1984, Wesselbaum 1984). Figure 1 depicts this dependence for a typical course of the initial screening period (Banaszewski 1990). At the moment, when the material is provided to the screen with blocked holes, this state is defined by blocking coefficient f_0 . This means that the screen has not performed any pulsating movement and blocked holes are present in the screen. Furthermore, with time t , the value of screen blocking coefficient f tends to the final value of f_∞ . The final state can be achieved along curve 1 or 2. Curve 1 demonstrates the case when $f_0 > f_\infty$ while curve 2 when $f_0 < f_\infty$.

Figure 2 shows the course of a typical function $f = f(t)$ marking the points being characteristic for this plot. Attaining f_∞ occurs after t_u regarded as the time of establishing the process equilibrium. This time is usually longer than the duration time of an industrial process t_{pwc} , to the residence time of a statistical grain on a screen

sieve. Therefore, there were introduced two blocking coefficients f_1^* and f_2^* . The coefficient of sieve blocking f_1^* is a ratio of the mean coefficient and the duration time of the process t_{pwc} , i.e. residence time for an industrial sieve. The material residence time on an industrial sieve, in general is from several to 60 seconds. For the blocking coefficient f_2^* of a sieve, time of establishment of process equilibrium is equal to 200-600 s. The present study is devoted to determination of effective screen blocking coefficients.

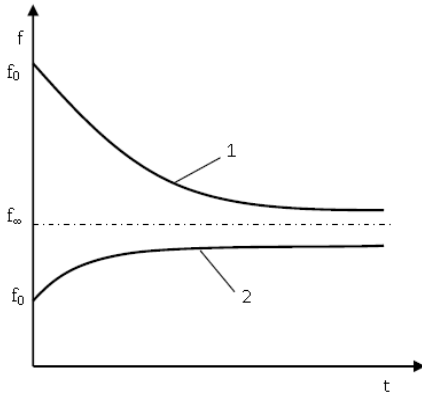


Fig. 1. Generalized plot of function $f = f(t)$

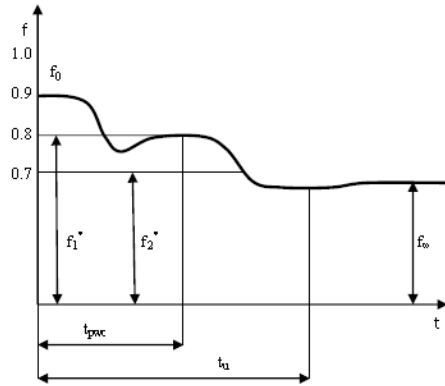


Fig. 2. A typical course of dependence $f = f(t)$ with marked characteristic points

The present study is based on the results of investigations performed on laboratory screens for a regulated toss indicator. As the investigated medium dry sand and agalite of 0.1 – 2.5 mm in size were applied.

2. Process of blocking of screen holes

The course of screen blocking coefficients f as a function of time is defined as:

$$f = f_\infty + (f_0 - f_\infty)e^{-K_0t} \tag{1}$$

where K_0 is the blocking constant which is expressed by the formula:

$$K_0 = \frac{1}{t_n} \ln \left| \frac{f_0 - f_\infty}{f_n - f_\infty} \right|. \tag{2}$$

Figure 3 shows $f = f(t)$ for a mixture of sands for various values of toss coefficient K .

The course of the curve depends on $f_0 - f_\infty$. One may notice that for all values of toss coefficient K , coefficient f_0 (f for time $t=0$) is the same. Therefore, parameter f_∞ has a decisive influence on the course of the $f = f(t)$ function. The lowest values of f_∞ occur when the toss indicator is equal to K_{min} . In this case the blocking is the highest and

deblocking is the lowest and K_{max} causes the greatest deblocking of blocked holes ($f_{\infty} \approx 1$). Values of the blocking coefficients for different toss coefficients K are shown in Table 1.

Figure 4 shows the dependence of $f = f(t)$ for spherical agalite. The conclusions are the same as in the case of sand.

Table 1. Values of f_0 and f_{∞} for various dynamic coefficients

| | K_1 | K_2 | K_{min} | K_{max} |
|--------------------|--------|--------|-----------|-----------|
| f_{∞} | 0.908 | 0.907 | 0.677 | 0.947 |
| f_0 | 0.796 | 0.796 | 0.796 | 0.796 |
| K_0 | 0.177 | 0.868 | 0.0164 | 0.230 |
| $f_0 - f_{\infty}$ | -0.112 | -0.111 | 0.119 | -0.151 |

Basing on the plots, it can be stated that the course of the $f = f(t)$ curve depends first and foremost on the value of the toss coefficient K .

A series of investigations was also carried out for mixtures of different:

- shapes of materials
- compositions of the lower and higher size fraction
- contents of grains that are difficult to screen x_t
- ratios of the mean grain size \bar{d} to the screen hole l .

Considering that the course of function to a considerable extent depends on the toss indicator, we can be certain that the course of the function, to a large extent, depends on the value of the toss indicator and that the value K has an impact on the value of f^* (Fig. 5).

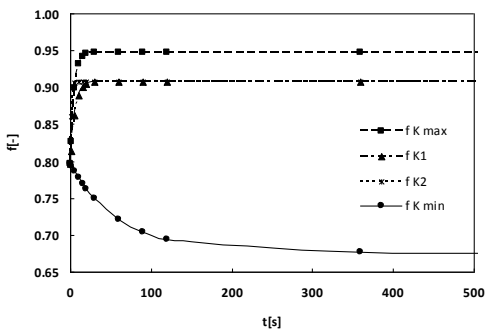


Fig. 3. Dependence $f = f(t)$ for mixture of sands for various values of toss coefficient K

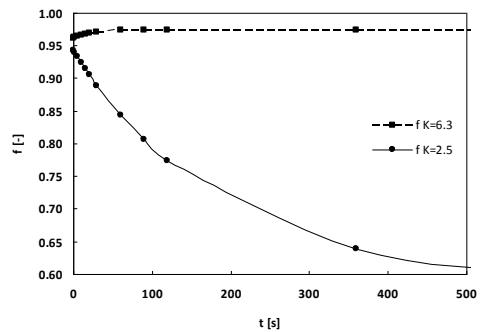


Fig. 4. Dependence $f = f(t)$ for mixture of agalites for various values of toss coefficient K

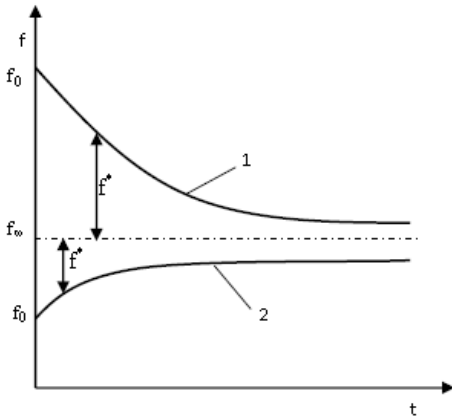


Fig. 5. The courses of dependence $f = f(t)$ with characteristic coefficients

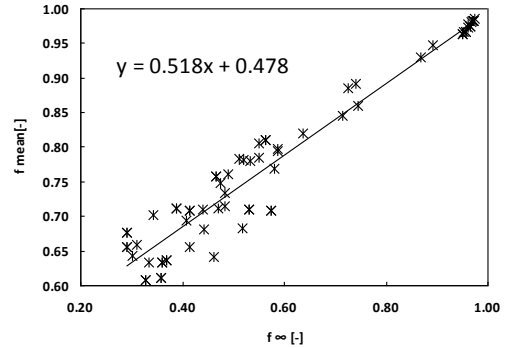


Fig. 6. Result $f_{\text{mean}} = f(f_{\infty})$ for the toss coefficient $K < 1$

To determine the value of the effective coefficient f^* for the investigated material/screen systems the mean value of blocking coefficient of screen holes f_{sr} has to be established. Basing on the course of the $f = f(t)$ dependence (e.g. Fig. 3) for given periods of time one can calculate f_{mean} as an arithmetic mean of f values using time intervals from $t=0$ to $t=t_u$ (without f_0 and f_{∞} values). Therefore, for different values of the toss indicator dependencies $f_{\text{mean}} = f(f_{\infty})$ (Figs. 6, 7, and 8) has to be prepared. By approximation of the data points one can obtain linear dependencies for three intervals of the toss indicator.

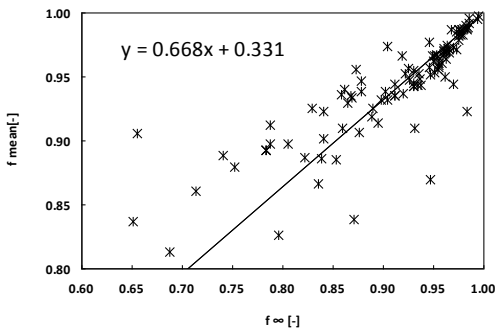


Fig. 7. Result $f_{\text{mean}} = f(f_{\infty})$ for the toss coefficient $K < 1, 3.5 >$

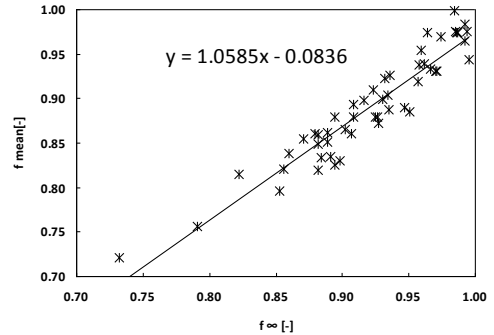


Fig. 8. Result $f_{\text{mean}} = f(f_{\infty})$ for the toss coefficient $K > 6.2$

3. Conclusions

The present study concerns the effective blocking coefficient of f^* as a function f_{∞} . The results are shown in Table 2.

It was proved that the most relevant parameter influencing the course of the plot of the screen blocking coefficient f is a function of toss coefficient K . Therefore, the

coefficient decides about the monotonicity of the function $f = f(t)$ and this influences the value of blocking coefficient f_∞ . The example dependencies $f = f(t)$ taking into consideration the values of f^* are shown in Figs. 9-14.

Table 2. $f^* = f(f_\infty)$ for different values of toss coefficient K

| Value of the toss coefficient K | $f^* = f(f_\infty)$ |
|-----------------------------------|----------------------------------|
| $K < 1$ | $f^* = 0.518 f_\infty + 0.478$ |
| $K < 1, 3, 5 >$ | $f^* = 0.668 f_\infty + 0.331$ |
| $K > 6$ | $f^* = 1.0585 f_\infty - 0.0836$ |

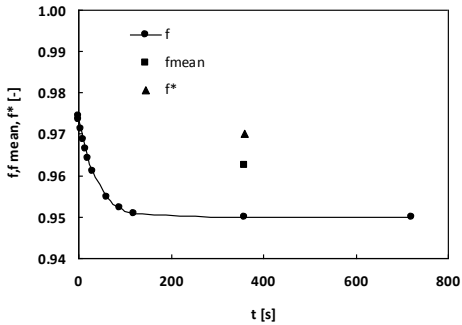


Fig. 9. $f = f(t)$ for agalite, sieve size 0.63 mm, $K=0.62, x_t = 20\%$

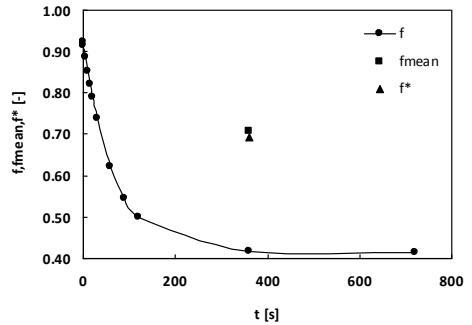


Fig. 10. $f = f(t)$ for agalite, sieve size 1 mm, $K=0.62, x_t = 70\%$

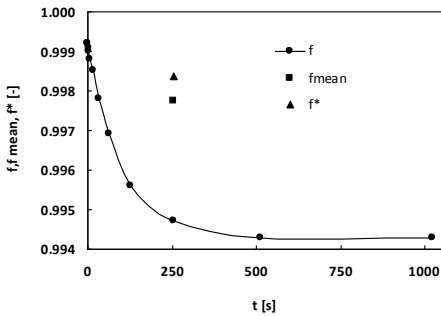


Fig. 11. $f = f(t)$ for sand, sieve size 1 mm, $K=1.5, x_t = 0\%$

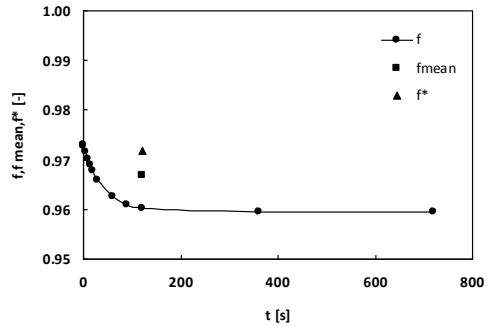


Fig. 12. $f = f(t)$ for agalite, sieve size 0.5 mm, $K=3.5, x_t = 40\%$

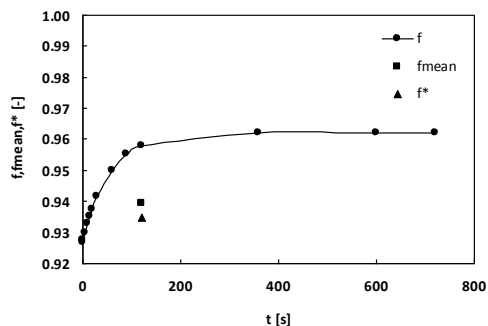


Fig. 13. $f = f(t)$ for agalite, sieve size 1 mm, $K=6.3$, $x_t = 50\%$

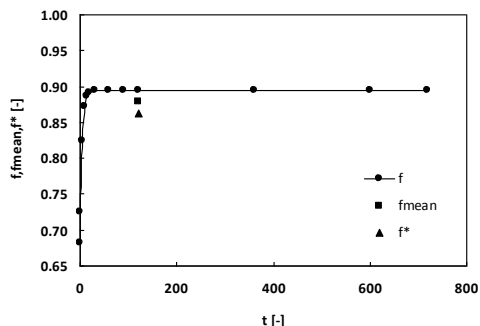


Fig. 14. $f = f(t)$ for sand, sieve size 0.5 mm, K_{\max} , $x_t = 40\%$

Acknowledgments

This study was performed as a part of chartered assignment W-10/1/2011/Dz.St.

References

- APLING A.C.,1984, Blinding of screens by sub-sieve sized particles, Transactions of the Institution of Mining and Metallurgy, C93, 92–94.
- BANASZEWSKI T., 1990, Przesiewacze, Wydawnictwo „Śląsk”, Katowice.
- BEECKMANS J.M., HU E.,GERMAIN R.,MCLNTYRE A.,1985, Performance characteristics of a probability screening machine, Powder Technology 43(3), 249–256.
- WESSELBAUM FRANZ-JOSEF, 1984, Methoden und Einrichtungen zum Freihalten von Siebmaschinen, Maschinenmarkt, 90(71), 1604–1607.

Received May 12, 2011; reviewed; accepted July 30, 2011

ADSORPTION OF CRYSTAL VIOLET FROM AQUEOUS SOLUTION ON ACTIVATED CARBON DERIVED FROM GÖLBAŞI LIGNITE

Tolga DEPCI *, Ali Riza KUL **, Yunus ONAL ***, Erkan DISLI ****,
Salih ALKAN **, Z. Funda TURKMENOGLU *

* Yuzuncu Yil University, Faculty of Engineering and Architecture, Department of Mining Engineering, 6580, Van, Turkey

** Yuzuncu Yil University, Faculty of Arts and Science, Department of Chemistry, 6580, Van, Turkey, Tel.: +90 432 225 10 81 ; fax: +90 432 225 11 14, alirizakul@yyu.edu.tr, (A.R. KUL)

*** Inonu University, Faculty of Engineering, Department of Chemical Engineering, 44280 Malatya, Turkey

**** Yuzuncu Yil University, Faculty of Engineering and Architecture, Department of Environmental Engineering, 6580, Van, Turkey

Abstract. Activated carbon (AC) was obtained from lignite of the local resource, Gölbaşı – Adıyaman (Turkey) by chemical activation. The Gölbaşı lignite was chosen as the precursor for its availability and low cost. The BET surface area of the activated carbon was found 921 m²/g. The AC was used as an adsorbent for Crystal Violet (CV) in aqueous solution. The adsorption properties of CV onto the activated carbon are discussed in terms of the adsorption isotherms (Langmuir and Freundlich) and the kinetic models (pseudo-first-order, pseudo-second-order and intraparticle diffusion model). It was shown that the experimental results best fitted by the Langmuir model, and the second-order kinetic equation. The thermodynamic parameters show that the adsorption process is endothermic. The experimental results point out that the obtained activated carbon is a viable candidate for sorbent removing CV from aqueous solutions.

keywords: crystal violet; activated carbon; Turkish lignite; adsorption

1. Introduction

In the textile industry, one of the main problems is removal of dyes and pigments from the wastewaters. It is known that most dyes are toxic, carcinogenic and mutagenic to aquatic organisms, so they have to be removed. Several methods, such as, filtration, coagulation, chemical oxidation, adsorption, etc., are used in order to remove dyes from wastewater (Mohan et al., 2002; Senthilkumaar et al., 2006). Among them, the liquid-phase adsorption process, in which activated carbon is usually

used, is a promising method for removal of dyes from industrial wastewaters. Activated carbon is of interest because of its relatively great adsorption capacity and the ease of production.

Crystal violet is used to colourize diverse products such as paper, leather, fertilizers, anti-freezes, detergents, and also as a component of inks for ball-point pens. It is also used in veterinary medicine, such as a dermatological drug, and for expelling intestinal parasites and fungi from the body (Adak et al., 2005). However, like other common dyes, CV is highly toxic to living organisms. Therefore, it should be removed from the wastewater.

As mentioned above, the liquid-phase adsorption process is a promising method for removal of dyes from wastewater. According to the literature survey, recently the following adsorbents were used to remove CV from wastewater: a surfactant-modified alumina (Adak et al., 2005), sludge biomass (Chu and Chen 2002), fly ash (Wang et al., 2005), sepiolite (Eren and Afsin, 2007; Eren et al., 2010), bottom ash, a power plant waste, and de-oiled soya (Mittal et al., 2010), NaOH-modified rice husk (Chakraborty et al., 2010), palm kernel fibre (El-Sayed, 2011).

The recent publications on adsorption of crystal violet on activated carbon have been reported by Senthilkumar et al. (2006), Önal (2006), Akmil-Basar (2006), Malarvizhi and Ho, (2010). These authors used activated carbons obtained from agricultural wastes. For instance, Senthikumar et al. (2006) used male flowers of coconut tree, Önal (2006) and Akmil-Basar (2006) used waste apricot, and Malarvizhi and Ho (2010) used wood apple rind as the precursors.

Activated carbon is a generic name of family of highly porous, amorphous carbonaceous materials and it cannot be characterized by a structural formula or chemical analysis (McDougall et al., 1980). Activated carbons exhibit an extended surface area, highly developed pore structure (in particular, micropore) and a high surface reactivity (Bansal and Goyal, 2005), so they are generally used to remove hazardous dyes and heavy metals from aqueous solution.

Two aims are accomplished in the current research. One is to evaluate lignite of the local resource, Gölbaşı – Adıyaman (Turkey), the original material for production of activated carbon. Since production of activated carbon is rather expensive, different alternative sources of cheap and readily available materials are regarded as the precursors, having in mind to reduce the costs. Besides, it is known that lignite has high ash and high moisture content. In developed countries like the U.S. instead of burning lignite, pyrolysis products are obtained and used as industrial solvents. Therefore, in addition to burning lignite in Turkey, end products like activated carbon should be produced to gain greater added value to Turkish economy. The second purpose of this study is to investigate the adsorption isotherm, kinetics and the thermodynamic parameters of CV adsorption onto activated carbon derived from the Gölbaşı lignite and to compare the adsorption capacity of the activated carbon with the literature data.

2. Materials and Methods

2.1 Materials

Test solutions (50, 100, 200 and 300 mg/dm³) containing crystal violet (CV) dye were prepared by diluting of stock solution of the dye which was obtained by dissolving weighed quantity of crystal violet (supplied by MERCK) in double distilled water.

2.2 Preparation of activated carbon

Activated carbon was prepared from Gölbaşı–Adıyaman (Turkey) lignite which was chosen as the precursor for its availability and low cost. The experimental procedure was based on the study carried out by Onal et al. (2006). Lignite samples were crushed and sieved to -60+40 mesh size fraction. It was mixed with ZnCl₂ (lignite/ZnCl₂ weight ratio of 1:1) and required amount of distilled water was added on this mixture. Then, this mixture was dried at 378 K in furnace to obtain the impregnated sample. Impregnated sample was heated to the activation temperature of 773 K for 1 hour under N₂ flow (100 cm³/min) at the rate of 283 K·min⁻¹. After the activation process, product was cooled down under N₂ flow then 0.5 N HCl was added on the samples. This mixture was filtered and it was washed with distilled water several times to remove residual chemicals and chloride ion until filtrate did not give any reaction with AgNO₃. Finally, the samples were dried at 378 K for 24h and stored in a desiccator until use. The activated carbon was ground in a standard ring mill and sieved under 400 mesh sizes (-0.038 mm).

2.3. Instrumentation

A Tri Star 3000 (Micromeritics, USA) surface analyzer was used to measure nitrogen adsorption isotherm at 77K in the range of 10⁻⁶ to 1 relative pressures. Prior to the measurement, the sample was degassed at 400°C for 2 h. The BET surface area, total pore volume, average pore radius (4V/A by BET), micropore area were obtained from the adsorption isotherms. Mesopore volume was determined by subtracting the micropore volume from total pore volume. The spectral determination of CV concentration in solutions was performed using a Shimadzu UV-VIS spectrophotometer (Model UV-HITACH U-2900, Japan). The zeta potential of the activated carbon was measured by a Zeta Meter 3.0 (Malvern Inc.) equipped with a microprocessor unit. The pH of the test solution was adjusted to the desired value by dropwise addition of dilute NaOH (0.5 %) or HCl (0.1 N).

2.4. Adsorption experiments

Adsorption studies were conducted in routine manner by batch technique. A number of stoppered Pyrex glass Erlenmeyer flasks containing a definite volume of solutions of desired concentration were placed in a thermostatic shaking assembly. For

the studies with activated carbon, 0.1g activated carbon was treated with 50 cm³ of the dye solution at 400 rpm. Adsorption experiment were carried out at different temperatures (298 K, 303 K and 313 K) using four dye solutions which were prepared at 50, 100, 200 and 300 mg/dm³ by using the stock solution (1000 mg/ dm³) at natural pH of the CV solution (pH of 5.8)

The amount of dye q (mg/g) adsorbed on activated carbons was calculated by the mass balance equation (1).

$$q = (C_0 - C)V / W \quad (1)$$

where, C_0 (mg/ dm³) is the initial dye concentration and C (mg/ dm³) is unadsorbed dye concentration in solution at time t , V (l) and W (g) is the volume of the solution and the weight of the dry activated carbons used respectively.

The effect of pH on the CV adsorption on the activated carbon was investigated by batch technique which was carried out at 50 mg/L initial dye concentration with 0.1 g/50 cm³ adsorbent dosage at 293 K for 60 min of equilibrium time and a constant stirring speed of 400 rpm. The pH values were adjusted in the range of 2 – 10.

The effect of stirring rate was also investigated by varying the stirring speed between 100 and 500 rpm for 60 min at a constant dye concentration (50 mg/ dm³) at pH of 5.8.

In order to determine the kinetic parameters, the stoppered pyrex glass Erlenmeyer flasks containing 500 ml volume of solutions of 50 mg/L concentration were placed in a thermostatic shaking assembly. The AC sample of 1.0 g was put into the dye solution and the mixture was stirred at 400 rpm at 298 K at pH 5.8. Every 10 minutes, the samples of 5 cm³ were taken by micropipette without ceasing the system. The dye solution was filtrated with Whattman filter paper. Concentration of the dye (CV) was determined using the UV/VIS spectrophotometer.

Thermodynamic parameters were determined from the experiments carried out at the different temperatures, for the different dye concentrations.

3. Results and discussion

3.1. Characterization of activated carbons

In order to characterise porosity of the activated carbon, nitrogen adsorption at 77°K, which is the standard method for characterisation of adsorbents, was applied. The N₂ adsorption isotherm of the activated carbon is given in Figure 1. It can be classified as Type 1 - characteristic of micropore solids, according to the IUPAC classification (Sing et al., 1985).

Table 1 presents the porous structure parameters obtained by applying the BET equation to N₂ adsorption on the activated carbon, at 77 K. It shows that the activated carbon has remarkable surface area, primarily contributed by micropores.

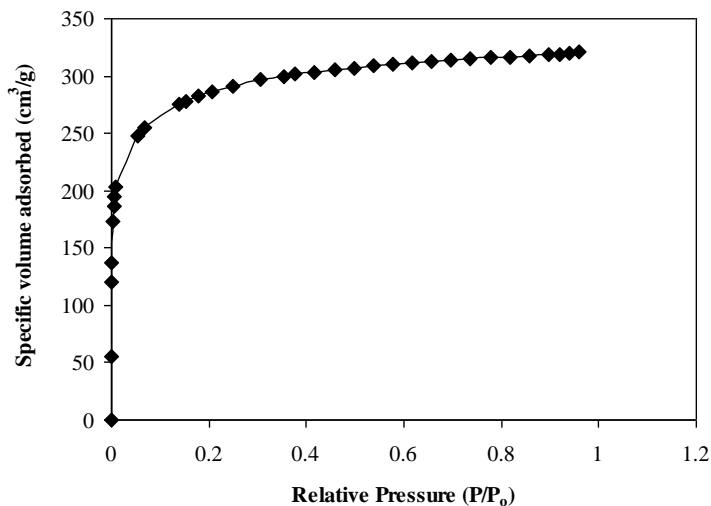


Fig. 1. Adsorption isotherm of nitrogen on the activated carbon, at 77K

Table 1. Total surface area (S_{BET}), areas of micro- and meso-pores (S_{micro} and S_{meso}) and the pore volumes (V_{micro} and V_{meso}) of the prepared activated carbon

| S_{BET} m ² /g | S_{micro} m ² /g | S_{meso} m ² /g | V_t cm ³ /g | V_{micro} cm ³ /g | V_{meso} cm ³ /g | D_p^* nm |
|--------------------------------|----------------------------------|---------------------------------|-----------------------------|-----------------------------------|----------------------------------|---------------|
| 921 | 812 | 109 | 0.476 | 0.427 | 0,049 | 2.11 |

* D_p denotes the average pore diameter determined from the BET equation; V_t denotes the total pore volume.

3.2. Effects of temperature and the dye concentration

The effects of temperature and the dye (CV) concentration on adsorption properties of the activated carbon are illustrated in Figure 2. It can be seen the percentage of dye removal at the adsorption equilibrium, showing a temperature-dependent character. It increases with the temperature raise which means that the adsorption process is endothermic. Sahu et al. (2009) and Singh et al. (2011) mentioned that the number of binding sites for the dye molecules on the adsorbent surface may be increased by the temperature raise. In addition, Almeida et al. (2009) mentioned that increase of the dye removal depending on the temperature can be explained by the increase of the mobility of the dye molecules.

On the contrary, the adsorption capacity of the activated carbon decreases with increasing the dye concentration. This may indicate that the adsorption is limited by number of the available active sites (Gupta et al., 1988) not sufficient for the high initial concentration of the dye (CV).

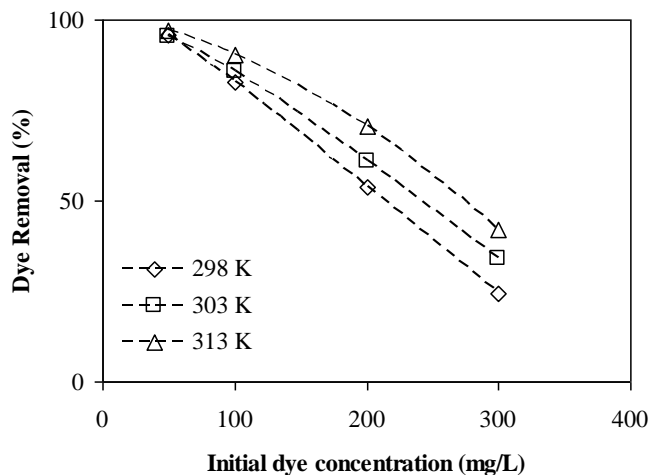


Fig. 2. Effect of temperature and initial dye concentration on equilibrium adsorption of crystal violet onto the activated carbon (0.1 g AC/50 cm³, pH of 5.8, 400 rpm)

3.3. Effect of contact time on the adsorption

From an economical point of view, the contact time required to reach equilibrium is an important parameter in waste water treatment. In order to investigate effect of contact time, the experiments were carried out for 10, 20, 30, 40, 50 and 60 min, using the fixed adsorbent dosage of 0.1 g at the natural pH (pH of 5.8) and the dye concentration of 50 mg/dm³. The results are shown in Fig. 3. It reveals that the equilibrium adsorption percentage increases with increasing the contact time and approaches to the equilibrium after about 50 min. Therefore 60 min. was accepted as optimal time for adsorption of CV on the activated carbon.

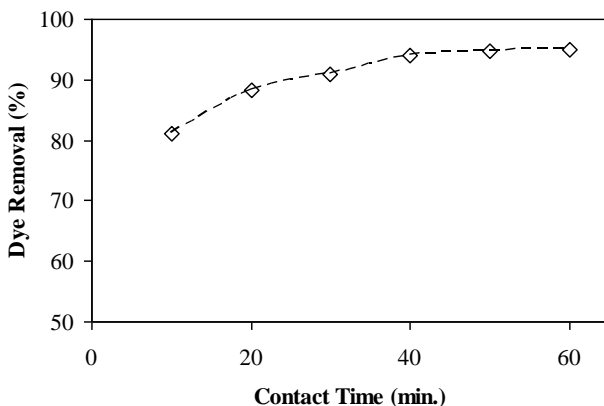


Fig. 3. Effect of contact time on equilibrium adsorption of crystal violet on the activated carbon, AC (0.1 g AC/50 cm³, pH of 5.8, 400 rpm, 298 K)

3.4. Effect of stirring rate

In order to determine the stirring rate effect on adsorption, the experiments were carried out varying the stirring speed between 100 and 500 rpm at dye concentration of 50 mg/dm^3 and stirring time of 60 min at natural pH of 5.8. Figure 4 shows the effect of stirring rate on the CV adsorption. As seen, the percentage of the dye removal increases depending on the increase in stirring rate. This result is very compatible with the studies done by Garg et al. (2004) and El-Sayed (2011). They claimed this situation depends on decreasing the thickness of the diffusion layer around the adsorbent surface due to the stirring rate. However, it is clearly seen in Figure 4 that the difference in the percentage increase is not very sufficient after 400 rpm value, so 400 rpm was considered as optimal stirring rate for the adsorption of the CV. Also, up to now, this issue is fixed in our experience for dye adsorption.

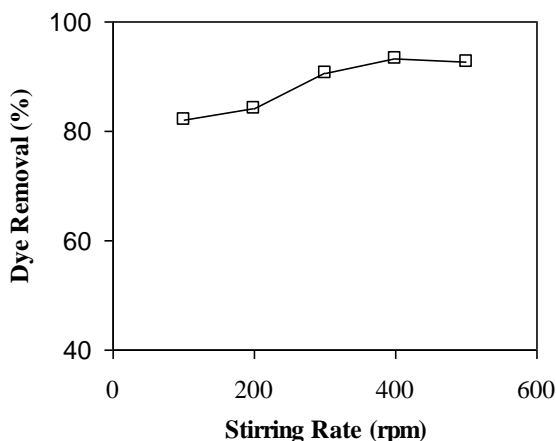


Fig. 4. Effect of stirring rate on adsorption of crystal violet on the activated carbon

3.5. Effect of pH

The pH of the distilled water used in the present study is 6.4 and after addition of the CV to obtain dye solution, pH of the solution was measured as 5.8 due to the cationic properties of CV. Then, the activated carbon was added the dye solution and adsorption experiment was started. The starting and the final pH of the mixture were noted and these values were noted as 4.13 and 4.48, respectively. This behaviour was also observed in the literature and it was explained with the ion exchange between the carbon surface and the cationic form of the dye molecule (Kurbatov et al., 1951; Kadirvelu et al., 2005; Ho, 2005; Malarvizhi and Ho, 2010).

The effect of the pH of solution on CV adsorption is shown in Fig. 5. The adsorption of CV on the activated carbon increases with increasing the pH of solution. After the pH range of 6 and 8, the difference in the percentage of the dye removal was not recorded at very significant amount. Similar trend of pH effect was observed in the

recent studies about adsorption of CV to be done by Jain and Jayaram (2010), Mittal et al., (2010), Chakraborty et al., (2010) and Singh et al., (2011). Thus, natural pH of the starting CV solution of 5.8 was considered as operational pH for the adsorption of the CV due to the considering of the cost and simplicity. Besides, it is clearly seen that the adsorption capacity of the activated carbon decreases with increasing the dye concentration. This observation supports the previous result which was presented in the effects of the dye concentration on adsorption part.

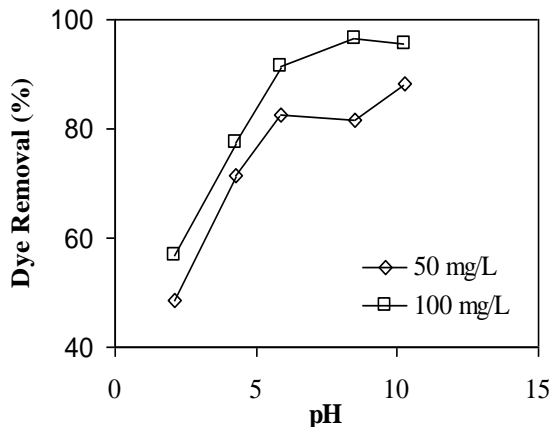


Fig. 5. Effect of solution pH on adsorption of crystal violet on the activated carbon

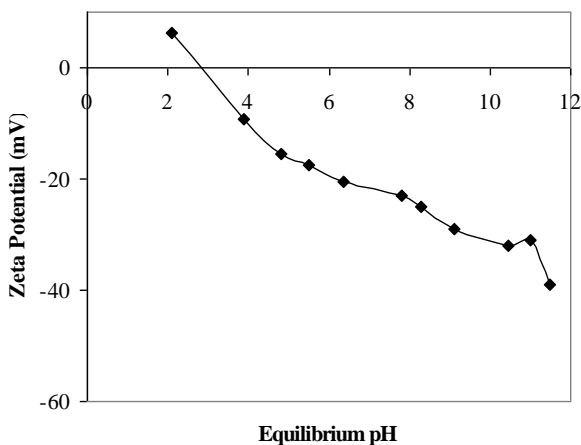


Fig. 6. Zeta potential of the activated carbon

Literature survey shows that pH of solution affect of the surface properties of the adsorbent and ionization/dissociation of the adsorbate molecule (Saeed et al., 2010; Chakraborty et al., 2010; Mittal et al., 2010). As mentioned, pH of the solution affects

the adsorption of CV. This observation can be explained by considering the zeta potential of the activated carbons. Therefore, in the present study, the zeta (ζ) potential variation of the activated carbon was investigated and this variation is given in Fig. 6. Zeta potential increases in the negative direction with increasing the pH and isoelectrical point (IEP), which represents no net electrical charge of surface at the specific pH, is approximately 2.8. If pH values is lower than the IEP (pH of 2.8), the surface of activated carbon surface has positive charged and protonation of the functional groups easily occurs on it. At this range, due to same charge of the cationic dye and the activated carbon, electrostatic repulsion takes place between them. Also in high acidic medium, lower adsorptive removal of the dye was due to the presence of excess hydrogen ions competing with the positively charged dye molecules (Mall et al., 2005; Wang et al., 2010; El-Sayed, 2011). As the pH of the dye solution increases, the surface of the activated carbon has negative charge due to the successive deprotonation of positive charged groups on the surface of activated carbon, and negative charge density on the surface increases. Therefore the electrostatic attraction between the negatively charged sites of the adsorbent and the positively charged dye molecules ($=N^+(CH_3)_2$) occurs (Chakraborty et al., 2010; Mittal et al., 2010). Depending on this feature, the adsorption of the CV on the activated carbon increases with increasing the pH of the solution.

3.6. Adsorption isotherms

Adsorption isotherms are mathematical models which describe distribution of the solute among two phases, i.e., the liquid and the adsorbed phases. In the present study, results of the adsorption at different temperatures were fitted with the Langmuir and Freundlich models which earlier have been found applicable to many dye sorption processes (Onal et al., 2006; Akmil-Başar 2006; Wang et al., 2010; Malarvizhi and Ho, Y.S., 2011; El-Sayed 2011; Ayed , 2011). The linearised Langmuir isotherm can be expressed by the following equation (Langmuir, 1918):

$$C_e / q_e = 1/Q_0 b + C_e / Q_0 \quad (2)$$

where C_e is the equilibrium solute concentration in the liquid phase (mg/dm^3), q_e is the adsorption capacity (mg/g), b (dm^3/mg) and Q_0 (mg/g) are the temperature-dependent Langmuir isotherm constants, where Q_0 signifies the theoretical monolayer capacity, i.e., the maximum amount that can be adsorbed. The Langmuir equation is applicable to homogeneous adsorption, i.e., when each sorbate molecule has equal sorption activation energy.

The Freundlich isotherm describes heterogeneous and reversible adsorption not restricted to formation of a monolayer. The Freundlich equation transformed to the linear form is as follows (Freundlich, 1906):

$$\log q_e = \log k_f + \log C_e / n \quad (3)$$

where, k_f (dm^3/g) is the Freundlich constant and $1/n$ (dimensionless) is the heterogeneity factor. Langmuir plots (C_e/q_e versus C_e) and Freundlich plots ($\log q_e$ versus $\log C_e$) for CV adsorption at different temperatures are depicted in Figs. 7 and 8, respectively. And the isotherm parameters calculated by applying the commonly accepted linear regression procedure to the linear representation of the isotherms, are summarized in Table 2.

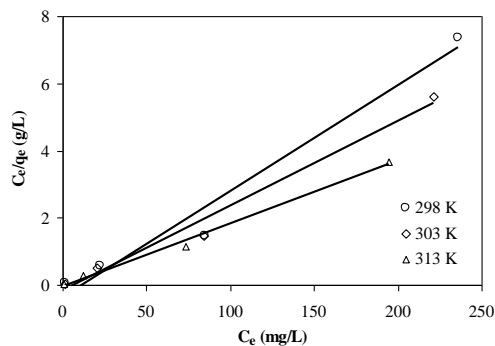


Fig. 7. Langmuir isotherm plots for adsorption of CV onto activated carbon at different temperatures

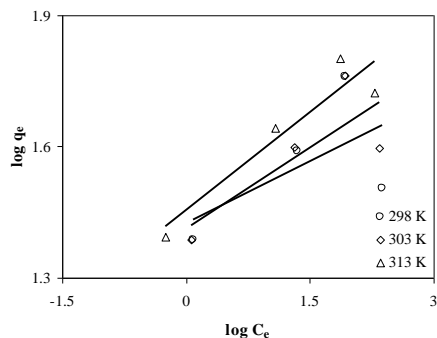


Fig. 8. Freundlich isotherm plots for adsorption of CV onto AC at different temperatures

Table 2. The fitted isotherm parameters for adsorption of CV onto the AC at different temperatures.

| | Temperature (K) | | |
|----------------------|-----------------|-------|-------|
| | 298 | 308 | 318 |
| Langmuir | | | |
| Q_0 (mg/g) | 60.8 | 61.2 | 65.8 |
| $b * 10^{-2}$ (L/mg) | 0.17 | 0.15 | 0.075 |
| R^2 | 0.971 | 0.988 | 0.995 |
| Freundlich | | | |
| k_f (L/g) | 10.64 | 8.08 | 6.72 |
| n | 26.67 | 25.81 | 28.52 |
| R^2 | 0.354 | 0.641 | 0.878 |

Comparing quality of fitting the Langmuir and Freundlich isotherms in terms of the correlation coefficient, R^2 , one may see that adsorption of CV on the activated carbon is quite well consistent with the Langmuir model, but not with the Freundlich one. The similar result was obtained in recent studies by done Wang et al. (2010), Malarvizhi and Ho (2011), El-Sayed (2011), Keyhanian et al. (2011). They found that the equilibrium adsorption data to be obtained for the adsorption of CV on different adsorbents were well described by the Langmuir model. Besides, it is seen from Table 2, the adsorption capacity (Q_0) - determined from the Langmuir model fit, increases with temperature raise showing that the adsorption process is endothermic. It may be concluded that raise in temperature accelerates transportation of dye molecules from solution to the adsorbent surface.

In order to determine whether the adsorption system is favourable or not, ‘ R_L ’ named as dimensionless separation factor, which is obtained from Langmuir model (Weber and Chakravorti, 1974; Hall et al., 1966) is defined by the following equation

$$R_L = 1/(1 + bC_o) \tag{4}$$

where R_L is a dimensionless separation factor, C_o is the initial dye concentration and b is Langmuir constant. The feasibility of the reactions are explained using the value of R_L ($R_L > 1$ -unfavourable, $R_L = 1$ -linear, $0 < R_L < 1$ - favourable, $R_L = 0$ – irreversible).

The values of R_L were found in the range of 0.016 – 0.114, indicating that the adsorption was favourable. Also the relationship between R_L and C_o depending on the temperature is presented in Figure 9. It seems that the raise in temperature of the system favours the adsorption.

Table 3. Adsorption capacities of various adsorbents for the adsorption of CV

| Adsorbents | Q_o (mg/g) | Reference |
|---|--------------|--------------------------|
| Phosphoric acid activated carbon | 60.42 | Senthilkumar (2006) |
| Sulphuric acid activated carbon | 85.84 | Senthilkumar (2006) |
| Activated carbon prepared from waste apricot | 57.80 | Akmil-Başar (2006) |
| Jute fiber carbon | 27.99 | Porkodi and Kumar (2007) |
| Kaolin | 47.27 | Nandi et al. (2009) |
| Semi-IPN hydrogels | 35.09 | Li (2010) |
| Sepiolite | 77 | Eren et al. (2010) |
| Ativated carbon from the waste biomass of wood apple rind | 16.5 | Malarvizi and Ho, (2010) |
| Magnetic nanocomposit | 81.70 | Signha et al. (2011) |
| Ginger waste | 19.8 | Kumar and Ahmad (2011) |
| Activated Carbon Derived from Gölbaşı Lignite | 60.8 – 65.8 | Present study |

In order to compare the adsorption capacity of the activated carbon derived from Gölbaşı Lignite, the adsorption capacities of various adsorbents for the adsorption of CV are given in Table 3. It seems that the activated carbon derived from Gölbaşı Lignite has a considerably high value of the adsorption capacity, showing that it is a better adsorbent compared to most of the adsorbents which are given in Table 3.

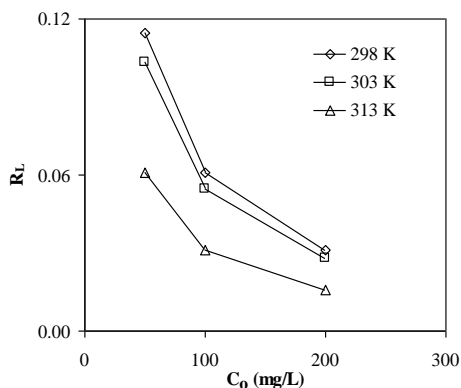


Fig. 9. Relation between C_0 and R_L for CV/AC system at various temperatures

3.7. Adsorption kinetics

Physical and chemical characteristics of adsorbents affect the adsorption process. To examine the rate limiting step of the adsorption process, several kinetic models are fitted to the adsorption results, such as, pseudo-first-order and pseudo-second-order kinetic models and the intraparticle diffusion one.

The pseudo-first-order equation is expressed as follows (Barret et al. 1951):

$$dq_t/dt = k_1(q_e - q_t). \quad (5)$$

The integrated form of the equation is as follows:

$$\log(q_e - q_t) = \log q_e - k_1 t / 2.303 \quad (6)$$

where q_e and q_t are the amounts (mg/g) of solute bound at the interface at the equilibrium and after time t (min), respectively, k_1 is the rate constant of the pseudo-first-order adsorption (min^{-1}).

The pseudo-second-order kinetic model expressed in the most commonly used form, formulated by Ho and McKay (1998; 1999), is as follows:

$$dq_e/dt = k_2(q_e - q_t)^2. \quad (7)$$

The integrated form of equation (7) is:

$$t/q_t = 1/k_2 q_e^2 + t/q_e, \quad (8)$$

where k_2 is the rate constant of the pseudo-second-order adsorption (g/mg min), q_t is the adsorbed amount at time t (mg/g).

The plots validating the pseudo-first-order model ($\log(q_e - q_t)$ versus t) and the pseudo-second-order model (t/q_t versus t) at various initial concentrations of the CV, at 298 K, are given in Figs. 10 and 11, respectively.

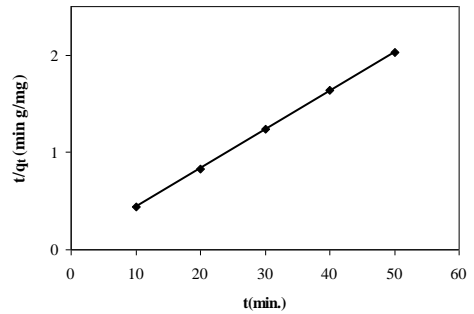
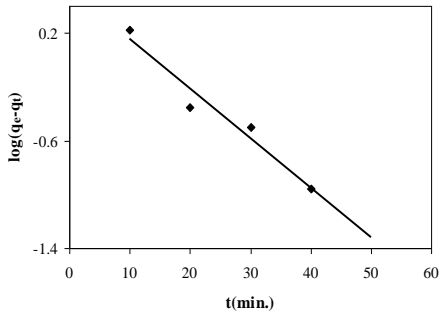


Fig. 10. Test of the pseudo-first-order adsorption kinetics for CV adsorption onto activated carbon

Fig. 11. Test of the pseudo-second-order adsorption kinetics for CV adsorption onto activated carbon

Parameters of the fitted kinetic models with the correlation coefficients, R^2 , are compared in Table 4. Examining fittingness of the models in terms of the R^2 value, it shows that the pseudo second order kinetic model describes the system much better than the pseudo first order kinetic model. Similar results have been reported in literature and according to this assumption, chemical sorption involving valence forces through sharing or exchange of electrons between adsorbent and adsorbate might significantly affect the rate-limiting step (Senthilkumaar et al., 2006; Gong et al., 2008; Chakraborty et al., 2010, El-Sayed. 2011).

Table 4. The parameters derived by fitting the adsorption models given by Eqs. 6 and 8 to the adsorption results

| Experimental | Calculated | | | | | |
|--------------------------------|------------------------------|--------------------------------|-------|-------------------------------|--------------------|-------|
| | First-order kinetic equation | | | Second-order kinetic equation | | |
| $q_{e \text{ exp.}}$ (mg/g) | q_e (mg/g) | k_1 (min^{-1}) | R^2 | q_e (mg/g) | k_2 (g/mgmin) | R^2 |
| 24.70 | 3.36 | 0.084 | 0.94 | 25.25 | 0.035 | 0.99 |

The rate parameter for the intraparticle diffusion model is determined using the following equation (Weber and Moris, 1963):

$$q_t = k_{\text{int}} \times t^{1/2} + C \tag{9}$$

where C is the intercept and k_{int} is the intraparticle diffusion rate constant ($\text{mg/g min}^{1/2}$). The test plot q_t versus $t^{1/2}$ is shown in Fig. 12. It indicates two adsorption ranges. The first one covering the time range between 10 and 20 min, which is very steep, is attributed to diffusion of CV through the solution film to the external surface of AC. The second range starting after 20 min, is described to the gradual adsorption limited by diffusion of solute in the liquid contained in pores of adsorbent particles and along the pores walls (intraparticle diffusion) (Li et al., 2003).

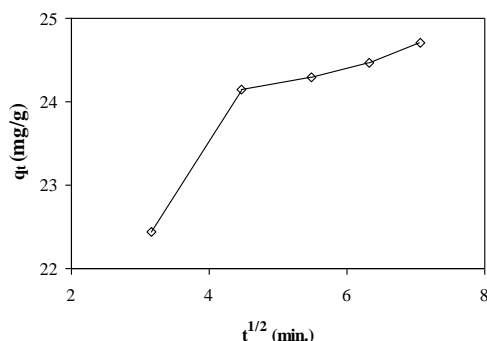


Fig. 12. Test of the intraparticle diffusion kinetics for CV adsorption onto activated carbon

3.8. Adsorption thermodynamics

In the present study, the effect of temperature on the adsorption course was investigated at different dye concentrations using the following equation (Ghosh and Bhattacharyya, 2002);

$$\Delta G^0 = -RT \ln K_c \quad (10)$$

where ΔG^0 is the standard free energy of adsorption, R is the gas constant, K_c is the adsorption equilibrium constant and T is the temperature. The K_c value was calculated from the following equation 11.

$$K_c = C_{Ae} / C_{Se} \quad (11)$$

where C_{Ae} and C_{Se} are the equilibrium concentrations of the dye ions in the adsorbed phase (mg/g) and in the solution (mg/ dm³), respectively.

The Standard enthalpy (ΔH^0) and entropy (ΔS^0) of adsorption can be estimated from the van't Hoff equation:

$$\ln K_c = \Delta S^0 / R - \Delta H_{ads}^0 / RT \quad (12)$$

The slope and the intercept of the van't Hoff plot ($\ln K_c$ vs. $1/T$) is equal to $-\Delta H_{ads}^0/R$ and $\Delta S^0/R$, respectively (Barrett et al., 1951). The van't Hoff plots for adsorption of CV onto the AC, at different dye concentrations, are given in Fig. 13.

The thermodynamic parameters are compared in Table 5. As one may the enthalpy (ΔH^0) values are found positive indicating endothermic process. The entropy (ΔS^0) values are also positive which indicates affinity of the AC for CV. The Enthalpy (ΔH^0) and entropy (ΔS^0) values decrease with increasing the dye concentration. In parallel, the percentage of the equilibrium dye adsorption decreases with increasing initial dye concentration (Fig. 2).

Degree of spontaneity of the adsorption process is determined by the Gibbs free energy. The values of standard free energy (ΔG) of adsorption were found negative.

It means that the adsorption process is thermodynamically favoured. The Gibbs free energy (the absolute value) gradually increases with the temperature raise which is in accordance with the endothermic process. On the other hand, the absolute value of ΔG decreases with the dye concentration. The analogous behaviour is seen also for K_c values.

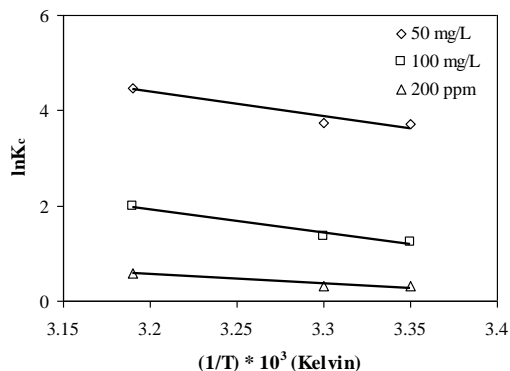


Fig. 13. The van't Hoff plots for CV adsorption onto the AC at different dye concentrations, at the natural pH

Table 5. Thermodynamic parameters for adsorption of CV onto the activated carbon

| Concn. (mg/dm ³) | ΔH (kJ/mol) | ΔS (J/mol) | $-\Delta G$ | | | K_c | | |
|---------------------------------|------------------------|-----------------------|-------------|----------|----------|-------|-------|-------|
| | | | (kJ/mol) | (kJ/mol) | (kJ/mol) | 298 K | 303 K | 313K |
| 50 | 42.84 | 173.57 | 9.18 | 9.44 | 11.66 | 40.67 | 42.40 | 88.29 |
| 100 | 40.17 | 144 | 3.09 | 3.40 | 5.18 | 3.48 | 3.86 | 7.33 |
| 200 | 15.76 | 55.07 | 0.77 | 0.80 | 1.43 | 1.36 | 1.37 | 1.73 |

4. Conclusions

The main conclusions of the present investigation are as follows.

1. Gölbaşı Lignite derived activated carbon is a promising adsorbent for removal of CV from aqueous solution. A small amount (4 g/ dm³) of the AC could almost decolorize aqueous solution of CV of 50 mg/ dm³.
2. The percentage dye removal increases with the temperature raise which implies that the adsorption process is endothermic.
3. The percentage removal of the dye increases depending on the increase in contact time and reaches the equilibrium after about 50 min.

4. The Langmuir model perfectly describes the adsorption results with the high correlation coefficient, R^2 , which increases with temperature in the range of 0.971-0.995. The adsorption capacity (Q_0) found from the Langmuir fit increases depending on the temperature raise.
5. Values of the dimensionless separation factor, R_L , were found between 0 and 1 for all concentrations and the temperatures which supports that CV is favourably adsorbed on the AC.
6. The adsorption process is well described by the pseudo second order kinetic equation indicating chemisorption. The adsorption capacity, q_e , calculated from the fit is very close to the experimental value, $q_{e\text{ exp}}$.
7. The enthalpy (ΔH^0) values are found positive indicating endothermic process. The standard free energy of adsorption, ΔG , was found negative which means that the adsorption process is thermodynamically favoured.
8. Comparing CV adsorption capacity of the activated carbon with many corresponding sorbents, it was found that the activated carbon derived from Gölbaşı Lignite has a considerably high value of the adsorption capacity. Finally, taking into consideration all results obtained in the present study, it can be concluded that the activated carbon can be used as a promising adsorbent to remove CV from aqueous solution.

Reference

- ADAK, A., BANDYOPADHYAY, M., PAL, A., 2005, Removal of crystal violet dye from wastewater by surfactant-modified alumina, *Separation and Purification Technology* 44, 139–144.
- AKMIL-BASAR, C., 2006, Applicability of the various adsorption models of three dyes adsorption onto activated carbon prepared waste apricot, *J. Hazard. Mater.* 135 (1–3), 232–241.
- ALMEIDA, C.A.P. DEBACHER, N.A. DOWNSC, A.J COTTETA, L. MELLO, C.A.D., 2009, Removal of methylene blue from colored effluents by adsorption on montmorillonite clay, *J. Colloid Interface Sci.* 332, 46–53.
- AYED, G. O., 2011, Removal of methylene blue and crystal violet from aqueous solutions by palm kernel fiber, *Desalination* 272, 225–232.
- BANSAL, R.C. GOYAL, M., 2005, *Activated Carbon Adsorption*, Taylor & Francis, New York, USA, p. 487.
- BARRETT, P.E.P. JOYNER, L.G. and HALENDA, P.P., 1951, The Determination of Pore Volume and Area Distributions in Porous Substances. I. Computations from Nitrogen Isotherms, *J. Am. Chem. Soc.* 73, p. 373.
- CHAKRABORTY, S., CHOWDHURY, S., & SAHA, P., 2010, Adsorption of Crystal Violet from aqueous solution onto NaOH-modified rice husk, *Carbohydrate Polymers*, doi:10.1016/j.carbpol.2011.06.058.
- CHU, K.H. CHEN K.M., 2002, Reuse of activated sludge biomass. II. The rate processes for the adsorption of basic dyes on biomass, *Process Biochem.* 37, 1129–1134.
- EL-SAYED, G.O., 2011, Removal of methylene blue and crystal violet from aqueous solutions by palm kernel fiber, *Desalination* 272, 225–232.
- EREN, E. AFSIN, B., 2007, Investigation of a basic dye adsorption from aqueous solution onto raw and pre-treated sepiolite surfaces, *Dyes and Pigments* 73, 162–167.
- FREUNDLICH, H.M.F., 1906, Uber dye adsorption in lusungen. *Z. Phys. Chem.* 57, 385.

- GARG, EL-S V.K., AMITA, M., KUMAR, R., GUPTA, R., 2004, Basic dye (methylene blue) removal from simulated wastewater by adsorption using Indian Rosewood sawdust: a timber industry waste, *Dyes Pigm.* 63, 243–250.
- GHOSH D. and BHATTACHARYYA K.G., 2002, Adsorption of methylene blue on kaolinite., *Appl. Clay Sci.* 20, 295 – 300.
- GUPTA, G. S., PRASAD, G. AND SINGH, V. N., 1988, Removal of color from wastewater by adsorption for water reuse. *J. Env. Sci. Health.* 23A (3), 205 – 217.
- HALL, K.R. , EAGLETON, L.C., ACRIVOS, A., VERMEULEN, T., 1966, Pore- and solid-diffusion kinetics in fixed-bed adsorption under constant-pattern conditions, *Ind. Eng. Chem. Fundam.* 5, 212–223.
- HO, Y.S. AND MCKAY, G., 1998, Circulation of solids and gas bypassing in an internally circulating fluidized bed with a draft tube, *Chem. Eng. J.* 70, 115-122.
- HO, Y.S. AND MCKAY, G., 1999, Pseudo-second-order model for sorption process, *Process Biochem.* 34, 451-465.
- HO, Y.S., 2005, Effect of pH on lead removal from water using tree fern as the sorbent, *Bioresour. Technol.* 96 1292–1296.
- JAIN, S., JAYARAM, R. V., 2010, Removal of basic dyes from aqueous solution by low-cost adsorbent: Wood apple shell (*Feronia acidissima*). *Desalination*, 250, 921.
- KADIRVELU, K. KARTHIKA, C. VENNILAMANI, N. PATTABHI, S., 2005, Activated carbon from industrial solid waste as an adsorbent for the removal of Rhodamine-B from aqueous solution: kinetic and equilibrium studies, *Chemosphere* 60, 1009–1017.
- KEYHANIAN, F., SHARIATI, S., FARAJI, M., HESABI, M., (2011) Magnetite nanoparticles with surface modification for removal of methyl violet from aqueous solutions *Arabian Journal of Chemistry* (in press).
- KURBATOV, M.H. WOOD, G.B. KURBATOV, J.D., 1951, Isothermal adsorption of cobalt from dilute solutions, *J. Phys. Chem.* 55, 1170–1182.
- KHARE, S.K. SRIVASTAVA, R.M. PANDAY, K.K. SINGH, V.N., (1988), Removal of basic dye (Crystal violet) from water using wollastonite as adsorbent, *Environ. Technol. Lett.* 9, 1163.
- LANGMUIR, 1918, The adsorption of gases on plane surfaces of glass, mica and platinum, *J. Amer. Chem. Soc.* 40, 1361 – 1368.
- LI, H. SHENG, G. TEPPE, B.J. JOHNSTON C.T. AND BOYD, S.A., 2003, Sorption and desorption of pesticides by clay minerals and humic acid–clay complexes, *Soil Sci. Soc. Am. J.* 67 122–131.
- MALARVIZHI, R., HO, Y.S., 2011, The influence of pH and the structure of the dye molecules on adsorption isotherm modeling using activated carbon *Desalination* 264, 97–101.
- MALL, I.D., SRIVASTAVA, V.C., AGARWAL, N.K., MISHRA, I.M., 2005, Adsorptive removal of malachite green dye from aqueous solution by bagasse fly ash and activated carbon-kinetic study and equilibrium isotherm analyses, *J. Colloid Surf. A* 264, 17–28.
- MCDOUGALL, G.J. HANCOOK, R.D. NICOL, M.J. WELINGTON, O.L. COPPERTHWAIT, R.G., 1980, The mechanism of the absorption of gold cyanide onto activated carbon *J S Afr. Inst. Min. and Metall.* 80, 344 – 356.
- MITTAL, A., MITTAL, J., MALVIYA, A., KAUR, D., GUPTA, V.K., 2010, Adsorption of hazardous dye crystal violet from wastewater by waste materials, *Journal of Colloid and Interface Science* 343, 463–473.
- MOHAN, D. SINGH, K.P. SINGH, G. KUMAR, K., 2002, Removal of dyes from wastewater using fly ash, a low-cost adsorbent, *Ind. Eng. Chem. Res.* 41, 3688–3695.
- ONAL, Y. AKMIL-BAŞAR C., EREN D., SARICI-ÖZDEMİR Ç., DEPCI T., 2006, Adsorption kinetics of malachite green onto activated carbon prepared from Tunçbilek lignite., *J. Hazard. Mater.* B128, 150-157.
- ONAL, Y., 2006, Kinetics of adsorption of dyes from aqueous solution using activated carbon prepared from waste apricot, *J. Hazard. Mater.* B137, 1719-1728.
- ÖZDEMİR, Ç. S. ÖNAL, Y.C. BAŞAR, A. ,2006, The effects of demineralization and swelling in producing active carbon from Turkish lignites, *Fuel Process. Technol.* 87, 979–986.

- SAEED, A., SHARIF, M., IQBAL, M., 2010, Application potential of grapefruit peel as dye sorbent: Kinetics, equilibrium and mechanism of crystal violet adsorption. *Journal of Hazardous Materials*, 179, 564–572.
- SAHU, J.N., ACHARYA, J., MEIKAP, B.C., 2009, Response surface modeling and optimization of chromium(VI) removal from aqueous solution using tamarind wood activated carbon in batch process, *J. Hazard. Mater.* 172, 818–825.
- SAFARIK, I. NYMBURSKA, K. SAFARIKOVA, M., 1997, Adsorption of water soluble organic dyes on magnetic charcoal, *J. Chem. Tech. Biotechnol.* 69, 1–4.
- SENTHILKUMAAR S., KALAAMANI, P., SUBBURAAM, C.V., 2006, Liquid phase adsorption of Crystal violet onto activated carbons derived from male flowers of coconut tree, *J. Hazard. Mater.* B136, 800–808.
- SING, K.W. EVERET, D.H. HAUL, R.A.W. MOSCOU, L. PIEROTTI, R.A. ROUQUERO, J. SIEMIENIEWASA, T., 1985, Physical And Biophysical Chemistry Division Commission On Colloid And Surface Chemistry Including Catalysis, *Pure Appl. Chem.* 57, 603 – 619.
- SINGH, K.P., GUPTA, S., SINGH, A.K., SINHA, S., 2011, Optimizing adsorption of crystal violet dye from water by magnetic nanocomposite using response surface modeling approach, *Journal of Hazardous Materials* 186, 1462–1473.
- WANG, S. BOYJOO, Y. CHOUEIB A., 2005, A comparative study of dye removal using fly ash treated by different methods, *Chemosphere* 60, 1401–1407.
- WANG, L., ZHANG, J., ZHAO, R., LI, C., LI, Y., ZHANG, C., 2010 Adsorption of basic dyes on activated carbon prepared from Polygonum orientale Linn: Equilibrium, kinetic and thermodynamic studies *Desalination* 254, 68–74.
- WEBER, W.J., MORIS, JR., J.C., 1963, Kinetics of adsorption on carbon from solution. *J.San, Eng. Div. ASCE Civil Eng.* 89, 31-39.
- WEBER, T.W. CHAKRAVORTI, R.K., 1974, Pore and solid diffusion models for fixed-bed adsorbers, *AIChe J.* 20, 228–238.

Received August 12, 2011; reviewed; accepted August 17, 2011

GRAVITY CONCENTRATION OF SUDANESE CHROMITE ORE USING LABORATORY SHAKING TABLE

Ahmed A. SEIFELNASR *, Tarig TAMMAM **, Abdel-Zaher M. ABOUZEID ***

* Faculty of Petroleum and Mining, Suez Canal University, Dept. of Mining Engineering, Suez, Egypt

** Faculty of Engineering, Omdurman Islamic University, Dept. of Mining Engineering, Khartoum, Sudan

*** Faculty of Engineering, Cairo University, Dept. Mining Engineering, Giza, 12613, Egypt, Mobile: 0020 113095989, Home :0020 2 35864665, Fax: 0020 2 35723486, abdel.abouzeid@gmail.com

Abstract. The main raw materials for chromium metal is chromite. Geologically, chromite deposits are associated, by their nature of formation, with specific gangue minerals such as serpentine, olivine, and chlorite. These associated minerals are of lower densities than chromite. This criterion of density difference between chromite and the associated minerals suggests the use of gravity separation techniques for concentrating the low-grade chromite ores. This paper presents the results of an investigation on the concentration of a low-grade (30% to 35% Cr₂O₃) chromite ore from Chickay Mine, East of Sudan, using a shaking table. The studied parameters were the table tilt angle and the feed size distribution. The optimum table tilt angle was 60, and the best performance of the table was obtained when the feed was split into two size fractions, -1.168 + 0.18 mm and - 0.18 mm, without desliming. The concentrate assay, under these conditions, was 47.2% Cr₂O₃ at a recovery of 75 percent.

keywords: concentration of low-grade chromite ores, gravity separation, shaking tables, table tilt angle, feed size distribution

1. Introduction

Chromium is one of the most important industrial elements nowadays. The chromium metal is used in metallurgical, and chemical, industries, whereas in refractory, chromite, the main mineral of chromium, is a main constituent in the refractory bricks for lining of high temperature furnace. In metallurgy, chromium is used in stainless steels, tool and alloy steels, nickel-chromium heating elements, in metal plating, manufacture of ferro-chrome alloys, and in the manufacture of grinding media, balls and rods, and mill liners in grinding plants. In chemical industry, it is used in the manufacture of paint pigments and chemical compounds, as an oxidizing

agent in organic syntheses, as an electrolyte in chromium plating baths, and as an agent for tanning and dyeing of leather (USBM, 1992).

Chromite can be classified on the basis of the Cr/Fe ratio. The highest grade chromites are those having the Cr/Fe ratio of more than 2.0, and containing a minimum of 46% - 48% Cr₂O₃ (Hundhausen, 1947; Habashi and Bassyouni, 1982; Maliotis, 1996). Chemical and refractory grade chromites typically have Cr/Fe ratios ranging from 1.4 to 2.0. Low-grade chromites are those which have low Cr/Fe ratios and contain relatively small amounts of chromium.

Chromite occurs as a primary mineral of ultra-basic igneous rocks, peridotites, and their modifications, serpentine, talc carbonate, and chlorite. It also occurs in basic gabbros under suitable conditions. Usually the chromite deposits occur as small grains, but by the segregation of these grains, ore-bodies rich in Cr₂O₃ may be formed (Read, 1957).

2. Background

Although flotation offers an attractive technique for the separation of fine materials with minimum chromium losses, earlier flotation results of low-grade chromite ores were inferior to those obtained by tabling (Nafziger et al., 1979; Nafziger, 1982). Flotation requires fine grinding, which necessitates high slime losses and creates the slime coating problems, which needs careful reagent control and additional depressing and dispersing reagents. For this reason, fine-grained disseminated chromite ores do not respond well to this technique. Also the complicated aqueous chemistry due to dissociation of ions such as iron and lead require makes the system control extremely difficult. Chromite flotation could not be floated using anionic collectors below pH 6. The important phenomena like dimerization, miscellization, and precipitation are all involved and controlled by the system pH (Klassen and Krokhn, 1963). Knowledge of the PZC's of the constituting minerals in ore under investigation must be known. The following PZC values have been reported for the most common minerals in the chromite ores: chromite, pH of 5.6-7.2 (Palmer et al., 1975; Guney and Atak, 1997); serpentine, pH of 5.2 (Yerel, 2005); magnetite, pH of 4-6.5; talc, pH of 2.1; and quartz, pH of 2.8 (Branko et al., 1992).

Chromite ores are usually concentrated by gravity concentration techniques based on differences in specific gravity between chromite and the common associating gangue minerals and rocks such as serpentine and olivine. Jigging has been used to upgrade a California chromite ore containing 18.1% Cr₂O₃ to produce a concentrate assaying 43.5% Cr₂O₃ at a recovery of 77% with Cr/Fe ratio of 2.38 Batty et al., 1947). However, jigging failed to enrich the Topraktepe chromite ore due to inadequate liberation of the ore in the appropriate jigging size fraction (Tevfik, 2007). However, Humphrey spiral technique was successful in concentrating the Topraktepe chromite ore at a suitable size fraction, -0.3 + 0.212 mm. The concentrate obtained under these conditions assayed 54.6% Cr₂O₃ at a recovery of 94.9% (Topraktepe, 2007). Heavy media separation was attempted to concentrate the Seiad Lake chromite

ore at a feed size fraction +100 mesh (+150 μm) materials (Hunter and Sullivan, 1960). Considerable amount of coarse gangue minerals was rejected and a sink product assaying 35.0% Cr_2O_3 at a recovery of 86% was obtained. Concentrating the Elazig-Kefdag chromite ore in Turkey using a Multi-Gravity Separator, MGS, was reported by Gence in 1999. The obtained concentrate assayed 52.1% Cr_2O_3 at a recovery of 69.6% at the optimum operating conditions. The Multi-gravity Separator was also used for concentration of the Toprakepe chromite ore, and a concentrate assaying 57.5% Cr_2O_3 from an ore assaying 46.2% Cr_2O_3 was obtained. Shaking tables were used for concentration of the Stillwater chromite ore (Sullivan and Worktine, 1964). Although significant amount of the chromium content remained in the middling fraction, the chromite recovery was reasonable. Treating the middling fraction of this process by tabling in a second stage increased the chromium recovery. Using the shaking table for enriching an Egyptian chromite ore containing serpentine as the major gangue mineral was found to be effective in concentrating the ore under consideration (Yousef et al., 1970). In a second stage, they used a magnetic separator to further remove most of the iron minerals from the table concentrate. The final concentrate assayed 68% Cr_2O_3 at a recovery of 80 % with the Cr/Fe ratio of 3.7.

Magnetic separation was not effective in enriching the California chromite ore (Hunter and Sullivan, 1960). The grade of the concentrate did not exceed 42% Cr_2O_3 at a recovery of 62%. The limited chromite recovery may be due to coating of chromite particles with magnetite which removed part of the chromite to the waste product. The Kempersayi chromite ore was concentrated by two-stage magnetic separation; 5000 Oersted and 11000 Oersted ($4 \cdot 10^4$ A/m and $8.8 \cdot 10^4$ A/m) (Starun et al., 1960). The concentrate obtained assayed 55.6% Cr_2O_3 at a recovery of 82.8%.

Electrostatic separation at 15 to 20 kV produced a high grade concentrate assaying 54% Cr_2O_3 at a recovery of 58% and the Cr/Fe ratio of 2.42 from the California chromite ore (Hunter and Sullivan, 1960). The low recovery in this case was due to the high percentage of fines which was partially untreated and partially masked the particles and hence precluded selective separation. High-tension electrostatic separation of a table concentrate from the Montana chromite ore resulted in a final concentrate assaying 42% Cr_2O_3 at a recovery of 86%.

In Sudan, chromite ore deposits occur mainly in the Ingassana Hills in the Blue Nile region. Other occurrences have been reported at Hammissana, Sol Hamid in the Northern Red Sea Hills, the Nuba Mountains in Southern Kordofan, Jabal Rahib Northwest Sudan, and Jabal El-Tawil in Central Butana in Southern Sudan. The Ingassana chromite ore is considered as one of the largest chromite ore deposits in Sudan. Its chromite reserves was estimated to be 2 teragrams (Tg or million tons), with chromium oxide assay in the range from 20% to 51% Cr_2O_3 (Habashi and Bassyouni, 1982; Ahmed, 1998). The mining area at Ingessana Hills is connected to Khartoum, Port-Sudan and other important parts of Sudan with fairly maintained motor roads and railways through Damazine city, the capital of Blue Nile Governorate.

Chickay Chromite Mine in the Ingassana area is about 80 km from Damazine city. The chromite ore in the Chickay Mine is in the form of a vein of complicated shape. Due to depletion of high grade chromite ore, and the presence of a large amount of low-grade ore in the area, it was necessary to come up with a suitable mineral processing technique to upgrade these low-grade ores together with the leftover fines from the previous chromite mining operations. The flotation technique was attempted for enriching the Chickay chromite ore. The assay of the feed to the flotation cell was 20.3% Cr_2O_3 . Under optimum conditions, the chromite concentrate assayed 28.7% Cr_2O_3 at a recovery of 94.5%. Of course, the assay of the obtained concentrate is not satisfactory, which indicates that the flotation is not the right technique to concentrate this type of ore (Tammam, 2010; Seifelnasr and Tammam, 2011). The main objective of the present work is to investigate the amenability of the Chickay low-grade chromite ore to be concentrated by gravity methods, utilizing the relatively large difference in the specific gravity of the main constituting minerals, chromite and serpentine, in particular by using the shaking table.

3. Material, equipment, and procedure

3.1. Material

A low grade chromite sample of about 250 kg was collected from Chickay Mine, at the Ingassana Hills, Blue Nile Governorate, Eastern Sudan. The chromium oxide (Cr_2O_3) content in the sample under investigation was, on the average, 34.2% Cr_2O_3 . The major associated gangue mineral was serpentine (density 2.6 g/cm^3) together with little olivine mineral (3.3 g/cm^3). The density of the chromite mineral is about 4.6 g/cm^3 . This significant difference in specific gravities between the constituting minerals gives a *concentration criterion* of more than 2.0 and suggests using one of the gravity separation techniques for upgrading the chromite ore.

3.2. Equipment

One of the effective gravity techniques in this case is tabling. Shaking Table is a highly selective gravity separator. A laboratory shaking table of 50 cm x 90 cm was used for the concentration of the chromite sample. Figure 1 shows a schematic drawing for the used shaking table. The fixed operating parameters were: 300 stroke/min, 11 mm stroke length, 50 g/min dry solids feed rate fed at a solid/liquid ratio of 1:4, 9 dm^3/min wash water flow rate. The positions of the products (tailings, middlings, and concentrate) splitters were fixed during the whole investigation. The studied variables were: the tilt angle of the table and the feed size.

3.3. Procedure

The table was set at the pre-assigned operating conditions, and the material was continuously fed into the feed box of the table at a constant feed rate until the system attains a steady state. The products (tailings, middlings, and concentrate) were

collected in their respective collecting pans, filtered, dried, weighed and analyzed for Cr_2O_3 .

4. Results and discussion

The chromite ore was ground to pass 1.2 mm which was a suitable size for tabling with minimum amount of fines. The study of the degree of liberation was performed for various size fractions of the ground ore by counting the free chromite particles in each fraction under the microscope. It was found that the highest counts for the free chromite particles, 56.7 %, were in the size range -200+100 microns.

Two series of separation experiments were carried out; one for different tilt angles of the table, and the other for different particle size ranges of the feed material to the table. In some experiments the ore sample was deslimed at 75 micrometers. The feed size fractions were prepared using a hydrocyclone to obtain equal settling particles.

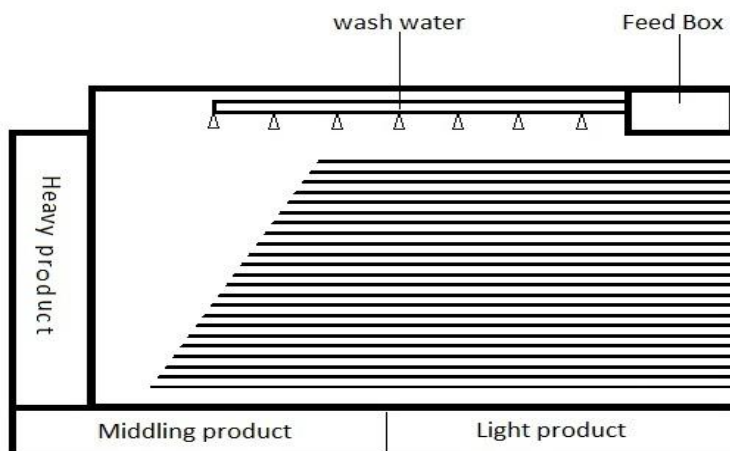


Fig. 1. A schematic layout of the shaking table

4.1. Effect of tilt angle

The table was tilted at three different tilt angles: 4° , 6° , and 8° . The feed to the table was a deslimed material whose size fraction was -1.168+0.075 mm. The -0.075 mm contains about 9.0% of the chromite contained in the feed sample. Figure 2 shows the grade and recovery of the concentrate fractions obtained at each tilt angle. The grade of the concentrate at 4° and 6° tilt angles was very close, 49.9% and 48.8.0% Cr_2O_3 , respectively, whereas at a tilt angle of 8° the grade of the concentrate was 54.2% Cr_2O_3 . The best recovery, 63.19%, was obtained at a table tilt angle of 6° , whereas the worst recovery, 13.6%, was obtained at a tilt angle of 8° . The reason for the deterioration of the recovery at the high table tilt angle is probably due to the higher downward pushing force of the particulate system flowing on the table surface by the

washing water flowing downward. The washing action, under these conditions, pushes the material more towards the middlings and the tailings sections. This is confirmed by a high yield of the chromite, 73.5%, in the middling fraction when the table tilt angle was 8° , whereas the chromite yield in the middlings was 38.4% and 27.1% at tilt angles of 4° and 6° , respectively (Fig. 3). The higher assay of both the concentrate and middlings at table tilt angle of 8° is again due to the enhanced gravitational force of the wash water by the increased tilt angle, which was able to push down larger amount of the rich chromite ore particles before it reaches the concentrate collection area. Based on the above discussion, a tilt angle of 6° was chosen for the second series of experiments. Table 1 summarizes the effect of the tilt angle of the table on the concentrate parameters, grade and recovery.

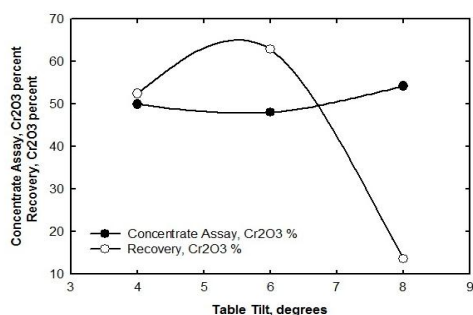


Fig. 2. The trend of Cr_2O_3 assay and recovery of the concentrate as a function of the table tilt angle in degrees

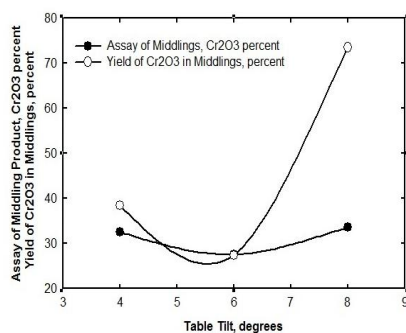


Fig. 3. The trend of the Cr_2O_3 assay and yield in the middling fraction at different table tilt angles in degrees

4.2. Effect of feed size fraction

To study the effect of the feed size fraction on the grade and recovery of the chromite concentrate four alternatives were attempted.

- 1) The deslimed ore ($-1.168 + 0.075$ mm) was used as the table feed and the slimes, -0.075 mm, was excluded. This alternative was discussed in the above section, Table 1. The grade and recovery of the concentrate were 48.8% Cr_2O_3 and 63.2% Cr_2O_3 , respectively.
- 2) In this alternative, an attempt was made to split the deslimed feed into two fractions $-1.168 + 0.25$ and $-0.25 + 0.075$ mm. Table 2 presents the results obtained in this series of experiments. The combined concentrate assays 48.1% Cr_2O_3 at a recovery of 66.6% Cr_2O_3 .
- 3) The table feed in this case was a whole feed, i.e., -1.68 mm without desliming or fractionation. The concentrate assays 47.35% Cr_2O_3 at a recovery of 68.2%. Table 3 presents the results obtained in this case. The tailings contain only about 6% of the valuable constituent.

- 4) The fourth series of experiments was designed to use the whole sample without desliming, but it was split into two fractions; $-1.68 + 0.180$ and -0.180 mm, and each fraction was used as a separate feed to the table. Table 4 presents the grades and chromite distributions in the various products of the feed fractions and the combined concentrate in this series of experiments. The combined concentrate assays 47.22% Cr_2O_3 at a recovery of 74.9%.

Table 1. Effect of the tilt angle of the shaking table on the concentration of the Sudanese chromite ore. The feed to the table is a deslimed ore of $-1.168 + 0.75$ mm

| Tilt Angle, degrees | Product | Weight, % | Assay, Cr_2O_3 , % | Cr_2O_3 Distribution, % |
|---------------------|-------------|-----------|------------------------------------|---|
| 4° | Concentrate | 37.4 | 49.9 | 52.3 |
| | Middlings | 42.1 | 32.5 | 38.36 |
| | Tailings | 2.1 | 10.4 | 0.61 |
| | Total | 81.6 | | 91.27 |
| 6° | Concentrate | 45.0 | 48.8 | 63.19 |
| | Middlings | 34.2 | 27.5 | 27.08 |
| | Tailings | 2.3 | 12.3 | 0.8 |
| | Total | 81.5 | | 91.07 |
| 8° | Concentrate | 7.9 | 54.2 | 13.54 |
| | Middlings | 69.4 | 33.5 | 73.51 |
| | Tailings | 4.8 | 20.5 | 3.1 |
| | Total | 82.1 | | 90.22 |

Table 2. Effect of the feed size fraction of the deslimed ore on the shaking table performance for concentrating of the chromite ore. The tilt angle of the table is 6 degrees.

| Particle size, mm. | Product | Product, Wt. % | Assay, Cr_2O_3 , % | Cr_2O_3 Distribution, % |
|----------------------------|-----------------|----------------|------------------------------------|---|
| $-1.68 + 0.25$ | Concentrate (1) | 37.1 | 49.2 | 52.80 |
| | Middlings | 18.6 | 27.0 | 14.34 |
| | Tailings | 0.20 | 12.1 | 0.05 |
| | Subtotal | 55.9 | 41.68 | 67.19 |
| $-0.25 + 0.075$ | Concentrate (2) | 11.0 | 44.47 | 14.0 |
| | Middlings | 15.6 | 24.33 | 10.92 |
| | Tailings | 2.4 | 11.34 | 0.80 |
| | Subtotal | 29.0 | 30.89 | 25.72 |
| Combined Concentrate (1+2) | 48.1 | 48.12 | 66.61 | |

Table 3. Effect of the whole feed size fraction without desliming (-1.168 mm) on the shaking table performance for concentrating of the chromite ore. The tilt angle of the table is 6 degrees

| Product | Product, Wt. % | Assay, Cr_2O_3 % | Cr_2O_3 Distribution, % |
|-------------|----------------|----------------------------------|---|
| Concentrate | 48.8 | 47.35 | 68.16 |
| Middlings | 34.0 | 28.85 | 25.92 |
| Tailings | 16.6 | 12.01 | 5.93 |
| Total Feed | 100.0 | 33.91 | 100.1 |

Table 4. Effect of the feed size fractions of the non- deslimed ore on the shaking table performance for concentrating of the chromite ore. The tilt angle of the table is 6 degrees

| Pricle size, mm | Product | Product, Wt. % | Assay, Cr ₂ O ₃ , % | Cr ₂ O ₃ Distribution, % |
|----------------------------|-----------------|----------------|---|--|
| -1.168+0.180 | Concentrate (1) | 40.2 | 48.88 | 60.32 |
| | Middlings | 23.8 | 24.59 | 17.9 |
| | Tailings | 0.4 | 5.5 | 0.06 |
| -0.180 | Concentrate (2) | 11.5 | 41.35 | 14.63 |
| | Middlings | 7.9 | 16.19 | 3.92 |
| | Tailings | 16.1 | 6.39 | 3.17 |
| Total | Feed | 99.9 | 32.60 | 100.0 |
| Combined Concentrate (1+2) | | 51.7 | 47.22 | 74.9 |

These four alternatives can be grouped into two sets; tabling of a deslimed feed and tabling of non-deslimed feed. The deslimed feed was treated once as a whole deslimed feed and the other series of experiments was carried out by splitting the deslimed feed into two size fractions, alternatives 1 and 2. The non-deslimed feed was also treated once as a whole feed and in the other series the sample was split into two fractions, alternatives 3 and 4. In both groups, the assay of the concentrate was almost the same whether the feed to the table was one fraction or two fractions, whereas the recovery was higher when the feed was split into two fractions than the case of one fraction. This trend is probably due to the way the particulates rearrange themselves during stratification on the table surface, where the heavy species gets better chance to segregate to the table surface, travelling towards the concentrate end, leaving the light species on the top to be washed off by the wash water. Also, it can be noticed that the chromite recovery is considerable higher in alternative 4 than in alternative 2, while the assay of the final concentrate is almost the same for both alternatives. This is possibly because the feed in alternative 4 was not deslimed, and hence the losses in the fine fraction was less and most of the chromite particles were recovered.

5. Summary and conclusions

The chromite reserves in Sudan are mostly of low-grade. The chromite content ranges from 20% to 35% Cr₂O₃. This grade is too low for industrial uses. The froth flotation technique failed to upgrade this type of ore to the marketable grade. As a result of the reasonable difference in specific gravity between the chromite mineral and the main associated ingredients, gravity separation was a possible solution for concentrating such ore. In the present work, a laboratory shaking table has been used for upgrading this type of low-grade chromite ore. Several series of experiments were carried out to investigate the effect of the table tilt angle and the feed size range on the table performance, grade and recovery. The assay of the feed ranged from 30% to 35% Cr₂O₃. The optimum mesh of grind, liberation, was in the size fraction of 200 µm to 100 µm. Encouraging results were obtained. The table tilt was varied from 4 degrees to 8 degrees. A table tilt of 6 degrees gave the best results as compared with the other tilt angles, where the concentrate assays 49% Cr₂O₃ at a recovery of 63%. With

respect to the table feed size distribution, it was found that closer feed size range is better than wider size range, which is logical for the table performance. Another conclusion was that splitting the feed into size fractions without desliming is more advantageous than desliming the feed. This latter finding is logical because the fine chromite fraction would have been lost if the feed is deslimed. The final concentrate which was obtained at tilt angle of 6 degrees and the feed was split into two fractions without desliming, $-1.168 + 0.18$ mm and -0.18 mm, assayed 47.2% Cr_2O_3 at a recovery of 75%.

References

- Ahmed, A.M., 1998, Sudanese Industrial Minerals and Rocks, Center for Strategic Studies, Khartoum, Sudan, 76–86.
- Batty, J.V.; Mitchell, T.F.; Havens, R.; Wells, R.R., 1947, "Beneficiation of chromite ores from Western United States, US Bureau of Mines, Report of Investigation #4079, Jun., 26.
- Branko, S.; Dragan, K.; Suzana, F., 1992, "Measurement and application of zeta potential, Rudarsko-Geološko-Naftni Zbornik, Zegreb, vol. 4, 147–151.
- Gence, N.; 1999, Beneficiation of Blazig-Kefdag Chromite by Multy Gravity Separation, Tr. J. Engineering and Environmental Science, vol. 23, 473–475.
- Guney, A.; Atak, S., 1997, "Separation of chromite from olivine by anionic collectors," *Fizykochemiczne Problemy Mineralurgii*, vol. 31, 99–106.
- Habashi, F.; Bassyouni, F.A., 1982, Mineral Resources of the Arab Countries, second Edition, Quebec, Canada, 46.
- Havens, R., 1946, "Froth flotation of chromite with fluoride," US Patent 2,412,217, 7.
- Hundhauen, R.J., 1947, "Chromiferous sand deposits in the Coos Bay Area, Coos County, Oregon, US Bureau of Mines, Report of Investigations 4001, 18.
- Hunter, W.L.; Sullivan, V., 1960, "Utilization studies on chromite from Seiad Creek, California," US Bureau of Mines, Report of Investigations 5576, 37.
- Klassen, W. I.; Krokhin, S.I., 1963, "Contribution to the mechanism of action of flotation reagents," Mineral Processing, Proceedings of the 6th International Congress, Cannes, 397–406.
- Maliotis, G., 1996, Chromium uses and markets, Industrial Minerals Information, Ltd.
- Nafziger, R.H., 1982, "A review of the deposits and beneficiation of low-grade chromite," *Journal of the South African Institute of Mining and Metallurgy*, vol. 27, 205–226.
- Nafziger, R.H.; Tress, J.E.; Paige, J.I., 1979, "Carbothermic reduction of domestic chromites," *Aletall. Trans. Section B*, vol. 10 B, No. 1, 5–14.
- Palmer, B.R.; Fuerstenau, M.C.; Aplan, F.F., 1975, "Mechanism involved in the flotation of oxides and silicates with anionic collectors, Part 2," *Trans AIME*, vol. 258, 261–270.
- Read, H.H., 1957, *Rutley's Elements of Mineralogy*, 24th Edition, Thomas Murby & Co., London, 458.
- Seifelnasr, A.A.; Tammam, T., 2011, "Flotation behavior of Sudanese chromite ores," Accepted for publication in *Journal of Engineering Sciences*, Faculty of Engineering, Assiut University.
- Sullivan, G.V.; Worktine, G.F., 1964, "Beneficiating low-grade chromites from the Stillwater Complex, Montana," US Bureau of Mines, Report of Investigations No. 6448, 29.
- Starun, V.G.; Dudabskiy, I.Ye.; Davydove, I.P.; Kolsnik, M.I.; Ryazantsev, V.D.; Samoylov, I.G.; Dokuchayeva, 1960, "Concentration of chromite from the Kempersayi deposit by magnetic separation," *Refractories and Industrial Ceramics*, vol. 1, No. 3, 89–91.
- Tammam, T.A., 2010, "Upgrading of a low-grade Sudanese chromite ore," M S Thesis Submitted to Omdurman Islamic University, Faculty of Engineering, Mining Engineering Department.
- Tevfik, A.; Zedef, V.; Aydogan, S., 2007, "Beneficiation of low-grade chromite of abandoned mine at Topraktepe," *Acta Montanistica Slovaca Rocnik*, vol. 12, ceslo 4, 323–327.

- USBM, 1992, Minerals Yearbook, vol. 1, Metals and Minerals, US Department of the Interior, Bureau of Mines, Washington D.C.
- Yerel, S.; Ozbay, N.; Gence, N, 2005, "Effect of pH on the micro-electrophoretic behavior of chromite and serpentine in aqueous solutions," F. U. Fen ve Muhendislik Bilimleri Dergisi, vol. 17, No.2, 435-441.
- Yousef, A. A.; Boulos, T.R.; Arafa, M.A., 1971, "Concentration of low-grade chromite ores for metallurgical and chemical purposes," Journal of Minerals, Metals, and Fuels, vol. 18, No. 1, 12-18.

Received July 31, 2011; reviewed; accepted September 15, 2011

ADSORPTION AND CO-ADSORPTION OF PEO-PPO-PEO BLOCK COPOLYMERS AND SURFACTANTS AND THEIR INFLUENCE ON ZETA POTENTIAL OF MAGNESITE AND DOLOMITE

Anna BASTRZYK, Izabela POLOWCZYK, Ewa SZELAG, Zygmunt SADOWSKI

Wroclaw University of Technology, Wybrzeze Wyspianskiego 27, 50-370 Wroclaw, Poland, zygmun.sadowski@pwr.wroc.pl

Abstract. The influence of adsorption and co-adsorption of PEO-PPO-PEO triblock copolymers (Pluronic) as well as surfactants on the zeta potential of magnesite and dolomite aqueous suspension are addressed here. Four Pluronic of various molecular weight were used in these studies. They have been mixed with cationic (CTAB) or anionic (SDS) surfactants. The adsorption isotherms of copolymers and copolymer-surfactant mixture onto magnesite and dolomite have been determined. The adsorbed amount of Pluronic increases with the increasing concentration and reaches plateau. An increase in the adsorbed amounts of both cationic and anionic surfactants onto the mineral surfaces (magnesite and dolomite) has been observed in the presence of Pluronic copolymers. A positive nature of zeta potential was observed in the presence of cationic surfactant, except magnesite without or with a low CTAB concentration. However, an attendant copolymer causes a decrease of zeta potential due to the deformation of an electrical double layer, comparing the presence of an individual cationic surfactant. The adsorbed non-ionic Pluronic layer partially screens the surface charge of mineral particles, and thus, reduces the zeta potential. On the other hand, the adsorption of anionic surfactant and copolymer caused a decrease in the negative value of the zeta potential of both investigated minerals due to increased SDS adsorption. The viscosity measurements were also performed to determine the thickness of adsorbed layer.

keywords: Pluronic, adsorption, synergism, zeta potential, dolomite, magnesite, surfactant, SDS, CTAB, polymer layer thickness

1. Introduction

The use of adsorbing copolymer and surfactant to modification of mineral surface and colloidal dispersion behaviour is significant for industrial applications. For instance, the pharmaceutical industry requires an adjustment of the drug surface to the human body environment. Thus, the use of amphiphilic macromolecules adsorbed onto the biodegradable materials is a new way of medicine delivery (Rapoport, 1999; Batrakova and Kabanov, 2008). Pluronic have been applied in both drug and gene

delivery systems (Shar et al., 1999; Govender and Swart, 2008), as a biological protector of bacterial cell and protein adhesion (Kabanov et al., 2002; Wesenberg-Ward et al., 2005). The application of Pluronics can increase the membrane hydrophilicity and fouling-resistance ability (Taylor et al., 2007).

Pluronics are triblock copolymers of polyethylene oxide (PEO) and polypropylene oxide (PPO). The adsorption of Pluronic macromolecules depends on the hydrophobicity of the sorbent surface. In the case of hydrophilic surface, two terminal PEO_n blocks attach to the surface, whereas the adsorption onto the hydrophobic surface is realized by PPO block which anchors to the surface. The conformation of adsorbed Pluronic molecules onto different surfaces depends on the PPO/PEO ratio (Terayama et al., 2001, Kapilashrami et al., 2003). The adsorption layer density of triblock copolymers at the solid-liquid interface is greater than that of diblock ones. Pluronics can adsorb at the surfaces either in a pancake or brush-like configuration. Polymer brushes are usually made of uncharged polymers rather than polyelectrolyte, most often polyethylene oxide (PEO).

Polymer-surfactant interactions were subjected to intensive theoretical and experimental investigations, especially at both the solution-air and solid-solution interfaces (Torn et al., 2003; Greenwood et al., 1995; Ortona et al., 2006; Zhang R. et al., 2007). Mixed adsorption of polymers and surfactants at the solid-liquid interfaces has been studied far less. A majority of these investigations have been focused on the adsorption onto the hydrophobic surfaces. Relatively low quantities of papers concerns the polymer-surfactant adsorption onto hydrophilic surfaces. It was shown, that the adsorption of Pluronic F108 onto silica was extremely sensitive to SDS concentration and ionic strength (Braem et al., 2001).

This paper involves a detailed study of the adsorption of Pluronics and ionic surfactants (cationic and anionic) on magnesite and dolomite. Subsequently, the zeta potential and viscosity of these systems have been analyzed. As will be shown, different behaviour of magnesite and dolomite suspensions suggests different conformations of the Pluronic-surfactant complexes at the mineral-water interface.

2. Materials and methods

2.1. Materials

2.1.1. Minerals

A natural dolomite from old quarry Kletno (Lower Silesia, Poland) and magnesite from magnesite mine Grochow (Lower Silesia, Poland) were used as mineral samples. The X-ray diffraction analysis of magnesite showed the sample contains impurities, such as silica and Fe-compounds, while the dolomite is relatively pure. Chemical analysis showed that the magnesite and dolomite contain 88% and 98 % of carbonates, respectively. The mineral samples were ground and classified. The -40 μm fraction was used in the adsorption experiments. The magnesite and dolomite samples had density 2.60 g/cm^3 and 2.77 g/cm^3 , respectively. The BET specific surface area was

determined using FlowSorbII 2300 apparatus (Micromeritics) and was found to be 1.92 m²/g for dolomite and 23.06 m²/g for magnesite. The particle size distribution measurements were carried out by using a Mastersizer2000 laser diffractometer, equipped with a HydroMu dispersion unit (Malvern Instruments), and showed that the mean particle diameter was about 7.7 and 17.3 μm for magnesite and dolomite, respectively.

2.1.2. Chemicals

Amphiphilic block copolymers of poly(ethylene oxide)-poly(propylene oxide)-poly(ethylene oxide) – Pluronics, with different molar mass and different contents of hydrophilic and hydrophobic segments were obtained as a gift from BASF Corporation. The general information about Pluronics PE 10500 and PE 6800 are presented in Table 1.

Cetyltrimethylammonium bromide (CTAB) (C₁₆H₃₃)N(CH₃)₃Br and sodium n-dodecyl sulphate (SDS) were used. They were purchased from Alfa Aesar GmbH & Co and were used without further purification. Tannic acid was obtained from Fluka.

Table 1. Characteristics of applied Pluronics

| Pluronic | Structure | Average molecular weight | Molar mass of PO block |
|----------|--|--------------------------|------------------------|
| PE 3500 | EO ₁₁ PO ₁₆ EO ₁₁ | 1900 | 950 |
| PE 6400 | EO ₁₃ PO ₃₀ EO ₁₃ | 2900 | 1750 |
| PE 6800 | EO ₇₂ PO ₂₈ EO ₇₃ | 8000 | 1750 |
| PE 10500 | EO ₃₇ PO ₅₆ EO ₃₇ | 6500 | 3250 |

2.2. Methods

2.2.1. Adsorption experiments

Adsorption isotherms were determined by solution depletion method, where the amount of Pluronics or surfactants adsorbed at the particle surface was determined from the difference between the initial and final concentration. The single component adsorption isotherms were established by mixing 50 cm³ copolymer or surfactant solution with 0.5 g of the mineral sample. After 24 hours, the dispersed solid was separated using a centrifuge at 2000 rpm for 10 minutes and the supernatants were analyzed. The concentration of Pluronics in the supernatants was measured according to tannic acid method described by Tsurumi et al. (Tsurumi et al., 2006). The reaction between tannic acid and PEO block of Pluronic results in a turbidity of solution. The turbidity was established by measuring the absorbance at 600 nm using Helios Gamma UV-Vis spectrophotometer (Thermo Electron Corporation). The equilibrium concentration of CTAB was detected by a colorimetric method with SDS, while sodium dodecyl sulfate concentration was determined using a two-phase titration method with Hyamine 1622 (Zhang S.J. et al., 2007). Adsorption of surfactant-copolymer mixtures was carried out according to the single surfactant isotherm

determination procedure described above. The mixture of two components were prepared in a flask and combined with a mineral sample immediately.

2.2.2. Zeta potential measurements

Zeta potential values of magnesite and dolomite sample were measured depending on the amount of copolymer and surfactant using ZetaSizer Nano ZS (Malvern Instruments). The zeta potential measurements were carried out at constant ionic strength of 0.1 mM NaCl. The pH of suspensions was the natural value imposed by the minerals and was 8.5 and 10.4 for magnesite and dolomite, respectively. The results were averaged over four independent measurements.

2.2.3. Viscosity measurements

The viscosity measurements of mineral suspensions were conducted using dynamic stress rheometer CVO 50 (Bohlin Instrument). The mineral suspensions for the adsorbed layer thickness measurements were prepared according to the procedure described above in a section 2.2.1. Since dolomite suspensions showed a strong coagulation, the viscosity measurements were carried out only for the magnesite suspensions.

All experiments were carried out at room temperature, i.e. 25°C.

3. Results and discussion

3.1. Adsorption isotherms of copolymers and copolymer-surfactant mixtures on the carbonates mineral surface

The isotherms of Pluronics adsorption onto the hydrophilic surfaces of magnesite and dolomite are presented in Fig. 1 and Fig. 2.

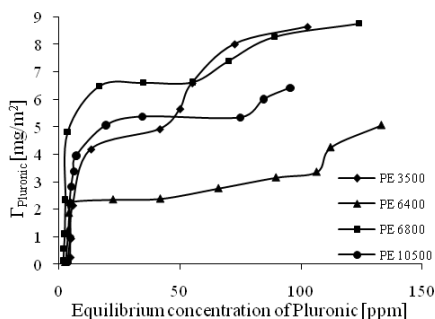


Fig. 1. Adsorption isotherms of Pluronics on magnesite (pH 8.5 and $C_{\text{NaCl}}=1 \cdot 10^{-4}\text{M}$)

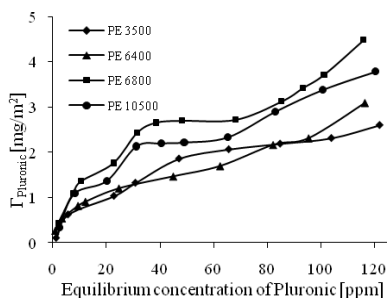


Fig. 2. Adsorption isotherms of Pluronics on dolomite (pH 10.4 and $C_{\text{NaCl}}=1 \cdot 10^{-4}\text{M}$)

The results for magnesite mineral showed that the adsorbed amount of investigated copolymer sharply increased up to 6.7, 5.4, 4.7 and 2.3 mg/m^2 , reaching the first plateau for PE 6800, PE 10500, PE 3500 and PE 6400, respectively. Further increase

in initial Pluronics concentration led to the formation of the second plateau. This observation corresponds to research of Pluronics adsorption on hydrophilic surfaces reported in literature. Tiberg and co-workers (1991) investigating the adsorption of PE 6200 copolymer onto silica surface concluded that sudden increase of adsorption densities of block copolymers on silica surface at high Pluronic concentration corresponded to the formation of more than one layer on surface. It was also observed that the multilayer can be only formed on the hydrophilic surfaces, where the adsorption occurs by terminal PEO group of copolymer (Paterson et al., 1999). In the case of dolomite mineral, the adsorbed amount of investigated copolymer slowly increased with the concentration and the regions observed for magnesite are barely apparent.

The adsorption of copolymer molecules onto carbonate minerals surface depends on the polymer molecular weight. One can see that the copolymer of PE 6800 exhibited the greatest adsorption affinity to the surface, whereas the worst adsorption was observed in system containing PE 6400 copolymer. Data presented in Table 1 show that PE 6800 copolymer has the highest molecular weight, 8000 g/mol and the largest number of PEO group, whereas PE 6400 is characterised by low molecular weight, 2900 g/mol and the smallest amount of PEO group. This finding is in a good agreement with the results published elsewhere (Dijt et al., 1990; Fler et al., 1993; Holmberg, 2002; Sakar-Deliormanli, 2007). Higher molecular weight of copolymer (M_w) means higher flexibility of the entire molecule which results in better protection of PPO block and better adsorption of molecules onto hydrophilic surfaces. But if we compare the adsorption behaviour adsorption of PE 3500 and PE 6400, as it is seen in Figure 1, PE 3500 with lower molecular weight ($M_w = 1900$ g/mol) and higher PEO part showed higher adsorption onto magnesite surface than PE 6400. Very similar results were observed in literature. Sakar-Deliormanli (2007) noticed that copolymer F 68 ($M_w = 8400$ g/mol, EO = 80%) adsorbed better at silica surface than copolymer F 127 ($M_w = 12600$ mg/g, EO = 70%). It has been suggested that the larger portion of segments of PEO groups were in macromolecules, the larger amount of copolymer was adsorbed onto silica surface, even if the molecular weight of Pluronic was smaller. It was attributed to the adsorption of block copolymer onto silica surface by hydrogen bonding between the ether oxygen and the silanol groups (Colic et al., 1998; Kawaguchi et al., 2001). In our investigated systems the magnesite sample contained 88% of carbonates and 12% of traces of minerals like talc, silicates and quartz. We can supposed that in our case, Pluronics have not only adsorbed onto silicates and quartz but also onto magnesite surface by complex formation. The mineral dissolution experiments in aqueous medium at pH 9 showed that concentration of Mg^{2+} in suspension was $3.50 \cdot 10^{-4}$ M. Magnesium cation may play crucial role in interaction between Pluronic molecules and the carbonate surface. It is well-known that poly(ethylene oxide)-based nonionic polymers are able to bind metal ions from solution and form a "pseudopolycations" which are capable of interacting with negatively charged species. It was also observed that POE chains in surfactant are

adsorbed to minerals surface through hydrogen bonding between oxygen atoms in POE chains and water molecules in the hydration layers of exchangeable cations such calcium and magnesium (Deng et al., 2006).

The results of cationic surfactant adsorption onto the magnesite and dolomite surface are presented in Fig. 3 and Fig. 4, respectively. The presence of copolymer caused greater adsorption of surfactant from mixed solution than from individual one. It can result from the synergistic interaction between block copolymer and cationic surfactant. In such system, cationic surfactant molecules anchor to the hydrophobic parts of copolymer molecules as it is schematically presented in Fig. 5. The surfactant molecules act as a bridge between the mineral surface and hydrophobic part of copolymer. This scheme was created based on the data published by Torn and co-workers (2003), which regard the structure of PVD-SDBS complexes. In the case of magnesite, the synergistic effect is significant for both investigated copolymers, which concentration in the mixture was 120 ppm. For PE 6800 and PE 10500 the plateau amount of CTAB was 8 and 12 mg/m², respectively. For the latter one, the value reached is twice as for an individual surfactant. Similar results were observed for dolomite sample, where the plateau value of CTAB in the presence of copolymer PE 6800 and PE 10500 was twice and three times greater than for an individual surfactant, respectively. It was observed that the presence of copolymer PE 10500 was more influencing on the adsorption of cationic surfactant than copolymer PE 6800. It can be explained by longer hydrophobic part in PE 10500 molecule to which the surfactants molecules or aggregates can be attached as it was shown in Fig. 5.

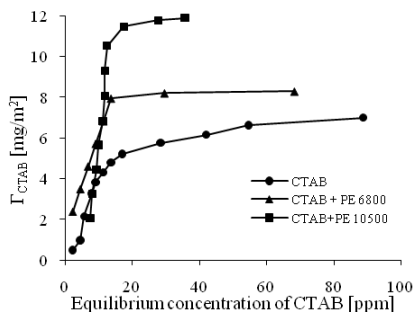


Fig. 3. Cationic surfactant adsorption on magnesite from mixed solutions (Pluronic concentration - 120 ppm, pH 8.5, $C_{\text{NaCl}} = 1 \cdot 10^{-4}$ M)

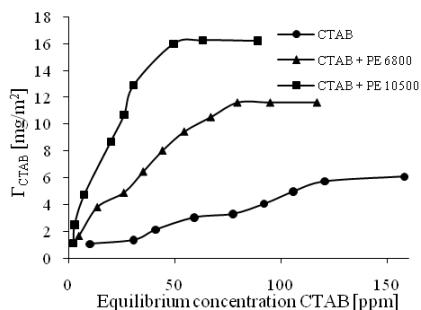


Fig. 4. Cationic surfactant adsorption on dolomite from mixed solutions (Pluronic concentration - 120 ppm, pH 10.4, $C_{\text{NaCl}} = 1 \cdot 10^{-4}$ M)

The adsorption isotherms of Pluronics onto carbonates minerals in the presence of cationic surfactant are shown in Figs. 6 and 7. The obtained data revealed that PE 6800 and PE 10500 molecules have greater affinity to both investigated mineral surfaces in the presence of CTAB, which initial concentration was 120 ppm. The plateau value of PE 6800 and PE 10500 in mixed system, was 9 and 11 mg/g² for magnesite and 10 and 18 mg/g², respectively. Earlier studies presented by Ivanova et

al. (2001), and Sastry and Hoffmann (2004) showed that hydrophobic part of CTAB monomers at concentration below cmc adsorb at PPO segments making it more hydrophilic because of the hydrophilic part of surfactants molecules exposed to solution. A greater adsorption of PE 10500 than PE 6800 at magnesite and dolomite surface can result from longer hydrophobic domain in molecule of PE 10500. The longer this domain was in molecules, the greater adsorption of CTAB at this segment occurred and the better affinity of copolymer-cationic surfactant mixture was observed.

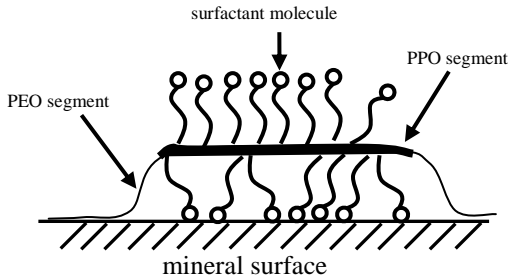


Fig. 5. Schematic diagram of Pluronic-surfactant system onto hydrophilic surface

The effect of Pluronics addition on anionic surfactant adsorption from the polymer-surfactant mixture is shown in Fig. 8 and 9. In this case, the similar behaviour was observed as for cationic surfactant. However, the plateau value of surfactant was lower in comparison to cationic one due to the mechanism of SDS adsorption onto carbonates minerals, described by Celik et al. (1998).

Figures 10 and 11 present the adsorption isotherms of Pluronics onto carbonates minerals in the presence of anionic surfactant. The obtained amounts of adsorbed PE 6800 and PE 10500 molecules were much greater in the presence of SDS for both investigated minerals. These results were similar to data obtained in the system containing CTAB, described above.

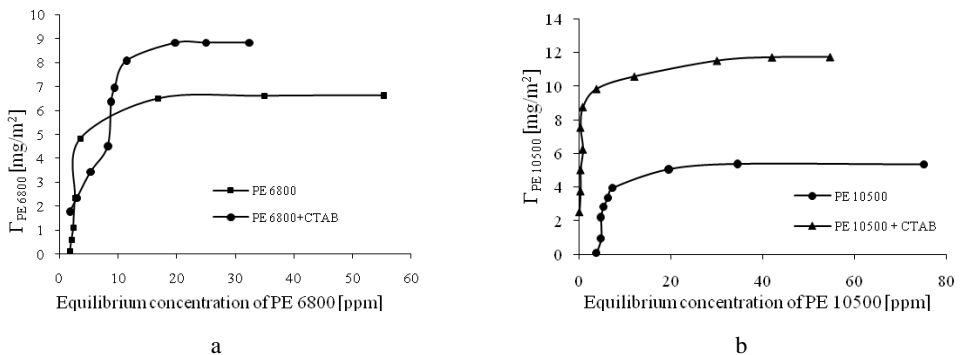


Fig. 6. Adsorption isotherms of Pluronic PE 6800 (a) and PE 10500 (b) on magnesite from mixed solution (CTAB concentration - 120 ppm, $C_{NaCl}=1 \cdot 10^{-4}M$, pH 8.5)

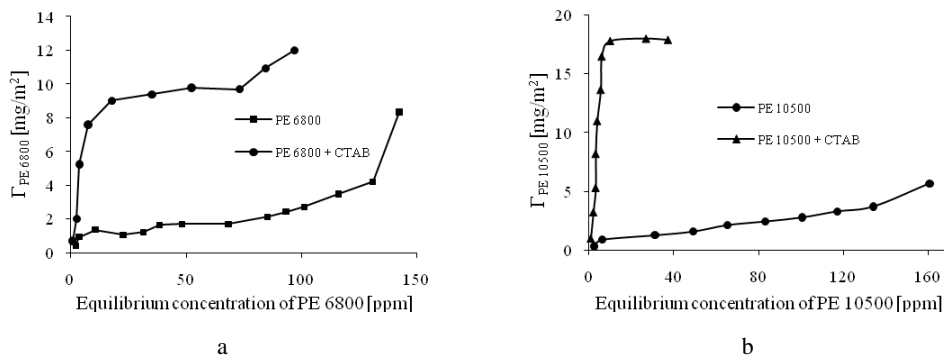


Fig. 7. Adsorption isotherms of Pluronic PE 6800 (a) and PE 10500 (b) on dolomite from mixed solution (CTAB concentration - 120 ppm, $C_{NaCl}=1\cdot 10^{-4}$ M, pH 10.4)

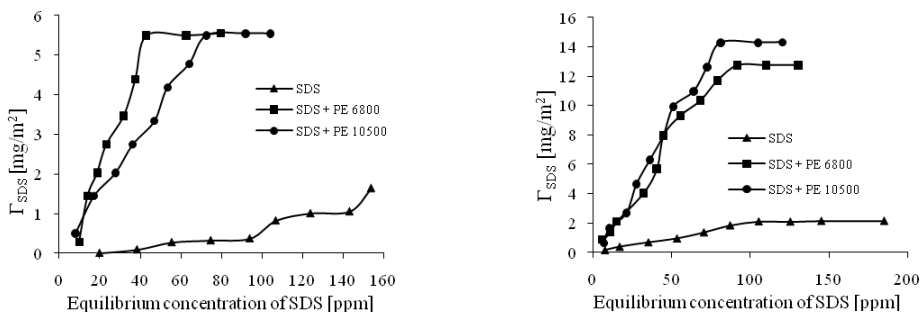


Fig. 8. Anionic surfactant adsorption isotherms onto magnesite from mixed solution from Pluronic-SDS solutions (Pluronic concentration - 120ppm, $C_{NaCl}=1\cdot 10^{-4}$ M, pH 8.5)

Fig. 9. Anionic surfactant adsorption isotherms onto dolomite from mixed solution from Pluronic-SDS solutions (Pluronic concentration - 120ppm, $C_{NaCl}=1\cdot 10^{-4}$ M, pH 10.4)

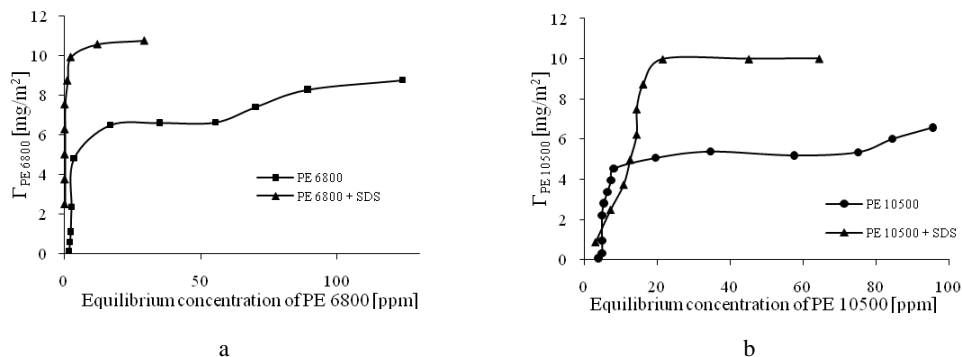


Fig. 10. Adsorption isotherms of Pluronic PE 6800 (a) and PE 10500 (b) on magnesite from the mixed solution (SDS concentration - 120 ppm, $C_{NaCl}=1\cdot 10^{-4}$ M, pH 8.5)

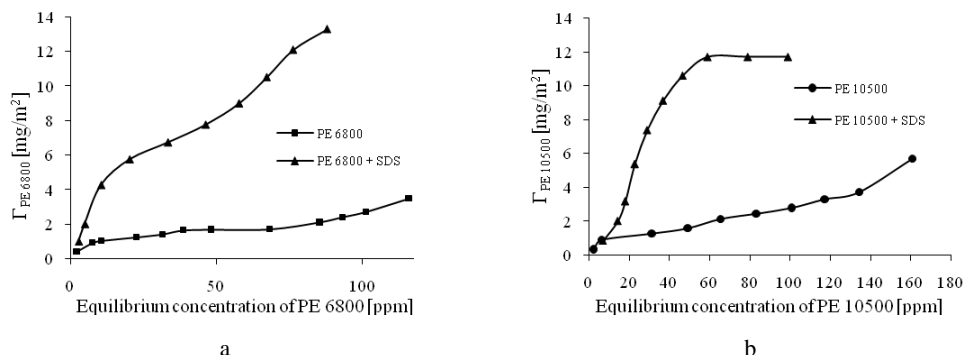


Fig. 11. Adsorption isotherms of Pluronic PE 6800 (a) and PE 10500 (b) on dolomite from the mixed solution (SDS concentration - 120 ppm, $C_{NaCl}=1 \cdot 10^{-4}$ M, pH 10.4)

3.2. Influence of the presence of copolymer, surfactant and the complex of copolymer-surfactant on the zeta potential of carbonate minerals

Natural magnesite particles had a negative zeta potential at natural pH of suspension which was 8.5, whereas the natural pH of dolomite suspension was equal 10.4. The isoelectric point of dolomite was in the vicinity of this pH.

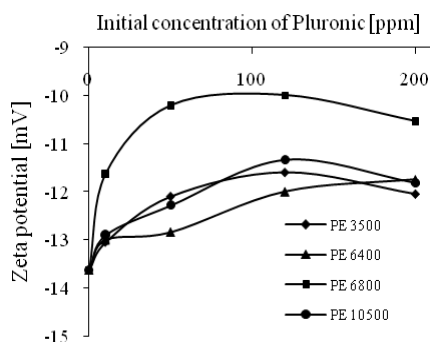


Fig. 12. Zeta potential of magnesite in the presence of Pluronic as a function of copolymer concentration ($C_{NaCl}=1 \cdot 10^{-4}$ M, pH 8.5)

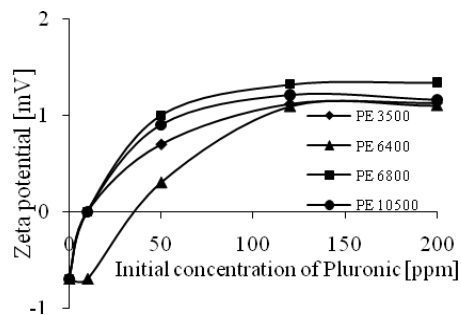


Fig. 13. Zeta potential of dolomite in the presence of Pluronic as a function of copolymer concentration ($C_{NaCl}=1 \cdot 10^{-4}$ M, pH 10.4)

Figures 12 and 13 show that the adsorption of nonionic copolymers (Pluronic) onto investigated minerals slightly changes the zeta potential value of carbonate mineral particles due to a shift in the place of slipping plane (Vincent, 1974; M'Pandou and Stiffert, 1987). Experimental data revealed (Fig. 14 and Fig. 15) that the zeta potential value of these particles in the presence of cationic surfactant (CTAB) and Pluronic-CTAB mixture was more positive. It may be explained by the structure of complex

Pluronic-CTAB formed in such solution, which is presented in Fig. 5. The cationic surfactant can be adsorbed at hydrophobic part of expanded Pluronic molecules, shifting the zeta potential value to more positive. However, an attendant copolymer causes a decrease of zeta potential due to the deformation of an electrical double layer, comparing the presence of an individual cationic surfactant. It may be attributed to the screening effect of Pluronic molecules (Liu and Xiao, 2008). In the presence of anionic surfactant the value of zeta potential of investigated minerals was more negative due to the presence of negatively charged surfactant molecules (Fig. 16 and Fig. 17). On the other hand, the co-adsorption of anionic surfactant and copolymer caused a decrease in the negative value of the zeta potential due to increased SDS adsorption. A special configuration of surfactant molecules in Pluronic-surfactant complex (Fig. 5) leads to higher negative zeta potential.

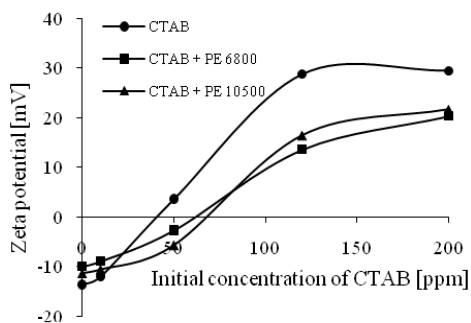


Fig. 14. Zeta potential of magnesite in Pluronic-CTAB mixed solution as a function of cationic surfactant concentration (Pluronic concentration – 120 ppm, $C_{NaCl} = 1 \cdot 10^{-4}$ M, pH 8.5)

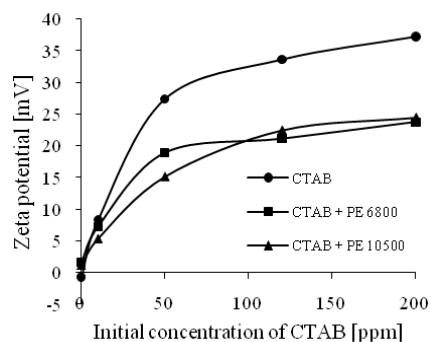


Fig. 15. Zeta potential of dolomite in Pluronic-CTAB mixed solution as a function of cationic surfactant concentration (Pluronic concentration – 120 ppm, $C_{NaCl} = 1 \cdot 10^{-4}$ M, pH 10.4)

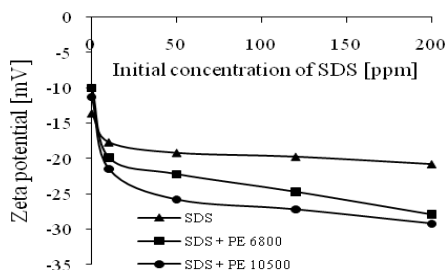


Fig. 16. Zeta potential of magnesite in Pluronic-SDS mixed solution as a function of anionic surfactant concentration (Pluronic concentration – 120 ppm, $C_{NaCl} = 1 \cdot 10^{-4}$ M, pH 8.5)

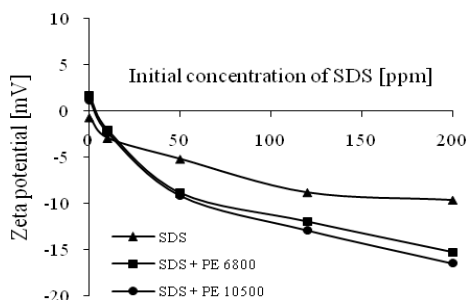


Fig. 17. Zeta potential of dolomite in Pluronic-SDS mixed solution as a function of anionic surfactant concentration (Pluronic concentration – 120 ppm, $C_{NaCl} = 1 \cdot 10^{-4}$ M, pH 10.4)

3.3. The thickness of adsorbed layer of copolymer and copolymer-surfactant complex onto carbonate minerals

The zeta potential values for dolomite particles without reagents were within the range of -1.0 to +1.5 mV. Mineral suspensions with such a low zeta potential tend to coagulate. For this reason, the viscosity measurements were performed only for the magnesite suspensions, which was stable at the natural pH (pH=8.5).

The adsorbed layer thickness can be calculated from an elastic module data (Greenwood-Ward et al., 1995; Postmus et al., 2007). The adsorbed layer is correlated with the effective volume fraction (ϕ_{eff}). This relation can be described by following equation:

$$\Phi_{\text{eff}} = \phi(1+\delta/a)^3$$

where: δ is the thickness of adsorbed layer and a is the particle radius.

The adsorbed layer thickness was calculated using this equation. The results are shown in Table 2. These results were obtained for magnesite suspension in the presence of single Pluronic and Pluronic-surfactant mixture.

Table 2. Thickness of Pluronic and Pluronic-surfactant layers on the magnesite surface obtained from viscosity measurements

| Layer | δ (nm) |
|---------------------|---------------|
| Pluronic 6800 | 2.0 |
| Pluronic 10500 | 2.3 |
| Pluronic 6800-CTAB | 3.7 |
| Pluronic 10500-CTAB | 3.9 |
| Pluronic 6800-SDS | 3.4 |
| Pluronic15000-SDS | 3.7 |

The thickness of copolymer layer was about 2.0 and 2.3 nm for PE 6800 and PE 10500, respectively. It is due to longer hydrophobic loops of PE 10500 expanded from the mineral surface comparing PE 6800. As can be seen from these data, the adsorption of Pluronic-ionic surfactant complex caused an increase in the adsorbed layer thickness. Attendant ionic surfactant molecules at the copolymer chain may impose loose conformation of the chain due to electrostatic repulsion between surfactants heads. Slightly thicker layers formed in the presence of CTAB may be explained by greater hydrophilic moiety of the cationic surfactant.

4. Conclusions

Amount of Pluronic adsorbed on the dolomite and magnesite surfaces depends on the PEO/PPO ratio. When adsorption occurred in mixed system, an increase of Pluronic and surfactant adsorbed amounts was observed. It suggests the existence of a synergistic effect between Pluronic and surfactant adsorbed on minerals surfaces. Adsorption of Pluronic-anionic surfactant complex onto the mineral surface causes an

increase in negative values of zeta potential in comparison with adsorption of the single surfactant. The observed change in zeta potential of both magnesite and dolomite particles as a result of adsorption of the nonionic polymer (Pluronic) and cationic surfactant can be explained by the Pluronic molecules screening effect. Under natural pH condition the dolomite suspensions were strongly coagulated (pH=10.4) and the thickness of adsorbed layers has not been analyzed for this mineral. From viscosity measurement results for the magnesite suspensions, the conclusion can be drawn that the adsorbed copolymer layer thickness increases in the presence of ionic surfactant.

Acknowledgments

The authors thank Dr. Patkowski (UMCS Lublin) for his help with viscosity measurements. This work was financially supported by the Polish Ministry of Science and Higher Education (grant No. N240 290134).

References

- Batrakova, V.E., Kabanov, A.V. 2008, Pluronic block copolymers: Evolution of drug delivery concept from inert nanocarriers to biological response modifiers, *J. Controlled Release*, 130, 98–106.
- Braem, D.A., Prieve, D.C., Tilton, R.D. 2001, Electrostatically tunable coadsorption of sodium dodecyl sulfate and poly(ethylene oxide)-b-poly(propylene oxide)-b-poly(ethylene oxide) triblock copolymer to silica, *Langmuir*, 17, 883–890.
- Celik, M., S., Yasar, E., El-Shall, H., 1998, Flotation of Heterocoagulated Particulates in Ulexite/SDS/Electrolyte System, *J. Colloid Interface Sci.*, 203, 254–259.
- Colic, M., Fisher, M.L., Fuerstenau, D.W. 1998, Electrophoretic behaviour and viscosities of metal oxides in mixed surfactant systems. *Colloid Polym. Sci.*, 276, 72–80.
- Dijt, J.C., Cohen Stuart, M.A., Hofman, J.E., Fleer, G.J. 1990, Kinetics of polymer adsorption in stagnation point flow, *Colloids Surf.*, 51, 141–158.
- Deng, Y.J., Dixon, J.B., White, G.N. 2006, Bonding mechanisms and conformation of poly(ethylene oxide)-based surfactants in interlayer of smectite, *Colloid. Polymer Sci.*, 284, 347–356.
- Fleer, G.J., Cohen Stuart, M.A., Scheutjens, J.M.H.J., Cosgrove, T., Vincent, B. 1993, *Polymers at Interfaces*, Chapman and Hall, London.
- Govender, S., Swart, P. 2008, Surfactant formulations for multi-functional surface modification, *Colloids Surf.*, 331, 97–102.
- Greenwood, R., Luckham, P.F., Gregory, T. 1995, The effect of particle size on the layer thickness of a stabilizing polymer adsorbed onto two different classes of polymer latex, as determined from rheological experiments, *Colloids Surf.*, 98, 117–125.
- Holmberg, K., 2002. *Handbook of Applied Surface and Colloid Chemistry*, Wiley&Sons, New York.
- Ivanova, R., Alexandridis, P., Lindman, B., 2001, Interaction of poloxamer block copolymers with cosolvents and surfactants *Colloids Surf.*, 183-185, 41–53.
- Kabanov, V.A., Batrakova, E.V., Alakhov, V.Y. 2002, Pluronic block copolymers as novel polymer therapeutics for drug and gene delivery, *J. Controlled Release*, 82, 189–212.
- Kapilashrami, A., Malmsten, M., Eskilsson, K., Benjamins, J.-W., Nylander, T. 2003, Ellipsometric studies of nonionic block copolymers adsorbed at the solid/water and oil/water interfaces, *Colloids Surf.*, 255, 181–192.
- Kawaguchi, M., Yamamoto, T., Kato, T. 2001, Rheological Properties of Silica Suspensions in Aqueous Solutions of Block Copolymers and Their Water-Soluble Components, *J. Colloid Interface Science*, 241, 293–295.

- Liu, H., Xiao, H. 2008, Adsorption of poly(ethylene oxide) with different molecular weights on the surface of silica nanoparticles and the suspension stability, *Materials Letters*, 62, 870-873.
- M'Pandou, A., Stiffert, B., 1987, Polyethyleneglycol adsorption at the $\text{TiO}_2\text{-H}_2\text{O}$ interface: Distortion of ionic structure and shear plane position, *Colloids Surf.*, 24, 159-172.
- Ortona, O., D'Errico, G., Paduano, L., Vitagliano, V. 2006, Interaction between cationic, anionic, and non-ionic surfactants with ABA block copolymer Pluronic PE6200 and BAB reverse block copolymer Pluronic 25R4, *J. Colloid Inter. Sci.*, 301, 63-77.
- Paterson I.F., Chowdhry B.Z., Carey P.J., Leharne S.A., 1999, Examination of the adsorption of ethylene oxide-propylene oxide triblock copolymers on soil, *J. Contaminant Hydrology*, 40, 37-51.
- Postmus, R.B., Leermakers, M.A.F., Koopal, K.L., Cohen Stuart, A.M. 2007, Competitive adsorption of nonionic surfactant and nonionic polymer on silica, *Langmuir*, 23, 5532-5540.
- Rapoport, N. 1999, Stabilization and activation of Pluronic micelles for tumor-targeted drug delivery, *Colloids Surfaces B: Biointerfaces*, 16, 93-111.
- Sakar-Deliormanli, A. 2007, Synergistic effect of polymer-surfactant mixtures on the stability of aqueous silica suspensions *Journal of European Ceramic Society*, 27, 611-618
- Sastry, N.V., Hoffmann, H. 2004, Interaction of amphiphilic block copolymer micelles with surfactants, *Colloids Surf.*, 250, 247-261.
- Shar, A.J., Obey, T.M., Cosgrove, T. 1999, Adsorption studies of polyethers. Part II: adsorption onto hydrophilic surfaces, *Colloids Surf.*, 150, 15-23
- Taylor, F.J.D., Thomas, R.K., Penfold, P. 2007, Polymer/surfactant interactions at the air/water interface, *Advanced Colloid Inter. Sci.* 132, 69-110.
- Terayama, H., Okumura, K., Sakai, K., Tprigoe, K., Esumi, K. 2001, Aqueous dispersion behavior particles by addition of surfactant and polymer, *Colloids Surf. B*, 20, 73-77.
- Tiberg, F., Malmsten, M., Linse, P., Lindman, B. 1991, Kinetic and Equilibrium Aspects of Block Copolymer Adsorption, *Langmuir*, 7, 2723-2730.
- Torn, H.L., de Keizer A., Koopal, L.K., Lyklema, J. 2003, Mechanism adsorption of poly(vinylpyrrolidone) and sodium dodecylbenzenesulfonate on kaolinite, *J. Colloid Inter. Sci.*, 260, 1-8.
- Tsurumi, D., Yoshimura, T., Esumi, K. 2006, Adsorption of 2-naphthol into adsorbed layer of PEO-PPO-PEO triblock copolymers on hydrophilic silica, *J. Colloid Inter. Sci.*, 297, 565-469.
- Vincent, B., 1974, The effect of adsorbed polymers on dispersion stability *Adv. Colloid Interface Sci*, 4, 193-277.
- Wesenberg-Ward, E.K., Tyler, B.J., Sears, J.T. 2005, Adhesion and biofilm formation of *Candida albicans* on native and Pluronic-treated polystyrene, *Biofilms*, 2, 63-71.
- Zhang, R., Liu, C., Somasundaran, P. 2007, A model for the cooperative adsorption of surfactant mixtures on solid surfaces, *J. Colloid Inter. Sci.*, 310, 377-384.
- Zhang, S.J., Lee, S., Lee, J.W. 2007, Does SDS micellize under methane hydrate-forming conditions below the normal Krafft point, *J. Colloid Inter. Sci.*, 315, 313-318.

Received July 18, 2011; reviewed; accepted August 15, 2011

CULLET AS FILTER MEDIUM FOR SWIMMING POOL WATER TREATMENT

Aleksandra KORKOSZ, Aleksandra PTASZYNSKA, Andreas HANEL
Marcin NIEWIADOMSKI, Jan HUPKA

Department of Chemical Technology, Gdansk University of Technology, 80-233 Gdansk, Narutowicza 11/12, Poland, e-mail: jhupka@pg.gda.pl

Abstract. The control of water quality in swimming pool is accomplished by treatment, including filtration and application of disinfectants. Contamination of pool water cannot be always effectively controlled by normal treatment. Swimming pool sediments were investigated previously and insufficient filtration efficiency for sand filters was noticed. In presented experiments two filtration medium materials were compared: silica sand and recycled glass (cullet). Results show, that despite larger negative zeta potential of cullet particles, filtration efficiency was comparable and recycled glass can be a useful material for optional filtration medium.

keywords: swimming pools water treatment, filter medium, cullet as filter medium, laboratory filter

1. Introduction

The main aim of filtration is removal of turbidity to achieve appropriate water clarity. This is a key factor in ensuring the safety of swimmers. Poor underwater visibility is a contributing factor to injuries. Filtration is also the critical step for the removal of *Cryptosporidium* oocysts and other microorganisms (Angenent et al., 2005). There are a number of different types of filters available, whereas their choice is based on several factors including water source quality, amount of filter area available and number of filters, filtration rate, ease of operation, method of backwashing, and filtration rate (higher flows lower separation efficiency).

The cleaning of a filter bed clogged with solids is referred to as backwashing. It is accomplished by reversing flow, fluidizing the filter material and passing pool water back through the filters to wastewater stream.

Medium-rate sand filters can filter suspended particulates down to about 7 μm in size with the addition of a suitable coagulant, such as polyaluminum chloride or aluminum hydroxychloride. Cleaning of sand bed is achieved by manual reverse flow backwashing, with air scouring to achieve removal of body oils and fats and improve

the backwash efficiency. For indoor heated pools, the sand medium typically has a life from five to seven years. Medium-rate sand filters have typically large diameters, can operate under pressure and require large plant rooms. Regarding sand filters efficiency for microorganisms removal, drinking water treatment has shown that when operated with a coagulant, sand filters can remove over 99% of *Cryptosporidium* oocysts.

Swimming pool sediments were investigated previously and insufficient filtration efficiency for sand filters was noticed. This led to a conclusion, that other filtration material can show better results (Korkosz et al., 2011). One of the possibilities for recycling waste glass is the preparation of cullet that can be a filter medium (Horan and Lowe, 2007). The use of recycled glass as a filter material can replace sand and gravel in filtration of various types of water. This can be an alternative to direct recycling application of cullet, which is also important due to increasing number of places where glass filters medium can be used.

The aim of the experiments was to evaluate cullet medium performance in comparison to sand at a larger scale, optimization of the media performance, and establishment of the material cost and so-called commercial viability. The results concluded that glass particles were as effective as sand, both at the filtration and backwashing stage.

Utilization of wastes as recycled materials is necessary for sustainable waste management. Additionally, there are many benefits that come out of glass recycling and using it as a filtration medium. Glass is a manufactured product and can be tailored to suit specific waters. What is more, it has lower specific density than sand and can be cheaper, lighter to transport and handle. It is known that glass is also smoother and more porous than sand, improving backwash efficiency, and making it easier to clean. It is also possible to add different properties to the glass media surface to achieve different results due to adsorption, and moreover, to encourage bio-film growth for nitrification and de-nitrification within the filter. What can also be concluded is that glass lasts longer than sand what is certainly a cost benefit, but can cause problems when the glass particles themselves have to be thrown away.

The cullet, which was used in present experiments, is a commonly used soda-lime-glass. The soda is used as a flux to decrease the melting temperature and the lime is added giving stability to the silica. The introduction of alkali metals lead to the formation of terminal $-\text{Si-O-M}$ groups, where alkali earth metals lead to the formation of bridging $-\text{Si-O-M-O-Si}-$ groups (Melcher et al., 2010). The introduction of these network modifiers plays an important role in the properties and durability of the glass. Corrosion of glass by liquids is well investigated in the literature. In general, ion-exchange processes leach out the mono- and bivalent network modifiers. H^+ , H_3O^+ and water molecules fill the released spaces leading to a hydrated layer. The thickness of this layer depends on the glass composition, properties of the liquid, temperature and exposure time (Melcher et al., 2010). For example, a low pH and low ionic strength increase the corrosion rate.

2. Experimental

Filtration experimental setup is presented in Figure 1. Experimental conditions were set as close to those during treatment of pool water as it was possible in our laboratory.

Parameters of filtration column are presented in Table 1. Material of the filtration column was selected to be transparent in order to be able to observe filter while operating. The column is equipped with pressure sensors in its bottom part. The setup is also equipped with compressed air assembly, that was not, however, used during presented experiments. Height of the filtration bed was smaller for sand: 800 mm, compared to cullet: 1100 mm.

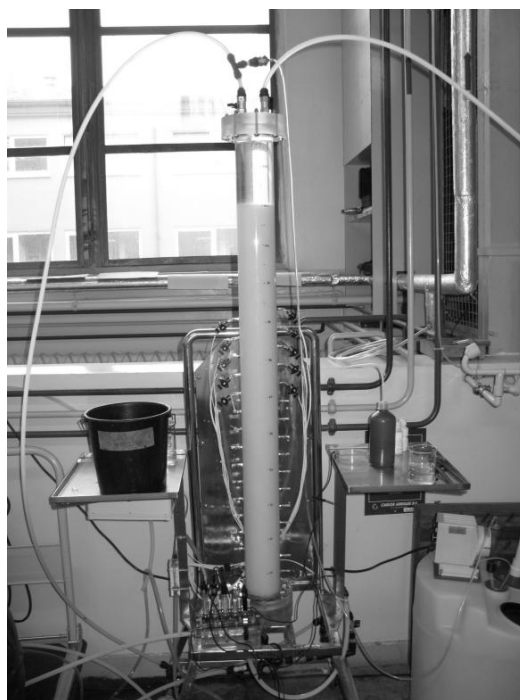


Fig. 1. Experimental filtration setup

Tabela 1. Parameters of experimental filtration column

| Parametr | Data/Value |
|--|--------------------------------|
| Material | polymethyl methacrylate (PMMA) |
| Height of filtration column | 1350 mm |
| External diameter of filtration column | 100 mm |
| External diameter of filtration column | 80 mm |
| Filtration bed height – sand | 800 mm |
| Filtration bed height – cullet | 1100 mm |

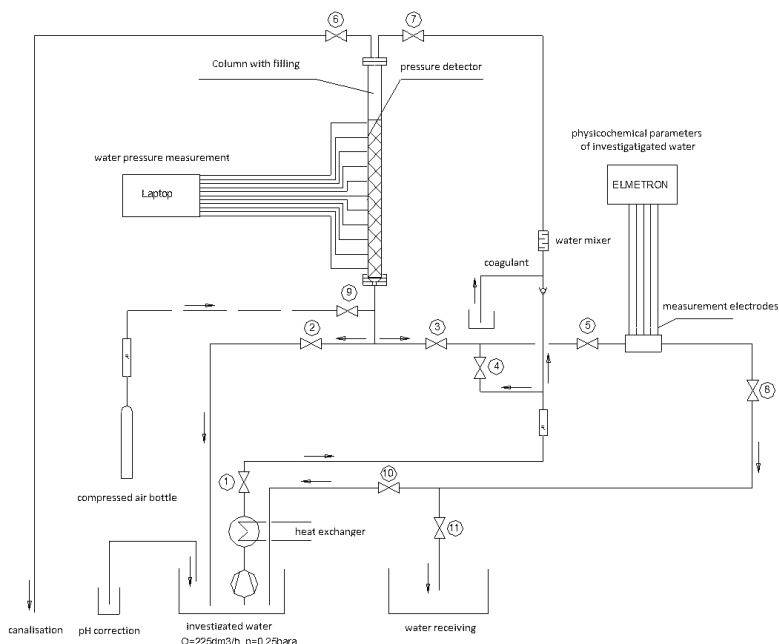


Fig. 2. Schematic of filtration experimental setup

Size distribution of sand particles and cullet is presented in Fig. 3 while characteristics of filtration media and filtration beds is shown in Table 2. Cullet had less uniform size and its filtration bed void fraction was greater: 53.9% compared to 42% in case of sand bed. Both materials had similar particle size range, 300 to 1,000 μm .

A model contaminated swimming pool water was prepared using collected from a pool “vacuum” cleaner sediment, which was mixed with tap water. After filtration experiments, samples of filtration beds were collected with a special pipe probe of length 16 cm and internal diameter 2.1 cm. Samples were subsequently split into four equal length sections and investigated for zeta potential of particles filtered and stopped by the filter. Amount of water contaminants in each section was also determined by mixing of filtering material from each section with water and total organic carbon (TOC) was measured.

Table 2. Characteristics of filtration media and filtration beds

| | Sand | Cullet |
|--|----------|----------|
| Particle size range, μm | 300-1000 | 300-1000 |
| Effective size (d_{10}), μm | 528 | 380 |
| Coefficient of uniformity | 1.23 | 1.64 |
| Filter bed void fraction, % | 42.0 | 53.9 |
| Particle density, g/cm^3 | 2.65 | 2.50 |

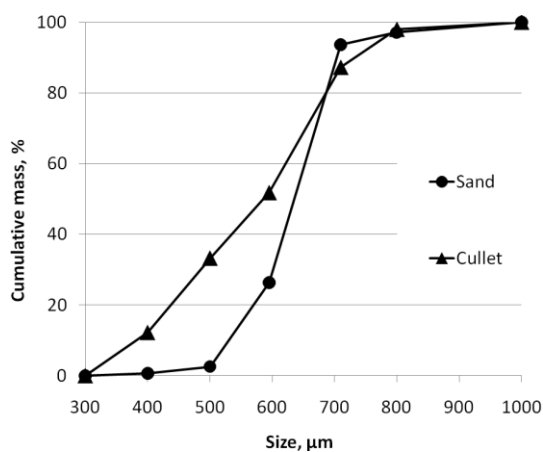


Fig. 3. Size distribution of sand and cullet particles used for filtration bed

3. Results and discussion

Filtration efficiency is presented in Table 3. Both filtration bed types were able to significantly decrease water turbidity to values below 1 NTU. Initial turbidities varied between 246 and 9.6 NTU. This result indicates, that regardless of bed differences, they similarly stopped suspended particles.

In order to explain filtration observations, zeta potential of the fine filtration particles of sand and cullet was measured and compared with zeta potential of particles collected from the filtration beds after experiments. Table 4 shows zeta potential values: sand, -13.4 mV, and cullet, -24.9 mV. Figure 5 presents zeta potential of sand particles for four sections of sampled filtration beds. Particles collected from the sand bed had zeta potential values varying between -11.3 and -18.9 mV, while particles collected from cullet bed between -13.5 and -14.9 mV. Thus, contaminant particles were not apparently affected by the filtering medium type.

Measurements of TOC and determination of contaminant amount in each of the four centimeter bed section did not show any definitive trend. It can be concluded, that for the present filtration setup, 16 cm length sampling was insufficient to find optimum filtration bed depth.

According to Stephan and Chasse (2001), zeta potential on both filtration medium and filtered particles needs to be compared to predict filtration efficiency. In the pH range 7.0 to 8.0, that was measured in treated water during the experiments, zeta potential did not exceed -24.9 mV and particles mostly exhibited values between -11 and -20 mV. This can indicate, that despite repulsion between similarly charged particles, the investigated filtration beds were able to significantly reduce water turbidity.

Table 3. Turbidity of swimming pool water before and after filtration

| Filter medium | Before filtration | After filtration |
|---------------|-------------------|------------------|
| Sand | 21.9 | 0.47 |
| | 26.3 | 0.74 |
| Cullet | 9.6 | 0.56 |
| | 246 | 0.57 |

Table 4. Zeta potential of filtration medium

| Filtration medium | Zeta potential, mV |
|-------------------|--------------------|
| Sand | -13.4 |
| Cullet | -24.9 |

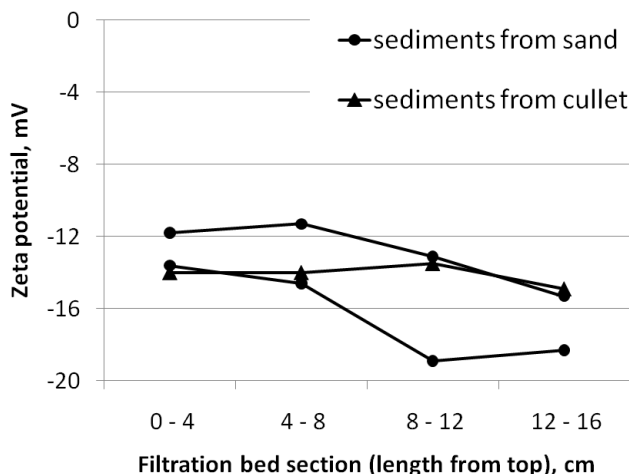


Fig. 5. Zeta potential of sediment particles obtained from filtration bed sampling

4. Final comments

Application of recycled glass (cullet) as filtration medium showed comparable results to filtration on sand regardless of larger negative zeta potential of cullet particles when compared to silica sand. It can be expected, that modification of glass can lead to enhancing filtration medium surface properties yielding better separation efficiency.

Acknowledgements

This research was partially supported by the Voivodeship Fund for Environmental Protection and Water Management in Gdansk, grant No. RX-10/2009, and the Gdansk University of Technology, contract DS No. 014668/03.

References

- ANGENENT, L.T., KELLEY, S.T., AMAND, A.S., PACE, N.R., HEMANDEZ, M. T., 2005, Molecular identification of potential pathogens in water and air of a hospital therapy pool, *Proceedings of the National Academy of Sciences of the United States of America*, 102(13), 4860–4865.
- HORAN, N.J., LOWE, M., 2007, Full-scale trials of recycled glass as tertiary filter medium for wastewater treatment, *Water Research* 41, 253–259.
- KORKOSZ, A., NIEWIADOMSKI, M., HUPKA J., 2011, Investigation of properties of swimming pool water treatment sediments, *Physicochemical Problems of Mineral Processing*, 46, 243–252.
- MELCHER, M., WIESINGER, R., SCHREINER, M., 2010, Degradation of Glass Artifacts: Application of Modern Surface Analytical Techniques. *Accounts of chemical research*, 43(6), 916–926.
- STEPHAN, E.A., CHASE G.G., 2001, A preliminary examination of zeta potential and deep bed filtration activity, *Separation and Purification Technology* 21, 219–226.

Received May 12, 2011; reviewed; accepted August 19, 2011

CHEMICAL CHARACTERIZATION OF PATNOS SCORIA (AĞRI, TURKEY) AND ITS USABILITY FOR PRODUCTION OF BLENDED CEMENT

Tolga DEPCI *, Tugba EFE **, Mucip TAPAN ***, Ali OZVAN **,
Mustafa ACLAN **, Tijen UNER **

* Yuzuncu Yil University, Faculty of Engineering and Architecture, Department of Mining Engineering, 6580, Van, Turkey, Tel.: +90 432 225 10 24 ; fax: +90 432 225 17 32, tdepce@gmail.com

** Yuzuncu Yil University, Faculty of Engineering and Architecture, Department of Geological Engineering, 6580, Van, Turkey

*** Yuzuncu Yil University, Faculty of Engineering and Architecture, Department of Civil Engineering, 6580, Van, Turkey

Abstract. This paper reports results of investigations on suitability of scoria (PTS), collected from Patnos (Ağrı) in Turkey, for blended cement production. Scoria (basic pumice) was chosen as cement replacement materials due to its availability and cost in Ağrı in Turkey. The portland cement was replaced by scoria within the range of 0, 5, 10, 20, 30, 40 and 50%. Characterization of scoria was subjected by the X-ray fluorescence (XRF), X-ray diffraction (XRD), Fourier Transform Infrared (FTIR) spectroscopy, Scanning Electron Microscopy (SEM), BET surface area and porosity, zeta potential (ζ) and thin sections. The standard tests were conducted for the obtained fresh and hardened states of scoria blended cement paste. Furthermore, the obtained cements were characterized by the XRF. According to experimental results, scoria up to 20% ratio could be added into clinker and it has a good potential of manufacturing blended scoria cement.

keywords: scoria, blended cement, Patnos

1. Introduction

Cement industry utilizes natural pozzolans as substitutes for portland cement due to environmental (CO₂ emission reduction), economical (cost reduction) and chemical (reduction of alkali aggregate reaction and increased chemical resistance) advantageous (Fu et al., 2003; Sersale 1987; Saraswathy et al., 2003; Vuk et al., 2002; Binici and Aksoğan 2006; Yilmaz, 2009).

Pumice is one of the natural pozzolan and is a volcanic origin rock formed during explosive eruptions. It has a highly porous structure which is formed by dissolved

gases precipitated during cooling as lava hurtles through the air. Generally, it has not a crystalline structure and SiO_2 , Al_2O_3 and Fe_2O_3 constitute major contents of pumice (Gündüz et al., 1998; Lura et al., 2004; Ersoy, 2010).

Turkey has important potential pumices reserves (68% of the reserve of the world). Although pumice has been used in the world industry for a long time, it has been evaluated and its importance has been recognized by Turkish industry for the last 30 years. Fifty six per cent of pumice reserves (acidic pumice and scoria) in Turkey occupies a large surface area in the East Anatolia Region depending on the recent volcanic activities (T.R. Report, 2001). Therefore, it is important to assess pumice reserve in Eastern Turkey for its use in the cement industry.

There are two aims of the current research. One is to characterize scoria from Patnos (Ağrı, Turkey). A literature survey showed that no academic studies have investigated this scoria for its use in the construction industry. Therefore, the second purpose of this study is to determine the potential use of scoria from Patnos in the cement industry as a replacement material.

2. Materials and methods

2.1. Sample preparation

More than 50 kg of scoria sample was collected from scoria deposit in Patnos (Turkey). In order to reduce the amount of sample, sampling was performed using the cone and quartering method and riffles, since sampling must have mineralogical, physical and chemical homogeneity. The sample was crushed and ground using a laboratory dodge jaw crusher, rod mill and ball mill to reduce their size to 200 mesh (74 μm) for mineralogical and chemical analyses. Five hand samples were prepared for thin section studies. Cutting, polishing and thinning processes were performed using an oil system. Glue that hardened under UV light was used.

2.2. Characterization of scoria samples

Chemical analysis of the scoria sample was carried out using the X-ray fluorescence (XRF Spectro IQ) technique.

The composition of the scoria sample was checked by the X-ray Powder Diffraction. By comparing positions of diffraction peaks against those of the ICDD cards, the target material could be identified. The XRD data were collected using the Rigaku X-ray Diffractometer (Model RadB-DMAX II) with $\text{Cu K}\alpha$ (30 kV, 15 mA, $\lambda=0.154051$ nm) radiation at room temperature. Scanning was done between $5^\circ < 2\theta < 70^\circ$. The measurements were made with 0.01 and 0.05 degree steps and 1 degree/minute rate. The divergence slit was variable. The scattering and receiving slit were 4.2 degree and 0.3 mm.

As a further characterization method, the FTIR analysis was carried out in order to investigate functional groups of scoria. The IR spectrum of material was measured in

the range of 400 to 4000 cm^{-1} by the KBr pellet method using the Perkin Elmer Spectrum One device. IR pellet was prepared using spectroscopic grade KBr with a sample (KBr-to-sample ratio of 100 mg : 3 mg). KBr was dried at 180°C for 12 hours before the preparation of pellet.

Surface area and porosity values of the scoria sample were determined using a Tri Star 3000 (Micromeritics Instrument Co. USA) surface analyzer which was used to measure nitrogen adsorption isotherm at 77 K in the range of relative pressures from 10^{-6} to 1. Before measurement, the sample was degassed at 400°C for 2 h.

The zeta potential of the scoria sample was measured by a Zeta Meter 3.0 (Malvern Instruments Ltd.) equipped with a microprocessor unit. The zeta potential was calculated automatically using the Smoluchowski equation and as a function of pH of the solution according to the electrophoresis method with high sensitivity. A sample of 0.5 g was taken from each pumice sample and then transferred into a glass beaker and 100 cm^3 of aqueous solution was added. The mixture was stirred using a magnetic shaker and the pH of the test solution was adjusted to the desired value by drop-wise addition of diluted NaOH (0.5%) or HCl (0.1 N). After stirring the solution, the suspension was stored to let larger particles to settle.

In order to investigate the morphology of the pumice sample, the Leo EVO 40 scanning electron microscope, which does not need palletizing, was used. SEM images were obtained from the scoria samples in powder form.

To investigate petrographical characteristics of the scoria sample, thin sections of 5 rock samples were prepared and determined using the LEICA Polarizer Microscope.

In order to measure the true densities of the scoria sample and cement, pycnometer was used.

2.3 Preparation of test specimens

A reference cement (ordinary portland cement, OPC) was produced by mixing portland cement clinker, 96% in weight, and gypsum, 4% in weight. This mixture was then ground for 40 minutes in a laboratory-type ball mill. Scoria blended cement samples (PBC) were obtained using 5%, 10%, 20%, 30%, 40% and 50% (by weight of clinker) pumice replacement by mixing and inter-grinding. The gypsum content was kept constant in all cements as 4%. Before grinding operation, portland cement clinker, scoria and gypsum were crushed, and sieved through a 9.5 mm sieve. The purpose of sieving was to keep the uniformity between each specimen through using the same feed sizes. Gypsum was dried at 40°C prior to crushing whereas the natural pozzolans were dried at 110°C.

2.4. Tests conducted on the scoria blended cements

The chemical compositions of the control specimen and scoria blended cements were performed by the X-ray spectrometer (XRF). Physical analyses were performed in accordance with TS EN 196-6. Fineness of the scoria blended cement samples was

determined by measuring the Blaine fineness and amount of material retained on 45, 90, and 200 μm sieves after vacuum sieving.

Following tests were carried out on the scoria blended and control cements: fineness, specific surface area by Blaine instrument, normal consistency, setting time, soundness by the Le Chatelier method and compressive strength. The amount of water necessary for the cements to have normal consistency was determined according to TS EN 196-3. Then, the pastes having normal consistency was used to determine the setting time and soundness through conducting tests as described in this standard. Compressive strength and flow values of the mortars were determined according to TS EN 196-1. Preparation of cement mortar mixtures was completed according to TS EN 196-1. In these tests, 450 ± 2 g of cement and 1350 ± 5 g of standard sand were used. PBC mortars were prepared with 225 cm^3 of water whereas the water content of the blended cement mortars were adjusted to have a w/c ratio of 0.5 as stated in the standard. The prepared mortars were poured into rectangular-prism-shaped three-part mortar molds $40 \times 40 \times 160$ mm and compressive strength tests were performed by an automated strength testing instrument in accordance with TS EN 196-1. The compressive strength of the mortars was determined after 1, 2, 7 and 28 days. Three cube specimens were tested for each day.

3. Results and discussion

3.1. Mineralogical and chemical characterization of scoria

3.1.1. X-ray fluorescence (XRF) and geochemistry

The result of chemical analysis of the scoria sample is given in Table 1. Chemical analysis indicates that SiO_2 , Al_2O_3 , Fe_2O_3 and CaO constitute major contents of the pumice samples. As it is known, pumice is an amorphous porous volcanic rock, which is composed mainly of SiO_2 . Pumices show acidic and basic properties and are named acidic pumice and scoria (basic pumice), depending on the SiO_2 content. According to the XRF results, the pumice sample used in the present study can be classified as scoria (basic pumice) due to the relatively low SiO_2 and high Fe_2O_3 contents (Gündüz et al., 1998).

According to TS 25, natural pozzolans should have specific chemical properties to be used in the cement industry. These requirements and comparison with scoria (PTS) are given in Table 2. The results in Table 2 indicate that the scoria samples collected from Ağrı (Turkey) satisfies the TS 25 requirements and therefore can be used in cement industry as a cement additive.

Table 1. Chemical composition of scoria sample

| | PTS |
|---|-------|
| SiO ₂ | 54.92 |
| TiO ₂ | 2.55 |
| Al ₂ O ₃ | 16.92 |
| Fe ₂ O ₃ | 10.31 |
| MgO | 2.01 |
| CaO | 6.47 |
| Na ₂ O | 2.17 |
| K ₂ O | 1.87 |
| P ₂ O ₅ | 0.39 |
| SO ₃ | 0.29 |
| LOI | 0.86 |
| Reactive silica | 31.52 |
| Puzzolonic activity (kg/cm ²) | 100 |

Table 2. Comparative study of chemical properties according to TS 25 standard

| Chemical Properties | TS 25 Standard | PTS |
|--|----------------|-------|
| | wt. % | wt. % |
| SiO ₂ + Al ₂ O ₃ + Fe ₂ O ₃ | > 70.0 | 81.73 |
| MgO | < 5.0 | 2.12 |
| SO ₃ | < 3.0 | 0.29 |
| Reactive silica | > 25 | 31.52 |
| Cl | < 0.1 | 0.009 |

3.1.2. X-ray diffraction (XRD)

The XRD pattern of scoria is given in Fig. 1. As stated before, pumice is an amorphous volcanic rock. X-ray diffraction data (Fig. 1) indicates that scoria has mainly amorphous structure (Arrigo et al., 2007; Ersoy et al., 2010), but some little crystalline mineral phases, anorthite (JCPDS Card File No. 73-1435), hornblende (JCPDS Card File No. 71-1062) and crystalline quartz (JCPDS Card File No. 76-0823) are also observed in the XRD pattern.

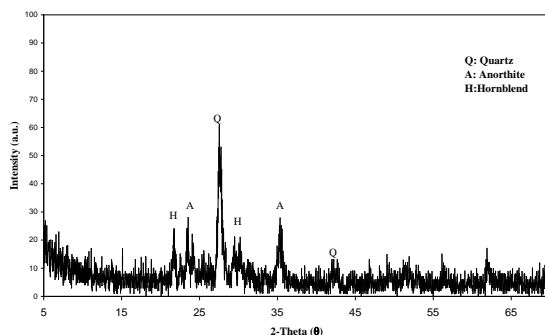


Fig. 1. XRD patterns of scoria

3.1.3. FTIR spectra

The infrared spectrum of scoria is given in Fig. 2. In the IR spectrum, the strong bands observed in the frequency range of $1000\text{--}1040\text{ cm}^{-1}$ is characteristic of silica. As seen, this peak is very broad, confirming the highest silica content in the scoria sample. On the other hand, the bands belonging to other metal oxides could be observed in the mentioned range as oxide or Si-O-M form. The broadening of the peak may be attributed to this. This explanation is also compatible with the literature data. In the literature, symmetric vibrations at 1049 cm^{-1} was attributed to Si-O-Al bonds (Perraki and Orfanoundaki, 2004; Blanco et al., 2006). Beside, the band in the $780\text{--}790\text{ cm}^{-1}$ region is attributed to Si-O bending strength vibrations of amorphous quartz. The band observed around 3000 cm^{-1} is characteristic for water (OH stretching vibrations). According to the FTIR bands, it could be seen that the main structure of the scoria samples is amorphous silica confirmed by the XRF and XRD results. Amorphous silica reacts with $\text{Ca}(\text{OH})_2$ and forms cementitious materials, which are important for concrete in terms of durability and the rate of gaining strength (Hossain, 2005).

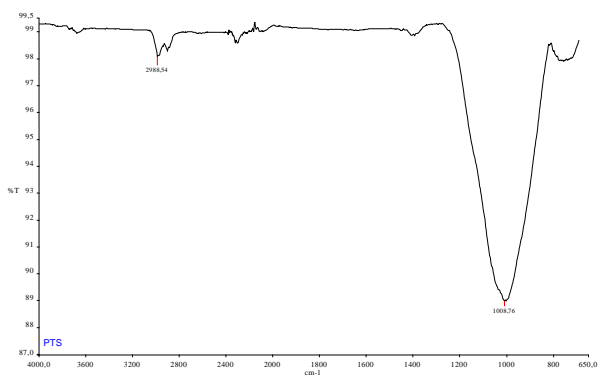


Fig. 2. FTIR spectrum of scoria

3.1.4. Electro-kinetic property

ζ potential variation of scoria is given in Fig. 3. The zeta potential increases in the negative direction with increasing the pH. The isoelectrical point (IEP), which represents no net electrical charge of surface at the specific pH, is not observed for scoria. A literature survey also shows that the same result was observed for pumices by Tunc and Duman (2009) and Ersoy et al. (2010).

According to the XRF, XRD and FTIR results, the scoria sample is composed mainly of SiO_2 . Therefore, the zeta potential of quartz was also measured and given in Figure 3. The IEP, like literature values (Huang and Fuerstenau, 2001; Prasanphan and Nuntiya, 2006) for quartz was at pH 2. For scoria and quartz, the negative zeta potential can be attributed to surface charge on a solid which may originate from ion adsorption, surface dissociation and isomorphous replacement of ions of the solid phase by others of a different charge.

Yılmaz (2009) mentioned that clinker has positive zeta potential values depending on the Ca^{2+} ions in crystal structure. Figure 3 indicates that the zeta potential of scoria is negative. As is known, electrically different charges attract each other. Thus, PTS and clinker pull each other and their particles easily come together.

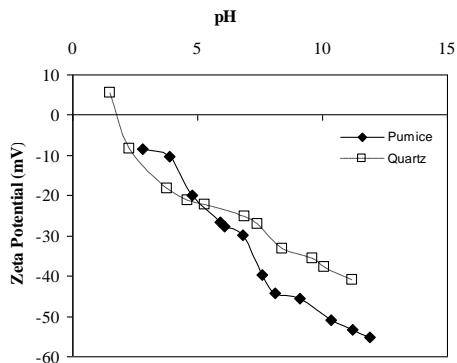


Fig. 3. Zeta potential vs. pH of the scoria sample

3.1.5. BET surface area and pores volume and size of tested pumice samples

Surface areas and porosity of pumice are given in Table 3. It can be seen that the basic pumice sample (> 200 mesh) has not a big surface area and micro- and mezzopore structure.

Table 3. Surface area and porosity value

| Pumice Samples | S_{BET} (m^2/g) | S_{ext} (m^2/g) | S_{mic} (m^2/g) | S_{mezo} (m^2/g) | V_t (cm^3/g) | V_{mic} (cm^3/g) | V_{meso} (cm^3/g) | D_p (nm) |
|----------------|---|---|---|--|-------------------------------------|--|---|---------------|
| PTS | 0.67 | 0.22 | 0.45 | 0.22 | 0.003 | 0.0003 | 0.0027 | 15.41 |

$D_p: 4V/A$ by BET, $S_{\text{ext}} = S_{\text{meso}} + S_{\text{macro}}$

3.1.6. SEM images

The SEM images of scoria samples are given in Fig. 4. They indicate that the scoria sample have irregular morphology, non uniform plate shape and glassy form (amorphous structure).

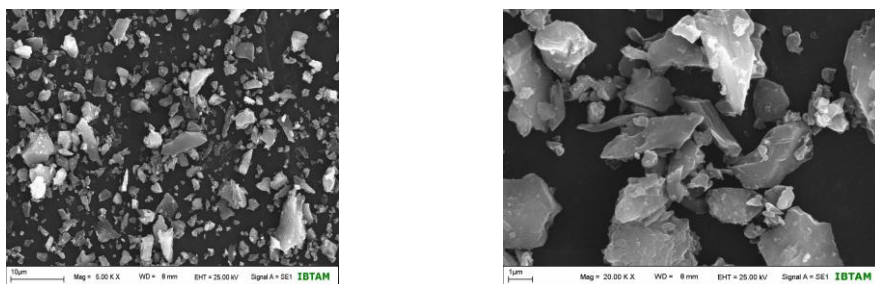


Fig. 4. SEM images of the scoria samples at different magnifications

3.1.7. Thin section

The thin sections, which were randomly selected from the images, are given in Fig. 5. The thin sections studies reveal that the scoria sample has mainly hyalopilitic-porphyrific texture, and from place to place, vitrophyric-porphyrific texture is also seen. Scoria is mainly composed of volcanic glass and there are phenocrysts of plagioclase, pyroxene and rarely hornblende in the matrix. Plagioclases in the matrix show polysynthetic twins and the minerals are classified as a long rod-shaped (Figs. 5 a–c). Pyroxene is easily distinguished with live color tone (Fig. 5 b) and lots of gas gaps are observed in the matrix (Fig. 5).

A literature survey shows that pozzolan can be considered as a good component for the cement industry, if it contains high amounts of zeolite minerals and volcanic glass (Planungs Report, 1984). The thin section studies show that scoria is mainly composed of volcanic glass, so the Patnos scoria pumice is a good pozzolan for the cement industry.

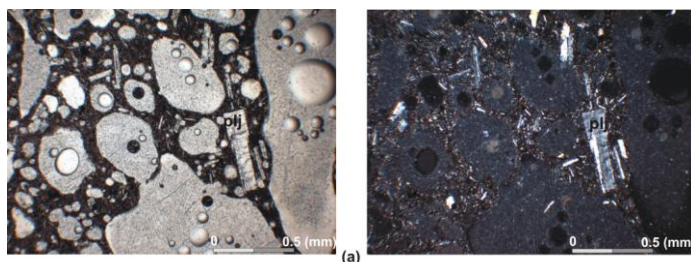


Fig. 5. Thin sections of the scoria sample: (a) plagioclase minerals and gas gaps in volcanic glass matrix. (b) pyroxene minerals seen in volcanic glass and plagioclase, (c) phenocrysts of plagioclase, pyroxene and gas gaps

(continued)

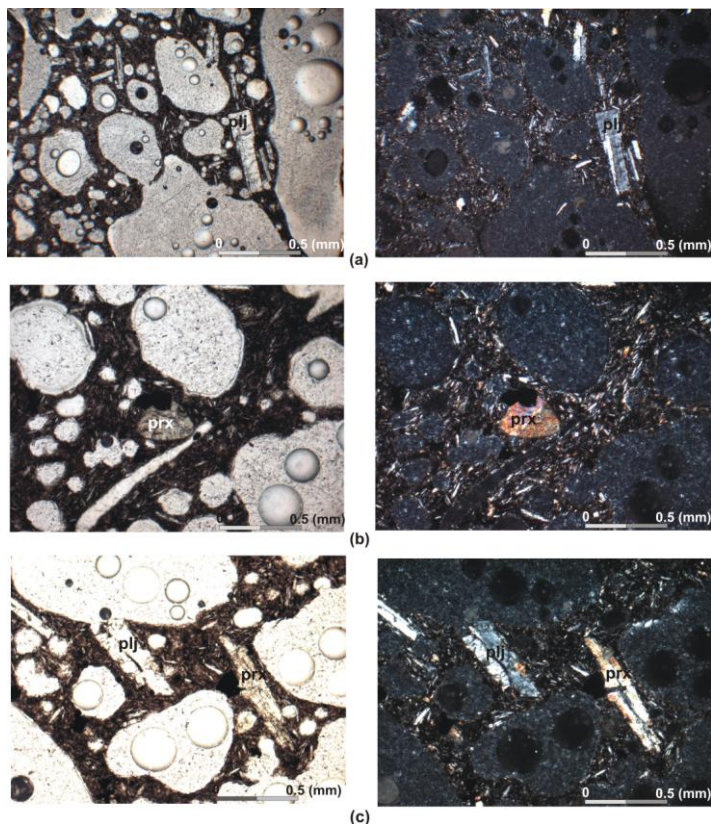


Fig. 5. Continued

3.2. Chemical and physical properties of scoria blended cement

Chemical analyses of the scoria blended cements and control specimen are given in Table 4. The chemical composition of the portland cement indicates that the CaO/SiO_2 ratio is greater than 2 and the percent of MgO content is smaller than 5%. These values satisfy the main composition requirements imposed by the TS EN 197– 1 standard. Depending on the scoria content, SiO_2 , Al_2O_3 and Fe_2O_3 contents increase and CaO content decreases with increasing the pumice ratio in the cement mixture.

Physical and mechanical properties of control (OPC) and the scoria pumice blended cements are given in Table 5.

The scoria blended cement mortars to be used for compressive strength testing were prepared to have a w/sbc of 0.50 as stated in TS EN 196-1. Table 5 shows the compressive strength values after 1, 2, 7, and 28 days. The trends, observed as variation of comparative strength with the percentage of scoria, indicate a decrease with the increase of scoria content in cement as expected. The literature survey shows that the comparative strength decreases, depending on the pumice content due to the

reduction of clinker content in the cement mixture (Yazıcıoğlu and Demirel 2006; Mehta, 1981; Hossain, 2003; TCMB research 2003). In TS EN 197 – 1, early strength (2 days) values should be greater than 10 MPa and standard strength (28 days) values should be between 42.5 MPa and 62.5 MPa. When the obtained results are compared to the standard, it can be seen that the strength requirements were satisfied by the blended cements up to 20 % scoria content.

Table 4. Chemical composition of control (OPC) and scoria blended cements

| Oxides | PTS | | | | | | |
|--------------------------------|-------|-------|-------|-------|-------|-------|-------|
| | OPC | 5% | 10% | 20% | 30% | 40% | 50% |
| SiO ₂ | 21.31 | 22.76 | 24.42 | 27.75 | 29.07 | 34.41 | 37.73 |
| Al ₂ O ₃ | 5.37 | 5.88 | 6.45 | 7.59 | 8.01 | 9.87 | 11.01 |
| Fe ₂ O ₃ | 3.74 | 4.39 | 4.75 | 5.46 | 5.50 | 6.88 | 7.59 |
| MgO | 2.54 | 2.49 | 2.46 | 2.41 | 2.13 | 2.30 | 2.25 |
| CaO | 60.52 | 58.11 | 55.39 | 49.96 | 46.92 | 39.09 | 33.66 |
| Na ₂ O | 0.56 | 0.65 | 0.74 | 0.90 | 0.85 | 1.23 | 1.39 |
| K ₂ O | 0.82 | 0.85 | 0.90 | 1.00 | 1.07 | 1.20 | 1.30 |
| SO ₃ | 2.08 | 1.98 | 1.89 | 1.71 | 1.89 | 1.36 | 1.18 |
| HM | 1.99 | 1.74 | 1.54 | 1.21 | 1.10 | 0.76 | 0.59 |
| SM | 2.34 | 2.27 | 2.24 | 2.18 | 2.15 | 2.11 | 2.08 |
| AM | 1.43 | 1.45 | 1.47 | 1.51 | 1.46 | 1.56 | 1.57 |
| LSF | 1.99 | 77.16 | 68.38 | 54.07 | 49.69 | 33.94 | 26.59 |

Comparing the setting time of the portland and blended cements, the portland cement and cements including 5 % and 10 % PTS have close setting time and setting time increases with increasing the amount of PTS. This result is very compatible with literature. In the literature, it is mentioned that the setting time considerably increases by the addition of greater natural pozzolan amounts (30–70% in mass) (Öner et al., 2003; Yetgin and Çavdar 2006; TS 25; Targan et al., 2003). The variation of setting time can be explain by reduction of the cement content in the mixture and a low specific surface area. As seen in Table 4, the values for blended cements are smaller than for the control cement. The low specific surface area and clinker content may decrease the rate of the hydration process which increases the setting time. The result is in a good agreement with the literature (Aydin and Gül, 2007).

Table 5. Physical and mechanical properties of control and the scoria blended cements

| | | PTS | | | | | | |
|----------------------------|---------|-------|-------|-------|-------|-------|-------|-------|
| | | 5% | 10% | 20% | 30% | 40% | 50% | OPC |
| Compressive Strength (MPa) | 1 day | 10.58 | 9.21 | 8.33 | 7.74 | 6.66 | 5.19 | 13.13 |
| | 2 days | 18.62 | 17.64 | 15.48 | 13.13 | 13.72 | 11.17 | 26.46 |
| | 7 days | 40.67 | 40.18 | 39.00 | 26.66 | 24.30 | 19.60 | 45.57 |
| | 28 days | 50.18 | 49.00 | 43.71 | 36.26 | 33.32 | 27.44 | 55.66 |
| Range Dimension | 200 µm | 0.5 | 0.6 | 0.4 | 0.6 | 0.7 | 0.2 | 0.2 |
| | 90 µm | 1.5 | 1.7 | 1.1 | 1.8 | 1.6 | 1 | 3.2 |
| | 45 µm | 12.4 | 13.1 | 13 | 14.6 | 12.7 | 11.4 | 12.6 |
| Blain, cm ² /gr | | 3897 | 3793 | 3740 | 3525 | 3620 | 3694 | 4011 |
| Setting Time (min.) | Initial | 115 | 120 | 150 | 170 | 165 | 230 | 100 |
| | Final | 160 | 160 | 200 | 220 | 190 | 285 | 140 |
| Water demand, % | | 26 | 27.4 | 27 | 27.4 | 27.4 | 27.9 | 26.3 |
| Density, g/cm ³ | | 3.08 | 3.06 | 3.02 | 2.98 | 2.97 | 2.94 | 3.13 |
| Soundness, mm | | 3 | 3 | 3 | 3 | 2 | 2 | 4 |

The OPC and PTS blended cements (for all scoria content) have nearly the same water demand ratio. A literature survey shows that the chemical structure, porosity and specific surface area of cement mixtures affect water demand (Lea, 1976). In the present study, a big difference between water demand ratios was not observed. This may be explained by the BET results. The BET data show that scoria (>200 mesh) has not a big surface area and big porosity values. Because of this, the water content does not change considerably.

As seen in Table 5, soundness of the portland and blended cements are different. Scoria addition reduces the volume expansion since the total CaO (see XRF results of blended cement) and free CaO amounts depend on amount of pozzolan. Çavdar and Yetkin (2009) mentioned that, as a result of CaO, the reaction temperature and rate decrease and the material crystallizes perfectly. Therefore, reduction of the volume

expansion of scoria blended cements can be explained by reduction of CaO amount in the scoria blended cement structure.

4. Conclusion

In the light of the experimental results, the following conclusions were obtained.

1. The scoria sample (PTS) is mainly composed of amorphous silica, Al_2O_3 and Fe_2O_3 .
2. PTS has mainly hyalopilitic-porphyrific texture and from place to place, vitrophyric-porphyrific texture. Scoria is mainly composed of volcanic glass and there are phenocrysts of plagioclase, pyroxene and rarely hornblende in the matrix.
3. PTS possess sufficient pozzolanic characteristics to be used as an additive during cement production, since it satisfies the standard requirements.
4. Tests conducted on the scoria blended cements suggest the manufacture of the blended scoria cement with a maximum replacement of 20%.
5. Finally, it can be said that use of scoria found in Patnos (Ağrı, Turkey) can be beneficially used for cement production and this will help to reduce clinker consumption.

Acknowledgment

This research is partially funded by Yuzuncu Yil University (Project Number: 2010- FBE-YL107). The authors would like to thank the Quality Control Team of Askale Van Cement Factory, for their contributions in performing standard cement tests.

Reference

- ARRIGO I, CATALFAMO P, CAVALLARI L, DI PASQUALE S., 2007, Use of zeolitized pumice waste as a water softening agent, *Journal of Hazardous Materials*, 147, 513–517.
- AYDIN A.C. AND GÜL R., 2007, Influence of volcanic originated natural materials as additives on the setting time and some mechanical properties of concrete, *Construction and Building Materials* 21, 1277–1281
- BİNİCİ H and AKSOGAN O., 2006, Sulfate resistance of plain and blended cement, *Cement Concrete Comp.*, 28:39–46.
- BLANCO VARELA M. T., MARTÍNEZ RAMÍREZ S., EREÑA, I., GENER M. AND CARMONA P., 2006, Characterization and Pozzolanicity of Zeolitic Rocks from Two Cuban Deposits, *Applied Clay Science*, V. 33, No. 2, 149–159.
- ÇAVDAR A. and YETGİN Ş., 2007, The Effect of Particle Fineness on Properties of Portland Pozzolan Cement Mortars, *Turkish Journal of Science & Technology*, Volume 4, No 1, 17–23
- ERSOY B., SARIİSİK A., DİKMEN S., SARIİSİK G., 2010, Characterization of Acidic Pumice and Determination of Its Electrokinetic Properties in Water, *Powder Technology*, 197, 129–135.
- FU X, WANG Y, HUANG S, HOU X, HOU W., 2003, The influences of siliceous waste on blended cement properties, *Cement Concrete Res.*, 33: 851–6.
- GÜNDÜZ L, SARIİSİK A, DAVRAZ M, UĞUR İ, ÇANKIRAN O., (1998), *PomzaTehnolojisi Cilt-1*. SDÜ Yayını, 285s. Isparta (in Turkish)
- HOSSAIN K.M.A., 2004, Properties of volcanic pumice based cement and lightweight concrete. *Cement and Concrete Research*, 34, 283–291.
- HOSSAIN K. M. A., 2005, Volcanic ash and pumice as cement additives: pozzolanic, alkali–silica reaction and autoclave expansion characteristics, *Cement and Concrete Research* 35, 1141– 1144

- HUANG, P. AND FUERSTENAU, W., 2001, The Effect of the Adsorption of Lead and Cadmium Ions on the Interfacial Behavior of Quartz and Talc, *Colloids and Surface A: Physicochemical and Engineering Aspects*, 177: 147–156.
- LEA FM., 1976, *The chemistry of cement and concrete*, 3rd ed. London: Edward Arnold, Ltd.
- LURA, P., BENTZ, D. P., LANGE, D. A., KOVLER, K., AND BENTUR, A., 2004, Pumice aggregates for internal water curing. Kovler, K., Marchand, J., Mindess, S., and Weiss, J., eds., *Proceedings of International RILEM Symposium on Concrete Science and Engineering: A Tribute to Arnon Bentur*, 137–151. Evanston: RILEM Publications S.A.R.L.
- MEHTA, P.K., 1981, *Studies On Blended Portland Cements Containing Santorin Earth, Cement and Concrete Research*, 4, 507–518.
- ÖNER M., ERDOĞDU K., GÜNLÜ A., 2003, Effect of components fineness on strength of blast furnace slag cement, *Cement and Concrete Research* 33, 463–469.
- PRASANPHAN S. and NUNTIYA A., 2006, Contributed Paper Electrokinetic Properties of Kaolins, Sodium Feldspar and Quartz, *Chiang Mai J. Sci.* 33(2) : 183–190.
- PERRAKI T., AND ORFANOUDAKI A., 2004, Mineralogical Study of Zeolites from Pentalofos Area, Thrace, Greece, *Applied Clay Science*, V. 25, No. 1–2, 9–16.
- PLANUNGS ENGINEERING MANAGEMENT (PEM), 1984, On investigations of Turkish natural pozzolans as cement admixtures, *Planungs Engineering Management Report*. Ankara, Düsseldorf.
- SARASWATHY V, MURALIDHARAN S, THANGAVEL K, SRINIVASAN S., 2003, Influence of activated fly ash on corrosion–resistance and strength of concrete, *Cement Concrete Res.*, 25:673–80.
- SERSALE G.P., 1987, Portland–zeolite–cement for minimizing alkali–aggregate expansion. *Cement Concrete Res.*, 17:404–10.
- TARGAN S, OLGUN A, ERDOGAN Y, SEVINC V., 2003, Influence of natural pozzolan, colemanite ore waste, bottom ash and fly ash on the properties of portland cement, *Cement and Concrete Research* 33 1175–1182.
- TS 25, 2008, Natural pozzolan (Trass) for use in cement and concrete – Definitions, requirements and conformity criteria. In *Turkish Standards*
- TSE EN 197 – 1, 2002, Cement– Part 1: Compositions and conformity criteria for common cements. In *Turkish Standards*
- TSE EN 196 – 1, 2002, Methods of testing cement–Part 1: Determination of strength. In *Turkish Standards*
- TSE EN 196 – 3, 2002, Methods of testing cement–Part 3: Determination of setting time and soundness. In *Turkish Standards*
- T.R. PRIME MINISTRY, STATE PLANNING ORGANIZATION REPORT, 2001, (in Turkish).
- TUNÇ S. and DUMAN O., 2009, Effects of Electrolytes on the Electrokinetic Properties of Pumice Suspensions, *Journal of Dispersion Science and Technology*, 30, 548 – 555.
- Türkiye Çimento Müstahsilleri Birliği Araştırmaların Gözden Geçirilmesi ve Durum Değerlendirmesi Raporu; *Traslar ve Traslı Çimentolar.*, 2003, TÇMB/AR–GE Enstitüsü, Ankara (in Turkish).
- VUK T, GABROVSEK R, KAUCIC V., 2002, The influence of mineral admixtures on sulfate resistance of limestone cement pastes aged in cold $MgSO_4$ solution. *Cem. Conc. Comp.*, 32:943–8.
- YAZICIOĞLU S. and DEMİREL B., 2006, The Effect of the Pumice of Elazığ Region used as a Pozzolanic Additive on the Compressive Strength of Concrete in Increasing Cure Ages, *Science and Eng. J of Fırat Univ.* 18 (3), 367–374.
- YETGİN Ş. and ÇAVDAR A., 2006, Study of Effects of Natural Pozzolan on Properties of Cement Mortars, *Journal of Materials in Civil Engineering*, 18/6, 813–816.
- YILMAZ B., 2009, Effects of Molecular and Electrokinetic Properties of Pozzolans on Hydration, *ACI Materials Journal* 106 (2), 128–137.

Received April 22, 2011; reviewed; accepted August 20, 2011

ADSORPTION OF POLY(ACRYLIC ACID) ON THE SURFACE OF TiO₂ IN THE PRESENCE OF DIFFERENT SURFACTANTS

Stanislaw CHIBOWSKI, Malgorzata PASZKIEWICZ, Jacek PATKOWSKI

Department of Radiochemistry and Colloid Chemistry, Maria Curie Sklodowska University, 20-031 Lublin, Pl. Curie-Sklodowska 5, Poland, stanislaw.chibowski@umcs.lublin.pl, fax: +48 (81) 533 28 11

Abstract. Results presented in this paper consider research on the influence of the presence of surfactants (cationic CTAB, anionic SDS) on adsorption of poly(acrylic acid) (PAA) at the titanium dioxide/solution interface. Research was carried out as a function of concentration of surfactants and the way of introduction of reagents to measured mixtures (PAA-CTAB-TiO₂-NaCl and PAA-SDS-TiO₂-NaCl). In order to compare obtained results of adsorption amount of PAA in mixed systems, measurements of adsorption amount of PAA on titanium dioxide without surfactant addition were also conducted. Observed changes in adsorption amount in the presence of surfactant are a result of an emerging complex polymer-surfactant and competitive adsorption of the two components on the TiO₂ surface.

keywords: adsorption, surfactant, polymer, titanium dioxide, polyacrylic acid

1. Introduction

Adsorptive behaviour of polymer/surfactant mixtures on the interface solid/solution is important not only for industrial but also in household applications. Wide possibilities of application of polymers and surfactants encourage scientists to make research on mentioned high-molecular weight substances. A mechanism of creation of complexes of polymer and surfactants in water solutions is well known. There is much less literature data on such interactions at the interface solid-solution. The problem considers not only competitive adsorption of polymer and surfactant but also adsorptive possibilities of creating complexes polymer-surfactant (Goddard, 1986, Goddard and Ananthapadmanabhan, 1998).

Composition and structure of co-adsorbing layers are dependent on the order in which components of the solution (polymer and surfactant) are added or if the adsorption process is conducted directly from mixtures. Research shows that when sequential adsorption is running, obtained structures that are a result of it are impossible to obtain via normal adsorption (with only one component). Emerging structures of adsorbed by-surface layers significantly influence stability of dispersed systems. This stability is very important not only in paint industry, cosmetics,

pharmaceuticals but also in mineral processing. Adsorption of polymers, surfactants or polymer-surfactant complexes can greatly influence surface properties of various minerals. Thus, the process of their separation and enrichment can be conducted with much greater efficiency (Somasundaran et al., 1998; Besra et al., 2002). That is why the aim of present research was to estimate the influence of cationic and anionic surfactant and the order of introduction of separate components (polymer, surfactant) into mixed systems (PAA-CTAB-TiO₂-NaCl and PAA-SDS-TiO₂-NaCl) on the mechanism of adsorption of polymer at the TiO₂/solution interface.



2. Materials and methods

Titanium dioxide P-25 by Evonic was used as adsorbent. TiO₂ P-25 is a mixture of 80% of anatase and 20% rutile. Specific surface of the mentioned oxide measured with the BET method was equal to 64.15 m²g⁻¹. Poly(acrylic acid) (PAA) by Aldrich, molecular weight (M_w) 60 000 was used as a polymer. Poly(acrylic acid) is a compound which belongs to a group of ionic polymers. It has only one type of functional groups, carboxylic groups, which makes it an anionic polymer.

A solution of poly(acrylic acid) (PAA) was processed by filtration on cellulose membrane produced by Millipore, type YM30 (NMWL: 30 000). Filtration was carried out in order to remove inorganic impurities and eliminate a low molecular weight polymer fraction.

Surface active agents used in the presented research were two surfactants, which characteristics are presented in Table 1. NaCl was used as a background electrolyte.

Table 1. Characteristics of surfactant used (Besra et al., 2002)

| Surfactant | Molecular formula | Molecular weight, [g/mol] | Ionic type | Chemicals Structures | Critical micelle concentration (cmc), [mM] |
|---|---|---------------------------|------------|--|--|
| Cetyl Trimethyl Ammonium Bromide (CTAB) | C ₁₆ H ₃₃ N(CH ₃) ₃ ⁺ Br ⁻ | 364.4 | Cationic |  | 0.9 |
| Sodium Dodecyl Sulphate (SDS) | n-C ₁₂ H ₂₅ SO ₄ Na | 288.3 | Anionic |  | 8.2 |

2.1. Adsorption measurements

2.1.1. Calibration curve for PAA/NaCl

In order to obtain adsorption amount of poly(acrylic acid), the method proposed by Crummett and Hummel (1963) was used. Five solutions of electrolyte of 1·10⁻³ M NaCl and PAA of concentrations from 1 ppm to 200 ppm were prepared. Next, 5 cm³ of each of the solutions were introduced into volumetric flasks where 1 cm³ of 20%

NaOH was added and, using various concentrations of HCl, pH was set to a value of 10. One cm³ of 1% hyamine 1622 solution was then added to such prepared solutions and filled with water up to 25 cm³. Resulting turbidity was measured after 15 minutes since addition of hyamine, at the wavelength of $\lambda=500$ nm.

2.1.2. Adsorption in the PAA/NaCl/TiO₂ system

Ten cm³ of polymer solution of final concentration equal to 10 ppm, 50 ppm, 70 ppm, 100 ppm, and 150 ppm as well as 10⁻³ M NaCl were introduced to 25cm³ Erlenmayer flasks. Next 0.04g of titanium dioxide was added. The Erlenmayer flasks were shaken for 24 hours at 25°C. After this time, suspensions were centrifuged, 5cm³ of the clear solution was taken and concentration of the polymer measured according to the above procedure. The difference between absorbance for pure PAA (calibration curve) and absorbance after the adsorption process of PAA onto TiO₂ was calculated and adsorption amount was the result of those calculations.

2.1.3. Adsorption in mixed polymer-surfactant systems

The measurement of adsorption of PAA and surfactant onto the surface of TiO₂ was conducted in the same way as described above. The only difference was the addition of either cationic (CTAB) or anionic (SDS) in such an amount that a final concentration of the surfactant was 1·10⁻⁵ mol/dm³ and 1·10⁻⁴ mol/dm³.

3. Results and discussion

3.1. Adsorption measurements in the PAA-TiO₂-NaCl system

An analysis of adsorption isotherms of poly(acrylic acid) onto titanium dioxide (Fig. 3) showed that mentioned PAA has a significant polydispersity degree. The measure of polydispersity of a sample of polymer is called the polydispersity index (PI), which is defined as a ratio between the average molecular mass (Mw) and average number molecular mass (Mn). For monodisperse polymers (PI equal to 1) the adsorption isotherm is ideally sharp. It is characterized by a sudden increase of adsorption at very low polymer concentration and shows a distinctive plateau in a broad range of concentrations (Santhiya et al., 1999).

The shape of the adsorption isotherm (Fig. 1, rounded shape, no plateau) provides information that in the analysed systems the PI index was much greater than 1.

In research concerning adsorption process of polymers it is essential to take into account pH. Previous research (Somasundaran et al., 1991) showed, that amount of adsorbed polymer is dependent on the change of pH, the change of surface groups of the adsorbent, degree of dissociation of functional groups present of macromolecules as well as conformation changes in polymer chains.

Figure 2 presents an influence of pH on adsorption amount of poly(acrylic acid) onto titanium dioxide.

An analysis of the data presented in Figure 2 shows a significant decrease of PAA adsorption with increasing pH of the solution. Observed decrease of adsorbed amount of poly(acrylic acid) with increasing pH of the solution is a result of the increase of degree of ionization of carboxylic groups in the PAA chain. Macromolecules of PAA ($pK_a = 4.5$) (Gebhard and Fuerstenau, 1983) in acidic environment, up to $pH=4.5$ have mostly undissociated $-COOH$ groups. With increasing pH, the amount of dissociated $-COO^-$ groups in the polymer chain increases, which makes interaction between polymer and more negatively charged titanium dioxide surface even harder. As a consequence of this fact, a decrease of adsorption of PAA is observed.

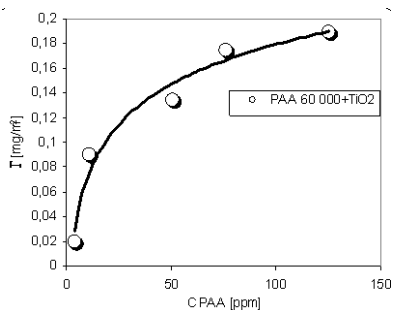


Fig. 1. Adsorption isotherm of poly(acrylic acid) (PAA) onto titanium dioxide (natural pH, 10^{-3} M NaCl)

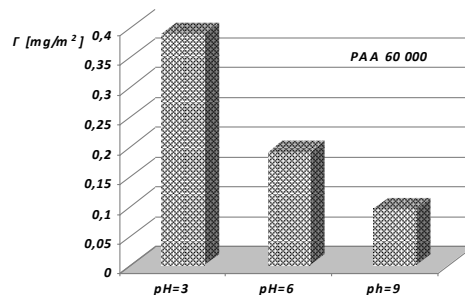


Fig. 2. Adsorption amount of PAA onto TiO_2 as a function of pH in solution of NaCl ($C_{NaCl}=10^{-3}$ M, $C_{PAA}=100$ ppm)

An existence of adsorption of PAA at pH higher than pH_{pzc} (pH_{pzc} for $TiO_2=6.3$) indicates that in this pH range adsorption of a polymer is caused mostly by specific interactions. At pH lower than pH_{pzc} , besides interaction of hydrogen bonding type, a significant role is played by electrostatic interaction between $-TiOH_2^+$ groups and still ionized $-COO^-$ groups, which are still present although not in great amount, in a chain of PAA. As a consequence, the highest adsorption of PAA is observed at pH lower than pH_{pzc} .

Table 2. Dissociation of PAA and the concentration of surface groups of TiO_2

| pH | $[COOH]/[COO^-]^a$ | Concentration of surface groups ^b | | |
|-----|--------------------|--|----------|---------|
| | | $-TiOH_2^+$ | $-TiO^-$ | $-TiOH$ |
| 3 | 31 | 32 | 0.002 | 179 |
| 4.5 | 1 | 16 | 0.003 | 162 |
| 6 | 0.031 | 4.4 | 0.01 | 156 |
| 9 | 0.000031 | 1.3 | 0.11 | 133 |

^a Values of $\log(\alpha/(1-\alpha))$ calculated from classical dependency $pH - pK_a$ (Pettersson et al., 2000)

^b Data calculated from numerical optimization of electrical double layer model (Davis and James, 1978).

Table 2 presents dissociation degree of PAA with increase of pH of solution, as well as calculated values of concentration of surface groups of titanium dioxide

expressed in $[\mu\text{C}\cdot\text{cm}^{-2}]$, ($C_{\text{NaCl}} 1\cdot 10^{-3} \text{ mol}\cdot\text{dm}^{-3}$) versus the pH of a solution ($C_{\text{NaCl}} = 1\cdot 10^{-3} \text{ mol}\cdot\text{dm}^{-3}$).

Because of high concentration of surface groups $-\text{TiOH}$ (Table 2) no matter what pH is used, one might say that those groups are very important in adsorption of poly(acrylic acid) onto TiO_2 . In reality, PAA macromolecules adsorb on the surface of titanium dioxide interacting with $-\text{TiOH}$ surface groups via hydrogen bonding (Xu and Vasudevan, 1991).

3.2. Adsorption measurements in mixed systems: polymer–surfactant onto TiO_2

Literature data bring information that type of interaction in mixed systems polymer-surfactant is dependent only on character of reagents. If both components, i.e. polymer and surfactant are ionic, a process of their interaction might be dependent on electrostatic interactions, repulsing and attracting (Somasundaran and Krishnakumar, 1998). One might say, that these interactions may significantly influence the process of polymer or surfactant adsorption when this process is conducted from mixed solutions. Adsorption measurements conducted in such systems are performed to get answer to the question whether and how the order of addition of components to the mixture and type of used surfactant influence the amount of adsorption of poly(acrylic acid) at the titanium dioxide-aqueous solution interface. The obtained results were place in Figs. from 3 to 6. They presented adsorption data for mixed systems (PAA/CTAB/ TiO_2 /NaCl and PAA/SDS/ TiO_2 /NaCl). Adsorption of poly(acrylic acid) (PAA/ TiO_2 /NaCl) is also presented.

3.3. Simultaneous addition of reagents to investigated PAA-CTAB - TiO_2 and PAA-SDS- TiO_2 systems

Figures 5 and 6 present the influence of concentration of measured surfactants (CTAB and SDS) on adsorption amount of poly(acrylic acid) on titanium dioxide, when the polymer and surfactant were introduced to a system simultaneously. Measurements were done at pH = 6. When reagents were introduced simultaneously to the mixed systems (PAA-CTAB- TiO_2 and PAA-SDS- TiO_2) at a constant (100 ppm) polymer concentration and changing concentrations of surfactants, adsorption amount of PAA on titanium dioxide compared to the adsorption amount of PAA on titanium dioxide without surfactants was lower for both used surfactants. A decrease of PAA adsorption on TiO_2 of approximately 35% was recorded in presence of CTAB and SDS with their concentration equal to $1\cdot 10^{-5}\text{M}$ and approximately from 15 to 20% decrease of adsorption of PAA for higher concentration of surfactants ($1\cdot 10^{-4}\text{M}$).

The observed decrease of adsorption of PAA on TiO_2 (Figs. 3 and 4) in presence of analysed surfactants (cationic CTAB and anionic SDS), while both polymer and surfactant were introduced to the system simultaneously is a result of a competitive adsorption of created complexes between polymer and analysed surfactants and free, non-bonded, molecules of CTAB or SDS.

Competitive adsorption results in a blockade of the active sites on the surface of titanium dioxide, which results in lower adsorption of PAA in the presence of analysed surfactants. The conducted measurements show that creation of PAA-CTAB complex and PAA-SDS complex begins with concentrations of surfactants equal to approximately $5 \cdot 10^{-5}$ M and $1 \cdot 10^{-4}$ M, respectively. Efficiency of creation of complexes increases with the increase of surfactant concentration. The obtained results of adsorption amount of PAA from pure solutions of PAA and mixed solutions may suggest that the non-bonded surfactant has a greater tendency to block active sites on the surface of TiO_2 than the created polymer-surfactant complexes. As a result of that, at lower concentrations of surfactant a greater decrease of adsorption of PAA was observed, because at these concentrations the complexes are practically non-existent. What is more, a creation of the PAA-surfactant complex in the bulk solution and its adsorption on the surface of TiO_2 results in a decrease of the amount of polymer from the solution. That is why at higher ($1 \cdot 10^{-4}$ M) concentrations of surfactant a higher adsorption of PAA was observed compared to concentration of $1 \cdot 10^{-5}$ M.

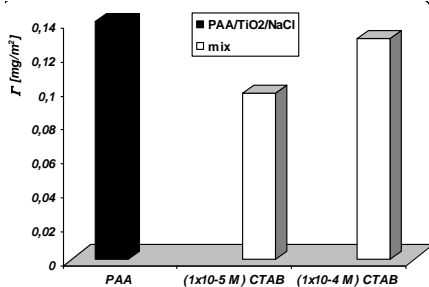


Fig. 3. Adsorption amount of PAA on TiO_2 in presence and absence of CTAB with simultaneous addition of reagents into the system ($C_{\text{PAA}}=100$ ppm). Concentration of NaCl in measured systems was $1 \cdot 10^{-3}$ M

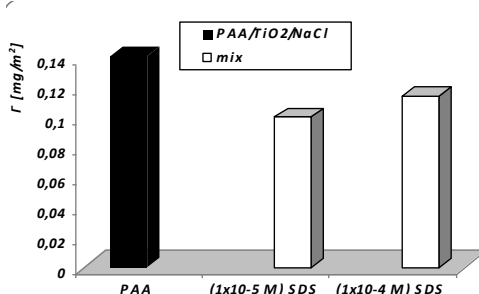


Fig. 4. Adsorption amount of PAA on TiO_2 in presence and absence of SDS, with simultaneous addition of reagents into the system ($C_{\text{PAA}} = 100$ ppm). Concentration of NaCl in measured systems was $1 \cdot 10^{-3}$ M

3.4. Influence of the order of addition of adsorbates on adsorption of PAA

A next stage of the research was to analyse the influence of order of addition of adsorbates (polymer, surfactant) into the system and whether this order will have influence on adsorptive behaviour of PAA onto TiO_2 . Appropriate data are presented on Figs. 5 and 6.

To understand changes of adsorption of PAA onto TiO_2 , Figs. 5 and 6 present data on adsorption amount of PAA onto TiO_2 for both pure PAA/ TiO_2 system as well as mixed PAA-SDS, PAA-CTAB systems. An analysis of Figs. 5 and 6 shows that distinct changes of adsorption of PAA onto TiO_2 are a result of both the order of addition of reagents to the system and ionic character of the analysed surfactants.

For a cationic surfactant–anionic polymer system (Fig. 5) there is a significant increase of adsorption of PAA onto the surface of oxide, when surfactant was introduced as first into the system, compared to pure PAA/ TiO_2 and when both reagents were introduced simultaneously.

An increase of adsorption of poly(acrylic acid) on titanium dioxide having previously adsorbed cationic surfactant (Fig. 5) is most probably caused by the fact, that in by-surface layer of adsorbed surfactant its concentration is much lower when compared to the bulk solution. As a consequence of that, it leads to more efficient creation of complexes with adsorbed CTAB on the surface of oxide, than it might be observed in the solution. This results in an increased adsorption. The obtained result suggests that previously adsorbed CTAB is a factor that favours adsorption of PAA, and that creation of polymer-surfactant complexes on the surface of solid may take place at much lower concentrations of surfactant when compared to the solution.

Completely opposite results were gained (Fig. 6) for the anionic polymer (PAA) – anionic surfactant (SDS) system. When the first substance added to the system was SDS, and then after reaching equilibrium, a polymer, adsorption of macromolecules of PAA significantly decreased, both compared to adsorption from pure solution of PAA and a mixed PAA-SDS system. In this case the reason for the decreased PAA adsorption on the surface of an oxide with previously adsorbed surfactant is a competitive adsorption of SDS compared to PAA. Previously adsorbed surfactant on the surface of TiO_2 blocks active sites on the surface of the oxide, giving a macromolecule of PAA a more difficult access. Adsorption of PAA by previously adsorbed SDS is not so easy as in the case of cationic surfactant. It is connected with the fact that both SDS and PAA have anionic character, which makes creation of a complex much more difficult. Literature data (Esumi et al., 2000; Fan et al, 1999) prove that anionic polymer-anionic surfactant complexes are created much more difficult than anionic polymer-cationic surfactant. This is proved in analysed systems.

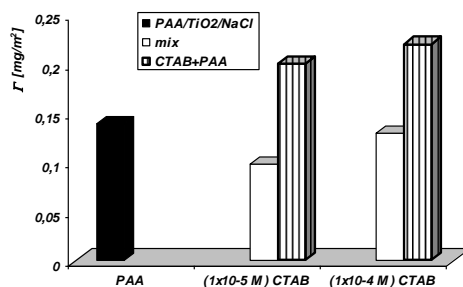


Fig. 5. Adsorption amount of PAA onto TiO_2 as a function of the order of addition of reagents to the system (cationic surfactant – anionic polymer) ($C_{\text{PAA}}=100$ ppm), $\text{NaCl } 10^{-3}\text{M}$

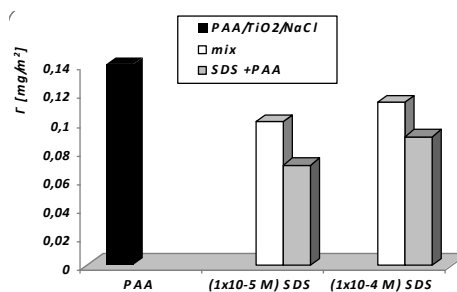


Fig. 6. Adsorption amount of PAA onto TiO_2 as a function of the order of addition of reagents to the system (anionic surfactant – anionic polymer) ($C_{\text{PAA}}=100$ ppm), $\text{NaCl } 10^{-3}\text{M}$

4. Conclusions

To sum up, the obtained results on a decrease of adsorption of PAA onto TiO₂ with previously adsorbed SDS follow from a significant blockade of the surface of an oxide by adsorbed molecules of SDS and much less favourable conditions of creation of the PAA-SDS complex.

Generally, one can say, that a presence of an anionic surfactant decreases measured adsorption amounts of anionic polymer on the surface of TiO₂, no matter what was the way of conducting an experiment. A much more beneficial influence on the measured adsorption amount of PAA onto the surface of titanium dioxide was noted for the cationic surfactant – anionic polymer system, but only when a surfactant was added as a first component.

References

- Besra L., Sengupta D.K., Roy S.K., Ay P., 2002, Studies on flocculation and dewatering of kaolin suspensions by anionic polyacrylamide flocculant in the presence of some surfactants, *Int. J. Miner. Process.*, 66, 1–28.
- Crummett W.B., Hummel R.A., 1963, The determination of traces of polyacrylamides in water, *J. Am. Water Works Assoc.*, 55, 209–220.
- Davis J.A., James R.O., Leckie J.O., 1978, Surface ionization and complexation at the oxide/water interface. I. Computation of electrical double layer properties in simple electrolytes, *J. Colloid Interface Sci.*, 63(3), 480–499.
- Esumi, K., Iitaka, M., Torigoe, K., 2000, Kinetics of Simultaneous Adsorption of Poly(vinyl pyrrolidone) and Sodium Dodecyl Sulfate on Alumina Particles, *J. Colloid Interface Sci.*, 232, 71–75.
- Fan, A., Somasundaran, P., Turro, N. J., 1999, Role of sequential adsorption of polymer/surfactant mixtures and their conformation in dispersion/flocculation of alumina, *Colloids Surf. A: Physicochem. Eng. Aspects*, 146, 397–403.
- Gebhardt J. E., Furstenau D. W., 1983, Adsorption of polyacrylic acid at oxide/water interfaces, *Colloids Surf.*, 7, 221–231.
- Goddard, E.D., Ananthapadmanabhan, K.P, editors, 1998, *Surfactant science series*, vol. 77. Marcel Dekker.
- Goddard, E.D., 1986, Polymer-surfactant interaction. Part I. Uncharged water-soluble polymers and charged surfactants, *Colloids Surf.*, 19, 255–300.
- Pettersson A., Marino G., Pursiheimo A., Rosenholmo J.B., 2000, Electrosteric Stabilization of Al₂O₃, ZrO₂, and 3Y–ZrO₂ Suspensions. Effect of Dissociation and Type of Polyelectrolyte, *J. Colloid Interface Sci.*, 228, 73–81.
- Santhiya D., Subramanian S., Natarajan K.A., Malghan S.G., 1999, Surface Chemical Studies on the Competitive Adsorption of Poly(acrylic acid) and Poly(vinyl alcohol) onto Alumina, *J. Colloid Interface Sci.*, 216, 143–153.
- Somasundaran, P., Krishnakumar, S., 1997, Adsorption of surfactants and polymers at the solid-liquid interface, *Colloids Surfaces*, 123–124, 491–513.
- Somasundaran, P., Snell, E. D., Q. Xu, 1991, Adsorption behavior of alkylarylethoxylated alcohols on silica, *J. Coll. Inter. Sci.*, 144, 165–173
- Somasundaran P., Yu, X. and Krishnakumar, S., 1998, Role of conformation and orientation of surfactants and polymers in controlling flocculation and dispersion of aqueous and non-aqueous suspensions, *Colloids Surf. A: Physicochem. Eng. Aspects*, 133, 125–133.
- Xu, Q., Vasudevan, T. V., 1991, Stabilization of kaolinite suspensions by anionic-nonionic surfactant mixtures, *J. Disper. Sci. Technol.*, 12, 83–93.

Our books are available in Tech bookstore
plac Grunwaldzki 13
50-377 Wrocław, D-1 PWr., tel. (071) 320 32 52
Orders can also be sent by post

ISSN 1643-1049

Physicochemical Problems of Mineral Processing, 48(1), 2011